Chemical, Mechanical, and Thermal Control of Substrate-Bound Carbon Nanotube Growth

by

Anastasios John Hart

B.S.E., University of Michigan, 2000
S.M., Massachusetts Institute of Technology, 2002

Submitted to the Department of Mechanical Engineering
in partial fulfillment of the requirements for the degree of

Doctor of Philosophy

at the

MASSACHUSETTS INSTITUTE OF TECHNOLOGY

September 2006

Signature redacted

Author .....
Department of Mechanical Engineering
August 19, 2006

Signature redacted

Certified by .....
Alexander H. Slocum
Professor of Mechanical Engineering, MacVicar Faculty Fellow
Thesis Supervisor

Signature redacted

Accepted by .....
Lallit Anand
Chairman, Department Committee on Graduate Students

Chemical, Mechanical, and Thermal Control of Substrate-Bound Carbon Nanotube Growth

by

Anastasios John Hart

Submitted to the Department of Mechanical Engineering
on August 19, 2006, in partial fulfillment of the
requirements for the degree of
Doctor of Philosophy

Abstract

Carbon nanotubes (CNTs) are long molecules having exceptional properties, including several times the strength of steel piano wire at one fourth the density, at least five times the thermal conductivity of pure copper, and high electrical conductivity and current-carrying capacity. This thesis presents methods of CNT synthesis by atmospheric-pressure thermal chemical vapor deposition (CVD), where effective choice of the catalyst composition and processing conditions enables growth of tangled single-wall CNTs or structures of aligned multi-wall CNTs, on bare silicon, microstructured silicon, and ceramic fibers. Applying mechanical pressure during growth controls the structure of a CNT film while causing significant defects in the CNTs. This mechanochemisty approach is used to "grow-mold" CNTs into 3D-shaped microforms.

A new reactor apparatus featuring a resistively-heated suspended platform enables rapid ($\approx$100 °C/s) temperature control and versatile *in situ* characterization, including laser measurement of CNT film growth kinetics, and imaging of stress-induced film cracking. By thermally pre-treating the reactant mixture before it reaches the substrate platform, aligned CNTs are grown to 3 mm length in just 15 minutes.

A microchannel array is created for combinatorial flow studies of nanomaterials growth, having velocity range and resolution far exceeding those of conventional furnaces. A detailed design methodology considers compressible slip flows within the microchannels and flow leaks across the array, and the devices are fabricated by KOH etching of silicon. Initial experiments with this system demonstrate chemically-driven transitions in CNT yield and morphology along the microchannels, and flow-directed alignment of isolated CNTs and CNT strands.

Applications of aligned CNTs in reinforced composites and electromechanical probes are enabled by the CNT synthesis technologies presented here, and show significant initial promise through collaborative research projects. Overall, controlling the packing density and matrix reinforcement of aligned CNTs gives material attributes spanning from those of energy-absorbing foams to stiff solids; however, significant increases in CNT length, growth rate, and packing density must be achieved to realize macroscopic fibers and films having the properties of individual CNTs. New machines can be created for studying the limiting aspects of growth reactions, for exploring new reaction regimes, and for producing exceptionally long nanostructures, looking ahead to fabrication of CNT-based materials in a continuous and industrially-scalable fashion.

Thesis Supervisor: Alexander H. Slocum
Title: Professor of Mechanical Engineering, MacVicar Faculty Fellow

Acknowledgments

Graduate school has been an incredibly rewarding experience, both personally and professionally. It has been a wonderful privilege to study at MIT—a place with a boundless urge for creativity, and with the guts and discipline to funnel creativity into new technology having impactful applications. Thanks to many for making this thesis possible, and for making the past years such a pleasure for me:

- Alex Slocum for being an enthusiastic and supportive research advisor, and a great friend.
- The Fannie and John Hertz Foundation, for granting me a fellowship which gave me the freedom to explore the topic of this thesis.
- The MIT Deshpande Center for Technological Innovation, for an Ignition Grant which supported our project in 2004–2005.
- Luuk van Laake, Laure Royer, and Michael Franzkowiak for visiting MIT and working with me on aspects of this project.
- Collaborators and fellow students working on CNTs: Ryan Bennett, Sreekar Bhaviripudi, Enrique Garcia, Gilbert Nessim, Alfonso Reina, and Prof. Brian Wardle at MIT; Dr. Bojan Boskovic at the University of Cambridge; and Prof. Don Lucca at Oklahoma State University.
- Fellow members of the Precision Engineering Research Group over the years: Joachim Sihler, Alexis Weber, Onnik Yaglioglu, and many others.
- The staffs of the MIT Microsystems Technology Lab and Center for Materials Science and Engineering for guidance with microfabrication and characterization.
- My thesis committee: Profs. Yet-Ming Chiang, Jing Kong, Martin Schmidt, Francesco Stellacci, and Jefferson Tester.
- Prof. Yet-Ming Chiang for graciously sharing his lab space for our furnace systems.
- Many friends at MIT, in Boston, and around the world, and fun times playing squash, watching baseball, skiing, traveling, and so on.
- Last but most importantly, my mother Elizabeth Hart and late father Gordon Hart, and family, for their love and support.

Contents

Chapter 1

Motivation and Outline

Engineering of materials and devices by controlling properties and interactions at molecular and atomic scales is impacting wide-ranging aspects of science and society. As seamless cylinders of carbon atoms arranged in a hexagonal lattice, carbon nanotubes (CNTs) are the third allotropic form of carbon in addition to diamond and graphite [5]. The nature of CNTs as long continuous molecules imparts exceptional material properties, including several times the strength of steel piano wire at one-fifth the density, at least five times the thermal conductivity of copper, and high electrical conductivity and current-carrying capacity [6, 7]. These fundamental properties, along with application-oriented characteristics [8–10] such as high surface area, diverse capabilities for chemical modification and functionalization, and strong interactions with polymers and composite host materials, are generating broad demand for control of CNT growth as a manufacturing process spanning from the nano- to macro-scales.

CNTs are distinguished by their number of concentric layers (walls, with spacing $\approx$0.34 nm), and their chirality (wrapping angle). The most distinct CNT structures in terms of numbers of walls are single-wall CNTs (SWNTs), double-wall CNTs (DWNTs), and multi-wall CNTs (MWNTs), which are illustrated in Fig. 1-1. Further, many supramolecular constructs have been demonstrated, such CNTs packed with fullerenes (C_{60}); these are called "peapods" [11]. Typically, SWNTs are 0.4–5 nm in diameter, and MWNTs are up to 100 nm in diameter.

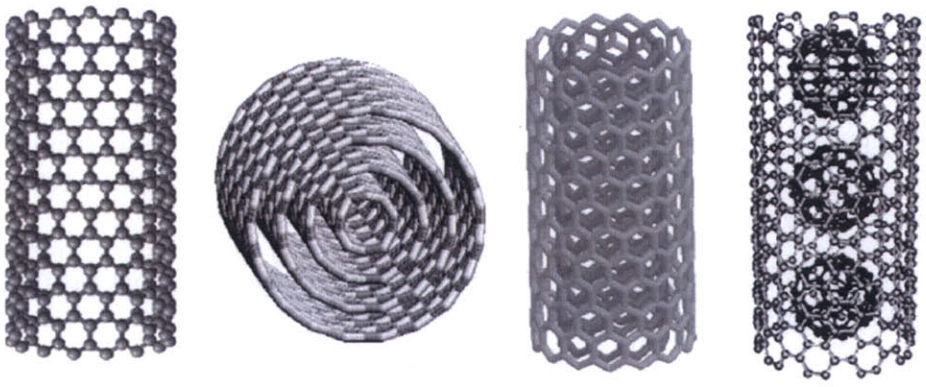

Figure 1-1. CNT structures: (from left to right) single-wall CNT (SWNT), multi-wall CNT (MWNT), double-wall CNT (DWNT), and SWNT "peapod" (from [12]).

1.1 History of CNT research and applications

While research and development in science and applications of CNTs has boomed during the past 15 years, filamentous carbon has been studied and used for over a century. Many researchers unknowingly worked with CNTs well before the atomic structure of a CNT was first observed by Sumio Iijima of NEC Research Laboratories in 1991, using high-resolution transmission electron microscopy (TEM) [13, 14]. Iijima's publication identified the possibility for unique properties depending on the chirality of CNTs, thereby igniting a broad base of research. The following is a summary of significant events in the history of research and applications of filamentous carbon materials:

- **1889:** T. Hughes and C. Chambers patent production of carbon filaments for use as glow discharge elements in lamps. Their process uses methane (CH_4) and ethylene (C_2H_4) as carbon sources, and the filaments nucleate on the surface of an iron crucible [15]. Since the 1870's, T. Edison had utilized carbon wires in his incandescent light bulbs [16], and in 1890 he patented a method for carbonizing natural fibers (e.g., hemp, bamboo, jute) by dipping the fibers in sugar and subsequently heating them to form a conductive lamp filament [17].

- **1952:** L. Radushkevich and colleagues in the U.S.S.R. describe synthesis of carbon filaments by disproportionation of CO over Fe catalyst, and show TEM images of hollow filaments with metal particles at their tips.

- **1953:** W. Davis and colleagues examine carbon filaments as small as 10 nm diameter, produced on firebrick in a CO atmosphere, and identify the role of Fe particles as catalysts which remain at the tips of growing structures [18].

- **1957:** H. Kauffman, D. Griffiths, and J. Mackay grow carbon fibers (4 μm diameter) on walls of a tubular reactor by cracking of hydrocarbon/hydrogen mixtures, and improve yield significantly by adding a small amount of hydrogen sulfide (H_2S) to the reactants [19].

- **1960:** R. Bacon of the National Carbide Company produces sub-μm diameter graphite nanoscrolls, and is first to distinguish between catalytic "base" and "tip" growth of carbon filaments [20].

- **1972:** R. T. K. Baker studies growth of cup-stacked carbon filaments using *in situ* TEM [21, 22], and suggests that the activation energy for filament growth is equal to that for carbon diffusion through the bulk of the metal catalyst particle.

- **1972:** The first consumer product using carbon fiber composites, a new fishing rod, reaches the market in Japan.

- **1976:** A. Oberlin and M. Endo report growth of carbon filaments having single-layer cylindrical graphite cores [23], where the cores are (in retrospect) SWNTs. The presence of the central core confirms the role of the catalyst in precipitating neat carbon layers, and individual filaments are thickened to ~100 μm diameter and lengthened to ~10 cm.

- **1979:** P. Wiles and J. Abrahamson find carbon filaments having "several layers of crystalline carbon wrapped together" in deposits from arc discharge [24][1].

- **1985:** H. Kroto, R. Smalley, and colleagues synthesize C_{60} [25] and call it the "Buckminsterfullerene" as its molecular structure is an embodiment of the geodesic dome invented by Buckminster Fuller.

- **1988:** M. Endo develops a floating catalyst process for continuous gas-phase synthesis of carbon nanofibers, which appear to be large-diameter MWNTs [26]. This process has been implemented for large-scale commercial production.

- **1991:** S. Iijima observes MWNTs in arc discharge deposits, and this publication ignites CNT science worldwide [13][2].

- **1993:** S. Iijima and D. Bethune observe SWNTs [14].

- **2005:** Showa-Denko (Japan) produces approximately 40 tons/yr of MWNTs and Hyperion (USA) produces approximately 100 tons/yr. The market price is about $100/kg compared to $10–40/kg for carbon fiber. MWNTs are used commercially as bulk additives in conductive plastics, composite tennis racquets and golf clubs, and lithium-ion batteries [27].

Broad efforts in large-scale synthesis of carbon fibers starting in the 1950's were motivated by pursuit of lightweight and strong structural materials for aircraft and spacecraft structures. This pursuit remains forceful and has driven development of a variety of materials including polymer, glass, and carbon fibers, and many nanomaterials including CNTs. However, the properties of CNT-based materials produced today cannot approach those of individual CNTs, because relevant quantities of CNTs can only be produced in disordered forms, and because there are many difficulties in making strong and stiff composites using disordered CNTs (section 4.5; [28,29]).

Nowadays, SWNTs are also produced commercially, yet high-purity SWNTs sell for $100–$500/g (July 2005), which far exceeds marginal production cost. On one hand, given current production cost there is no advantage to SWNTs over MWNTs, for use in established applications which rely on large amounts of disordered bulk CNTs. On the other hand, manufacturing techniques cannot yet control the properties (e.g., metallic vs. semiconducting) and arrangement (e.g., isolated, aligned, and/or organized network placement) of SWNTs for use in applications such as electronics which would require small amounts of high-quality and high-purity SWNTs and would be able to pay a strong premium for this product. At large quantities, without achieving long-range alignment, strong interconnection, and dense packing among CNTs, the properties of CNT-based materials cannot approach the truly exceptional mechanical, thermal, and electrical properties of individual CNTs.

[1] This work was published as a conference abstract, but was not published in a journal so perhaps it did not receive the widespread attention it deserved.

[2] According to the ISI Web of Science, Iijima's paper has been referenced in 5,261 scientific articles, as of July 27, 2006.

1.2 Motivation

CNTs are one example of broad emerging need for bulk-scale production of materials having exquisite size-dependent and structure-dependent properties. However, present laboratory-scale and industrial techniques to develop and synthesize these materials typically utilize equipment which is unable to control the manufacturing processes at the relevant length, time, and property scales. Particularly, these apparatuses do not facilitate measurements (e.g., growth rate, defect density) of the products during the reaction, which could be used to control the reaction conditions if the systems were capable of rapid response. Further, the time scales and length scales of control which could be achieved if feedback techniques were coupled with existing apparatuses, far exceed those of the growth reactions. For example, a typical tube furnace can be heated at 0.1–1 °C/s and has nearly isothermal conditions over ≈10 cm lengths. It takes ≈60 s to establish a steady gas composition inside such a tube at atmospheric pressure. However, CNTs can nucleate in less than 0.001 s, and as demonstrated in this thesis, significant changes in CNT structure, yield, and morphology can occur over only a few millimeters due to thermal, chemical, hydrodynamic, and diffusive non-uniformities in conventional reaction systems.

In part because we do not effectively manage chemical, mechanical, and thermal fluctuations which the catalytic sites and nanostructures experience during growth, we are hindered from further understanding many limiting aspects of the growth reactions, such as selectivity among single-wall, double-wall, and multi-wall CNTs, selectivity among chiralities of CNTs, and termination of growth or deactivation of the catalysts. Further, these processes typically use bulk high-temperature environments, and there is significant potential to improve energetic balances between the activity of the reactants and the performance of the catalysts. Alternative methods of delivering energy such as microwave [30, 31], ultrasonic [32, 33], and electrochemical methods [34] may be used to rapidly, locally, and precisely control reaction events, and to improve the compatibility of nanostructure growth processes with other materials for device fabrication and integration. Mechanochemical phenomena [35], particularly the effects of directed forces on the reactivity of molecules and on reaction kinetics [36, 37], have been studied for biological molecules such as DNA and proteins [38–40], and these effects should be investigated for controlling the growth rate and morphology of nanowires and nanotubes.

This thesis is an exploration of technologies for growth of CNTs by thermal CVD on catalyst-coated substrates, with an emphasis on studying the effects of gradients in process conditions on growth in traditional tube furnace systems, and in building and utilizing new apparatuses for precise chemical, mechanical, and thermal control of substrate-bound CNT growth. These new apparatuses are suited toward studying limiting aspects of the growth reactions, and developing industrially-scalable manufacturing processes for ordered CNT materials such as aligned films and long fibers. Certain applications, such as electromechanical probes and interlaminar-reinforced composites, are realistic given production technology presented here; many others, such as fibers of macroscopically-long CNTs and CNT-based materials having chirality-selected electrical properties, require significant further advances across this broad and exciting field.

1.3 Thesis outline

This thesis project began with the concept of growing and aligning CNTs using directed gas flows in microchannels, with aim to fabricate macroscopic-length (i.e., 1 meter and longer) strands of continuous CNTs. This idea both necessitated and catalyzed a broader investigation into CVD synthesis of CNTs. While our original idea remains unfulfilled beyond initial verification of flow-aligned CNT growth, much fundamental progress has been made in controlled synthesis of CNT films, in development of new reactor systems, and in utilization of these systems for new types of growth experiments, as is detailed in the following chapters:

Chapter 2 summarizes the current state-of-the-art understanding of the science, synthesis, and applications of CNTs. There are particular foci on the mechanical properties of CNTs, and the mechanism of CNT nucleation and growth by catalytic chemical vapor deposition.

Chapter 3 presents growth and characterization of films of tangled SWNT films on silicon substrates, including the first process for growing CNT films conformally on micromachined surfaces. Changing the size and configuration of the substrate sample inside a tube furnace reveals how thermally-induced evolution of the reactant mixture can significantly affect the yield and quality of CNTs.

Chapter 4 presents growth and characterization of aligned architectures of MWNTs, including millimeter-thick films and patterned microstructures on silicon substrates, and conformal coatings on commercially-available ceramic fibers. This chapter also presents the first study of mechanochemical effects on CNT film growth; applying mechanical pressure during growth controls the film alignment while causing defects in the CNTs, and enables direct "grow-molding" of CNTs into 3D-shaped microforms.

Chapter 5 presents the design and fabrication of a microchannel array for combinatorial studies of nanomaterials growth. The flow range and resolution of this device far outperform conventional furnace and flow delivery hardware, and reversible mating of the device with a catalyst pattern enables *ex situ* characterization of the reaction products.

Chapter 6 presents the design and construction of furnace systems used for the CNT growth experiments in this thesis: atmospheric pressure tube furnaces, a flow-reversal furnace configuration for conducting short-time growth experiments, and a novel reactor apparatus using a suspended heated platform. The suspended platform apparatus enables rapid control of reaction temperature, *in situ* characterization of the reaction surface, and versatile packaging of microchannel devices for high-temperature operation.

Chapter 7 presents results of CNT growth experiments using new apparatuses: short-time CNT film growth using the flow-reversal furnace configuration; enhanced rate growth and *in situ* measurement of film growth kinetics using the suspended heated platform reactor; and flow-aligned growth of isolated CNTs and CNT strands by confinement in microchannel arrays.

Chapter 8 presents artistic visualizations of CNT structures. These have catalyzed enjoyable opportunities to communicate our work more broadly and to showcases the beauty and complexity of CNT self-assembly in response to gradients in chemical and mechanical reaction conditions.

Chapter 9 summarizes the findings of this thesis, poses key unanswered questions as we seek to understand and scale the manufacturing of CNTs and like nanomaterials, and outlines upcoming research activities designed to help answer these questions.

Chapter 2

Introduction to the Science, Synthesis, and Applications of CNTs

This chapter assesses our current understanding of the science, synthesis, and applications of CNTs. The structure of CNTs is described in comparison to other filamentous carbon materials. The electronic, mechanical, thermal, and multifunctional properties of CNTs are presented, with emphasis on the scalability of these properties and applications in fibers and composite materials. The mechanism of CNT synthesis by catalytic chemical vapor deposition, which forms the basis of this thesis, is presented in detail. This seeks both an engineering understanding of the critical dependencies of the synthesis process, as well as a mechanistic understanding of the critical phases of catalyst pre-treatment, CNT nucleation, and CNT growth.

2.1 Structure and electronic properties of CNTs

CNTs are a structurally "perfect" member of a broader family of filamentous carbon structures [41], and must be distinguished from the materials described below.

- Carbon fibers (CFs), typically several μm diameter, which are produced by spinning of polymer melt solutions (e.g., polyacrylonitrile). The spun fibers are annealed at very high temperatures (e.g., 3000 °C) to reorganize the carbon into graphite fragments ("turbostratic graphite") which are generally aligned along the fiber axis but are not continuous. This general processing technique is specialized to give many types of CFs, having application-suited stiffness, strength, and thermal and electrical conductivities [42], which are wound and woven into cloth, tubes, and many other forms suitable for large-scale processing.

- Graphite whiskers, typically 1–10 μm diameter, which are produced in the discharge of a DC arc between carbon electrodes, operated at ~10 atm gas pressure. Whiskers form by winding of large graphite sheets into scrolls, are up to several cm long [41], and have high stiffness and electrical conductivity. Arc-production of CNTs, as Iijima first demonstrated [13], occurs at much lower gas pressures.

- Vapor-grown carbon fibers (VGCFs), typically 1–100 μm diameter, which start as thin carbon filaments which precipitate from metal catalyst particles flowing in a hydrocarbon

atmosphere. However, unlike CVD synthesis of CNTs (section 2.5) this reaction is operated under heavily pyrolytic conditions so the initial filament is overcoated by carbon deposited on its sidewalls. After growth, VCGFs are typically annealed like CFs; annealing substantially improves VGCF properties by ordering carbon into graphene ribbons. Endo and colleagues demonstrates (much in retrospect after their initial work in 1976 [23]) that the core of a VCGF can be a CNT (Fig. 2-1a-b). Tibbetts and colleagues extensively studied substrate-bound VCGF synthesis by pyrolysis of natural gas, contributing useful models of the nucleation, lengthening, and thickening processes [43–50].

- Carbon nanofibers (CNFs), typically <1 μm diameter, which are generally more ordered than VGCFs. Here, Endo's work in the 1980's pioneered the development of catalytic decomposition of hydrocarbons to produce large quantities of sub-μm diameter VGCFs, which are effectively large-diameter MWNTs [26]. There are also "stacked" CNFs, having planar graphitic layers perpendicular to their axis (Fig. 2-1c); and "herringbone" or "cup-stacked" CNFs, having cone-shaped graphitic layers (Fig. 2-1d). Both are produced by CVD methods where the carbon layers precipitate from metal catalysts, and have relatively poor tensile properties because they are held together only by interlayer surface forces. More recently, cup-stacked filaments having hollow cores have arisen [51]. Further, many plasma-enhanced CVD processes give filaments comprising layers of graphite which are stacked at an angle to the central axis [52].

We strictly designate CNTs as having seamless cylindrical graphene walls which are continuous along the length and parallel to the central axis of the CNT. If we visualize the formation of a CNT as the action of rolling a graphene sheet into a seamless cylinder, the chirality of a CNT is established by the orientation of the graphene lattice with respect to the axis of rolling. The chirality is denoted by (n,m) indices (Fig. 2-2) according to a convention developed by Dresselhaus [5, 54]. The chirality determines the band gap, and therefore the electronic properties of a CNT. For example, "armchair" SWNTs, which have a straight edge of the hexagonal lattice perpendicular to the tube axis, have a small band gap and are typically metallic. Conversely, "zigzag" SWNTs, which have a straight edge of the hexagonal lattice parallel to the tube axis, are metallic in one-third of cases and semiconducting in two-thirds of cases. There are hundreds of possible CNT structures having different diameter and chirality pairings. Geometric and energetic calculations suggest that the pentagon/hexagon arrangement in the cap uniquely determines the chirality of a CNT [55].

The band gap of a CNT is inversely proportional to the tube diameter. All CNTs larger than approximately 3 nm in diameter have band gap energies less than the thermal energy at room temperature, and therefore exhibit metallic behavior. Therefore, while SWNTs can be semiconducting or metallic, MWNTs are almost always metallic. This makes SWNTs more frequently studied for use in next-generation transistor devices [56–58], while MWNTs are more frequently studied for their high current-carrying capacity ($>10^9$ A/cm^2 [59]) as demanded by microelectronic interconnects [60, 61].

Room-temperature ballistic electron transport has been demonstrated over μm-scale distances in SWNTs [57, 62] and through parallel channels in MWNTs [63]. Making low-resistance electrical contact to CNTs has been a practical challenge, and relies on intimate engagement between the metal and the conduction path through the CNT. Ohmic contact to metallic CNTs

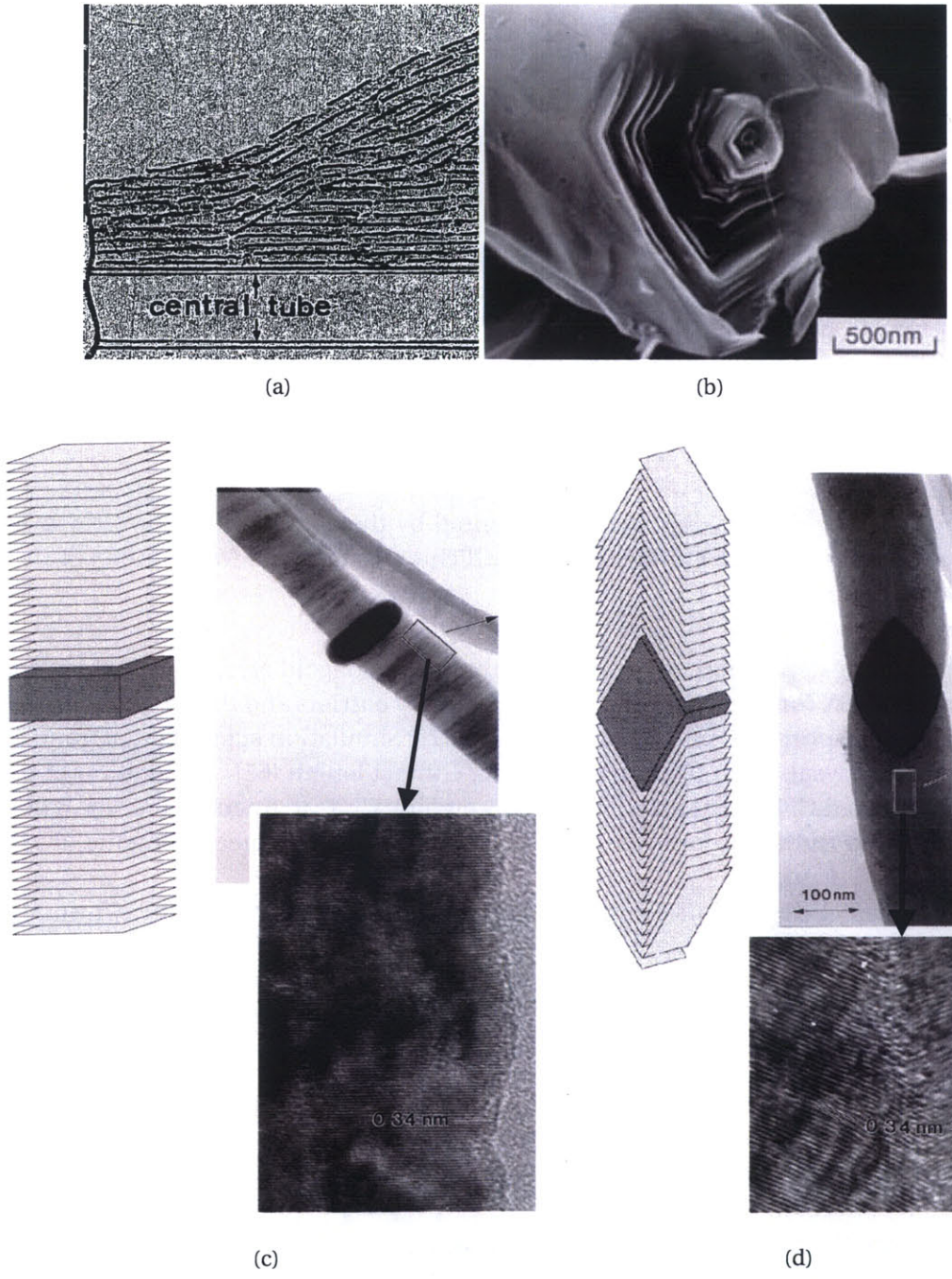

Figure 2-1. Various non-CNT carbon filaments: (a) schematic of hollow tube along central axis of VGCF, coated with turbostratic graphite (from [23]); (b) fracture surface of VGCF, revealing ≈5 nm diameter hollow core (from [41]); (c) schematic of structure and TEM images of sheet-stacked CNFs (from [53]); and (d) schematic of structure and TEM images of cup-stacked CNFs (from [53]).

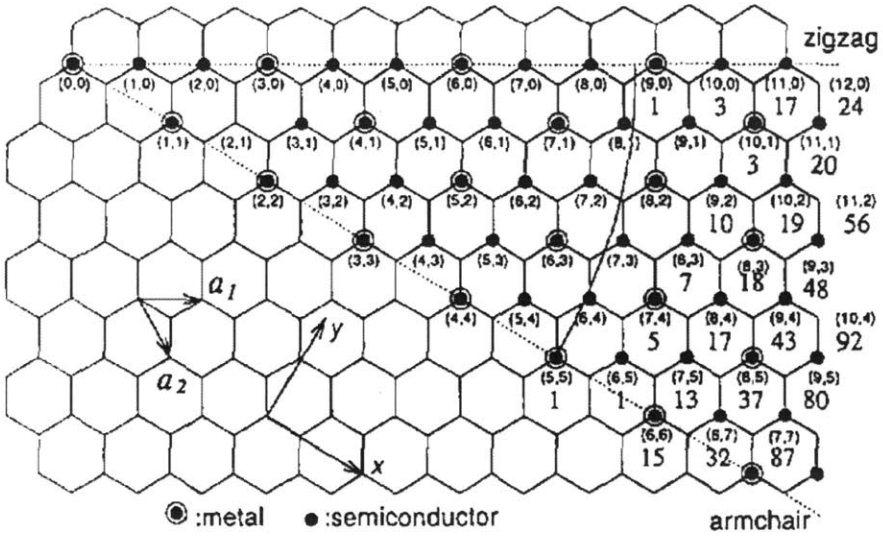

Figure 2-2. Chiral orientations of CNTs, represented by the alignment of the CNT axis with particular lattice points of the graphene sheet, which determine the (n,m) index of the CNT (from [54]).

was first achieved by deposition and subsequent annealing of gold electrodes [64], and later it was found that Pd-CNT interfaces do not exhibit Schottky barriers and thereby enable observation of ballistic transport in semiconducting tubes [57]. Simulation suggests that good metal-CNT contacts have weak hybridization over a long contact length [65]. Integration of parallel electrically-contacted CNTs could be improved by etching CNTs to open their ends [66], as has been demonstrated through room-temperature superconductivity measurements of MWNTs having ends rooted in Au [67].

Defects in a SWNT degrade its electrical properties, and the defect density is intimately related to the growth process [68]; overall the relationship between defects and CNT properties requires much further experimental and theoretical study before scalable applications are realized. Further, electronic characteristics of CNTs are sensitive to the surrounding atmosphere; this can be a blessing for chemical sensing [69, 70], and trouble for devices which require stable operation [71].

2.2 Mechanical and thermal properties of CNTs

The density-normalized mechanical stiffness and strength of CNTs exceed those of all known natural and synthetic bulk materials (Fig. 2-3, Table 2.1). As a CNT is comprised of graphene sheets, its tensile elastic modulus is closely approximated by the in-plane modulus of single-crystal graphite, which is $\approx$1000 GPa. Theoretically, this value is independent of the nanotube diameter, except for a possible decrease due to curvature effects in very narrow SWNTs [12], and has been confirmed by a wide body of experimental work. However, one must take care in considering the area over which is value is calculated; here, a SWNT is considered as a hollow tube with a wall thickness equal to the interlayer spacing of graphite (0.34 nm).

The modulus as measured by cantilever bending decreases from ≈1 TPa to ≈100 GPa as the tube diameter increases beyond $d \cong 12$ nm. In these larger-diameter CNTs, bending induces wave-like distortions of the lattice which relieve strain and decrease the effective stiffness [72, 73]. It has further been shown that the bending stiffness of a MWNT as derived from the electrostatically-induced resonance measurements, is inversely proportional to the density of defects in its sidewalls, where the defect density is approximated by the electrical resistivity of the CNT [74].

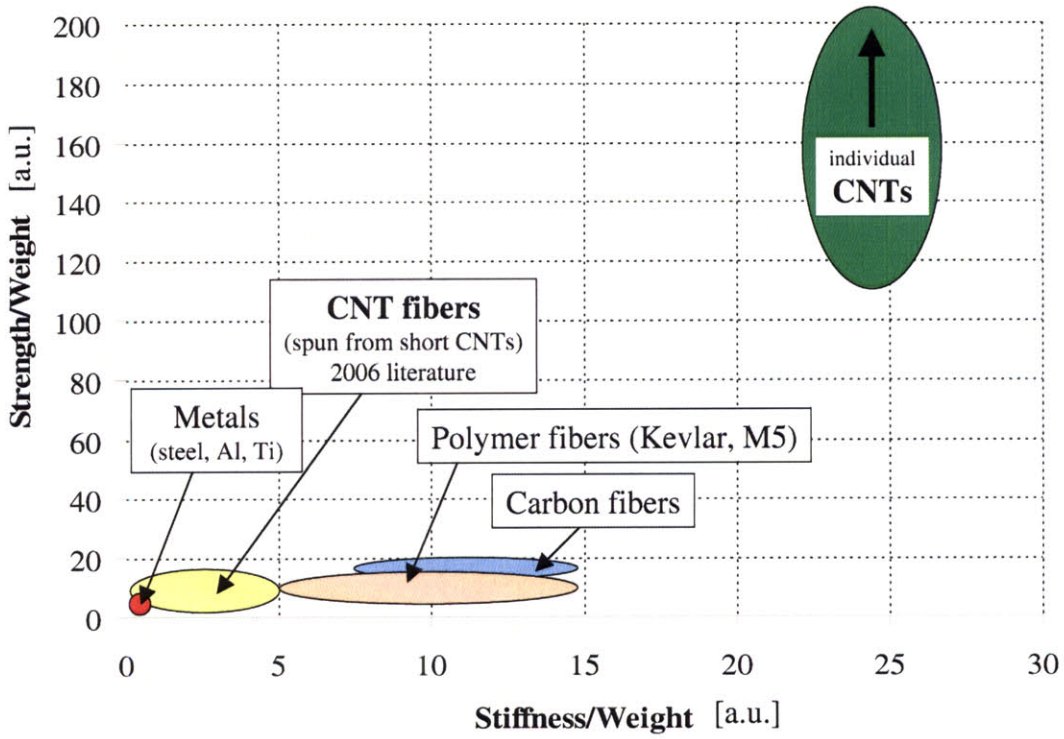

Figure 2-3. Comparison of density-normalized stiffness and strength of individual CNTs, to synthetic fibers and structural materials (data compiled from many sources).

Theory predicts that the ultimate tensile strength of a material is approximately one-tenth of its elastic modulus, or ≈100 GPa for small-diameter CNTs; however, the inevitable presence of defects prevents this limit from being realized. Strength tests on MWNTs produced by arc discharge, where the CNTs were mounted between a pair of AFM tips, gave strengths of 11–63 GPa [84]. Testing of CVD-grown MWNTs gave a tensile strength distribution (by Weibull statistics), where 25% of the CNTs fail at or below 55 GPa, and 75% of the CNTs fail at or below 148 GPa [76]. While the arc-grown MWNTs are expected to have a lower defect density and therefore be stronger than the CVD-grown MWNTs, the authors hypothesize that defect-induced ripples in the sidewalls improve stress transfer through the structure and thereby increase the strength. This mechanism may be compelling for applications of MWNTs in reinforced composite materials.

Further experiments have strained SWNTs to ≈6% elongation before breakage [85]. Superplastic elongation to strains exceeding 250% has been demonstrated by pulling a SWNT in a

Material	Stiffness E [GPa]	Tensile Strength σ [GPa]	Density ρ [g/cm^3]	Specific Stiffness (E/ρ)	Specific Strength (σ/ρ)	Thermal Cond. [W/m-K]
CNT [75–77]	1000	20–200	1.4[a]	28	110–1100	>3000
PAN/Pitch CF	500	4	1.8	11	19	500
CVD-spun CNTF [78,79]	15	1.0	2	0.3	4	-
Dry-spun CNTF [80]	15	0.3	0.8	0.7	3.0	-
Polymer-CNTF [81,82]	100	0.9	1.5	4	8	-
Glass fiber	74	3.5	2.6	1.1	11	-
Kevlar	87	3.0	1.4	2.3	16	-
M5 fiber	375	7.6	1.7	9	35	-
Steel (1080)	1	205	8	1	1	48
Aluminum (6061)	69	0.3	3	1.0	0.9	170
Titanium (8Al-1Mo-1V)	120	0.9	4	1.1	1.6	6
Copper (UNS C10100)	115	0.4	9	0.5	0.3	380

[a]The density of CNTs is reported for a hexagonally-packed array of SWNTs, each having outer diameter of 1.0 nm.

Table 2.1. Mechanical and thermal properties of CNTs, CNT fibers (CNTFs) and various other materials. The listed values of specific strength and specific stiffness are normalized relative to those of steel. Properties of metals were obtained from [83]. Properties of carbon and synthetic fibers are as listed in [42]. Thermal conductivities of polymer and CNT fibers were not obtained; these are generally much less than for carbon fibers.

TEM while resistively heating it to above 2000 °C [86]. Quantum mechanical computations offer predictions of the strength of SWNTs depending on their chirality, and on applied load, temperature, and time [87]. Overall, much further understanding of how CNT strength relates to the density and nature of defects, and the nature of loading conditions, is required.

Along with their outstanding electrical and mechanical characteristics, high-quality CNTs have thermal conductivity exceeding the in-plane thermal conductivity of graphite, which is the highest value among all known materials [88]. The room-temperature thermal conductivity of an individual suspended SWNT has been measured as 3500 W/m-K [89], and ballistic phonon transport through MWNTs has been experimentally verified [90].

2.3 Electromechanical properties and devices

CNTs also exhibit useful electromechanical properties, as their electrical characteristics can be significantly affected by mechanical deformation to their structure. Tombler and colleagues first observed that bending a SWNT (using an AFM tip) can reversibly increase its electrical resistance by two orders of magnitude [91]. Later work by Cao et al. characterized the piezoresistance of suspended SWNTs under tensile stress [92], showing that small band-gap semiconducting CNTs undergo the largest change in resistance. Relationships between mechanical strain and electronic structures of CNTs have been studied using Raman spectroscopy, where

pressures and loads cause the resonance peaks to shift [93, 94].

Many unique nanoscale devices demonstrate the unique structure and mechanical characteristics of individual CNTs. For example, telescoping "sword-in-sheath" extension of a MWNT provides a demonstration for a nanoscale linear bearing, having no measurable wear between the sliding wall surfaces [95]. Extending this idea, a section of Cr/Au film (≈300×300 nm) is anchored at the midpoint of a suspended MWNT, while the outer wall is removed at the supports, enabling freely-rotating electrostatic actuation of the film as a nanoscale torsional mirror [96]. Another device has a Au/Cr pendulum anchored to a suspended SWNT, and in this case the pendulum is actuated by charging in an electron microscope, resulting in reversible torsional deformation of the SWNT to 70° over a suspended length of ≈400 nm [97]. Further, a telescoping MWNT is built as a tunable electromechanical resonator, having ~200 MHz oscillation frequency [98].

A single suspended SWNT has been implemented as the transducer element in a microfabricated pressure sensor, where deflection of a suspended Al_2O_3 membrane strains the SWNT and thereby changes its I-V characteristics [99]. The concept of a nonvoltatile electromechanical memory using CNTs in a cross-bar array is demonstrated between a pair of SWNTs positioned on a substrate by mechanical manipulation [100]. However, because of challenges in directed growth and/or manipulation, individual CNT devices largely remain single proof-of-concept demonstrations. Interestingly, the crossbar memory concept is in final stages of development using lithographically-patterned ribbons of tangled SWNTs suspended over etched trenches [101], rather than individual CNTs. Adaptation of CNTs as a new material in an existing manufacturing infrastructure will perhaps make this the first commercial microdevice which uses CNTs.

2.4 Perspective on scalability of CNT properties

Astounding comparisons between properties of CNTs and other materials should not let us think CNTs can readily be "super" materials. Individual molecular chains boast similarly exceptional properties as CNTs, and the great challenge is in assembling these chains into macroscopic materials which exhibit nanoscale properties. However, CNTs offer unique promise here because unlike many other molecules, CNTs can grow to macroscopic lengths.

The longstanding inspiration for producing fibers from continuous long molecules is rooted in the origins of polymer science, and particularly by the work of Hermann Staudinger. The following passage summarizes Staudinger's contributions, for which he was awarded the 1953 Nobel Prize in Chemistry [102]:

> "In 1922 Staudinger and J. Fritschi proposed that polymers are actually giant molecules (macromolecules) that are held together by normal covalent bonds, a concept that met with resistance from many authorities. Throughout the 1920s, the researches of Staudinger and others showed that small molecules form long, chainlike structures (polymers) by chemical interaction and not simply by physical aggregation. Staudinger showed that such linear molecules could be synthesized by a variety of processes and that they could maintain their identity even when subject to chemical modification. Staudinger's pioneering work provided the theoretical basis for

polymer chemistry and greatly contributed to the development of modern plastics. His researches on polymers eventually contributed to the development of molecular biology, which seeks to understand the structure of proteins and other macromolecules found in living organisms."

A wide variety of high-strength polymer fibers are produced nowadays, and this started with with Dupont's poly(*p*-phenylene terephthalamide), or PPTA, commonly known as Kevlar, in the early 1970's. Recently, the production techniques for polymer fibers have been adopted to produce fibers containing CNTs; however, Staudinger's idea of a "continuous crystal" which would replicate the properties of individual polymer chains at macroscopic scales, has not been realized in either effort.

Polymer fibers can achieve at least 90% of the theoretical elastic modulus for a crystal comprised of connected polymer chains, yet like with preliminary strength tests of individual CNTs, practical yield strengths of polymers are often no more than 25% of theoretical values [103]. This is because spinning processes can achieve exceptional alignment and dense packing of chains, yet the connections between chain ends are weak, and stress concentrations at these points cause fracture of the fiber (Fig. 2-4). Secondary bonding between chain ends is one-to-two orders of magnitude weaker than intramolecular covalent bonds within the chains. The elastic modulus is dominated by the stiffness of the intramolecular bonds within the chains; therefore, under a tensile stress, a polymer fiber stretches as the chains of the polymer fiber are elongated, and then fails when a stress concentration builds and fracture propagates from a discontinuity among the parallel chains.

Fibers and yarns spun from short CNTs—in direct CVD [78, 79], from aligned arrays [80], or in acid or polymer solutions [81, 82]—do not yet offer compelling properties. One technique, where CNTs are spun from a solution of super-concentrated H_2SO_4, can achieve $\approx$80% density of CNTs in the fibers, yet the fibers break relatively easily due to poor end-to-end connections (e.g. voids) among the CNTs [104]. Because of the tendency of CNTs to bundle and rope (e.g. 100–500 nm diameter aggregates) due to strong inter-tube surface forces, it will be challenging to produce fully-dense CNT fibers. Further, if continuous CNTs were grown directly into long fibers from fixed catalyst sites, the fibers must be densified and/or twisted after growth to compact the space between neighboring CNTs which is necessitated by the spacing between the catalyst particles on the substrate. Overall, fibers and yarns comprised of short CNTs which have been produced to date fail to reflect the mechanical properties of individual CNTs primarily because of slip between adjacent substructural units of the fiber, stress concentrations at voids within the fiber, and difficulties in making robust mechanical connection to the fiber [105]. Comparatively, carbon fibers are nearly as stiff but not nearly as strong as individual CNTs, so the true potential for CNT fibers lies in their strength and multifunctional properties.

To create high-performance bulk materials utilizing CNTs we must further understand and control the molecular-level interactions among CNTs and between CNTs and the host material, and discover how bulk properties scale based on the fraction, type, and properties (e.g., length, diameter, defect density) of the CNTs. At weight fractions of $\ll$1%, CNT-polymer composites typically exhibit electrical conductivity by percolation, where the electrical conductivity increases sharply when the CNT loading crosses a percolation threshold, and then current travels through a loose network CNTs throughout the material [106–108]. Because it is relatively straightforward to mix small fractions of CNTs in polymers and because percolation can be

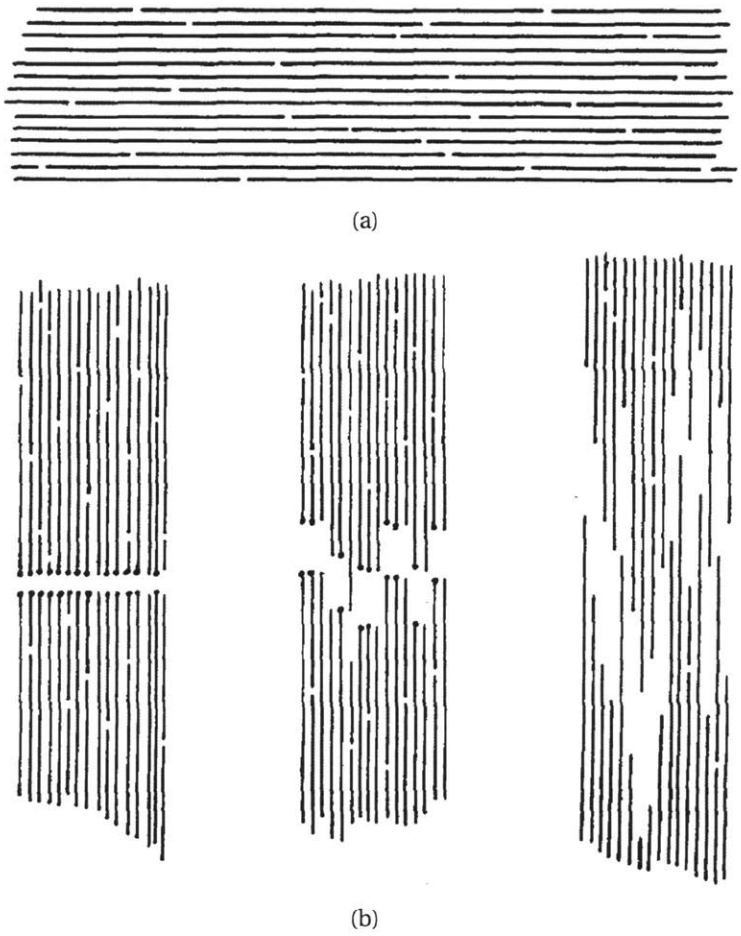

Figure 2-4. Structure of polymer fibers (from [103]): (a) fiber of aligned elongated chain molecules, with molecules having adjacent yet disconnected ends; (b) schematics of fiber failure, by (left) chain scission, (middle) chain scission and chain slip/pullout, (right) chain slip/pullout.

achieved using low-quality disordered and large-diameter CNTs, electricaly conductive plastics containing CNTs became commercially available in the early 1990's, particularly for electrostatic discharge applications and for electrostatically-assisted painting of plastic components.

However, compelling thermal and mechanical properties of CNT composites are not realized until CNTs are loaded at higher weight fractions, which must be closer to the typical loadings of carbon or ceramic fibers in structural composites (≈65%). Unfortunately, bulk mixing of CNTs with matrix materials at weight fractions exceeding a few percent typically leads to agglomeration and non-uniform dispersion [29]. This proves an imperative for growing assemblies of densely aligned CNTs, along with new dispersion techniques such as molecular-level mixing [109], *in situ* polymerization [110], and direct growth of CNTs on composite host materials (section 4.5).

Studies so far indicate that polymers adhere very strongly to CNTs, which is good news if challenges in bulk synthesis and alloying of CNTs are overcome. CNT-polymer interfacial

strength increases with CNT diameter, and reaches a steady-state for CNT diameter ≥10 nm [111]. Experiments show that CNTs fail (SWNT fracture, or sword-in-sheath extension of a MWNT) before the CNT-matrix interface fails. CNT-polymer adhesion strength of 100's of MPa has been measured by pulling individual CNTs and CNT ropes from a matrix using a scanning probe tip [112, 113], which exceeds the interfacial strength in current fiber-based composites. This suggests covalent bonding between the CNTs and matrix, which is possibly best at defect sites on the CNTs. Further experimental evidence shows that polymers are good at wetting in spaces among CNTs, and CNT-polymer interaction significantly increases the mechanical properties of a tangled mat of CNTs [114]. One mechanism of interaction is crystallization of a thin layer of polymer around the outer wall of a CNT, as has been observed for poly(vinyl alcohol) (PVA) [115]. Molecular dynamics studies of physisorption between individual polymer chains and CNTs have shown that aromatic rings interact strongly with SWNT sidewalls, and poly(*p*-phenylenevinylene) (PPV) is particularly good at bonding to CNTs due to the planar arrangement of aromatic rings along the backbone of the chain [116]

2.5 Synthesis of CNTs: the CVD method and mechanism

There are many methods of synthesizing, or "growing" CNTs, and these can be roughly divided into methods where CNTs grow from metal catalyst particles, and methods where CNTs grow without catalyst particles. In all cases, carbon is reorganized into a CNT from a prior form such as graphite, amorphous carbon, or a molecular precursor species (e.g., a gaseous or liquid hydrocarbon). The energy required for CNT growth is typically supplied by heating the precursor species and/or the catalyst. Dangling carbon bonds correspond to high energy states, and this energy is greater than the strain energy required to "bend" graphite into closed cages such as C_{60} and CNTs. CNT formation is favorable after a reaction first organizes carbon into a graphitic cap which acts as the nucleus of a CNT, and then tube is lengthened from its open end.

Since the mid 1990's[1], catalytic chemical vapor deposition (CCVD or CVD) has emerged as the most versatile and scalable method of CNT synthesis, owing to its low reaction temperatures (relative to arc, laser, and flame methods), high yield, and versatility for gas-phase ("floating catalyst") or substrate-bound ("fixed catalyst") growth [52, 117, 118]. Iijima's initial confirmation found CNTs in the deposit on the carbon electrode of a DC electric arc [13]; this apparatus was very similar to that reported for synthesis of large quantities of C_{60} [119]. In addition to arc discharge, CNTs can be produced in flames [120–122][2], by laser ablation of carbon [125], by direct conversion of carbon using microwave energy [126], and by many occasional procedures which are too numerous to mention. In concert with the focus of this thesis, this section addresses CVD methods in detail. Table 2.2 compares performance characteristics of major

[1]However, Endo's floating catalyst CVD process developed in the mid 1980's [26] gave large quantities of what later became known as MWNTs.

[2]After Kroto and colleagues' discovery of C_{60}, there was broad speculation that CNTs could be synthesized. One particular example is that Jack Howard's group in the Department of Chemical Engineering at MIT made C_{60} in a $C_6H_6/O_2/Ar$ flame [120]. Long after Iijima's first arc results, Howards's group reported CNT synthesis using flames [121], and have since further developed the technique and understanding of the growth mechanism [122, 123]. Simply enough, carbon nanofibers and possibly CNTs were much later found in diesel exhaust particulates from a Rover 218 TD [124]!

Method	Operating temp. [°C]	CNT length [μm]	CNT growth rate [μm/s]	Yield	Quality	Purity
Arc discharge	≈4000	~1	up to 10^7 [a]	Low	Low	Low
Laser ablation	RT–1000 °C [b]	~1	~0.1	Low	High	Med
Flame [c]	≈1500	1–10	10–100	Low	High	Med
Thermal CVD	500–1200	0.1–10^5	0.1–10	High	Med	Med-High
PECVD [d]	100–800	0.1–10	0.01-1	Low	Low-Med	Med

[a] In arc plasmas, CNTs grow for very short times at astonishing rates of 1–10 m/s, before self-terminating because of stochastic instabilities in the growth conditions [127]. More recently the yield and quality of arc-generated CNTs has been improved by running the arc underwater [128].

[b] This is the temperature of the surrounding furnace [129,130]; the local temperature at the ablation site is much higher.

[c] Values for SWNT growth in premixed $C_2H_2/O_2/Ar$ flame [122].

[d] These values are for PECVD growth on substrates [52]. Some processes use plasmas to enhance CNT growth from floating catalysts, giving much higher yields [131], and at high energies are essentially hybrid plasma-flame-CVD techniques. A more recent advance produces MWNTs without a catalyst by impinging a plasma flame jet (≈4000 °C) of alcohol vapor jet against a graphite target [132].

Table 2.2. Process characteristics of mainstream CNT synthesis methods.

methods of CNT synthesis; further discussion of non-CVD synthesis techniques is left to the literature.

In the widely-developed CVD method, CNTs form by organization of carbon on a nanoscale metal catalyst particle in a high-temperature carbon-containing atmosphere. The carbon dissociates from the source compound and adds to the CNT through surface and/or bulk diffusion at the catalyst. This mechanism (Fig. 2-5) is analogous to Vapor-Liquid-Solid (VLS) crystal growth, which was first studied during the 1960's with respect to growth of silicon whiskers [133]. In the VLS model, a vapor-phase precursor dissolves into a liquid growth site (catalyst), and a solid crystal precipitates from the growth site. CNT growth from metal catalysts generally agrees with the VLS model as a working example; however, under certain circumstances (e.g., at high temperature and if the catalyst is liquified) carbon may diffuse through the bulk of the catalyst, while under other conditions (e.g., at lower temperature) surface diffusion may dominate [134–136]. The VLS mechanism is more directly applicable to growth of semiconductor nanowires [137], such as silicon nanowires which precipitate from gold nanoparticle catalysts in a silane (SiH_4) atmosphere [138,139].

CVD growth can be performed in a variety of closed-atmosphere furnace apparatuses, in which pressure, temperature, and gas flow are controlled (Fig. 2-6). These apparatuses are typically suited to either "fixed-catalyst" (substrate-bound) CNT growth, where the CNTs grow from catalyst particles arranged on a substrate such as a silicon wafer, or to "floating-catalyst" growth where the catalyst particles are held in a fluidized bed or pass through the furnace continuously in the gas phase.

In substrate-bound growth, CNT-CNT or CNT-substrate surface interactions in addition to the arrangement and activity of the catalytic sites determine if CNTs grow in an isolated, tangled, or aligned configuration (Fig. 2-7). For example, isolated SWNTs can be grown to millimeter- or centimeter-lengths [141,142] when suspended during growth by a gas flow; how-

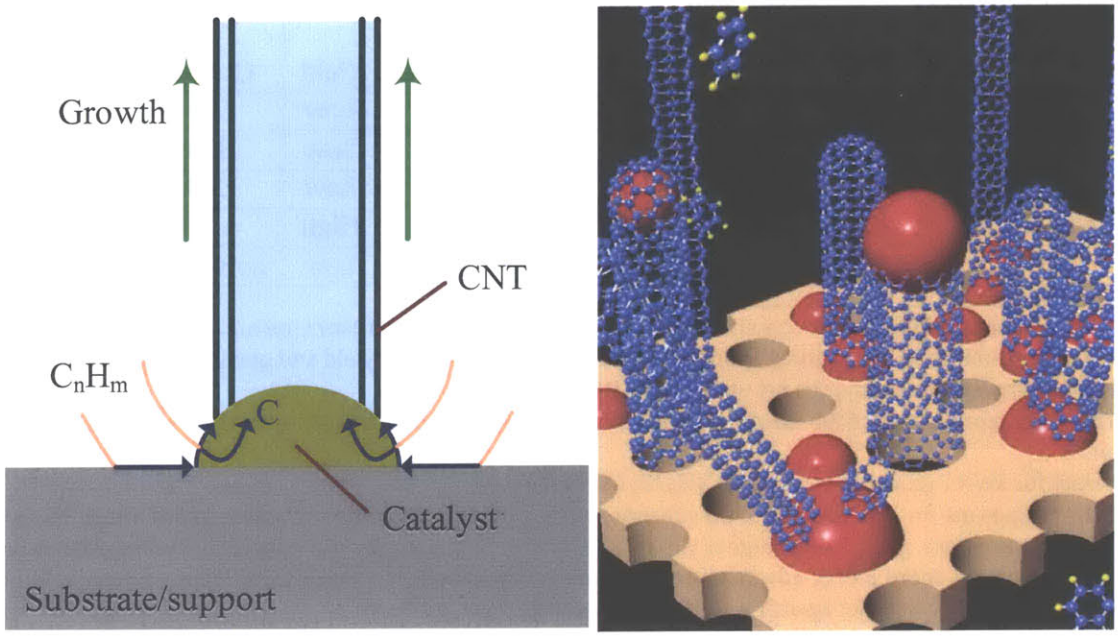

(a) (b)

Figure 2-5. Schematics of individual substrate-bound CNTs growing by CVD: (f) "base growth" of a CNT, where a gaseous carbon source diffuses at a metal catalyst particle which remains attached to the substrate, and a CNT grows upward from the surface of the particle; (b) base- and tip-growth of CNTs rooted in a nanoporous (e.g., zeolite) substrate (from [140]).

ever, the density of catalytic sites must be very low to prevent entanglement among CNTs. At a high catalyst density and CNT growth rate, a vertically-aligned CNT (VA-CNT) growth mode is typical whereby the CNTs self-orient perpendicular to the substrate surface due to initial crowding and continue to grow upward in this direction [143, 144]. The catalyst particle can remain rooted on the substrate during CNT growth ("base growth"), or can lift from the substrate and remain at the tip of the advancing CNT ("tip growth"). In both cases, carbon is added at the catalyst site. The growth kinetics, catalyst-substrate surface interactions, and forces acting on the catalyst particle (e.g., forces induced by an electric field in plasma-enhanced CVD [145]) determine whether base growth or tip growth occurs [146].

CNT growth by CVD involves many process parameters, and therefore a multi-dimensional parameter space must be explored to develop an empirical model of a particular growth scheme, and to relate the characteristics of the CNTs to the process conditions. The main process parameters include those listed below, and further discussion of parameter dependencies in CVD reactions is grown through chapters 3, 4, and 7. CNT characteristics of interest include diameter, wall structure and chirality, defect density, and length, as well as the many physical properties which result from these basic characteristics.

Catalyst and support

- *Catalyst material* – Catalysts are typically transition metals such as Fe, Co, and Ni [147, 148], which have a high solubility for solid or liquid carbon [149], or bi-metallic alloys

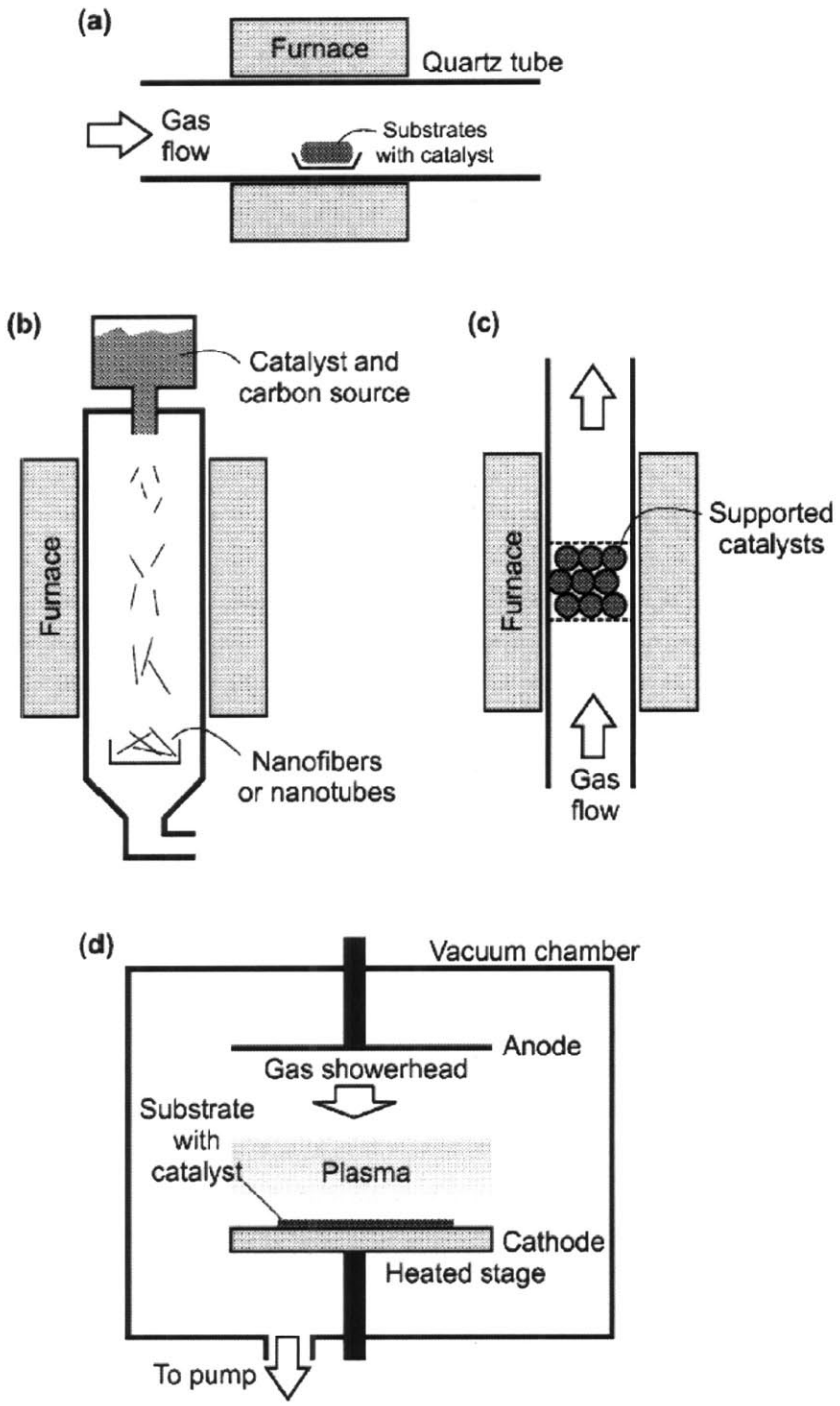

Figure 2-6. Classical furnace designs for CVD synthesis of CNTs and like nanostructures (from [52]): (a) horizontal tube furnace with fixed catalyst; (b) vertical tube furnace with floating catalyst; (c) vertical tube furnace with fixed gas-permeable or fluidized bed catalyst; (d) low-pressure plasma-enhanced (PECVD) chamber with heated stage.

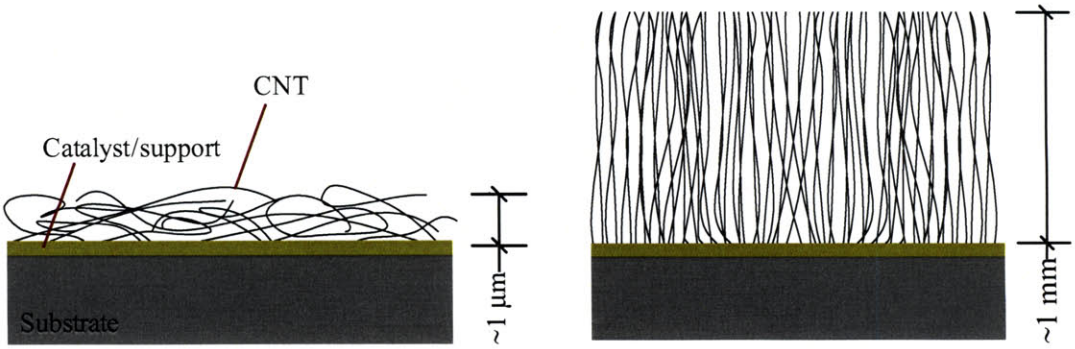

Figure 2-7. Classical morphologies of CNTs grown on substrates: (a) tangled film, which terminates at ~μm thickness due to steric hindrance among CNTs; (b) vertically-aligned film, which can grow uniformly to ~mm thickness.

such as Fe/Mo and Co/Mo where the first element is the catalyst and the second element likely has stabilizing and promotional functions [150]. The catalyst can be deposited as a thin film (which coarsens or dewets into particles upon heating), deposited from a metal precursor solution or from a solution of metal nanoparticles, or delivered in the gas phase by evaporation or sublimation of an organometallic compound (e.g., $Fe(C_5H_5)_2$) [59, 151] or by introduction of an aerosol [152, 153].

- *Catalyst size* – The catalyst particle size (diameter) roughly determines the CNT diameter [154], although in some cases bundles of SWNTs or DWNTs may grow from a single catalyst particle [155].

- *Substrate/support material* – The substrate must withstand the reaction temperature. The support (the material in contact with the catalyst metal) "grips" the catalyst particles and can promote favorable electronic and/or catalytic interactions which affect the CVD reaction. Typical supports are oxides such as Al_2O_3, MgO_2, SiO_2, and TiO_2.

Reaction parameters

- *Reactant composition and flow rate* – Most of the readily available carbon-containing compounds have been used to grow CNTs by CVD. Typically the reactant is a hydrocarbon or alcohol (e.g., C_2H_2, CH_4, C_2H_4, C_2H_5OH, C_6H_6, C_7H_8, C_8H_{10}), and is introduced in the vapor phase. Energetic compatibility between the carbon source and the catalyst is important for high CNT yield. Empirically, higher-activity (less stable) reactants are compatible with catalysts in which carbon diffuses more easily at lower temperature. A classic combination is acetylene (C_2H_2) with Ni [21]; as the most active (least saturated) hydrocarbon, C_2H_2 thermally decomposes into poly-aromatic hydrocarbons at temperatures above 700 °C [156]. The carbon source is typically balanced with one or more complementary species, which suppresses gas-phase pyrolysis of the carbon source at high temperature and/or etches dangling (amorphous) carbon from the catalyst and thereby

increases the quality and lifetime of growth. These additivies include H_2, NH_3, and H_2O-vapor.

- *Temperature* – CVD growth typically occurs at 500–1200 °C. Growth at lower temperatures has been achieved by separately dissociating the carbon source using a plasma; however, CNT quality generally increases with reaction temperature.

- *Pressure* – High-quality CNTs can be grown at both low and atmospheric pressures; generally, lower pressure limits the supply of reactant to the catalyst, yet a higher gas mean free path at lower pressure improves the uniformity of gas diffusion and therefore the uniformity of CNT growth (e.g., the thickness of a VA-CNT film) across a large area. Atmospheric-pressure processes are more readily scalable to industrial quantities and bulk yields, whereas low-pressure processes are more readily useful for precisely-controlled growth of small numbers of CNTs such as for electronics or field emitters.

The design of the overall reaction sequence is vital. Statistical design of experiments can be used to capture a broad space in a relatively short experimental load, and using this technique it was demonstrated that temperature, catalyst composition, and gas composition are the most important variables in determining CNT yield and quality from a Mo/Fe catalyst supported on MgO, in C_2H_2 [157]. However, there are many other parameters which are not usually or easily quantified or controlled. These include the flow profiles within the CVD furnace, the forces acting on the CNTs during growth, and trace contaminants in the reactants or on the reactor walls. These factors are likely responsible for non-repeatabilities in typical laboratory-scale CVD operations.

2.5.1 Details of the CVD growth mechanism

While there is not yet a comprehensive understanding of the overall reaction space for CNT growth, much empirical work has certified general trends among the important variables, and much modeling and simulation has addressed the energetics and kinetics of the reaction [22, 45, 46, 158–162]. To lead a more rigorous understanding of the mechanism of CNT growth by CVD, we can divide the process into three stages (Fig. 2-8): pre-conditioning the catalyst, nucleating the CNT on the catalyst surface, and growing the CNT from the catalyst surface until the reaction terminates.

2.5.1.1 Pre-conditioning of the catalyst

The procedure for pre-conditioning the catalyst—increasing the furnace and catalyst/substrate to the reaction temperature—affects the chemical state of the catalyst, and thereby modulates its suitability and efficiency for decomposing and reorganizing carbon once the growth stage begins. However, current understanding is inconclusive as to whether an oxidized state or a metallic catalyst state is more efficient for CNT growth; likely, both are suitable for CNT growth under particular conditions. Most nanoscale metal particles are easily oxidized in ambient conditions, and empirical observations such as those presented in this thesis (Chapters 3 and 4) show that reducing atmospheres are necessary for high-yield CNT growth.

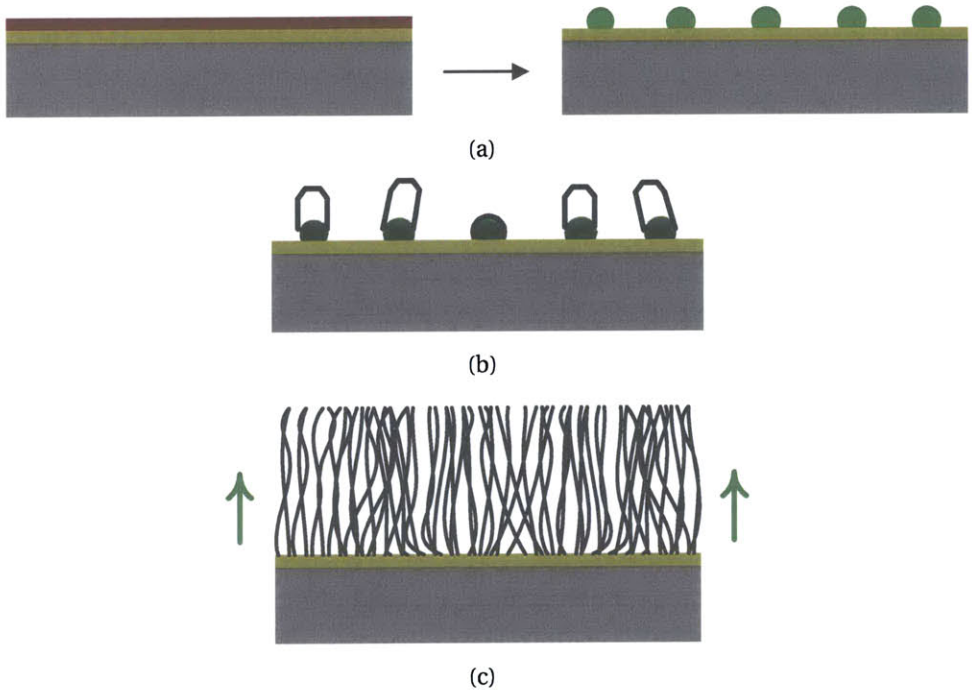

Figure 2-8. Schematic representation of three critical stages of CNT synthesis: (a) *pre-treatment* of the catalyst, such as de-wetting of a metal film into nanoclusters and reduction of their chemical state; (b) *nucleation* of CNTs on the catalyst particles, which determines the CNT chirality and wall structure; and (c) *growth*, which balances accumulation of carbon into the CNT, with accumulation of amorphous carbon which may overcoat the exposed areas of catalyst and terminate the growth process.

For example, Fe can typically be oxidized as FeO (ferrous oxide), $\alpha - Fe_2O_3$ (ferric oxide, "hematite"), $\gamma - Fe_2O_3$ (ferric oxide, "maghemite"), or Fe_3O_4 (ferrous ferric oxide, "magnetite"). By pre-treating Fe foils in oxygen and steam atmospheres and subsequently comparing the yield of carbon filaments grown in C_2H_2, Baker et al. concluded the order of activity is FeO > Fe ~ Fe_3O_4 [163]. However, here as in many present-day cases it is difficult to decouple possible effects of the pre-treatment atmosphere on the surface structure (e.g., particle size and surface roughness) of the catalyst from effects on the oxidation state of the catalyst. *In situ* X-ray diffraction studies during substrate heating showed that Fe evolves into Fe_2O_3 [164]. Because this occurred in pure He, the authors suggest that adsorbed moisture on the catalyst surface can cause oxidation. Upon introduction of C_2H_2 for CNT growth, Fe_2O_3 was reduced to Fe, and then growth began. Further, modeling of the CO disproportionation reaction, as used in the "HiPCo" [165] and "CoMoCat" processes [166] has suggested that only a metallic catalyst particle is stable, because oxygen reacts with carbon dissolved in the catalyst particle, forming CO.

2.5.1.2 Nucleation and structure determination

Nucleation is the process by which carbon initially organizes at the catalyst particle and starts growth of a CNT. It is widely accepted that the catalyst acts as a template for the cap of the CNT, and assembly of the tube walls begins after the cap is formed. CNT nucleation routinely happens very rapidly, in milliseconds or fractions thereof [159], and the nucleation time likely varies depending on the catalyst diameter and process conditions. Many aspects of reaction kinetics involving nanoscale particles exhibit size-dependent behavior; as catalyst particle size decreases, melting point decreases, carbon solubility increases, and equilibrium vapor pressure increases [167]. The catalyst particle can be liquid during SWNT nucleation and growth [168, 169], yet other experiments and simulations demonstrate that CNFs, MWNTs, and SWNTs can nucleate from solid particles [135]. Crystalline nanoparticles can rapidly change shape without liquefying [170], so perhaps it would be more suitable to establish whether or not the catalyst particle remains crystalline, and how far carbon penetrates into the particle during nucleation and during growth.

In situ studies using controlled-atmosphere TEM have directly viewed nucleation and short-time growth of carbon filaments [21,22,171,172]. Perhaps the most notable of these is by Helveg et al. [173], who show tip-growth nucleation of MWNTs from Ni catalyst particles in CH_4/H_2 at 500 °C during simultaneous HRTEM examination (Fig. 2-9a). Their images reveal that the Ni catalyst elongates as graphene sheets initially form on its surface, then the catalyst "jumps" from its support base while simultaneously contracting, leaving a short segment of CNT in its path. This cycle of expansion and contraction propels the catalyst forward throughout the growth process, while the catalyst remains crystalline. Growth appears to terminate when the catalyst is encapsulated by graphene and no metallic surface area is exposed to receive additional carbon. Observations along with supporting simulations contend that carbon adsorbs preferentially at atomic step edges on the Ni surface, and is transported on the catalyst by surface diffusion. *Ex situ* HRTEM imaging of SWNTs grown from Co/SiO_2 indicate that nucleation occurs at step edges, and that the step edge withdraws along the catalyst surface as the SWNT cap grows and lifts away from the catalyst particle (Fig. 2-9b) [174].

Molecular dynamics simulations involving liquefied catalyst particles predict that the catalyst becomes highly supersaturated with carbon prior to nucleation [175]. Carbon organizes to form graphitic islands on the particle surface, these islands lift off to form a cap for each layer of the CNT, and the carbon concentration drops to a steadily saturated level once growth begins (Fig. 2-10). Other simulations predict that SWNT growth can occur entirely by surface diffusion, where carbon atoms adsorb and reorganize on an Fe surface [176].

When the requirements for nucleation are not met, a catalyst metal particle will not start to grow a CNT. Following from Seidel et al. [177], two nucleation "failure modes" are

- (Fig. 2-11a) Encapsulation of the catalyst by thin graphitic layers, when the rate of carbon supply to the catalyst is insufficient or the catalyst cannot sufficiently process carbon for CNT growth. This may also happen if the reaction temperature is too low, or if the catalyst is not appropriately pre-treated.

- (Fig. 2-11b) Direct deposition of carbon on the substrate, which buries the catalyst and supporting layer. This may occur when the rate of carbon supply is too high, such as when the reaction temperature is too high and gas-phase pyrolysis occurs.

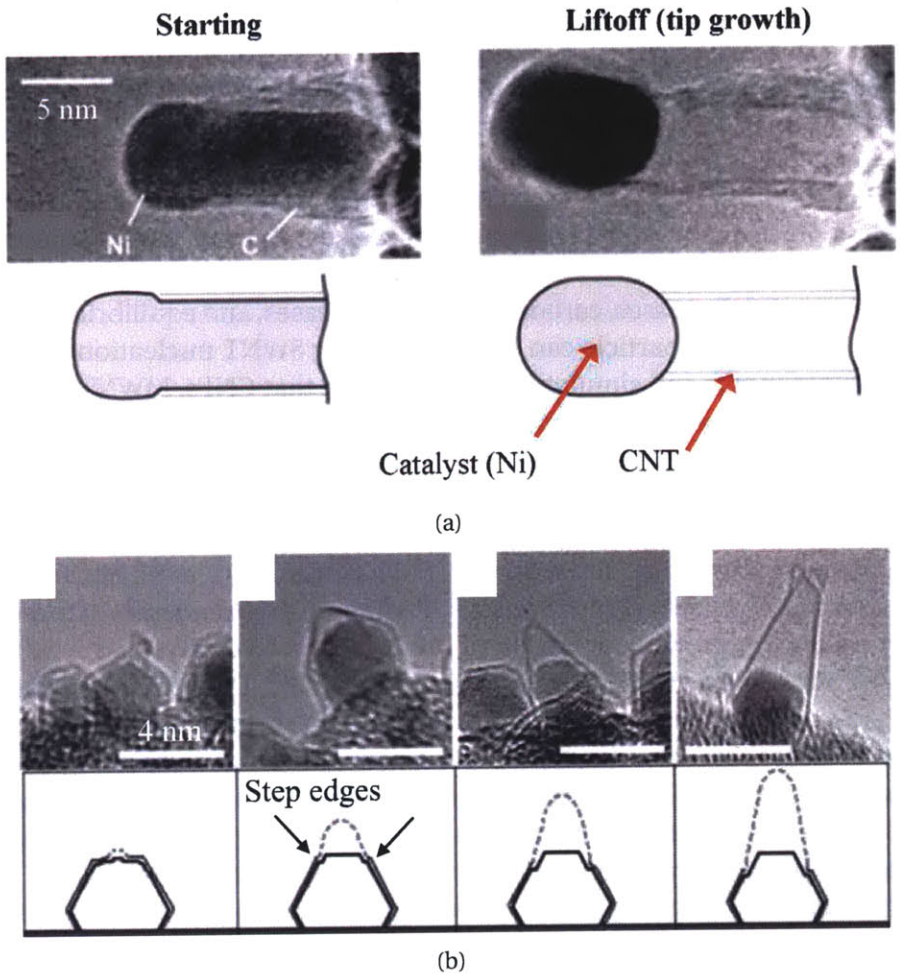

Figure 2-9. Observation of CNT nucleation by CVD: (f) lift-off of a Ni catalyst particle, leaving a MWNT structure behind, observed *in situ* during growth in controlled-atmosphere HRTEM (adapted from [173]); (b) time series of SWNT nucleation from Co, showing growth of cap at step edges, observed *ex situ* by HRTEM (adapted from [174]).

These explanations are highly simplified, and intricate phenomena such as surface diffusion of carbon on the supporting layer and catalyst-support interactions also play significant roles in nucleation.

Further, the relationship between the nucleation conditions and CNT chirality is not understood, and all current growth processes give polychiral ensembles of CNTs. Catalytic decomposition of CO on Co/Mo catalysts has given samples where more than 50% of the semiconducting SWNTs have (6,5) and (7,5) chirality [178], and these "dominant" chiralities are selected by the reaction conditions [179]. For example, changing from $Co/Mo/SiO_2$ to Co/Mo/MgO maintains the SWNT diameter but shifts the (n,m) distribution; changing the reactant composition shifts both diameter and (n,m) distributions; and increasing the reaction temperature increases the SWNT diameter but maintains the (n,m) distribution. The authors conclude that changing the reaction kinetics and the morphology of the catalyst by varying the CVD conditions and

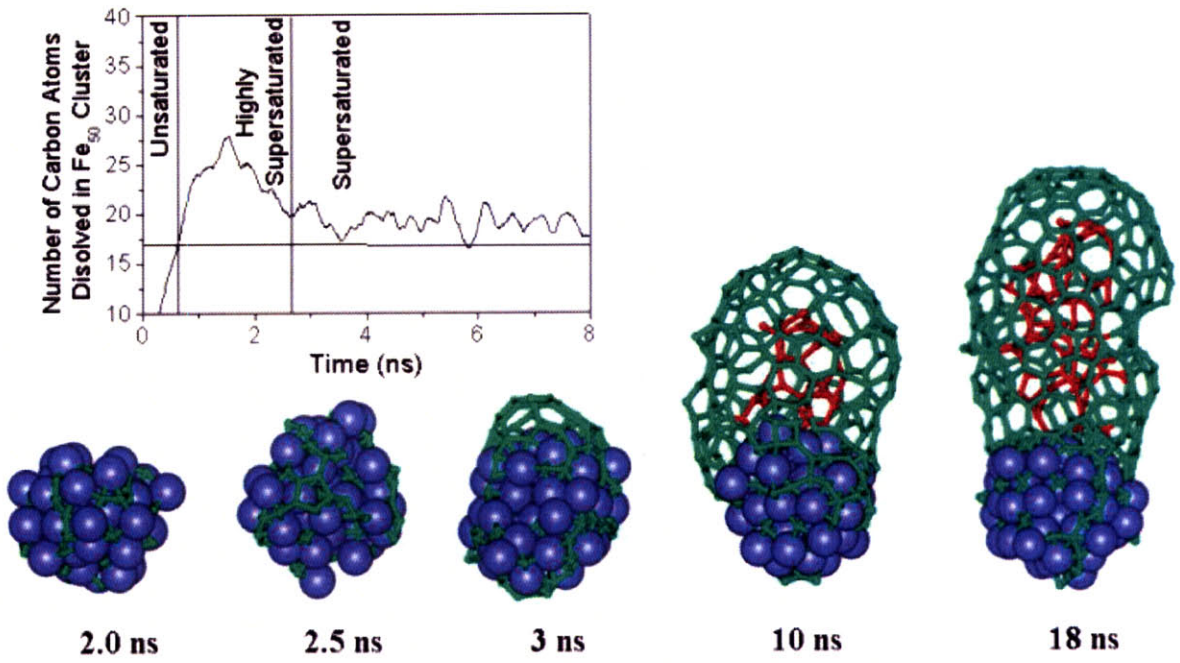

Figure 2-10. Molecular dynamics simulation of SWNT nucleation from a catalyst nanoparticle of liquid Fe, predicting that the catalyst is highly supersaturated before the cap lifts off, and is supersaturated during quasi-steady growth (from [175]).

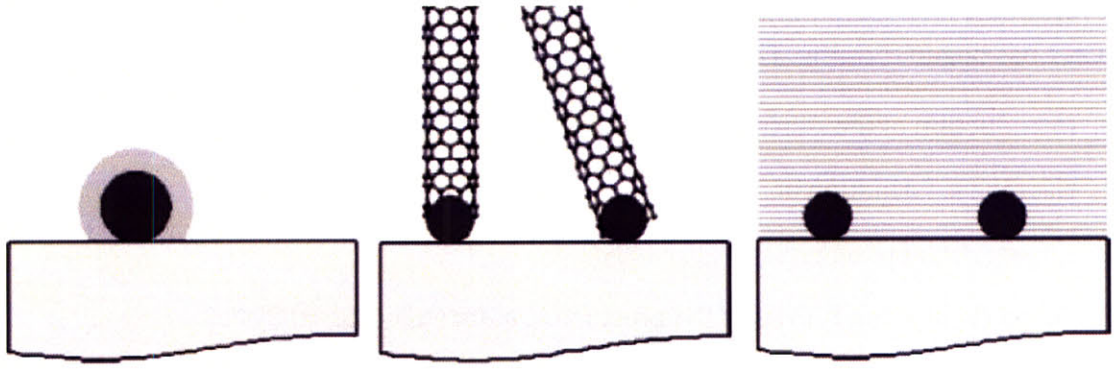

Figure 2-11. Limiting scenarios of carbon deposition, diffusion, and precipitation under CVD reaction conditions (from [177]): (b) rate of carbon supply or conversion is too low, and the catalyst particle is encapsulated by graphitic layers; (c) nucleation and growth conditions are appropriate and CNTs grow normally; (d) rate of carbon supply is too high and carbon coats the catalyst and substrate before nucleation occurs.

metal-support interaction determines which cap structure is stable during nucleation, which in turn establishes the chirality. A similar abundance of (6,5) and (7,5) SWNTs has been found in samples produced using Fe/Co catalysts supported on zeolite, with alcohol as the carbon source [180].

Chiral order within MWNTs, where all layers of a particular MWNT have the same chirality and are in crystallographic register but the MWNTs have a broad distribution of chiralities, has been found in aligned films grown in a nitrogen-containing atmosphere [181, 182]. It appears that nitrogen functions in ordering the walls, as register is not found among MWNTs grown in a nitrogen-free atmosphere. Electron diffraction characterization of small bundles of DWNTs grown from Co/MgO catalyst in CH_4 showed that all inner walls and all outer walls in particular bundles have the same respective chirality, but separate bundles have different preferential chirality pairs [183]. This has not been reported for other DWNT syntheses; further, this unique result suggests that entire DWNT bundles can grow from individual catalyst particles.

2.5.1.3 Growth

The growth phase starts when a CNT cap lifts off from the catalyst particle, and ends when the CNT length stops increasing due to termination of the reaction conditions or deactivation of the catalyst. Like for nucleation, a delicate compatibility among many reaction parameters is necessary for steady CNT growth; however, precisely different sets of conditions may be independently suitable for high-activity nucleation and for high-yield growth. Because *in situ* TEM examination can view growth only for relatively short lengths (<1 μm) under very limiting (low pressure) reaction conditions, and because simulations are computationally feasible for relatively small numbers of atoms and short times, most knowledge about CNT growth dynamics following nucleation is based on empirical studies and adaptation of kinetic models to data.

We can trace a growth "event" as the journey of a carbon atom from its starting constitution (e.g., bonded in a molecule of hydrocarbon gas) to its ending constitution in the CNT lattice. This process is important for nucleation as well; however here we consider the dynamics after the CNT has begun forming. The "path" of carbon is (after [136]):

0. Introduction of the starting reactant mixture;
1. Gas-phase formation of precursors from the starting mixture;
2. Adsorption of precursors at the catalyst;
3. Dissociation of carbon from the precursors, assisted by the catalyst;
4. Carbon transport over/through the catalyst;
5. Reorganization and incorporation of carbon into the CNT structure.

It is vital to realize that the precursor which reaches the catalyst is not likely the same as the reactant which enters the CVD system, primarily due to gas-phase reactions which occur as the reactant flows through the system and is heated as it approaches the growth site. Many studies including those presented in this thesis suggest that thermal or catalytic treatment of

the reactants[3], prior to the interaction with the catalyst, has vital effects on the yield and quality of CNTs [184–189]. Thermally-induced decomposition of a hydrocarbon gives many stable and unstable products along with H_2; for example, C_2H_4 homogeneously reforms into C_2H_2, CH_4, C_2H_6, C_3H_6, C_3H_8, C_4H_4, C_4H_6, and H_2 [190].

Therefore, identification of direct precursors, or more immediately the active intermediates which are formed at the growth conditions, is a key research issue for establishing scalability and controllability of CNT synthesis. This is complicated because the conversion rate of starting reactant to CNTs is typically very low in laboratory-scale CVD methods. Further, as the characteristic times of CVD operation and gas analysis techniques are large compared to the those of growth events, it is difficult to assess the reaction progress in real-time. Eres et al. seek to prevent gas-phase reactions by impinging the substrate with a high-speed gas jet in a low-pressure reactor [191], and thereby demonstrate that C_2H_2 can be a direct precursor to SWNT growth.

However, even if a single precursor is isolated, there are multiple pathways when the precursor adsorbs on a catalytic metal surface. La cava et al. suggest a network of intermediate steps, resulting in growth of fibrous carbon along with "encapsulating" carbon (Fig. 2-12) [192]. The encapsulating carbon stops the reaction by covering the catalyst surface. The primary routes are:

- (1→2→4): Adsorption of a hydrocarbon molecule on the catalyst surface, direct dissociation of atomic carbon, and contribution to the growing filament.
- (1→2→5): Adsorption of a hydrocarbon molecule on the catalyst surface, direct dissociation of atomic carbon, and contribution to encapsulating carbon.
- (6→7→8): Gas-phase polymerization of hydrocarbon molecules, adsorption of a polymerized molecule, and contribution to encapsulating carbon.
- (1→3→8): Adsorption of a hydrocarbon molecule on the catalyst surface, polymerization with additional hydrocarbon molecules on the surface, and contribution to encapsulating carbon.

[3]Moisala et al. [167] give excellent commentary on the high-temperature behavior of hydrocarbons in relation to CNT synthesis:

> "Increasing the number of carbon atoms in saturated hydrocarbons (CH_4, C_2H_6, and C_3H_8) leads to a decrease in the stability of the molecules. Methane is the most stable hydrocarbon and its thermal decomposition begins at approximately 900 °C. Unsaturated hydrocarbons (C_2H_2 and C_2H_4) have more easily disrupted π-bonds in their structure and are thus more reactive and unstable. According to thermodynamic calculations, the decomposition of unsaturated hydrocarbons is already favourable at the lowest calculated temperature (200 °C). As an example, acetylene is thermodynamically unstable already at 25 °C and decomposes to numerous products (including CH_4 and C_2H_4) according to complex kinetics... At high temperatures the decomposition proceeds readily and the reaction products may undergo further reactions, such as decomposition and polymerization. Due to this complex self-pyrolysis, the concentration of hydrocarbons must be controlled in order to prevent catalyst deactivation by amorphous carbon accumulation."

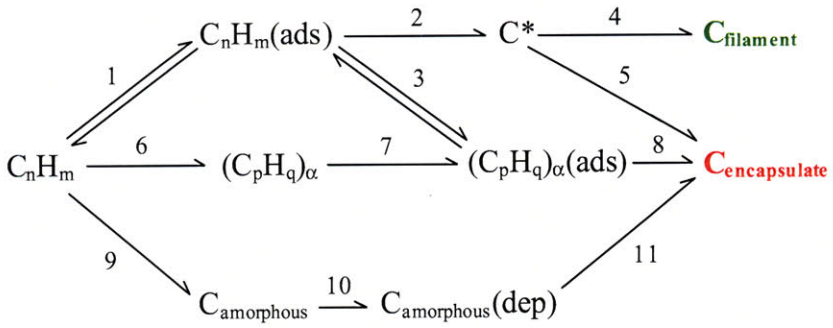

Figure 2-12. Schematic routes for carbon deposition from a hydrocarbon which reacts with a metal surface, resulting in growth of filamentous carbon and deposition of encapsulating carbon (adapted from [192]). This generalized pathway was related to experimental observations of carbon filament growth on Ni, Fe, and Cu foils.

Adsorption is reversible, so a hydrocarbon molecule or chain which sticks to the catalyst does not necessarily contribute to carbon deposition. Further, these routes suggest that polymerized molecules cannot contribute to filament growth, which is contrary to theories of CNT formation from carbon chains and rings [191, 193–195].

Growth terminates when the catalyst is no longer effective at reorganizing carbon into a CNT. Catalyst deactivation may happen gradually or abruptly, for many reasons including accumulation of amorphous (encapsulating) carbon on the catalyst surface (which blocks the area for adsorption of source carbon), contamination of the catalyst by impurities in the growth atmosphere or by interdiffusion with the substrate or supporting layer, or because of a change in the chemical state of the catalyst [160]. Alvarez et al. studied SWNT growth by CVD of CO on Co/Mo/oxide, and observed that Co was oxidized during CNT growth and metallic after growth terminated [196].

Measuring the kinetics of CNT growth, or the progress of CNT length versus reaction conditions and elapsed time, is challenging because it is difficult to access CNTs for measurement in a typical reaction system. The CNTs must grow without external hindrance to give a meaningful estimate of the kinetics of the chemical process itself. When CNTs grow on a substrate, surface interactions among CNTs and with the substrate can slow and terminate growth when the CNTs get stuck or entangled. Therefore, it is most useful to measure the thickness of an aligned film or the length of a suspended individual CNT, either *in situ* or in most cases by examining many samples from a series of reaction conditions and durations. Due to these difficulties along with the wide variation among CVD growth processes, there is not a comprehensive understanding of the limiting kinetics of growth. Further, the balancing attributes (e.g., carbon supply rate, deposition rate, and etching rate) which necessarily vary among processes reveal different kinetic behaviors.

CNFs catalyzed by Fe in CH_4/H_2 were observed to lengthen linearly with time and then abruptly stop growing [47]. The growth rate of individual SWNTs monitored *in situ* by TEM first increases, then attains a quasi-constant value, then gradually decreases, and then growth stops; however, the final CNT length here is only ≈60 nm. The growth rate of VA-CNT films is typically observed to decrease gradually with time. This is attributed to either diffusion limitation as the

reactant must travel through an increasing thickness of CNT film to reach the catalyst at the substrate [159, 161, 197], or to gradual poisoning of the catalyst [162]. For sparse CNT films, it is more likely that catalyst poisoning precedes diffusion limitation, and for dense films it is more likely that diffusion limitation precedes poisoning. A typical present-day thermal CVD process nucleates CNTs at a catalyst activity of ≈5% [198], which gives a film with a CNT volume fraction of only ≈1% [4]. An exceptional result reports catalytic activity of 83% yet a VA-SWNT film grown in this process has a CNT volume fraction of only 3% [199].

Puretzky et al. build a detailed model of VA-CNT film growth by fitting kinetic parameters to *in situ* measurements of film thickness made by monitoring the decaying reflectivity of a silicon substrate as it is masked by the growing film [160]. This model considers competition between growth and accumulation of amorphous carbon which gradually deactivates the catalyst, and thereby qualitatively predicts the dependence of film growth rate and terminal thickness on the growth temperature and partial pressure of the C_2H_2 feedstock. It works better for lower growth temperatures, and therein does not comprehend the dynamics of gas-phase reactions of the carbon source, and their contribution to growth and catalyst deactivation (which are more important at higher temperature).

2.5.2 Roles of additives in CVD

For both for CNT nucleation and growth, it is necessary to balance the counteracting pathways of accumulating desired (CNT) carbon versus undesired (amorphous) carbon. A common strategy is to add an "etching" agent or a combination of such agents to the CVD atmosphere, such as H_2, NH_3, O_2, CO_2, a sulfur-containing compound, or H_2O-vapor. By favorably balancing the decomposition reactions, these additives can significantly increase the nucleation frequency, growth rate, and structural quality of CNTs.

H_2 is perhaps the most common additive to hydrocarbon atmospheres, and its role has been studied for a wide range of catalytic reactions, particularly for reforming of hydrocarbons where solid carbon is an undesirable product [200]. Hydrogen plays two roles in mediating carbon deposition by combining with carbon to reverse decomposition reactions: it reduces gas-phase pyrolysis of a hydrocarbon; and it causes desorption of unstable carbon fragments from the catalyst surface [148, 201]. There are many possible products of hydrogen transfer to or from a hydrocarbon or carbon structure, both in the gas phase and on the metal surface, as studied for decomposition of C_2H_4 and H_2 on bulk Ni by Yoshida et al. (Fig. 2-13) [202]. Unfortunately, the Yoshida et al. study and much related work addresses growth of CNFs rather than CNTs, and therefore does not comprehend possible effects on structural selectivity (e.g., growth of SWNTs versus MWNTs).

A recent study by Zhang et al. [203] reveals that nucleation and growth of small-diameter SWNTs is favored by presence of O_2 in a plasma-enhanced thermal CVD environment of CH_4/H_2. The plasma dissociates H_2 into radicals (H·), which are highly active in etching SWNTs; these radicals must be balanced by O_2[4] in order to have high-yield SWNT growth. Comparison is made to CVD synthesis of diamond, which is commonly conducted in H·-rich atmospheres, where the reactive H· species are known to etch sp^2-hybridized carbon (i.e., CNTs) to give sp^3

[4]Oxygen combines with H radicals by the reaction H + O_2 → OH + O. This reaction has a much higher rate constant than direct oxidation of C into CO.

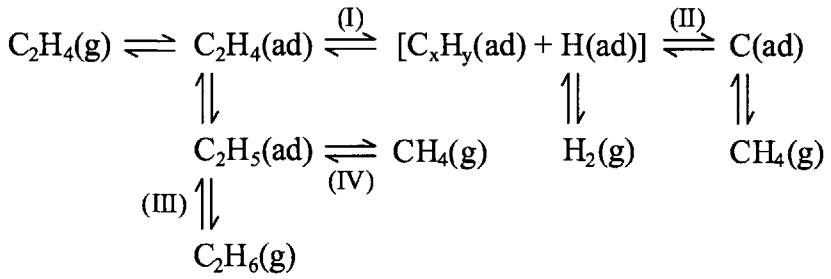

Figure 2-13. Reaction scheme between C_2H_4 and H_2, when reacting in the gas phase and on a catalytic metal surface (adapted from [202]). Legend: (I,IV) dehydrogenation; (II) hydrogenolysis; (III) hydrogenation; (ad) adsorbed species; (g) gaseous species.

carbon (diamond). H· species are are an inevitable byproduct of hydrocarbon deposition, and here the H· concentration is enhanced by plasma-induced dissociation. This both emphasizes the capability of H_2 to etch nuclei of small-diameter SWNTs, and enables direct scavenging of H by adding O_2. Since larger-diameter CNT structures are more stable against H· etching, this work may help to explain why it has been difficult to synthesize SWNTs at high yield, while relatively high-yield MWNT growth has been achieved more routinely. A heavily oxidizing support layer such as Al_2O_3 could also provide an O_2-like promotional effect in stabilizing CNT nuclei.

The O_2-assistance mechanism may also be at work in low-pressure thermal CVD growth of VA-SWNT films using ethanol [204], where each ethanol molecule contains an oxygen atom. Further, rapid growth of mm-thick VA-SWNT films has been achieved by adding ≈100 ppm[5] H_2O-vapor to C_2H_4/H_2 in thermal CVD [205]. The authors hypothesize that H_2O etches amorphous carbon from the catalyst and therefore increases the catalyst lifetime; however, the particular conditions for high-yield nucleation of SWNTs in addition to rapid growth in this process are not clear. Further, the SWNTs grown by H_2O-assisted CVD are ≈3 nm diameter which is much larger (and therefore more stable against etching by H·) than those grown by the method of Zhang et al.

In PECVD processes where a plasma is established directly above the substrate (Fig. 2-6d), in order to dissociate the carbon source and enable growth at low substrate temperatures, NH_3 is frequently added to mediate excessive deposition of amorphous carbon on the substrate [52]. In light of the Zhang et al. study, it makes sense that direct PECVD using NH_3 has typically produced highly disordered CNTs. Recent work using PECVD of pure C_2H_2 after catalyst pretreatment in NH_3 has gives thin films of VA-SWNTs at a substrate temperature of 350 °C [206]. Aside, this result indicates that SWNTs can grow by surface diffusion.

Sulfur, which is typically added as H_2S gas in a fixed-catalyst CVD process [49] or as thiophene (C_4H_4S) in floating catalyst processes [78, 207, 208], has been utilized to increase the yield of CNT growth. Here, sulfur likely improves the rate of carbon diffusion at the catalyst by alloying with Fe [209].

Impurity levels of O_2 and H_2O are common in most CVD systems; these can affect the growth reaction positively or negatively, and in many cases may account for significant non-

[5]This is far less than the a typical water concentration in ambient air, e.g., 50% relative humidity at 21 °C (70 °F) is ≈12,000 ppm H_2O.

repeatabilities in results. For example, a study of SWNT synthesis from aerosol-generated Fe catalyst particles in CO revealed that CO_2 is essential for SWNT growth in this system, and that adding ~500 ppm of CO_2 or H_2O significantly improves the growth results [210]. Variability among initial experiments led to the discovery that Fe adsorbed on the reactor wall formed trace quantities of CO_2 and H_2O by reaction with CO.

2.6 Organization and processing of CNTs

Many applications require organization of CNTs during or after growth, ranging from controlled placement of individual CNTs on substrates to alignment of millions of CNTs in parallel bundles. Organization of CNTs during growth typically involves applying forces to the CNTs or relying on self-assembly to arrange the CNTs in desired configurations and orientations, and notable approaches include those listed below.

- Growth of CNTs suspended between micromachined posts, where a CNT growing from a first post has a free end and adopts a random or flow-directed growth orientation, and eventually anchors to the second post by surface interactions [211–213].
- Growth of mm- to cm-long individual horizontally-aligned CNTs, which are suspended by a gas flow through a tube furnace [142, 214, 215].
- Growth of horizontally-aligned CNTs oriented by electrostatic interactions related to the crystallographic orientation of the substrate [216, 217], or by atomic step edges on the substrate [218].
- Growth of aligned CNTs while applying an electric field, where the electric field induces a torque in the CNT, influencing it to orient itself parallel to the field lines [219, 220].
- Vertically-aligned growth of individual MWNTs and SWNTs due to electric fields induced in PECVD [221, 222], and due to gravity [223, 224].
- Vertically-aligned growth by confinement of the catalyst within a nanoporous template, where the pores guide the CNTs to grow vertically [225, 226], and hierarchical branching of CNTs induced by confinement in branched pores [227]. Growth of vertically-aligned CNT films and microstructures, where CNTs self-orient due to crowding, is discussed thoroughly in Chapter 4.

Organization after growth is complicated by the typically tangled nature of CNTs which result from bulk synthesis processes. As a result, much work focuses on purifying and dispersing disordered assemblies of CNTs to facilitate further processing in solutions or polymers. Further, widespread effort is rapidly advancing our understanding of the surface chemistry of CNTs, and this chemistry could be harnessed by functionalizing CNTs (adsorbing or bonding molecules on the surface) for a multitude of purposes [228–230]. In addition to the fiber spinning and composites fabrication processes mentioned in section 2.4, and beyond the further discussion of CNT-polymer composites in section 4.5, some notable approaches to post-growth processing and organization of CNTs are listed below.

- Fluidically-directed deposition and orientation of CNTs (and other molecules including nanowires and DNA) on substrates, where the flows are confined in microfabricated channels [231–234].
- Formation of intricate CNT patterns on substrates by evaporation of a liquid [235–237].
- Dispersion of CNTs in liquid crystal solutions, and deposition of films in which the CNTs are oriented by the nematic liquid crystal matrix [238, 239].
- Deposition and patterning of CNT films by contact printing from solutions [240].
- Filtering and drying of CNT solutions to make paper [186].
- Separation of metallic and semiconducting CNTs by dielectrophoresis in solution, where metallic CNTs are preferentially attracted to electrodes [241].
- Separation of CNTs by chirality-specific wrapping using DNA strands [242, 243].
- Crosslinking of CNTs by high-temperature annealing in the presence of boron [244], and by electron beam irradiation [245], and coalescence of DWNTs by high-temperature annealing [244].
- Manipulation of the end conformation of CNTs, by annealing in an oxidizing atmosphere to open the ends, and by annealing in vacuum to close the ends [246].
- Purification and etching of CNTs using H_2O_2 [247], HCl [247], HF [248, 249], HNO_3 [249], by oxidation in air [248, 250], by mechanical action and ultrasonication [251], and by microwave heating [252].

Building on these and many other processing methods, the potential applications of CNTs are far too numerous, and are developing too rapidly to make a thorough and lasting presentation here. Some applications, such as electrically-conductive plastics and lithium-ion batteries involving small weight fractions of dispersed low-quality CNTs have been realized commercially, while may others such as transistors requiring individually contacted semiconducting CNTs still face significant research and development challenges. This topic is best left to review articles [8, 9, 253] which are regularly refreshed.

Chapter 3

Synthesis of Tangled Single-Wall CNTs on Silicon Substrates

This chapter discusses growth of films of tangled SWNTs on bare and microstructured silicon substrates by atmospheric pressure CVD, from a catalyst film of $Mo/Fe/Al_2O_3$ deposited by entirely electron beam evaporation. High-density films having a tangled morphology and a Raman G/D ratio of at least 20 are grown over a temperature range of 750–900 °C. H_2 is necessary for CNT growth from this catalyst in a CH_4 environment, and at 875 °C the highest yield is obtained from a mixture of 10%/90% H_2/CH_4. We demonstrate for the first time that physical deposition of the catalyst film enables growth of uniform and conformal CNT films on a variety of silicon microstructures, including vertical sidewalls and silicon "micrograss" fabricated by reactive ion etching, and angled surfaces fabricated by anisotropic wet etching. Our results confirm that adding Mo to Fe promotes high-yield SWNT growth in H_2/CH_4; however, $Mo/Fe/Al_2O_3$ gives poor-quality multi-wall CNTs (MWNTs) in H_2/C_2H_4. Alternatively, an exceptional yield of vertically-aligned MWNTs grows from only Fe/Al_2O_3 in H_2/C_2H_4.

Experiments using long substrate samples, and samples in different flow configurations inside a tube furnace, reveal profound effects of thermal and catalytic decomposition of the reactants, on the CNT growth reaction. These experiments further illustrate the importance of precisely controlling the reactivity of the carbon source for uniform and high-yield growth in desired applications. The flow and substrate configurations featured here can later be used to map the selectivity between CNT properties and the chemistry of the reactant atmosphere.

The results presented in this chapter emphasize the synergy between the catalyst and gas activity in determining the morphology, yield, and quality of CNTs grown by CVD, and enable direct growth of CNT films in micromachined systems for a variety of applications. More immediately, growth of nanostructures such as CNTs on microstructured surface topographies gives hierarchical microscale and nanoscale surface textures. Such substrates could be used to study cell and neuronal growth, influence liquid-solid wetting behavior, and as functional elements in microelectronic and micromechanical devices.

3.1 Growth of conformal films of single-wall CNTs (extended from [1,2])

While many prospective applications require control of the position and orientation of individual or groups of CNTs, there are also many applications for films of tangled CNTs as functional device elements such as thin-film transistors [254], chemical sensors [255], flow sensors [256], and electrical contacts [257]. These films may be grown directly on substrates and subsequently processed by lift-off patterning, functionalization, contact metal deposition, CVD deposition of structural layers, and other methods; alternatively the CNTs may be grown in bulk and selectively deposited onto devices by wet chemical methods [240,258].

Synergy between the catalyst, carbon source, and growth conditions such as temperature and flow rate is vital for obtaining a high yield of high-quality CNTs by CVD. The performance of a catalyst in nucleating and continuing the growth of CNTs depends on several factors in addition to its elemental composition, including the size and surface properties of the catalyst particles and the interactions between the catalyst and the support. The supporting layer can significantly promote or hinder CNT growth by the nature of its physical, chemical, and electronic interactions with the catalyst [259,260]. Especially effective material combinations for CNT growth include Al_2O_3-supported Mo/Fe with CH_4 [261], Ni or Co with C_2H_2 [262], and SiO_2-supported Mo/Co with CO [166] or alcohol [263].

The performance of a catalyst is also coupled to the deposition process, which can roughly be categorized as a physical method such as magnetron sputtering or e-beam evaporation, or a chemical method for preparing metal clusters in solution and subsequently depositing the clusters on a substrate. For sputtering deposition, Shin et al. demonstrated that the temperature and background pressure of the sputtering process, which affects the grain size and density of Ni thin films, is directly related to the length and diameter of vertically-aligned CNTs grown by thermal CVD of C_2H_2 [264]. In comparison, chemical methods [261,265,266] enable direct control of particle composition and particle size, which can give direct control of CNT diameters [154]. However, deposition methods for these solutions, including spin-coating [261,267], dip-coating [268], and contact printing [269,270], are less favorable than physical methods for uniformity over large areas, and for coating of microstructures. For example, with contact printing it is difficult to coat oblique features; with dip-coating the solution tends to collect and dry in recessed areas; and with spin-coating, surface tension effects oppose uniform coating of topography and non-uniformity is especially prevalent as solutions wick away from edges and corners of features. It is also straightforward to pattern physically-deposited metal films to micron-scale dimensions using liftoff of standard image-reversal photoresist in acetone, and therefore dictate uniform area-selective growth of CNTs on large substrates.

This section presents a parametric study of CNT growth from a Mo/Fe/Al_2O_3 catalyst deposited by e-beam evaporation, and demonstrates uniform and conformal growth of CNT films by atmospheric-pressure thermal CVD on a variety of silicon microstructures. Presence of H_2 in addition to CH_4 is necessary for CNT growth in our process, and dense films of high-quality SWNTs are grown over a wide range of conditions from a H_2/CH_4 mixture. Our experiments confirm that Mo promotes SWNT growth from CH_4, and indicate that Mo hinders MWNT growth from C_2H_4. Alternatively, a Fe/Al_2O_3 film in C_2H_4 gives an exceptional yield of vertically-aligned MWNTs.

3.1.1 Materials and methods

3.1.1.1 Catalyst film

A catalyst film of 20 nm Al_2O_3, 1.5 nm Fe, and 3 nm Mo is deposited by e-beam evaporation in a single pump-down cycle using a Temescal VES-2550, with a FDC-8000 Film Deposition Controller. The substrates are (100)-orientation 150 mm diameter silicon wafers (p-type, 1-10 Ω-cm, Silicon Quest International), which have been cleaned using a standard "pirahna" (3:1 H_2SO_4:H_2O_2) solution. After catalyst deposition, no further cleaning or dedicated oxidation is necessary prior to CNT growth. The Al_2O_3 is deposited by direct evaporation from a crucible of high-purity crystals, rather than by evaporation of Al with a slight background pressure of O_2 [271,272], or by other methods such as spin-coating of a sol-gel precursor [193]. While CNT growth from catalyst metals deposited on a layer of Al has been reported [273,274], Al must be oxidized to prevent damage to the catalyst by formation of an Al-Si eutectic at 577 °C [275].

CNT growth from Mo/Fe catalysts is well-known, and addition of a small amount of Mo (as low as 20% [273]) to Fe significantly enhances catalytic activity for CNT growth. Furthermore, while Fe is a sufficient monometallic catalyst under a wide range of conditions, CNT growth from pure Mo (supported on Al_2O_3 particles) has been reported only in CO at 1200 °C [165]. Deng et al. suggest from simulations that certain bimetallic catalysts give a higher CNT yield than monometallic catalysts because one metal (in the case of Mo/Fe, Mo) is responsible for nucleation, and the other metal is responsible for growth and defect repair [150]. However, considering much experimental evidence that Fe is necessary for nucleation and that an unfavorable ratio of Mo/Fe significantly affects yield, the complex interaction of Fe and Mo may not be divisible into primary behaviors. It has also been hypothesized that molybdenum carbide forms from Mo in a hydrocarbon environment, which causes aromatization of CH_4, which in turn improves nanotube growth from Fe [193,276].

Further, compared to other support materials including TiN and TiO_2, Al_2O_3 is an especially effective support layer for Fe catalysts for CNT growth [193,277,278]. The performance of Al_2O_3 can be attributed to strong dispersion effects which limit agglomeration of Fe clusters on the Al_2O_3 surface [260], the nature of metal-support interactions in promoting electron transfer between the catalyst and the support [259], high surface roughness and porosity which improves the diffusion of reactant gases to the catalyst clusters [277,279], and enhanced decomposition of hydrocarbons on the Al_2O_3 surface [177,280]. Some reports indicate the crystallinity of the support material critically affects CNT growth, whereas others indicate that amorphous support materials are better supports. For example, Hongo et al. demonstrate that SWNT growth on Fe-coated Al_2O_3 is affected by both the film thickness and the crystallographic orientation of the substrate, which determines the interaction energy with Fe. On the other hand, Vander Wal et al. qualitatively show that fumed (amorphous) oxides give higher yield than powdered crystalline oxides. In this study, the effect of crystallinity may be masked by the increased surface area allowing more uniform dispersion of the metal catalyst particles. Furthermore, the support layer should be sufficiently thick to prevent interdiffusion of the catalyst metal into the substrate. Therefore, while it has been demonstrated that the CNT growth is also highly sensitive to support layer thickness [281,282], relatively steady behavior should be observed beyond a certain thickness.

3.1.1.2 CVD procedure

CNT growth is performed in a conventional single-zone atmospheric pressure quartz tube furnace, having an inside diameter of 22 mm and a 30 cm long heating zone (section 6.1). Flows of argon (Ar, 99.999%, Airgas), methane (CH_4, 99.995%, BOC), ethylene (C_2H_4, 99.5%, Airgas), and hydrogen (H_2, 99.999%, BOC) are metered using manual needle valve rotameters (Matheson Tri-Gas and Gilmont Instruments). The rotameters were purchased new and were calibrated. We estimate 1-2% relative accuracy and repeatability of the flow ratios, and 5% accuracy of the total flows. For best consistency, the parametric studies of growth conditions used samples taken from the same wafer.

After loading the sample in the tube, the furnace is flushed with 400 sccm Ar for 10 minutes to displace atmospheric air. Next, the furnace temperature is ramped linearly to the setpoint temperature, for 30 minutes, with a flow of 400 sccm Ar. The Ar flow is maintained for an additional 15 minutes while the furnace temperature stabilizes at the setpoint, and then the reactant gases are introduced for the growth period of typically 15 minutes. 400 sccm Ar is again introduced for 10 minutes to displace the growth gases from the tube and then the Argon flow is reduced to a trickle ($\approx$10 sccm) while the furnace cools to below 150 °C.

3.1.1.3 CNT characterization

Scanning electron microscopy (SEM) of as-grown samples is performed using a Philips XL30 FEG-ESEM in high-vacuum mode, at 5 keV. X-Ray photoelectron spectroscopy (XPS) is performed using a Kratos AXIS Ultra Imaging Spectrometer.

Resonant Raman spectroscopy [283] is performed using a Kaiser Hololab 5000R Raman Microprobe, with 514.5 nm (2.41 eV) Argon-Ion excitation (Coherent), and a 100X magnification objective which is focused to maximize the intensity of the Si signal. Spectra are taken with a single 15 s accumulation at each of five points per sample, and the individual spectra are shifted to match at the 521 cm^{-1} silicon peak and then averaged. The G/D peak intensity ratio is used as a rough measure of sample quality, indicating the relative response of graphitic carbon (at 1589 cm^{-1}) to defective carbon (at 1350 cm^{-1}) from intrinsic defects in the CNTs or amorphous carbon on the CNTs and the substrate. The G/Si ratio is an ordinal approximation of CNT yield. However, it must be cautioned that an increase in the quantity of CNTs both increases the G-band intensity and decreases the visibility of the substrate. The catalyst film and any amorphous deposits on the substrate decrease the Si signal. The relative intensity of the D-bband peak increases and the Si peak decreases with higher magnification (smaller spot size). Therefore, it is imperative to use the same magnification and focus for examining each sample.

Section 3.2 discusses further details of CNT characterization by SEM imaging and Raman spectroscopy.

3.1.2 Growth on flat silicon substrates

3.1.2.1 Study of growth temperature

To study the effect of growth temperature, otherwise identical experiments are conducted using the Mo/Fe/Al_2O_3 film on Si, with 40/360 sccm H_2/CH_4, at temperatures ranging from 725–1025 °C. The wafer is manually scribed and cleaved into 1×1 cm samples. Fig. 3-1 shows SEM images of representative samples. No growth occurs at 725 °C, while at 750–900 °C a film of densely tangled small-diameter CNTs is grown. At 925 °C, CNTs protrude from cracked clusters of large particles on the substrate, and CNTs rarely grow from the substrate areas in between the clusters. Because of the low density, we observe that these CNTs are individually at least several μm long, and are sometimes straight and suspended between neighboring clusters. At 1025 °C, soot forms in the furnace tube, likely due to the self-pyrolysis of CH_4. The soot particles, shown in Fig. 3-2, are approximately spherical with a diameter of 1 μm. Large-diameter fiber structures grow on the Mo/Fe/Al_2O_3 film at 1025 °C, and are also shown in Fig. 3-2.

The Raman spectra in Fig. 3-3 indicate that the films of Fig. 3-1 contain a large proportion of high-quality single-wall CNTs. This judgment is based on the position of the G peak near 1589 cm^{-1}, the high G/D ratio, and the presence of strong RBM peaks, and is confirmed by TEM examination. Several RBM peaks are observed on each sample in the range of 160–310 cm^{-1}, indicating SWNT diameters of approximately 0.8–1.6 nm. Fig. 3-4 plots the average G/D and G/Si ratios for each sample, confirming the observation from SEM imaging that the CNT yield reaches a sharp maximum at approximately 825 °C, and showing the quality is relatively constant at $G/D \approx 25$ for 775–875 °C. The variation in G/D and G/Si values from spectra taken at different points on the 825 °C sample is much less than samples grown at neighboring temperatures, demonstrating that this condition also gives a very uniform film texture.

3.1.2.2 Study of gas composition

To evaluate the effect of gas composition on CNT growth, otherwise identical experiments are conducted using 1×1 cm samples at 875 °C and a total flow of 400 sccm, varying the partial flows of H_2 and CH_4. No CNT growth occurs from these samples in a pure CH_4 atmosphere, and CNT growth is first observed for $H_2/CH_4 \approx 0.04$. Fig. 3-5 shows SEM images of selected samples, and Fig. 3-6 shows the G/D and G/Si ratios from the Raman spectra. CNT yield rapidly reaches a maximum at $H_2/CH_4 \approx 0.09$, and is locally minimal at $H_2/CH_4 \approx 0.20$. Quality is first locally maximized at $H_2/CH_4 \approx 0.06$, then decreases as H_2 content increases, and then increases to a second maximum at $H_2/CH_4 \approx 0.20$. Although uncertainty in our data precludes a more certain conclusion, it appears that the maximum yield coincides with the first local minimum in quality, and that the local minimum of yield and maximum of quality at $H_2/CH_4 \approx 0.20$ are also coincident. An analogous behavior is observed on single long samples (1×10 cm) processed in pure CH_4. On these samples, CH_4 thermally and catalytically decomposes into an evolving mixture containing H_2 and CH_4 as the gas flows along the surface of the sample, which causes the morphology, quality, and yield of CNTs to change significantly. These experiments are discussed in section 3.3.1.

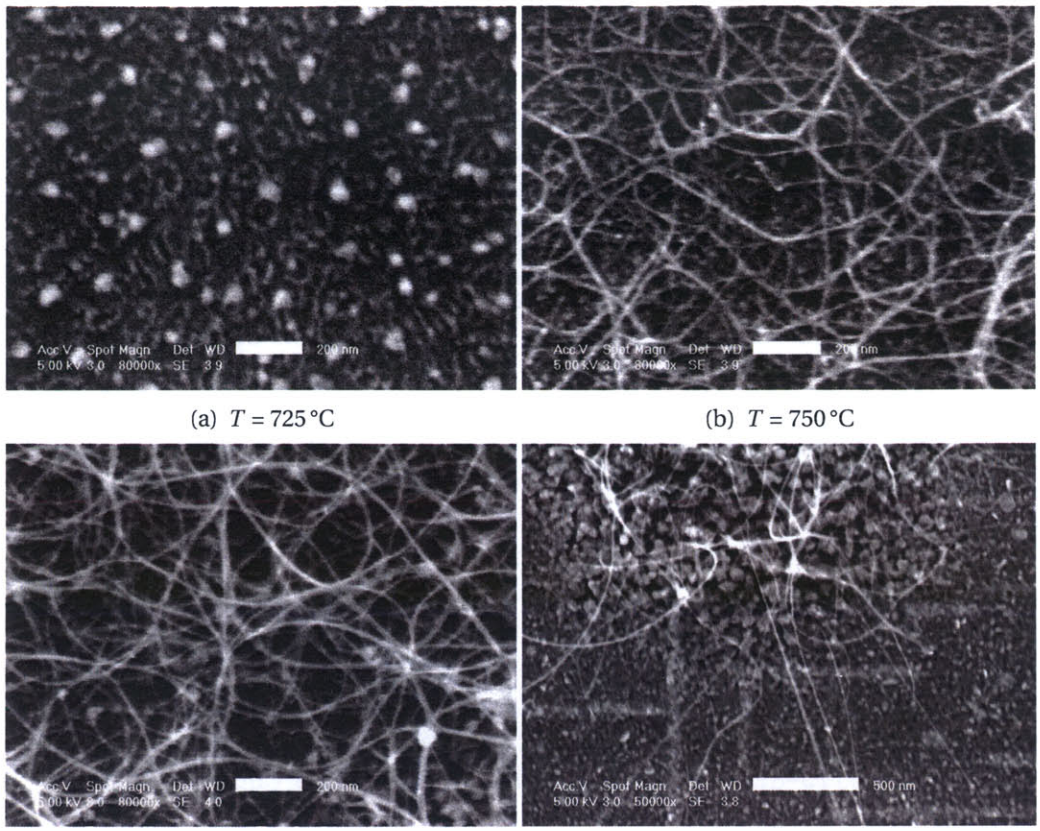

(a) $T = 725\,°C$ (b) $T = 750\,°C$

(c) $T = 825\,°C$ (d) $T = 925\,°C$

Figure 3-1. SEM images of $Mo/Fe/Al_2O_3$ film processed in 400 sccm of 80:20 H_2/CH_4, at 725–925 °C. Scale is 0.2 μm on (a)–(c), and 0.5 μm on (d).

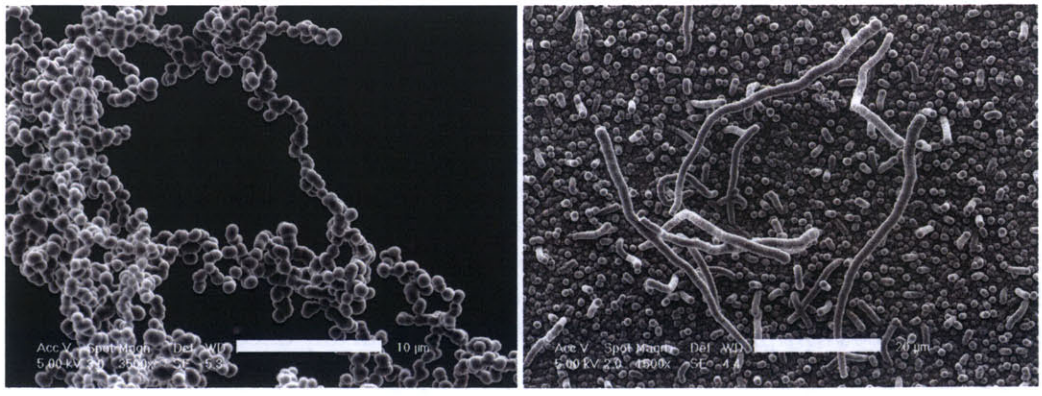

(a) (b)

Figure 3-2. Products formed at 1025 °C: (a) soot in furnace tube from pyrolysis of CH_4, scale 10 μm; (b) fibrous structures on $Mo/Fe/Al_2O_3$ film, scale 20 μm.

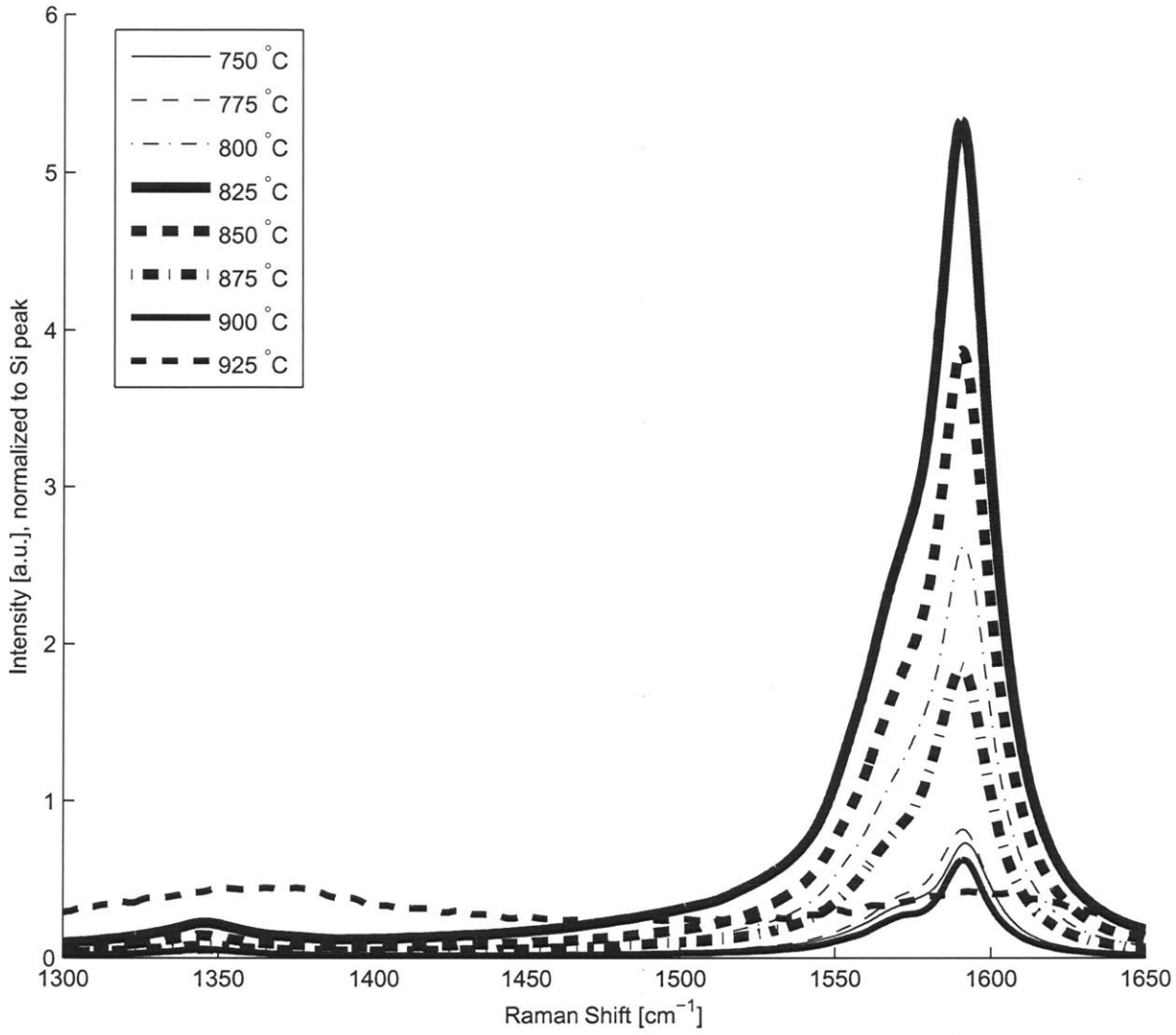

Figure 3-3. G and D band regions of Raman spectra for samples with growth temperature of 750–925 °C, normalized to height of Si peak.

3.1.2.3 Study of flow rate

Within the limits of our flowmeters, increasing the total flow rate for a given H_2/CH_4 ratio increases both CNT quality and yield, whereas below a given flow rate no CNT growth occurs. Fig. 3-7 compares the Raman spectra of samples grown at total flows of 200, 400, and 1200 sccm, at 875 °C, with H_2/CH_4 = 0.11. Adding a slight flow of Ar (e.g., 100 sccm) to the mixture decreases CNT yield. With much more Ar (e.g., 800 sccm) in addition to 40/360 sccm H_2/CH_4 (H_2/CH_4 = 0.11), there is no CNT growth at 825 °C. We have not conducted a systematic study of this effect; however, the surface reaction which grows CNTs may be hindered by adsorption of Ar at the catalyst [284,285].

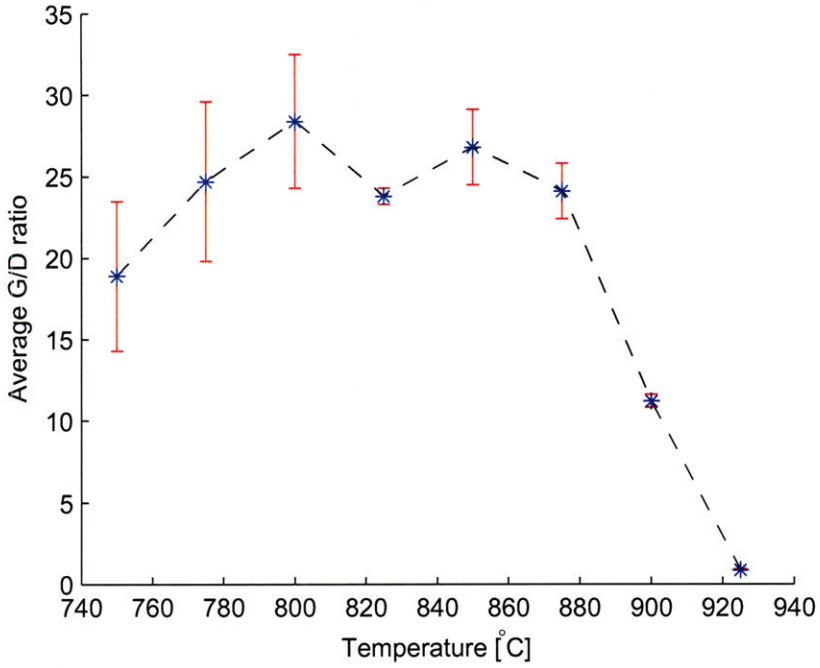

(a)

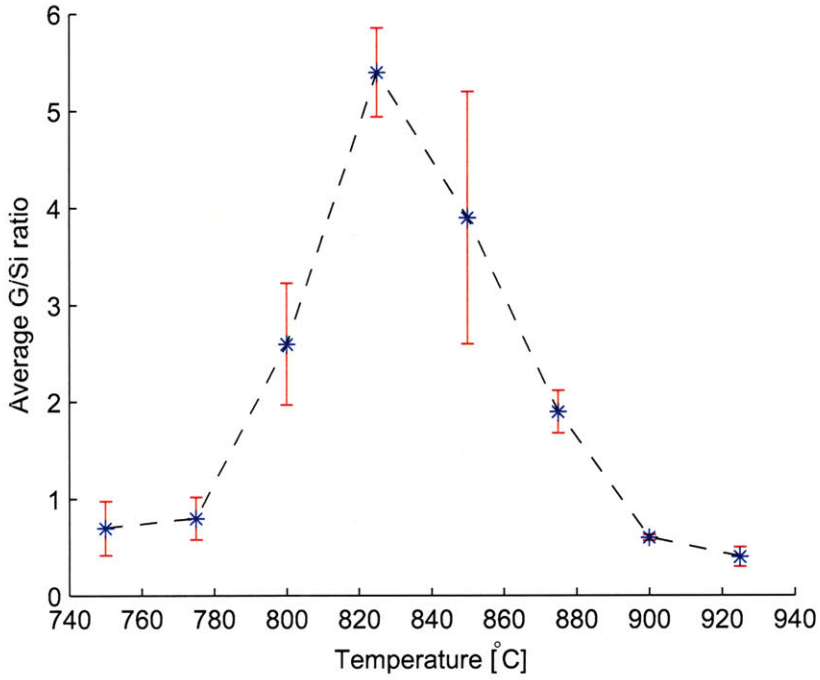

(b)

Figure 3-4. Peak intensity ratios from Raman spectra (Fig. 3-3) of samples grown at 750–925 °C: (a) G/D ratio, indicating sample quality; (b) G/Si ratio, indicating sample yield.

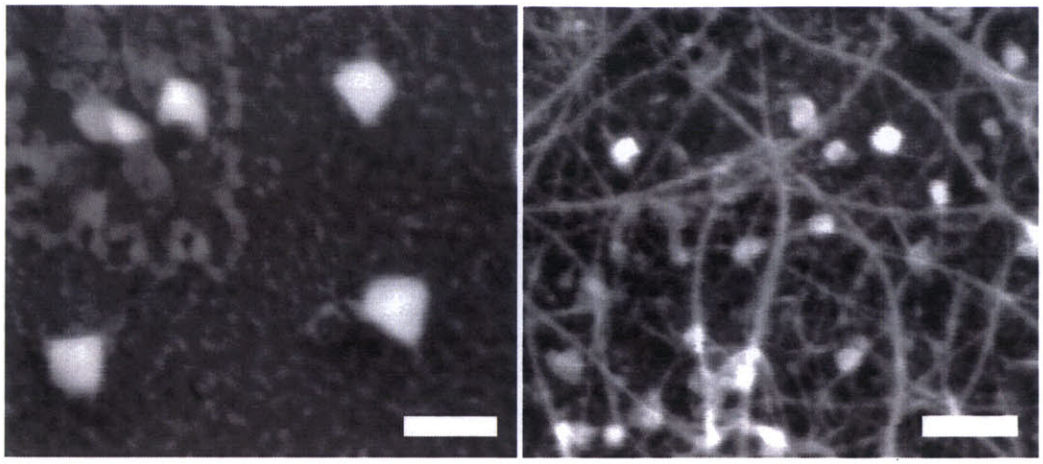

(a) (b)

Figure 3-5. Samples processed in 400 sccm of H_2/CH_4 at 875 °C, with (a) $H_2/CH_4 = 0.02$, insufficient for CNT growth; (b) $H_2/CH_4 = 0.09$, which gives highest yield. Scales 0.2 μm.

3.1.2.4 Study of annealing and heating atmospheres

CNT growth from the $Mo/Fe/Al_2O_3$ film is also affected significantly by "pre-baking" the catalyst sample, and by changing the atmosphere in which the catalyst is heated to the growth temperature. First, we consider a sample which is pre-baked in Ar for 30 minutes at 875 °C, subsequently cooled to room temperature, and then treated with the previously described ("normal") Ar heating and H_2/CH_4 growth sequence. The G/Si ratio and the G/D ratio decrease by 10–20% compared to a sample that was not pre-baked. When the catalyst is not pre-baked and is heated to the growth temperature in an atmosphere of 5% H_2 in Ar, no CNT growth occurs. However, when the sample is first pre-baked in Ar, cooled to room temperature, and then heated in 5% H_2/Ar before the growth step, there is moderate CNT yield and the G/Si ratio is about 50% less than on a sample that is not pre-baked and was grown by the normal sequence (Fig. 3-8, Fig. 3-9). However, the G/D ratio is 80% higher than for the normal procedure without pre-baking, indicating a significant increase in CNT quality. When a sample is first treated in 5% H_2/Ar at 875°C, then cooled, and then processed normally, the CNT yield is very low, as confirmed by a sparse network of CNTs seen on the substrate and a G/Si ratio of only 0.05.

Ex situ X-ray photoelectron spectroscopy (XPS) data shown in Fig. 3-10 indicates that the Mo layer in the catalyst film is continuous as deposited. This is apparent because only Mo(3p) and Mo(3d) appear in the spectrum of an as-deposited sample, while peaks for Al, Fe, and Mo appear in the spectrum of a sample annealed in Ar for 30 minutes at 875 °C. Angle-resolved XPS measurements, in which the penetration depth of the X-ray beam is varied by tilting the sample stage, show qualitatively how the chemical states of the elements change through the thickness of the film, due to interdiffusion upon annealing in Ar at 875 °C. The penetration depth is a maximum of 3–4 nm when the stage is horizontal (0° tilt), and decreases as the stage is tilted to the maximum angle of 70°. Fig. 3-10b shows that each element is more strongly oxidized near the surface of the film, because the peaks shift to higher binding energy as the stage tilt angle decreases [286]. The Al 2p spectrum shows the characteristic peaks of Al at approximately 72 eV and Al_2O_3 at approximately 75 eV, and the relative strength of the Al_2O_3 peak increases at the

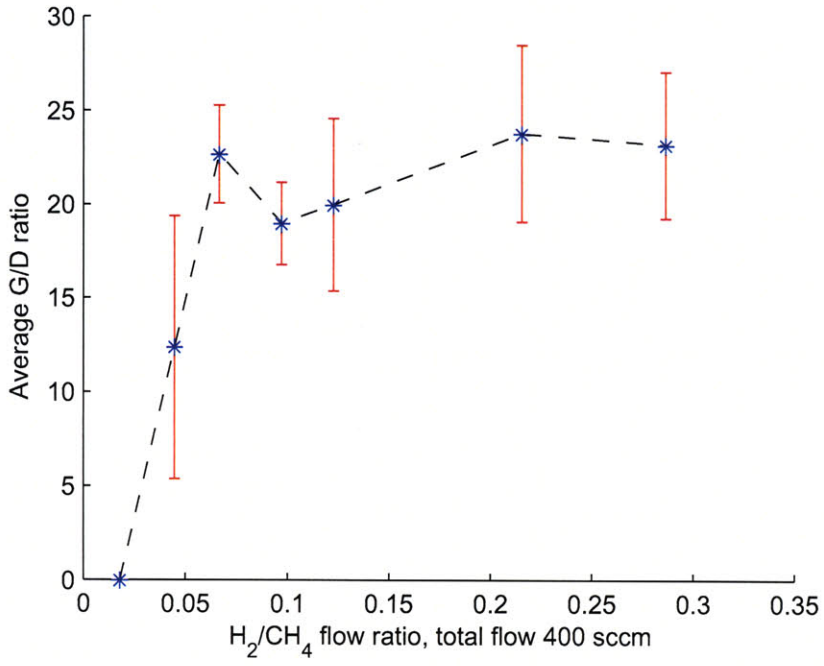

(a)

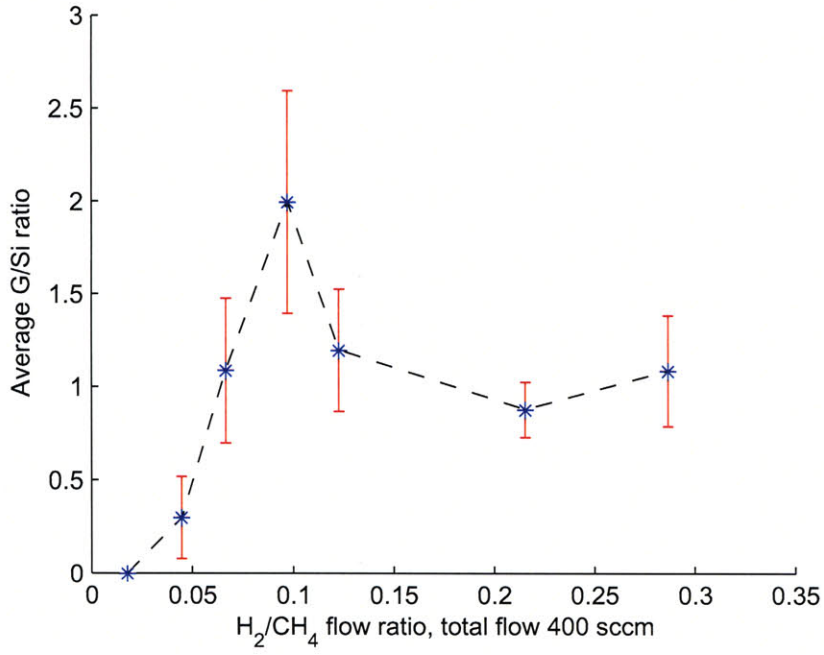

(b)

Figure 3-6. Peak intensity ratios from Raman spectra of samples processed in varying H_2/CH_4 environments: (a) G/D ratio; (b) G/Si ratio.

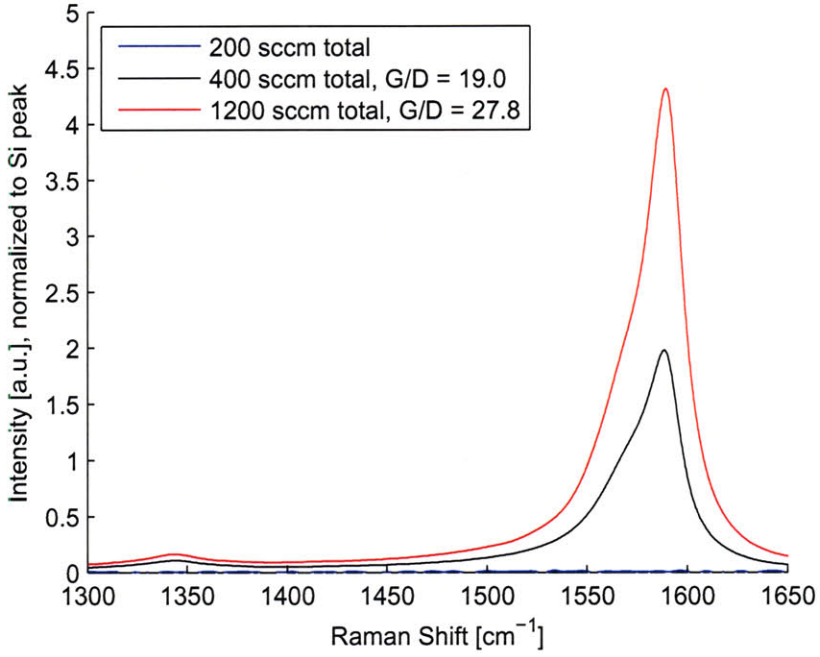

Figure 3-7. Effect of total flow rate on samples processed with H_2/CH_4 =0.11, at 875 °C.

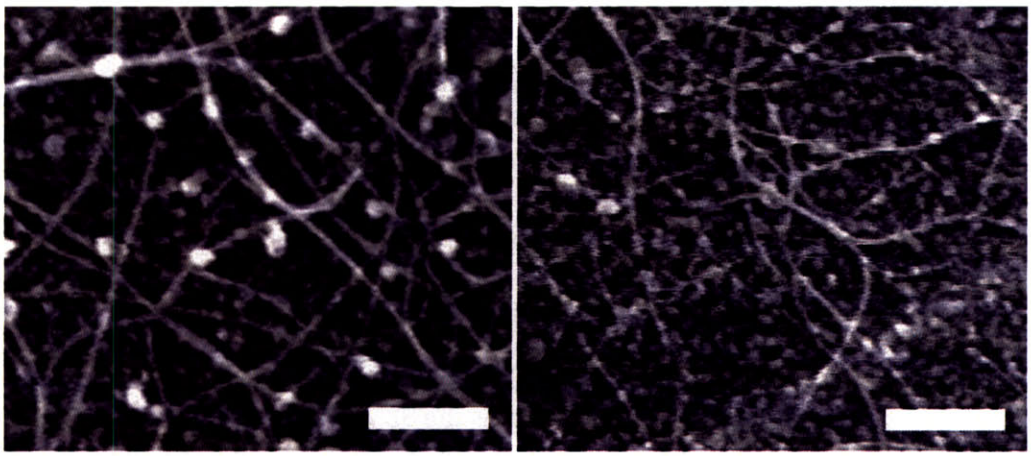

(a) (b)

Figure 3-8. Effects of annealing and pre-heating procedure: (a) sample annealed in Ar and heated in H_2/Ar; (b) sample annealed in H_2/Ar and heated in Ar. Scales 0.2 μm.

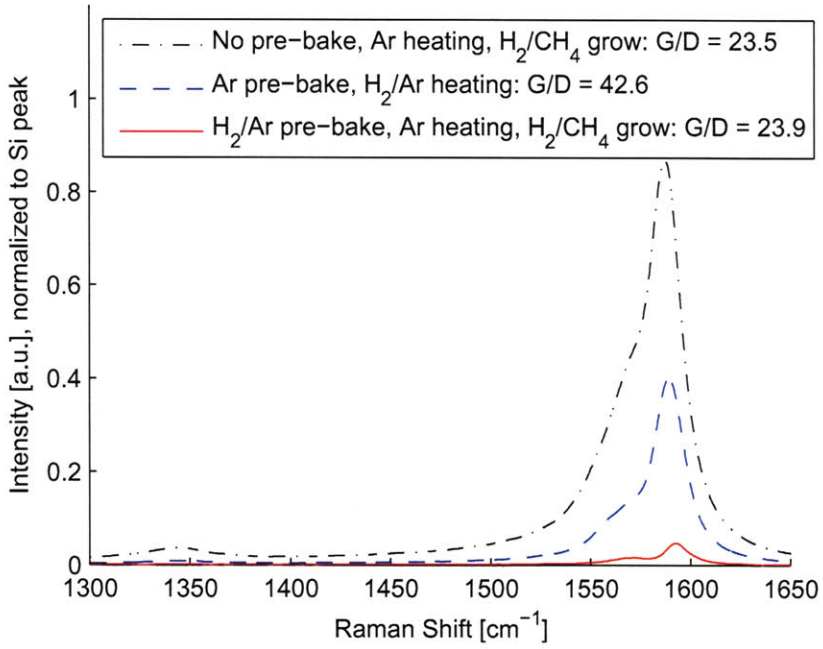

Figure 3-9. Raman spectra of samples prebaked and heated in Ar and H_2/Ar atmospheres.

surface. The doublet in the Fe 2p spectrum shows Fe_2O_3 ($2p_{3/2}$ at 711 eV and $2p_{1/2}$ at 725 eV), with a weak shift toward elemental Fe ($2p_{3/2}$ at 707 eV and $2p_{1/2}$ at 720 eV) as the penetration depth increases [287]. The Mo 3d signature suggests an increasing proportion of MoO_3 ($3d_{5/2}$ at 233 eV and $3d_{3/2}$ at 236 eV) near the surface, relative to Mo ($3d_{5/2}$ at 228 eV and $3d_{3/2}$ at 231 eV).

3.1.2.5 Process variability

The Mo/Fe/Al_2O_3 catalyst film was deposited on silicon wafers in eight instances, with desired and measured (by quartz crystal monitor in the electron beam evaporator) layer thicknesses listed in Table 3.1.2.5. The measured thickness of Fe is typically 10–20% greater than the desired thickness; for Mo, the overshoot is typically 20–30%.

The variability of growth was evaluated by cleaving a single sample ($\approx 1 \times 1$ cm) from a wafer from each catalyst deposition and then processing all eight samples in the same growth experiment, at 825 °C, with 400 sccm flow ($H_2/CH_4 = 0.25$). The density and texture of all the films is very similar (Fig. 3-11), except for the sample from deposition #5 (run name "TL6"), which appears cleaner and has a substantially lower density of CNTs than the other samples. Raman spectroscopy of these samples (Fig. 3-11) confirms the SEM observations, revealing that #5 has the highest G/D ratio and the lowest G/Si ratio. Deposition #5 has the highest Mo/Fe ratio (2.94); however, since there is no apparent correlation between Mo/Fe ratio (otherwise ranging from 2.12–2.59) and the quality and yield of other samples, we cannot certainly attribute the differences in #5 to high Mo content. Excluding deposition #5, the average G/D ratio among the depositions is 26.5 $\pm$4.6 (2-σ variation), and the average G/Si ratio is 5.3 $\pm$2.1.

Last, the uniformity of catalyst deposition was evaluated by taking five samples from differ-

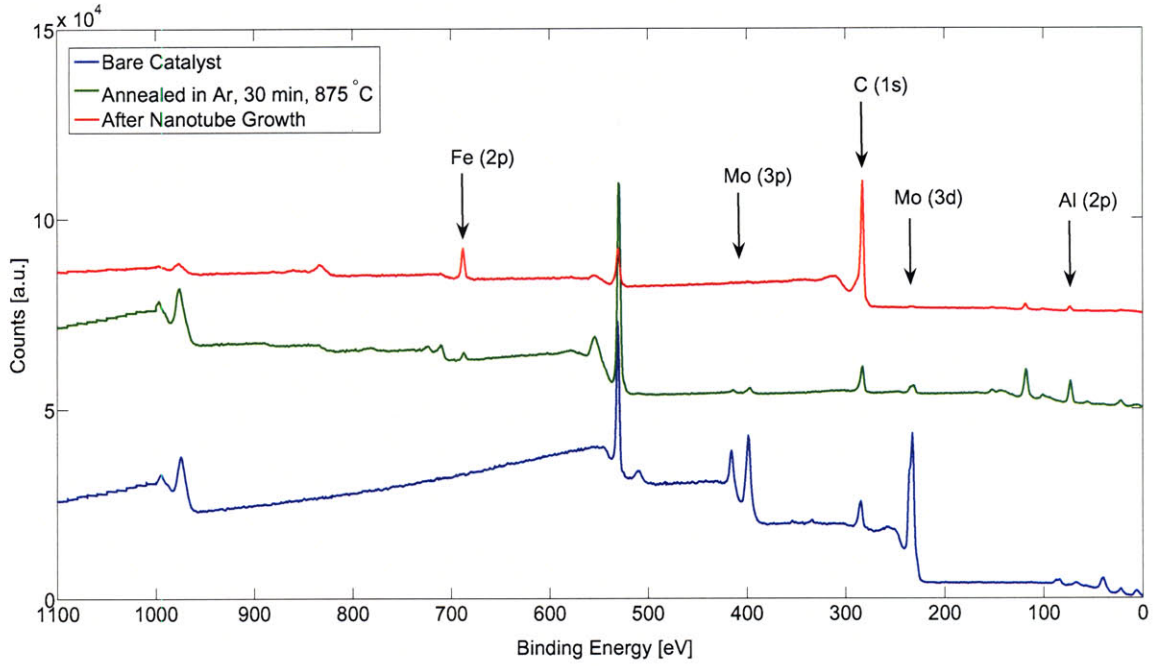

(a)

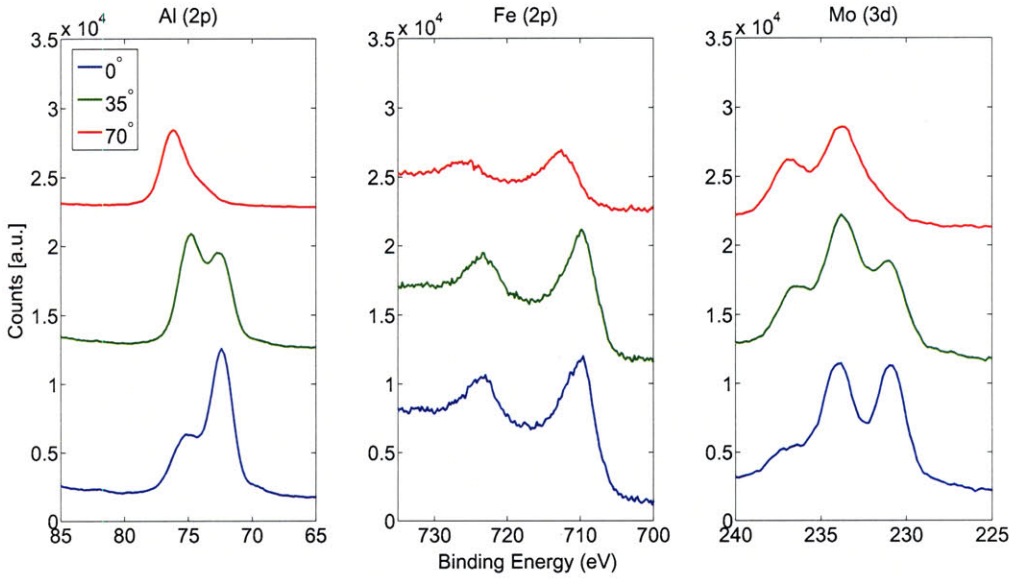

(b)

Figure 3-10. Structure and composition of $Mo/Fe/Al_2O_3$ catalyst film, measured by XPS: (a) comparison of as-deposited, annealed, and CNT samples; (b) through-thickness evolution of annealed sample, measured by angle-resolved XPS.

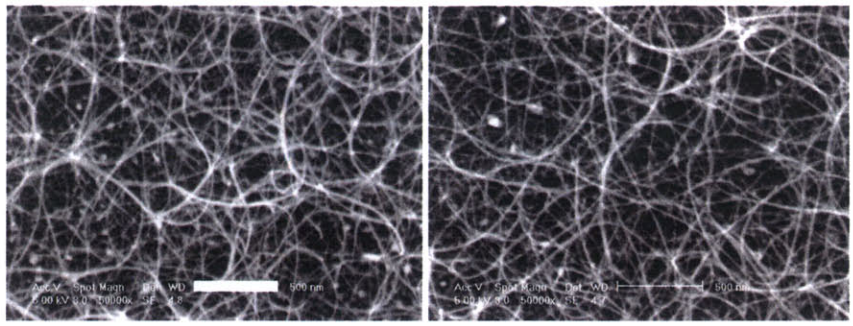

(a) TL2, "Deposition #1"

(b) TL3, "#2"

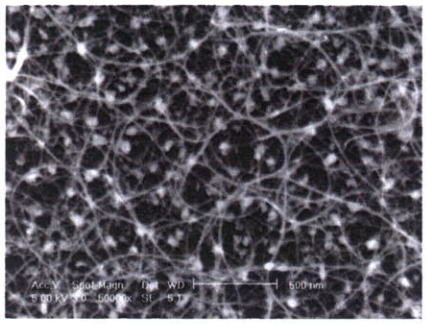

(c) TL4, "#3"

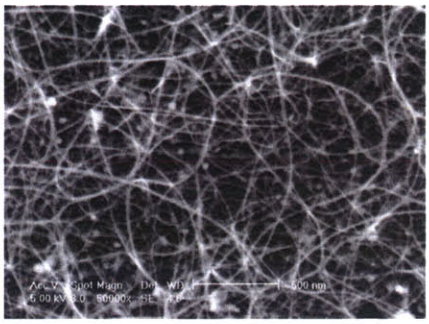

(d) TL5, "#4"

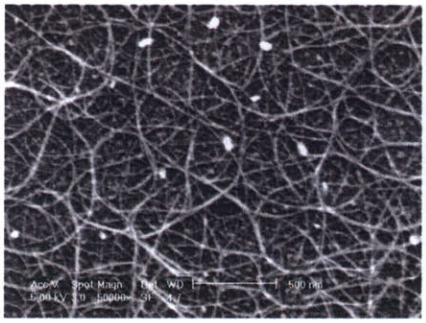

(e) TL6, "#5"

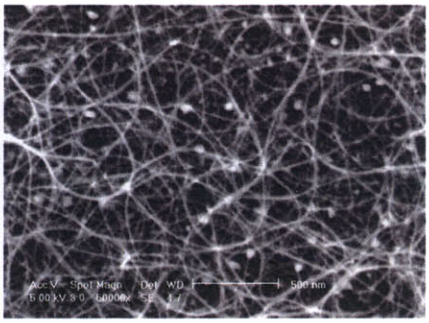

(f) TL7, "#6"

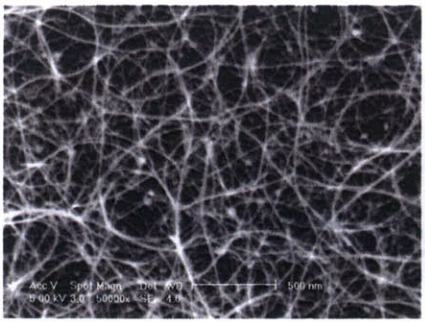

(g) TL8, "#7"

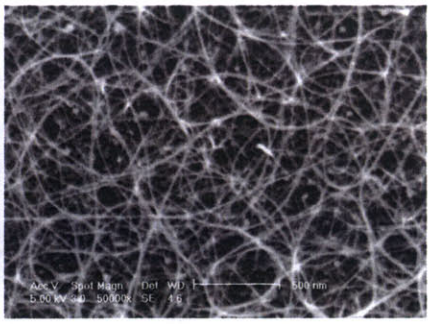

(h) TL10, "#8"

Figure 3-11. SEM images of CNT films on samples taken from eight different e-beam depositions of $Mo/Fe/Al_2O_3$ catalyst. All samples were processed in the same growth experiment, with $H_2/CH_4 = 0.25$, at 825 °C. The texture of the samples is very similar, except for sample #5 (deposition TL6), which has a high Mo/Fe ratio. Scales 0.5 μm.

Deposition		Mo/Fe/Al_2O_3Thickness [nm]		**Mo/Fe Ratio**	
Name	#	Desired	Measured	Desired	Measured
TL2	1	20.0/1.5/3.0	20.9/1.6/4.1	2.00	2.56
TL3	2	20.0/1.5/2.5	21.1/1.7/3.6	1.67	2.12
TL4	3	20.0/1.5/2.5	20.9/1.7/4.4	1.67	2.59
TL5	4	20.0/1.3/2.6	20.6/1.5/3.3	2.00	2.20
TL6	5	20.0/1.3/2.6	20.1/1.6/4.7	2.00	2.94
TL7	6	20.0/1.5/3.0	20.0/1.7/4.1	2.00	2.41
TL8	7	20.0/1.5/3.0	20.0/1.7/4.0	2.00	2.35
TL10	8	20.0/1.5/2.9	21.4/1.7/3.9	1.93	2.29

Table 3.1. Film thicknesses for eight depositions of Mo/Fe/Al_2O_3 catalyst layers. Desired values were programmed into the e-beam controller, and measured values are as reported by the quartz crystal monitor inside the e-beam chamber.

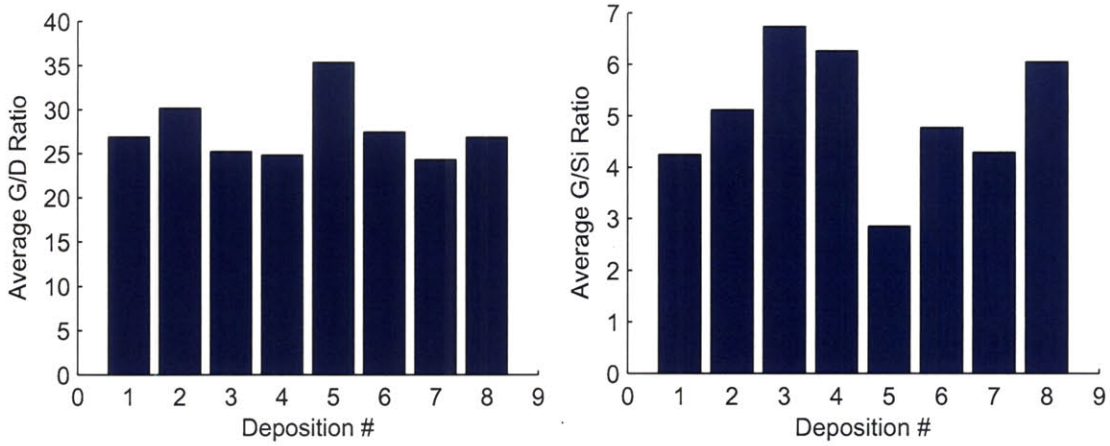

(a) (b)

Figure 3-12. Comparison of (a) G/D and (b) G/Si ratios from Raman spectra, averaged over five spots on each of Mo/Fe/Al_2O_3 depositions #1–8.

ent areas of a single wafer (#8, TL10), and processing these samples in the same growth experiment, at 825°C and H_2/CH_4, and characterizing the resulting CNT films by Raman spectroscopy (Fig. 3-13). This gives 2-σ variation of $G/D = \pm 3.1$ and $G/\text{Si} = \pm 0.25$.

3.1.2.6 Discussion

The G/D ratio of our films, which is greater than 20 for most growth conditions, exceeds values previously reported for Fe and Mo/Fe catalysts supported on films of oxidized Al or spun-on Al_2O_3 [193], indicating that the Al_2O_3 deposited by e-beam evaporation is especially effective as a supporting later for CNT growth catalysts.

We suspect that Al_2O_3 directly promotes CNT growth, perhaps by feeding carbon to the catalyst particles by surface diffusion, as Al_2O_3 is known to catalyze the reorganization and decom-

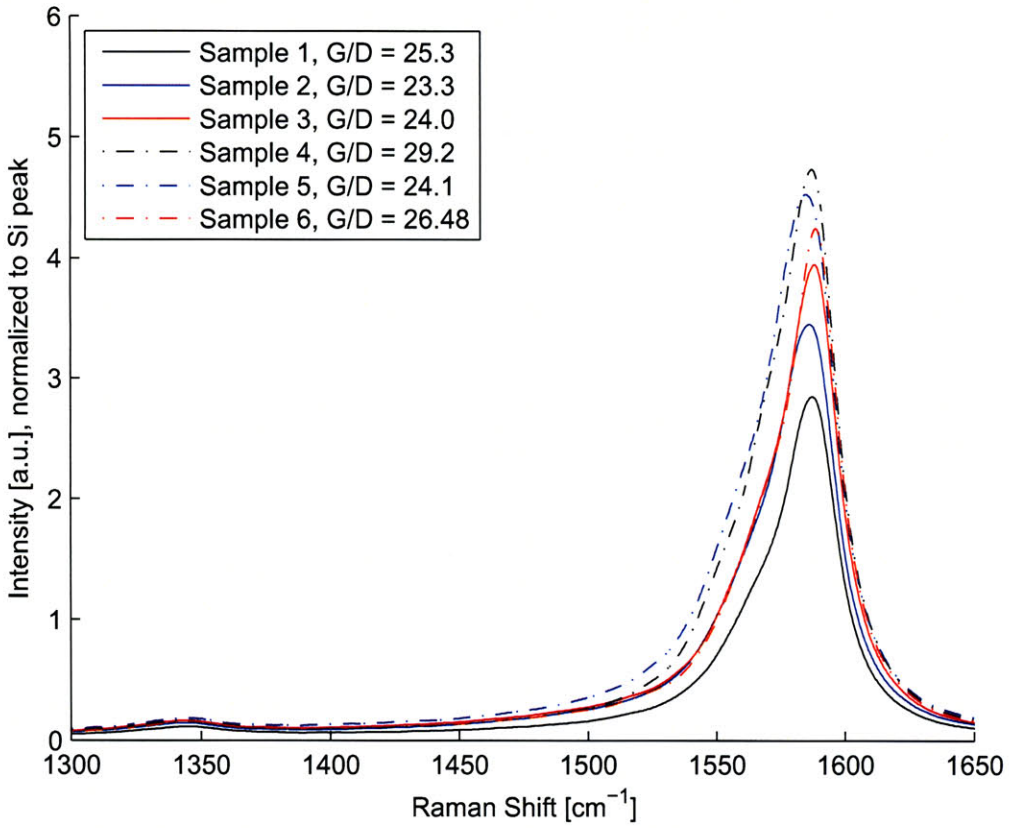

Figure 3-13. Evaluation of catalyst film uniformity, in terms of G/D ratio measured by Raman spectroscopy (400 sccm, $H_2/CH_4 = 0.25$, 825 °C).

position of hydrocarbons at temperatures as low as 300 K [288]. Similar to the effect of adding H_2 to the gas mixture there may be an equilibrium effect of Al_2O_3, and in general of the relative surface area of the oxide support. At one extreme, placing a large block of Al_2O_3 in the furnace tube prevents CNT growth on a $Mo/Fe/Al_2O_3$ sample; initially clean Al_2O_3 surfaces darken, indicating surface deposition of carbon at conditions which otherwise do not cause self-pyrolysis of CH_4. At the other extreme, films of Mo/Fe on Si and SiO_2 show significantly lower yield than the $Mo/Fe/Al_2O_3$ film when processed under the same conditions.

It is well-known that treatment in H_2 enhances sintering of metal nanoparticles and promotes re-precipitation of metals from supporting oxide layers [289]; therefore, it is not unexpected that CNT growth is absent on a film heated in H_2/Ar without pre-baking. However, noting that all samples first pre-baked in Ar show at least moderate CNT yield, it appears that high-temperature treatment in an oxidizing atmosphere stabilizes the film against the deleterious effects of H_2. Numerous past results demonstrate there is a particle size "window" for CNT growth [154, 290], where the carbon supply rate and activity must match the conditions for growth. When a thin film is heated, a broad distribution of particle sizes is created. This distribution is shifted by the annealing and heating atmosphere and process, but when the Fe/Mo catalyst remains oxidized prior to nucleation, SWNT growth occurs over a broad range of processing conditions.

We also tested CNT growth from a 3.0/1.5/20 nm Mo/Fe/Al film on bare Si, as suggested by Ward et al. [193]. After heating in Ar, we were unable to grow CNTs, likely due to formation of an Al-Si eutectic at 577 °C, which deactivates the catalyst metal [275]. Growth after dedicated oxidation of the Al layer, by holding in air at 450 °C for 30 minutes prior to introduction of Ar, and then further heating to the growth temperature, yielded only a low density of poor-quality CNTs. We initially expected a higher CNT density because thin Al layers oxidize rapidly in air [271]; however because the Mo top layer is continuous, it may slow oxidation of the Al until most of the Fe has diffused into the Al, giving a compound which is less effective for CNT growth.

Franklin et al. show that CNT growth from a solution-prepared $Mo/Fe/Al_2O_3$ catalyst occurs in a narrow composition window of H_2/CH_4 spanning from approximately H_2/CH_4= 0.06–0.10 [211]. They observe little or no yield from gas compositions outside this range; on one side there is an excess of active carbon species due to self-pyrolysis of CH_4, and on the other side there is a deficit of active species. While the highest yield from our system falls within these limits, we further show high activity from H_2/CH_4 =0.1–0.3. It would be instructive to conduct experiments at a higher H_2/CH_4 ratio; however, at this stage, the configuration of our CVD apparatus limited our experiments to the range of flow compositions presented here.

Further, we suspect that the interaction between Fe and Mo is qualitatively similar to that of the Co/Mo system, in which highly monodisperse clusters of Co are stabilized by an excess of Mo, giving a high yield of SWNTs with a narrow diameter distribution [166, 196]. Our catalyst has a definite excess of Mo (Mo/Fe = 2), and the excess Mo does not inhibit growth of SWNTs even though the solubility of Mo in Fe is only 7% and the total metal thickness of 5 nm likely produces metal clusters larger than the SWNT diameters we observed. It would be instructive to pursue a combinatorial approach to evaluate the effect of catalyst composition when there is an excess of Mo. A study spanning a range where Fe/Mo < 1, in which overlapping gradient films were deposited by pulsed laser deposition, demonstrates that Mo/Fe = 1/16 is the best ratio for growth of vertically-aligned MWNTs by thermal CVD of C_2H_2 [291].

Finally, to qualitatively evaluate the role of Mo and the hydrocarbon environment, we compared the performance of the $Mo/Fe/Al_2O_3$ film to a Fe/Al_2O_3 film, atmospheres of H_2/CH_4 and H_2/C_2H_4. Fig. 3-14 shows SEM images of CNT growth from these four conditions. Versus the high-density SWNTs grown from $Mo/Fe/Al_2O_3$, Fe/Al_2O_3 gives a much lower density of CNTs in H_2/CH_4. $Mo/Fe/Al_2O_3$ gives highly defective MWNTs in H_2/C_2H_4, whereas Fe/Al_2O_3 gives mm-high structures of vertically-aligned MWNTs. Therefore, Mo promotes growth of SWNTs from CH_4, but may retard the growth of MWNTs from C_2H_4. A complex interaction between Mo and Fe is further implied, because based on as-deposited thickness, we may expect the Fe film (1.5 nm) to give smaller particles than the Mo/Fe film (3.0/1.5 nm). We emphasize that the best parameters for CNT growth are tightly coupled for each catalyst and hydrocarbon environment; for example, the gas composition giving the highest yield changes with growth temperature, and the conditions for high yield do not necessarily give the highest quality.

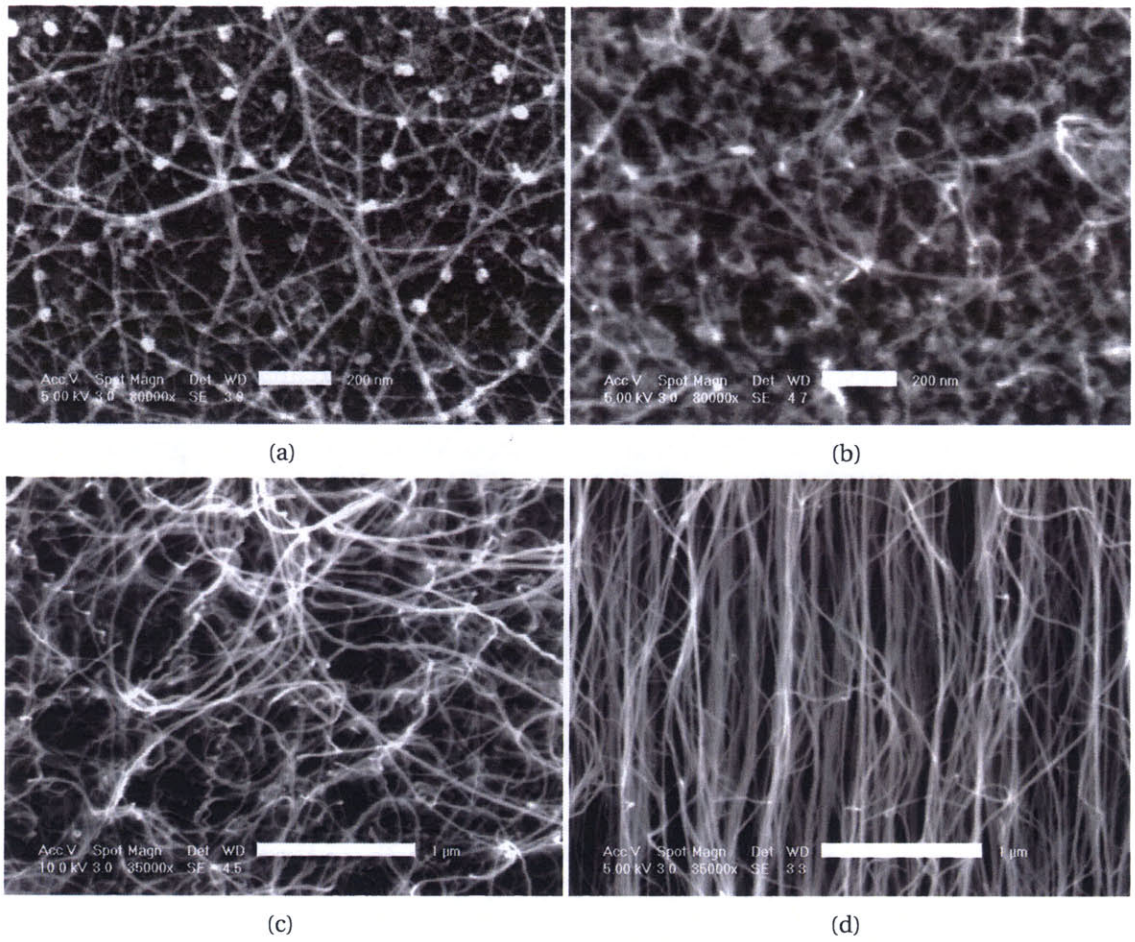

Figure 3-14. Qualitative study of effect of Mo on CNT film growth: (a) $Mo/Fe/Al_2O_3$ in H_2/CH_4, 875 °C (scale 0.2 μm); (b) Fe/Al_2O_3 in H_2/CH_4, 875 °C (scale 0.2 μm); (c) $Mo/Fe/Al_2O_3$ in H_2/C_2H_4, 750 °C (scale 1 μm); (d) Fe/Al_2O_3 in H_2/C_2H_4, 750 °C (scale 1 μm).

3.1.3 Growth on microstructured silicon substrates

Using the CVD procedure discussed in section 3.1.1.2, high-quality CNT films are grown directly and conformally on silicon microstructures. Bulk-micromachined structures are fabricated from (100) silicon wafers by deep-reactive ion etching (DRIE) using SF_6/C_4F_8 plasma, by reactive ion etching (RIE) using Cl_2 plasma, and by wet etching in aqueous KOH. The catalyst film of $Mo/Fe/Al_2O_3$ is deposited on the microstructures by the same process as for the flat silicon substrates; the wafer is placed horizontally and perpendicular to the evaporation source and during deposition the substrate holder is rotated in the horizontal plane.

Fig. 3-15 shows CNT films grown on a vertical sidewall etched by DRIE and on a pyramid structure within a microchannel etched in KOH. These films uniformly coat slanted surfaces (Fig. 3-15b) and make smooth transitions at corners (Figs. 3-15a and 3-15b). Suspended CNTs span distances of approximately 5 μm or less between nearby structures, such as across narrow vee-grooves etched in KOH. Raman spectra are nearly identical on all horizontal and slanted silicon surfaces covered with CNTs, verifying film uniformity. However, the signals from SWNTs are often stronger when the spot is focused over a narrow trench, indicating resonance from suspended SWNTs.

CNT film growth on microstructures is now extended to silicon surfaces having irregular topography, rather than regularly sloped features. When silicon is processed in Cl_2 plasma (LAM-490B, Lam Research), a surface of "micrograss" is produced (Fig. 3-16). Micrograss, which is alternatively called "black" silicon, forms because of micro-masking of the substrate during RIE etching. These micro-masks may be dust or other contaminant particles, native SiO_2, or more likely are sub-micron spots of SiO_2 which are sputtered from the masked areas of the wafer and are re-deposited within the areas of bare Si that remain exposed by the concurrent etching process [292, 293]. As etching proceeds, the micro-masks template formation of an irregular and dense forest-like matrix of sharp structures (Fig. 3-17). In our system, the etch rate is approximately 0.3 μm/min. The sloped footings of the micrograss are oriented with the [100] directions of Si, indicating that in-plane etching is faster along the [110] directions.

Fig. 3-18 shows CNT growth by thermal CVD[1] on the silicon micrograss, where each blade of grass is coated by a tangled mat of CNTs and blades of grass spaced by approximately 5 μm or less are connected by suspended CNTs. Isolated and bundled CNTs span trenches (Fig. 3-18c) and form suspended webs (Fig. 3-18d).

Further, we deposited Mo/Fe (3.0/1.5 nm) on a micrograss sample where the SiO_2 mask on the horizontal surfaces had been consumed entirely by the etching process, leaving SiO_2 only where it had been re-deposited as micro-masks. Thick and curly CNTs grow sparsely on horizontal surfaces of this sample, yet many straight suspended CNTs connect the tips of adjacent micrograss structures (Fig. 3-19a). Occasionally, CNTs as long as 250 μm connect across wide areas of micrograss (Fig. 3-19c).

It appears that growth of suspended CNTs is favored by catalyst support on areas of SiO_2 left near edges of features and at the tips of the micrograss. Also, the small size of these structures increases the chances that CNTs will grow with suspended ends until reaching adjacent structures, and will not be hindered by surface interactions with the substrate. On flat substrates, the yield and quality of CNTs from Mo/Fe on SiO_2 is much better than from Mo/Fe on Si, pre-

[1] CNF growth on micrograss by plasma-enhanced CVD was performed by B. O. Boskovic and A. T. H. Chuang at the University of Cambridge, and is discussed in [2]

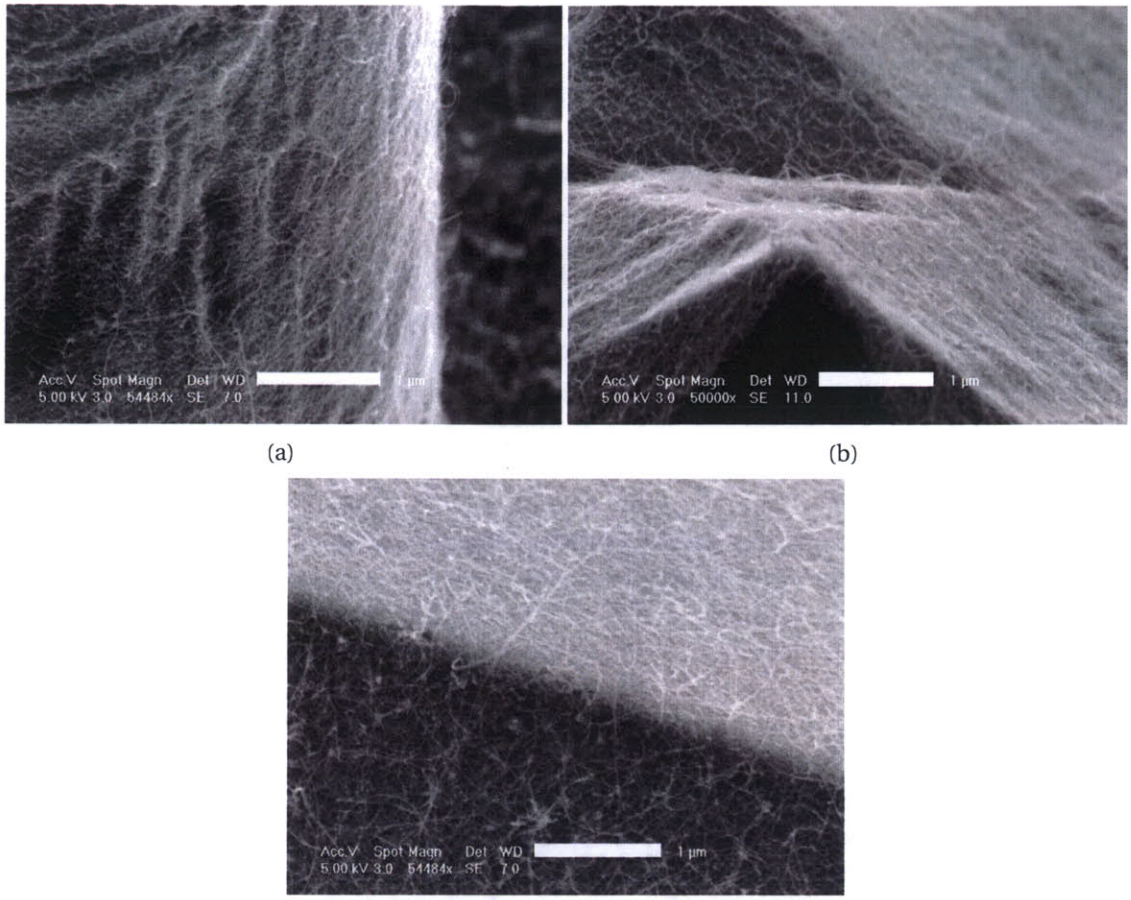

Figure 3-15. CNT growth from $Mo/Fe/Al_2O_3$ catalyst on bulk-micromachined silicon microstructures: (a) film on vertical sidewall of cylindrical post fabricated by DRIE; (b) uniform film on pyramid inside KOH-etched microchannel; (c) transition between sidewall and floor of microchannel. Scales 1 μm.

sumably due to diffusion of the catalyst into Si at the growth temperature [294]. Under SEM examination, the CNTs from Mo/Fe on Si and on SiO_2 appear to have larger diameters than those from $Mo/Fe/Al_2O_3$, owing to weaker metal-support interactions compared to Al_2O_3. This apparent selective growth from a uniform catalyst layer deposited on micro-masks can be an alternative to catalyst patterning for localized growth of CNTs from sharp microstructures.

CNT/CNF growth on micrograss was also conducted using PECVD of C_2H_2/NH_3, from a catalyst created from a colloidal solution of Co nanoparticles. These experiments were performed by our collaborators, Bojan Boskovic and colleagues at the University of Cambridge, and are detailed in our joint publications [2, 295].

Together these results show that deposition of a catalyst film by a physical method such as e-beam evaporation enables uniform CNT film growth on microstructured surfaces having arbitrary topography, even though oblique surfaces expose smaller projected areas and therefore receive thinner catalyst layers than surfaces that directly face the deposition source. Assuming

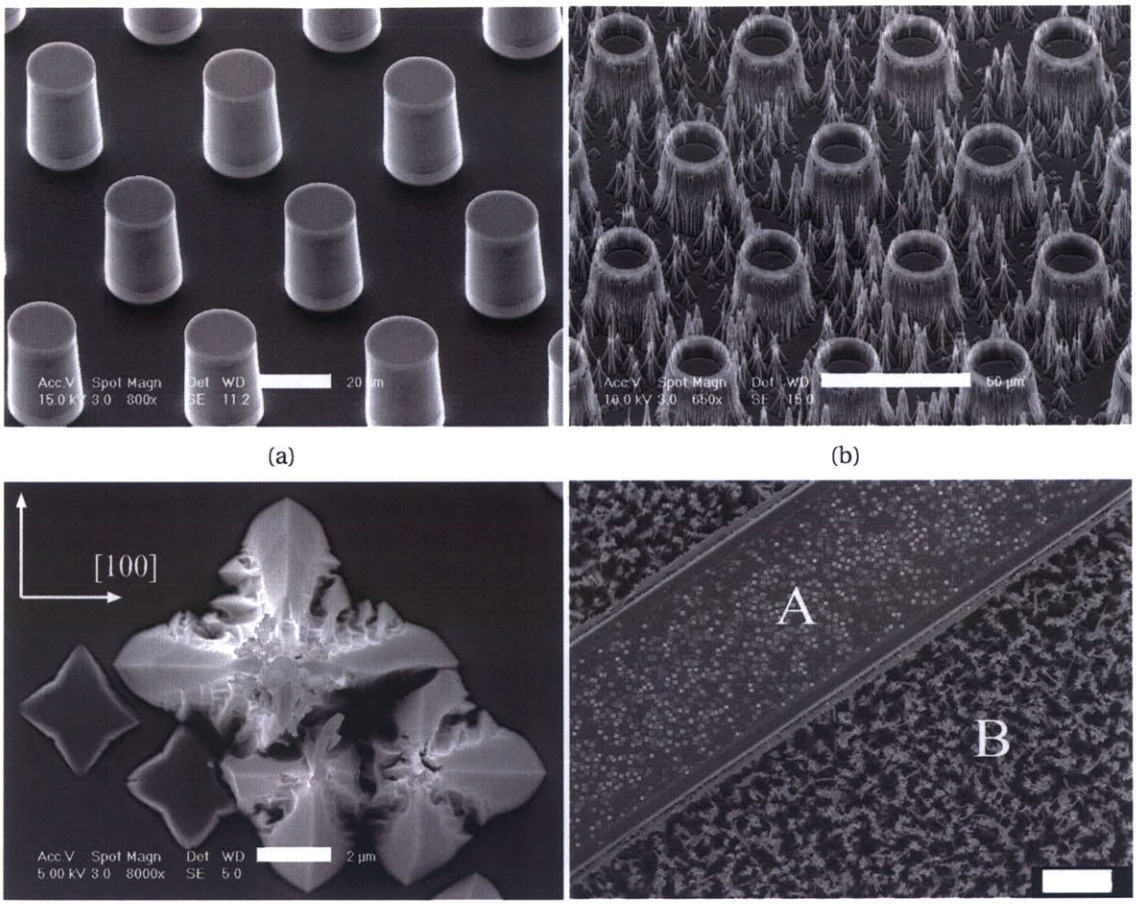

Figure 3-16. SEM images of RIE-etched silicon microstructures: (a) "clean" cylindrical posts, etched in SF_6/CF_4 plasma in STS-DRIE (scale 20 μm); (b) cylindrical posts with interstitial low-density silicon micrograss, etched in Cl_2 plasma in LAM-490B (scale 50 μm); (c) top view of micrograss, indicating (100) crystal directions (scale 2 μm); (d) top view indicating flat masked area A and high-density silicon micrograss area B (scale 10 μm).

a uniform vapor flux, the ratio film of the film thickness on an oblique surface to the thickness on a surface directly facing the evaporation source is proportional to the cosine of the angle between the normal to the oblique surface and the plane containing the evaporation source [296]. Therefore, the film thickness should be negligible on a surface which is perpendicular to the source. Growth on the DRIE-etched vertical walls is less dense than on slanted surfaces; however, the moderate CNT density on the vertical walls suggests that intermolecular collisions direct sufficient atoms to the sidewalls.

Using DC-PECVD, Chhowalla et al. show that the size of catalytic particles is directly related to the initial thickness of a metal film [221], which affects the suitability of the catalyst for CNT growth in both thermal CVD and PECVD environments. In PECVD, the initial film thickness affects both the CNT structure and diameter [297]. However, our results indicate that the activity of the $Mo/Fe/Al_2O_3$ catalyst film in thermal CVD does not significantly decrease when the

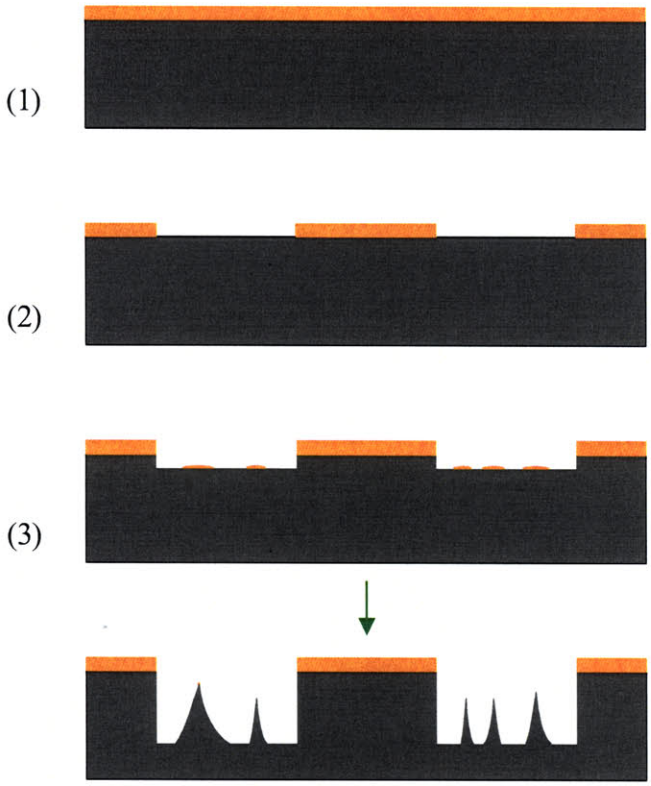

Figure 3-17. Formation process of silicon micrograss within desired pattern of microstructures: (1) grow thermal SiO_2; (2) etch SiO_2 in CF_4 plasma; (3) etch Si in Cl_2 plasma, which causes deposition and undercutting of micro-masks.

thickness is scaled by the "cosine" effect. This may be due to the role of Mo in increasing the catalytic activity of Fe in CH_4 [273], or in promoting formation of very small Fe clusters suitable for SWNT growth as has been found for the Co/Mo system [196].

Further, because metal deposition by magnetron sputtering is less directional than e-beam evaporation, sputtering may enable further enhancement of CNT film uniformity on oblique surfaces. Topography-driven effects on particle size and therefore on catalytic activity will vary widely among different catalyst and CVD methods, and it is expected that CNT growth on flat substrates occurs in a wider range of processing conditions than on arbitrary topography. Here, we chose to investigate limiting cases of surface structure (vertical sidewalls and micrograss) to demonstrate the performance of catalyst coating and the CVD process on CNT and CNF growth. Further quantification of how the catalyst film thickness, deposition method, composition, and resulting particle size differ among oblique and horizontal surfaces, requires further study using Rutherford backscattering spectrometry (RBS), XPS, TEM, and other techniques.

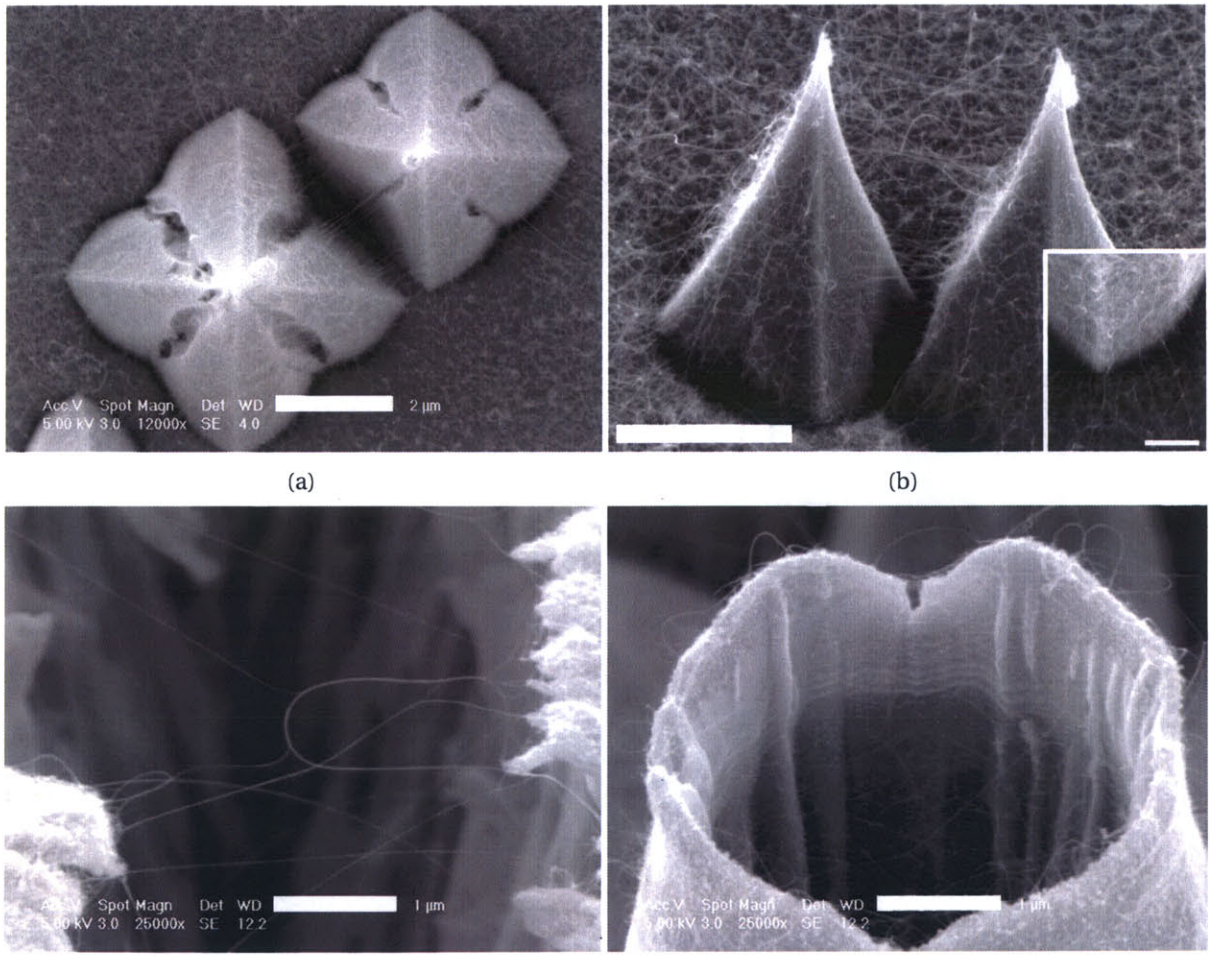

Figure 3-18. CNT growth from $Mo/Fe/Al_2O_3$ catalyst on silicon micrograss: (a) dense coating of neighboring grass "blades", with many straight CNTs connecting the nearest faces of the blades (scale 2 μm); (b) angled view of adjacent coated blades (scale 1.5 μm), with inset showing CNT network between the foot of the blade and the substrate (scale 0.5 μm); (c) CNTs suspended and tangled across a trench (scale 1 μm); (d) self-supporting web of CNTs suspended from lip of circular silicon island (through-etching of oxide mask left lip behind, scale 1 μm).

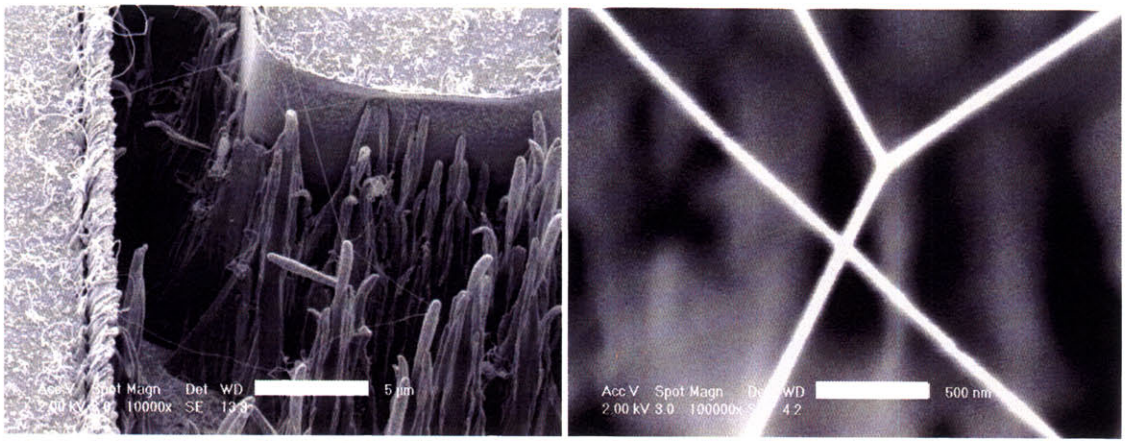

(a) (b)

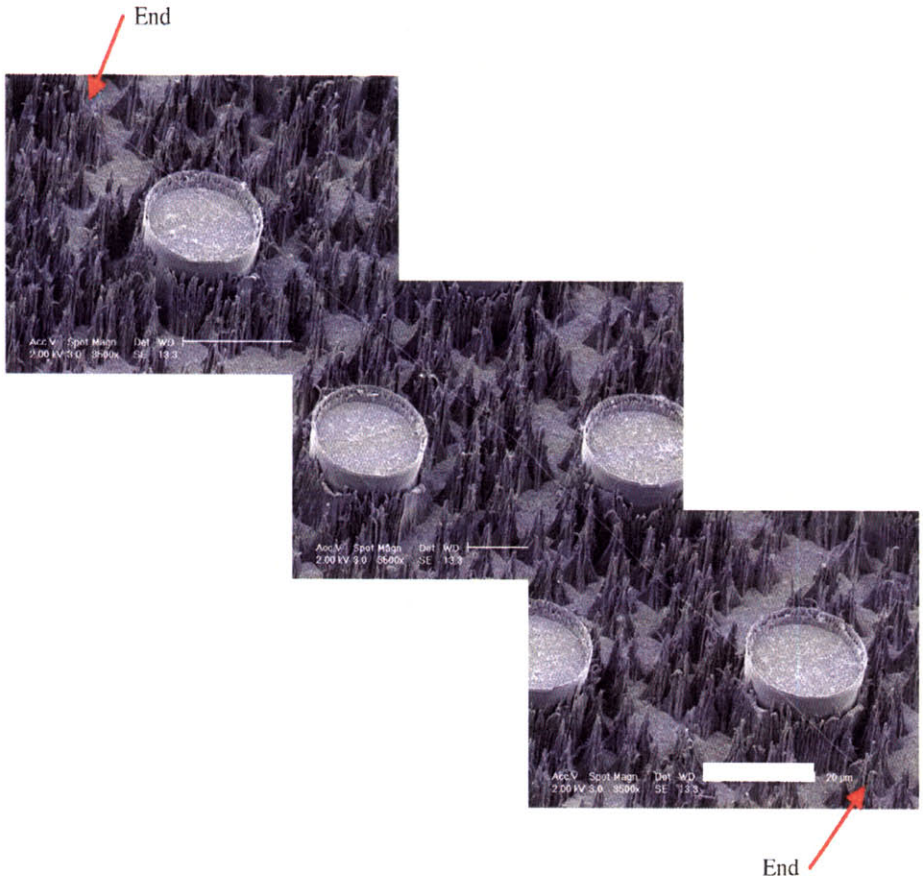

(c)

Figure 3-19. CNT growth from Mo/Fe catalyst on silicon micrograss: (a) thick and curly CNTs grow on horizontal surfaces, while straight CNTs grow across trenches and between adjacent blades of grass (scale 5 μm); (b) close-up of junction between suspended CNTs (scale 0.5 μm); (c) $\approx$200 μm long CNT spanning field of micrograss (scale 30 μm).

For truly three-dimensional substrates such as carbon fibers, surfaces which are not in view of the deposition source are fully "shadowed" and will not be coated with catalyst. While wet catalyst solutions have been successful for coating fibers [298] which have relatively uniform topography, manual dispersion of liquid catalysts on microstructures is hindered by local topography, wetting, and surface tension effects, which depend on the substrate material. In our experiments with silicon micrograss, manually-dispersed droplets of Co colloid form an uneven thickness of catalyst coating on the flat areas of the samples, while the solution penetrates the top layer of the micrograss and lands on the lower branches resulting in a distribution that is much less uniform than in the flatter areas (Fig. 3-16d, region A). This gives rise to dense "bunched" CNF growth on the flatter regions and sparse growth on the micrograss regions. Even a small surface roughness on the micrometer scale created by etching of the masked region of the micrograss substrate causes this effect of bunched CNF growth, compared to the uniform forest grown on the flat surface of non-etched Si using same DC PECVD system and similar growth conditions [299].

As demonstrated by the effects of the texture of the micrograss surface on CNF growth by PECVD, the catalyst deposition and CVD growth processes may be further tuned to increase the selectivity of growth based on surface texture. For example, a physically-deposited film and CVD process could be sought where the catalytic activity is affected considerably by cosine effects introduced by a desired surface texture, and thereby growth is selective to a particular surface orientation (e.g., horizontal or sloped beyond a certain angle). This would be the opposite of what we have demonstrated by conformal growth in thermal CVD. When the catalyst is deposited by a wet method, the surface texture and the nature of the catalyst-surface wetting interaction could be modified to increase the selectivity of growth. However, coating topography by physical or solution methods will be more challenging for high-aspect-ratio features such as narrow trenches.

Going forward, hierarchical control of the physical and chemical texture of surfaces offers opportunities to direct material-surface interactions, such as liquid-solid wetting behavior and compatibility with biological materials. For example, leaves of lotus and rice plants are superhydrophobic because of a combined effect of microscale and nanoscale roughness [300, 301], and elastic interactions between groups of hydrophilic hairs on the Lady's Mantle plant make the leaf surface hydrophobic [302]. The electrical conductivity of the CNTs and the ability to coat and chemically functionalize [228–230, 303] their surfaces enables further customization of these interactions.

3.2 Details of SEM and Raman characterization

3.2.1 SEM imaging of CNTs

The visibility of CNTs by SEM imaging varies strongly with the accelerating voltage; Fig. 3-20 shows the effect of varying the SEM accelerating voltage on the image of a tangled CNT film. At lower accelerating voltage, high contrast enables smaller diameter suspended CNTs to be seen [304]; however, the lower resolution means that the finest viewable details of CNT bundles and branches are not seen. As the voltage is increased, the lower background contrast makes it harder to see very small CNTs, especially those near the substrate. Higher voltage also increases the rate at which the Al_2O_3 underlayer charges, blurring the image. For our samples, an accelerating voltage of 5 kV seems to be a reasonable compromise between these competing effects.

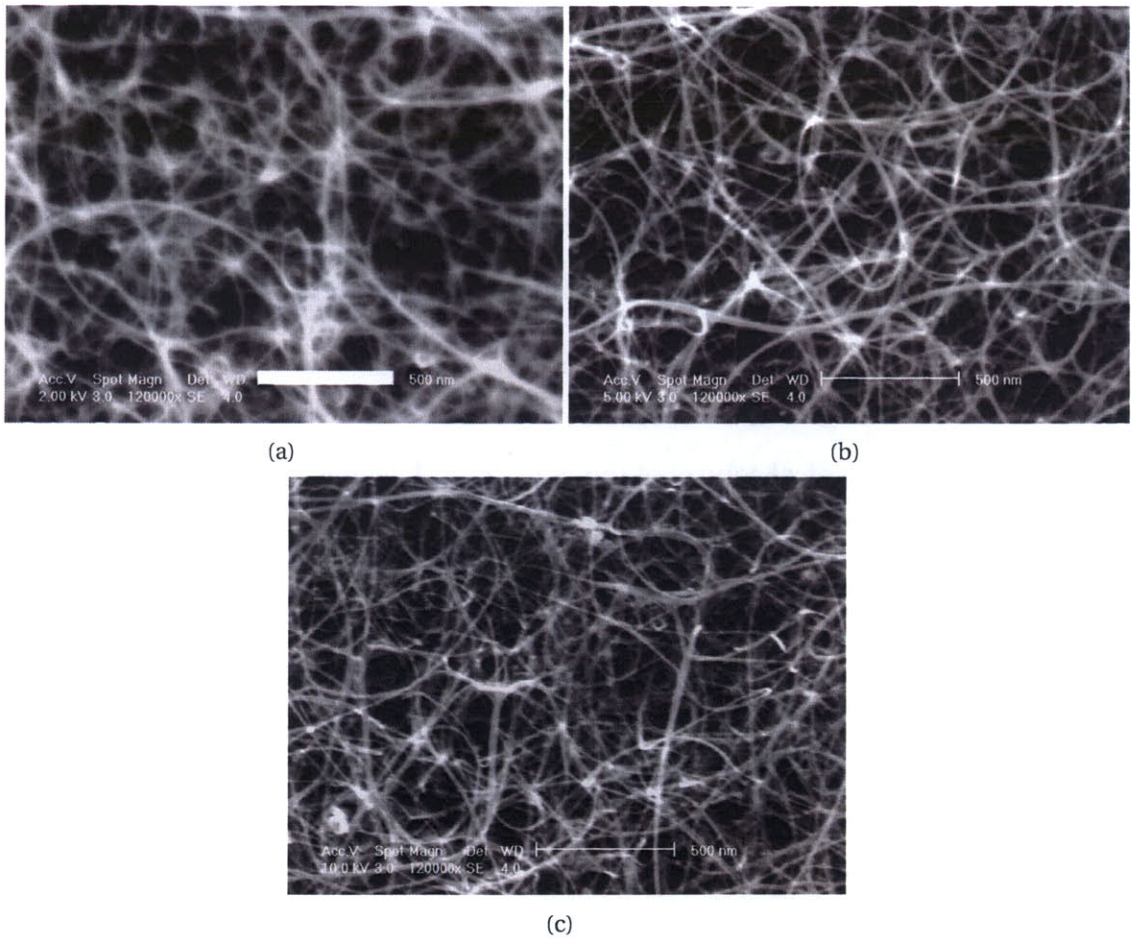

(a) (b)

(c)

Figure 3-20. Effect of SEM accelerating voltage on imaging of a tangled CNT film from $Mo/Fe/Al_2O_3$ catalyst on Si: (a) 2.0 kV; (b) 5.0 kV; (c) 10.0 kV. Scales 0.5 μm.

3.2.2 Raman spectroscopy of CNTs

3.2.2.1 Basics of analyzing Raman spectra

In resonant Raman scattering [305], a material is excited by a photon with energy matching that of a strong optical absorption electronic transition within the material. For a CNT (and unlike graphite) this occurs between electronic states which are in quantum confinement. Hence, for a given optical excitation frequency (energy), the Raman scattering behavior of small CNTs is determined by the CNT diameter, and the response of CNTs having the same diameter and chirality depends on the excitation energy [306]. A Raman spectrum of CNTs has three regions of prominent interest:

- The *G*-band, or "Graphitic" peaks, from 1582–1592 cm^{-1}, which represent stretching of the CNT lattice, tangential to the surface and along the axis of the tube (Fig. 3-21b). The position of the *G* peak depends strongly on the type of CNTs (Fig. 3-22a), and weakly on the CNT diameter (Fig. 3-22b). Because many samples are a mixture of semiconducting and metallic SWNTs, as well as some MWNTs, the *G* peak is often broader than the idealized shapes shown in Fig. 3-22a and can be roughly decomposed into a sum of individual peaks representing each type of CNT.

  For SWNTs alone, a two-peak "split" *G*-band is typically observed under a good resonance condition. The higher frequency (G_+) peak corresponds to stretching along the tube axis, and the lower-frequency (G_-) peak is from stretching perpendicular to the axis. In full, the *G*-band of a polydisperse sample of SWNTs can be decomposed into as many as six isolated peaks. For metallic CNTs, the spacing between the G_+ and G_- peaks is inversely related to the tube diameter [307].

  Most Raman response peaks of CNTs including the *G* peak can be approximated by a Lorentzian lineshape,

$$y = \frac{a}{1 + \left(\frac{x-b}{c}\right)^2}, \tag{3.1}$$

  where a is the peak amplitude, b is the center frequency, and c is a scaling factor (the half-width at half-maximum). The lineshape of the G_- peak is highly sensitive to whether a SWNT is semiconducting (giving a Lorentzian lineshape) or metallic (giving a Breit-Wigner-Fano lineshape).

- The *D*-band, or "Disordered" peaks, in the range 1250–1450 cm^{-1}. These peaks arise from defective non-CNT carbon, as well as defects inherent in the structure of well-formed CNTs [308]. The *D*-band intensity of a CNT itself is roughly proportional to the density of defects. Oxidation can change the *D*-band intensity of a sample, such as by etching of the CNTs at defect sites which increases the *D*-band, and/or by etching of amorphous carbon which decreases the *D*-band [309]. High-temperature annealing in vacuum can improve the graphitic order of CNTs and therefore decrease the *D*-band while increasing the *G*-band [310].

- The RBM-band, or "Radial Breathing Mode" peaks, from approximately 100–350 cm^{-1}. The RBM bands represent radial contraction and expansion of the cylindrical CNT structure (Fig. 3-21b). For our studies of tangled CNT films grown in CH_4/H_2, the 514.5 nm

wavelength (E_{laser} = 2.42 eV) was chosen because a large population of SWNTs is visible at lower laser energies (Fig. 3-23a); however, to comprehensively characterize the SWNT diameters it is necessary to take Raman spectra using multiple laser energies, (e.g., using a tunable laser).

The center frequency of the RBM peak and the SWNT diameter are related (Fig. 3-23b) as

$$\omega_{\mathrm{RBM},bund} = \frac{248}{d_t} \tag{3.2}$$

for isolated SWNTs, and

$$\omega_{\mathrm{RBM},isol} = \frac{234}{d_t} + 10 \tag{3.3}$$

for bundled SWNTs.

Using the Raman spectrum, we make qualitative assessments of the yield and quality of CNTs using the following parameters:

- G/D ratio, the intensity ratio between the maxima of the G and D peaks, which is therefore a measure of sample quality.
- G/Si ratio, the intensity ratio between the maxima of the G-band and Si peaks (521 cm^{-1}), which is therefore a measure of sample yield on a silicon substrate. Because an increase in the quantity of CNTs both increases the G-band intensity and decreases the visibility of the substrate, the G/Si ratio is a coarse ordinal approximation of yield. Further, the catalyst film and any amorphous deposits on the substrate decrease the Si signal.
- RBM/G ratio, the intensity ratio between the maximum of the highest[2] RBM peak and the maximum of the G peak, which is therefore a measure of the relative yield of SWNTs to all graphitic carbon.

Alternative to the G/D ratio, the "quality factor" of a CNT sample is defined,

$$Q = \frac{G_{max}}{G_{max} + D_{max}}. \tag{3.4}$$

This ratio is close to 1 for samples with $G/D > 10$; therefore, ranking high quality samples by the G/D ratio gives a more meaningful spread of data.

[2]Because only a few SWNTs within the focal spot can give a sharp RBM peak [283], this parameter typically varies significantly across a sample, and therefore many spots must be examined to get a good average value.

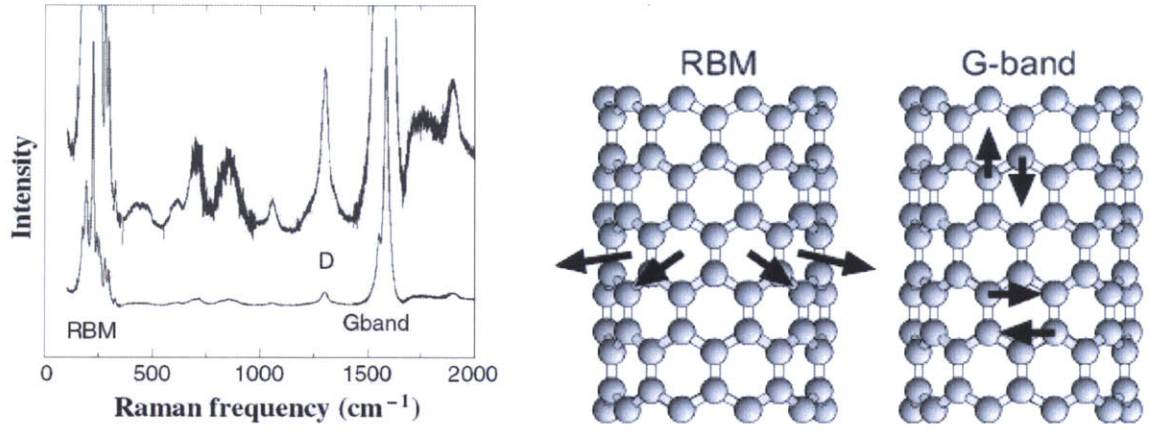

(a) (b)

Figure 3-21. Generalized resonant Raman emission of CNTs (from [283]): (a) Raman spectrum of CNTs, indicating radial breathing mode (RBM) and graphitic-band (*G*-band) regions (the top curve in the lower plot amplifies the background signal); (b) schematic of SWNT vibration under RBM and *G*-band excitations.

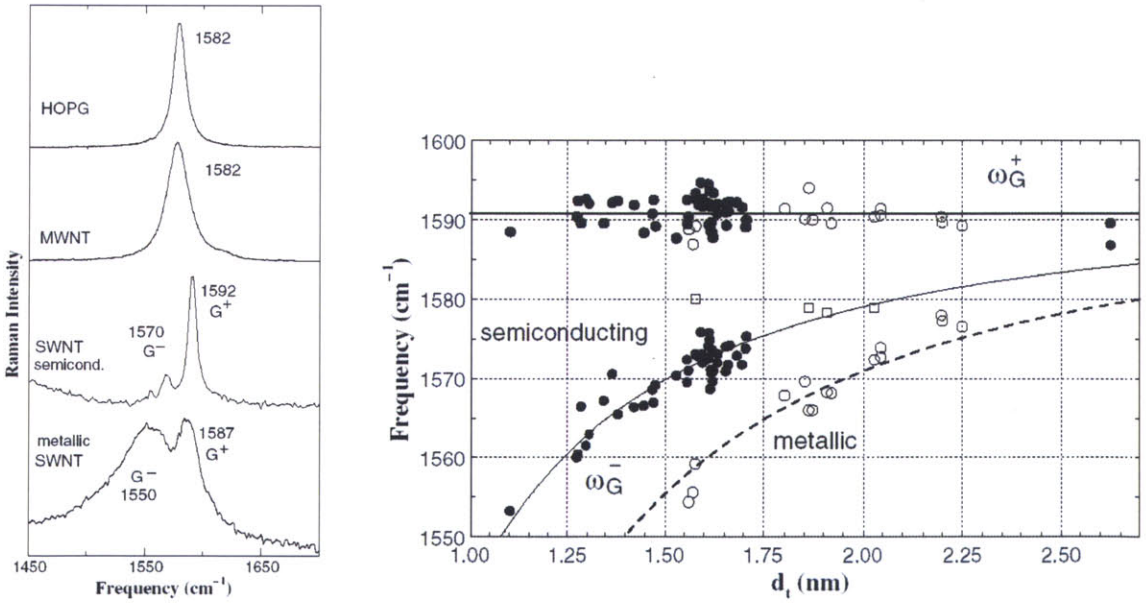

(a) (b)

Figure 3-22. CNT *G*-band emissions (from [283]): (a) characteristic *G* peaks for highly-ordered pyrolytic graphite (HOPG), MWNTs, semiconducting SWNTs, and metallic SWNTs; (b) measured relationships between *G*-band frequency and SWNT diameter.

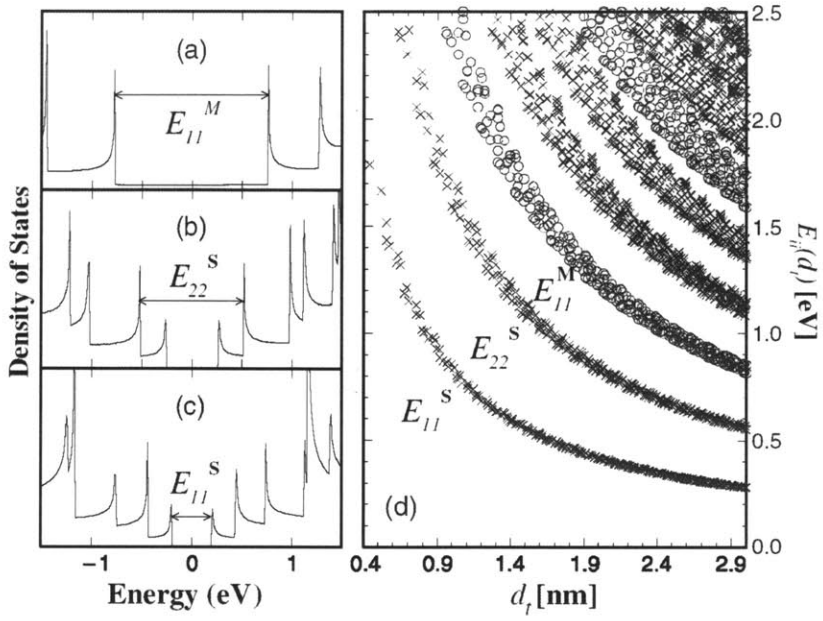

(a)

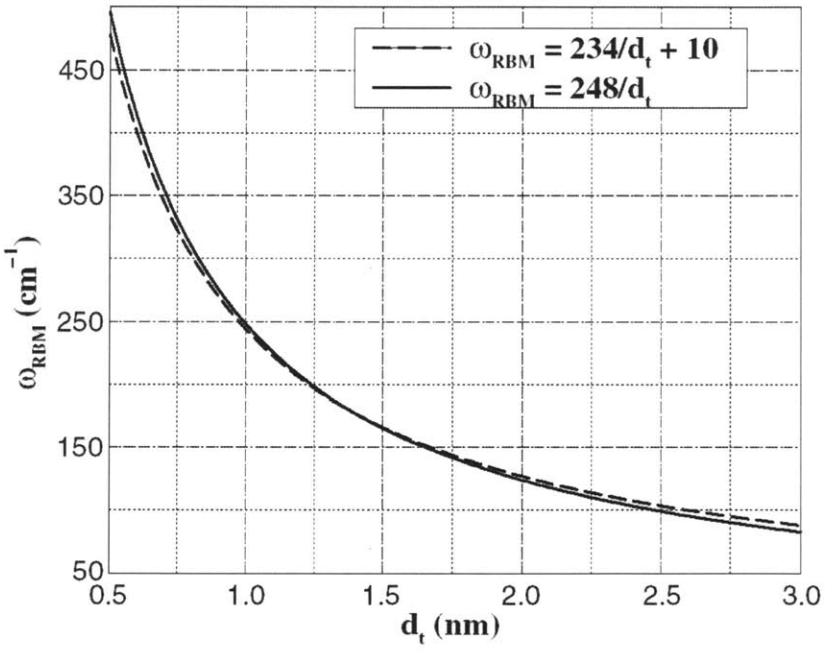

(b)

Figure 3-23. SWNT RBM emissions (from [283]): (a) Kataura plot giving "visibility" of SWNTs according to laser excitation energy, based on calculated density of states; (b) relationships between RBM frequency and diameter for isolated (dashed curve) and bundled (solid curve) SWNTs.

3.2.2.2 Effect of objective magnification

We notice a strong effect of objective magnification on the Raman spectra of CNT films on silicon substrates. The objective determines the depth of field and the spot size of the Raman collection. The Kaiser Microprobe used for our measurements is equipped with [10X,50X,100X] objectives, which have focal depths of [1.27,1.83,16.48] μm.

As the objective magnification is increased, the position of the G peak shifts to the left (Table 3.2), the relative intensity of the D-band increases, and the relative intensity of the Si peak decreases. This indicates stronger signals from MWNT "impurities" (having a G-band at 1582 cm^{-1}) and amorphous carbon, perhaps because of improved focus on defective CNTs near the surface and greater amplification of MWNT resonances which are weak relative to SWNT resonances. However, the relative intensity of the RBM peaks does not change with spot size, suggesting that a uniform population of SWNTs is visible at all spot sizes.

Objective	G/D	G/Si	RBM/Si
10X	32.5	6.0	0.34
50X	31.3	5.1	0.35
100X	23.7	4.1	0.32

Table 3.2. Peak intensity ratios from averaged raman spectra taken with 10X, 50X, and 100X objectives (FG-160).

Figs. 3-24 and 3-25 show the unprocessed and normalized spectra taken using the different objectives on a single sample. Repeated collections at the same spot are highly repeatable; however, there is moderate variation among individual collections at different spots. Therefore, it is sufficient to take a single collection at each spot, and necessary to average collections from multiple nearby spots on each sample. The G/D ratio also can vary significantly depending on the laser excitation wavelength and power [306], so it is important to compare only data taken with identical Raman settings.

3.2.2.3 Effect of laser power

The Raman spectra we measure also change with the laser power (Fig. 3-26); for example, at low power, the signal-to-noise ratio is high; yet at high power RBM signals from SWNTs are suppressed. This is possibly due to local oxidation (burning) of CNTs under high power, either by direct laser-induced heating of the CNTs or by laser heating of the substrate. The G/Si ratio is higher at low power, yet the G/D ratio is relatively invariant with power. A power setting of 10 mW is used for the studies in this chapter. Further study should find a power setting which gives suitable RBM intensity and is also stable (no burning) over long exposures.

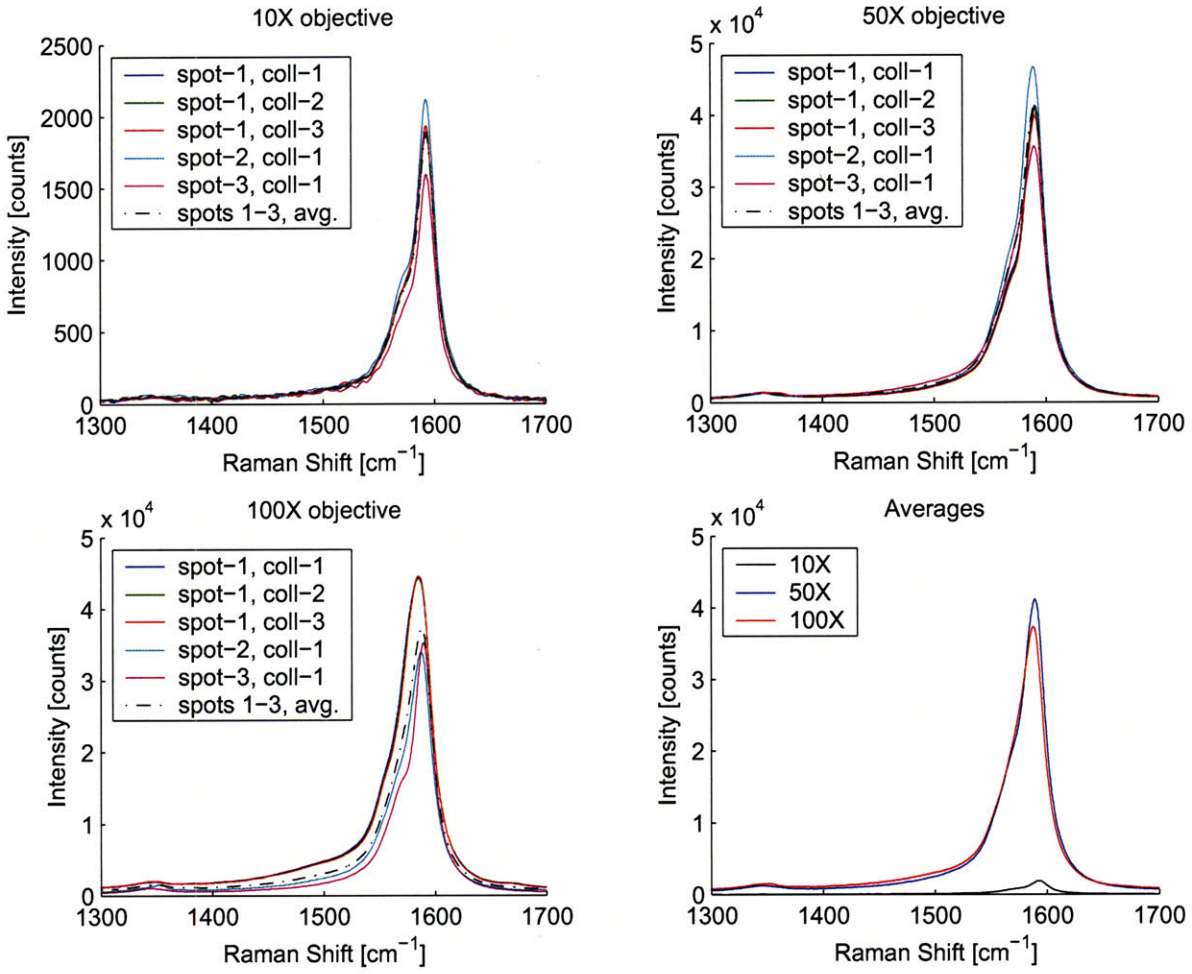

Figure 3-24. Unprocessed Raman spectra of a CNT film grown from $Mo/Fe/Al_2O_3$ in CH_4/H_2, compared for 10X, 50X and 100X objectives.

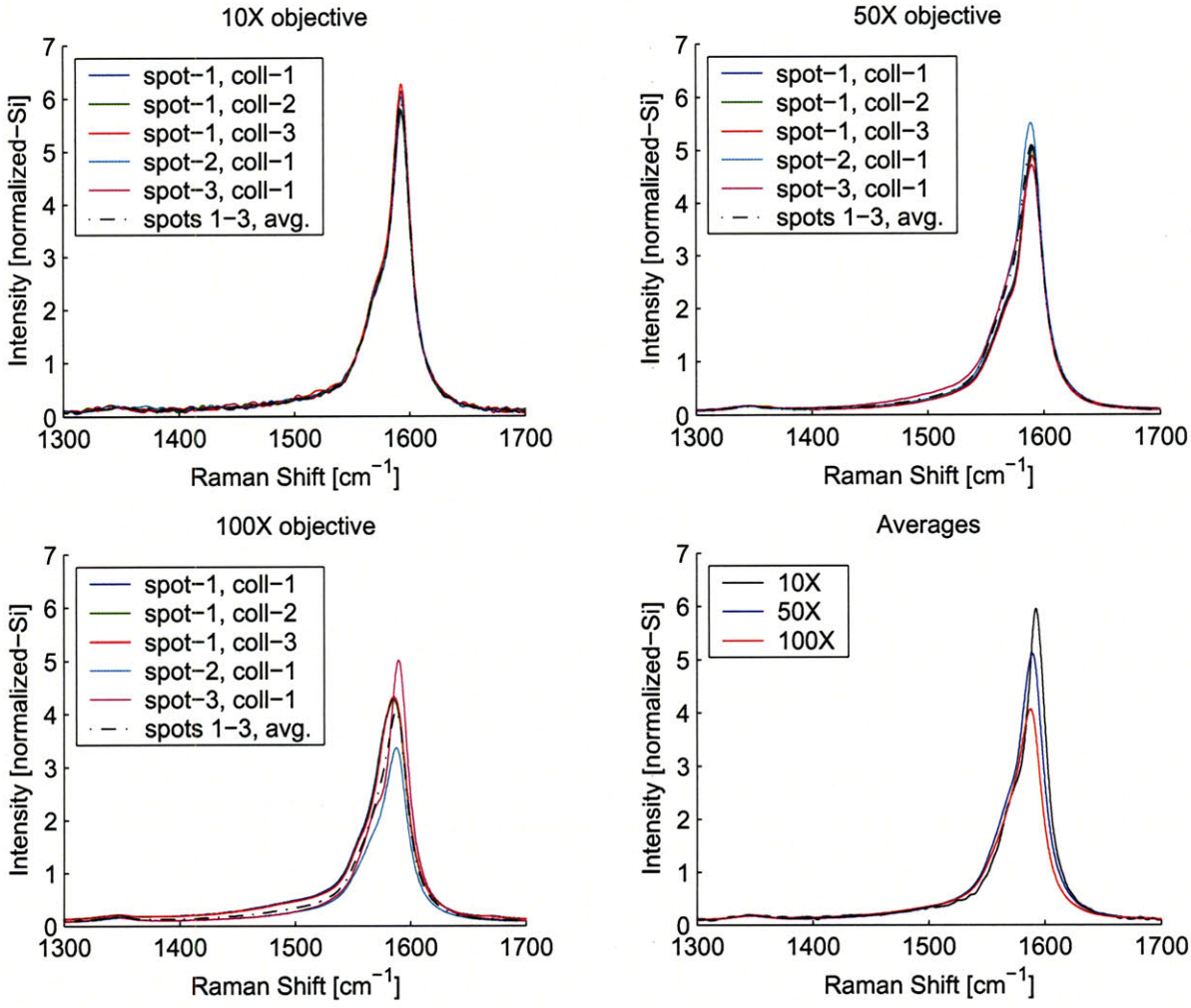

Figure 3-25. Raman spectra of a CNT film grown from $Mo/Fe/Al_2O_3$ in CH_4/H_2, compared for 10X, 50X and 100X objectives, normalized to height of Si peak at 521 cm^{-1}.

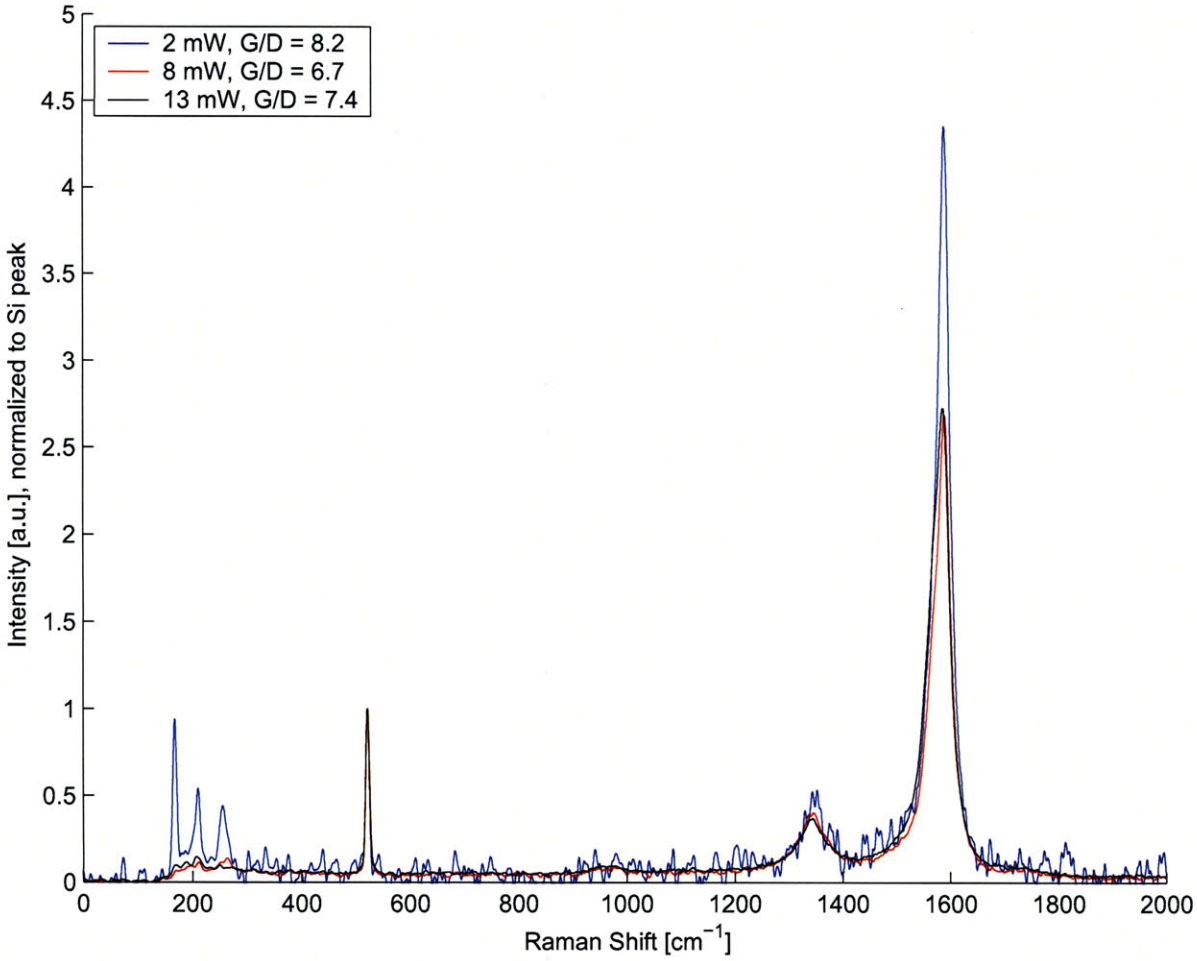

Figure 3-26. Raman spectra of a CNT film grown from $Mo/Fe/Al_2O_3$ in CH_4/H_2, acquired using 100X objective, compared for laser output powers of 2 mW, 8 mW, and 13 mW (measured without objective), and normalized to height of Si peak at 521 cm^{-1}. Note that the RBMs are much stronger under low power, suggesting that a relatively high power burns SWNTs.

3.2.2.4 Raman spectroscopy using 785 nm laser excitation

The CNT films from the study of growth temperature (Fig. 3-1) were also characterized using a Raman probe system (Kaiser Raman RXN) with 785 nm excitation and a ≈6 mm diameter spot, giving the Raman spectra shown in Fig. 3-27. In contrast to the microprobe system described previously, in which an optical microscope is used to focus the laser spot on the sample, the probe system collects over a working distance of several inches and distributes the beam power over a much broader area. Interestingly, the *G* peaks of spectra taken with the probe clearly show the G_- SWNT peak between 1550 and 1570 cm^{-1}, whereas the microprobe analysis shows only a slight knee in the *G*-band to the left of the the G_+ peak. Because it has a much smaller working distance, the microprobe sees more MWNTs and other carbon on the substrate, which blur the *G*-band signal. Overall, the probe system measurements confirm that our samples contain a high proportion of SWNTs; however, these results further emphasize that assessments of yield and quality based on Raman spectra should only be used to make ordinal comparisons.

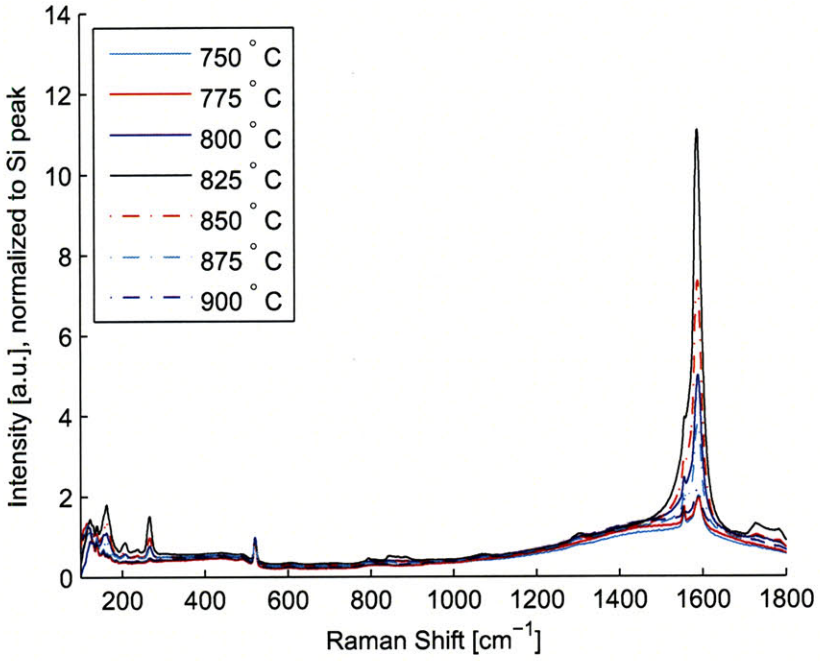

(a)

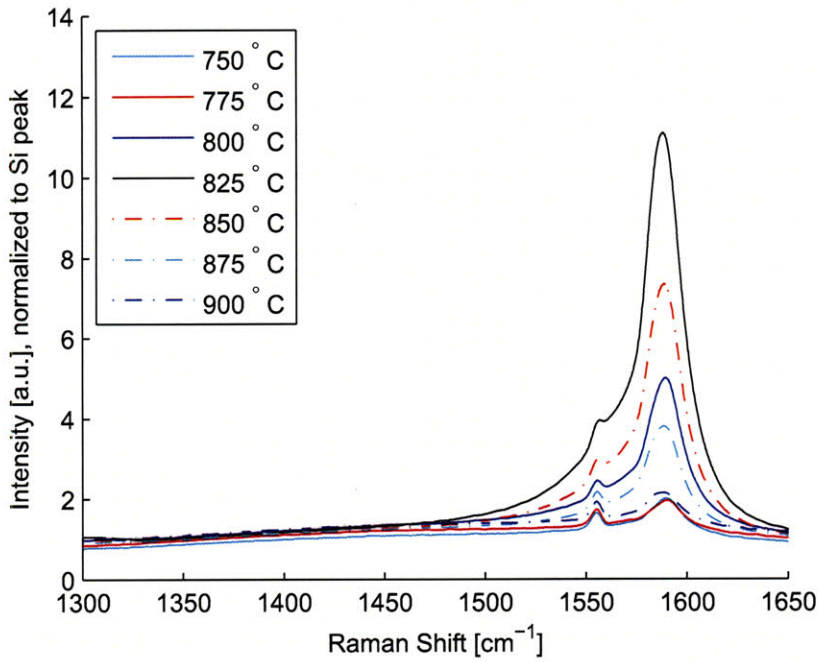

(b)

Figure 3-27. Raman spectra of $Mo/Fe/Al_2O_3$ samples processed in CH_4/H_2 at temperatures of 750–925 °C, normalized to height of Si peak, taken with ≈6 mm spot size and 785 nm excitation: (a) full spectra; (b) D–G band regions only.

3.3 Effects of substrate sample configuration and evolving gas reactivity on CNT yield and quality

3.3.1 Morphology transitions on long samples

While we do not obtain CNT growth in pure CH_4 on ≈1×1 cm samples of $Mo/Fe/Al_2O_3$ on Si, using a ≈10 cm×1 cm ("long") sample reveals how increased residence time of the reactant flow over the catalyst and in the tube furnace increases the reactivity of the gas. This more reactive gas grows CNTs downstream from the leading edge of the long sample. Fig. 3-28 shows a long sample processed in 290/130 sccm CH_4/Ar, at 875 °C, for 15 minutes. After processing, the surface of the sample exhibits U-shaped bands, changing from gray at the left (upstream) end of the sample, to light brown, to dark brown, and then gradually weakening to light brown again at the right end of the sample. SEM examination (Fig. 3-29) reveals that the light gray area contains clusters (≈0.2 μm diameter) with no surrounding CNTs; the light brown area contains relatively large-diameter structures "bursting" from the clusters along with a dense mat of small-diameter tubes; and the dark brown area contains a high-density mat of small-diameter tubes.

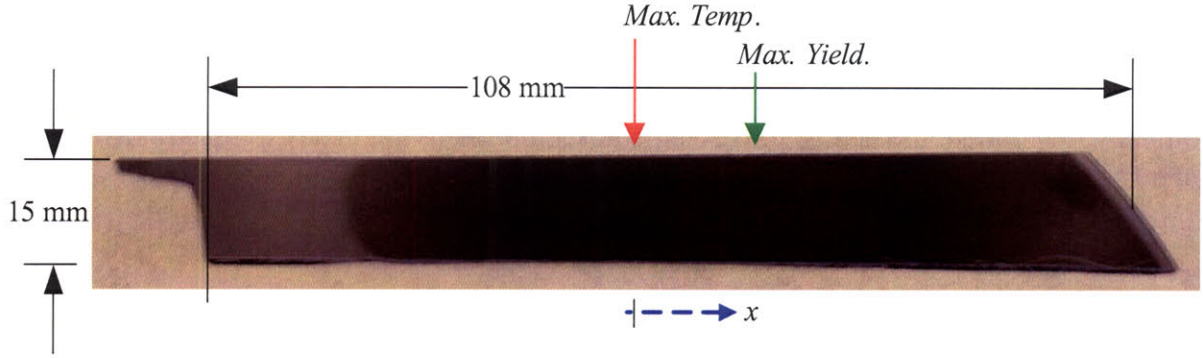

Figure 3-28. Long substrate sample after growth cycle in 290/130 sccm CH_4/Ar at furnace set-point of 875 °C.

More specifically, near x = -35 mm, a high density of smaller clusters appears on the substrate and large-diameter tubes appear to be "sprouting" from the larger clusters. Near x = -30 mm, the dense mat of small-diameter tubes begins. The deposit from this location was examined by high-resolution TEM (JEOL-2010 at 200 keV), and as shown in Fig. 3-30 the clusters have many stacked crystalline (possibly graphitic) layers which overlap in the image plane. *In situ* energy-dispersive X-ray (EDX) analysis indicates the clusters contain Fe and C, and occasional clusters also show some Al indicating that these contain some of the Al_2O_3 support layer. Additional investigation, perhaps involving X-ray diffraction (XRD) is needed to understand the composition and possible crystallinity of these clusters.

The U-shaped bands qualitatively match the shape of a laminar flow profile across the sample, where the gas velocity is highest and therefore the gas residence time is longest. We hypothesize that the gas chemistry changes as the boundary layer flow proceeds along the sample. This evolution occurs both from self-pyrolysis of CH_4, catalytic decomposition of CH_4 into H_2 and

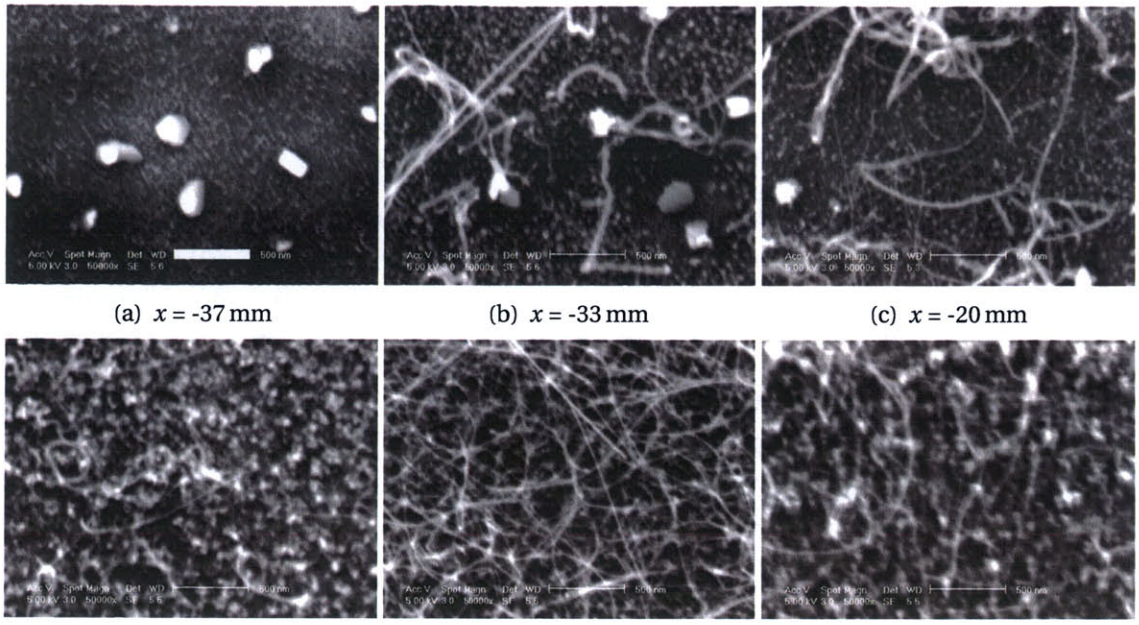

(a) x = -37 mm (b) x = -33 mm (c) x = -20 mm

(d) x = -8 mm (e) x = 17 mm (f) x = 40 mm

Figure 3-29. SEM images from selected locations on long sample (Fig. 3-28), showing morphology transition caused by thermal and catalytic development of gas atmosphere. Scales 0.5 μm.

other hydrocarbons, and deposition of elemental carbon. This might be expressed as a function of position x in the direction of flow over the sample:

$$CH_4 \rightarrow aCH_4 + bCH_x + (1-a-b)\,C_{(s)} + (2-bx/2)H_2, \tag{3.5}$$

where the coefficients a and b change with x.

Raman spectra (λ = 514 nm) taken along the mid-line of the sample give the G/D ratio and G/Si ratio profiles shown in Fig. 3-31. Each profile has two local maxima, and the maxima on both samples are near x = -25 mm and x = 15 mm. Relatively, the first pair of maxima has a low G/Si ratio and a high G/D ratio, and the second pair has a high G/Si ratio and a low G/D ratio. Between these maxima the signals are very weak, and there is almost no growth as confirmed by the SEM image taken at x = -11 mm. The temperature distribution along the central axis of the furnace tube is sufficiently uniform to discount that spatial variation in sample temperature causes this behavior. The double-peak trend is qualitatively similar to the variation of the G/D and G/Si ratios measured on regular samples processed in different H_2/CH_4 mixtures. On these samples, CNTs are first observed at $H_2/CH_4 \approx 0.04$; however, the maximum quality is observed at a higher H_2 concentration than the maximum yield.

Here, it appears that the residence time of the gas mixture over the catalyst, rather than the time at high temperature, is most important in determining the nature of the gas reactivity with the catalyst. Therefore, the catalyst is decomposing the gas mixture as it flows over the substrate sample, and the gas at a given downstream point on a long sample is more active than at the same point in the tube where a much smaller sample of catalyst-coated substrate is placed. This is demonstrated when the samples diagrammed in Fig. 3-33 are processed under

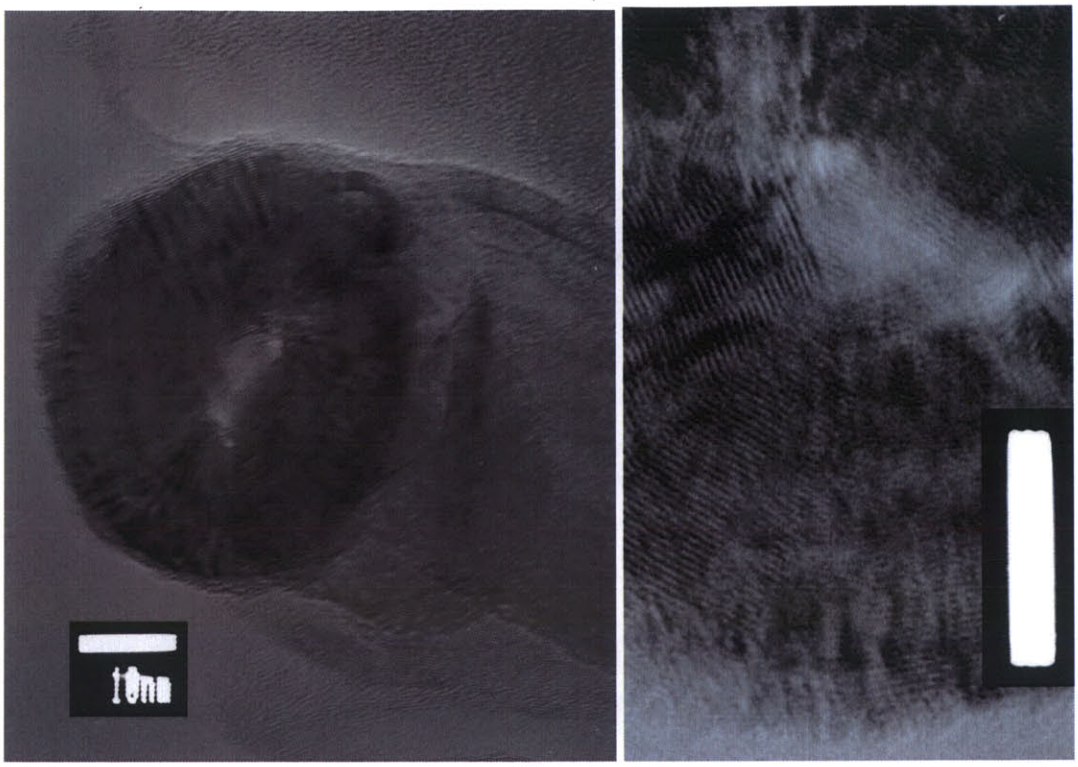

(a) (b)

Figure 3-30. HRTEM images of onion-like clusters observed near x =-30 mm on long sample. Scales 10 nm.

identical growth conditions. No growth occurs on a small sample placed either at the center of the furnace or at the point downstream of the center where the highest yield occurs on the long sample. When four small samples are spaced along the tube only sparse growth is observed on the last sample, and as the size of the small samples is increased and the spacing is decreased so the configuration approaches that of the long sample, growth is observed farther upstream.

Previous literature demonstrates that adding a catalytic compound upstream of the growth location can significantly enhance CNT yield by increasing the activity of the carbon species [184–187]. This mechanism is likely at work on our long samples as well. The technique of placing a continuous sample of catalyst in the furnace and examining the spatial variation of the products could be used to quickly understand the effect of evolving gas activity on a variety of catalytic reactions. This continuous sample might be a coated substrate, a coated fiber, or a "boat" containing powdered catalyst. Compared to a parametric study which uses a large number of "small sample" experiments processed individually at closely separated parameter sets (e.g. temperature, flow rates), a "long sample" parametric study could use a much narrower set of experiments at more spaced conditions.

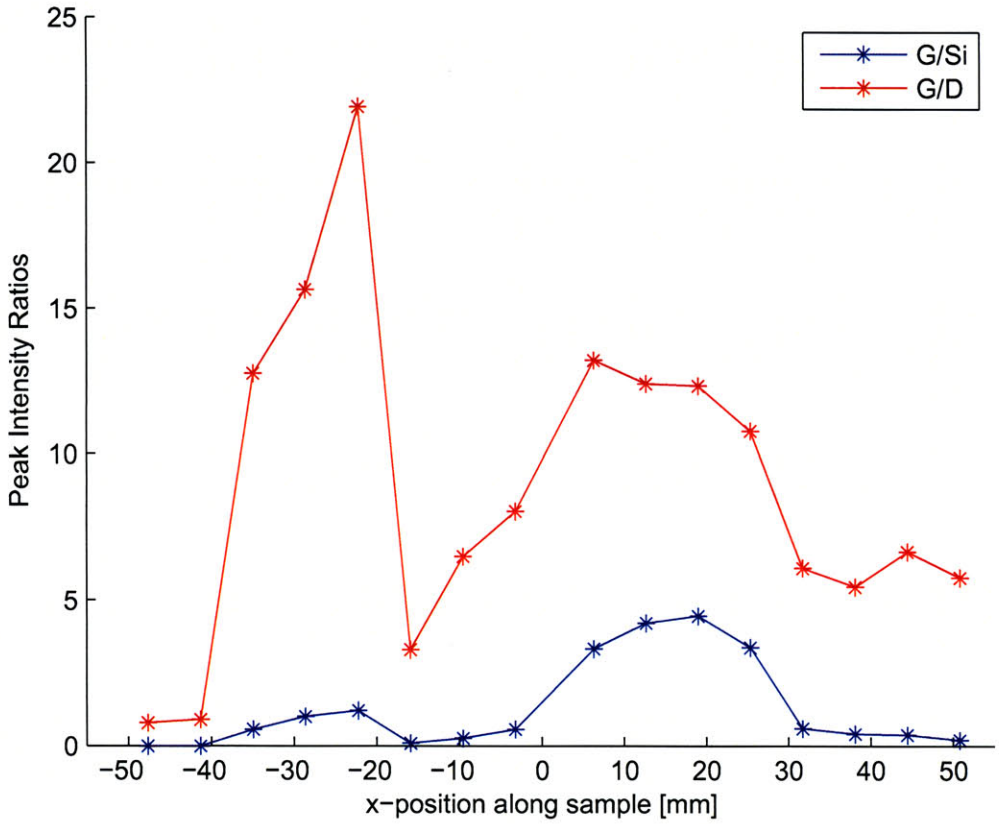

Figure 3-31. Spatial profiles of G/Si and G/D ratios calculated from Raman spectra taken along centerline of long substrate sample.

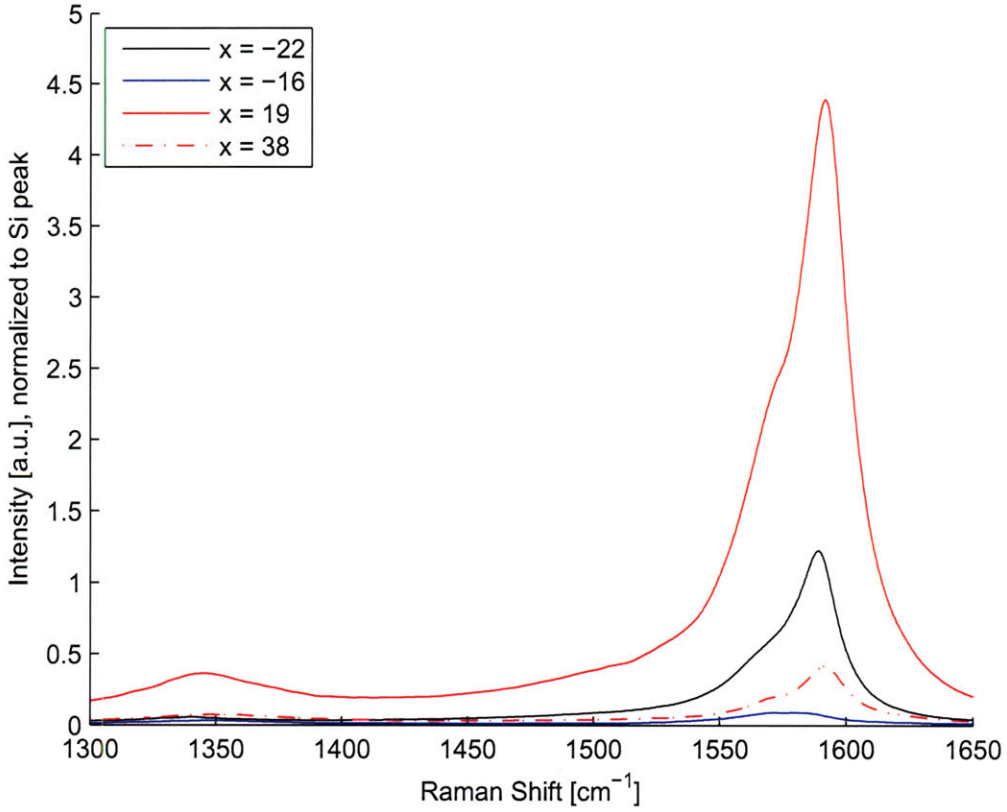

Figure 3-32. G and D bands from Raman spectra taken at selected positions on long sample (with corresponding G/D ratios as in Fig. 3-31), normalized to Si peak height.

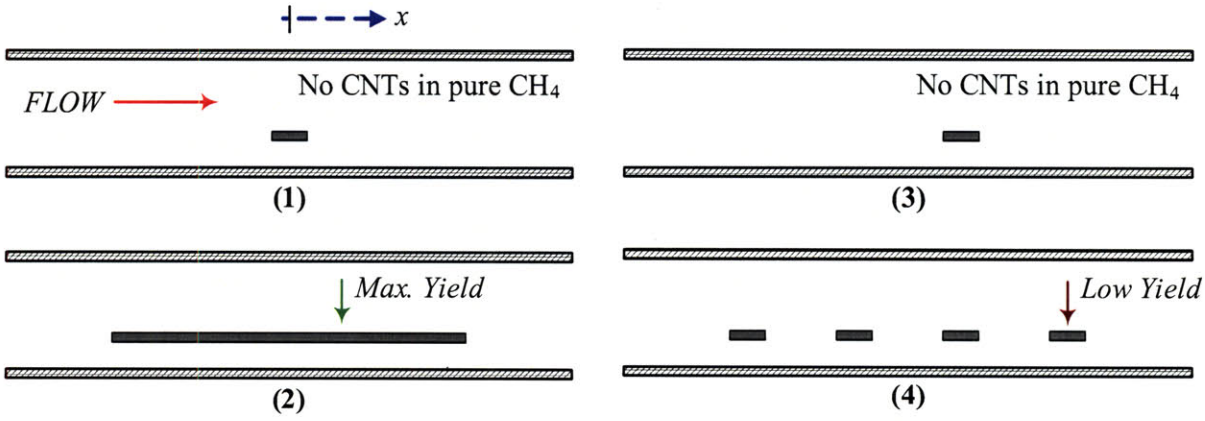

Figure 3-33. Sample configurations for qualitative assessment of how gas activity evolves with flow along furnace tube and over catalyst surfaces.

3.3.2 Diffusion-restricted growth by capping the sample

Realizing from the long sample experiments that the time spent at high temperature significantly affects the gas reactivity for CNT growth, we hypothesized that slowing or stagnating the gas flow over the catalyst substrate might allow it to reach a high reactivity over a shorter flow distance. One method is to simply place a second silicon sample as a "shield" or a "cap" over a catalyst-coated silicon sample (Fig. 3-34), requiring the gas to diffuse into the gap between the cap and the catalyst-coated sample surface. This shortens the spatial dependence of the gas chemistry, as the mixture flows through the gap and evolves within a few millimeters of the entry between the cap and the sample.

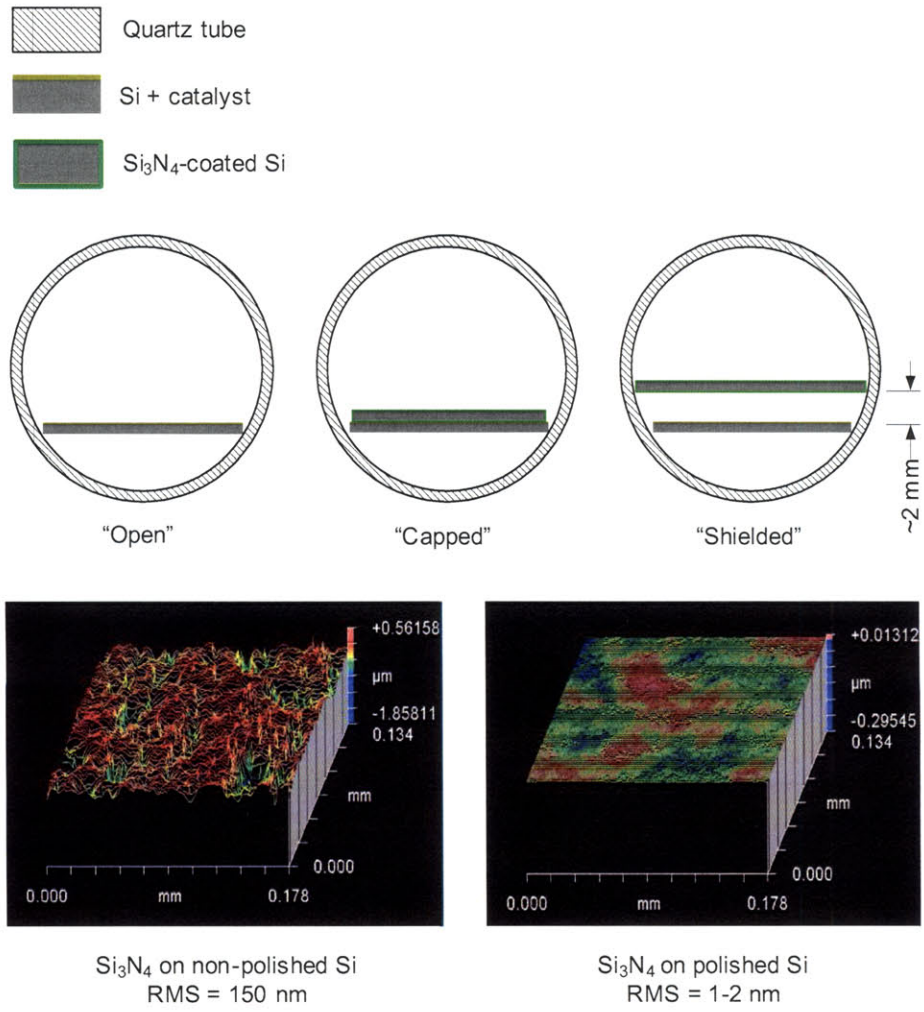

Figure 3-34. Open, capped, and shielded sample configurations, and comparison of surface roughnesses of Si_3N_4-coated non-polished and polished silicon surfaces measured using Zygo NewView optical surface profilometer.

Fig. 3-35 shows SEM images, and Table 3.3 and Fig. 3-36 summarize Raman spectroscopy data from the center of 15×30 mm (30 mm along the flow direction) samples processed in open, shielded, and capped configurations. Compared to an open sample processed under the same

conditions, capping the sample significantly increases the CNT yield and decreases the CNT quality. Interestingly, the highest yield and lowest quality are observed on the capped sample processed in 100% CH_4, which yields no CNTs in the open configuration. Like on a long sample, the increased residence time of the gas over the catalyst in the capped configuration causes pure CH_4 to decompose into a more complex (yet unknown) chemistry which is suitable for CNT growth.

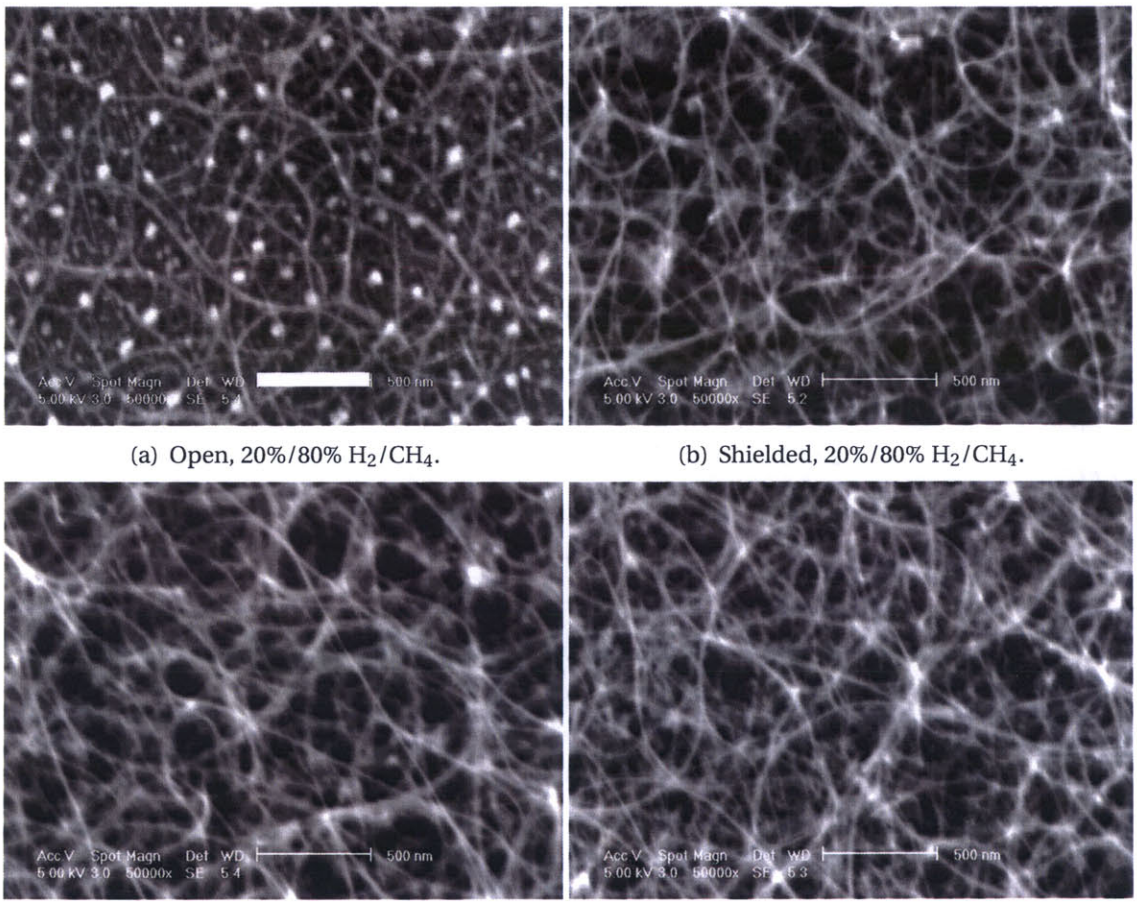

(a) Open, 20%/80% H_2/CH_4.

(b) Shielded, 20%/80% H_2/CH_4.

(c) Capped, 20%/80% H_2/CH_4.

(d) Capped, 100% CH_4.

Figure 3-35. SEM images comparing fully-developed film structures in center areas of samples processed in open, shielded, and capped configurations, at 875 °C for 15 minutes. Scales 0.5 μm.

In the shielded configuration, where the gas flow is slowed in the 2 mm gap between the sample and the shield but can proceed continuously over the full area of catalyst, the G/Si and G/D ratios are between the values measured from the open and capped samples.

When the cap is flipped so the polished side instead of the non-polished side contacts the catalyst film, the yield decreases and the quality increases, likely because of slower diffusion of gas through the smaller gap between the polished surfaces. Fig. 3-34 shows surface profiles of the polished and non-polished surfaces of silicon wafers coated with Si_3N_4; the roughness of the polished side is approximately 2 nm, and the roughness of the non-polished side is approximately 150 nm. While the samples were cleaned and blown dry just prior to capping, it is

ID	Conditions	G/D	G/Si	Rel. Yield	RBM/Si
238	Open, 20%/80% H_2/CH_4, 15 min.	25.0	1.3	1.0	0.08
362	Npol-cap, 20%/80% H_2/CH_4, 15 min.	16.2	4.7	3.6	0.37
364	Npol-cap, 20%/80% H_2/CH_4, 3 min.	14.5	3.2	2.5	0.43
368	Npol-cap, 100% CH_4, 15 min.	8.7	6.0	4.6	0.52
371	Pol-cap, 20%/80% H_2/CH_4, 15 min.	13.6	2.9	2.2	0.31
241	Shielded, 20%/80% H_2/CH_4, 15 min.	17.8	2.3	1.8	0.22

Table 3.3. Comparison of peak intensity ratios of Raman spectra of samples grown in open, capped, and shielded configurations, at 875 °C. All data are averages of 5 spectra taken with 100X objective at nearby locations in center area of sample.

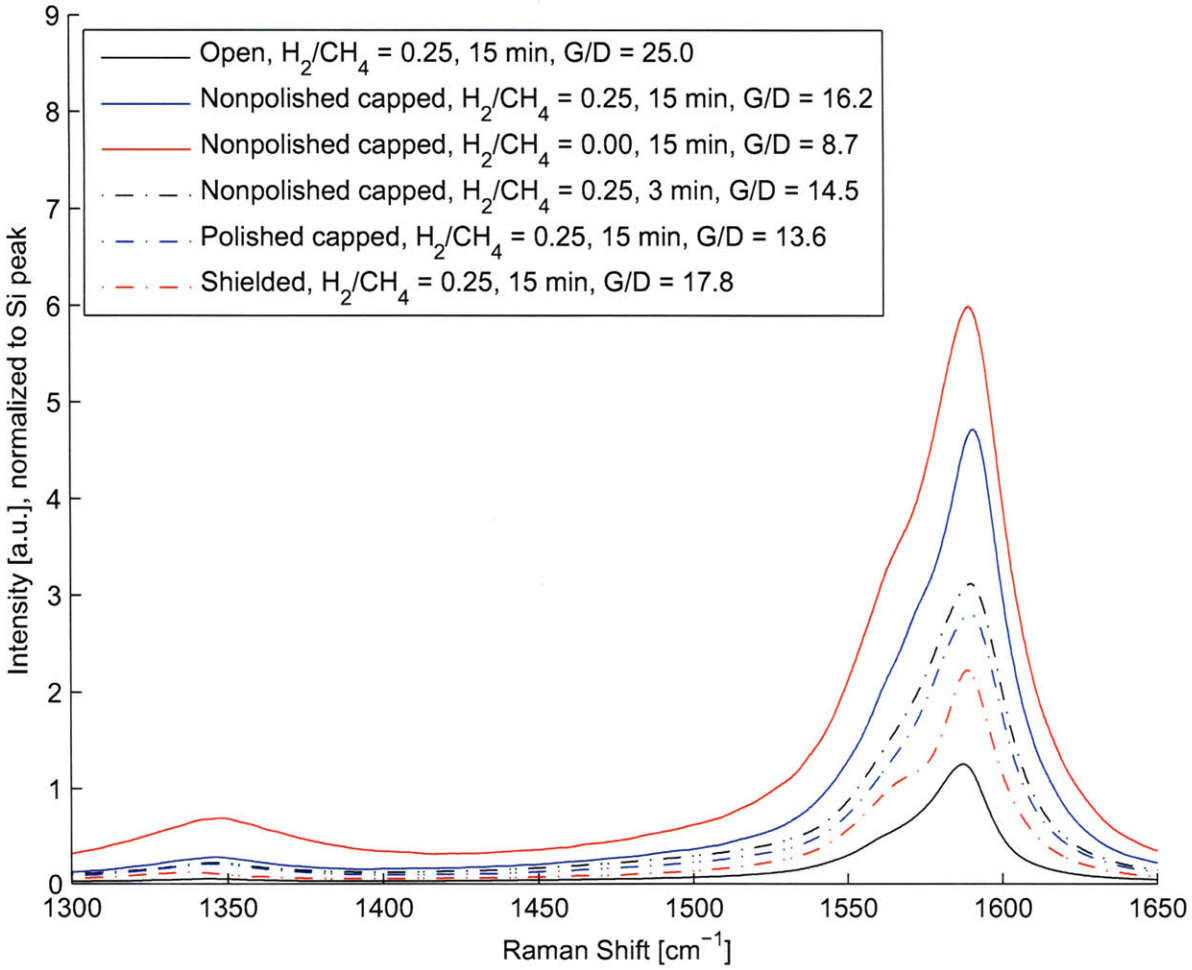

Figure 3-36. Raman spectroscopy analysis of CNT films grown in various substrate configurations, with 400 sccm total flow through tube furnace at 875 °C. Plot shows normalized Raman spectra, G and D bands only.

likely that particles increase the gap beyond the nominal value dictated by surface roughness; however, we are certain that the gap in the non-polished configuration is larger than the gap in the polished configuration.

Further, we observe a generally inverse relationship between CNT yield and quality on samples processed in the capped configuration. Conversely, there is no yield-quality correlation among samples processed in an open configuration at a wide variety of temperatures and gas compositions. In the open configuration, increasing the flow rate from 400 to 1200 sccm at $H_2/CH_4 = 0.25$ increases both yield and quality. In the open configuration, the reaction products are easily carried away with the gas flow, while when capped, the narrow gap between the cap and the sample may trap the products, plausibly leading to higher amorphous carbon content and a lower G/D ratio. These trends, in addition to the progression observed on long samples, emphasize that the relationship between the gas activity and the nature of the CNT products is non-monotonic and depends on the sample configuration and processing conditions.

Annealing the sample prior to growth in the open configuration does not change the G/D or G/Si ratio of the CNT film considerably (10–20% fluctuations, which fall within measurement error); however, if a sample is initially heated in the capped configuration, the catalyst film breaks into clusters, and only sparse growth of low-quality CNTs occurs when CH_4 or H_2/CH_4 is introduced. It appears that the film releases adsorbates and/or gases (possibly H_2O) when annealed, and these released species are trapped under the cap and cause the film to fragment. Breakup may be further attributed to the presence of Mo, since a similar film consisting of only Fe/Al_2O_3 does not fragment when first heated while capped. Therefore, before growing CNTs from capped samples, the samples were annealed in Ar for 30 min at 875 °C.

We also examined how the film morphology changes with the distance under the cap, which is analogous to the evolution of the film along the flow direction of long samples. On the 15×30 mm samples, the CNT yield and quality become fully-developed within 1 mm of the leading edge when processed in H_2/CH_4, while it takes approximately 4 mm for the film to develop in pure CH_4 (Fig. 3-37). SEM images support this observation and show how the film morphology evolves (Figs. 3-38 and 3-39) from clusters into a densely branched mat of small-diameter CNTs. For the sample capped in 100% CH_4, the clusters appear to "burst" into large-diameter tubes where the mat of small-diameter CNTs also starts growing, just like on the long sample. However, on capped samples the G/D and G/Si ratios do not show the bimodal profiles measured on the long sample, and instead reach relatively stable values with increasing distance under the cap.

In the open configuration, the width of the sample (normal to the flow direction, which determines the height at which the sample rests relative to the axis of the furnace tube) does not measurably affect the yield or quality. For capped samples, the CNT yield at the centerline is lower on wider samples (Fig. 3-40), because as the width increases, a lesser quantity of gas reaches the centerline of the sample. We expect that on even wider samples, the yield would decay significantly along the centerline of the sample, as the gas would be consumed and/or decomposed into a chemical state not suitable for CNT growth. By modelling the diffusive flow between the cap and the sample, along with the reaction at the catalyst surface it would be possible to estimate how the chemistry changes through the gap. This would give the distance it takes for the gas to reach a steady composition, a sort of "penetration length" at which the decomposition rate and flow rate are balanced. This also points us toward using porous substrates to establish spatial uniformity of gas flows to CNT growth substrates over large areas.

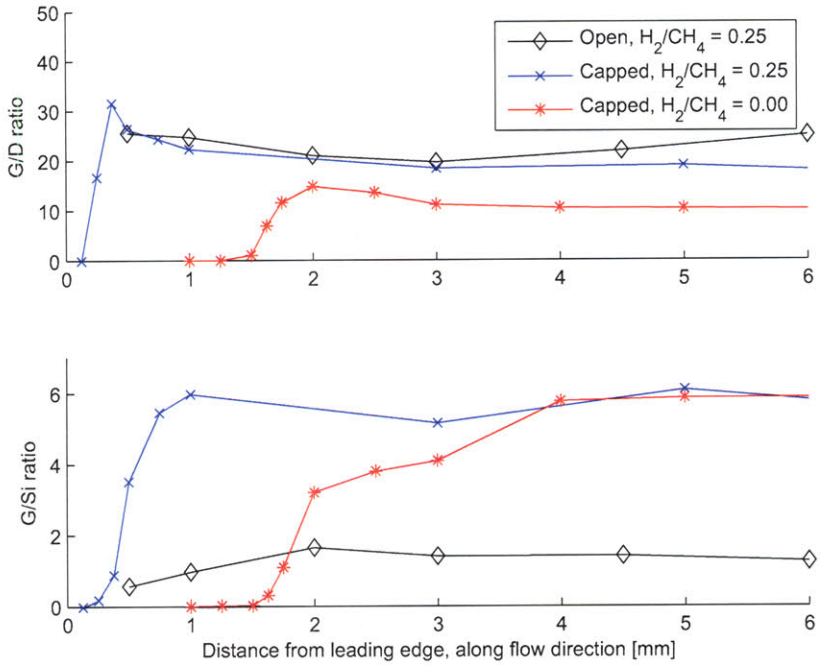

Figure 3-37. Comparison of film yield and quality profiles under cap, in H_2/CH_4 and CH_4 growth atmospheres; growth at 875 °C for 15 min.

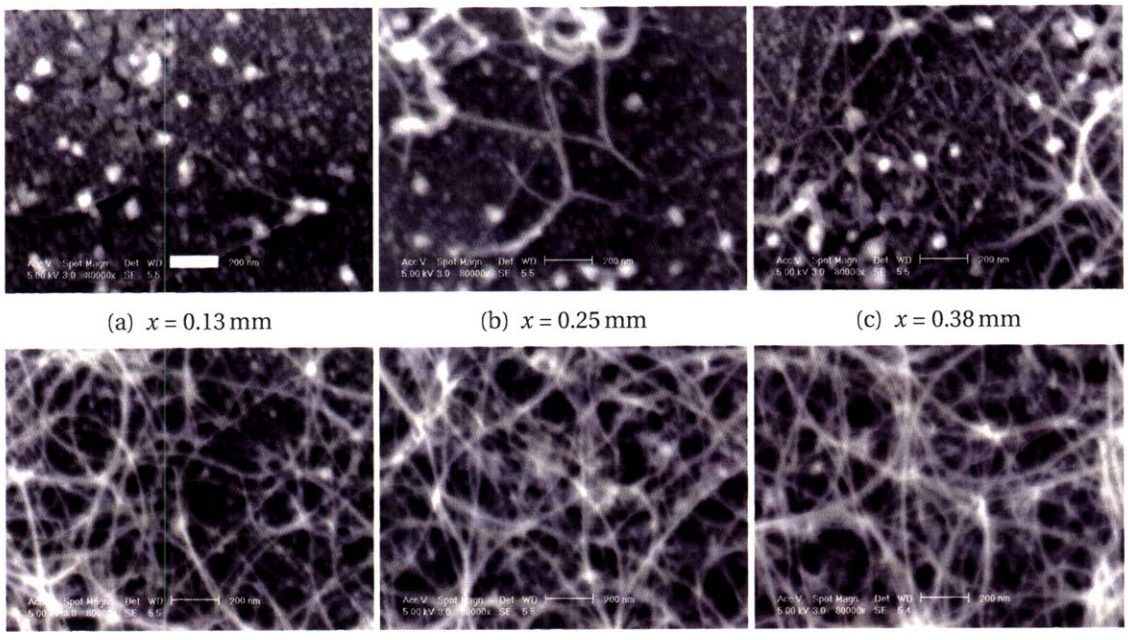

(a) $x = 0.13$ mm (b) $x = 0.25$ mm (c) $x = 0.38$ mm

(d) $x = 0.50$ mm (e) $x = 1.00$ mm (f) $x = 17.0$ mm (center)

Figure 3-38. SEM images showing development of CNT film structure under cap, measured from leading edge where the cap rests on the sample. $H_2/CH_4 = 0.25$, 400 sccm total flow, 875 °C, 15 min. Scales 0.2 μm

(a) $x = 1.13\,\text{mm}$ (b) $x = 1.25\,\text{mm}$ (c) $x = 1.63\,\text{mm}$

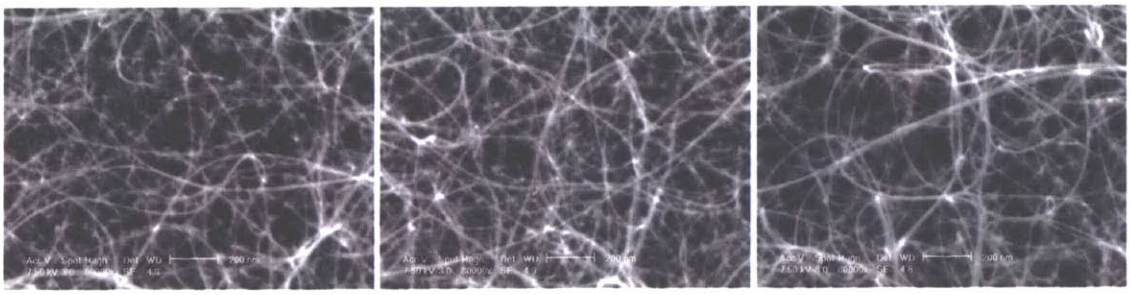

(d) $x = 1.88\,\text{mm}$ (e) $x = 2.00\,\text{mm}$ (f) $x = 17\,\text{mm}$ (center)

Figure 3-39. Development of CNT film structure under cap; 400 sccm CH_4, 875 °C, 15 min. Scales 0.2 μm.

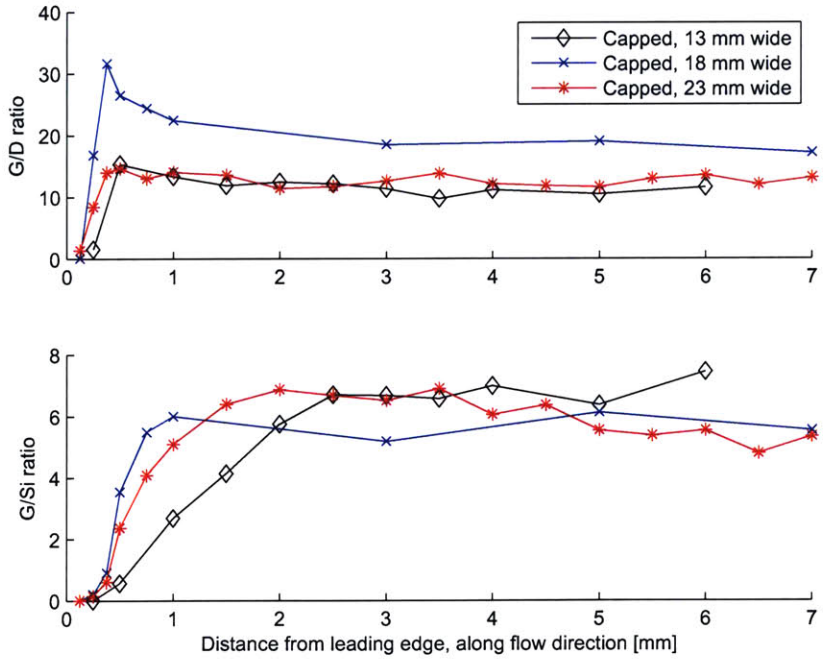

Figure 3-40. Effect of sample width on film yield and quality profiles under cap, for growth in 400 sccm of H_2/CH_4= 0.25, at 875 °C, for 15 min.

3.3.3 CNT-substrate interactions on patterned substrate samples

When we grow CNTs from $Mo/Fe/Al_2O_3$ on Si, where the film has been patterned by lift-off of image-reversal photoresist (procedure described in section 4.1.1), the CNTs which grow from the edges of the catalyst patterns onto the bare Si substrate appear to "melt" into faceted clusters (Fig. 3-41). These clusters look like those at the leading edge of the long or capped samples and among tangled CNTs on some short samples. Away from the edges of patterns, the CNTs are densely tangled on the catalyst. The clusters which interact with the Si substrate (Fig. 3-42) appear to be arranged in loop and curve layouts further suggesting that these are broken and transformed CNTs. The high density and large size of the clusters relative to original the size of the CNTs suggests that additional material is added to form the clusters, either by additional deposition from the reaction atmosphere or by contribution from the substrate. Many of the clusters seem to be growing upward from the substrate surface, suggesting the clusters are firmly rooted in the substrate and that the CNTs template cluster nucleation. The dissolution of the CNTs and growth of the clusters is more complete for longer processing times; almost no CNT segments are visible in SEM on samples processed in H_2/CH_4 for 60 min.

When the film is patterned on Si coated with $\approx 1\ \mu$m of thermal SiO_2, the CNTs grow smoothly onto the substrate and do not appear to transform in reaction with the substrate (Fig. 3-43). Therefore, unoxidized Si (assuming the native SiO_2 on Si is removed by H_2), along with one or more of C/Mo/Fe/Al, cause cluster formation. The CNTs may be carrying traces of Mo, Fe, and/or Al onto the Si substrate, and these traces could mix with Si and thereby nucleate transformation of CNTs into metal-C clusters. For reference, the eutectic of Fe-C forms above 1153 °C, and Fe-Si forms at 1196 °C. Experimentally, these compounds form readily at lower temperatures due to melting point suppression of nano-sized clusters [167,311].

Further, it is unlikely that these clusters are diamond nanocrystals, although many reports have studied the transformation of CNTs to sp^3-hybridized structures including diamond nanocrystals, diamond nanorods, and carbon "onions" [312–315]. Additional characterization by methods such as XRD, EDX, and TEM might reveal more about the structure and composition of these clusters, and enable a comparison to the clusters observed within the CNT film areas.

Also, we see a much more intricate image when the clusters are examined at a higher SEM accelerating voltage of 25.0 keV (Fig. 3-44). No traces of Fe, Mo, or Al are detected when the clusters are examined using EDX in our Philips XL-30 FEG-ESEM; however, the resolution of the EDX instrument is insufficient to detect the $Mo/Fe/Al_2O_3$ catalyst film in the first place.

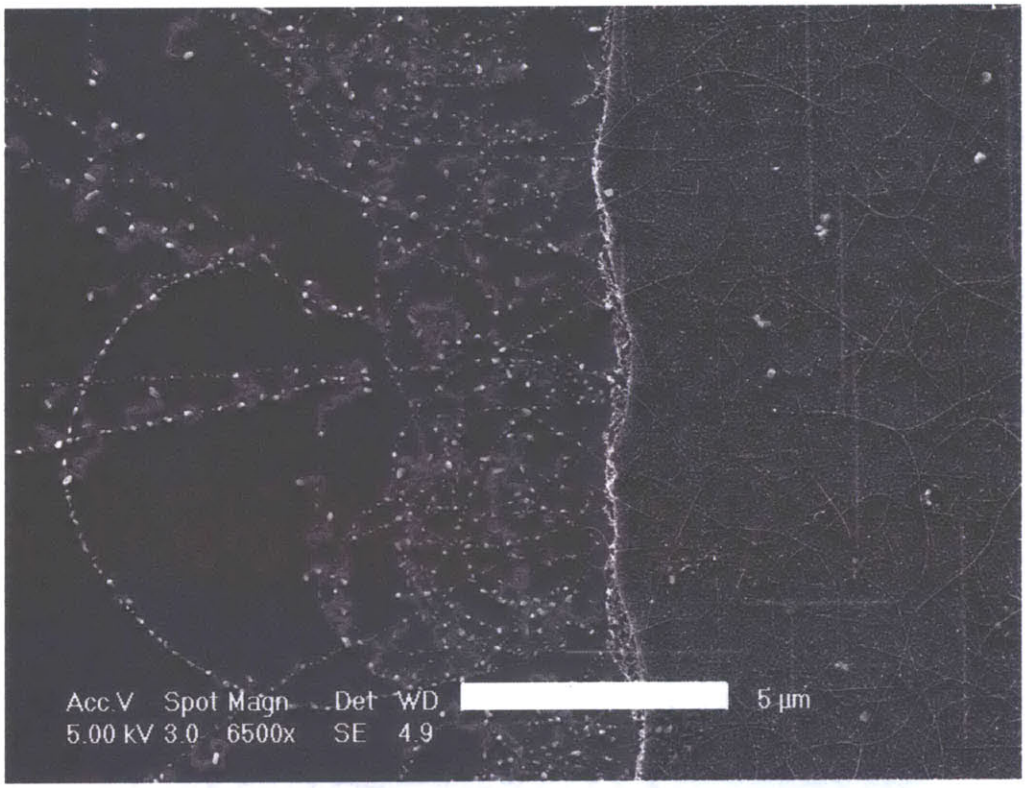

(a)

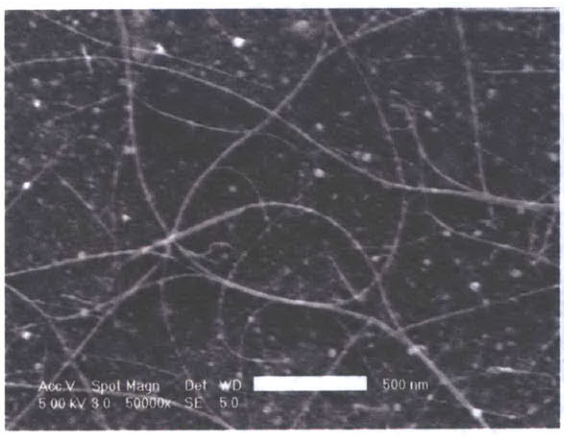

(b)

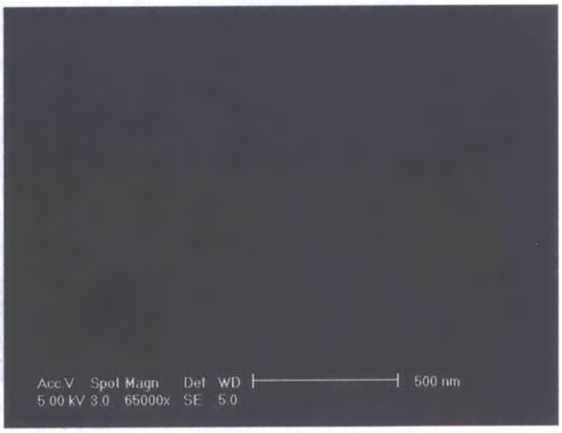

(c)

Figure 3-41. CNT growth from Mo/Fe/Al_2O_3 patterned on bare silicon by lift-off of image-reversal photoresist: (a) edge of catalyst patch, showing tangled CNTs over catalyst patch (at right side) and patterns of CNTs mixed with bright clusters on adjacent silicon area (at left side); (b) close-up of CNTs in center of catalyst patch; (c) close-up of bare substrate far from catalyst patch. Scales are 5 μm in (a), and 0.5 μm in (b) and (c)

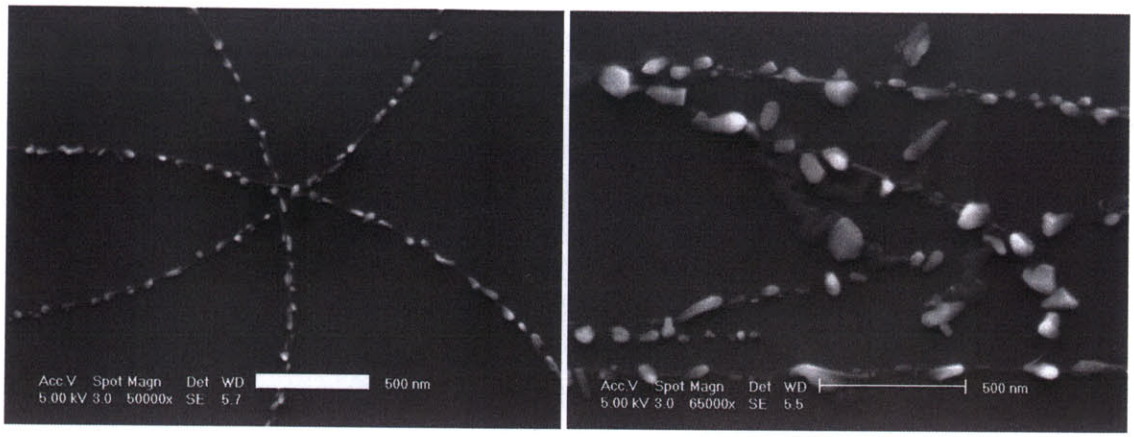

(a) (b)

Figure 3-42. Close images showing "melting" of CNTs into clusters on bare Si substrate processed in H_2/CH_4= 0.25. Scales 0.5 μm.

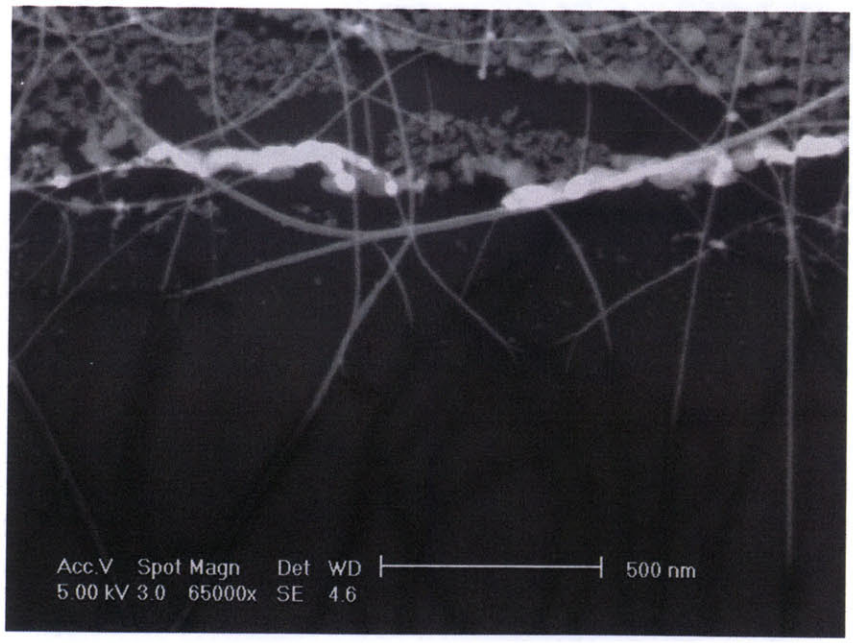

Figure 3-43. Catalyst patterned on SiO_2 by lift-off of image-reversal photoresist. CNTs appear to extend smoothly from the catalyst patches onto the substrate, and do not "melt" into the clusters seen when CNTs extend onto the bare Si substrates (FG-70). Scale 0.5 μm.

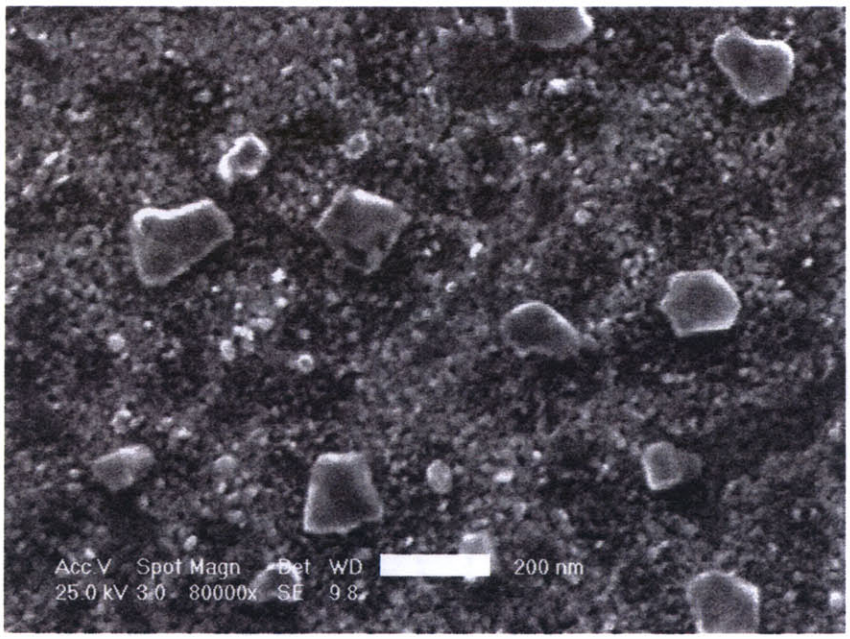

Figure 3-44. Clusters from $Mo/Fe/Al_2O_3$ substrate, examined at 25.0 keV. Scale 0.2 μm.

Chapter 4

Synthesis of Coordinated Architectures of Multi-Wall CNTs

This chapter discusses synthesis of coordinated architectures of small-diameter MWNTs, by atmospheric-pressure thermal CVD of $C_2H_4/H_2/Ar$ on Al_2O_3-supported iron catalysts. First, films and lithographically-templated microstructures of vertically-aligned CNTs (VA-CNTs) are grown on silicon substrates from a Fe/Al_2O_3 catalyst film deposited by electron beam evaporation. The structures grow to 1 mm height in 15 minutes, and reach close to 2 mm in 60 minutes. Spatial transitions between tangled and aligned morphologies are achieved by briefly pre-conditioning the substrate with H_2/Ar at the growth temperature, and by changing the configuration of the sample inside the furnace tube. The growth rate and final height of CNT microstructures grown from catalyst patterns depends strongly on the local areal density of catalyst, representing a reverse analogue of loading effects which occur in plasma etching processes. Periodically varying the gas composition in the furnace demonstrates the ability to pause, resume, deactivate, and reactivate growth, and enables fabrication of split multi-layer films. Detailed SEM examination of the film microstructure suggests how mechanical stresses could slow and limit CNT film growth. Comparative studies illustrate the effects of the supporting layer and catalyst heating rate on CNT yield from Fe in C_2H_4.

Using the same CVD reaction, we demonstrate that a VA-CNT film can exert mechanical energy as it grows, and in our experiments the average force output is approximately 0.16 nN per CNT, for CNTs having an outer diameter of 9 nm and five walls. The film thickness after a fixed growth time and the alignment of CNTs within the film decrease concomitantly with increasing pressure which is applied by placing a weight on the catalyst substrate prior to growth, and CNTs grown under applied pressure exhibit significant structural faults. The measured mechanical energy density of CNT growth is significantly less than the energies of primary steps in the CNT formation process, yet based on the film volume is comparable to the energy density of muscle, and based on the volume of CNTs is comparable to hydraulic actuators. We utilize this principle to "grow-mold" three-dimensional structures of CNTs which conform to the shape of a microfabricated template. This technique is a catalytic analogue to micromolding of polymer and metal microstructures; it enables growth of nanostructures in arbitrarily-shaped forms having sloped surfaces and non-orthogonal corners, and does not require patterning of the catalyst before growth.

Further, coatings of aligned MWNTs are grown directly on Al_2O_3 fibers coated by a Fe salt solution, at rapid and commercially-relevant rates. This technology has catalyzed a collaborative research effort in fabrication and testing of CNT-reinforced hybrid composites.

4.1 Rapid growth of millimeter-scale aligned CNT structures on silicon substrates (based on [3])

Synthesis of macroscopic CNT materials having mechanical, electrical, and thermal properties comparable to those of individual CNTs remains elusive, in large part due to incomplete knowledge of the growth behavior of CNTs. It is accepted that CNT growth by CVD involves surface and/or bulk diffusion of carbon at a metal catalyst particle. At a high catalyst density and CNT growth rate, a vertically-aligned growth mode is typical whereby the CNTs self-orient perpendicular to the substrate surface due to initial crowding and continue to grow upward in this direction [143, 144]. However, the mechanism of termination of vertically-aligned growth is not clearly known. At all stages of CNT growth, chemical and mechanical interactions are highly coupled, and these interactions must be further understood for efficient synthesis of CNT materials containing long CNTs having macroscopic lengths.

While CNT growth from floating catalytic sites [26, 78] is readily more scalable for bulk synthesis, growth from substrates offers greater control of the arrangement, density, and length of CNTs. Typically, growth of aligned CNTs on a substrate is achieved using an unsaturated hydrocarbon gas such as C_2H_2 [316, 317] or C_2H_4 [144, 318] and a predeposited catalyst film or by evaporating a solution of an organometallic catalyst precursor and a liquid hydrocarbon [319–321]. Millimeter-scale architectures of aligned MWNTs have been routinely achieved using floating catalyst precursors [322,323]; however, these structures typically have lesser crystallinity and higher impurity content (e.g., metal catalyst periodically along the tube axis) than structures grown from pre-deposited catalyst films. Further, by adding an optimal amount of ferrocene ($Fe(C_5H_5)_2$) to C_2H_2 feedstock during growth, Eres et al. [324] increased the terminal length of VA-MWNTs, grown from a Mo/Fe/Al catalyst film, from less than 0.5 mm to greater than 3 mm. This is attributed to $Fe(C_5H_5)_2$ increasing the effectiveness of C_2H_4 by promoting its dehydrogenation before reaching the catalyst site. Further study has shown that gas-phase reactions critically affect the CNT growth process in many systems, and that a minimum incidence rate of carbon-containing molecules is necessary for vertically-aligned growth [191].

Recently, the first atmospheric pressure synthesis of vertically-aligned SWNTs was reported [205], where introduction of a controlled concentration of H_2O vapor gives rapid growth of high-purity SWNT films to a thickness of up to 2.5 mm, possibly due to selective removal of catalyst-bound amorphous carbon by H_2O. Since, plasma-enhanced CVD growth of VA-SWNT [325] and VA-DWNT [326] films has been achieved, without using an oxygen-containing additive.

This section discusses growth of VA-MWNT films and microstructures from a Fe/Al_2O_3 catalyst film deposited by e-beam evaporation. The CNTs grow rapidly to at least 1 mm height when processed in $C_2H_4/H_2/Ar$ for 15 minutes. Incidentally, our CVD conditions are similar to those upon which the H_2O-assisted process has been studied [205]. Here, without the addition of H_2O, we synthesize thin MWNTs instead of SWNTs, yet maintain similar growth rates as the H_2O-assisted process [162]. We first studied synthesis of tangled SWNT films from

$Mo/Fe/Al_2O_3$ in CH_4/H_2, and then found that the same catalyst gives poor yield of MWNTs in an otherwise identical process using C_2H_4/H_2 at 750 °C, while VA-MWNT structures grow from Fe/Al_2O_3 in C_2H_4/H_2 (section 3.1, [1]).

4.1.1 Materials and methods

A catalyst film of 1.2/10 nm Fe/Al_2O_3 is deposited by electron beam evaporation in a single pump-down cycle using a Temescal VES-2550 with a FDC-8000 Film Deposition Controller. The film thickness is measured during deposition using a quartz crystal monitor, and later confirmed by Rutherford backscattering spectrometry (RBS) [327]. The substrates are plain (100) 6" silicon wafers (p-type, 1-10 Ω-cm, Silicon Quest International), which have been cleaned using a standard "piranha" (3:1 H_2SO_4:H_2O_2) solution. Because the Al_2O_3 is deposited by direct evaporation from a crucible of high-purity crystals, rather than by evaporation of Al [272,318], or by other methods such as spin-coating of a sol-gel precursor [193], we do not a dedicated oxidation or curing step prior to CNT growth. Catalyst patterns are fabricated by lift-off of a 1 μm layer of image-reversal photoresist (AZ-5214E): the photoresist is patterned by photolithography, catalyst is deposited over the entire wafer surface, and then the areas of catalyst on photoresist are removed by soaking in acetone for 5 minutes, with mild sonication.

CNT growth is performed in a single-zone atmospheric pressure quartz tube furnace (section 6.1), having an inside diameter of 22 mm and a 30 cm long heating zone, using flows of Ar (99.999%, Airgas), C_2H_4 (99.5%, Airgas), and H_2 (99.999%, BOC). The furnace temperature is ramped to the setpoint temperature in 30 minutes and held for an additional 15 minutes under 400 sccm Ar. The flows of Ar and H_2 used during growth are established typically 1–5 minutes prior to introducing C_2H_4, then the C_2H_4/H_2/Ar mixture is maintained for the growth period of 15–60 minutes. Finally, the H_2 and C_2H_4 flows are discontinued, and 400 sccm Ar is maintained for 10 more minutes to displace the reactant gases from the tube, before being reduced to a trickle (≈10 sccm) while the furnace cools to below 150 °C.

Samples are characterized by SEM using a Philips XL30-FEG-ESEM typically at 5 keV, by HRTEM using a JEOL-2010 typically at 200 keV, and by Raman spectroscopy with 647 nm excitation at 2 mW power. TEM samples are prepared by removing a piece of the aligned CNT film with tweezers, dispersing the CNTs in methanol by vortexing for 2 minutes and sonicating mildly for 30 minutes, and air-drying a drop of the solution on a copper grid coated with a holey carbon film. For Raman spectroscopy, the microscope is focused on the sidewall of the film to maximize the G-band intensity from CNTs oriented mainly perpendicular to the laser beam. The areal density of CNTs on the substrate is calculated using the average CNT diameter measured by HRTEM imaging, the film volume which is estimated by SEM imaging, and the mass determined by scraping the film from the substrate and weighing it using a thermogravimetric analyzer (TGA, Perkin-Elmer) at room temperature.

4.1.2 Results

4.1.2.1 Thick films and high-aspect-ratio microstructures

Millimeter-tall VA-CNT films are grown from the Fe/Al_2O_3 film processed in 100/500/200 sccm $C_2H_4/H_2/Ar$, at 750 °C, as shown in Fig. 4-1. The structures grow rapidly, reaching 0.9 mm height in 15 minutes, and terminating at 1.8 mm height after 60 minutes. The average growth rate of 1 μm/s during the first 15 minutes indicates that approximately 9,300 circumferential "floors" of carbon atoms per second are added to each CNT. The side view in Fig. 1b shows that the CNTs are oriented primarily perpendicular to the substrate. The CNTs are primarily arranged in strands as large as 0.1 μm diameter, in which the CNTs are held closely by surface forces, and there is significant bridging between nearby strands. HRTEM examination (Fig. 4-1c) shows that the CNTs are primarily multi-wall and tubular [328], without bamboo-like crossovers [329, 330]. The CNTs average approximately 8 nm OD and 5 nm ID, and most have 3–7 concentric parallel walls. By SEM examination, metal clusters are routinely observed at the roots of CNTs ripped from the substrate; however, in thorough TEM examination, we have not observed any metal particles along the CNTs. Therefore, the CNTs grow by a "base growth" mechanism [117], where the catalyst particle remains on the substrate and new carbon is added there. The density of CNTs on the substrate is estimated as 1.5×10^{10} CNTs/cm^2, and appears the same from the top to bottom of the film sidewall, suggesting that the CNTs extend fully through the thickness of the film.

A typical Raman spectrum (Fig. 4-2) of our VA-MWNT films has a G/D peak intensity ratio slightly greater than unity. This is compared to the spectrum of a film of tangled SWNTs grown from a $Mo/Fe/Al_2O_3$ film in CH_4/H_2 in an identical tube furnace [1], which has $G/D >$ 20. The MWNTs also have a strong G' band near 2650 cm^{-1} [331], and low-frequency modes at approximately 215 cm^{-1} and 340 cm^{-1}. The low-frequency modes could correspond to radial breathing of inner shells of MWNTs which by the relation $d = 224/\omega_{RBM}$ [332] gives d = (1.04,0.66) nm; however, by HRTEM we have not observed inner diameters smaller than 3 nm. The G-band is split broadly, and can be decomposed into Lorentzian-shaped peaks [283] centered at 1570 cm^{-1} and 1605 cm^{-1}.

The G/D ratio and the low-frequency modes do not change through the thickness of the film (i.e., at the bottom, middle, or top of the sidewall or on the top surface which is tangled), and are not significantly affected by the position of the sample in the furnace. However, the high-frequency component of the G-band is typically more prominent near the top of the film. A G/D ratio close to unity is typical for VA-MWNTs grown by other thermal CVD methods [160, 333], and the strong D-band arises both from defects in the CNTs and amorphous carbon on the sidewalls [308]. Overall, Raman characteristics of MWNTs have not yet been studied thoroughly in the literature. Additional work is needed to understand the origin of the low-frequency modes and the broad splitting of the G-band in our samples, as well as to characterize samples grown at a wide variety of temperatures and gas compositions.

When the catalyst film is patterned, CNT structures having identical cross-sections can be grown in large arrays (Fig. 4-3a), and complex shapes can be defined (Fig. 4-3b). Growth depends strongly on the areal density of catalyst, as the growth rate and the final height of a CNT structure vary with its cross-sectional size and shape, and with the size and arrangement of nearby features. This is a reverse analogue to "loading" and "microloading" effects [334, 335]

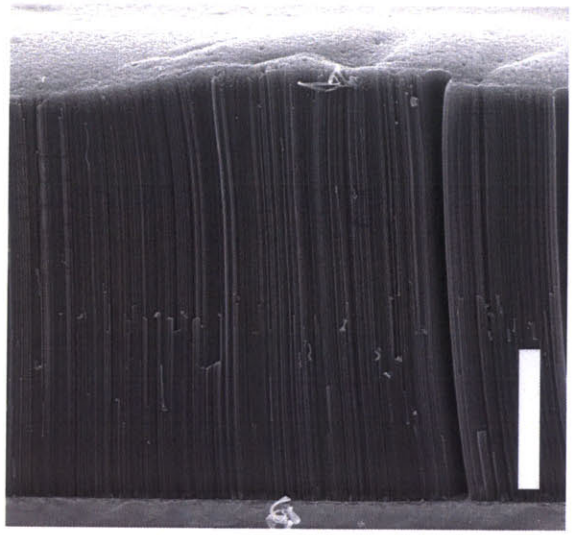

(a)

(b)

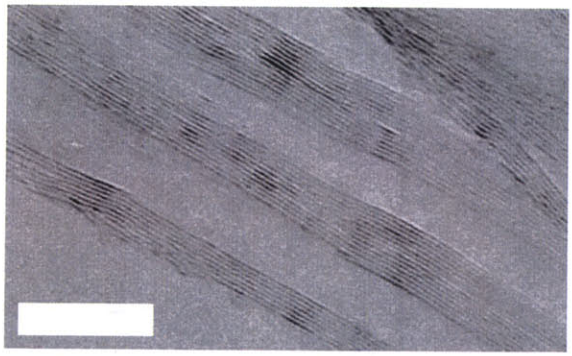

(c)

Figure 4-1. (a) Oblique view (stage tilted 70°) SEM image of aligned CNT film, approximately 1.8 mm high, grown in 60 minutes from 100/500/200 sccm $C_2H_4/H_2/Ar$ (scale 650 μm); (b) typical alignment of CNTs within film, viewed from side (scale 0.5 μm); HRTEM images of MWNTs from film (scale 10 nm). In (b), the rectangle indicates a large strand and the circle indicates bridging between strands.

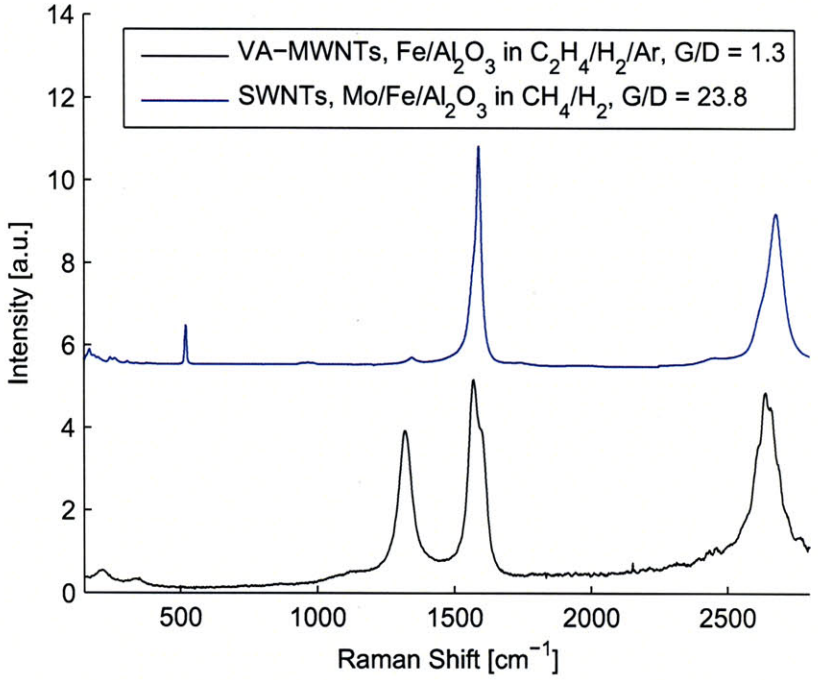

(a)

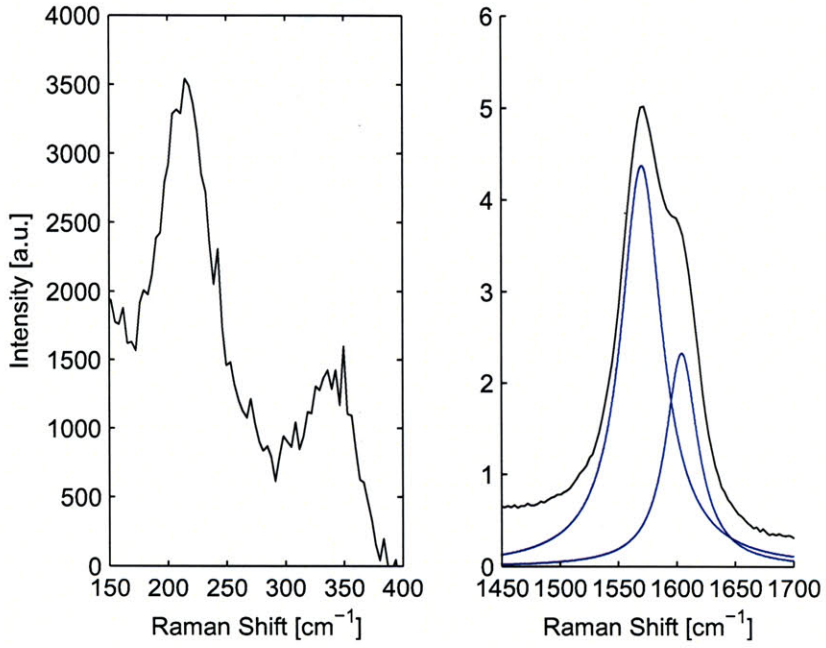

(b)

Figure 4-2. Typical Raman spectrum of VA-MWNT film grown at 750 °C: (a) comparison to spectrum of tangled SWNT film grown from $Mo/Fe/Al_2O_3$ in CH_4/H_2; (b) low-frequency modes (left) and Lorentzian-fit *G*-band region (right) of VA-MWNT spectrum. These spectra were taken with the assistance of Hyungbin Son.

observed in plasma etching processes, where the etch rate is affected by the local pattern density, and high-density patterns etch at a slower rate due to local depletion of etchant species. In general, for catalyst shapes having roughly equal length and width such as squares and circles, larger cross-sections grow into taller CNT structures, and high-density arrangements of shapes grow taller than low-density arrangements. For example, the center feature of the complex shape shown in Fig. 4-3b grows taller than the surrounding shapes. We suspect this behavior is mediated by the local supply of active reactant to the catalyst, where larger features "starve" smaller features of reactant. Additional images of arrays of high-aspect-ratio VA-CNT microstructures are shown in Fig. 4-4.

Significant loading effects (Fig. 4-3e) are typically observed over 0.1–1 mm distances on the substrate, and are more pronounced when a high partial flow of Ar is used. At these length scales, and among growing structures which obstruct the gas flow, flow near the substrate is dominated by diffusion and natural convection. The observed loading effects further suggest that "preconditioning" the reactants by thermal and/or catalytic treatment can significantly increase CNT yield [184, 186, 187]. Accordingly, the film thickness varies by as much as an order of magnitude based on the position of the growth substrate along the hot zone of our furnace, and we find a "sweet-spot" giving the highest yield at 40–80 mm downstream from the location of the thermocouple. We obtain maximum film thickness at the growth temperature of 750 °C. At 750 °C and 15 minutes growth time, the film thickness is linearly proportional to the flow of C_2H_4 for 10–75 sccm (in addition to 500/200 sccm H_2/Ar), and saturates at 75–200 sccm C_2H_4.

CNT structures having smaller cross-sectional shapes are more prone to bend and collapse during growth, particularly due to differences in growth rate across the base of the structure. As illustrated in Fig. 4-3c, circular features wider than approximately 20 μm typically remain self-standing. The CNTs growing from the smallest patterned features (3 μm diameter circles) are roughly aligned with one another and form single structures, which are often sharply bent and rest on the substrate. CNTs growing from even much smaller patterned areas of catalyst may not be self-aligned, as has been recently demonstrated on silica particles [336]. Oblong catalyst shapes, which grow into aligned CNT "blades", are very prone to leaning. Self-stability depends strongly on the packing density of CNTs within the aligned structure, which is related to many factors including the structure and particle density of the catalyst film, as well as the initial activity of the growth process in nucleating CNTs from the catalyst particles. However, gravitational effects are insignificant for millimeter-scale growths, as the height of CNT structures is no different when the substrate is inverted so the catalyst faces downward during growth.

The edges and corners of CNT structures grown from the patterned Fe/Al_2O_3 film are very sharp (Fig. 4-3d). In our process, the sharpness is limited by the edge rounding ($R \approx 0.25$ μm) of features on the laser-written lithography mask and by blurring during the exposure and development steps. However, higher-precision lithography for patterning the catalyst should enable CNT structures with edges which are defined by only a small number of long and parallel CNTs.

The CNT films and structures adhere weakly to the substrate, and can easily be removed in bunches using tweezers or as free-standing films by gently separating the film from the substrate using a razor blade. This was also observed by Hata et al. for thick films grown by the water-assisted CVD method, and is desirable for applications which warrant harvesting and/or transplanting of CNTs [337, 338]. On the other hand, irradiation treatment [245, 339, 340] or annealing [341] may be investigated for strengthening the CNT-substrate adhesion following growth. We also observe indications of significant residual stresses in thick CNT films, which

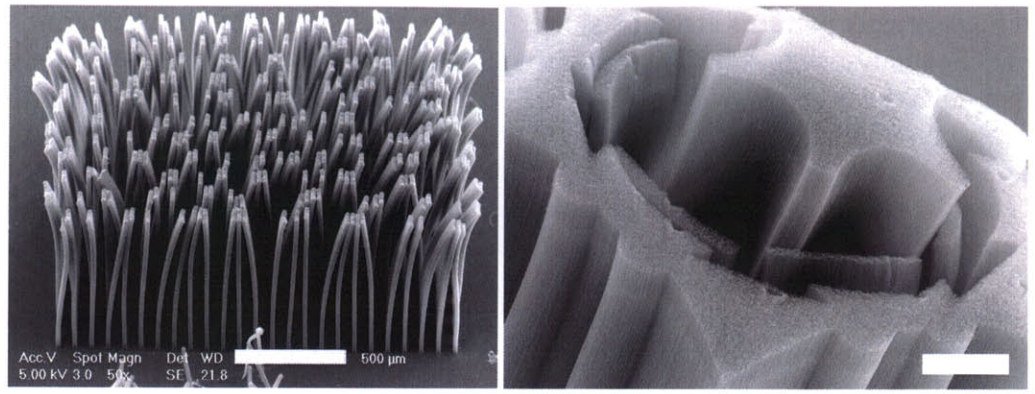

(a) (b)

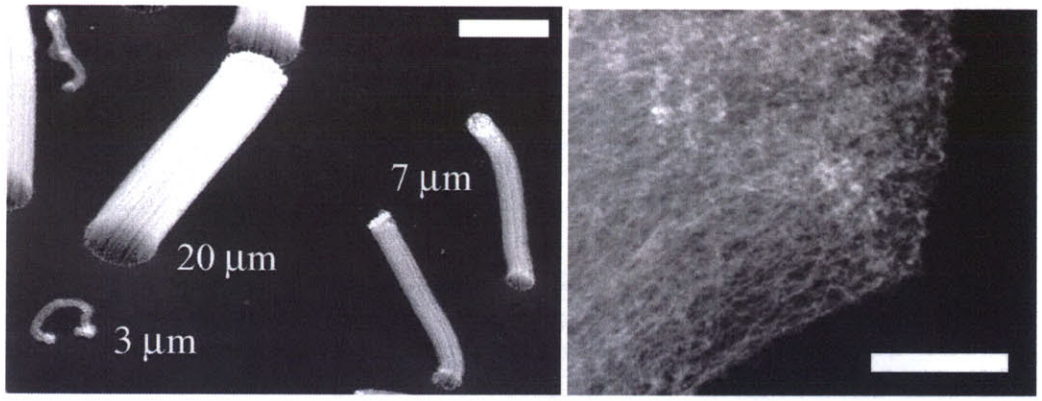

(c) (d)

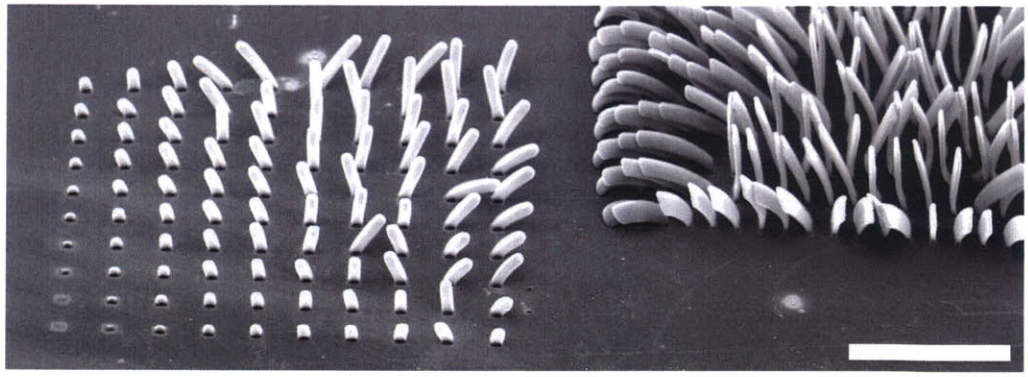

(e)

Figure 4-3. CNT microstructures grown from lithographically-patterned Fe/Al_2O_3 catalyst: (a) array of pillars, approximately 1 mm high, grown in 15 minutes (scale 500 μm); (b) complex pattern which grew taller near its center, and having sharp features reproduced from high-resolution lithography mask (scale 50 μm); (c) loss of free-standing behavior as pillar diameter decreases (scale 25 μm); (d) sharp corner of patterned feature from (b) (scale 5 μm); (e) significant loading effects on pattern grown with high partial flow of Ar (scale 500 μm).

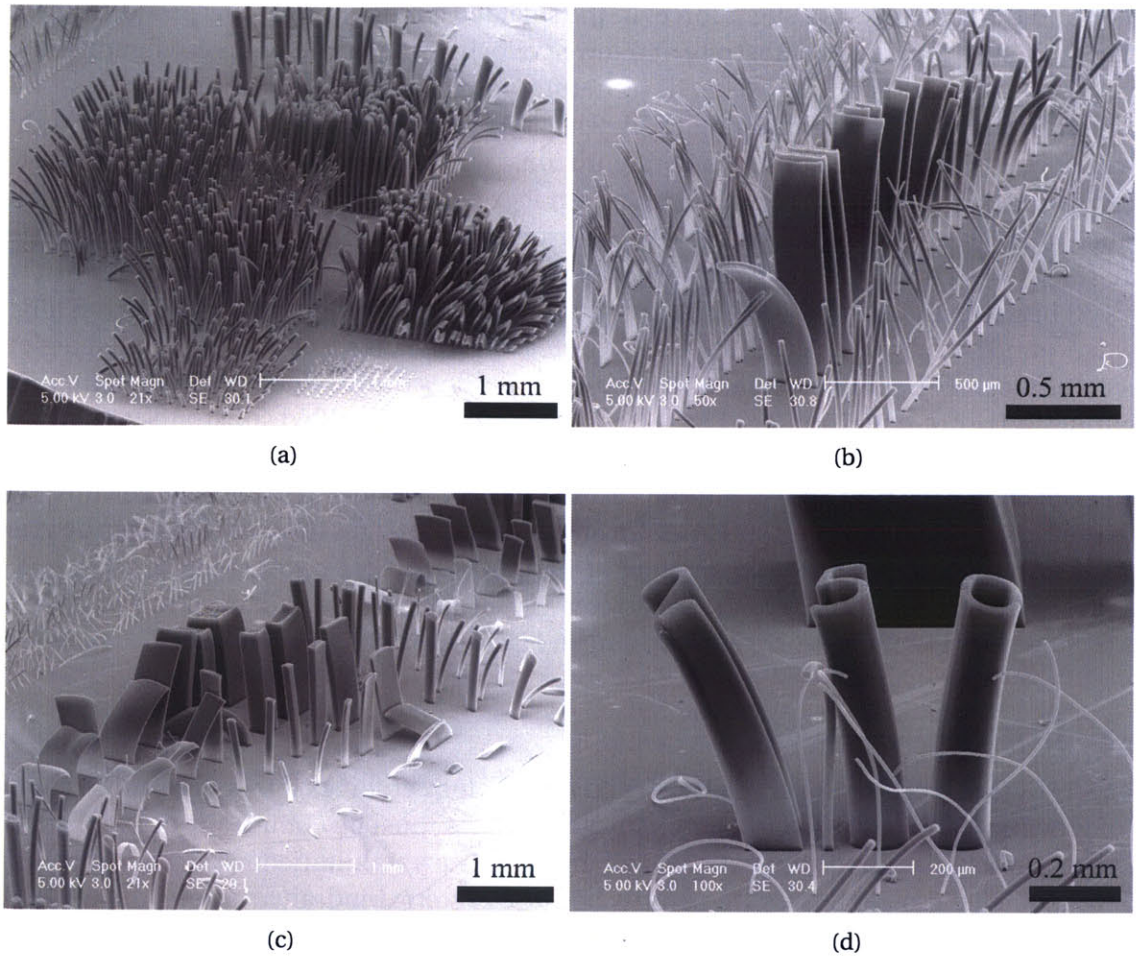

(a) (b)

(c) (d)

Figure 4-4. High aspect ratio CNT microstructures grown from lithographically-patterned catalyst, at "best" growth condition of 100/500/200 sccm $C_2H_4/H_2/Ar$ and 750 °C. Significant loading and mechanical stability effects are also observed at this condition of a low partial flow of Ar, yet small features grow much taller than with a high partial flow of Ar (Fig. 4-3d).

can cause delamination of the film from the substrate and may contribute to slowing or termination of growth, and are studying these effects in more detail.

4.1.2.2 Flow-mediated growth patterns

The pattern of VA-CNT growth depends on the placement of the substrate in the furnace and the duration of H_2 pre-conditioning before introduction of C_2H_4. We have studied these effects using the substrate configurations diagrammed in Fig. 4-5a: "open", where the growth substrate is rested in the center of the furnace tube, 40 mm downstream of the control thermocouple; "capped", where a bare Si_3N_4-coated silicon substrate is placed on top of the growth substrate and held by gravity; and "shielded", where a wider Si_3N_4-coated silicon substrate is spaced above the growth substrate by approximately 2.5 mm. In the capped configuration, gas reaches the catalyst by diffusing into the gap ($\approx$1 μm) between the substrates, and VA-CNT growth lifts

the cap and therefore exerts a slight force. In the shielded configuration, flow proceeds through the gap and over the growth substrate at a lower velocity than in the open configuration, and flow circulation in the gap is "smoothed" by natural convection between the substrates.

When H_2 is introduced simultaneously with C_2H_4, predominately tangled ($\approx$1 μm thick) growth occurs for all three substrate configurations, with occasional thin ($\approx$100 μm) VA-CNT growth in the darkest areas of the photographs in Fig. 4-6a. When H_2 is introduced 1 minute in advance, thick (0.8–1.0 mm in 15 min) VA-CNT growth occurs over larger areas. The open substrate (Fig. 4-5b) has aligned growth primarily around the periphery, with abrupt transitions[1] (Fig. 4-7) between the aligned and tangled regions. The capped substrate (Fig. 4-5b) has aligned growth around the periphery, with gradually decreasing thickness leading to a tangled region in the center area. The shielded substrate (Fig. 4-5b) is fully covered with VA-CNTs. For 2.5 and 5 minutes of H_2 pre-conditioning (Fig. 4-6b-c), the open and shielded substrates are fully covered with thick films of VA-CNTs, and the capped substrate shows increased VA-CNT coverage toward the center area. In all 1–5 minute cases, the film thickness on the shielded substrate is more uniform than on the open substrate, owing to the smooth gas flow pattern over the growth substrate. For H_2 pre-conditioning exceeding 5 minutes, VA-CNT coverage decreases, and occurs primarily at the periphery of the substrates as well as in circular pillars at the center areas. This is shown for 15 minutes pre-conditioning in Fig. 4-6d.

4.1.3 Discussion

When CNT growth begins, a vertically-aligned morphology emerges if there is a sufficient density of growing CNTs to cause crowding. The growth sites must be chemically active, and there must be a sufficient carbon supply to feed all the active sites simultaneously. If alignment is not achieved, tangled growth terminates shortly because of steric hindrance among the CNTs.

The supply of gas to the catalyst is affected by the flow circulation within the boundary layer over the substrate, and the shape of flow field around the substrate affects the pattern of growth because rapid growth of a VA-CNT film converts a large quantity of gaseous carbon into solid carbon. For example, assuming a 1% conversion rate of the hydrocarbon source, growth of VA-MWNTs (1% areal coverage, 5 walls per CNT) at 60 μm/min. requires approximately 16 sccm C_2H_4, while growth of 1 cm^2 of tangled SWNTs (0.1% areal activity of catalyst film) at 1 μm/min. requires approximately 0.35 sccm CH_4. In the latter case, the CNT growth rate is easily limited by the reaction rate at the catalyst particle and uniformity of growth is relatively unaffected by the flow profile around the substrate; in the former case, the conversion rate is a substantial fraction of the total carbon supply flowing through the furnace, and therefore spatial and temporal non-uniformities in the flow directly affect the growth pattern in areas where the catalyst does not receive enough feedstock.

In our experiments, continuous spatial gradients in the rate of carbon supply to the catalyst result in nearly discrete spatial transitions from tangled to aligned growth. Therefore, as observed on the open substrate with 1 minute H_2 pre-conditioning, areas in the "wake" of the leading edge do not receive a sufficient supply of active carbon species, leading to tangled growth in these areas. On capped substrates, gaseous carbon is consumed by the VA-CNT growth re-

[1] Perhaps we see a similarity with nature, where the end of a region of VA-CNTs is like an abrupt tree-line (`http://en.wikipedia.org/wiki/Tree-line`).

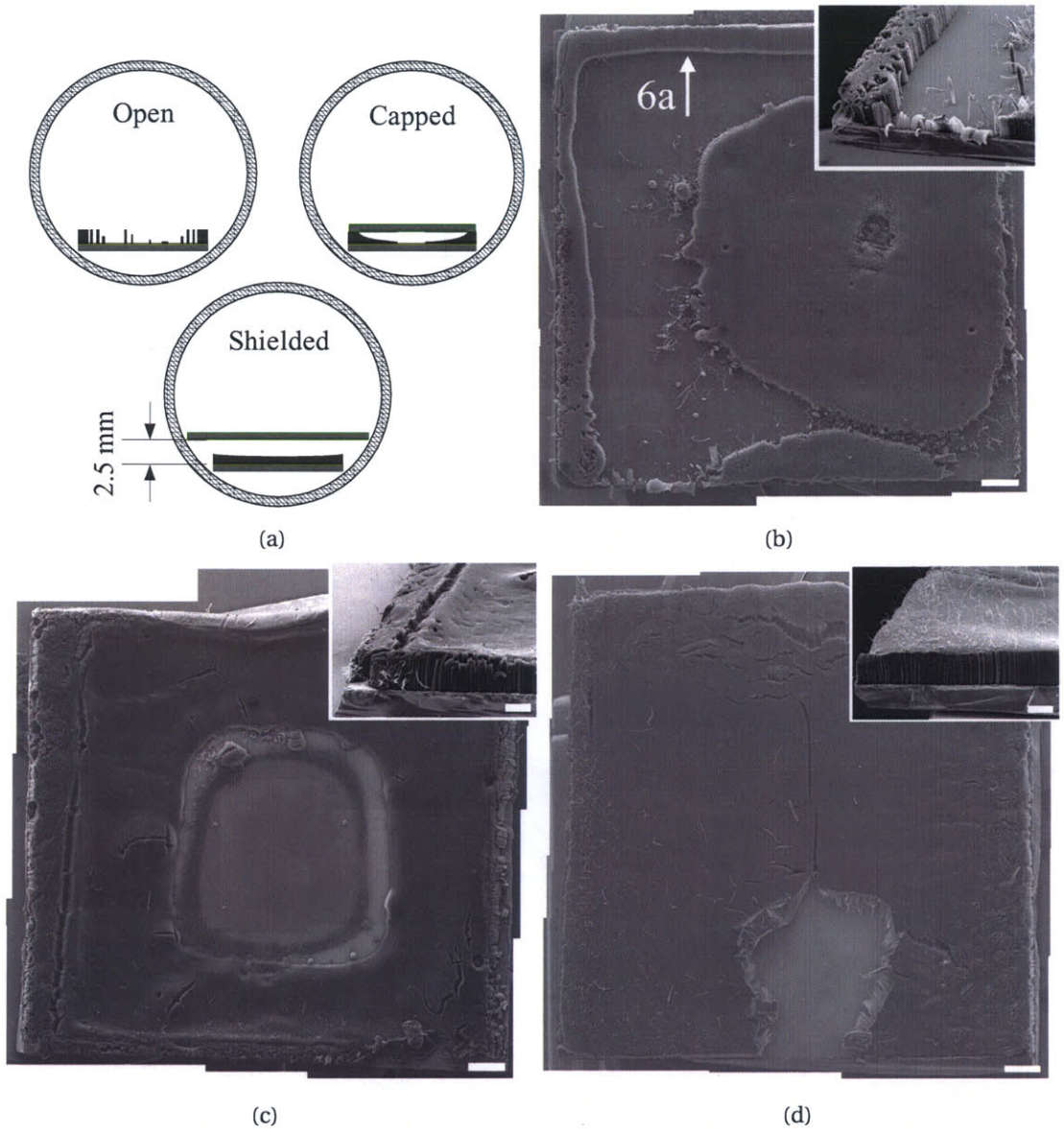

Figure 4-5. (a) Substrate configurations used to establish different flow profiles over Fe/Al_2O_3-coated ≈15×15 mm silicon substrate, and representations of resulting growth patterns after 1 minute of pre-conditioning in 500/200 sccm H_2/Ar and 15 minutes of growth in 100/500/200 sccm $C_2H_4/H_2/Ar$; (b) top-view composite SEM image of sample grown in open configuration (scale 1 mm); (c) sample grown under same conditions, capped (scale 1 mm); (d) sample grown under same conditions, shielded, with small area of film torn away by tweezers (scale 1 mm). Insets to (b)–(d) show oblique view SEM images of leading-edge corner of each sample (scales 0.5 mm).

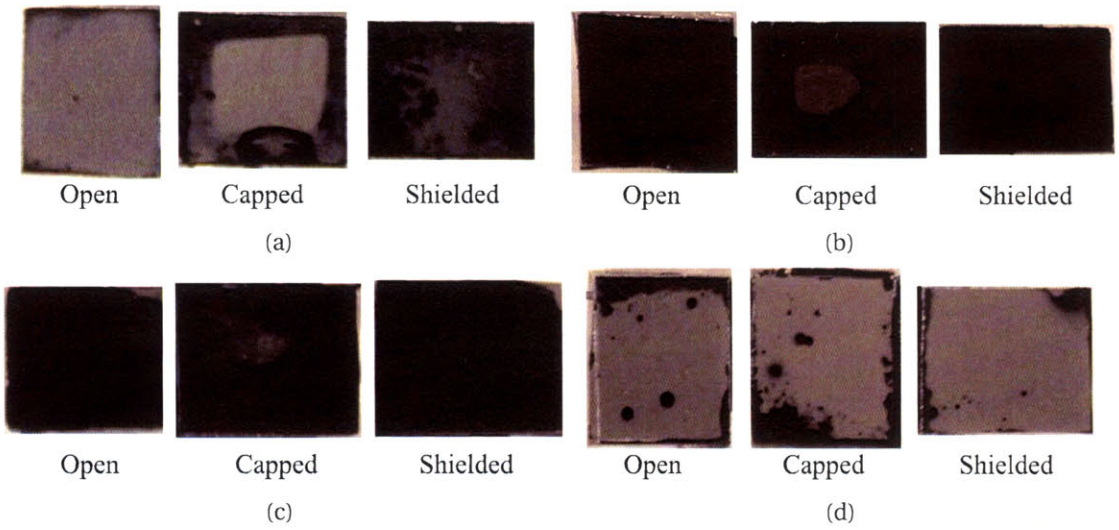

Figure 4-6. Optical top-view images of ≈15×15 mm samples grown in open, capped, and shielded configurations, with different durations of H_2/Ar pre-conditioning before introduction of C_2H_4: (a) 0 minutes; (b) 2.5 minutes; (c) 5 minutes; (d) 15 minutes.

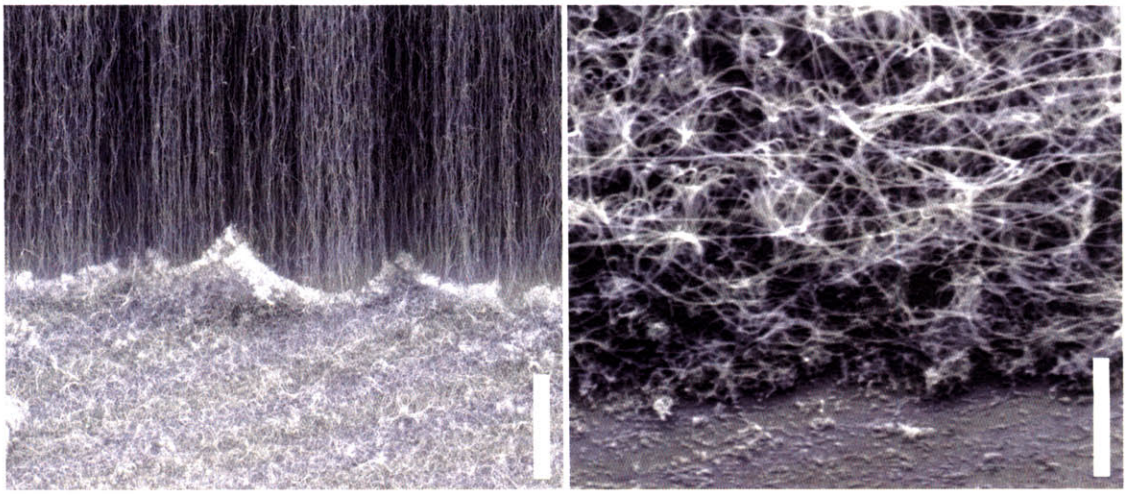

Figure 4-7. (a) Abrupt transition between tangled and vertically-aligned growth regions, on open sample with viewing angle indicated by arrow in Fig. 4-5b (scale 5 μm); (b) tangled region, where film has been scratched with tweezers (in lower portion of image) to reveal thickness of approximately 1 μm (scale 1 μm).

action around the periphery, and tangled growth occurs in the center area because the gas is restricted from and/or consumed before reaching the center area. For a given substrate size, the flow field around the substrate is relatively independent of the gas mixture, so changing the mixture to increase the concentration of active carbon species also increases the area on which vertical growth is active. However, once VA-CNT growth is established, it can proceed in a lesser supply of active species than is necessary for initiation.

It is evident that H_2 pre-conditioning increases the initial conversion rate of hydrocarbon to CNTs on the substrate, so areas receiving relatively less circulation of C_2H_4 at the start of the growth period are activated in the VA-CNT mode. Generally, H_2 can increase the activity of metal catalysts for cracking hydrocarbons, as well as "clean" catalytic surfaces by etching polycyclic hydrocarbon species which tend to encapsulate metal surfaces [148, 192]. Reduction of the catalyst to metallic Fe by H_2 may promote improved CNT nucleation [164], yet prolonged treatment with H_2 may suppress growth by causing sintering of metal particles or altering metal-support interactions [289].

Further, synergy between the metal catalyst and the supporting material is critical for an efficient and high-yield CVD growth process. CNT growth from Al_2O_3-supported catalysts has been studied widely [193,261], and the enhanced catalytic activity of a metal nanoparticle is attributed to many effects including strong dispersion, enhanced electron transfer, high surface roughness, and enhanced decomposition of hydrocarbons on the Al_2O_3 surface [177,259,277, 279,280]. In our process, Fe-coated SiO_2 substrates give only occasional areas of aligned CNTs, and Fe-coated bare Si substrates give no aligned CNTs and only sparsely tangled and highly defective CNTs. However, VA-CNTs grow at high yields on Fe/Al_2O_3 substrates we prepare by a variety of methods, and process under identical CVD conditions as the Fe/Al_2O_3 film on Si. For example, CNT films exceeding 500 μm thick grow in 15 minutes on Si substrates which are coated with 10 nm Al_2O_3 by e-beam evaporation and then soaked in 0.01 M $Fe(NO_3)_3$ in isopropanol for 5 minutes and dried in ambient air. Aligned CNTs grow radially from 20 μm diameter Al_2O_3 fibers cut from a commercially-available cloth, which is similarly loaded with Fe by soaking in the $Fe(NO_3)_3$ solution. We also note that millimeter-high VA-CNTs are grown from Fe/Al_2O_3 films which are rapidly heated to the growth temperature in only 1–2 minutes, indicating that the normal 30–45 minute heating and annealing duration is not needed to form nanoparticles from the physically-deposited catalyst film. Among all cases, the products are MWNTs having comparable diameters and crystallinity which grow as rapidly as 1 μm/s on average.

4.2 Further study of VA-CNT film growth

This section presents further studies of VA-CNT film synthesis, along with perspectives toward understanding more fundamental aspects of the growth process. To further enable growth of VA-CNT films in a manufacturing process, as for continuous production of thicker, more uniform, higher-density, CNT films on large substrate areas, these paramount questions include:

- What limits the growth rate at short times? Is the reaction limited by the supply of carbon to the growth sites on the substrate, or by the reaction rate in converting source carbon into CNTs at the substrate?
- What limits the ultimate thickness of a VA-CNT film? Does growth stop because of deactivation and/or evolution of the catalyst, because of diffusion limitations as the film gets thicker and prevents source carbon from reaching the growth sites at the base of the film, and/or because of mechanical stresses? How do our results compare to published models of film growth kinetics?
- Can VA-CNT film growth be paused and resumed, and stopped and reactivated?
- What do we learn by temporally adjusting the gas flows and growth temperature? Can this isolate separate "best" conditions for nucleation and growth?
- What are the sizes of catalyst particles which nucleate CNTs in our experiments? How many CNTs grow from each particle?

Preliminary investigations of these issues lead us to conclude that:

- The "best" conditions found for growth of VA-MWNT films from 1/10 nm Fe/Al_2O_3 in our tube furnace system are 100/500/200 sccm $C_2H_4/H_2/Ar$ at 750 °C. For C_2H_4 flow less than ≈ 50 sccm, results indicate the growth rate is limited by the C_2H_4 supply, and at higher flow rates the growth rate is limited by the reaction rate.
- Growth stops when the C_2H_4 flow is terminated. When C_2H_4 is paused while H_2 and Ar are maintained, it appears that H_2 etches at the growth site, and growth resumes when C_2H_4 is resumed. When C_2H_4 and H_2 are paused and only Ar is maintained, growth does not resume when C_2H_4 is resumed.
- Growth can be reactivated by oxidizing the substrate in air after cooling following a normal growth sequence. We have not determined if our process reactivates growth from catalyst particles which grew CNTs in the first growth instance, or if new catalyst particles are activated by the oxidation sequence in the first instance.
- Mechanical stresses arise during growth of VA-CNT films, and increase in magnitude with film thickness as different areas of the film grow at different rates. In turn, these stresses may slow growth.

- A high concentration of C_2H_4 is best for uniform nucleation of a VA-CNT film on a substrate in our system; after this, growth can proceed in an environment with a relatively low C_2H_4 concentration. Conversely, a low initial C_2H_4 concentration gives non-uniform nucleation. Recently, we have grown extremely uniform films using He instead of Ar as the carrier gas, and it appears that annealing the Fe/Al_2O_3 catalyst in He/H_2 promotes immediate nucleation of a VA-CNT film.
- Limited observations indicate that a single CNT grows from each catalyst particle, and that the catalyst particles are retained within the roots of the CNTs and separated from the substrate following growth.

Results to support these conclusions are presented in the remainder of this section, along with very limited discussion. Typically the results of a growth experiment are compared in terms of the film thickness and uniformity of the film on the substrate. The uniformity is categorized with the following indices:

0: Primary coverage of tangled CNTs, with < 10% coverage of VA-CNTs.

1: Partial coverage of tangled CNTs, with > 10% coverage of VA-CNTs.

2: Full coverage of VA-CNTs, with significant non-uniformities in film thickness (e.g., stress-induced ripples in the sidewalls, and cracks and ripples in the top surface).

3: Full coverage of aligned VA-CNTs, with uniform film thickness.

At each condition, individual samples were typically processed in the "open", "capped", and "shielded" configurations (Fig. 4-5a).

4.2.1 Parametric study of growth conditions

4.2.1.1 Study of growth temperature

VA-CNT film growth occurs in our tube furnace system at growth temperatures ranging from approximately 675–800 °C, and the maximum growth rate is observed at 750 °C. The film thickness after a fixed growth time increases with growth temperature up to the maximum point, and then sharply decreases with temperature (Fig. 4-8). We observe a similar trend for growth of tangled SWNT films from $Mo/Fe/Al_2O_3$ in CH_4/H_2 (Fig. 3-4). A "negative" activation energy is apparent for higher temperatures [342], as the growth rate decreases as temperature increases, likely due to excessive gas-phase pyrolysis (i.e., formation of longer-chain hydrocarbon molecules) of the reactant mixture as it flows through the furnace tube prior to reaching the catalyst.

Assuming a constant growth rate (final thickness divided by growth time) during the 15 minute duration of these experiments, we estimate the activation energy (E_a) using the Arrhenius relation [161, 200]. The growth rate ($\dot{h}$) is proportional to the reaction rate (k), such that

$$\dot{h} \propto k = e^{\frac{E_a}{RT}}, \tag{4.1}$$

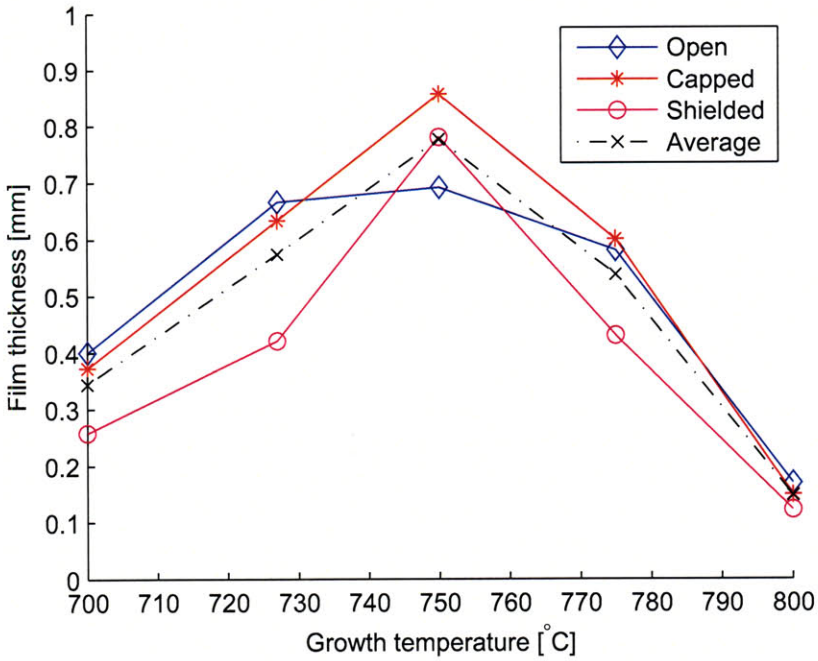

Figure 4-8. Variation of CNT film thickness with growth temperature, for samples processed in open, capped, and shielded configuration, in 100/500/200 sccm $C_2H_4/H_2/Ar$, for 15 minutes. H_2/Ar was introduced 5 minutes prior to C_2H_4. Samples were taken from the same wafer, and were placed 40 mm downstream of the control thermocouple of the tube furnace.

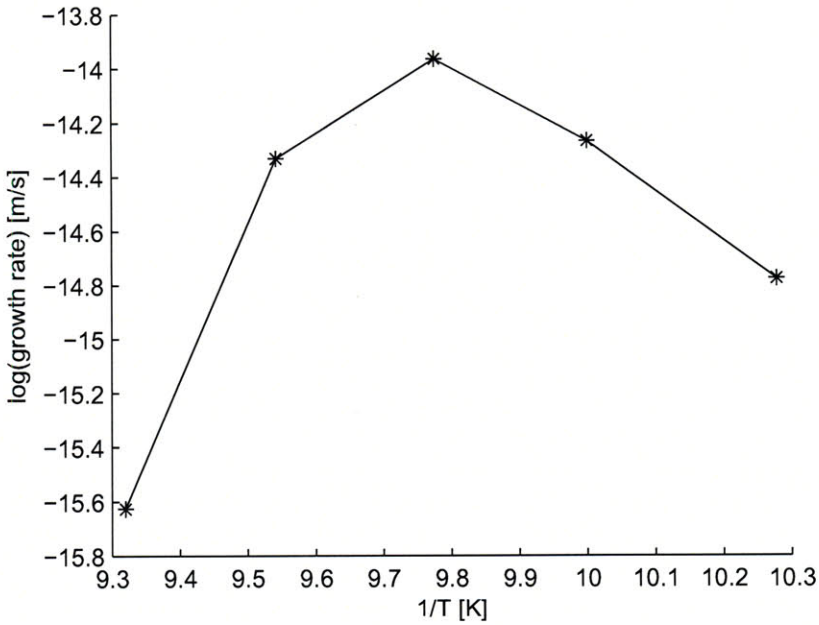

Figure 4-9. Arrhenius plot of average data presented in Fig. 4-8. The apparent activation energy of the reaction is estimated using the data for 700–750 °C (maximum and right-hand portion of curve).

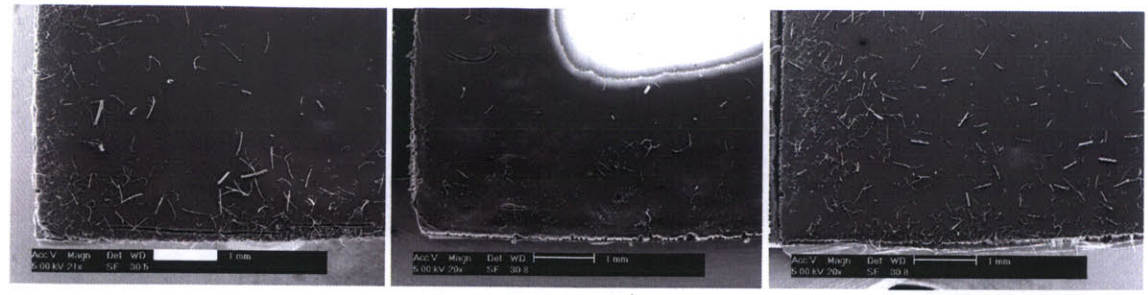

(a) 700 °C, Open (b) 700 °C, Capped (c) 700 °C, Shielded

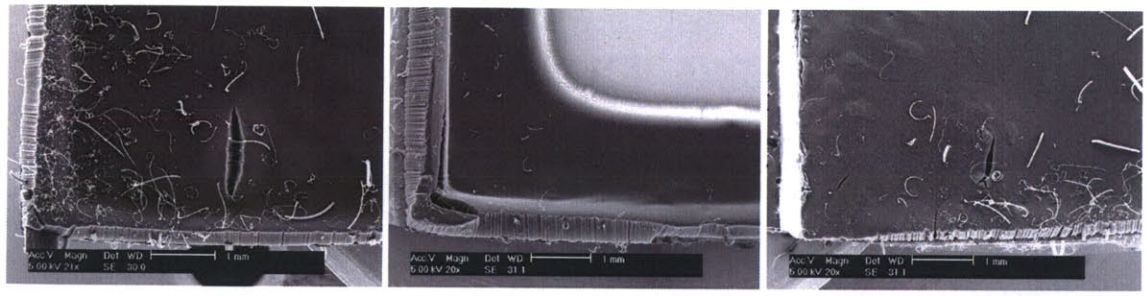

(d) 750 °C, Open (e) 750 °C, Capped (f) 750 °C, Shielded

(g) 775 °C, Open (h) 775 °C, Capped (i) 775 °C, Shielded

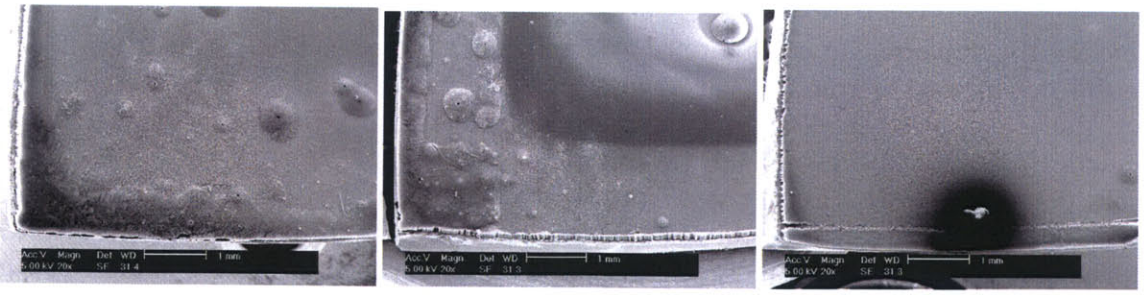

(j) 800 °C, Open (k) 800 °C, Capped (l) 800 °C, Shielded

Figure 4-10. Coverage of aligned CNT film for growth temperatures ranging from 700–800 °C. Samples were processed in open, capped, and shielded configurations, in 100/500/200 sccm $C_2H_4/H_2/Ar$, for 15 minutes. H_2/Ar was introduced 5 minutes prior to C_2H_4. Samples were placed 40 mm downstream of the control thermocouple of the tube furnace. Scales 1 mm.

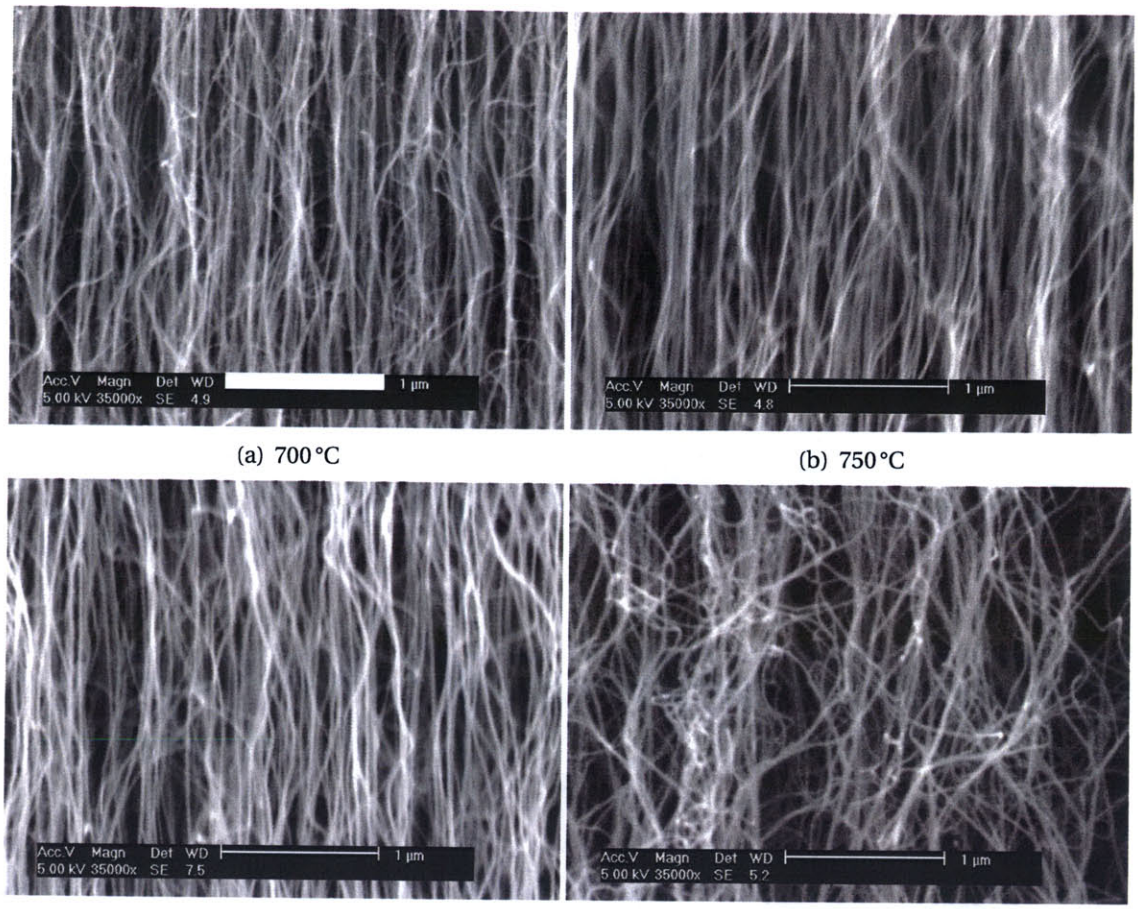

(a) 700 °C (b) 750 °C

(c) 775 °C (d) 800 °C

Figure 4-11. Alignment of CNT film for growth temperatures ranging from 700–800 °C. Samples were processed in shielded configuration, in 100/500/200 sccm $C_2H_4/H_2/Ar$, for 15 minutes. Scales 1 μm.

where R is the universal gas constant (8.314 J/mol) and T is the reaction temperature [K]. Considering only the region from 700–750 °C where the growth rate increases with reaction temperature, the activation energy is simply the slope of a linear fit to a plot of $\ln \dot{h}$ versus $1/T$. This calculation gives $E_a = 135$ kJ/mol = 1.4 eV/atom.

The decrease in VA-CNT coverage (Fig. 4-10) and alignment (Fig. 4-11) also suggest that the activity of the catalyst decreases. It may be that an increasing proportion of catalyst sites is initially "poisoned" by accumulation of amorphous carbon, which forms due to increased gas-phase decomposition of C_2H_4 at higher temperature.

4.2.1.2 Study of ethylene flow rate

Varying the partial flow of C_2H_4 among experiments at otherwise identical growth conditions (Fig. 4-12) reveals the dependence of the initial growth rate (assumed constant within the first fifteen minutes of growth) on the amount of carbon supplied to the catalyst. The alignment within the VA-CNT film improves with increasing C_2H_4 flow, reaching approximately steady

state at 50 sccm C_2H_4. This suggests that fewer CNTs nucleate (and perhaps have more defects) when the supply of carbon to the catalyst is insufficient.

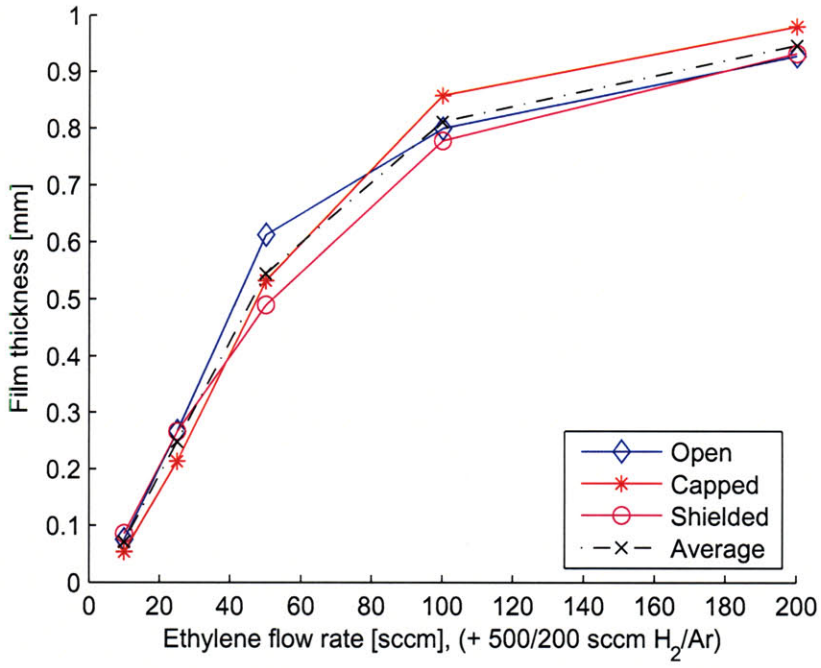

Figure 4-12. Variation of CNT film thickness with C_2H_4 flow rate, for samples processed in open, capped, and shielded configurations, at 750 °C, for 15 minutes. The remainder flow is 500/200 sccm H_2/Ar, and H_2/Ar is introduced 5 minutes prior to C_2H_4. Samples were taken from the same wafer (catalyst deposition 'VA-14'), and were placed 40 mm downstream of the control thermocouple.

(a) 10 sccm C_2H_4, Open (b) 10 sccm C_2H_4, Capped (c) 10 sccm C_2H_4, Shielded

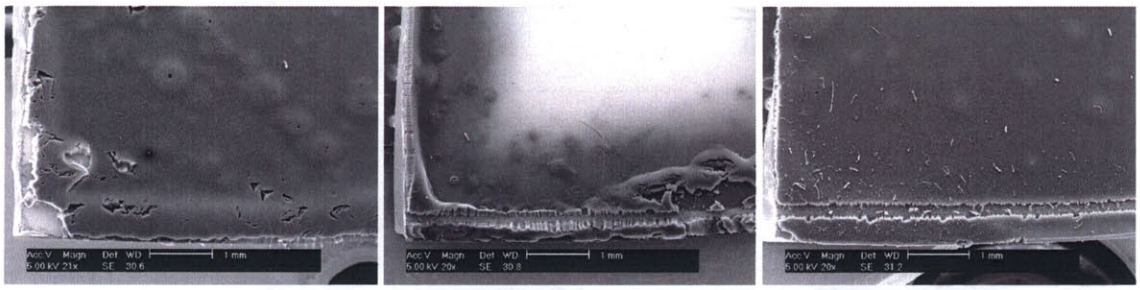

(d) 25 sccm C_2H_4, Open (e) 25 sccm C_2H_4, Capped (f) 25 sccm C_2H_4, Shielded

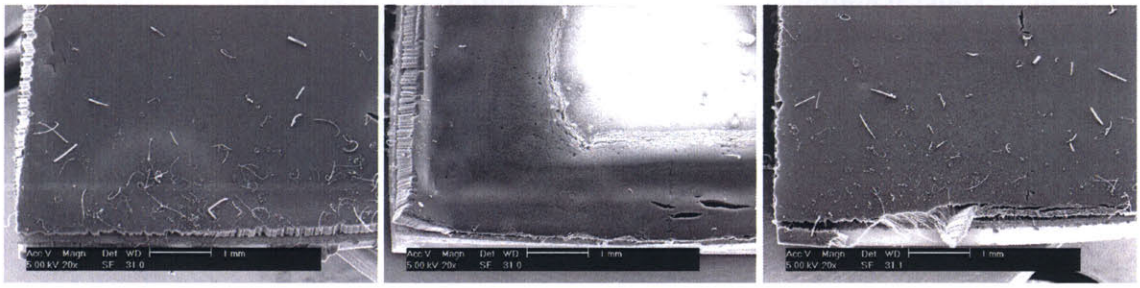

(g) 50 sccm C_2H_4, Open (h) 50 sccm C_2H_4, Capped (i) 50 sccm C_2H_4, Shielded

Figure 4-13. Coverage of aligned CNT film at different C_2H_4 flow rates, at conditions described in Fig. 4-12. Scales 1 mm.

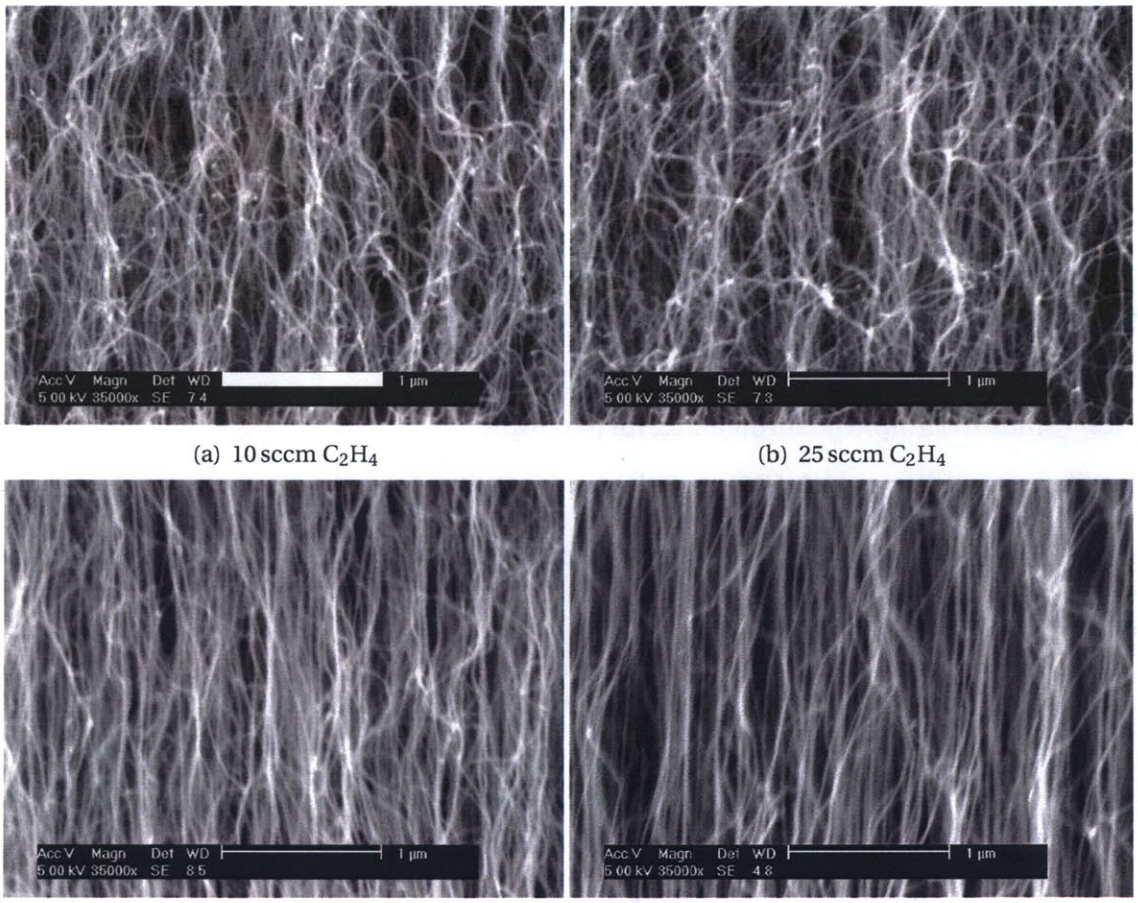

(a) 10 sccm C_2H_4 (b) 25 sccm C_2H_4

(c) 50 sccm C_2H_4 (d) 100 sccm C_2H_4

Figure 4-14. Alignment of CNT film at different C_2H_4 flow rates, for samples processed in shielded configuration at conditions described in Fig. 4-12. Scales 1 μm.

4.2.1.3 Study of pre-conditioning sequence

As discussed in 4.1.2.2, the nucleation of a VA-CNT film in our process is very sensitive to both the sample configuration and the duration of pre-conditioning with H_2/Ar prior to introduction of C_2H_4. The thickness and coverage of CNT samples are quantified in Table 4.1.

Going forward, we are now studying how the H_2 flow and the heating atmosphere affect the size, morphology, and chemical state of the catalyst film.

	Film thickness [mm]				Coverage		
H_2 pre-cond. [min.]	*Open*	*Capped*	*Shielded*	**Avg.**	*Open*	*Capped*	*Shielded*
0	0.01	0.21	0.85	**0.4**	0	0	0.5
1.0	0.96	1.04	0.90	**1.0**	0.5	1	3
2.5	0.86	1.01	0.83	**0.9**	2	1	3
5.0	0.84	0.96	0.89	**0.9**	3	1	3
15.0	0.53	0.74	0.29	**0.5**	1	1	0.5

Table 4.1. CNT film thickness after varying pre-conditioning duration of H_2/Ar, followed by growth with 100/500/200 sccm C_2H_4/H_2/Ar, at 750 °C, for 15 minutes.

4.2.1.4 Study of sample position along furnace tube

The uniformity and rate of VA-CNT growth also depend on the position of the sample along the furnace tube, as thermally-induced decomposition of the reactant mixture significantly affects its activity for CNT growth. The sample position is measured from the location of the control thermocouple (Fig. 6-1), in the direction of the gas flow through the tube. In our system, the coverage and thickness of a VA-CNT film grown for 15 minutes is generally best at about 80 mm downstream from the thermocouple when the sample is pre-conditioning with H_2 for 5 minutes prior to C_2H_4, and is closer to 60 mm downstream (Figs. 4-15 and 4-16) This precise relationship varies with the mixtures of H_2/Ar and C_2H_4/H_2/Ar used for pre-conditioning and growth, and for each step two mixtures were tested as listed in Table 4.2.

A	500/200 sccm H_2/Ar
B	500/600 sccm H_2/Ar
C	100/500/200 sccm C_2H_4/H_2/Ar
D	100/500/600 sccm C_2H_4/H_2/Ar

Table 4.2. Gas flows used in study of sample position on VA-CNT film thickness and coverage: (A, B) are pre-conditioning mixtures, and (C,D) are growth mixtures.

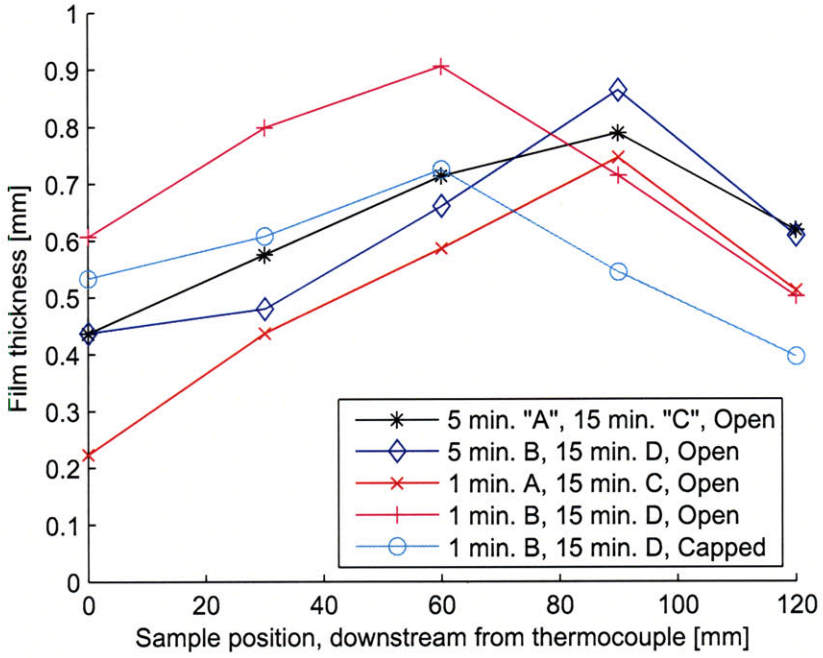

Figure 4-15. Variation of CNT film thickness with sample position along furnace tube, at growth temperature of 750 °C. Samples were taken from the same wafer (deposition 'VA-14').

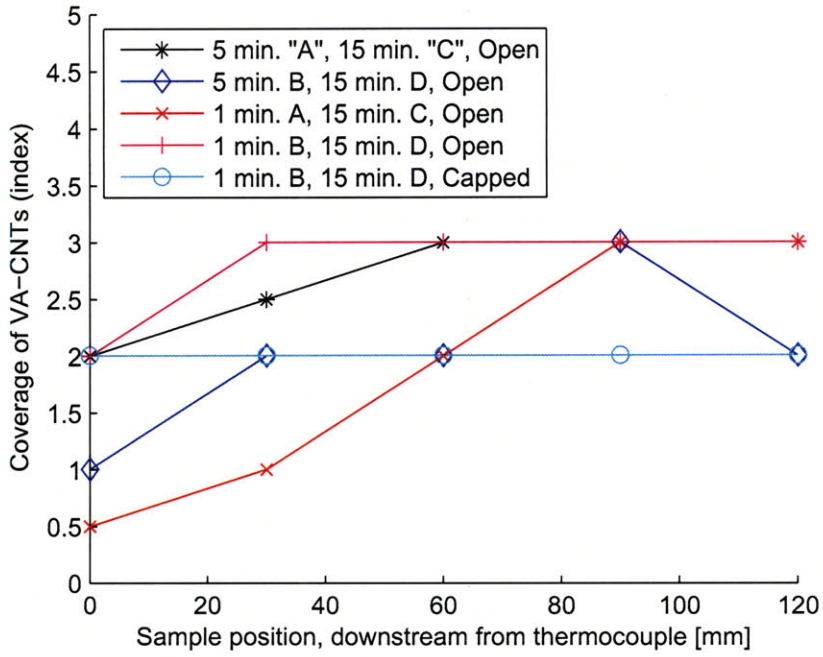

Figure 4-16. Variation of VA-CNT coverage with sample position along furnace tube, at growth temperature of 750 °C. Samples were taken from the same wafer (deposition 'VA-14').

4.2.2 Temporal adjustment of temperature and ethylene flow rate

Realizing the need for a relatively high supply of C_2H_4 for uniform nucleation of a VA-CNT film, we sought to determine if temporal adjustment of the growth temperature and C_2H_4 flow rate can let us isolate a separately superior condition for steady-state VA-CNT film growth, which may give more rapid growth or a longer catalyst lifetime. However, these experiments (Table 4.3) did not give results which exceeded those expected by superimposing results from experiments conducted with temporally-uniform conditions. Further study should utilize the heated platform reactor apparatus (section 6.2), which is capable of rapid temperature control and *in situ* monitoring of film thickness.

	Film thickness			
	Open	*Capped*	*Shielded*	Avg.
100/500/200 sccm $C_2H_4/H_2/Ar$, 750 °C, 60 min.	1.17	1.28	1.17	1.0
100/500/200 sccm $C_2H_4/H_2/Ar$, 750 °C, 15 min.	0.74	0.77	0.86	0.8
100/500/200 sccm $C_2H_4/H_2/Ar$, 750 °C, 5 min. 100/500/200 sccm $C_2H_4/H_2/Ar$, 750–800 °C, 2 min. 100/500/200 sccm $C_2H_4/H_2/Ar$, 800 °C, 8 min.	0.60	0.65	0.54	0.6
100/500/200 sccm $C_2H_4/H_2/Ar$, 750 °C, 5 min. 25/500/200 sccm $C_2H_4/H_2/Ar$, 750–800 °C, 2 min. 25/500/200 sccm $C_2H_4/H_2/Ar$, 800 °C, 8 min.	0.33	0.34	0.44	0.4
100/500/200 sccm $C_2H_4/H_2/Ar$, 750 °C, 5 min. 50/500/200 sccm $C_2H_4/H_2/Ar$, 750 °C, 55 min.	0.61	0.64	0.60	0.6

Table 4.3. Summary of thickness measurements from temporal adjustment experiments.

4.2.3 Pausing, resuming, and reactivating growth using pulsed gas flows

While temporal adjustment of the growth temperature and reactant composition did not yield results exceeding those for temporally uniform conditions, we next studied how growth might be paused or stopped, and resumed or reactivated, by periodically varying the gas composition. The experiments were performed using catalyst samples taken from the same wafer (deposition 'VA-15'); however this catalyst was less efficient than the catalyst used in our other experiments, as it gave an ultimate thickness of only ≈1.0 mm in 30 minutes of growth (Fig. 4-17a). Samples which have reached the terminal thickness exhibit a thin (≈20 μm high) layer of "collapsed" CNTs at the interface with the substrate (Fig. 4-18); this is consistent with our hypotheses on mechanical stress effects in VA-CNT film growth, which is discussed in section 4.2.4.

Experiments were conducted with a periodic gas flow sequence: introducing the usual gas mixture of 100/500/200 sccm $C_2H_4/H_2/Ar$ for 10 minutes, and then discontinuing ethylene while maintaining H_2/Ar or only Ar for 2–5 minutes, and then repeating this sequence for up to three cycles. SEM images of film structures are shown in Fig. 4-17b-d, and thickness measurements are listed in Table 4.4. From these results, we summarize our capability for transient control of VA-CNT film growth by pulsing the gas composition:

- Deactivating the catalyst: discontinuing C_2H_4/H_2 and introducing Ar.
- Pausing growth: discontinuing C_2H_4 but maintaining H_2/Ar.
- Resuming growth: resuming C_2H_4 after flowing H_2/Ar.

The hypothesized mechanical stresses can also induce discontinuities or splits (Fig. 4-19) in the CNT films when growth is paused and resumed. Here, it appears that continuing H_2/Ar after discontinuing C_2H_4 maintains the activity of the catalyst while etching carbon and possibly CNTs at or near the catalyst. CNT growth resumes when C_2H_4 flow resumes.

A split interface has one face of "sharp-tipped" CNTs (or well-aligned ends) which were rooted at the substrate before the flow pulse; and one side of tangled CNTs, which is like the top surface of any VA-CNT film growing from catalyst at the base. This interface structure suggests that exposure to H_2/Ar detaches previously grown CNTs from the substrate, and that growth resumes with CNTs having free ends which must recover a vertically-aligned conformation. The sharp-tip CNT surface may be useful for making electrical contact through many parallel CNTs, and further investigation and/or processing could be pursued to establish the CNTs with a uniform (i.e., capped or open) end condition [343]. Further, mechanical adhesive strength exceeding that of the well-known Gecko's foot has been demonstrated for VA-CNT surfaces [344], and it would be interesting to study this phenomenon with the sharp-tip and tangled CNT surfaces revealed here.

The pulsed flow experiments also give insight to the time evolution of film thickness. For example, a film of 1.0 mm thickness grows in 30 minutes of temporally uniform flow, and pulsed growth (C_2H_4/H_2/Ar–H_2/Ar 10/5/10/5/10 minutes) only produces two discernible sections of CNTs totalling 1.0 mm thick. These two sections are produced during only 20 (10+10) minutes of C_2H_4 flow, and the second section is rooted with a collapsed layer suggesting termination of growth. Further, the first section is 0.6 mm thick, indicating that most growth happens during the initial 10 minute period; however, it is not clear if growth proceeds at a constant rate and terminates suddenly, or if growth slows before terminating. Conversely the single-section film grown in pulsed C_2H_4/H_2/Ar–Ar does not have a collapsed bottom layer, indicating growth was terminated prematurely by pulsing with only Ar. Spatial variations in the total film thickness, exemplified by the appearance of three sections in some areas of the film processed with C_2H_4/H_2/Ar–H_2/Ar 10–2–10–2–10 min. (Fig. 4-17d) further confirm variations in the catalyst activity due to chemical and mechanical effects, including the duration of the pause period.

Along a similar path of investigation, a "growth mark" method for revealing the thickness of CNT films versus time was published recently [161], where the authors sweep Ar over the substrate sample to pause growth for 10–30 seconds. This introduces a ripple in the film sidewall, which like our method is viewed as a "ruler" on the sidewall of the CNT film after growth. While we have not studied pulse durations shorter than 2 minutes, it may be possible to resume growth after short pulses of only Ar in our system as well. More generally, these experiments could be more precisely conducted in a "flow-reversal" configuration of a tube furnace as described in section 6.1.3.

Further, we successfully reactivated growth by following a previously published recipe for reactivation of catalysts for low-density growth of SWNTs [345]. We first grow a VA-CNT film by the normal growth sequence with 15 minutes of 100/500/200 sccm C_2H_4/H_2/Ar, then cool the sample, and then reheat in air to 400 °C, and hold for 30 minutes. Next, the furnace is sealed

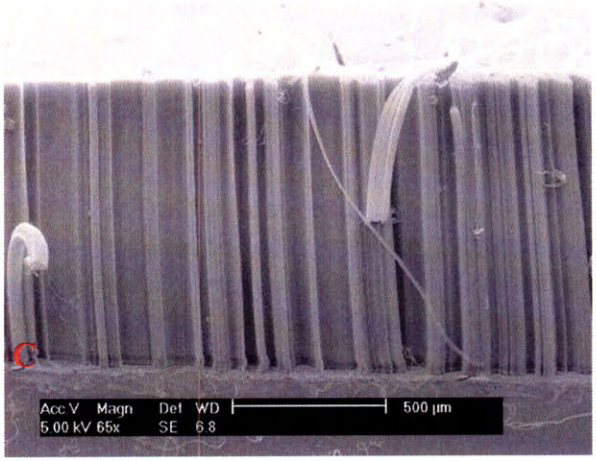

(a) Constant $C_2H_4/H_2/Ar$, 30 min.

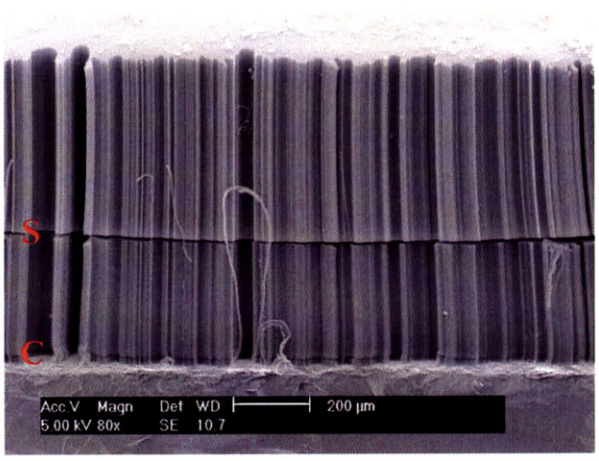

(b) Pulsed $C_2H_4/H_2/Ar$–H_2/Ar, 10–5–10–5–10 min.

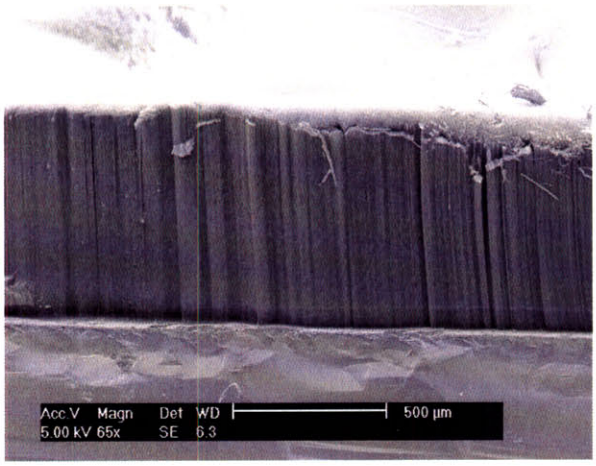

(c) Pulsed $C_2H_4/H_2/Ar$–Ar, 10–5–10–5–10 min.

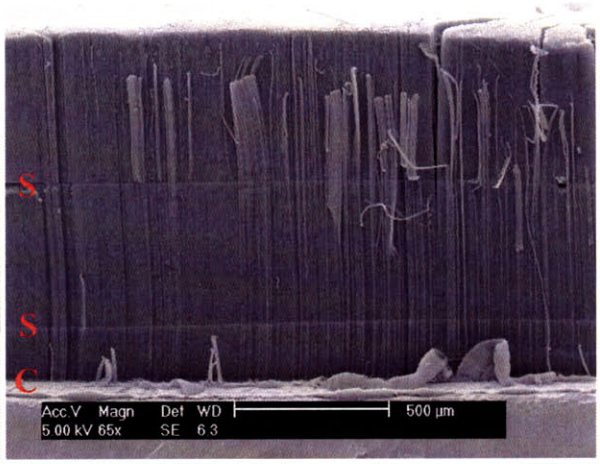

(d) Pulsed $C_2H_4/H_2/Ar$–H_2/Ar, 10–2–10–2–10 min.

Figure 4-17. Fabrication of split multilayer VA-MWNT films by periodic pulsing of gas flow composition. Nominal reactant mixture is 100/500/200 sccm $C_2H_4/H_2/Ar$, at 750 °C. "C" denotes collapsed layer at bottom of film present at growth termination, and "S" denotes a split or ripple in film wall caused by cycling the reactant mixture between $C_2H_4/H_2/Ar$ and H_2/Ar.

	Film thickness				
	Open	*Capped*	*Shielded*	Avg.	Collapse layer?
100/500/200 sccm $C_2H_4/H_2/Ar$, 30 min.	0.86	0.98	1.07	1.0	Y
$C_2H_4/H_2/Ar$–H_2/Ar, 10–5–10–5–10 min.	0.99	0.98	0.88	1.0	Y
$C_2H_4/H_2/Ar$–H_2/Ar, 10–2–10–2–10 min.	0.98	1.01	1.22	1.1	Y
$C_2H_4/H_2/Ar$–Ar, 10–5–10–5–10 min.	0.63	0.69	0.68	0.7	N

Table 4.4. Summary of thickness measurements from pulsed-flow experiments, demonstrating that growth can be resumed after stopping C_2H_4 but maintaining H_2/Ar, but is deactivated when both C_2H_4 and H_2 are stopped. All samples processed with 5 minutes of H_2/Ar preconditioning (500/200 sccm).

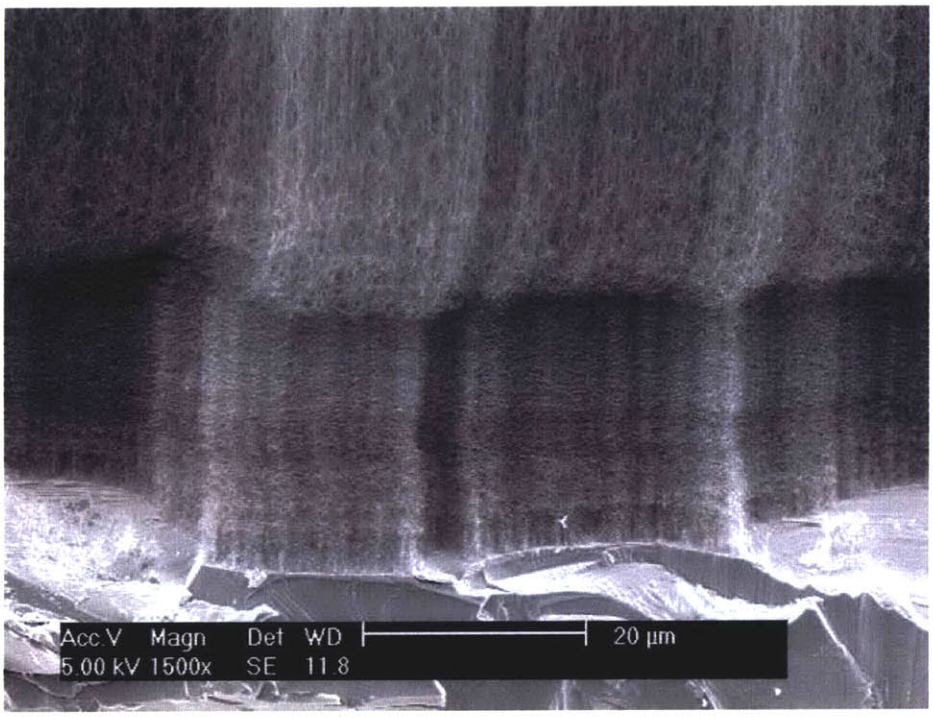

Figure 4-18. Collapsed layer at bottom of film, $C_2H_4/H_2/Ar–H_2/Ar$, 10–5–10–5–10 min., 750 °C.

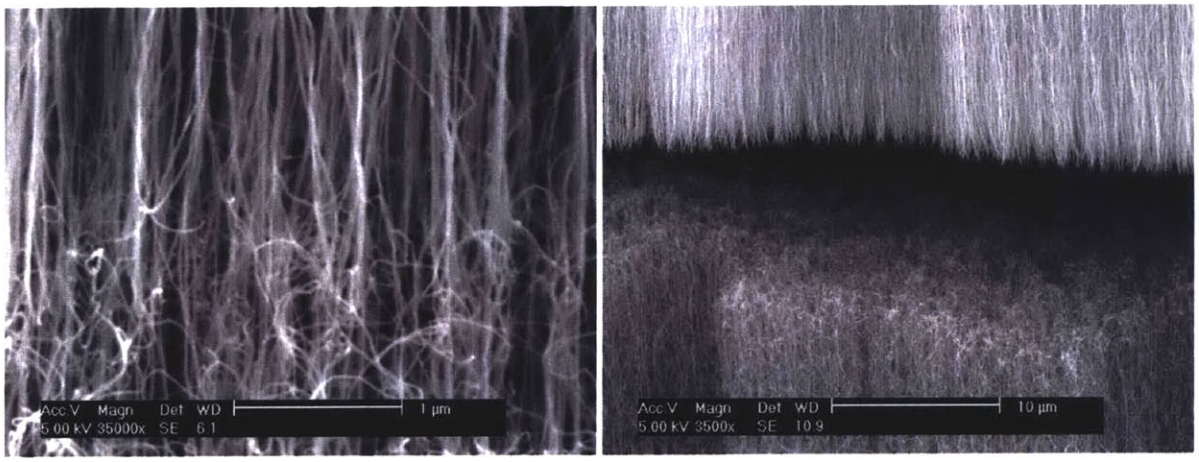

(a) (b)

Figure 4-19. "Pulse marks" on sidewall of film, introduced by cycling between $C_2H_4/H_2/Ar$ and H_2/Ar: (a) transition in order where some CNTs appear contiguous and others are split, yet the sidewall is not split; (b) split area, where the bottom of the upper layer is uniform and flat.

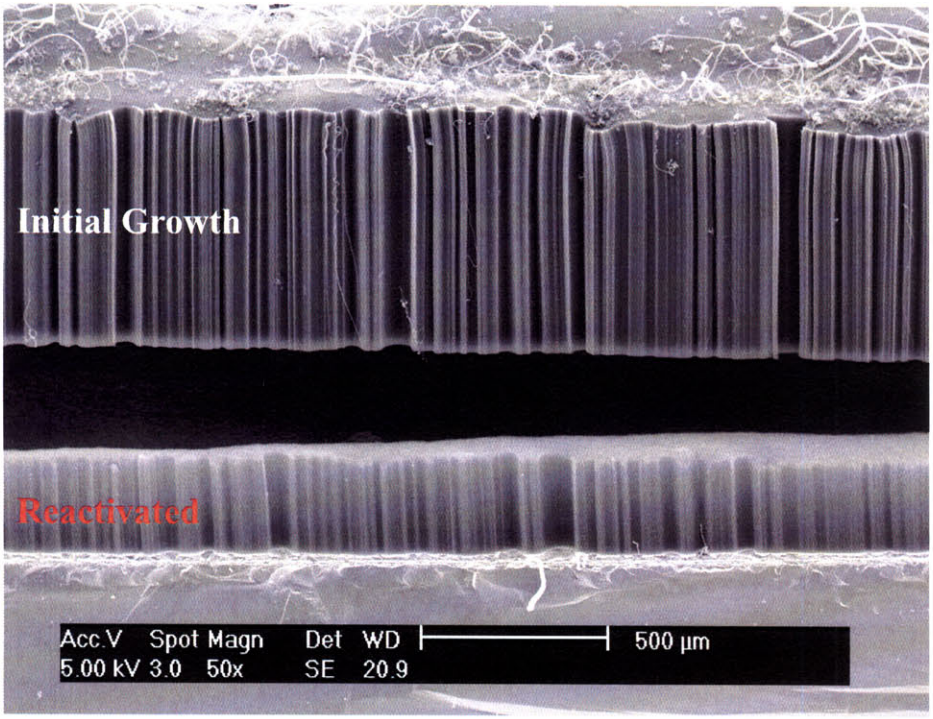

Figure 4-20. Reactivation of VA-CNT growth by first annealing CNT film in air for 30 min. at 400 °C [345] prior to re-running typical growth sequence of 15 minutes 100/500/200 sccm $C_2H_4/H_2/Ar$ at 750 °C.

and the normal heating and growth sequence is repeated, producing a second VA-CNT section (Fig. 4-20) which is split from and grows under the section from the first growth sequence. By SEM examination, the alignment and density of the second (reactivated) section are not as strong as the first section. Further, we have not investigated if the second sequence reactivates catalyst particles which were active during the first sequence, or if the second sequence activates new catalyst particles which were inactive during the first sequence. In studies of VA-CNT film growth from Fe nanoclusters templated by block copolymer films organized on Al_2O_3/Si [198,346], we find that only 5% of the Fe nanoclusters become active for CNT growth in the first growth sequence. Hence, in our study of reactivation from a Fe/Al_2O_3 film it is practical that enough inactive catalyst particles remain from the first sequence to seed a VA-CNT layer in the second sequence.

4.2.3.1 Damage to CNTs by sonication and electron beam exposure

Preparation of CNT samples for TEM imaging is a delicate process. The CNTs must be sufficiently exfoliated so dispersion on an imaging grid gives isolated CNTs which are suspended over the holes in the grid. However, ultrasonication in a solvent, a typical method of assisting dispersion of CNTs in solution, can easily damage the CNTs (Fig. 4-21). Further, the CNTs are prone to severe damage by the electron beam in the TEM (Fig. 4-22).

As a result, it is necessary to delicately disperse the CNTs (with little or no sonication, giving irregular clumps of CNTs on the grid) and to minimize electron beam exposure to have most

accurate images of "as-grown" CNTs. Uniform dispersion of our long CNTs, such as would be necessary for solution-based processing, remains a challenge.

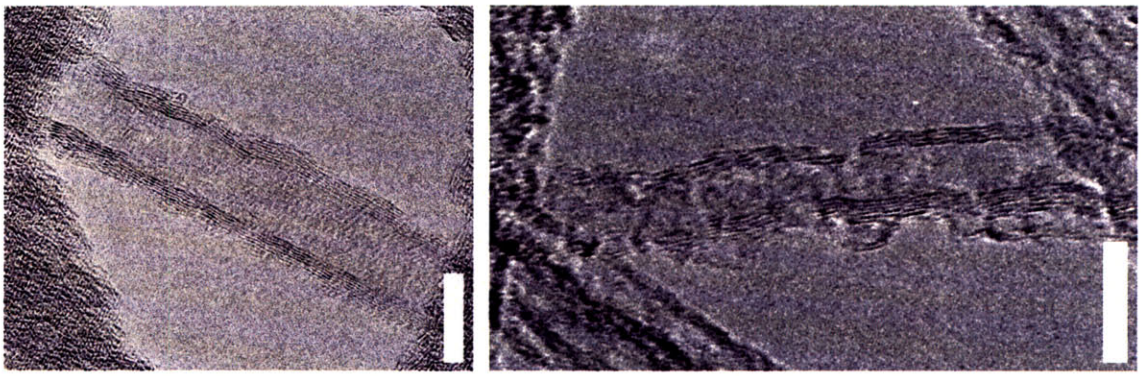

(a) (b)

Figure 4-21. Damage to MWNTs by ultrasonication during TEM sample preparation: (a) isolated CNT, from sample dispersed in methanol without sonication (scale 5 nm); (b) isolated CNT showing significant wall damage, from sample dispersed in methanol with heavy sonication (scale 5 nm). Growth in 100/500/200 sccm $C_2H_4/H_2/Ar$, 750 °C. Imaged using JEOL-2010 by Sreekar Bhaviripudi.

4.2.3.2 Thermogravimetric analysis (TGA)

TGA involves heating a sample at a prescribed rate, in a controlled atmosphere, while simultaneously measuring the mass of the sample. TGA of a VA-CNT film grown from 100/500/200 sccm was performed by scraping the VA-CNT film from the substrate and placing the CNTs in the hanging basket of the TGA instrument (Perkin-Elmer), and heating in air. The oxidation temperature is where $|dM/dT|$ is maximum [347], and for our CNTs this is ≈730 °C (Fig. 4-23). This is higher than values of ≈500 °C reported for VA-MWNTs synthesized by spray pyrolysis, and is closer to the oxidation temperature of high-purity graphite at ≈850 °C [348]. The high oxidation temperature of our CNTs may be due their very high purity, as each CNT grows from a fixed catalyst particle at the base. The presence of significant amounts of metal catalyst in CNTs or along with graphite can significantly lower oxidation temperatures [348].

We quantify the purity (yield) of our process by dividing the mass of carbon by the mass of catalyst, assuming each CNT is seeded by a single catalyst particle having the same diameter as the CNT. For a 1.0 mm long MWNT with 10 nm diameter, this ratio is 28,000 (Table 4.5). However, we already know that each catalyst particle does not seed a CNT, so the process yield could be more formally expressed based on the measured mass of the CNT film divided by the total mass of catalyst on the substrate.

Broadly, high thermal stability is a very desirable characteristic for applications of CNTs. Oxidative treatment of CNTs has also been sought to purify CNTs by removing amorphous carbon which burns at a lower temperature than the CNT walls [349], and to open caps of CNTs [350]. Further, higher-temperature annealing (e.g., at 2800 °C [310]) in vacuum could improve the graphitization of the walls and therefore heal defects, which we expect would significantly improve the electrical properties [351] of the CNTs.

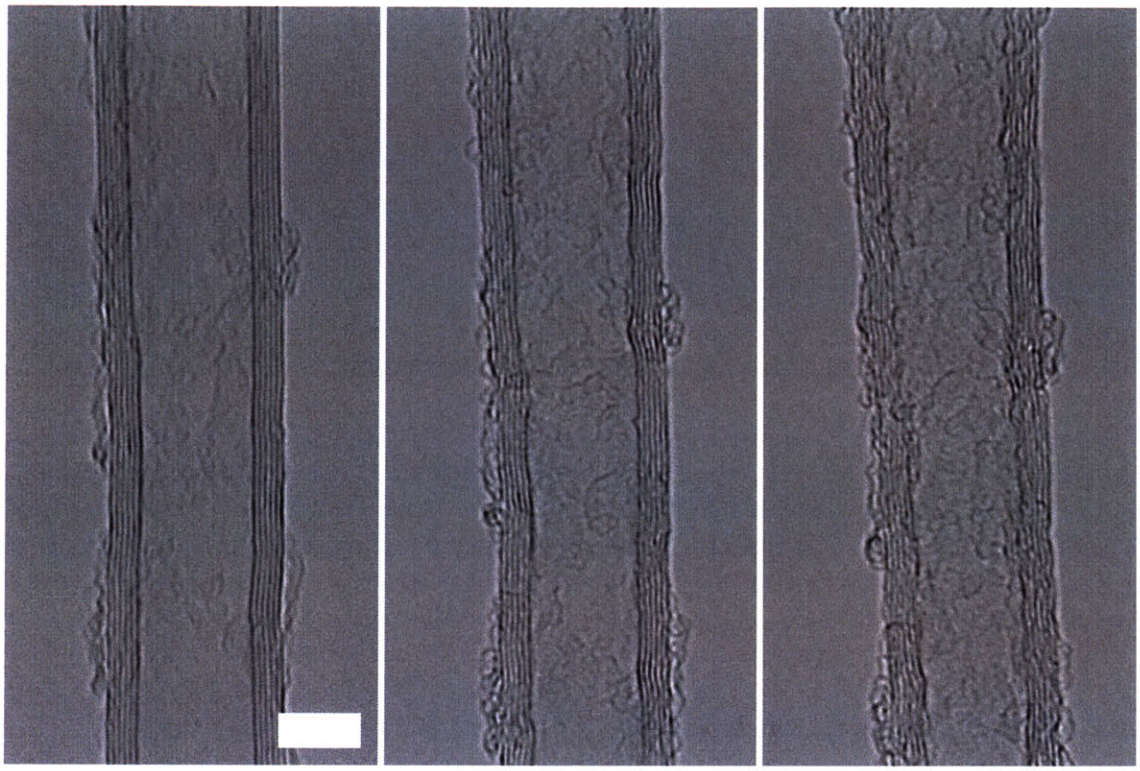

(a) $t = 10\,\mathrm{s}$ (b) $t = 30\,\mathrm{s}$ (c) $t = 180\,\mathrm{s}$

Figure 4-22. Damage to a MWNT by electron beam exposure during TEM imaging (JEOL-2011 at 200 keV). Scales 5 nm.

		CNT length [mm]		
		0.1	*0.5*	*1.0*
Catalyst diameter [nm]	*2*	14,000	70,000	140,000
	10	2,800	14,000	28,000
	20	1,400	7,000	14,000

Table 4.5. Yield of VA-CNT growth process using Fe metal catalyst, expressed as mass of carbon per unit mass of catalyst. This assumes that the catalyst particle is spherical, and that the concentric layers within the CNTs have the bulk density of graphite ($2.2\,\mathrm{g/cm^3}$).

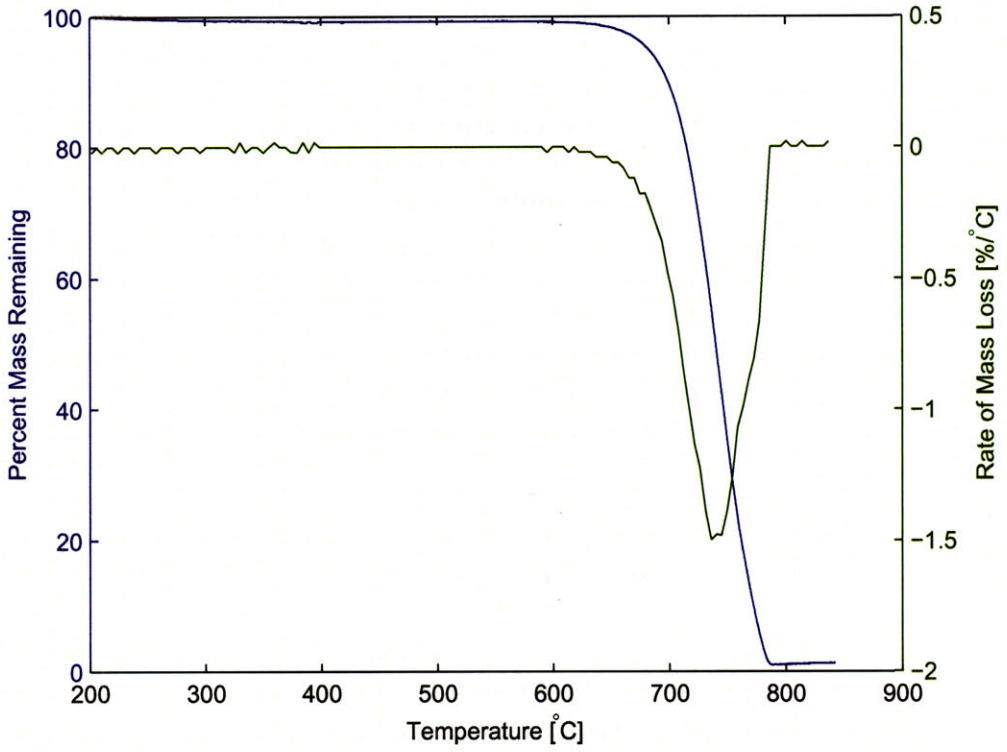

Figure 4-23. TGA plot from VA-CNT film, heated in air at 5 °C/minute, and revealing oxidation temperature of ≈730 °C.

4.2.4 Apparent effects of mechanical stresses during growth

4.2.4.1 Collapse, wrinkling, and peeling of VA-CNT films

Typically on samples which have been processed beyond termination of growth (occurring at 30–60 minutes in the tube furnace), we observe that a thin layer of CNTs near the substrate has collapsed into a coil-like arrangement, as shown in Fig. 4-24a. This morphology transition occurs over a vertical distance of 10-100 μm, with the CNTs becoming "wavy" with increasing amplitude and decreasing period, and then becoming fully collapsed through at least the final 20 μm above the substrate. In the collapsed area, the bends in many CNTs appear very bright (Fig. 4-24c) in the SEM, suggesting that the CNTs are buckled or kinked [352,353] at these points. Sectioning the substrate reveals that the collapsed layer extends into the center area of the film.

It is unclear whether collapse causes premature termination of growth, or if collapse occurs after growth terminates and as mechanical interactions between nearby CNTs may be strengthened by accumulation of amorphous carbon on the outer walls of the CNTs or simply by prolonged high-temperature treatment. However, based on film collapse, and the presence of significant wrinkles (Fig. 4-24b) in the sidewalls of films which have been processed for extended durations, we hypothesize that non-uniformities in the growth rate across the film can introduce significant stresses in the film, which mechanically restrict continued growth.

Residual stresses in thin films such as oxides and metals typically cause film delamination or induce curvature of the substrate [354]. In this case, the CNT layer is very flexible compared to the rigid Si substrate. We hypothesize that in-plane stresses are translated into axial stresses along the CNTs, and axial stresses are introduced directly as neighboring regions of the film grow at slightly different rates and/or as growth terminates unevenly. Because the bottoms of the CNTs are anchored to the substrate, the film cannot compensate for stresses by expanding or contracting in-plane near the substrate. Therefore, stresses more readily cause bending of a portion of a CNT near the substrate interface, either immediately after it emerges from the catalyst particle, or as growth attempts to "push" it upward through the highly stressed region of the CNT film. At the growth temperature of 750 °C, film collapse at the interface is mechanically favored over delamination; however, when a sample is heated to 1200 °C in Ar following growth, the CNT film fully and cleanly delaminates from the substrate and rests freely in a concave "bowl" shape (Fig. 4-24d). A hypothesis of stress-induced termination fits certain observations that the growth rate of a VA-CNT film declines with time but stops suddenly, and that the time and thickness at which growth stops fluctuates from sample-to-sample [355].

4.2.4.2 Growth of free-standing CNT "superstructures" from silicon chips

Aligned CNT strands grow from catalyst-coated silicon chips which are created when we scribe the silicon substrate with a diamond-tipped pen and subsequently break it into samples. These chips fall onto the substrate surface and growth from the catalyst-coated surfaces of the chips gives aligned CNT "superstructures" which rest on the top of the film (Fig. 4-26a–b). The fibers grow simultaneously with the film, and are lifted upward by the growth of the film. When the catalyst surface of a chip initially faces the catalyst surface of the substrate, the chip is lifted upward by growth of the strand and remains at the tip of the strand (Fig. 4-26c); when the catalyst on the chip initially faces upward (Fig. 4-26d), it remains on the top surface of the film and the strand grows from a fixed base. Chips which are lifted upward typically give longer strands.

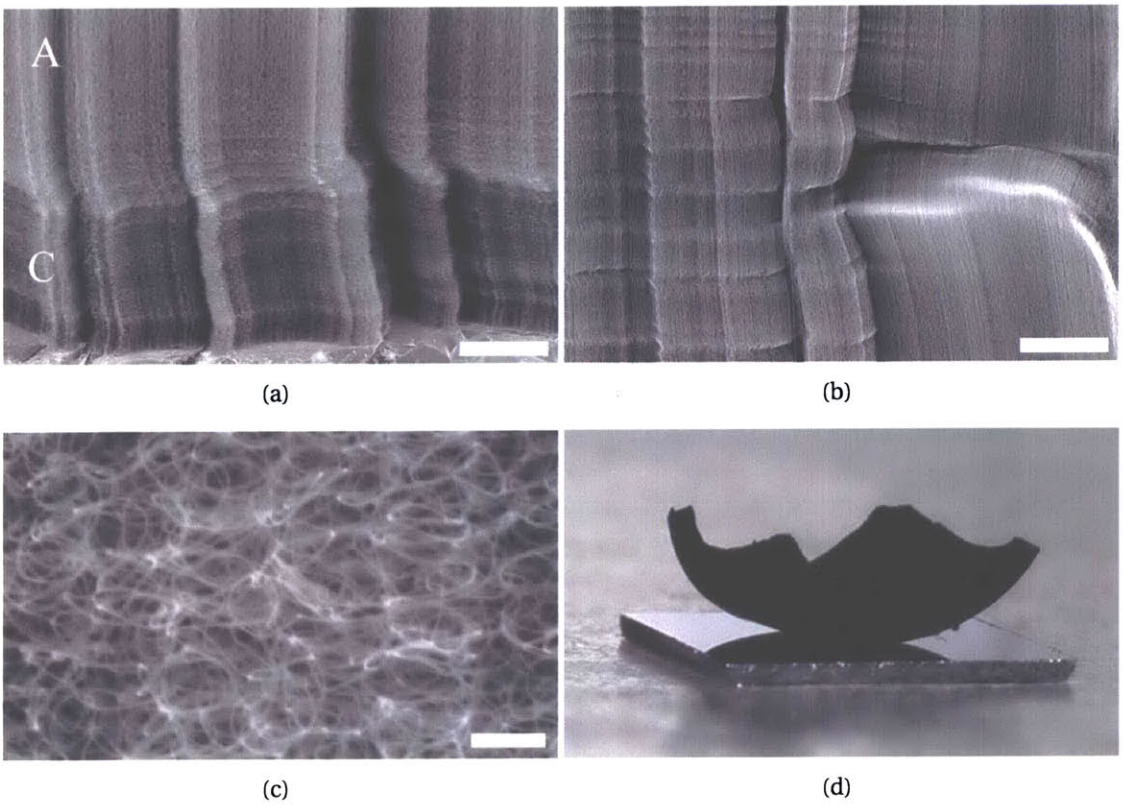

Figure 4-24. Stress-induced collapse, wrinkling, and peeling of a VA-CNT film: (a) region of film just above substrate, showing transition between aligned region (A) and collapsed region (C) (scale 20 μm); (b) wrinkles in sidewall of film, approximately halfway through film thickness (scale 20 μm); (c) tangled, coil-like morphology in collapsed region (C) shown in (a) (scale 0.5 μm); (d) peeled film resting on 15 × 15 mm Si substrate, after post-growth annealing in Ar for 5 minutes at 1200 °C.

The chips are typically 1–100 μm wide and a few μm thick, and as also observed with the lithographically patterned structures, strands growing from smaller chips are generally shorter and are more likely bent and/or kinked. However, a strand grown from a chip is often longer than a strand grown from a patterned area of catalyst having approximately the same cross-sectional size and shape, and the length of strands with at least a 25 μm "diameter" cross-section can be greater than the thickness of the underlying CNT film by as much as 50%. This suggests that growth is faster and prolonged because of improved gas access to the catalyst, and because the strands are not bound within the film by mechanical stress. The strands flutter and easily fall over or detach from the film when we blow gently over the substrate; therefore, we suspect that even longer strands are formed during growth, and are detached from the film and carried downstream by fluctuating forces induced by the gas flow in the furnace tube.

Synthesis of much shorter and larger-diameter aligned CNTs from SiO_2 flakes was previously achieved using injection CVD [321]. Self-aligned strands could be produced continuously in a floating substrate system, and may be suitable fillers for enhancing the properties of composite materials.

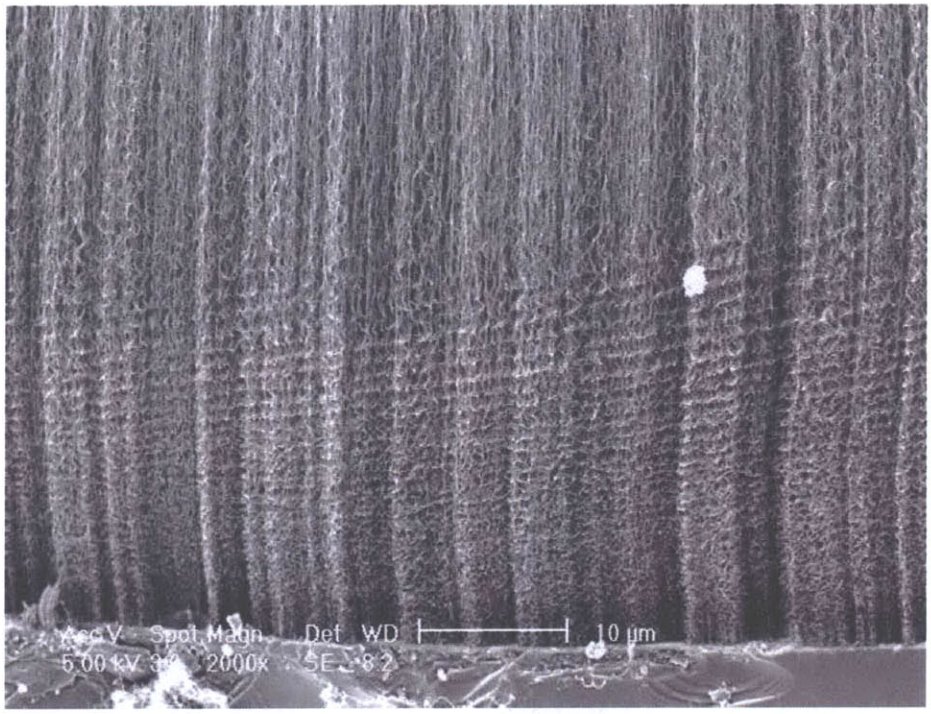

(a)

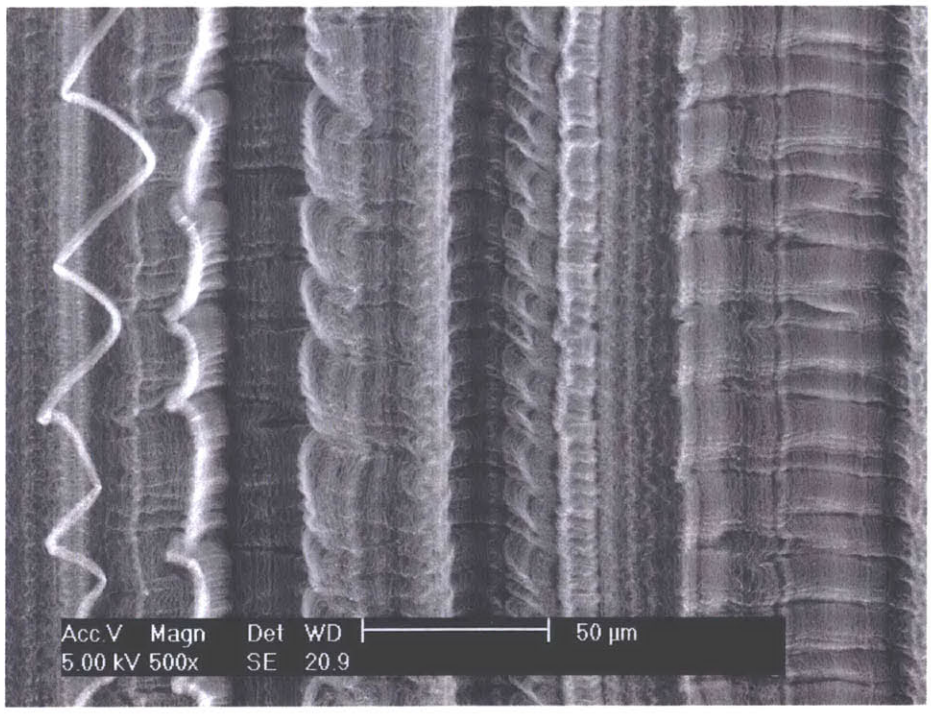

(b)

Figure 4-25. Intricate ripple and wrinkle patterns on the sidewall of a VA-MWNT film.

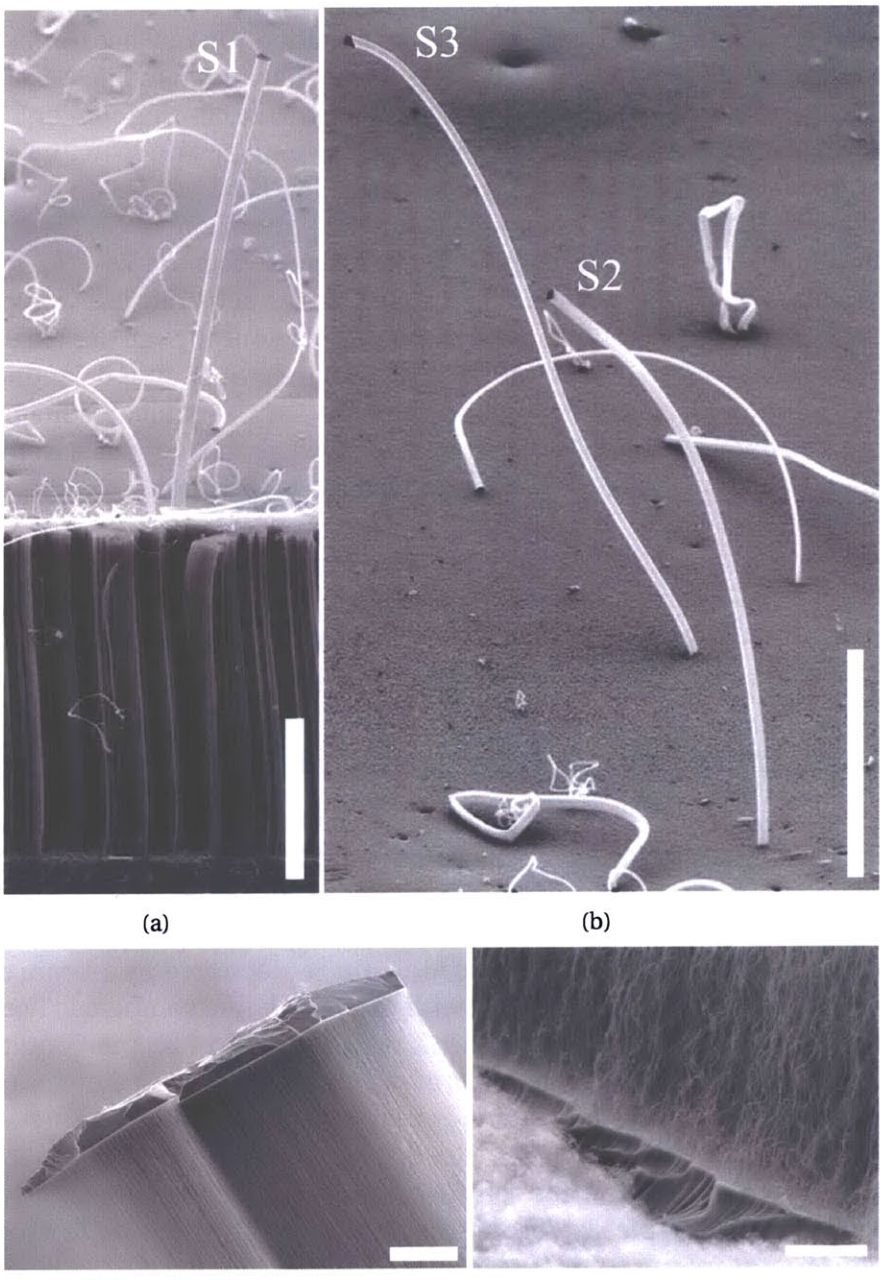

Figure 4-26. CNT strand "superstructures" grown from silicon chips created during scribing of the silicon substrate: (a)-(b) free-standing and collapsed strands on top surface of VA-MWNT film, where length of free-standing strands (S1,S2,S3) = (1.5,1.7,1.5) mm, exceeding film thickness of 1.1 mm (scales 500 μm); (c) silicon chip at tip of strand (scale 10 μm) (d) silicon chip at base of strand, resting on top of film (scale 2 μm).

4.2.5 Examination of bottoms of CNTs

Because the CNTs in our films are very long and each grow from a single catalyst site, it is difficult to find catalyst particles during routine TEM examination. On rare occasions we observe a catalyst particle at an apparent root of a MWNT, such as that shown in Fig. 4-38e. The oblong shape of the catalyst may arise during growth or after growth (i.e., during cooling), and with this limited *ex situ* examination it is not useful to comment the shape and structure of the catalyst in light of previous *in situ* observations of growth [173, 356]. However, we do note that the catalyst particle fits within the CNT, and it appears that the bottom end of CNT is loosely capped by closed graphitic layers. This may explain why it is easy to peel the VA-CNT films from the substrate, as in this form a CNT would not be "rooted" in the substrate but would be "resting" against the substrate or supporting layer and perhaps is held only by van der Waals forces.

Also, we observed the bottom structure of the CNT film by SEM after delamination using a razor blade, as shown in Fig. 4-27. Here we see how the CNT alignment is maintained down to the CNT-substrate interface (before termination of growth), and it appears from the highest-magnification image that many of the CNTs are clustered at their bottom ends. This warrants further investigation.

Dry transfer of CNTs to a TEM grid, e.g., by "lifting" a thin layer of CNTs from the sidewall of a film while maintaining alignment of the CNTs, has shown promise in an initial experiment and will let us examine a large population of bottom ends of CNTs, and further analyze the CNT/catalyst structure and the possibility of end grouping.

4.2.6 Effect of supporting layer and heating rate

To qualitatively evaluate the effect of the supporting layer on CNT growth in the $C_2H_4/H_2/Ar$ atmosphere, we derive catalysts from a Fe salt solution [261, 278] and load these catalysts on Si substrates having different supporting layers. Samples are prepared by soaking $\approx 1 \times 1$ cm substrates for 5 minutes in 10 mM $Fe(NO_3)_3 \cdot 9H_2O$ dissolved in 2-propanol, and then drying the substrates in ambient air. Substrates of 10 nm Al_2O_3 on Si (deposited by e-beam evaporation), 1 μm thermally-grown SiO_2 on Si, and bare Si with native SiO_2, are compared. The CNT growth procedure is exactly as described in section 4.1.1, with 1 minute of H_2 pre-conditioning. Simple air-drying causes non-uniform aggregation of salt on the substrates; therefore growth is not highly uniform. However, this method lets us quickly evaluate the quality of metal-support interaction.

When the substrates are heated, the salts decompose into metal nanoclusters which seed CNT growth; metal nitrates typically decompose at 150–190 °C [357]. For Fe on Al_2O_3/Si, VA-CNTs exceeding 0.5 mm grow in 15 minutes (Fig. 4-28a-b), for Fe on SiO_2/Si there are only isolated areas of VA-CNT growth (Fig. 4-28c-d), and for Fe on Si there is only sparse growth of tangled CNTs (Fig. 4-28e-f). This demonstrates the importance of Al_2O_3 as a supporting layer for the number of reasons discussed in section 3.1, as well as the versatility of the Fe/Al_2O_3 system for high-yield growth of CNTs from the C_2H_4 carbon source [358].

When the substrates are processed in an alternative "rapid heating" growth sequence, CNT yield is more consistent among the different supporting materials. Here, the tube furnace is equipped with an extra-long quartz tube (125 cm compared to 75 cm). The samples are placed in the sealed tube, in the section which remains outside of the furnace while the furnace tem-

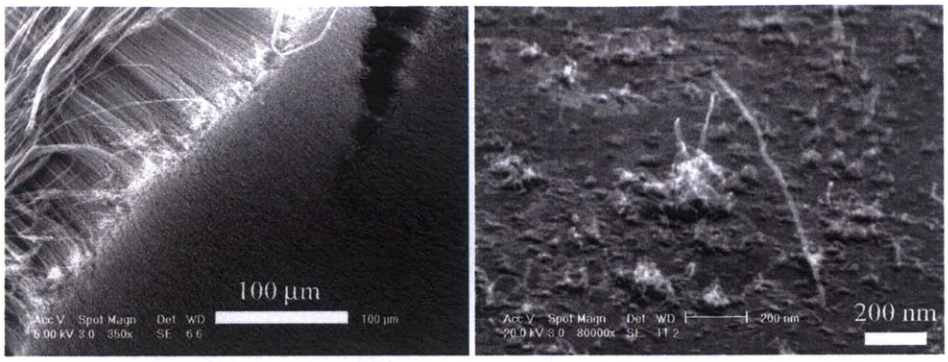

(a) (b)

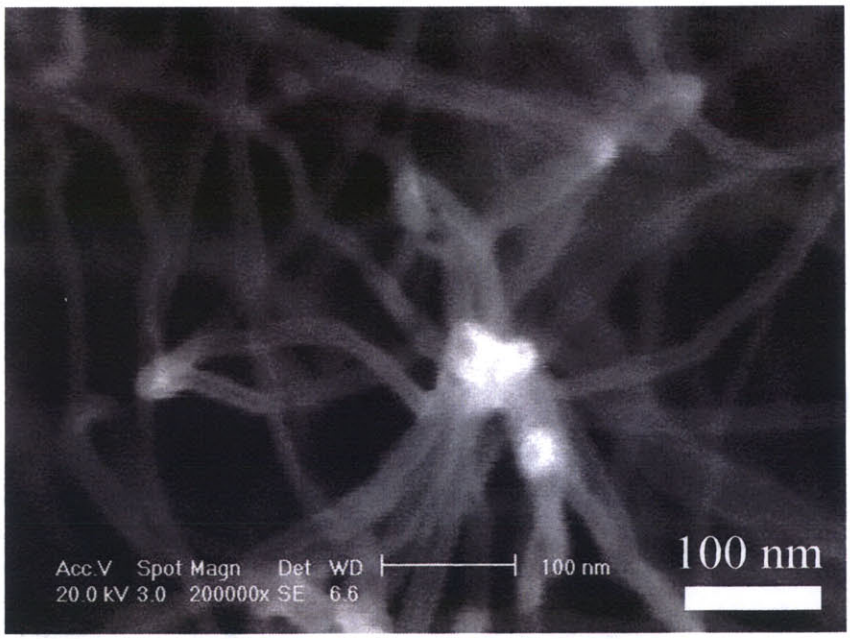

(c)

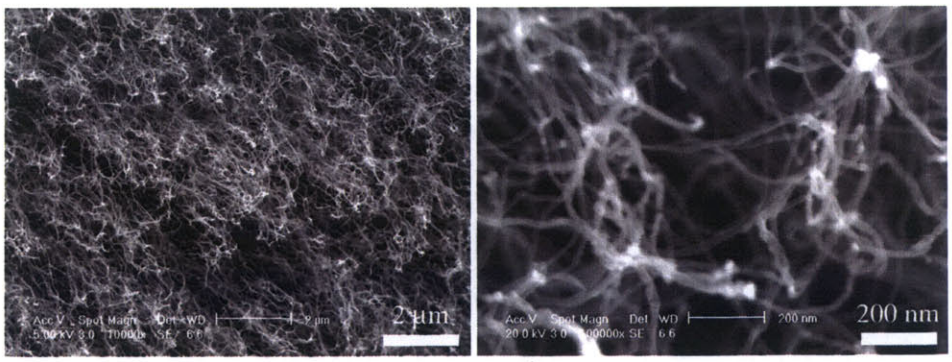

(d) (e)

Figure 4-27. SEM examination of bottom surface of CNT film manually peeled from silicon substrate: (f) bottom of peeled film surface; (b) substrate surface after film delamination (c) close view peeled film surface, showing apparent junctions at bases of CNTs; (d) and (e) alternate magnifications of (c).

perature is ramped and stabilized under Ar. Then the tube is rapidly shifted to place the samples just downstream of the control thermocouple, and after one minute the "normal" growth sequence is followed, with 1 minute 500/200 sccm H_2/Ar pre-conditioning at 750 °C. With rapid heating, the yield and uniformity of growth is increased compared to results with normal heating, and the Al_2O_3 > SiO_2 > Si hierarchy of support performance is maintained (Fig. 4-29). This indicates that nanoparticles for CNT growth can form upon rapid heating of $Fe(NO_3)_3 \cdot 9H_2O$, and also that the rapid heating process prevents unfavorable interactions such as formation of Fe silicide [294] which likely stunts growth from unsupported Fe in the normal heating sequence.

E-beam deposited Fe/Al_2O_3 on Si was also processed by rapid heating, giving limited and apparently flow-mediated nucleation of mm-high VA-CNT pillars (Fig. 4.2.6). Incidentally, this sample gave the curious "bottle" structures (the tops of pillars shown) which are used in the "Absolut Nano" and "|NANO|!" renderings (Chapter 8). Going forward, it will be interesting to study the time evolution of the catalyst film into nanostructured topography, such as by AFM imaging of substrates pre-conditioned for short durations using the suspended resistively-heated platform (section 6.2).

As measured by Raman spectroscopy, the quality (G/D ratio) of CNTs grown by the rapid heating process is comparable yet inconclusively ordered (slightly lower for Fe/Al_2O_3/Si, and slightly higher for $Fe(NO_3)_3 \cdot 9H_2O$-Al_2O_3/Si) compared to CNTs grown by the normal process (Fig. 4-31).

4.2.7 Screening of other catalyst film combinations

Finally, in an effort to isolate initial conditions for VA-CNT growth, other catalyst films which were reported in literature to yield VA-CNTs in a CVD atmosphere of C_2H_4 were evaluated (Figs. 4-32–4-34). Our initial experiments grew tangled CNTs yet failed to produce VA-CNTs from these films, on both Si and SiO_2 substrates.

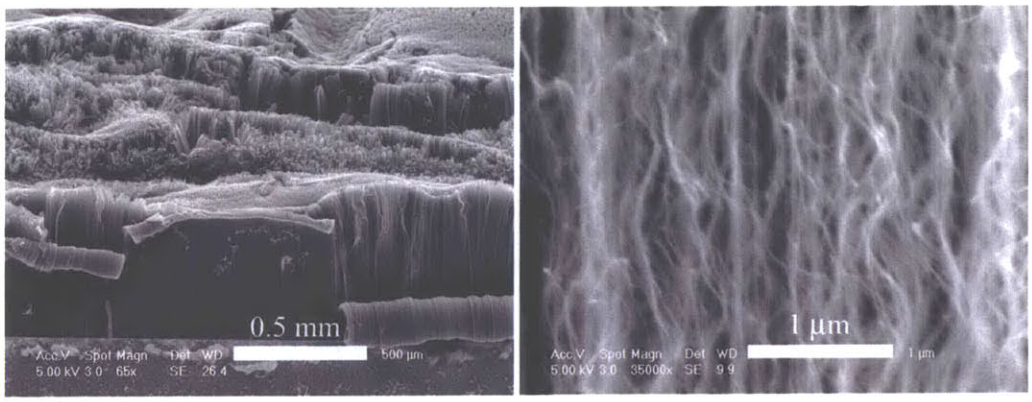

(a) (b)

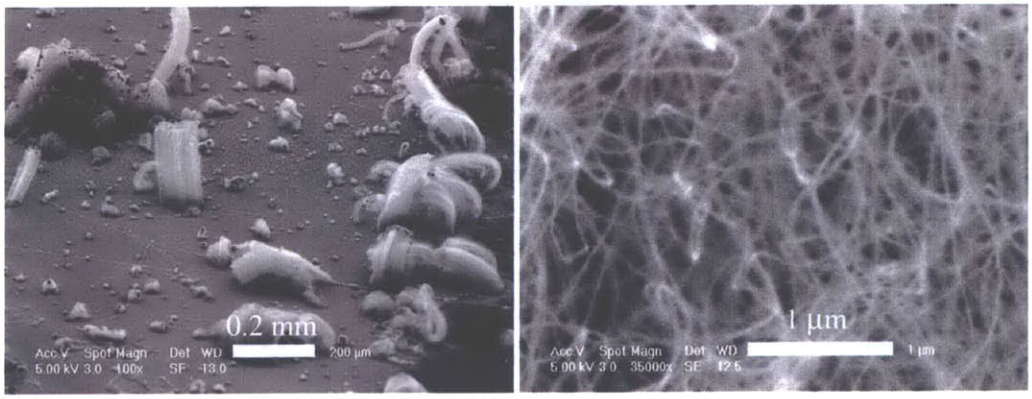

(c) (d)

(e) (f)

Figure 4-28. CNT growth from $Fe(NO_3)_3$-derived catalysts, processed by "normal" growth sequence in 100/500/200 sccm $C_2H_4/H_2/Ar$, 750 °C: (a,b) $Fe(NO_3)_3$ on 10 nm Al_2O_3 on Si; (c,d) on 1 μm SiO_2 on Si; (e,f) on Si with native SiO_2 only.

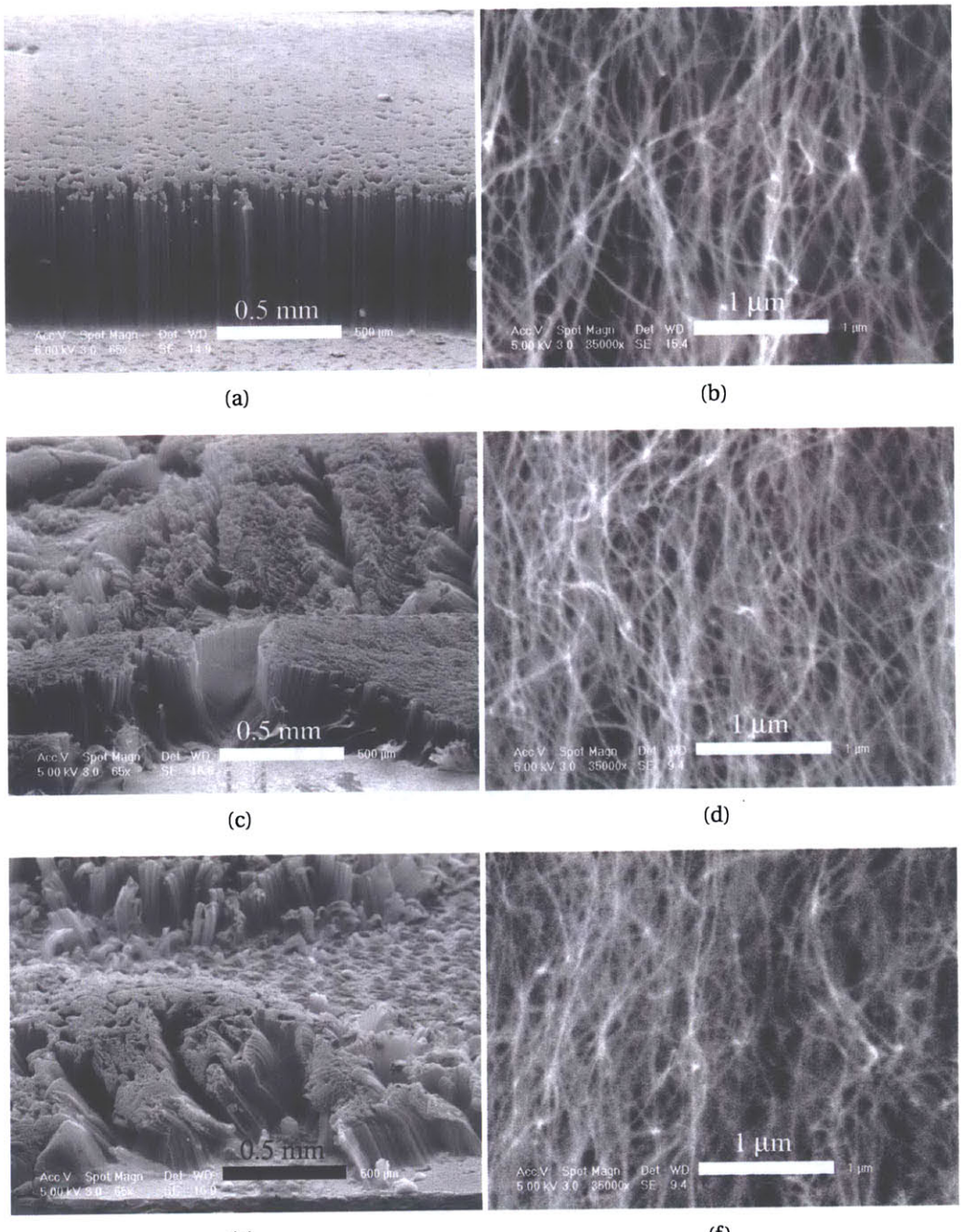

Figure 4-29. CNT growth from $Fe(NO_3)_3$-derived Fe catalysts, processed by "rapid" heating growth sequence: (a,b) $Fe(NO_3)_3$ on 10 nm Al_2O_3 on Si; (c,d) on 1 μm SiO_2 on Si; (e,f) on Si with native SiO_2 only.

(a)

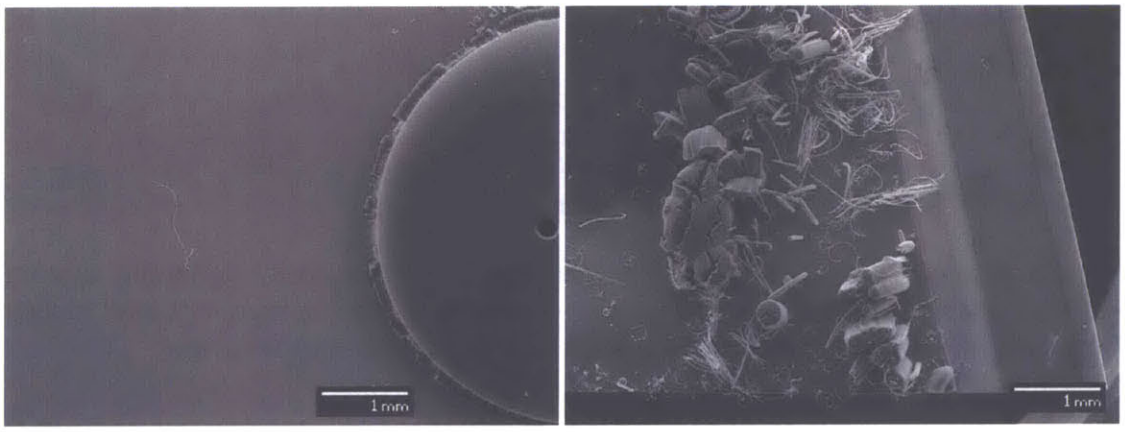

(b) (c)

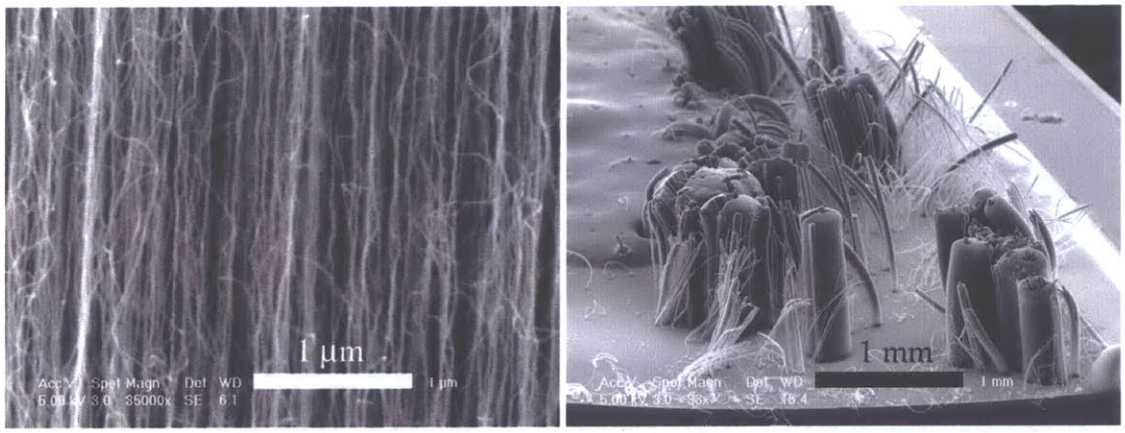

(d) (e)

Figure 4-30. (a) CNT growth from long sample of Fe/Al_2O_3 film on Si, processed by rapid heating method in 100/500/200 sccm $C_2H_4/H_2/Ar$, exhibiting flow-mediated growth pattern; (b) close view of area 1; (c) close view of area 2. Left edge of sample was placed at center (thermocouple location) of furnace tube, and gas flow direction is left-to-right with reference to (a).

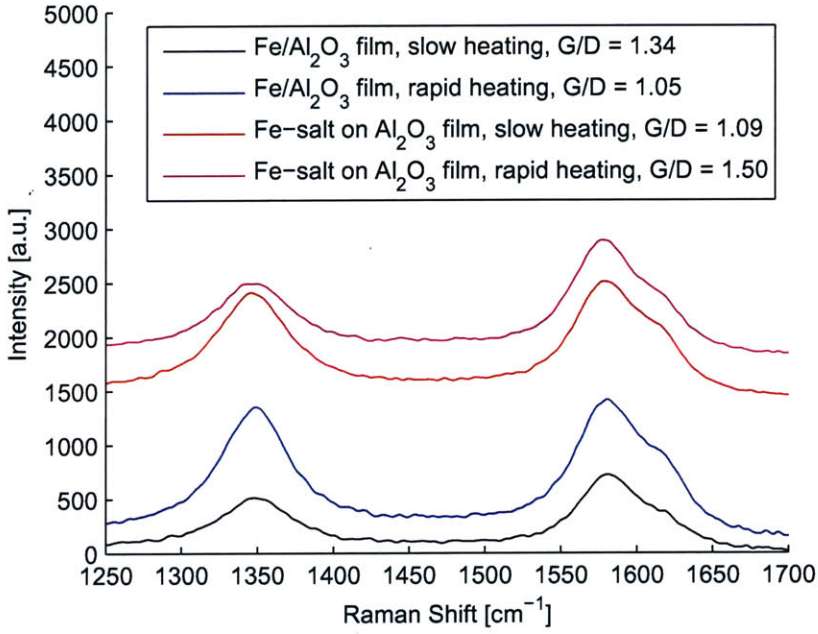

Figure 4-31. Comparison of *G*- and *D*-band regions of Raman spectra (514 nm excitation) of VA-CNTs grown from Al_2O_3-supported Fe. Fe is deposited by e-beam evaporation or deposition of Fe salt, and the CNTs are synthesized using a slow or rapid heating sequence.

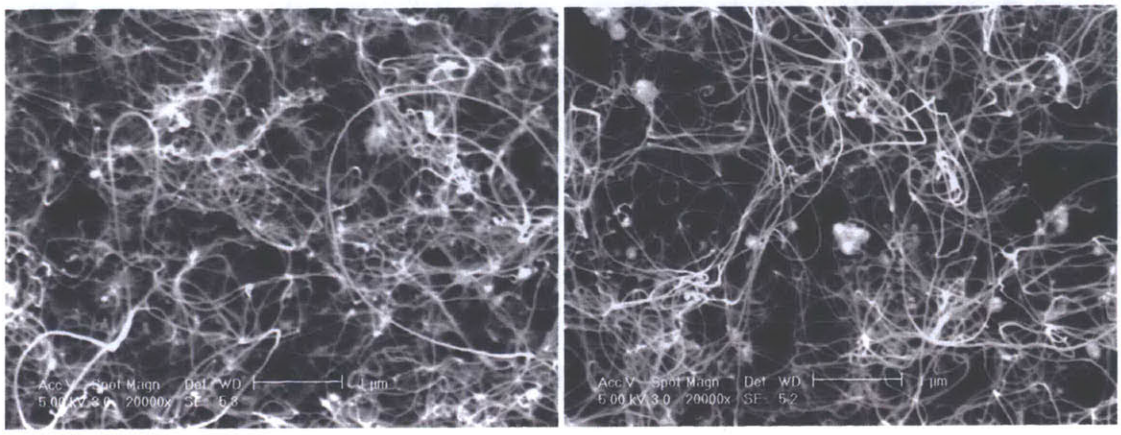

(a) Bare Si substrate.

(b) SiO_2 substrate.

Figure 4-32. Growth from 5 nm Fe catalyst film deposited on Si by e-beam evaporation then annealed in air for 9h at 300 °C (after [144]). CVD was performed in 1000 sccm C_2H_4 at 700 °C.

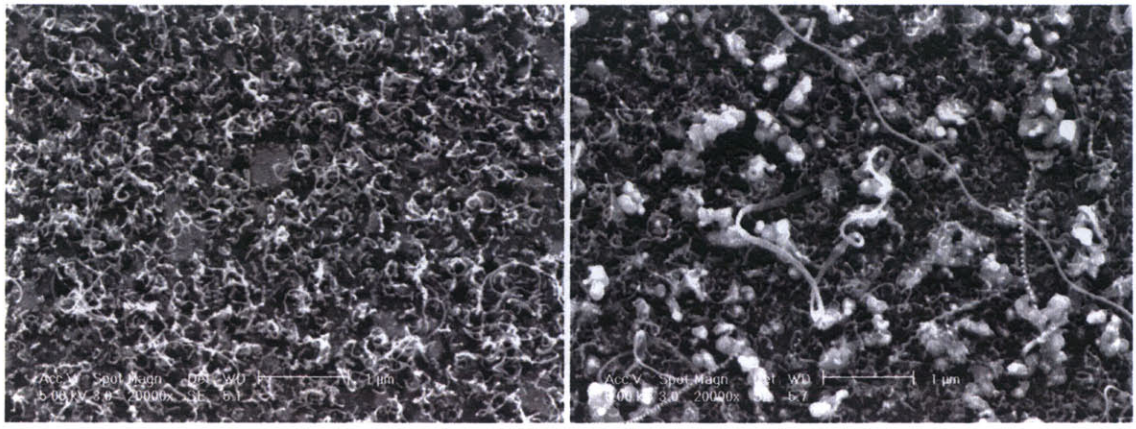

(a) Bare Si substrate. (b) SiO_2 substrate.

Figure 4-33. Growth from 5/20 nm Ni/Al catalyst film deposited on Si by e-beam evaporation (after [318]), in 1000 sccm C_2H_4 at 750 °C.

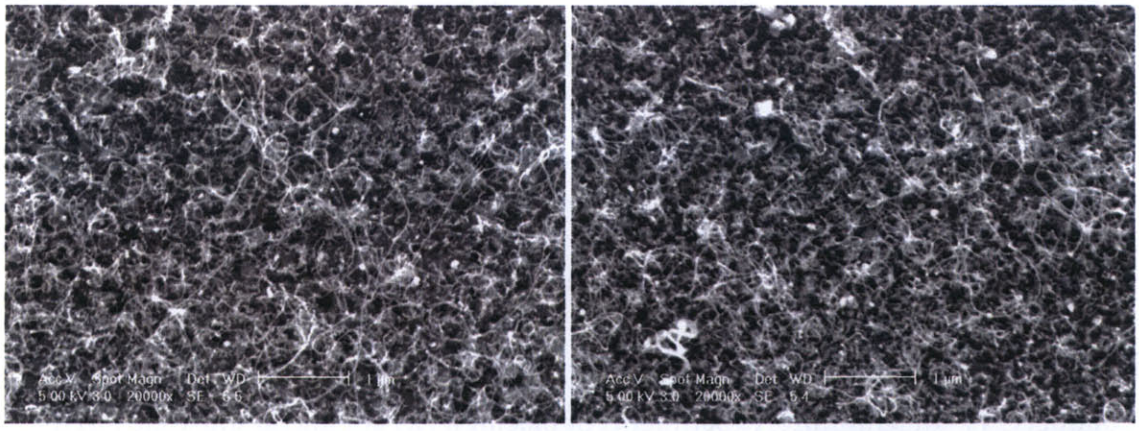

(a) Bare Si substrate. (b) SiO_2 substrate.

Figure 4-34. Growth from 5/20 nm Ni/Al catalyst film deposited on Si by e-beam evaporation then annealed in air for 1h at 400 °C. CVD was performed in 1000 sccm C_2H_4 at 750 °C.

4.3 CNT film growth under mechanical pressure: force output and control of film structure (based on [4])

While the chemical kinetics of CNF and CNT growth by catalytic CVD have been studied widely [22,45,46,158–162], the effects of mechanical forces on CNT growth have only been explored using non-contact methods to guide the direction of growth. For example, isolated SWNTs can be grown to millimeter or centimeter lengths when suspended by gas flow during growth [141,142]. Application of an electric field during growth can exert a force on a nanotube and/or a catalyst particle [145], to achieve aligned and direction-controllable growth in plasma-enhanced CVD processes [221,359,360], and to achieve growth of aligned CNTs spanning gaps between microfabricated electrodes [219]. Further, fluid flows and surface tension forces at fluid interfaces can direct post-growth assembly of CNTs into patterns and structures on surfaces [235,236,361].

This section presents growth of VA-CNT films under mechanical pressure. The pressure affects the film microstructure and CNT wall structure, and facilitates measurement of the force which can be exerted collectively by large numbers of CNTs during growth. We use this principle to fabricate three-dimensional structures of CNTs which conform to the shape of a microfabricated template. This technique is analogous to microinjection or microtransfer molding, [362–364] where microstructures are fabricated by flowing a precursor material such as a resin or powder into a microfabricated mold and subsequently curing the material. In our process, a gaseous feedstock is catalytically transformed into CNTs within the mold, filling the cavities with a scaffold of solid nanostructures which is embossed by the mold as mechanical pressure builds during CNT growth within the cavities.

Our previous work in VA-CNT film growth (section 4.1) demonstrates that placement of a piece silicon wafer as a "cap" on top of the growth substrate moderates the gas flow to the catalyst, and the CNT film lifts the cap as it grows. Other studies show that CNT growth can lift a film which is deposited on top of the catalyst [365,366], and that stacked CNT multilayers can be grown when catalyst is intermittently supplied to the catalyst-substrate interface, where each additional layer lifts the previously-grown layers [367,368]. Here we provide the first indication of mechanochemical effects [35] on CNT growth reactions, where a mechanical force applied to the growth site affects the morphology and growth rate of CNTs in a densely-packed film. Film growth under mechanical pressure may be suitable for a wide variety of nanostructures in addition to CNTs, such as inorganic and semiconducting nanowires. Further, CNT layers having controlled structure and permeability are useful for applications in electrochemical energy storage, membranes and electrodes in fuel cells, and fluid filtration [369,370].

4.3.1 Materials and methods

We conduct CNT "weightlifting" experiments by placing a 1×1 cm silicon substrate (p-type, 1-10 Ω-cm, Silicon Quest International) coated with a 1.2/10 nm Fe/Al_2O_3 film deposited by e-beam evaporation, under a tungsten weight as shown in Fig. 4-35a. The catalyst surface is separated from the weight by a Si_3N_4-coated silicon cover which is slightly larger than the substrate, and the non-polished surface ($R_a \approx 150$ nm) of the cover is in initial contact with the catalyst film. The weight is a stack of coupons (1×3–9 cm) which are cut from a tungsten sheet (99.95+%,

Midwest Tungsten) using an abrasive waterjet (Omax[2]), and then sonicated in acetone and rinsed with DI-H_2O. Incidentally, patches of tangled and aligned CNTs are also observed on the waterjet-cut edges of the tungsten weights (section 4.6), possibly due to inclusion of microparticles of garnet abrasive from the cutting process. However, placing a tungsten coupon immediately upstream of the growth substrate does not affect the characteristics of the CNT film grown from the Fe/Al_2O_3 catalyst.

For physically-templated growth, the catalyst-coated substrate is clamped against a microfabricated silicon template using a quartz fixture as drawn in Fig. 4-35b, and the assembly is preloaded using Al_2O_3 bolts and high-temperature spring washers. The template is fabricated by standard photolithography and etching using aqueous KOH (20 wt% in DI-H_2O, 80 °C). The pattern is etched on the non-polished side of the wafer to prevent bonding of the template to the growth substrate during the shape transfer process.

CNT growth is performed in a single-zone atmospheric pressure quartz tube furnace, according to the process described in section 4.1.1, with 1 minute of H_2 pre-conditioning and 15 minutes of growth with 100/500/200 sccm $C_2H_4/H_2/Ar$.

Characterization is performed by SEM using a Philips XL30-FEG-ESEM at 5 keV, and by HRTEM using a JEOL-2011 at 200 keV. TEM samples are prepared by dispersing a section of CNT film gently in isopropanol, and air-drying the solution on a holey carbon grid (Quantifoil). An "average" CNT from our process has an outer diameter of 9 nm and five walls, as observed by TEM imaging. The films contain approximately 1.5×10^{10} CNTs/cm^2. This is calculated using the mass of an average CNT (based the dimensions measured by TEM and the density of graphite), the film volume which is estimated by SEM imaging, and the film mass determined by weighing the film using a thermogravimetric analyzer (TGA, Perkin-Elmer) at room temperature.

4.3.2 Results and discussion

4.3.2.1 CNT film "weightlifting" and control of internal film structure

A growing VA-CNT film lifts the tungsten weight upward, demonstrating that CNT growth exerts an extrusive force. Fig. 4-36 plots the final thickness of the VA-CNT film, versus the applied pressure, at otherwise identical CVD conditions. The thickness of the VA-CNT film and the degree of alignment within the film decrease with increasing applied pressure, beyond a minimum pressure which is needed to suppress non-uniformities in the film which emerge in regions that grow at a relatively rapid rate. For these slight pressures ($\leq$500 N/m^2; $\leq$1 g), we observe no uniform effect of pressure on growth. The weight rests on the peaks of the top surface of the film, which has a waviness of approximately 20% ($\approx$200 μm) of the total thickness. For higher pressures, the film thickness decreases in an approximately linear fashion with the logarithm of applied pressure, and the top surface of the film is substantially flat (Fig. 4-37a, bottom). With increasing pressure beyond the threshold, the internal structure of the CNT films changes from well-aligned (Fig. 4-37b), to less-aligned with increased deformation of the CNTs (Fig. 4-37d), to predominately collapsed in a "serpentine" pattern, where a sample grown under 60,000 N/m^2 pressure exhibits a spatial wavelength of $\approx$300 nm (Fig. 4-37d). We observe that

[2]The tungsten sheet was cut using the built-in settings for cutting stainless steel of the same thickness, at the maximum edge quality of "5".

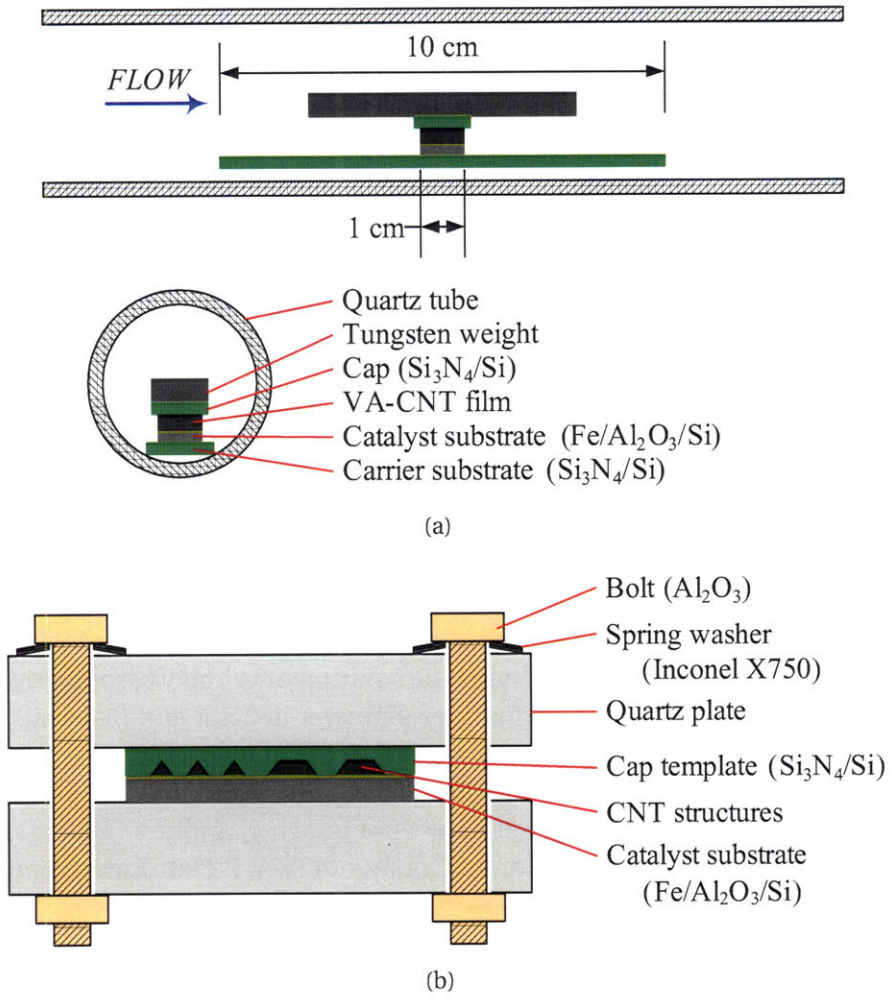

Figure 4-35. Substrate configurations for applying mechanical pressure to CNT films during growth: (a) placement of a catalyst-coated substrate under tungsten weight, where growth lifts the tungsten weight; (b) clamping a catalyst substrate against a microstructured template, where growth fills the cavities in the template.

the wavelength of the collapsed film structure is smaller for higher applied pressures; however, further study is necessary to quantify this relationship in detail.

TEM imaging (Fig. 4-38) reveals that mechanical pressure causes the CNTs to have a prevalence of significant structural faults and kinks in their sidewalls, compared to relatively straight CNTs which are more abundant in aligned films grown under little or no mechanical pressure. Isolated groups of CNTs show the serpentine CNT shape (Fig. 4-38d) which is microscopically realized within the collapsed films. Microscopic curves in the CNTs are accomodated by the sharp faults in the sidewalls and local changes in the inner and outer diameters, rather than by smooth curves in the lattice. Generally, the structure of CNTs grown under mechanical pressure is different than the structure expected from a CNT which is deformed after growth [72, 353]. Oblique forces on the catalyst particle may cause different rates of carbon precipitation across the catalyst particle, causing the observed defects in the wall structure [371].

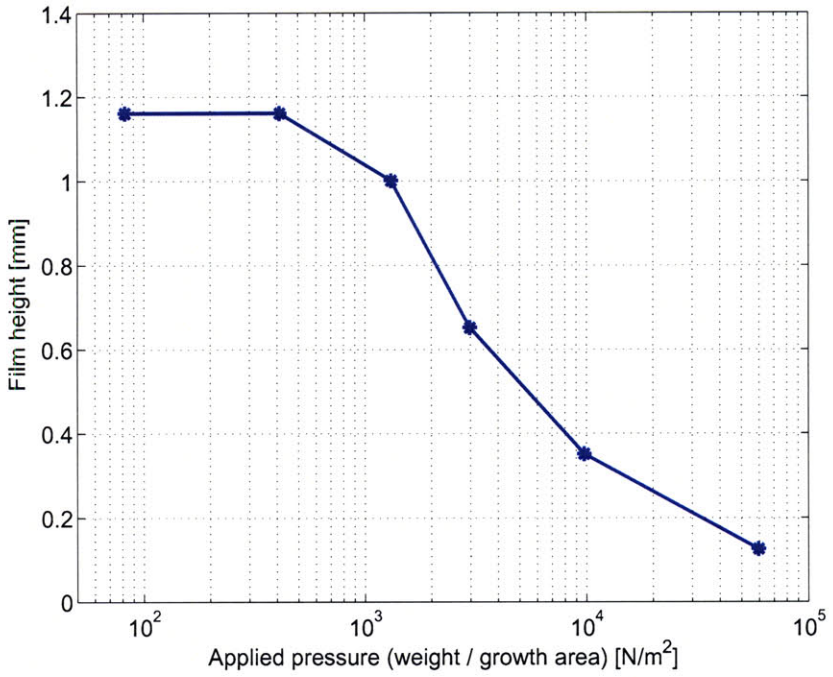

Figure 4-36. Measured relationship between CNT film height and pressure applied during growth, for 15 minutes of growth.

In the "capped" sample configuration (Fig. 4-35a), the gas flow to catalyst is restricted by the cap and gas reaches the catalyst by diffusing inward between the cap and substrate. As a result, VA-CNT growth occurs only around the periphery of the substrate, in an area where the initial gas supply is sufficient to activate growth in a vertically-aligned conformation. For a 1×1 cm substrate, the area of VA-CNT growth is typically 0.1–0.2 cm^2, and we calculate the applied pressure for each experiment by dividing the weight placed on the cap by the area of VA-CNT growth which is measured by SEM examination at low magnification. The area of VA-CNT growth necessarily fluctuates from run-to-run because of debris which establishes a slight initial gap between the catalyst substrate and the cap, and therefore modulates amount of gas which initially diffuses into the gap to initiate vertically-aligned CNT growth. However, the thickness of the VA-CNT region is invariant among many identical experiments in the capped configuration and in different sample configurations [3], confirming that the flow restriction introduced by the cap does not affect the steady growth rate.

Because applied pressure causes the CNTs in a film to be more closely packed, hindrance of gas diffusion through the film [159,160] may contribute to slower growth of CNTs under applied pressure. To evaluate this hypothesis, we also grew CNTs from lithographically-patterned samples where the catalyst is arranged so CNTs grow in regularly-spaced "pillars", so diffusion of gas to the catalyst is limited only by the half-width of the pillar cross-section, rather than by the thickness of the film or by the distance from the outer edge of the sample. For example, under equivalent applied pressures, an array of 200×200 μm pillars grows to approximately the same effective height a sample having a uniform film of catalyst (Figs. 4-39 and 4-40), suggesting that mechanical constraint rather than diffusion limitation plays a dominant role in decreasing the

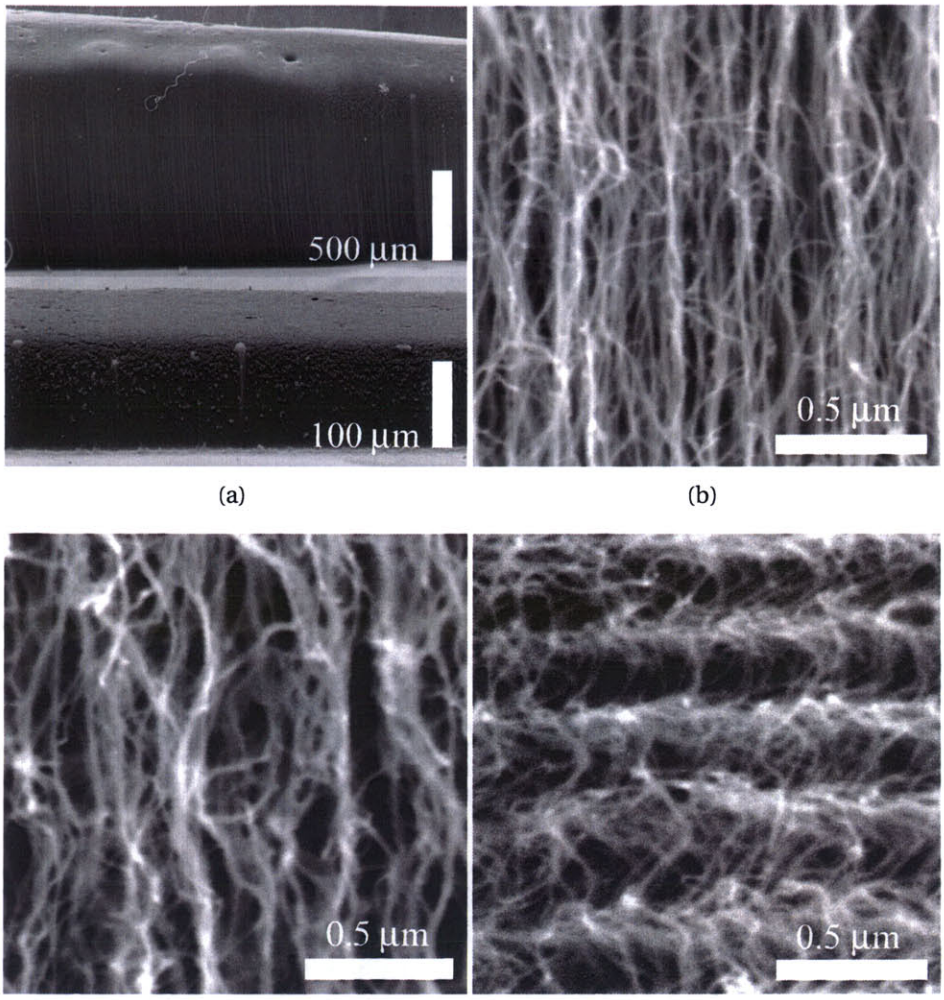

Figure 4-37. Morphology of CNT films grown under different applied pressures: (a) sidewall of film grown under 0.2 g weight (top) and 61 g weight (bottom); (b) alignment within film grown under 0.2 g silicon weight (≈80 N/m^2); (c) grown under 6 g tungsten weight (≈3000 N/m^2); (d) grown under 61 g tungsten weight (≈60,000 N/m^2).

growth rate of CNTs in our experiments.

Further, while the CNT length is approximately equal to the film thickness for a well-aligned film, the length of CNTs in a collapsed film substantially exceeds the film thickness. For example, in the film grown under 60,000 N/m^2 pressure (Fig. 4-37d), the CNT length is 40% (assuming an in-plane "zig-zag") to 90% (assuming the CNTs form helices) greater than the film thickness. Still, the "effective" CNT length, accounting for the collapsed microstructure, decreases significantly with applied pressure. Further analysis of the film microstructures is needed to determine a more precise relationship between CNT length and applied pressure.

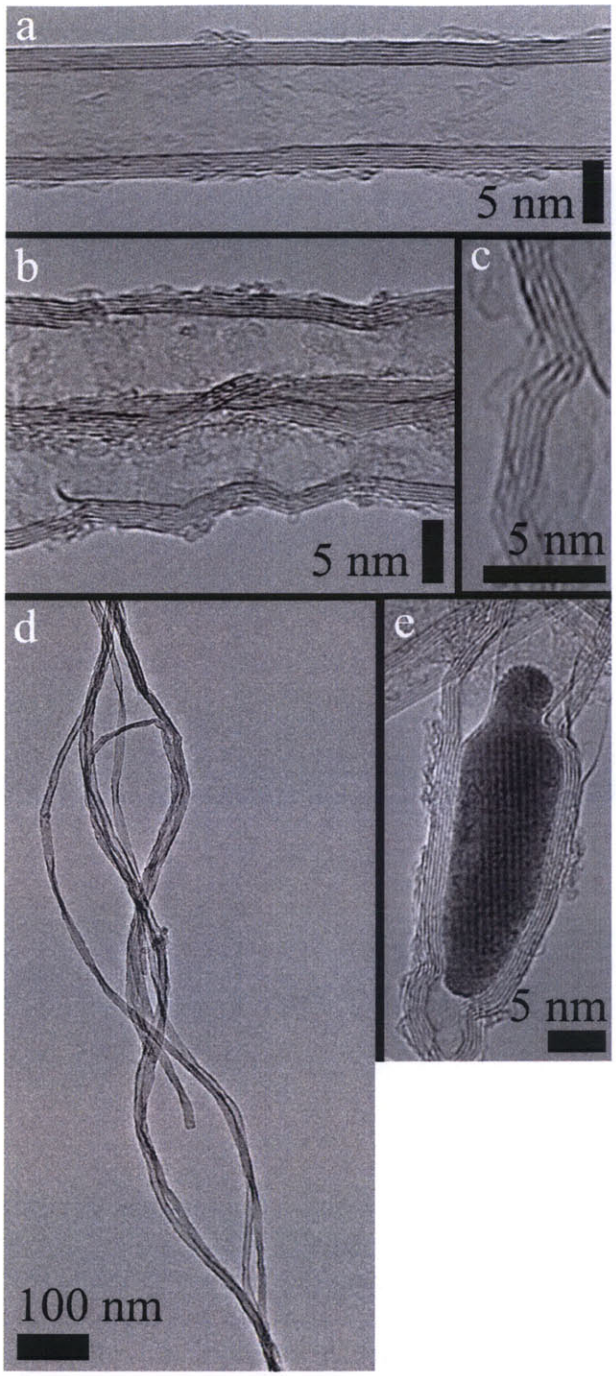

Figure 4-38. TEM images: (a) typically straight multi-wall CNT from aligned film; (b) defective CNTs with sidewall kinks and ripples, which are abundant in films grown under high applied pressure; (c) close-up of defective sidewall structure; (d) low-magnification image of "serpentine" CNTs isolated from film having collapsed microstructure, grown under 60,000 N/m^2 pressure, showing abundant sidewall defects and local changes in diameter; (e) Fe catalyst particle encapsulated at bottom end of CNT.

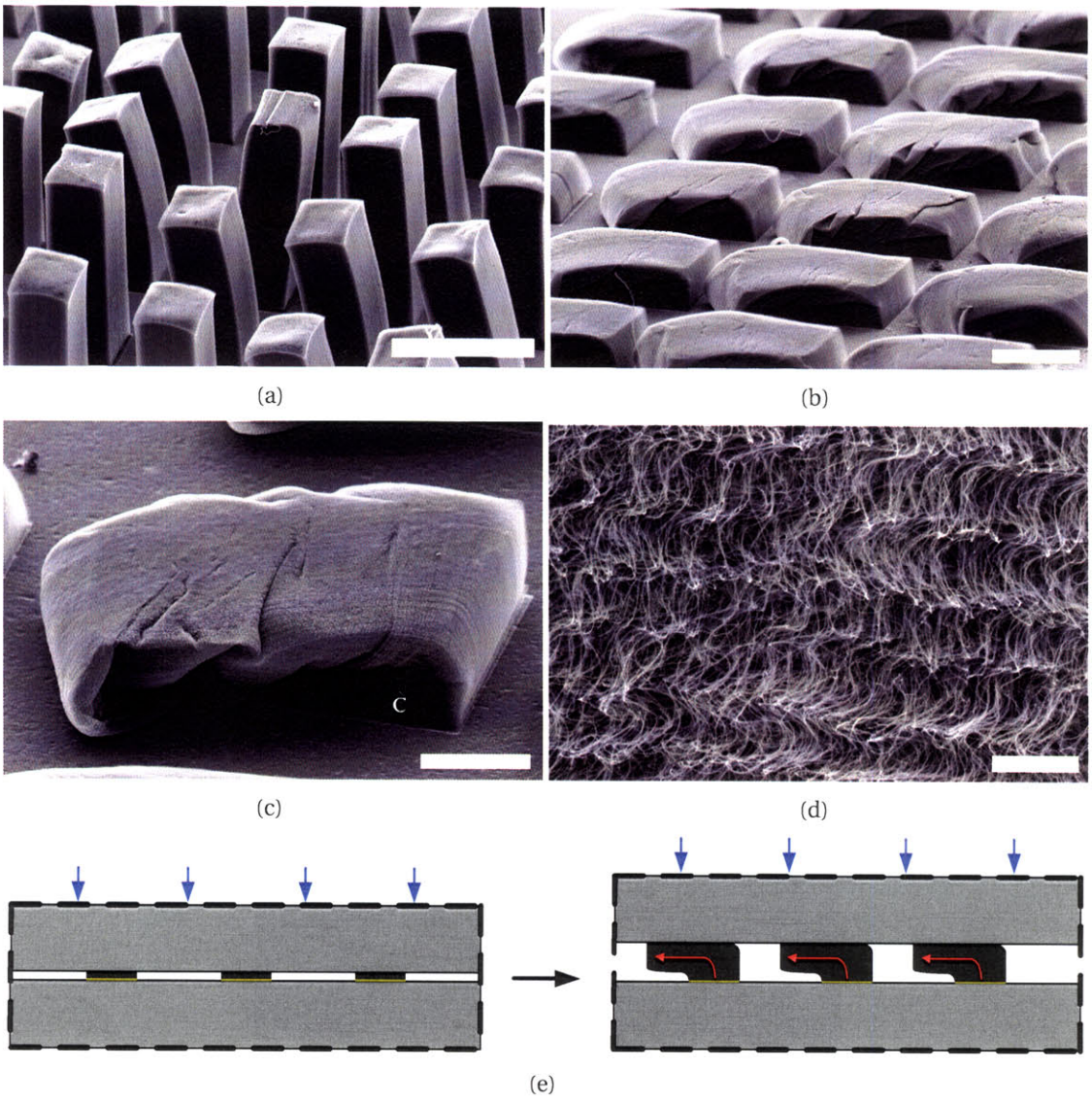

Figure 4-39. (a) CNT pillars grown from lithographically-patterned Fe/Al_2O_3 catalyst ($250\times250\,\mu m$ square patterns), under negligible mechanical pressure of $25\,N/m^2$ (scale $500\,\mu m$); (b) CNT pillars grown under mechanical pressure of $10{,}000\,N/m^2$, where pillars "turn" while growing to reduce mechanical constraint and bend and buckle during growth (scale $200\,\mu m$); (c) single CNT pillar from (b) (scale $100\,\mu m$); (d) collapsed morphology at bottom of pillar grown under $10{,}000\,N/m^2$, in area of (c) indicated by notation 'C' (scale $2\,\mu m$). The pressure is calculated by dividing the applied force (based on the mass of the tungsten weight) by the total area of CNT growth on the patterned sample. Interestingly, the pillars "turn" and grow horizontally under mechanical constraint. This behavior needs further study; however, the horizontal regions of the pillars do not substantially contact the substrate so the mechanical pressure is still calculated based on the area of the catalyst pattern.

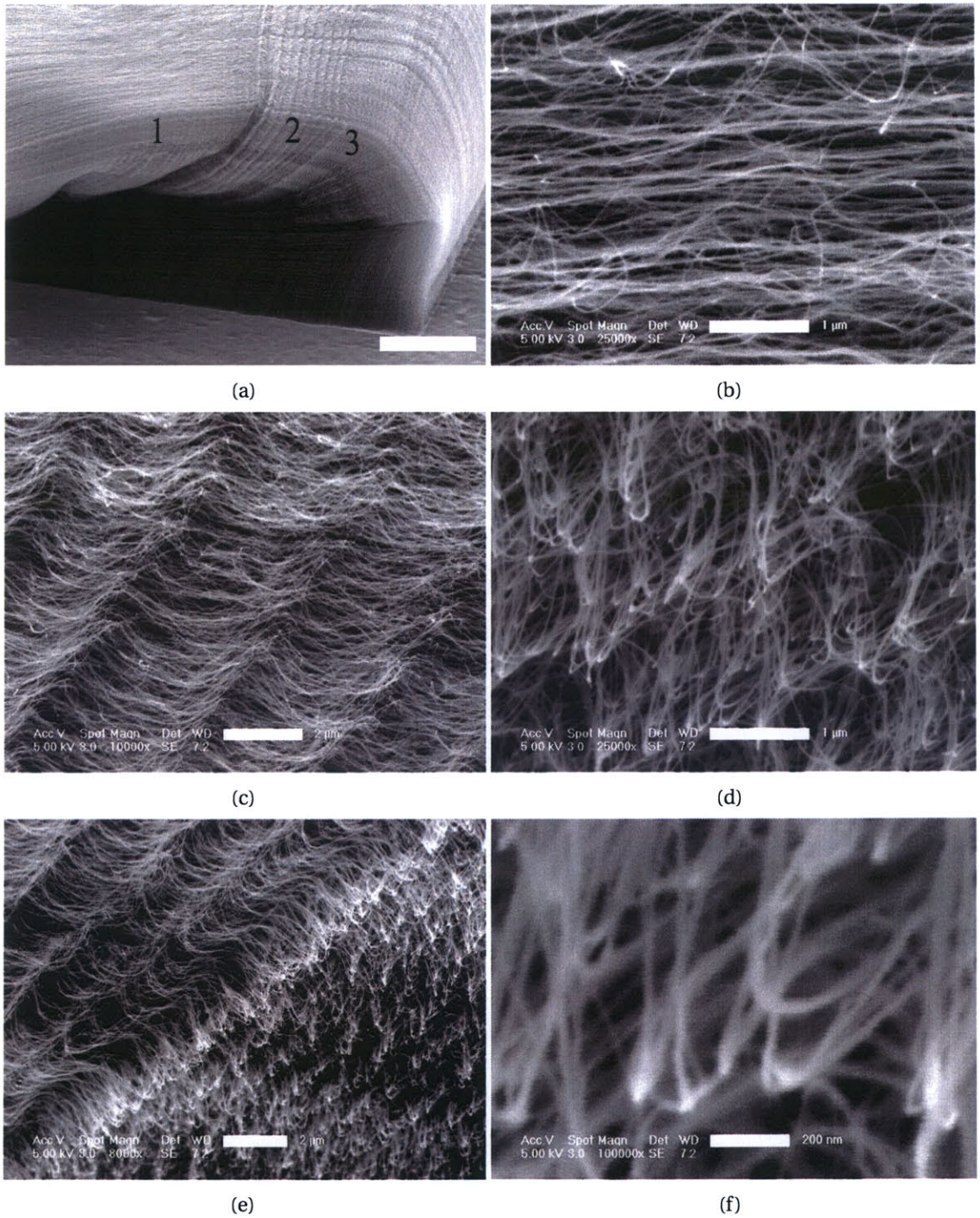

Figure 4-40. (a) Close-up of bend region of CNT pillar grown under 10,000 N/m^2 pressure (scale 40 μm); (b) region 1 (scale 1 μm); (c) region 2 (scale 2 μm); (d) region 3 (scale 1 μm); (e) abrupt transition between regions 2 and 3 (scale 2 μm); (f) close-up of "hairpin" kink bands in region 3 (scale 0.2 μm).

When a CNT film lifts a weight, the force exerted per CNT (F_{CNT}) is:

$$F = \frac{mg}{N_{CNT} A_G} \tag{4.2}$$

where m is the mass of the tungsten weight, g is the gravitational constant, N_{CNT} is the number of CNTs per unit area of vertically-aligned film (1.5×10^{10} CNTs/cm^2), and A_G is the area of vertically-aligned growth on the substrate. The value of F is computed for each experiment in the data set (Fig. 4-36), and averaged to give a representative value of 0.16 nN per CNT for our process. This is equivalent to a mechanical energy of 0.16 nJ per meter of CNT growth, or 1.5×10^{-4} eV/atom.

Table 4.6 compares the average mechanical energy exerted to estimated energies of processes involved in CNT formation. The total surface energy of the graphite layers on the inner and outer walls of a CNT, which are created when the CNT evolves from the catalyst particle, is

$$U_{surface} = \sigma_g \pi L (d_o + d_i), \tag{4.3}$$

where d_o is the outer diameter of the CNT, d_i is the inner diameter, and σ_g is the surface energy of graphite. A linear fit to Abrahamson's values [372] for the surface energy of graphite basal planes gives

$$\sigma_{g,s} = -5.85 \times 10^{-5} T + 0.15 \text{ J/m}^2, \tag{4.4}$$

which equals 0.089 J/m^2 at our growth temperature of 750 °C.

The strain energy required to bend a stack of graphene sheets into the cylindrical shape of a CNT is [43]

$$U_{strain} = \frac{\pi E_g \delta_g^2 L}{12} \ln \frac{d_o}{d_i}, \tag{4.5}$$

where $E_g = 1\times10^{10}$ N/m^2 is assumed for the Young's Modulus of graphite, and $\delta_g = 3.4\times10^{-10}$ m is the interlayer spacing between layers. While the catalytic growth process does not necessarily exert this energy because a CNT does not form by bending graphite into a cylinder, this quantity gives a measure of the mechanical energy which would be released if a CNT were cut along its length after growth, and therefore is the mechanical energy potential in a CNT. The activation energy for our growth reaction is 1.4 eV/atom, as estimated by an Arrhenius method (section 4.2.1.1) from the dependence of growth rate on temperature.

The mechanical energy exerted by growth is one-to-four orders of magnitude less than the other estimated energies, further suggesting that the observed change in film microstructure at relatively high applied pressures is governed by a finer effect of force on the production of defects as observed by TEM imaging. We believe the well-ordered serpentine arrangement in the films grown under pressure is influenced by lateral constraint introduced by neighboring CNTs. This space also gives the CNTs room to "wiggle" near the catalyst, allowing the direction of growth to change in concert with production of structural faults. The serpentine morphology is similar to previously observed multi-mode buckling of high-aspect-ratio micromachined beams [373] and laterally-constrained plates [374]. Further, post-growth foam-like compressibility of VA-MWNT films grown from a liquid hydrocarbon feedstock has been attributed to coordinated multi-mode buckling of the CNTs, where the CNT film collapses into a reversible serpentine-like arrangement upon application of a compressive load [375]. We observe sig-

Number of carbon atoms in a single CNT (9 nm OD, 5 walls)	6.55×10^{12}	atoms/m
Bulk density of graphite	2.2	g/cm^3
Mass of a single CNT	8.58×10^{-14}	kg/m
Measured mass density of VA-CNT array	8.1	kg/m^3
Areal number density of VA-CNT array	1.5×10^{10}	CNT/cm^2
Average CNT-CNT spacing on substrate	73	nm
Measured activation energy for our growth process	1.40	eV/atom
	2.24×10^{-19}	J/atom
Equivalent activation energy for growing a CNT	1.47×10^{-6}	J/m
Free surface energy of a single CNT at 1023 K	4.08×10^{-9}	J/m
	3.9×10^{-3}	eV/atom
Elastic strain energy of a single CNT	1.44×10^{-8}	J/m
	1.4×10^{-2}	eV/atom
Average total energy output by lifting, 1×1 cm VA-CNT array	2.4	J/m
Lifting output per CNT	1.6×10^{-10}	J/m
	1.5×10^{-4}	eV/atom
Force supported by each CNT	1.6×10^{-10}	N
	0.16	nN
Volumetric energy output by lifting (based on volume of grown film)	2.4×10^{4}	J/m^3
Volumetric energy output by lifting (based on volume of a hexagonally-packed VA-CNT film)	2.8×10^{6}	J/m^3
Specific energy output by lifting	3.0×10^{3}	J/kg

Table 4.6. Comparison of estimated energies involved in formation of a single CNT (9 nm OD, 5 walls) to energy output by a CNT film as it lifts a static weight during growth.

nificant irreversible compressibility of our films when compacted following growth, and are studying the post-growth mechanical properties of our CNT films in further detail.

Single-mode buckling of a CNT after growth can be modeled by treating the CNT as an Euler column [376]. Euler's equation for the critical force (F_C) needed for first-order buckling of a column is [377]

$$F_C = \frac{\pi^2 E_g I}{L^2}, \tag{4.6}$$

where $I = \pi(d_o^4 - d_i^4)/64$ is the second moment area of the cross-section. Based on this calculation, the CNT length for a buckling force of 0.40 nN is $\approx 2\,\mu$m (for 9 nm OD, 5 layers), which far exceeds the 300 nm wavelength of the serpentine morphology which is observed after growth under this force (Fig. 4-37d). Alternatively, approximately 10 nN would be required to buckle a CNT over 300 nm. The large discrepancy between the force exerted during growth and the force which may be required to create a similar structure by post-growth deformation suggests that a larger force is needed to deform CNTs after growth than during growth. This hypothesis is qualitatively confirmed by an experiment where we place the catalyst substrate under a weight, yet initially space the substrate from the weight so a uniform and well-aligned film grows be-

fore contacting the template. The resulting film (Fig. 4-41) has a well-aligned upper region and a collapsed lower region, where the wavelength of the pattern in the collapsed region decreases toward the bottom of the film. Mechanical resistance is introduced when top of the film contacts the template, and this resistance is transmitted through the film to the base where the growth sites exert an opposing force, which slows and perhaps eventually terminates growth.

Although CNT film growth is an impractical actuation technique because of its operating temperature, low speed, and irreversibility, the measured energy densities of growth have significant macroscopic equivalence. The volumetric energy density of CNT growth, based on the volume of the as-grown film, is

$$E_{Vf} = \frac{F_l h_f}{V_f} = 2.4 \times 10^4 \text{ J/m}^3, \tag{4.7}$$

where F_l is the force lifted by the film during growth, h_f is the film thickness after growth, and V_f is the film volume (area of VA-CNT growth × film thickness). F_l and h_f are taken as average values of the data in Fig. 2. The value of 2.4×10^4 J/m^3 is comparable to muscle.

The volumetric energy energy density of CNT growth, based on the volume of a film of CNTs which is closely-packed in a vertically-aligned array, is

$$E_{Vp} = E_{Vf} \frac{4}{0.907 \pi N_C d_o^2} = 2.8 \times 10^6 \text{ J/m}^3, \tag{4.8}$$

where N_C is the measured number density of CNTs on the substrate (1.5×10^{14} CNTs/m^2), d_o is the CNT outer diameter (9 nm), and 0.907 is the packing density of cylinders in a hexagonal array. The value of 2.8×10^6 J/m^3 is comparable to hydraulic actuators [378,379].

The energy output per unit mass is

$$E_M = \frac{E_V}{\rho_f} = 3.0 \times 10^3 \text{J/kg}, \tag{4.9}$$

where ρ_f is the measured film density (8.1 kg/m^3).

4.3.2.2 Micro-scale shape transfer: "grow-molding"

We utilize the force output capability of CNT growth to physically template growth of CNT three-dimensional CNT microforms by a "grow-molding" approach. Figs. 4-42 and 4-43 show CNT structures which are grown to replicate an etched silicon template which is held against the catalyst-coated substrate during CNT growth. The $C_2H_4/H_2/Ar$ mixture diffuses into the cavities between the template and the growth substrate. The template is cleanly removed (Fig. 4-44) following growth, leaving the free-standing structures on the growth substrate, and the template can then be reused. This technique surpasses traditional methods for growing CNT microstructures using two-dimensional catalyst patterns on substrates [143, 144, 205, 269], as it enables fabrication of arbitrary shapes having sloped and/or curved surfaces and non-orthogonal corners, and does not require patterning of the catalyst.

In our initial experiments, concave corners of the microform (convex corners of the template) are sharper than convex corners, yet are rounded to 5–10 μm (Fig. 4-42d). The finest repli-

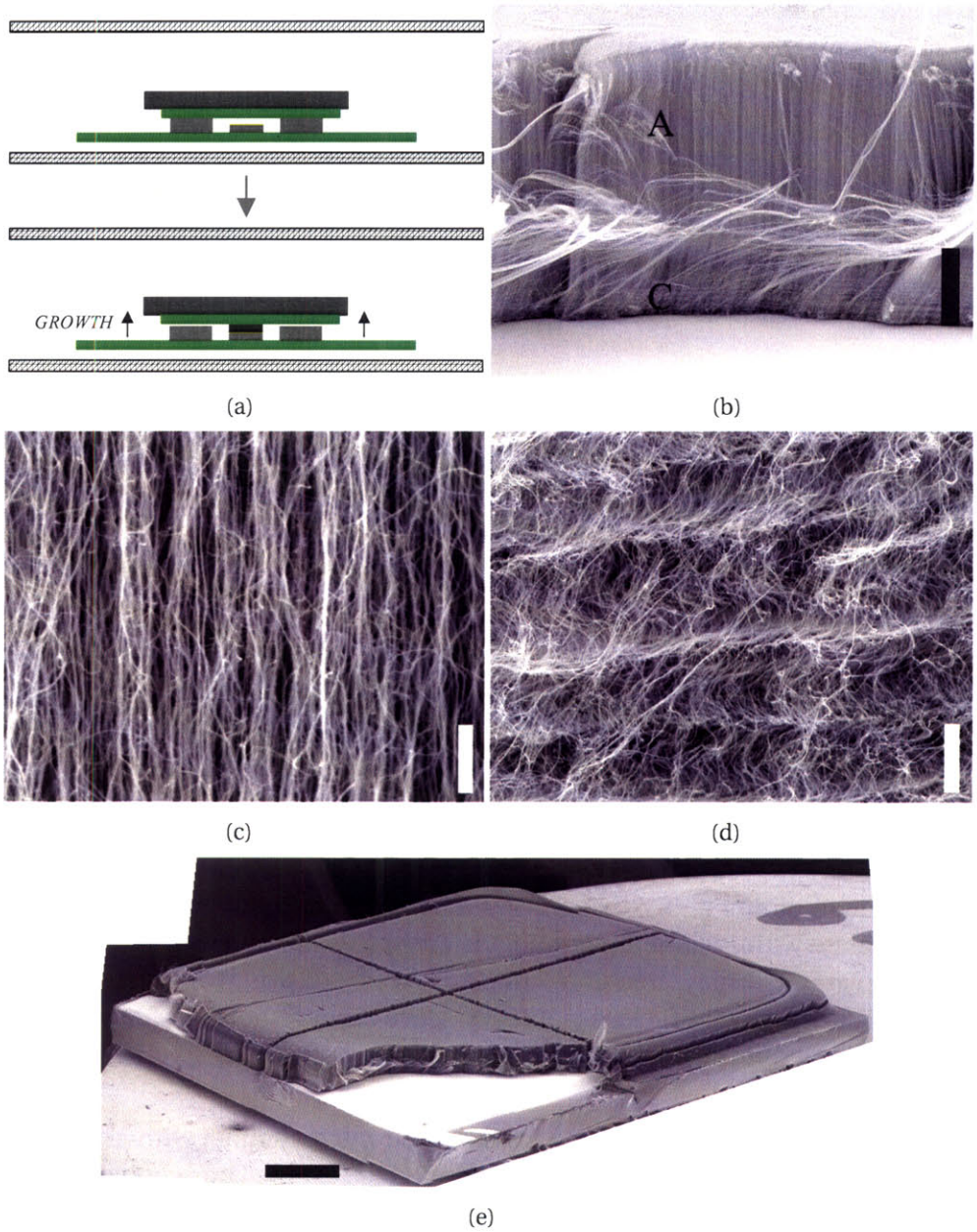

Figure 4-41. (a) "Weighted-shield" growth configuration, where film is grown under a flat template, but is initially spaced 300 μm above the template so unconstrained growth precedes constrained growth; (b) Interior wall section of film, showing aligned upper region (A) and collapsed lower region (C) (scale 100 μm); (c) Close view of aligned region (scale 1 μm); (d) Close view near top of collapsed region, and wavelength of pattern decreases toward bottom of film (scale 3 μm); (e) Full view (digitally stitched from 12 frames) of CNT film (corner section removed using tweezers), showing substantially uniform top surface due to mechanical constraint (scale 1 mm). The cross-pattern on the film is the result of scribing the substrate prior to growth. The crack around the periphery of the film developed as the film attempted to grow around the edge of the cap, as the cap did not fully cover the film.

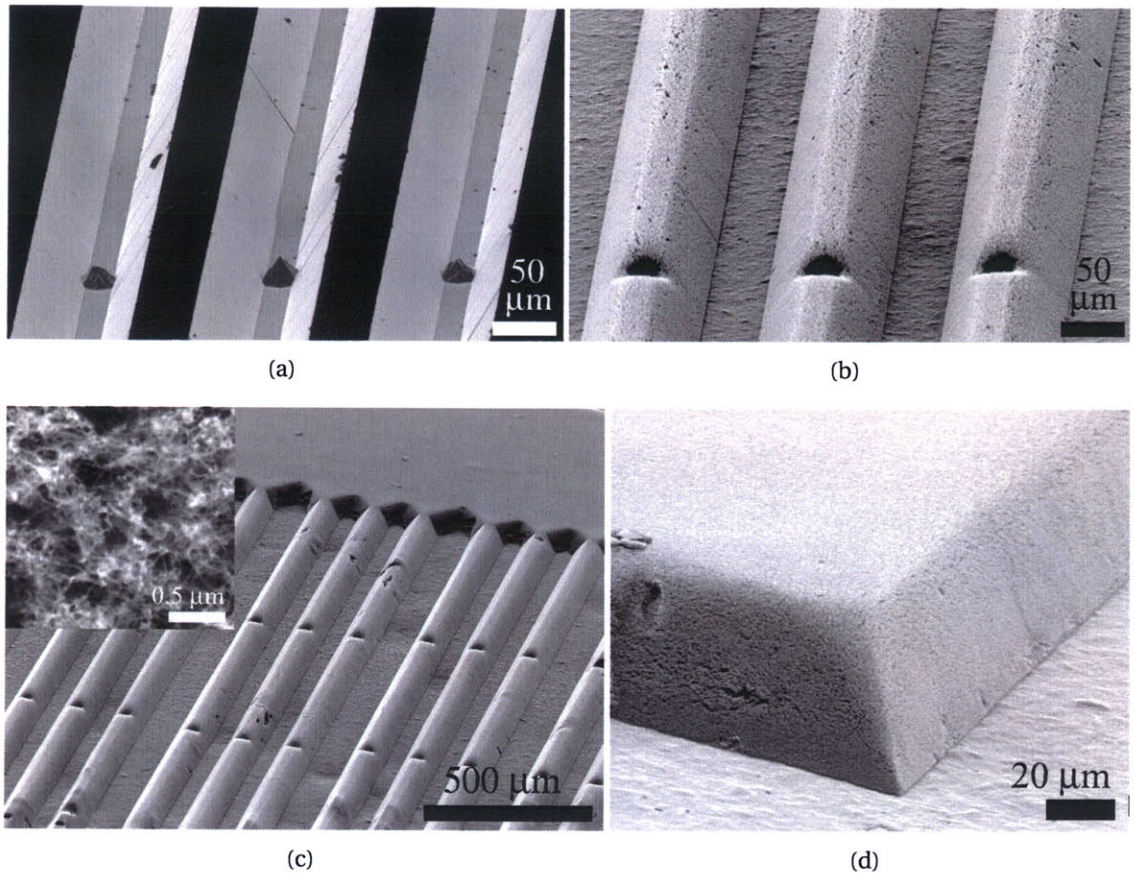

Figure 4-42. Grow-molding of 3D-shaped CNT microforms: (a) KOH-etched trapezoidal microchannel template with included pyramidal islands; (b) CNT microforms grown to fill and conform to template; (c) broad area of microforms (scale 500 μm), with inset showing typical outer surface of a microform; (d) close view of concave corner, showing sharply angled transition at interface of microform and substrate, and rounding of corner.

cation we have attempted is a 5 μm wide KOH-etched microchannel with a triangular cross-sections, and the apex of such a microform is rounded to $\approx$2 μm. The accuracy and resolution of shape replication depend on the areal density of CNTs growing from the substrate, and on the gas flow through the template. With appropriate and uniform gas flow, such as by using a porous template, these structures could be fabricated over large substrate areas. Further, application of an electric field between the growth substrate and template may be helpful to draw the CNTs into especially narrow template features and sharp corners, achieving shape transfer at a significantly higher resolution than demonstrated by our initial results.

Sectioning a CNT microform reveals how its structure evolves under mechanical constraint during growth, as shown in Fig. 4-45. Initially, a well-aligned CNT film grows upward into the cavity between the substrate and template. When a portion of the film reaches the template surface, compressive forces are transmitted to the bases of these CNTs. Because the film cannot freely move upward, CNTs begin to "bunch up" with additional growth at the base of the structure. In this example, the slanted sidewalls "pin" growth from the outer edges of the cross-

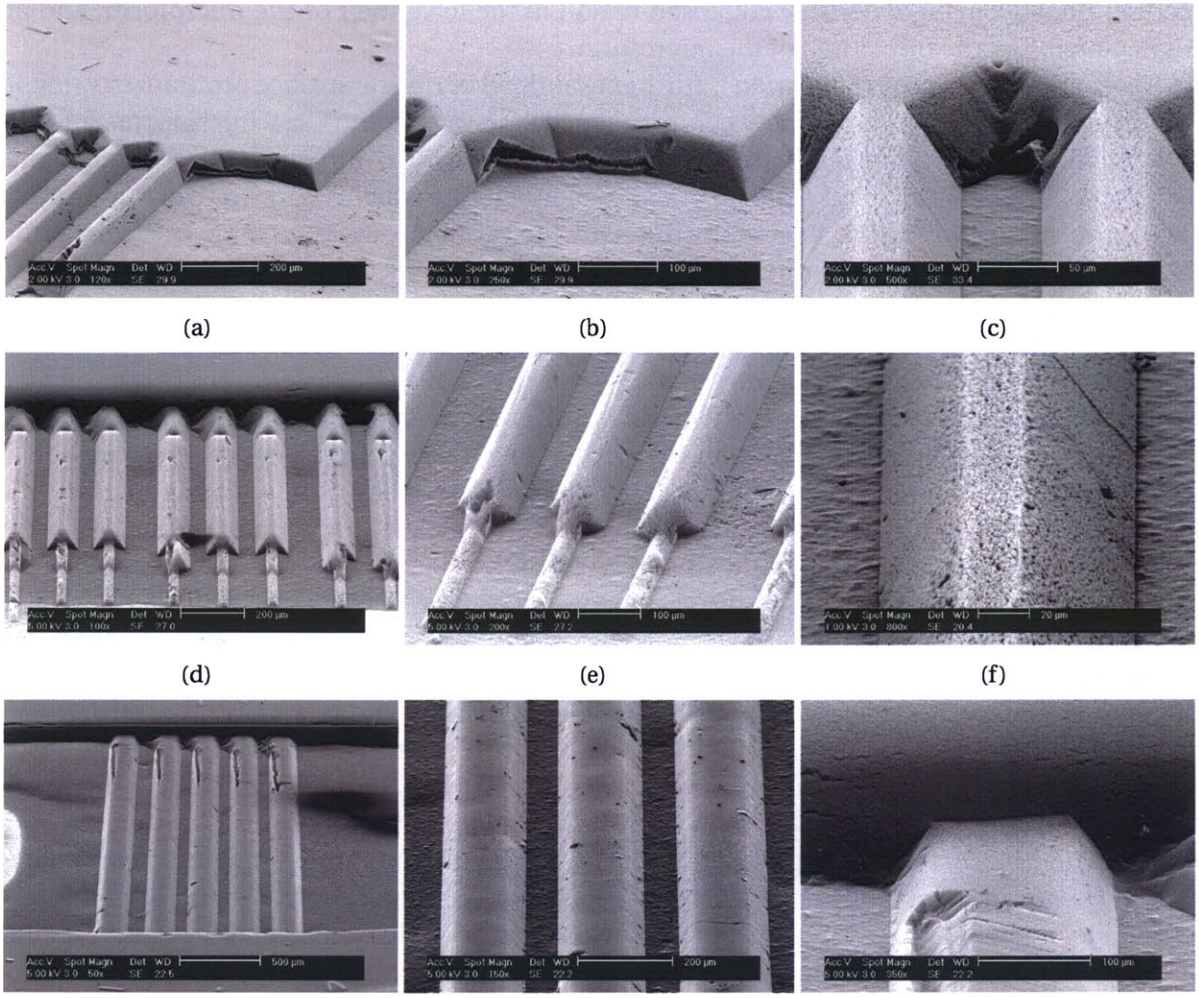

Figure 4-43. Additional CNT microforms, grown to replicate KOH-etched silicon template (of microchannel device presented in Chapter 4).

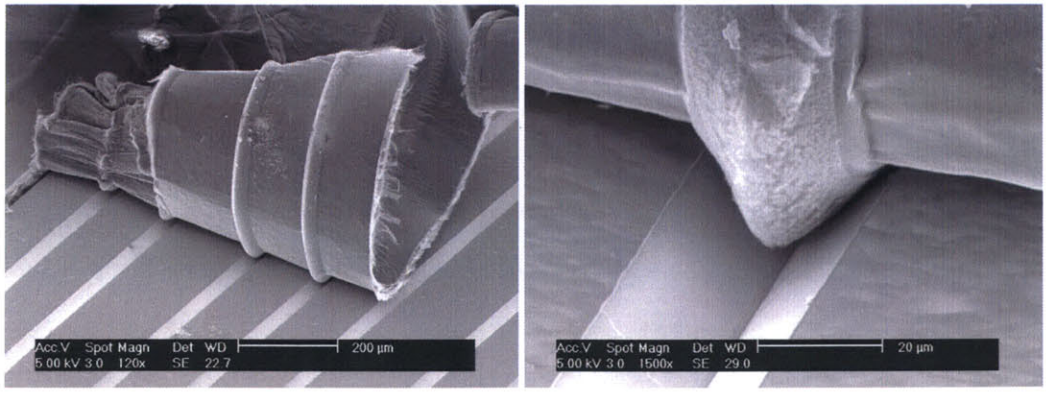

Figure 4-44. Delamination of CNT film and microform from triangular-channel template.

section, finally leaving a densely collapsed region in the lower half of the microform, and an aligned region in the upper half of the microform.

The accuracy of shape replication is further examined by optical surface profilometry (Fig. 4-46), revealing a smooth match between the sloped sidewalls of the CNT microforms and the KOH-etched microchannel template. However, the CNTs do not completely "fill" the microchannel shape. A higher growth rate and/or density, and therefore a higher growth "pressure" would give better shape replication, as demonstrated by the variability among various growth conditions (e.g. gas composition, temperature). The CNTs are not reflective to visible light; however, we expect the locally random surface of the CNT microform scatters enough light to construct a surface. Conversely, the sloped sidewalls of a fully specular surface (e.g. Si) could not be imaged if by this technique. In our measurements, the reflectivity of a CNT microform surface coated with 0.1 μm Au-Pd is only slightly higher than an an as-grown CNT microform surface.

Processing a sample with a templated cap in the weighted-shield configuration gives similar results to the flat film (Fig. 4-41); the VA-CNT film grows normally until reaching the cap, and then lifts the cap. Only slight imprints in the top surface of the film are observed (Fig. 4-48). Therefore, the "surface tension" of the film must be broken in order to create topography in the film, and that it is more difficult to break this tension as growth proceeds because the growth sites remain at the base of the film. Here again, further work on controlling the applied mechanical pressure as well as the growth pressure (CNT density and growth rate) could enable shape-engineered CNT microstructures having hierarchical geometry and internal structure.

Overall, this work demonstrates that CNT growth can exert a considerable extrusive force, which can be balanced by pressure exerted by an external template or by mechanical constraint from neighboring CNTs within the film. A CNT film can lift tens of thousands of times its own weight as it grows, evoking thoughts of fire ants which can lift "only" fifty times their own weight. This may warrant new applications for CNTs in microelectromechanical systems which take advantage of single-stroke force output and actuation capability, such as for initiating folding of microstructures [380], for embedding CNT layers as constrained energy dissipators [381], or for reducing thermal or electrical contact resistance by direct growth or physical templating of conformal CNT film structures at interfaces between components. Going forward, studying the force output of CNT growth as it depends on the growth conditions and density of CNTs in a film may give a more complete understanding of the reaction energetics, particularly of how compressive or tensile forces affect the production of defects in CNT structures during growth from catalytic particles by CVD.

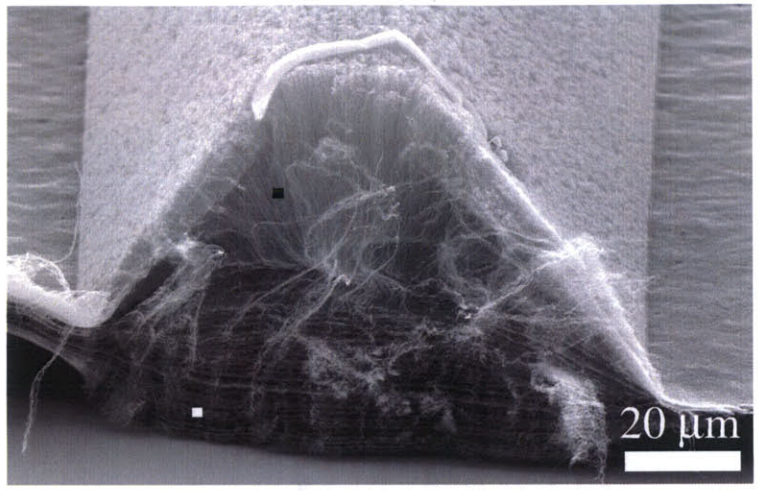

(a)

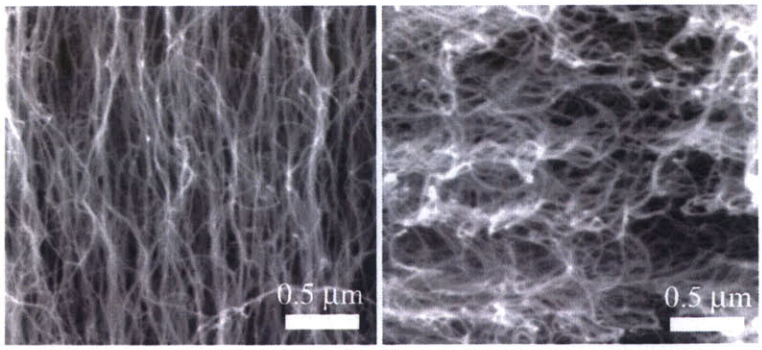

(b) (c)

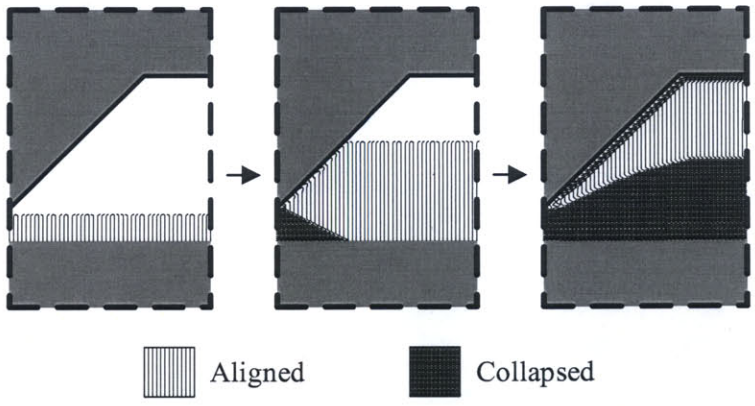

(d)

Figure 4-45. Internal structure of trapezoidal-channel CNT microform, revealed by sectioning using a razor blade: (a) full view, showing crowding of CNTs at bottom, which is induced by continued base-growth after CNTs initially fill the form; (b) close view of aligned region near top of cross-section (at black square in (a)); (c) close view of collapsed region near bottom of cross-section (at white square in (a)); (d) simplified illustration of how the internal structure of a microform evolves under mechanical constraint during the growth process.

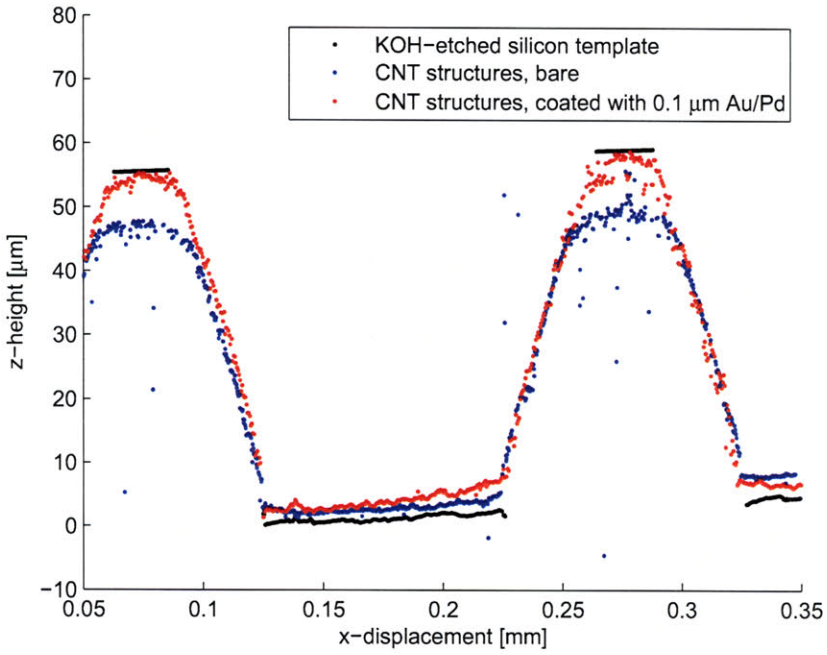

Figure 4-46. Optical surface profiles of CNT microforms (Zygo NewView 6300, taken with assistance of A. McClung of Zygo Corporation), comparing silicon template to bare (as-grown) and metal-coated microforms. Metal coating improved reflectivity of the surfaces, reducing background noise and enabling imaging with a lower magnification objective. The difference in profiles is representative of variations in process fidelity; in this case the coated sample exhibits better replication. In both cases, the replication of the sidewall surfaces is very good. The profilometer cannot image the sidewalls of the silicon mold, yet the profile can be interpolated by connecting adjacent horizontal surfaces at bottom and top elevations. The data was manually shifted and zeroed to make the profiles overlap.

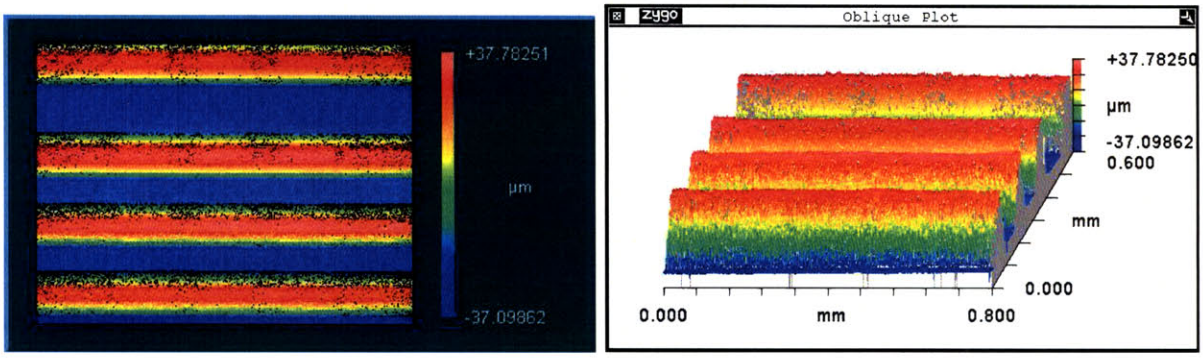

(a) (b)

Figure 4-47. Three-dimensional optical surface profile of metal-coated CNT microforms. The corresponding slice profile is shown in Fig. 4-46

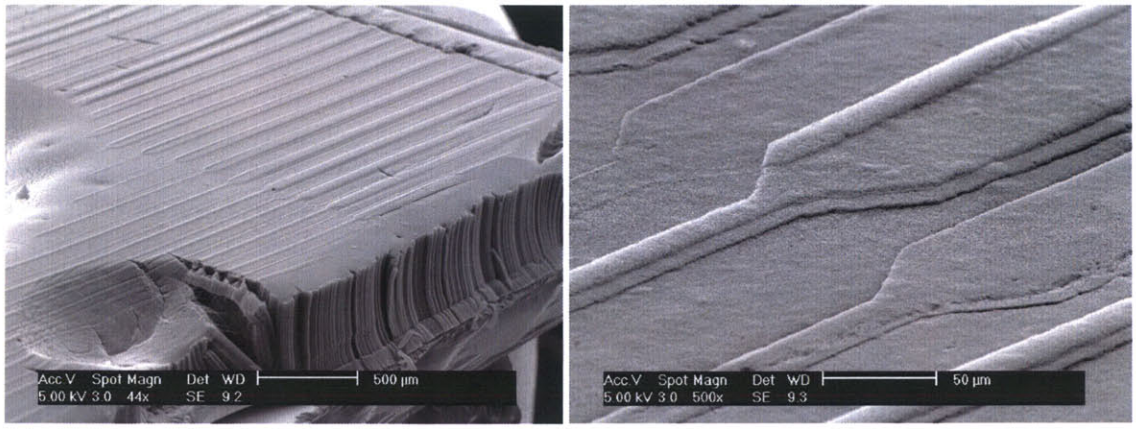

(a) (b)

Figure 4-48. "Imprinting" of film grown in weighted-shield configuration, into templated shield. In (b), we see that the template translated as it was lifted by the growing film.

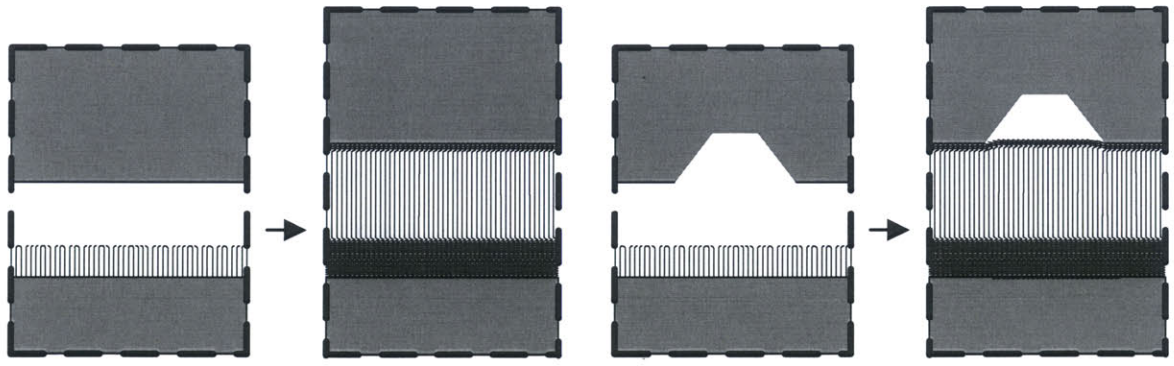

(a) (b)

Figure 4-49. Schematic of growth evolution in weighted-shield configuration: (a) flat shield, representative of experiment in Fig. 4-41; (b) template shield, representative of experiment in Fig. 4-48.

4.4 Chemical delamination of VA-CNT films

While the VA-MWNT films produced by CVD of $C_2H_4/H_2/Ar$ are easily removed from the substrate using a razor blade, this mechanical process is difficult to control by hand and often leads to bending, bunching, and/or tearing of the film. To this end, an alternative process is demonstrated where the film is chemically delaminated from the substrate using a HF/DI-H_2O solution (Fig. 4-50). Because the CNT film is hydrophobic[3], it remains above the solution surface when placed in the etch solution, while the substrate rests just below the surface. The etchant penetrates the base of the film, and over several minutes the film is cleanly delaminated from the substrate, leaving a free-standing film floating on the surface. The CNT film is simply removed from the surface of the bath by lifting it out with tweezers or (more robustly) by bringing a clean (hydrophobic) silicon substrate under the film and lifting it away.

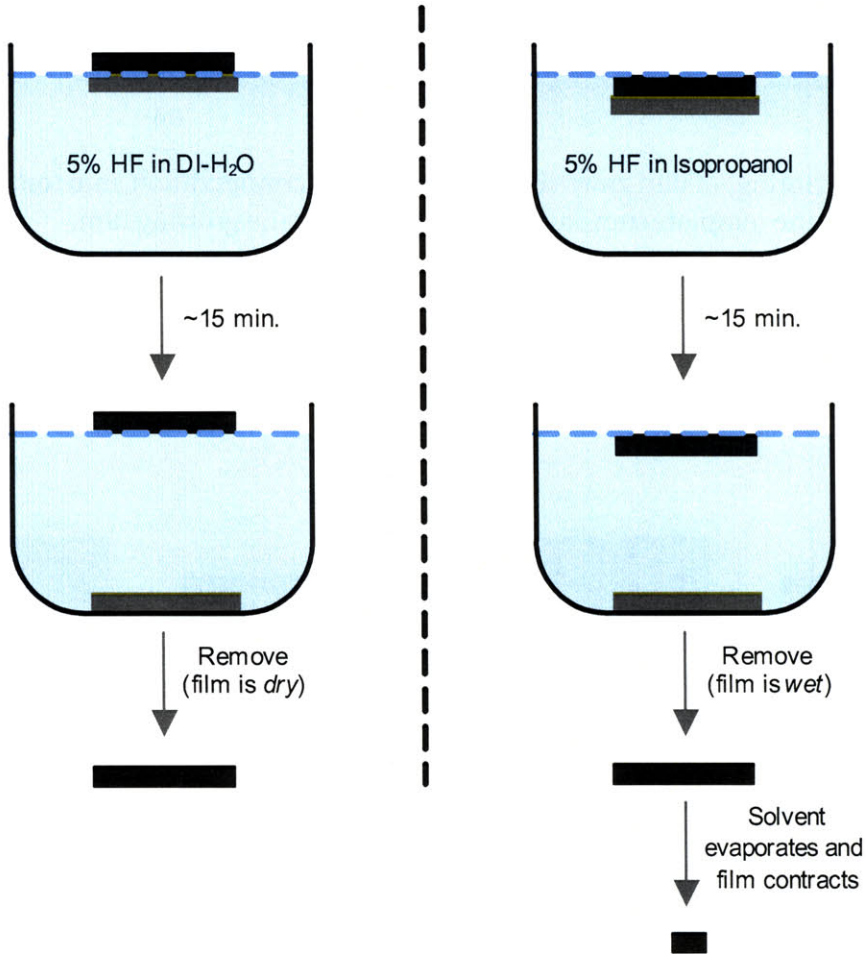

Figure 4-50. Process schematic for chemically-induced delamination of VA-MWNT films from silicon substrates.

[3]Hydrophobicity is typically observed for VA-CNT films [382], which is a combination of the surface condition of the CNTs and the configuration of the CNTs. Coating of CNT films to produce "superhydrophobic" surfaces having persistently strong non-wetting behavior has been demonstrated [303].

Conversely, if the etchant solution wets the CNT film (e.g., HF/2-propanol), both the CNT film and the substrate are initially submerged and floating just beneath the surface of the bath. The CNT film separates from the substrate and remains just below the surface, while the substrate sinks. The film is wet when removed from this solution, and subsequent drying causes extreme capillary-induced contraction of the film. For example, a $\approx 10 \times 10$ mm film shrinks to only a few mm^2 upon capillary-induced densification.

There has been much simultaneous work on removal of VA-CNT films from substrates. A solution of 1% HF in DI-H_2O, is used to remove a VA-SWNT films from SiO_2/Si [203], in a fashion otherwise identical to our process. Further, a VA-SWNT film grown on SiO_2 is delaminated by vertically submerging the substrate into pure DI-H_2O at 60 °C [383]. Here, a thermocapillary effect caused by the temperature difference between the CNT substrate and the H_2O drives the liquid along the substrate surface and splits the CNT film from the substrate as the substrate is submerged.

4.5 Growth of aligned CNT coatings on ceramic fibers: toward three-dimensionally reinforced CNT-fiber composites

Fiber composites are a ubiquitous materials technology, and multiscale architectures comprising CNTs within fiber/polymer composites are sought widely for reinforcement of composites and development of multifunctional properties [28, 29, 384, 385] such as thermal conductivity, electrical conductivity, and energy dissipation [386], in addition to stiffness and strength. Generally, properties of CNT composites benefit from increased surface area of CNT-polymer interaction [387]; therefore, uniform dispersion and adhesion of polymer among small-diameter CNTs will provide best results.

Utilizing process knowledge from growth of VA-MWNT films on Fe/Al_2O_3/Si, and the qualitative study of Fe-support effects in nucleation of aligned CNTs using $Fe(NO_3)_3 \cdot 9H_2O$, aligned CNTs were grown on commercially-available Al_2O_3 fibers. This was initially sought simply as a qualitative demonstration of the versatility of the CVD process comprising Al_2O_3-supported Fe in C_2H_4/H_2/Ar [358].

In our process, strands are cut from a commercially-available Al_2O_3 fiber cloth (McMaster-Carr, #1687T21), soaked for 5 minutes in a solution of $Fe(NO_3)_3 \cdot 9H_2O$ dissolved (by stirring and sonication) in 2-propanol, and allowed to dry overnight in ambient air. Each strand or "tow" consists of several hundred fibers each approximately 20 μm in diameter (Fig. 4-51). Two CVD processes are compared: "slow heating" and "rapid heating". In slow heating CVD, the process is identical to that for VA-CNT film growth on silicon substrates coated with Fe/Al_2O_3 (section 4.1.1: the temperature is ramped under flowing Ar for 15–30 minutes, then the temperature is stabilized for 15 minutes, and then growth is commenced with 100/500/200 sccm C_2H_4/H_2/Ar. Introducing H_2 2–5 minutes before C_2H_4 (and commensurately reducing the stabilization time) gives strong nucleation of CNTs on the fiber surfaces; however, a more systematic study of H_2 pre-conditioning has not been conducted for CNT growth on Al_2O_3 fibers. In rapid heating CVD, an extra-long furnace tube is used so the catalyst-coated fibers can remain in the sealed tube but just outside the furnace enclosure until the furnace is ready. The tube is rapidly translated so the fibers are introduced into the center of the furnace, followed by 2 minutes of

treatment in Ar, and then the normal growth sequence with H_2 pre-conditioning.

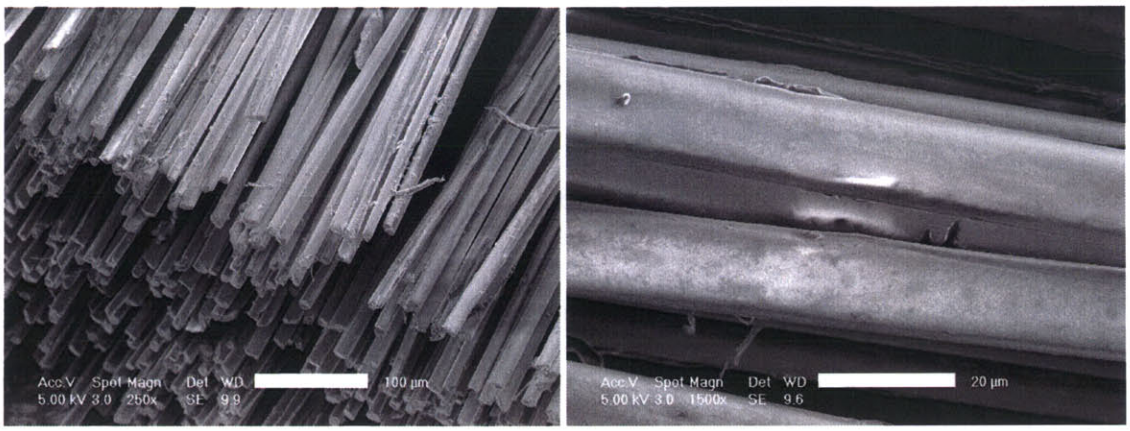

(a) (b)

Figure 4-51. Al_2O_3 fibers loaded with Fe by soaking in 10 mM $Fe(NO_3)_3$-IPA for 5 minutes: (a) end of fiber "tow", containing hundreds of fibers (scale 100 μm); individual fibers aligned in the tow, each approximately 20 μm diameter (scale 20 μm).

Aligned CNT coatings are grown on the surfaces of the fibers within the tows (Fig. 4-52); CNTs typically bunch into two or more aligned groups at equidistant "poles" of the fiber surface (Figs. 4-53 and 4-54). Growth spreads the tows open, creating space for the CNTs among adjacent fibers. The CNT coverage is much higher at the ends of the fiber tows, presumably because there is more catalyst at the ends due to capillarity-driven accumulation when the salt solution dries on the fibers. The CNT coverage increases along with the concentration of the precursor salt solution, and is promoted by rapid heating CVD.

Initial mechanical property tests by Enrique Garcia show that CNT growth on the Al_2O_3 fibers does not damag'e the mechanical integrity of the fibers, and that conventional room-temperature and photo-curable (e.g. SU-8) epoxies strongly and uniformly penetrate the CNT forests [388–390]. We have also grown CNT forests on ceramic fiber hose ($Al_2O_3/SiO_2/B_2O_3$ fibers; McMaster-Carr, #876575K4), as shown in Fig. 4-56. Compared to a cut strip of cloth which has loose edges, the hose is a useful geometry for preparing composite specimens as it can simply be "squashed" and infiltrated with epoxy to give a two-ply laminate.

Since the experiments presented here were completed, other methods have been presented for growing CNTs on ceramic fibers, such as by placing Al_2O_3 or SiC fibers in a furnace and delivering a solution containing both the catalyst precursor (typically an organometallic molecule such as $Fe(C_5H_5)_2$) and the carbon source, which gives coatings of aligned CNTs on the fiber surfaces [391]. A similar process grows CNTs on short SiC fibers, for use as brushes [341]. Tangled CNTs grow on batches of carbon fibers by sputtering of a stainless steel catalyst and subsequent thermal CVD of C_2H_2 [392], and by plasma-enhanced CVD on fibers coated with a Co colloid catalyst [298]. Further, CNTs are grown on the surfaces of elongated metal substrates by continuous feeding through a furnace, where the substrate is heated resistively by passing a current through the substrate, and the CNTs are removed from the substrate before the substrate exits the furnace [393]. CNTs are grown on a fused-SiO_2 rod by locally heating the substrate using a laser; the laser spot is fixed and the rod moves continuously through a deposition

(a) Before (b) After

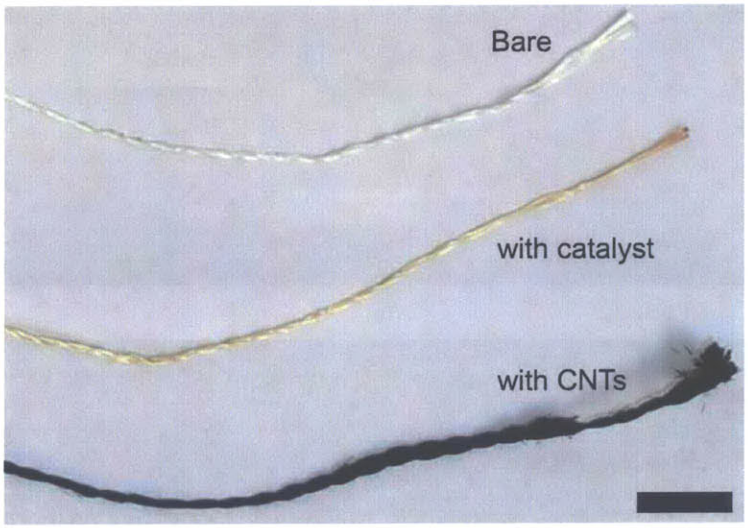

(c)

Figure 4-52. Al_2O_3 fiber tows before and after CVD cycle: (a) and (b) in tube furnace; (c) long strands outside furnace (scale 10 mm).

chamber [394]. However, CNTs resulting from these processes are typically short and sparse, contrasting to the long, dense, and aligned coatings achieved by the process presented here. Other work reinforces Al_2O_3 matrix materials with tangled CNTs [395–397].

A recent report [398] demonstrates enhanced interlaminar strength, damping, thermal conductivity, and electrical conductivity for a laminated fiber/polymer composite prepared using SiC fibers coated with surface-grown aligned MWNTs. This indicates further promise for engineering the CNT-on-fiber technique to achieve high local loadings of CNTs, and for development of growth processes for other (perhaps more commercially relevant, e.g., glass or carbon) fiber substrates. Overall, direct growth of CNTs on composite substrates addresses the primary drawbacks of agglomeration and non-uniform dispersion of CNTs suffered by mixing with matrix materials, which even if overcome are likely limited to realizing composites with low weight loadings of reinforcement, rather than locally high weight loadings as enabled by direct growth on fibers. Scalable manufacturing technologies could continuously produce aligned CNTs on fibers or CNT-reinforced fiber layers, and this is a major topic of our ongoing collaborative ef-

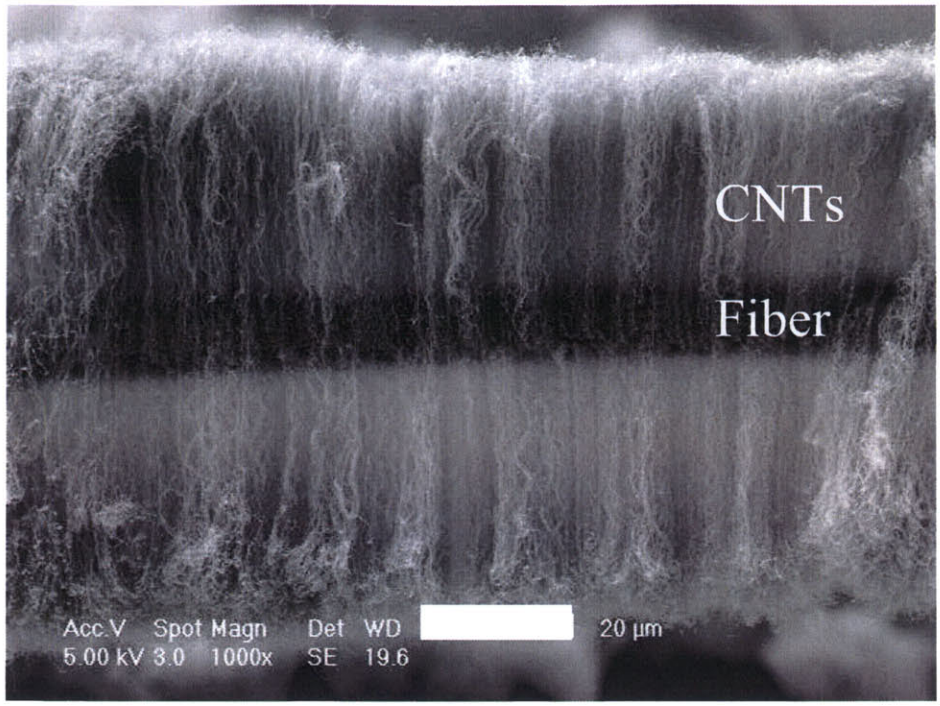

(a)

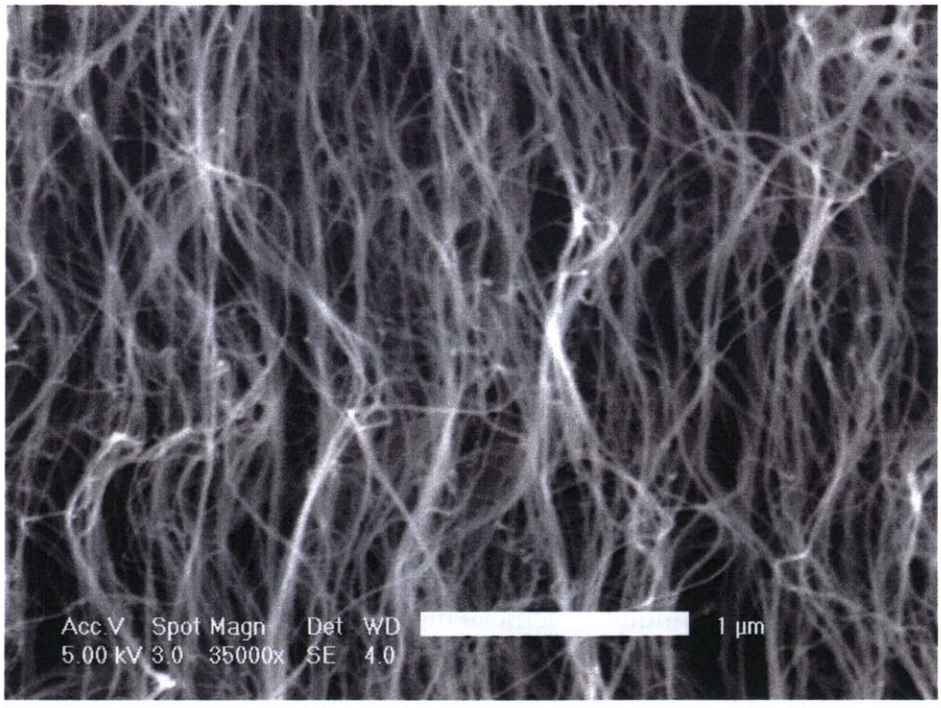

(b)

Figure 4-53. (a) CNT-coated Al_2O_3 fiber (10 mM solution) after slow heating CVD process with 15 minutes growth and 100/500/200 sccm $C_2H_4/H_2/Ar$ (scale 20 μm); (b) alignment within CNT coating (10 mM solution, rapid heating CVD; scale 1 μm)

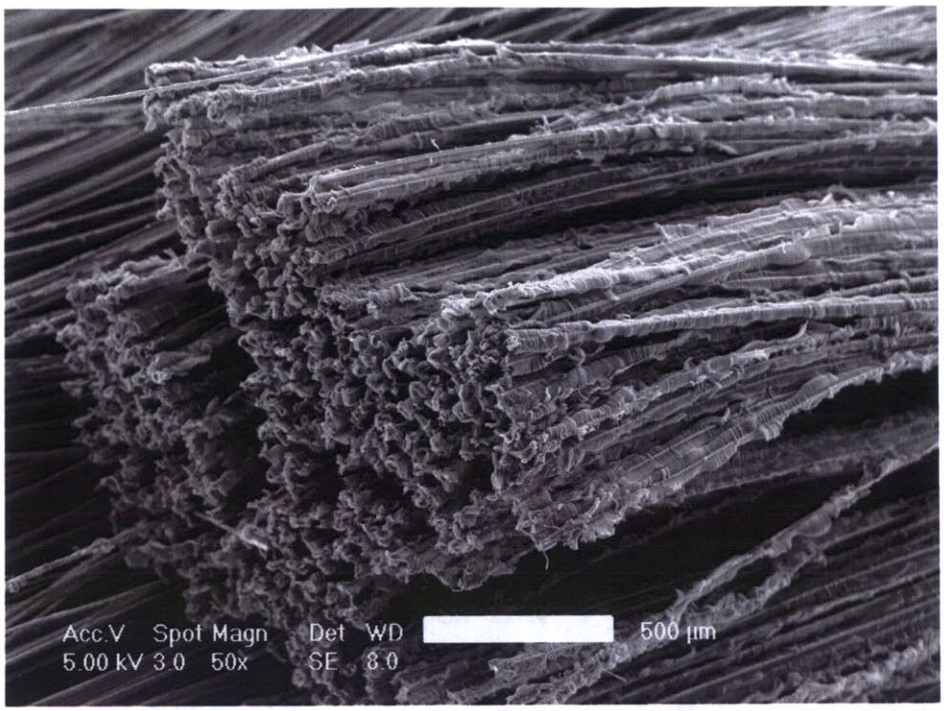

(a)

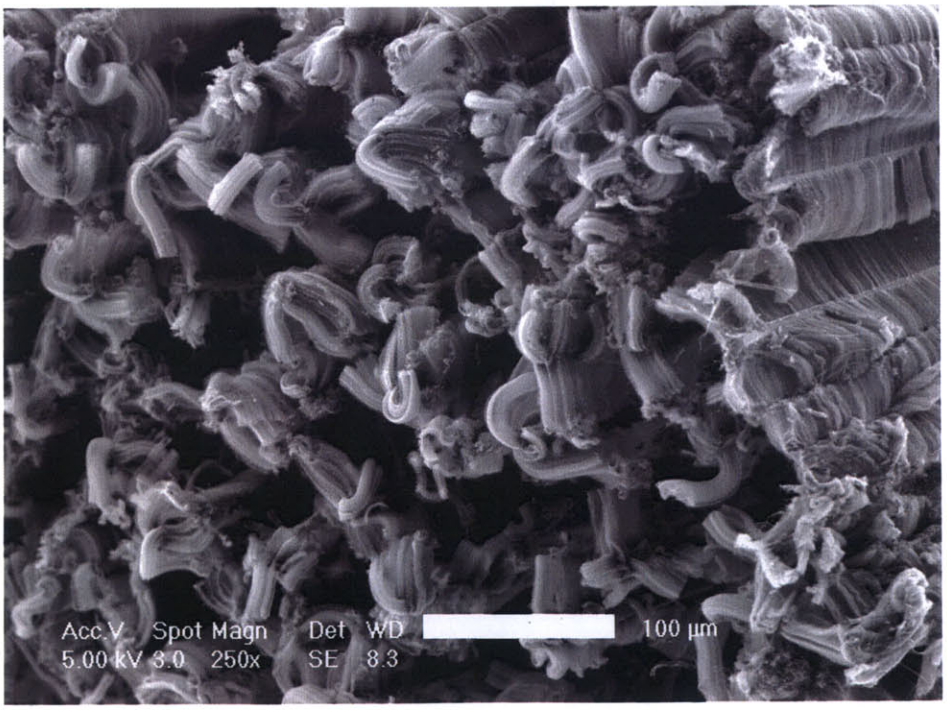

(b)

Figure 4-54. Tows of Al_2O_3 fibers with CNTs growth perpendicular to their surface, often bunched in diametrally-opposed locations (10 mM solution, slow heating CVD). Scale in (a) 500 μm; scale in (b) 100 μm.

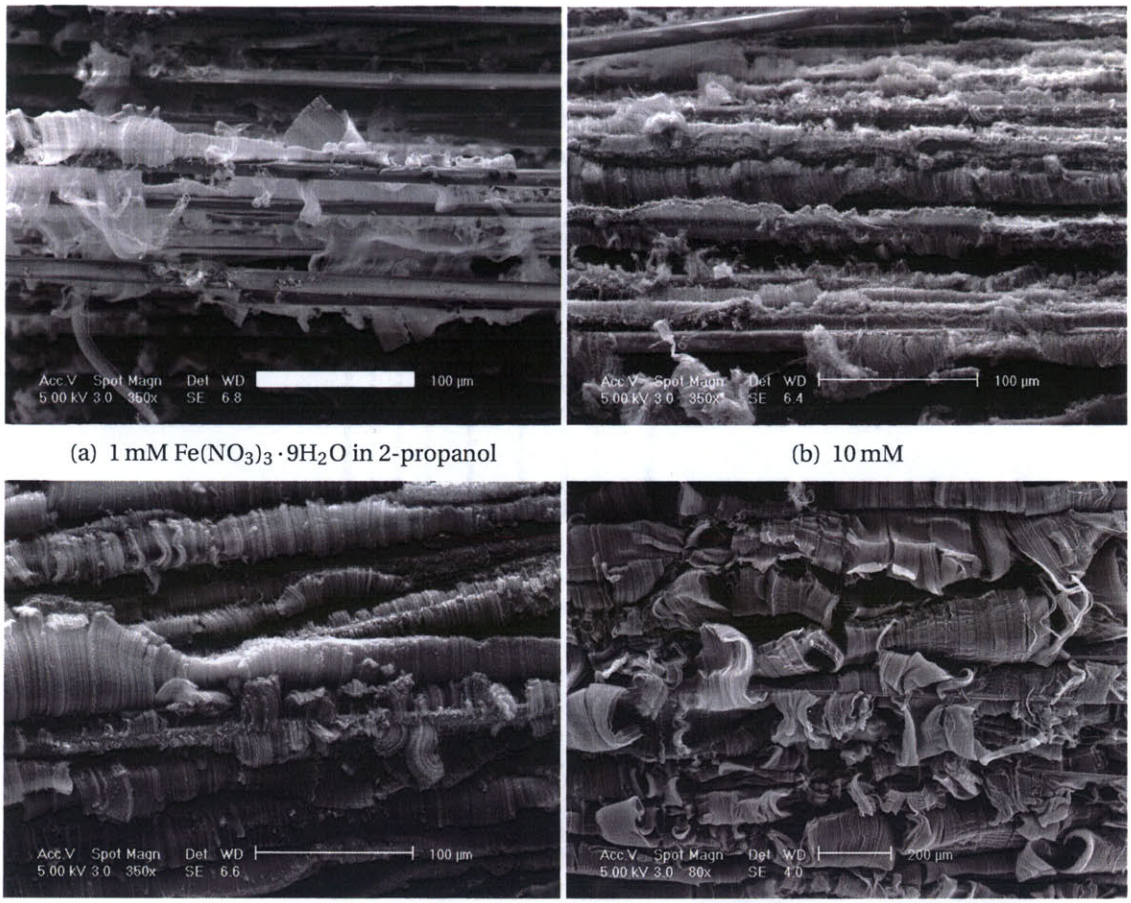

(a) 1 mM $Fe(NO_3)_3 \cdot 9H_2O$ in 2-propanol (b) 10 mM

(c) 100 mM (d) 100 mM, rapid heating

Figure 4-55. Increase in coverage of aligned CNTs on Al_2O_3 fibers soaked in high-concentration solution, and processed by rapid heating with 15 min. growth and 100/500/200 sccm $C_2H_4/H_2/Ar$. Scales 100 μm.

forts [399].

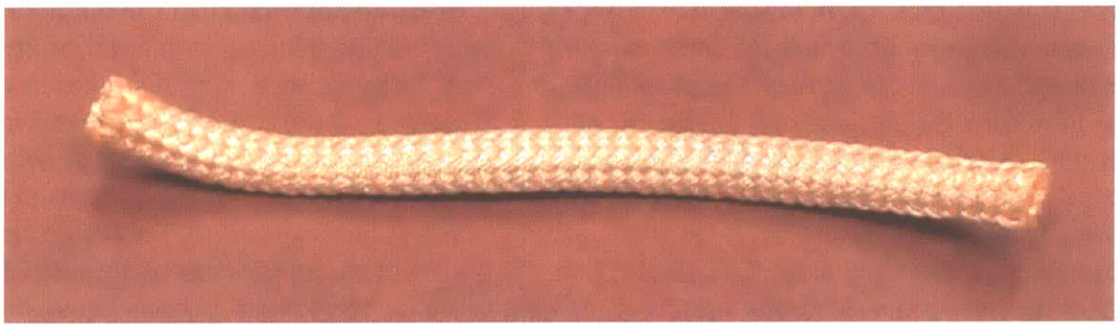

(a)

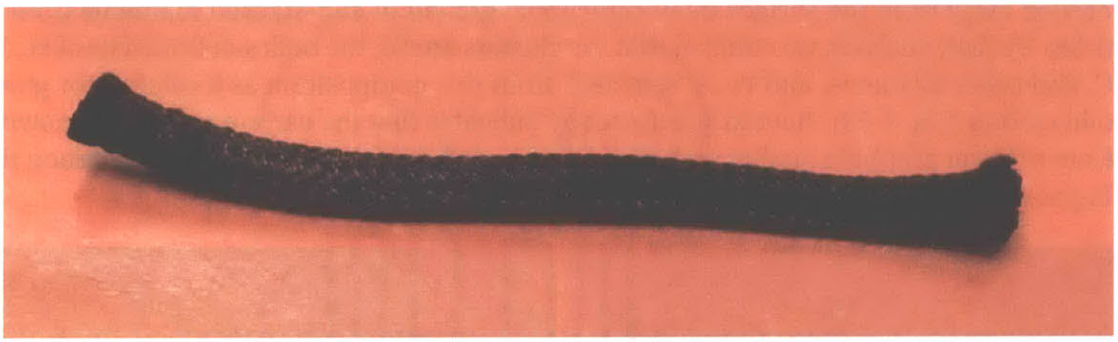

(b)

Figure 4-56. Ceramic hose (f) before and (b) after CVD cycle, which coats the fibers with aligned CNTs (10 mM solution, slow heating CVD).

4.6 Growth of carbon nanostructures on bulk metal surfaces

The $C_2H_4/H_2/Ar$ atmosphere used for VA-CNT growth from Fe/Al_2O_3 catalysts is also very active for growing carbon nanostructures on bulk metal surfaces containing the elements which are catalytically active in forming filamentous carbon. In the course of our experiments with various furnace configurations for CNT growth, we grew high yields (millimeter-scale "fuzz") of solid carbon on porous stainless steel (Figs. 4-57 and 4-59), nickel thermocouple wire (not shown), waterjet-cut edges of tungsten (Figs. 4-61–4-64), and garnet abrasive powder used for waterjet cutting (not shown).

Carbon growths on these surfaces have a wide range of sizes and structures, from ~nm-diameter filaments which could be CNTs based on their appearance in SEM, to ~μm-diameter filaments which grow in "octopus"-like clumps (Fig. 4-57a). An abundance of the filamentous nanostructures appear to have a faceted catalyst particle along their length with a carbon structure rooted in opposite sides of the particle (Fig. 4-57b). Referencing in-depth studies in previous literature, this represents a "bidirectional" growth mode, where carbon precipitates from both sides of a metal catalyst particle [400]. One model suggests that carbon filament growth on a Fe foil proceeds first by initial formation surface carbide phases when the foil is exposed to a hydrocarbon, and then breakup of the surface due to stresses because carbides occupy a larger volume than pure Fe (Fig. 4-58, [148,158]). Then, filaments grow from the clusters formed when the surface breaks up. A similar mechanism is plausible for our growth process on stainless steel, where the Fe clusters are segregated by the initial carbide formation process, and then are carried away from the surface by bi-directional growth of cup-stacked filaments from the particles. By EDX analysis, we confirm that the clusters are Fe; the bulk steel consists of Fe, Mo, Cr, C, and other elements, and Fe is "selected" from this composition as a catalyst for growth of solid carbon (Fig. 4-59). Raman spectroscopy indicates that the carbon structures grown on steel are of lower graphitic quality and contain more defective and/or amorphous carbon than CNTs grown from the Fe/Al_2O_3 film on Si or from Fe on Al_2O_3 fibers (Fig. 4-60).

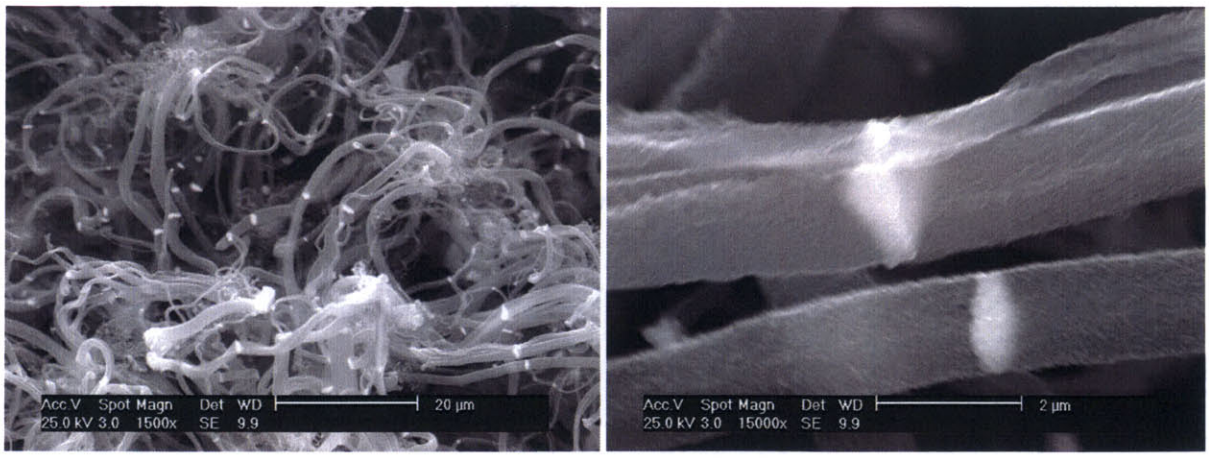

(a) (b)

Figure 4-57. SEM images of fibrous structures grown from bare porous stainless steel (Porcerax), processed in 100/500/250 sccm $C_2H_4/H_2/Ar$ at 750 °C, for 15 min. Apparent catalyst particles appear to be imbedded in the fibers, and are bright in the image.

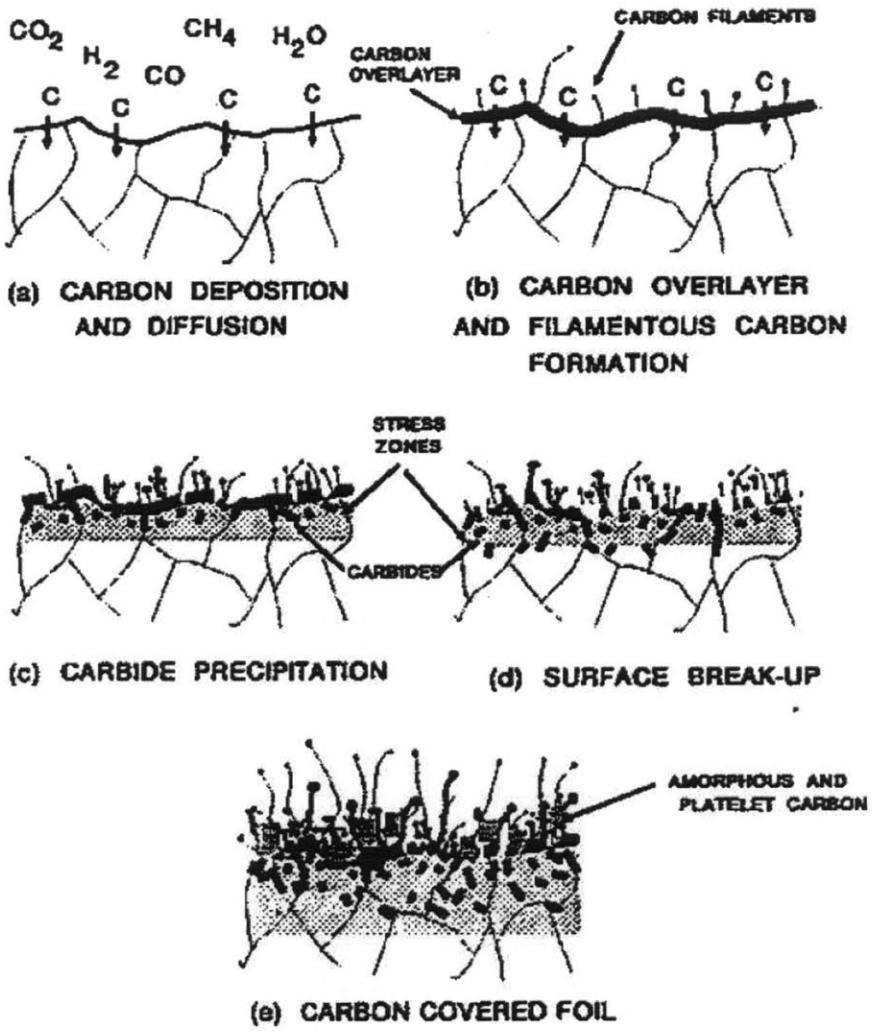

Figure 4-58. Proposed formation mechanism of filamentous carbon on metal foils, where stress-induced surface breakup produces catalytic particles (from [158])

Catalytic formation of carbon on bulk metal is of course widely known. Specific to this section, CNTs have been grown directly on stainless steel meshes [156, 401, 402] and on the oxidized interior surfaces of stainless steel tubing [403], and a layer of sputter-deposited stainless steel has been used to catalyze growth of tangled CNTs on the surfaces of carbon fibers [392]. Further, precipitation of metal particles from a stainless steel reactor has improved the rate of carbon fiber production by pyrolysis of natural gas [44].

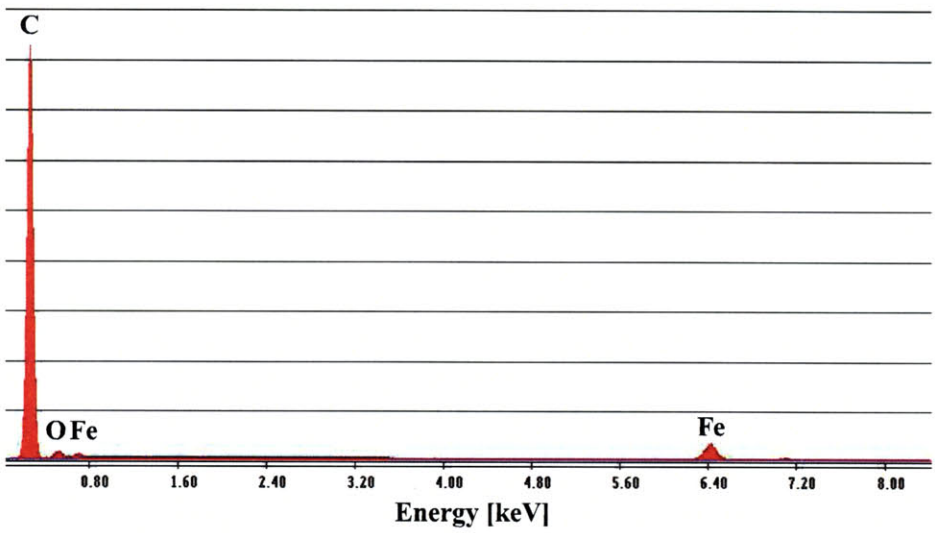

(a)

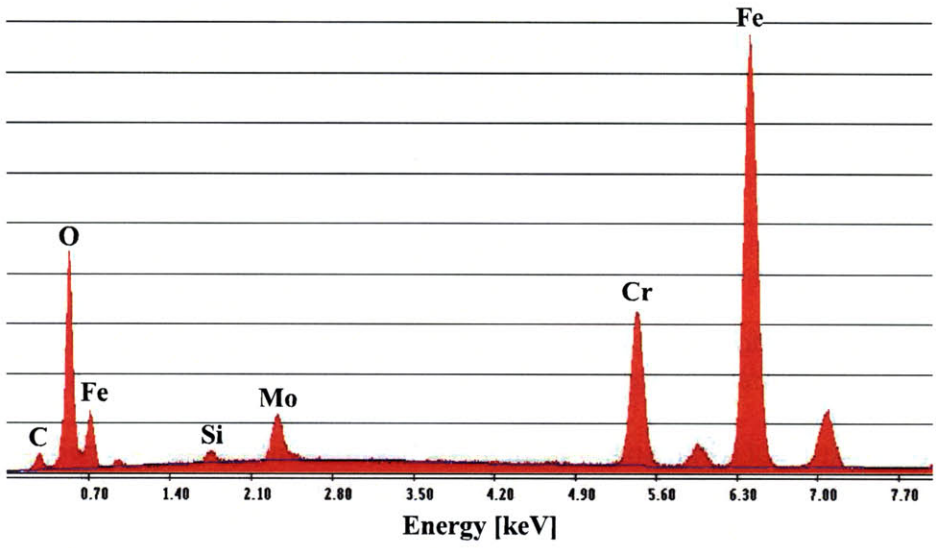

(b)

Figure 4-59. EDX spectra of (a) region of carbon filament containing apparent catalyst particle (Fig. 4-57b), and (b) bare porous stainless steel substrate. Spectra were taken at 25.0 keV in Philips XL30 FEG-ESEM.

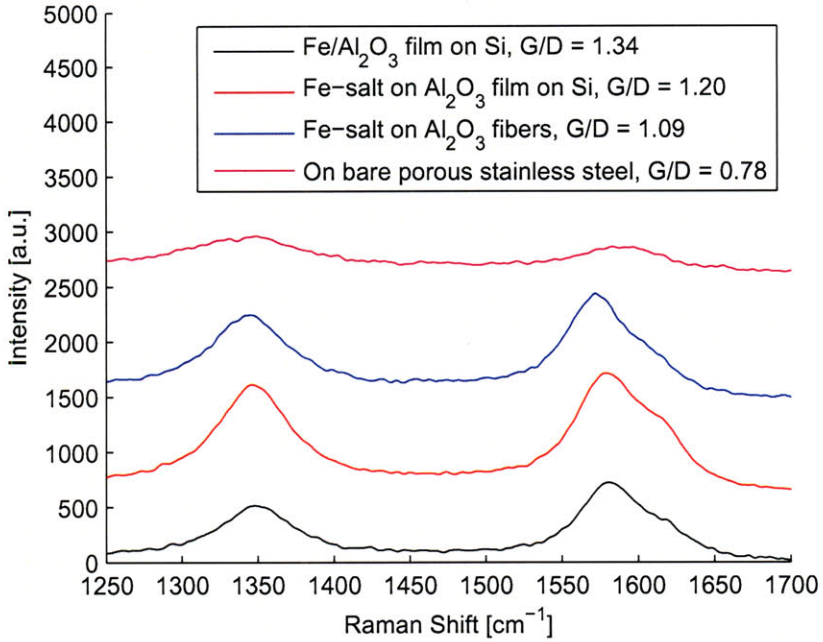

Figure 4-60. Comparison of *G*- and *D*-band regions of Raman spectra (514 nm excitation) of VA-CNTs on $Fe/Al_2O_3/Si$, VA-CNTs on Fe/Al_2O_3-fibers, and disordered carbon structures on porous stainless steel.

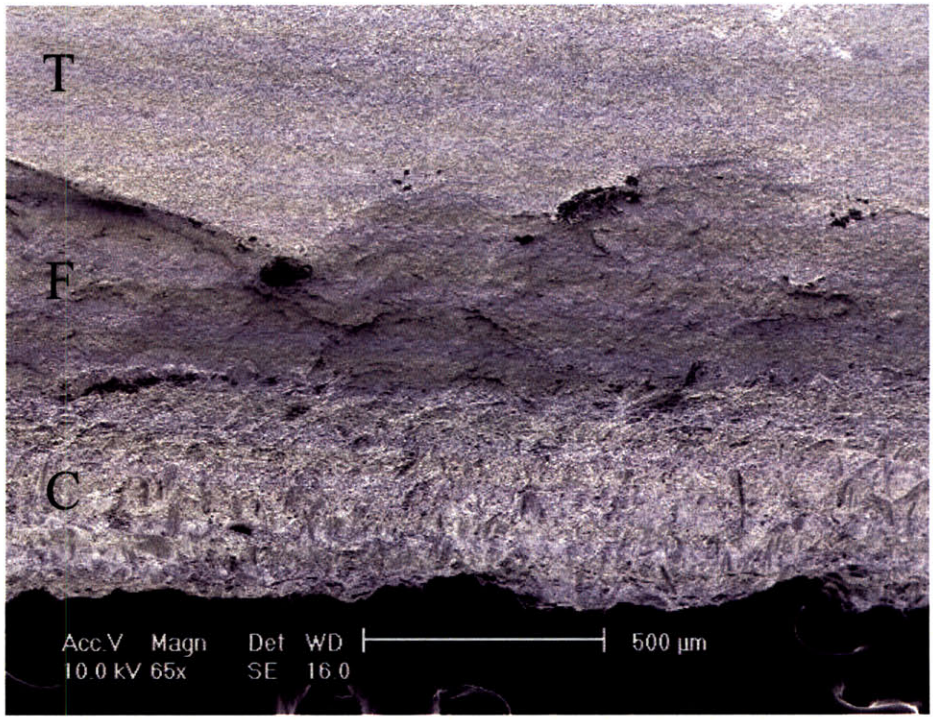

Figure 4-61. Edge of waterjet-cut tungsten piece: T, top surface; F, fractured surface which was chipped away during waterjet cutting; C, cut surface, parallel to jet. CNT growth is observed on cut surface.

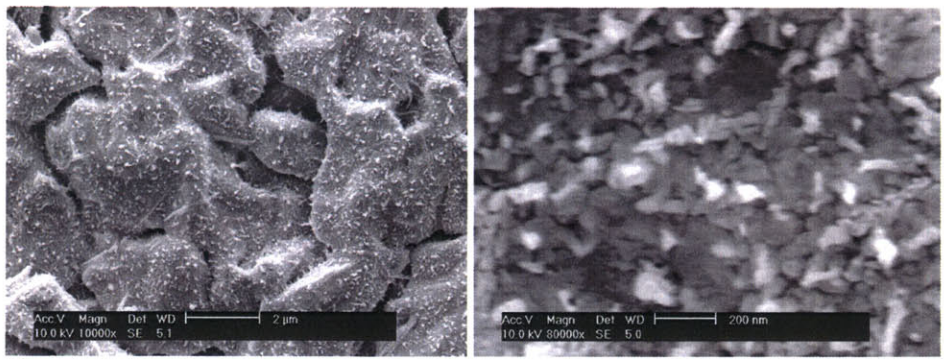

(a) (b)

Figure 4-62. Top (T) surface of tungsten piece after processing in 100/500/200 sccm $C_2H_4/H_2/Ar$, at 750 °C, for 15 min.

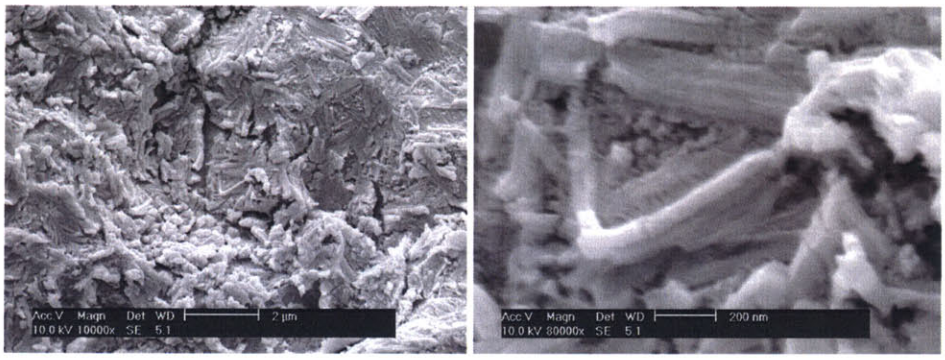

(a) (b)

Figure 4-63. Fractured (F) surface of tungsten piece after processing in 100/500/200 sccm $C_2H_4/H_2/Ar$, at 750 °C, for 15 min.

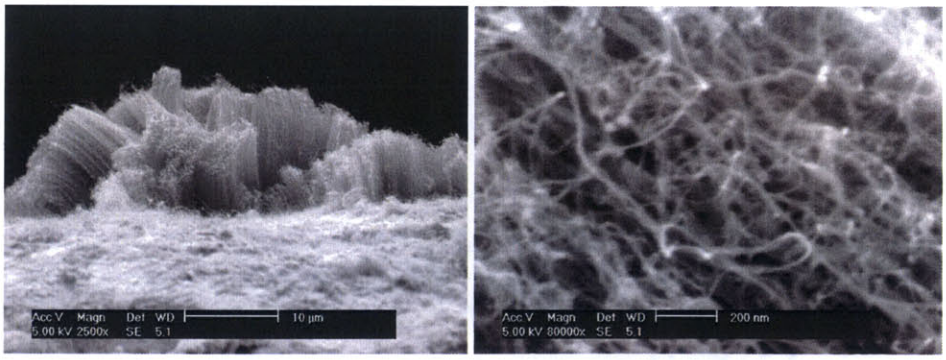

(a) (b)

Figure 4-64. Carbon nanostructure growth on waterjet-cut (C) surface of tungsten piece after processing in 100/500/200 sccm $C_2H_4/H_2/Ar$, at 750 °C, for 15 min.

Chapter 5

Microchannel Arrays for Combinatorial Flow Studies of Nanomaterials Growth

This chapter presents the design, modeling, and fabrication of a microchannel array device for conducting combinatorial studies of nanomaterials growth, particularly growth of CNTs [404, 405]. The device is fabricated by anisotropic etching of single-crystal silicon, which enables a novel two-stage microchannel design. By choosing the sizes of the "entry" channel regions, which act as the dominant fluidic resistors, a velocity variation of at least three orders of magnitude can be achieved among wide "growth" channels regions adjacent to the entry regions. For example, the fluid in the first growth channel may have an average velocity less than 0.001 m/s, while the fluid in the last growth channel may have a velocity of 1 m/s or greater. Dozens of experiments can be conducted at once, and the limiting kinetic conditions achieved in the microchannels would be difficult or impossible to achieve in traditional growth chambers such as tube furnaces.

A detailed design methodology considers compressible slip flows within the microchannels and determines the microchannel dimensions to achieve a specified velocity progression (e.g., a geometric sequence) between adjacent channels in the array. Further modeling considers flow leaks between adjacent leaks, and effects of variations in lithography dimensions and operating conditions on the hydrodynamic characteristics of the microchannels.

The device is sealed reversibly by mating a polished silicon surface against a non-polished silicon surface, and is operated by adjusting the pressure drop across the array, rather than using expensive mass flow controllers. Devices having a variety of velocity ranges and progressions have been fabricated to demonstrate the utility of the platform for CNT growth.

5.1 Introduction

In conventional approaches to growth of nanostructures by CVD using growth systems such as tube furnaces, it is very difficult to maintain uniformity and control of key process variables (e.g., temperature distribution, flow rate, reaction times) at the temporal and spatial resolutions needed to probe the dynamics of the growth reactions . For example, nucleation of a CNT from a catalyst nanoparticle can occur within milliseconds after the carbon source is introduced, yet a tube furnace is typically heated at 0.1–1 °C/s (Table 5.1). Furthermore, parametric studies

of these reactions are overwhelming due to the number of important process variables, and the resolution of these studies is limited by that of conventional gas delivery and temperature control hardware.

Growth reaction			**Tube furnace**		
CNT diameter	1×10^{-9}	m	Tube furnace size	0.1	m
Nucleation time	$<1\times10^{-3}$	s	Heat/cool rate	1	°C/s
Growth rate	$1\text{–}1000\times10^{-8}$	m/s	Gas introduction time	10–100	s
Power consumed (1 cm^2)	0.02	W	Power input	1,000	W

Table 5.1. Mismatch between spatial, temporal, and energy consumption dynamics of CNT growth, and control capability of a conventional tube furnace.

While microscale chemical and fluidic systems have been studied and implemented widely [406], state-of-the-art approaches to microfluidic processing of nanomaterials are restricted to single parameter sets per experiment, such as for synthesis of CdSe nanocrystals [407,408], and to fluidic deposition and patterning of pre-grown nanostructures on substrates, such as for deposition of horizontally-aligned silicon nanowires [232] and drying-mediated organization of CNTs [361]. Here we present a system and methodology for growing nanomaterials using precisely fabricated microchannel arrays as reactors, in which dozens of isolated flow experiments can be conducted simultaneously. This system is applied to study synthesis of CNTs by atmospheric pressure thermal CVD. Microfluidic systems for nanocrystal growth have been limited to relatively low temperatures of 300 °C, compared to 1000 °C which our microchannel apparatus can achieve while maintaining reversible sealing and reusability.

The array is built using a novel variable-depth microchannel design (Fig. 5-1), where each channel consists of an "entry" region having a triangular cross-section, and an adjacent and much wider "growth" region having a trapezoidal cross-section. KOH etching produces the long ($\approx$10 mm) microchannels in a standard (100) silicon wafer. The channel sidewalls intersect the wafer surface at 54.7° angles, because the etch rate of (111) planes is 50–500 times slower than the etch rate of (100) planes in KOH [296, 409]. When the pattern is left in the etchant long enough, rectangular "slit" openings self-terminate to have triangular cross-sections; alternatively, if the etch is terminated early, a trapezoidal cross-section results.

The fluidic resistance of a microchannel is highly sensitive to its cross-sectional dimensions, so for a given pressure drop across the array, a very large velocity range can be achieved within a relatively small range of cross-sectional dimensions. The total length of the entry and growth channel regions is fixed, and the width and length of the each entry region are chosen to achieve a desired average velocity in the growth region. Because of the microscale dimensions, flows remain laminar even at high (e.g., 10 m/s) flow velocities. For high temperature gas flows, as would be used to grow nanomaterials such as CNTs by CVD, it is demonstrated that compressible slip flow models must be used for the entry channels, while incompressible no-slip models are appropriate for the growth channels. An example array design contains 45 parallel two-stage channels (Fig. 5-2 giving a range of 0.001–1.0 m/s and a differential flow rate of $\sim10^{-5}$ sccm. This range and resolution cannot be achieved using traditional tube furnace systems or flow control equipment, and could enable ordinal optimization [410] studies of highly coupled multidimensional reaction spaces.

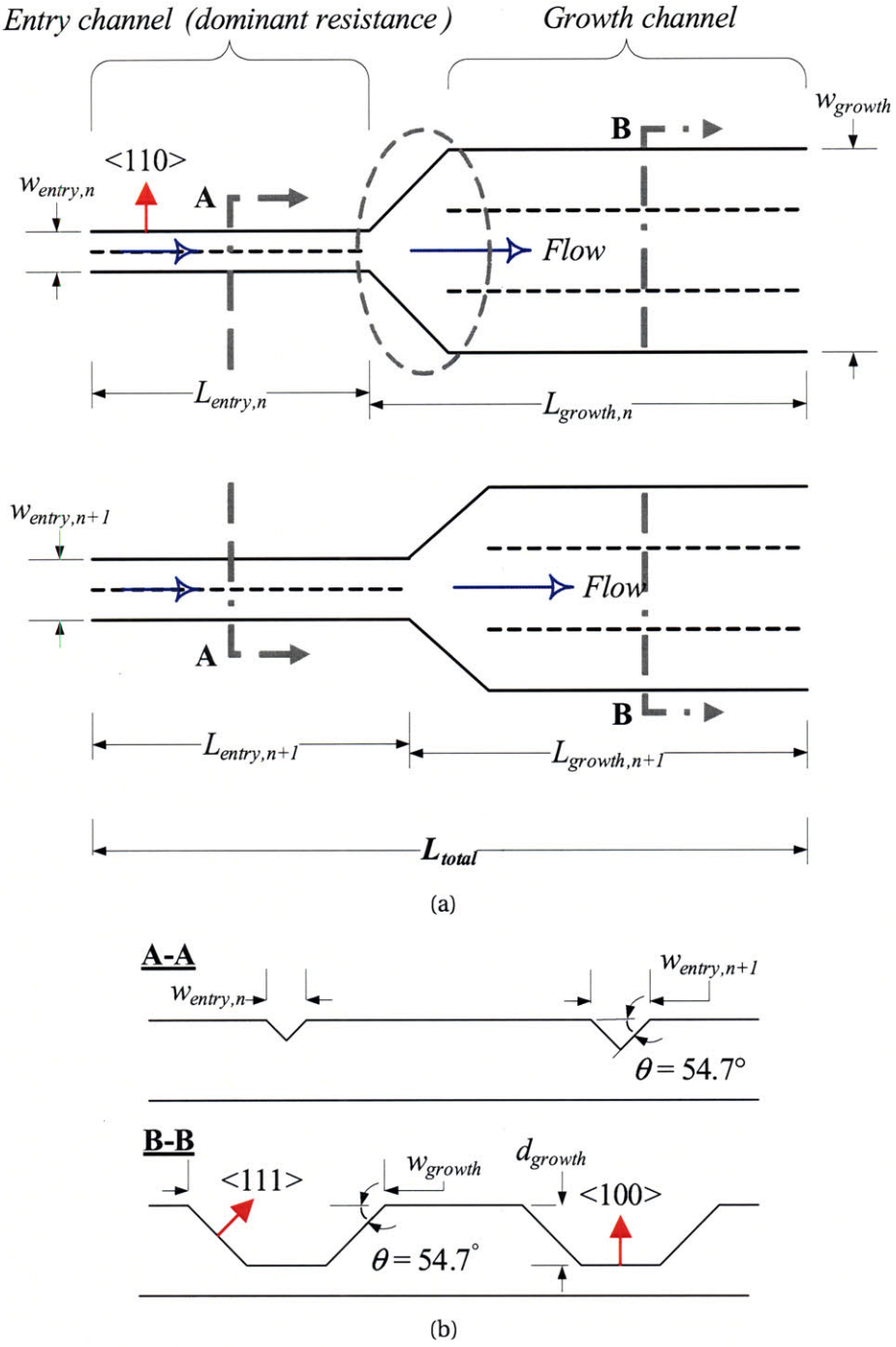

Figure 5-1. Schematic of variable-depth microchannel design fabricated by KOH-etching of silicon. Each channel has two regions: a variable-width, self-terminating "entry" region, which is the dominant fluidic resistance; and a much wider, time-terminated "growth" region. The total length of the two regions is constant, and the individual lengths are chosen to give desired increases in the average velocities in the growth channel regions, for specified (lithographically-limited) widths of the entry regions.

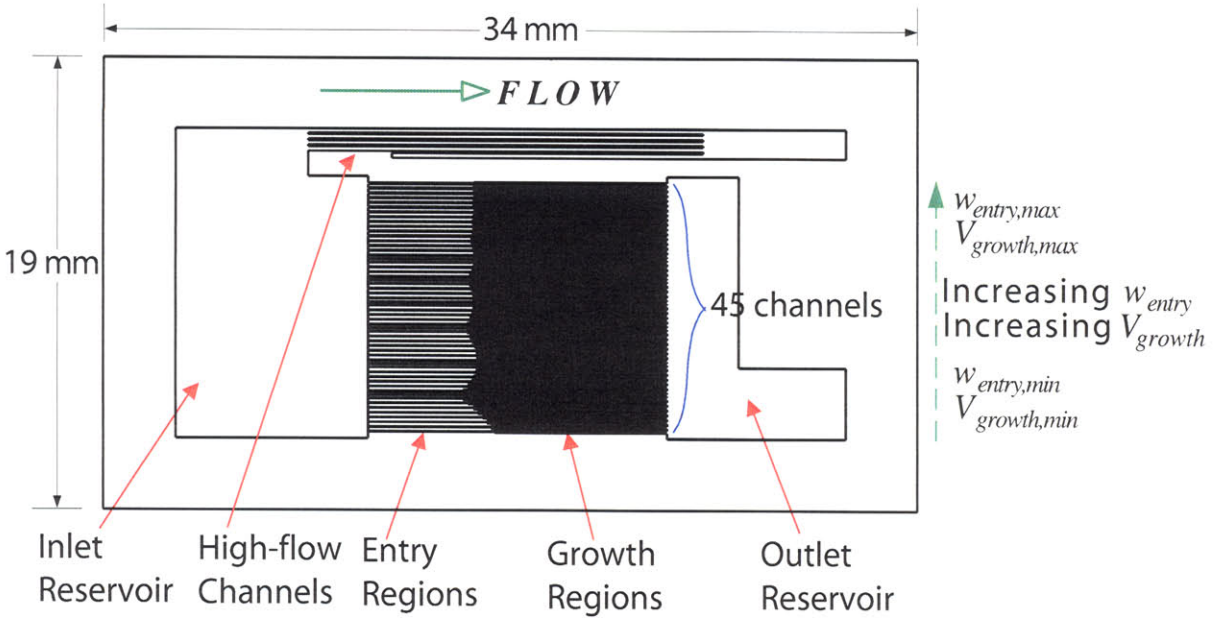

(a)

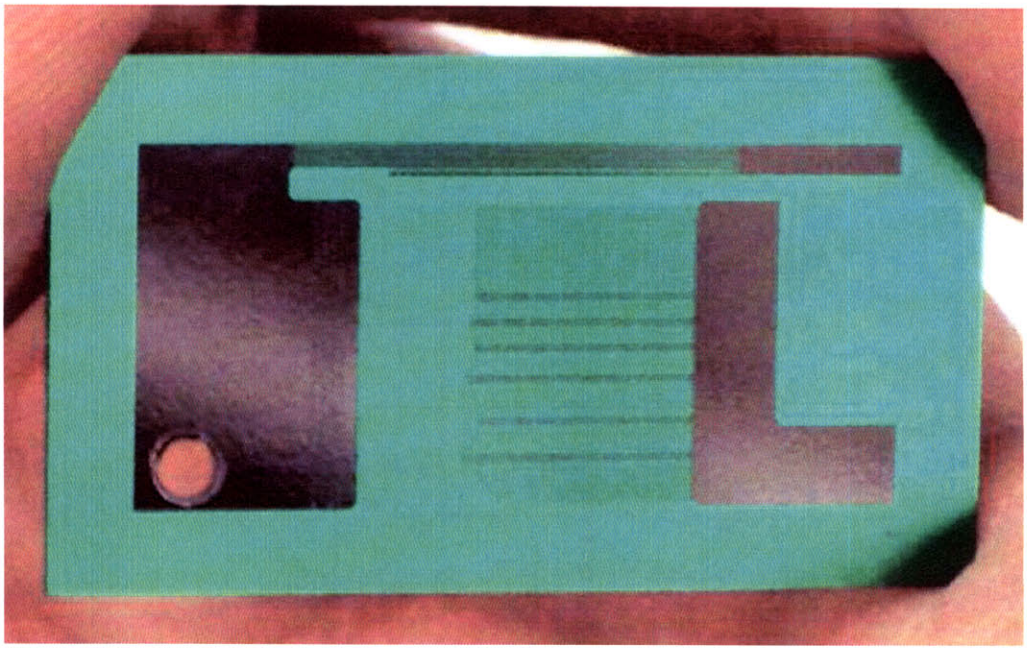

(b)

Figure 5-2. Schematic of example microchannel device, and picture of fabricated device. The device has an array of 45 channels plus 4 "sacrificial" high-flow channels for increasing the total flow rate through the device.

Looking ahead, combinatorial catalyst libraries [411,412] will be useful for studying new catalyst materials using microchannel systems, for example to investigate sequentially arranged catalysts and dopants as "conditioning" chemistries for type-selective (e.g., SWNTs versus DWNTs [186,187]) and possibly chirality-selective [181] growth of CNTs. Our array design could be modified to incorporate a mixing array, so different concentrations of two reactants are delivered to each channel; for example, where an equal flow of a certain reactant is delivered to each channel, independent of the total of the mixture in the channel. Furthermore, because of the small size of the growth chamber, reactants could be rapidly introduced to and flushed from the channels, and the reactant mixture could be controllably varied throughout the reaction. The remainder of this chapter discusses the details of the flow modeling, implementation, and fabrication of the microchannel devices.

5.2 Flow modeling

To predict the velocities in the channels of the array and thereby design a device to achieve a desired velocity range and progression, it is first necessary to develop models of flows through microchannels having the triangular and trapezoidal cross-sections which are etched using KOH. First, incompressible flow models are developed for no-slip and slip flow through circular pipes, and then numerical simulations are used to determine a correction factor for applying the circular pipe models to KOH-etched cross-sections. Finally, a compressible slip flow model developed after work of Arkilic et al. [413] shows that compressibility has a significant effect on the pressure drop through long microchannels and hence must be considered by our calculations.

5.2.1 Flow regimes

Intermolecular collisions cause momentum and energy transport and guarantee thermodynamic equilibrium within a fluid. Non-continuum effects, namely the non-zero slip velocity at surfaces (e.g., walls of microchannels), must be considered when modeling flows through microscale devices, as molecular collisions with the confining geometry of the device become relatively more important in describing the flow behavior.

Based on the geometric dimensions, fluid properties, temperature, and pressure, a gas flow problem can be classified into the no-slip, slip, transition, or free-molecular flow regime. A well-known parameter for characterizing a flow problem is the Knudsen number (Kn), which is the ratio between the mean free path (λ) of a gas and the relevant length scale (L),

$$\mathrm{Kn} = \frac{\lambda}{L}. \tag{5.1}$$

The mean free path is the average distance a gas molecule travels between collisions, and is related to the gas pressure (P), collision diameter (d), and temperature (T), by

$$\lambda = \frac{kT}{\pi P d^2 \sqrt{2}}, \tag{5.2}$$

where k is the Boltzmann constant. The collision diameter, which is the hard-sphere diameter

of a gas molecule according to the kinetic theory of gases, can be calculated from the viscosity (μ), molar mass (M), and temperature, and is between 2–5 Å for most gases [357].

A gas is considered "rarefied" when the magnitude of the mean free path is non-negligible with respect to the length scale of surrounding geometry. In general, no-slip assumptions are valid when $\mathrm{Kn} \leq 10^{-2}$, while a flow is in the free-molecular regime when $\mathrm{Kn} > 10$ [414]. Between these two limits, further classification gives slip flow for ($0.01 < \mathrm{Kn} \leq 0.1$) and transition flow for ($0.1 < \mathrm{Kn} < 10$). The regimes are separated by values of Kn, which is constant along lines plotted in terms of length scale and normalized number density (Fig. 5-3). The normalized number density (n/n_0) is determined by the ideal gas law according to the temperature and pressure of the fluid, such that

$$\frac{n}{n_0} = \frac{pT_0}{p_0 T}. \tag{5.3}$$

Hence, for CH_4 at 900 °C and 1.17 atm average pressure, the normalized number density is 0.30 (using T_0 =298 K and p_0 =1 atm). Therefore, channels with cross-sectional dimensions greater than approximately 20 μm are in the no-slip regime, while those from 2–20 μm are in the slip flow regime. Geometries smaller than 2 μm are in the transition regime; however, since the minimum channel width for the designs presented here is ≈5 μm, the transition regime is not important for our analysis.

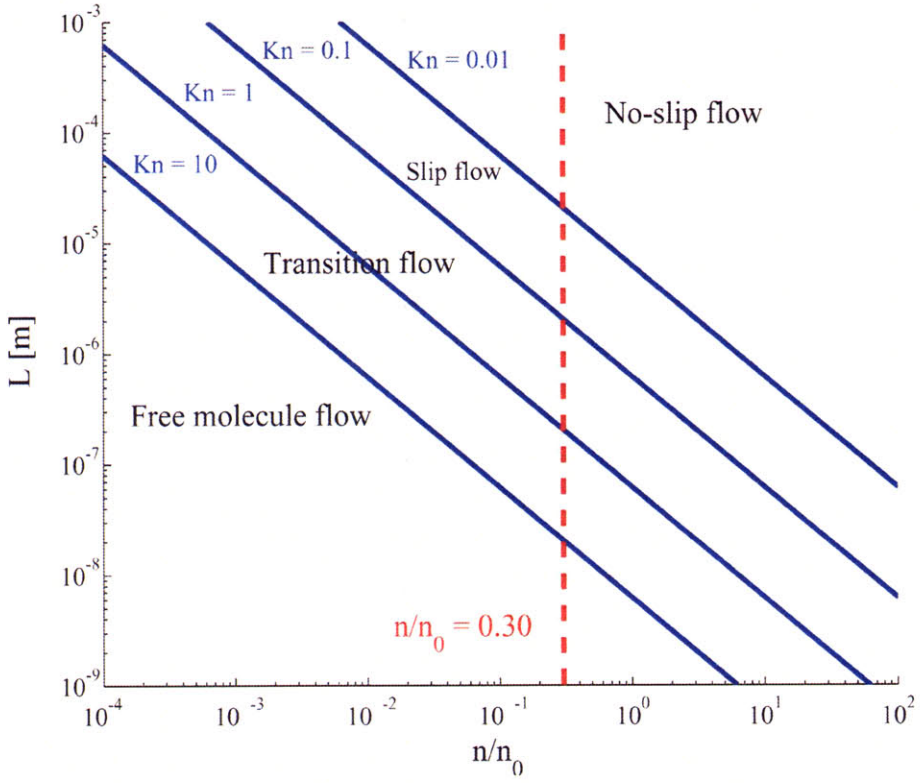

Figure 5-3. Relationship between length scale and normalized number density for CH_4, classifying gas flow regimes based on the Knudsen number [415].

5.2.2 Incompressible flow models

5.2.2.1 Circular pipe

The flow models start from the Navier-Stokes equations in cylindrical coordinates, and the resulting general solution for steady fully-developed flow in a pipe having a circular cross-section. Neglecting inertial terms, enforcing rotational symmetry, and assuming a fully-developed velocity profile, the reduced form of the Navier-Stokes equation is [416]

$$-\frac{1}{\mu}\frac{dp}{dz} = \frac{1}{r}\frac{d}{dr}\left(r\frac{dv(r)}{dr}\right), \tag{5.4}$$

with pressure change (p) and flow along the z-direction. Integrating this equation twice, the general velocity profile across a circular pipe is

$$v(r) = -\frac{dp}{dz}\frac{1}{4\mu}r^2 + C. \tag{5.5}$$

For incompressible no-slip flow, applying the condition of zero velocity at the outer radius of the pipe ($r = R$) the velocity profile is

$$v(r)_{n,i} = -\frac{dp}{dz}\frac{1}{4\mu}\left(R^2 - r^2\right). \tag{5.6}$$

The flow rate (Q) through the pipe is found by integrating the velocity profile over the cross-sectional area, such that

$$Q = 2\pi\int_0^R v(r)rdr = Q_{n,i} = -\frac{dp}{dz}\left(\frac{\pi R^4}{8\mu}\right). \tag{5.7}$$

This gives a constant pressure gradient,

$$\frac{dp}{dz}_{n,i} = -\frac{8\mu Q}{\pi R^4}. \tag{5.8}$$

When Kn > 0.01, the no-slip boundary condition is invalid, and the flow model must consider the momentum transfer between the gas molecules and the pipe wall. Accordingly, Maxwell proposed a slip boundary condition [417], which balances the differential frictional force exerted across a thin layer of gas near the wall with the pressure gradient along the flow direction. For a circular cross-section, Maxwell's slip boundary condition is

$$v(R) = -\frac{\mu}{\epsilon}\frac{dv}{dr}|_R. \tag{5.9}$$

The term μ/ϵ, often denoted as ζ and called the coefficient of slip, is the ratio of internal friction (μ) in the gas to friction against the wall. Maxwell defined the coefficient of slip as

$$\zeta = \frac{\mu}{\epsilon} = \frac{\mu}{\rho}\sqrt{\frac{\pi}{2R_u T_w}}\left(\frac{2-\sigma_v}{\sigma_v}\right). \tag{5.10}$$

Here, R_u is the universal gas constant and T_w is the wall temperature. In this analysis, the wall temperature is assumed to be uniform and equal to the bulk fluid temperature. The tangential momentum accommodation coefficient, σ_v, is

$$\sigma_v = \frac{\tau_i - \tau_r}{\tau_i}, \tag{5.11}$$

where τ_i and τ_r are the incoming and reflected tangential (along the wall direction) momentum values for molecules colliding with the wall. Hence, σ_v indicates how much tangential momentum a gas molecule loses when it collides with the wall, with respect to its incident tangential momentum. For specular reflection, $\tau_r = \tau_i$ and $\sigma_v = 0$, meaning that the tangential velocity of the molecules is unaffected by the collision; for diffuse reflection, $\tau_r = 0$ and $\sigma_v = 1$, and the molecules are completely retarded by the wall. Arkilic et al. [418] measured σ_v in micromachined silicon channels, giving values independent of Kn and ranging from 0.75 to 0.85 for argon, nitrogen, and carbon dioxide.

Substituting Maxwell's slip condition into Eq. (5.5) and solving gives the velocity distribution for slip flow in a pipe,

$$v(r)_{s,i} = -\frac{dp}{dz}\left(\frac{1}{4\mu}(R^2 - r^2) - \frac{R}{2\epsilon}\right). \tag{5.12}$$

The flow rate is

$$Q_{s,i} = -\pi\frac{dp}{dz}\left(\frac{R^4}{8\mu} + \frac{R^3}{2\epsilon}\right). \tag{5.13}$$

Substituting this into $v(r)$, the pressure gradient is

$$\frac{dp}{dz}_{s,i} = -\frac{2Q_{s,i}}{\pi\left(\frac{R^4}{4\mu} + \frac{R^3}{\epsilon}\right)}. \tag{5.14}$$

While the dimensions of the array designs give only continuum and slip flows, it is worthwhile to also examine the "unified" flow model of Karniadakis and Beskok [415], which is a modified slip flow solution of the Navier-Stokes equations that is valid for Kn > 0.1. For an isothermal flow, the unified flow model predicts a slip velocity of

$$v(R) = \left(\frac{2-\sigma_v}{\sigma_v}\right)\left(\frac{\mathrm{Kn}_D}{1 - b\mathrm{Kn}_D} 2R\frac{dv}{dr}|_R\right), \tag{5.15}$$

where $\mathrm{Kn}_D = \lambda/2R$. The coefficient b is used to adjust the slip condition to match numerical models based on the kinetic theory of gases, such as solutions of the Boltzmann equation and Monte Carlo simulations. The value of b ranges[1] from -1 to -2, over a wide span of Kn. The unified flow model also proposes a corrected viscosity,

$$\mu_{corr} = \mu\left(\frac{1}{1 + \mathrm{Kn}}\right), \tag{5.16}$$

to account for the increased frequency of wall collisions with respect to intermolecular collisions as Kn increases. While the finer points of the unified model are not important to our

[1] For $b = 0$, the unified model matches Maxwell's condition

analysis, Karniadakis and Beskok make a useful demonstration that a simple slip model can describe both continuum and non-continuum gas flows with reasonable accuracy in exchange for avoiding costly simulations.

Substituting the unified flow boundary condition into the general velocity distribution obtained by integrating the Navier-Stokes equation (Eq. 5.5) gives the velocity distribution

$$v(r)_{u,i} = -\frac{dp}{dz}\left(\frac{1}{4\mu_{corr}}\left(R^2 - r^2\right) + \frac{C_u R}{2\mu_{corr}}\right). \tag{5.17}$$

The flow rate is

$$Q_{u,i} = -\pi\frac{dp}{dz}\left(\frac{R^4}{8\mu_{corr}} + \frac{2R^3 C_u}{\mu_{corr}}\right) \tag{5.18}$$

and the pressure gradient is

$$\frac{dp}{dz} = -\frac{2\mu_{corr}Q}{\pi\left(\frac{R^4}{4} + C_u R^2\right)}, \tag{5.19}$$

where

$$C_u = 2R\left(\frac{2-\sigma_v}{\sigma_v}\right)\left(\frac{Kn}{1-bKn}\right). \tag{5.20}$$

Figs. 5-4, 5-5, and 5-6 compare the fully-developed velocity profiles for (5,25,50) μm diameter pipes carrying 0.001 sccm of methane at 900 °C (λ_{CH_4} = 253 nm). For the 5 μm (Kn = 0.05) diameter pipe, there is a significant difference—a much lower maximum velocity, and a slip velocity of approximately 20% of the maximum velocity—between the slip and no-slip solutions. For $D = 2R = 25$ μm (Kn = 0.01), the difference is only a few percent. For $D = 50$ μm (Kn = 0.005) the profiles are nearly identical, demonstrating that this flow is well-approximated by no-slip assumptions. For each case, note that the unified flow model (using μ_{corr}) matches the Maxwell slip solution.

Figs. 5-7 and 5-8 compare the pressure gradients calculated by each flow model, showing that slip flow decreases the pressure gradient by as much as 40% at $D = 5$ μm. Also, the pressure gradient calculated by the unified flow model matches the slip flow pressure gradient within 5% for $D > 5$ μm. When $D < 5$ μm, the pressure gradient calculated by the unified flow model drops considerably more, as the flow enters the transition regime and Maxwell's slip condition is no longer valid.

Figs. 5-9 and 5-10 show the effect of varying σ_v from the minimum of 0.75 (measured by Arkilic [418]) to the maximum of 1.0 (specular reflection). Within this range, σ_v affects the pressure gradient by approximately 10%, so 0.85 is chosen as an average value for and used in our analysis. In the FLUENT™ material property database, the default value of σ_v for CH_4 is 0.9137.

The no-slip and Maxwell slip solutions are also validated using FLUENT™ software[2]; simulation values are indicated in the figures, and demonstrate differences of less than 1% in velocity and pressure between the analytical and numerical solutions for no-slip and slip flows through circular pipes.

[2]A license to use FLUENT™ for this research was generously provided at substantially reduced cost by the General Motors PACE program.

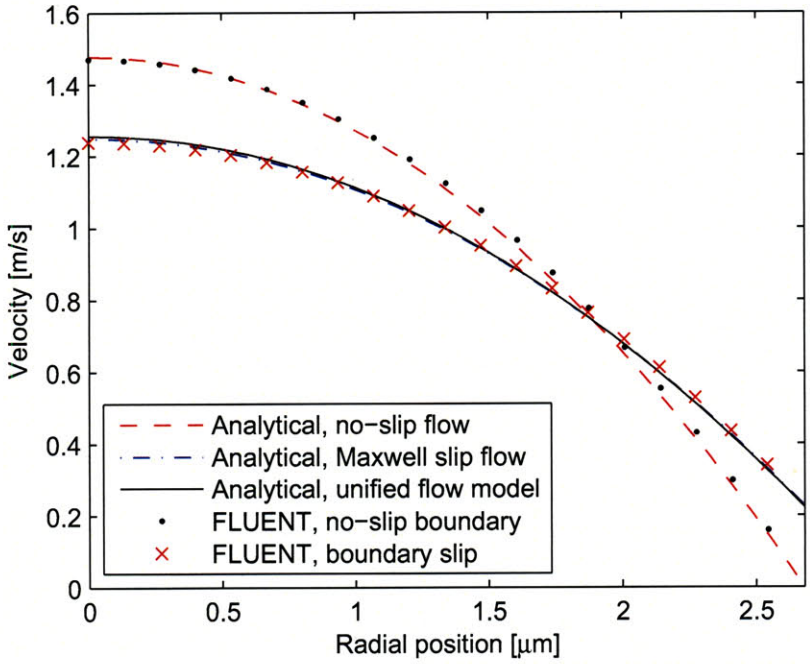

Figure 5-4. Velocity profiles predicted by incompressible no-slip, Maxwell slip, and unified flow models, for 0.001 sccm CH_4 flow at 900 °C through a 5 μm diameter pipe.

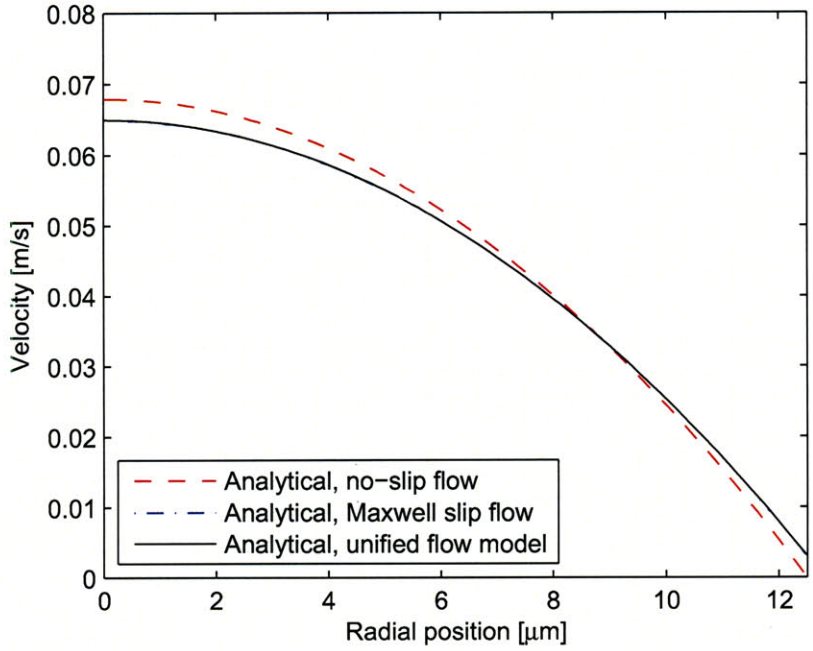

Figure 5-5. Velocity profiles predicted by incompressible no-slip, Maxwell slip, and unified flow models, for 0.001 sccm CH_4 flow at 900 °C through a 25 μm diameter pipe.

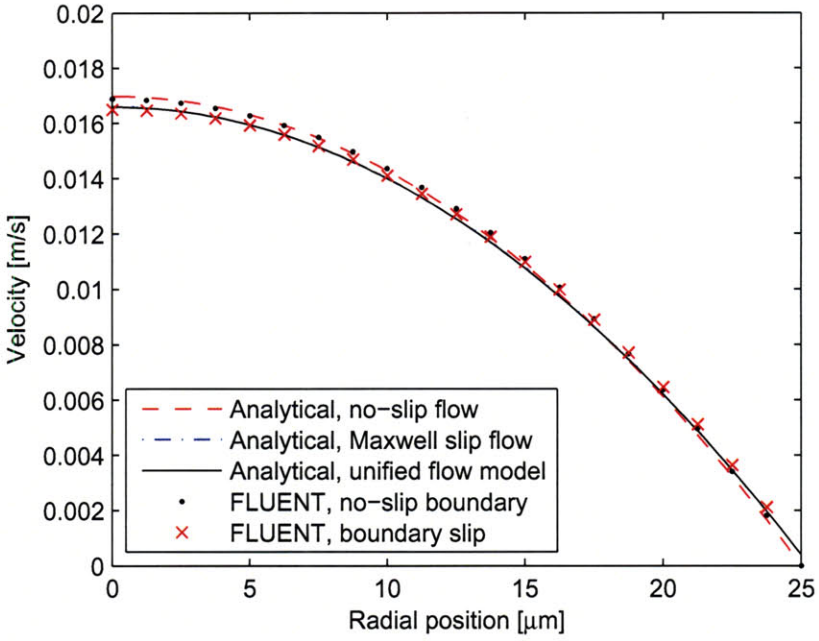

Figure 5-6. Velocity profiles predicted by incompressible no-slip, Maxwell slip, and unified flow models, for 0.001 sccm CH_4 flow at 900 °C through a 50 μm diameter pipe.

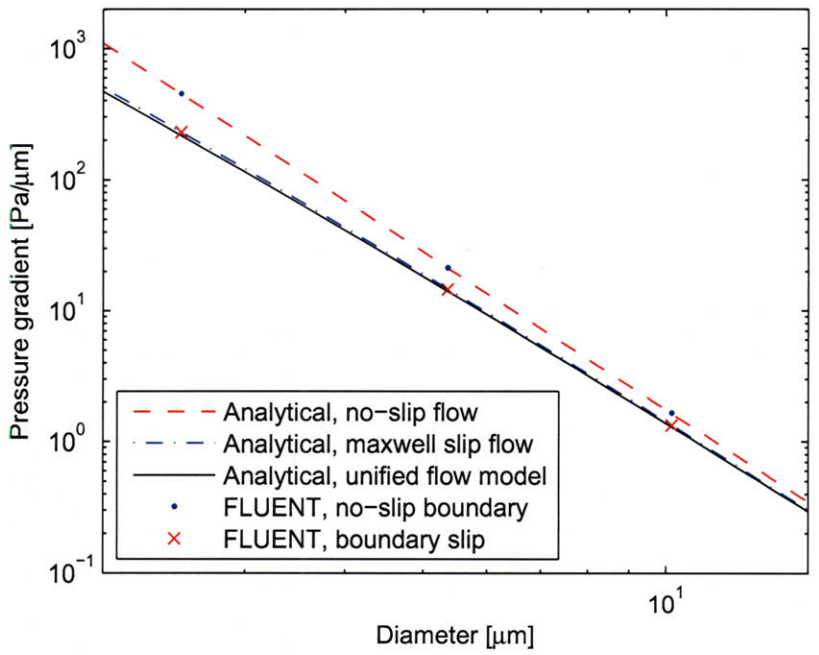

Figure 5-7. Pressure gradients predicted by incompressible no-slip, Maxwell slip, and unified flow models, for 0.001 sccm CH_4 flow at 900 °C through a microscale pipe.

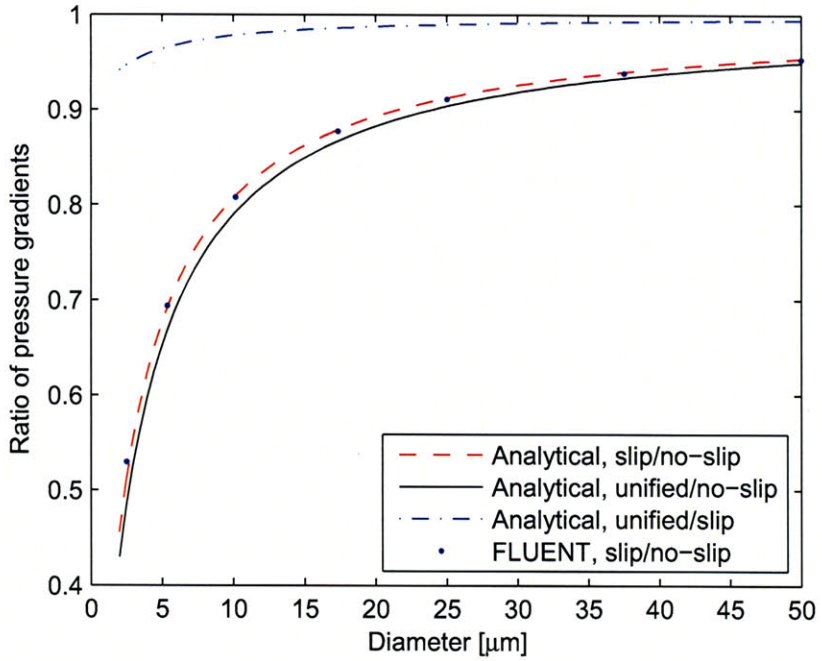

Figure 5-8. Ratios of pressure gradients predicted by incompressible no-slip, Maxwell slip, and unified flow models, for 0.001 sccm CH_4 flow at 900 °C through a microscale pipe.

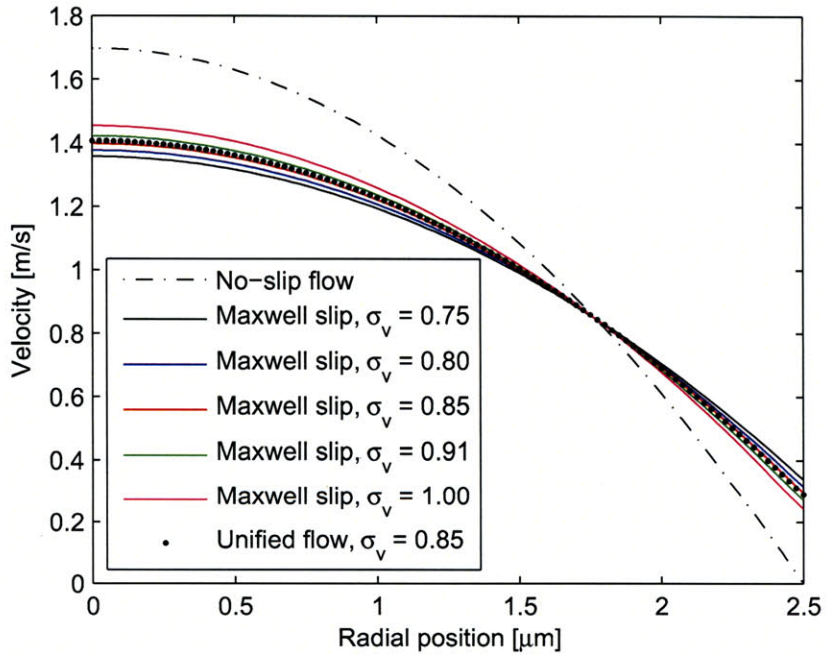

Figure 5-9. Effect of varying tangential momentum accommodation coefficient, σ_v, on velocity profile for incompressible slip flow of 0.001 sccm CH_4 at 900 °C through a 5 μm diameter pipe.

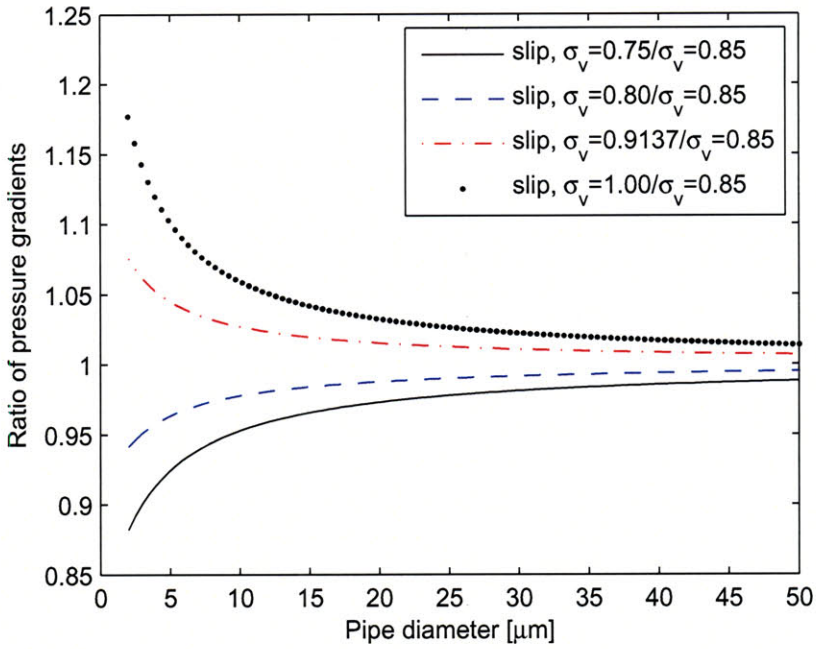

Figure 5-10. Ratios of pressure gradients predicted by incompressible Maxwell slip flow model for varying σ_v, for methane flow at 900 °C through a microscale pipe.

5.2.2.2 Flows through KOH-etched geometries: triangular and trapezoidal cross-sections

It is common practice to model pressure drops through non-circular cross-sections using a flow model for a circular cross-section of equivalent hydraulic diameter (D_h),

$$D_h = \frac{4A_c}{P}, \tag{5.21}$$

where A_c is the area of the cross-section and P is the perimeter. Applying this formula to the geometry of a KOH-etched triangle (Fig. 5-1, sec. B-B) gives

$$A_{c,tri} = \frac{w^2 \tan\theta}{4}, \tag{5.22}$$

and

$$D_{h,tri} = \frac{w \tan\theta}{1 + \frac{1}{\cos\theta}}. \tag{5.23}$$

For a KOH-etched trapezoid,

$$A_{c,trap} = wd - \frac{d^2}{\tan\theta}, \tag{5.24}$$

$$D_{h,trap} = \frac{4wd - \frac{4d^2}{\tan\theta}}{2w - \frac{2d}{\tan\theta} + \frac{2d}{\sin\theta}}. \tag{5.25}$$

For incompressible laminar flow of a fluid with density ρ through a duct of arbitrary cross-section, modelled as a circular pipe of length L and with flow rate Q, the pressure drop (Δp) is related to the hydraulic diameter as

$$\Delta p = f\frac{Q^2 \rho L}{A_c^2 D_h}. \tag{5.26}$$

The dimensionless friction factor (f) is determined analytically or experimentally for the cross-sectional shape. For an equilateral triangle cross-section, which is close to the 54.7° isosceles triangle fabricated by KOH etching, $f = 13.3/\mathrm{Re}$ [416]. Ma and Peterson [419] use a clever coordinate transformation to derive the velocity distribution, and hence determine the friction factor, for laminar no-slip flow through arbitrary cross-sections. For the KOH-triangle geometry, this gives $f \times \mathrm{Re} = 12.9$, and for a KOH-trapezoid $f \times \mathrm{Re} = 13$–$15$ for etch depths (d) of at least 40% of the opening width (w).

Eq. (5.26) shows that pressure drops for flows through different geometries of equal hydraulic diameter are simply related by ratio of their friction factor to cross-sectional area. Therefore, to give a simple analytical model of the pressure drop through the KOH-etched channel geometries, a correction factor was sought between a numerical solution for the triangular cross-sections, and the analytical solution for a circular pipe. Accordingly, we state that the pressure drop across a pipe of arbitrary cross-sectional shape (denoted with subscript G) is

$$\Delta p_G = C_G\left(\frac{A_{c,circ}}{A_{c,G}}\right)\Delta p_{circ}, \tag{5.27}$$

where C_G is the frictional correction factor calculated as the ratio between the pressure drop across a length of pipe having cross-section G to the pressure drop an equal length of circular pipe of D_H, at the same flow rate Q. For the a 54.7° KOH-triangle, $C_{tri} = 0.83$ is determined using FLUENT simulations. This is very close to the value of $f_{tri}/f_{circ} = 12.9/16 = 0.807$ calculated from values given in the literature [416,419]. For a KOH-trapezoid with $w/d = 0.5$, FLUENT simulations give $C_{trap} = 0.85$. Fig. 5-11 shows the simulated pressure gradients for triangular pipes of varying hydraulic diameter, along with the scaled analytical results calculated by applying the calculated C_G to the analytical model.

Hence, substituting the correction and geometry factors, the pressure drop for incompressible slip flow through a KOH-etched triangle is

$$\Delta p_{tri,sp,i} = 0.831\left(\frac{1}{w^2 \tan 54.7°}\right)\frac{16Q(L-x)}{\left(\frac{D_h^2}{8\mu} + \frac{D_h}{\epsilon}\right)}. \tag{5.28}$$

Similar substitutions can be made for the no-slip solution for the triangular cross-section, and for the trapezoidal cross-section. Note that the correction factor determined by FLUENT™ analysis is nearly identical for no-slip and slip flows ($C_{tri} = 0.831$ for no-slip and $C_{tri} = 0.828$ for slip), indicating that the difference in flow behavior is relatively independent of the boundary shape. The slip flow correction factor increases slightly as Kn approaches 0.1, where $C_{tri} = 0.86$ for $D_H = 2.5\,\mu$m; however, behavior beyond this limit is not important for the channel widths in our device, and therefore the correction factors stated previously are used. Aside, Morini et al. [420] compute values for the friction factor for rectangular, trapezoidal, and double trape-

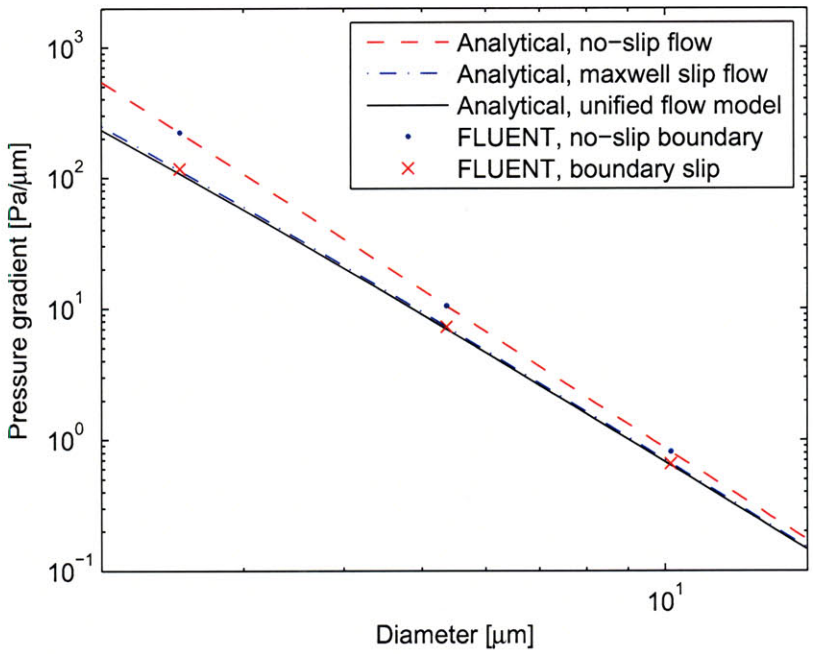

Figure 5-11. Simulated pressure profiles in triangular cross-section microchannel, and comparison to scaled analytical result for equivalent circular pipe. The computations are performed for incompressible flow of CH_4 at 900 °C.

zoidal cross-sections, using a numerical solution to the unified flow model.

5.2.3 Compressible flow models

In addition to slip at the channel walls, compressibility is important when modeling gas flows in microchannels, especially when the pressure drop is at least a few psi, and/or when the channel is very long [421]. A rule-of-thumb is that a microchannel flow must be considered compressible if the pressure drop is more than 5% of the inlet static pressure [420].

When compressibility is considered, the pressure gradient varies along the channel, and therefore the pressure distribution is nonlinear. Comparing an incompressible flow solution to a compressible flow solution for a channel having the same geometry, outlet pressure, and mass flow rate, the compressible solution will predict a lower pressure drop because the model considers a smaller (compressed) volume of gas upstream of the outlet. Arkilic, Schmidt, and Breuer [413] solve compressible no-slip and slip flows in a rectangular microchannel by applying conservation of mass to the velocity profile derived from the Navier-Stokes equation, and substituting the ideal gas law such that

$$\rho(z) = \frac{p(z)}{R_g T}. \tag{5.29}$$

From the velocity profiles developed previously for circular pipes, conservation of mass is applied as

$$\dot{m} = 2\pi\rho \int_0^R v(r) r dr = 2\pi \frac{p(z)}{R_g T} \int_0^R v(r) r dr. \tag{5.30}$$

For no-slip flow, a simple first-order differential equation results,

$$p(z)\frac{dp}{dz} = \frac{8\mu R_g T}{piR^4}. \tag{5.31}$$

Solving this equation, the pressure distribution for compressible no-slip flow in a pipe of length L is

$$p(z)_{n,c} = \sqrt{p_0^2 + \frac{16\mu\dot{m}R_g T}{\pi R^4}(L-z)}, \tag{5.32}$$

where p_o is the outlet pressure and z is the distance from the pipe inlet. In comparison, the pressure distribution for incompressible no-slip flow is

$$p(z)_{n,i} = p_o + \frac{8\mu Q}{\pi R^4}(L-z). \tag{5.33}$$

Applying the same procedure to the slip velocity profile derived previously (Eq. 5.12),

$$p(x)_{s,c} = \frac{-C_2 - \sqrt{C_2^2 - 2C_1\left(\dot{m}(L-z) - \frac{C_1 p_o^2}{2} - C_2 p_o\right)}}{C_1}, \tag{5.34}$$

where

$$C_1 = -\frac{\pi R^4}{8\mu R_g T}, \tag{5.35}$$

and

$$C_2 = \frac{\pi\rho R^3}{2\epsilon}. \tag{5.36}$$

Alternatively, for incompressible slip flow,

$$p(z)_{s,i} = p_o + \frac{2Q}{\pi\left(\frac{R^4}{4\mu} + \frac{R^3}{\epsilon}\right)}(L-z). \tag{5.37}$$

Figs. 5-12 and 5-13 plot the pressure distributions along 2500 μm long circular pipes of diameter 5 μm and 50 μm, for incompressible and compressible flows. As expected, the flow resistance is lower for compressible flow, and the effect of compressibility increases as the pipe diameter decreases. Further, the nonlinearity in the pressure distribution is stronger for smaller diameter pipes. More formally, the ratio of the compressible and incompressible no-slip mass flows, for identical circular pipes with the same inlet (p_i) and outlet (p_o) pressures is

$$\frac{\dot{m}_{n,c}}{\dot{m}_{n,i}} = \frac{1}{2}\left(\frac{p_i}{p_o} + 1\right), \tag{5.38}$$

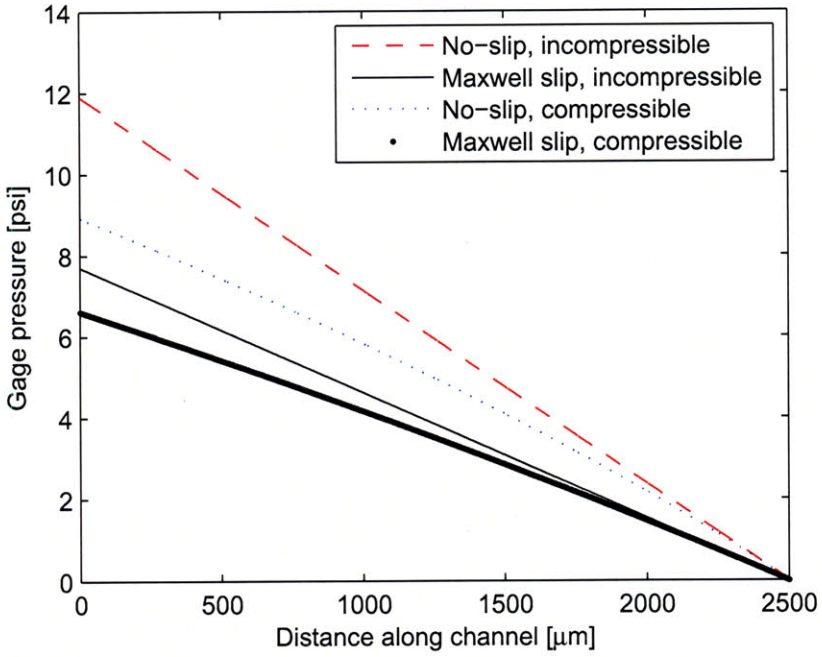

Figure 5-12. Pressure distribution (CH_4, 900 °C) along a 5 μm diameter circular pipe, according to compressible and incompressible flow models, calculated for $\dot{m} = 3.27 \times 10^{-12}$ kg/s.

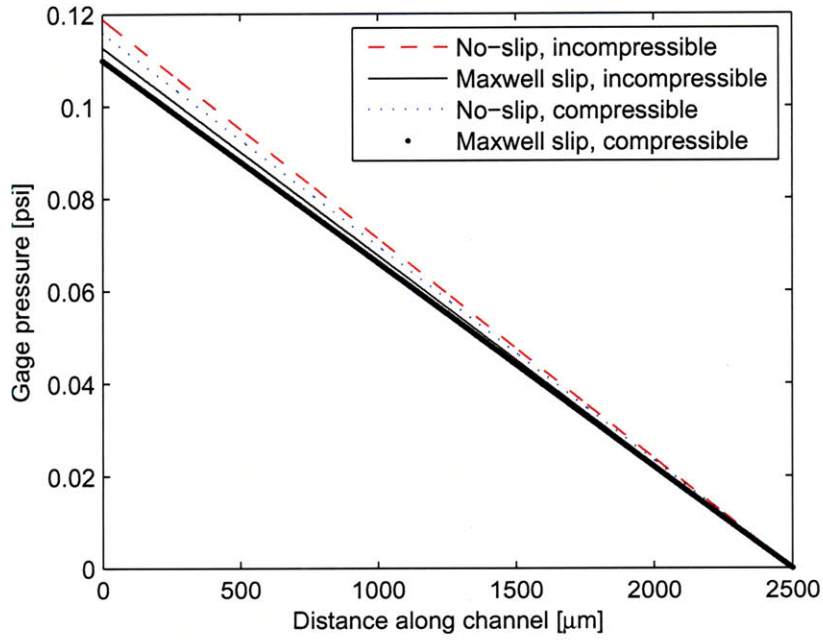

Figure 5-13. Pressure distribution (CH_4, 900 °C) along a 50 μm diameter circular pipe, according to compressible and incompressible flow models, calculated for $\dot{m} = 3.27 \times 10^{-10}$ kg/s.

which is identical to the result derived by Arkilic [413] for a microchannel having a rectangular cross-section. For slip flow, the ratio between compressible and incompressible mass flows is

$$\frac{\dot{m}_{s,c}}{\dot{m}_{n,c}} = 1 + \frac{4\mu}{\epsilon}\left(\frac{1}{\frac{p_i}{p_o}+1}\right) = 1 + 4\mathrm{Kn}\left(\frac{2-\sigma_v}{\sigma_v}\right)\left(\frac{1}{\frac{p_i}{p_o}+1}\right). \tag{5.39}$$

This is of the same form as Arkilic's solution for a rectangular cross-section. Eq. (5.39) verifies that the mass flow decreases as Kn increases, but this effect diminishes as the pressure ratio (p_i/p_o) increases. Because these solutions have the same form for different geometries, we can apply the correction factors derived for incompressible flow to the compressible flow solutions, to estimate the pressure drops for compressible flows in the triangular and trapezoidal sections. Computational verification of this assumption is necessary future work, such as by simulating compressible flows using FLUENT™.

5.3 Flow array design methodology

We can now design the KOH-etched microchannel array to have a desired distribution of (average) velocities in the growth sections of the channels. Note that the pressure drops in microchannel flows, and in pipe flows alike, are extremely sensitive to the channel diameter. For example, from Eq. (5.33), halving the channel diameter (D_h, or equivalently the width of a KOH-etched triangle) increases the resistance by a factor of 16. While this diminishes slightly in the slip regime, the pressure drop is still inversely proportional to at least D_h^3. The two-stage KOH-etched microchannel design (Fig. 5-1) takes advantage of this effect, allowing the depth of the self-terminating entry region to be varied across the array, while the depth of the growth section is equal for every channel. The depth of the entry channel is determined by the width (w) of the etch opening in the lithography mask, while the depth of the growth channel (d) is determined by the time of the KOH etch, and is therefore always greater than that of the deepest entry channel.[3]

A main goal of the array design is to achieve a wide velocity range across the array, with a uniform increment between the velocities in the growth regions of adjacent channels. However, the highly nonlinear relationship between pressure drop and channel width means that for very narrow channels, the sensitivity of the pressure drop exceeds the resolution of most conventional lithography processes for MEMS prototyping. For example, if a 10% increment in velocity is desired from one channel to the next, and the first entry channel is 5 μm wide, the entry next channel must be only 5.1 μm wide. It would be very difficult to establish this width increment using conventional techniques.

Instead of reaching vanishingly small width increments at low velocities and in areas of high sensitivity (e.g., very small differential flow rates between adjacent channels), the array design establishes a minimum allowable width increment (δw_{min}) between the entry regions of adjacent channels, and compensates the length of the entry region (L_e) to give the desired flow resistance and therefore the desired velocity in the growth region. This minimum increment is established by the lithography process, and for example is 0.25 microns for the conventional

[3] This is true as long as the etch time is not long enough for the growth region to also self-terminate; hence the growth channel is also much wider than the widest entry channel.

laser-written masks (Advance Reproductions) used for our process. All channels are of equal total length, which is the sum of the lengths of the entry and growth regions,

$$L_{total} = L_e + L_g. \tag{5.40}$$

5.3.1 Velocity scaling

To calculate the dimensions of the channels, the desired velocities in the growth regions must be known. Within the size constraints of the device and/or its package, the design accommodates an arbitrary progression of velocities among the growth channel regions of the array, and the progression is thoroughly treated here for some basic mathematical forms.

It is convenient to first establish the desired minimum ($V_{g,min}$) and maximum ($V_{g,max}$) average velocities among the growth channel regions, and to calculate the velocity range of the device as the number of orders of magnitude between these limits, which is

$$O_N = \log\left(\frac{V_{g,max}}{V_{g,min}}\right). \tag{5.41}$$

5.3.1.1 Scaling in logarithmic space

For a device spanning a wide velocity range, the velocities are conveniently scaled using a geometric sequence. First, the "middle" velocity, or the average velocity in logarithmic coordinates, is

$$V_{g,midlog} = V_{g,min}\left(10^{\frac{O_N}{2}}\right) \tag{5.42}$$

For an array of N channels, we index the channels by n and start with $n = 0$. By a geometric sequence, the growth velocity in the $(n+1)^{th}$ channel is equal to the velocity of the n^{th} channel, multiplied by a scaling factor. This is

$$V_{g,n} = V_{g,midlog}\left(10^{\frac{O_N}{2}}\right)^{S_n C_n{}^a}, \tag{5.43}$$

where

$$S_n = \text{sign}\left(n - \frac{N-1}{2}\right) \tag{5.44}$$

and

$$C_n = \text{abs}\left(\frac{2(n+1) - N - 1}{N-1}\right). \tag{5.45}$$

When the scaling factor is constant (corresponding to the case of $a = 1$ in Eq. 5.43), the distribution of velocities versus n is linear when the velocity axis is plotted on a logarithmic scale. If $a > 1$, the logarithm of the velocities varies parabolically with n.

This captures a multi-resolution approach to combinatorial flow experimentation. For example, a first array can be designed with $a = 1$ to explore a wide velocity range with uniformly scaled increments between adjacent channels, and a second array can be designed with $a > 1$ to explore a the behavior about a desired "nominal" velocity $V_{g,midlog}$, with high sensitivity.

Fig. 5-14 shows example velocity distributions given by linear-parabolic scaling, for $N = 45$ with $V_{g,min} = 0.001$ m/s and $V_{g,max} = 1.0$ m/s. In practice, the velocity magnitudes can also be scaled by adjusting the pressure drop across the device; therefore, if a point of interest is observed during experimentation with the first device, the pressure drop across the second device can be chosen so $V_{g,midlog}$ coincides with this point of interest (although there maybe side-effects of the pressure drop on the performance of the reaction of interest).

In contrast to the "two-sided" or "symmetric" distribution stated by Eq. (5.43), a "one-sided" distribution establishes a curve starting at $V_{g,min}$, given by

$$V_{g,n} = V_{g,min}\left(10^{O_N}\right)^{\left(\frac{n}{N-1}\right)^a}. \tag{5.46}$$

Fig. 5-15 shows example velocity progressions for this distribution.

5.3.1.2 Scaling in linear space

Another exemplary method of distributing the velocities in the array is to scale the values in a linear coordinate space, which typically gives a more narrow range of velocities than logarithmic scaling but enables a constant velocity increment between adjacent channels. In a linear space, the middle velocity is the normal average of the minimum and maximum velocities,

$$V_{g,midlin} = V_{g,min}\left(\frac{10^{O_N}+1}{2}\right). \tag{5.47}$$

For "two-sided" parabolic scaling in linear space,

$$V_{g,n} = V_{g,midlin}\left\{1+\left(\frac{10^{O_N}-1}{10^{O_N}+1}\right)S_n{C_n}^a\right\}, \tag{5.48}$$

where S_n and C_n are given by Eqs. (5.44) and (5.45), respectively. For "one-sided" scaling in linear space,

$$V_{g,n} = V_{g,min}\left\{1+\left(10^{O_N}-1\right)\left(\frac{n}{N-1}\right)^a\right\}. \tag{5.49}$$

Figs. 5-16 and 5-17 show example velocity progressions for the parabolic-linear scaling distributions.

Another method of distributing the velocities is to scale the increments using a power law. A symmetric distribution about $V_{g,midlin}$ scaled in this manner gives

$$V_{g,n} = V_{g,midlin}\left\{1+\left(\frac{10^{O_N}-1}{10^{O_N}+1}\right)S_n\left(\frac{b^{C_n}-1}{b-1}\right)\right\}, \tag{5.50}$$

where b is a scaling factor and $b = 1$ gives a linear progression. A one-sided distribution is given by

$$V_{g,n} = V_{g,min}\left\{1+\left(10^{O_N}-1\right)\left(\frac{b^{\frac{n}{N-1}}-1}{b-1}\right)\right\}. \tag{5.51}$$

Figs. 5-18 and 5-19 show example velocity progressions for the power-linear distributions.

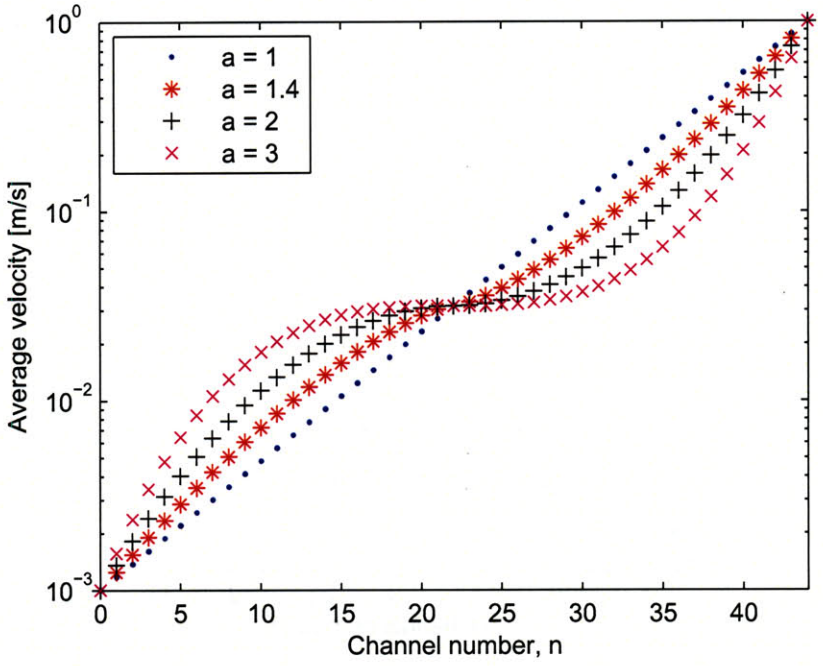

(a)

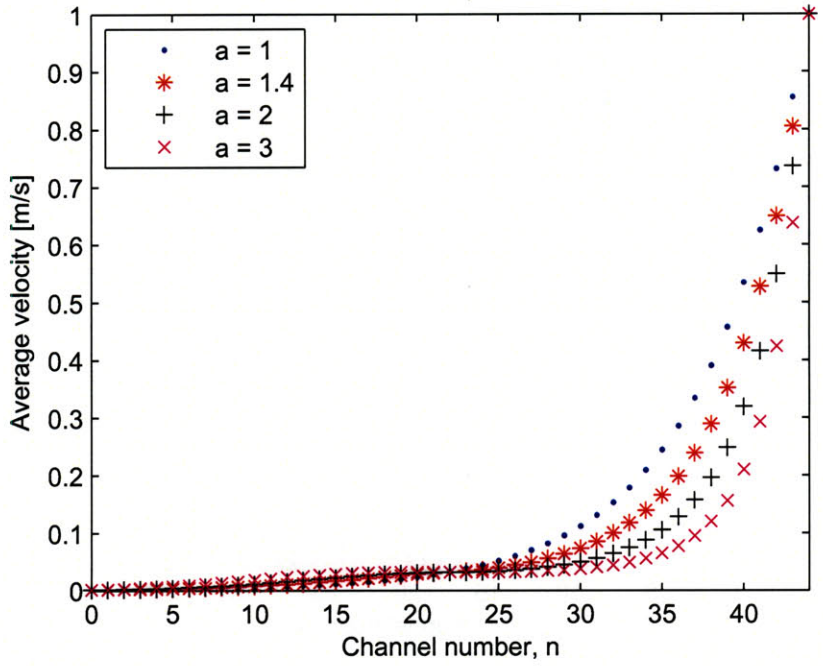

(b)

Figure 5-14. Example of "two-sided" parabolic velocity scaling in a microchannel array, in logarithmic coordinate space: (a) logarithmic scale plot; (b) linear scale plot.

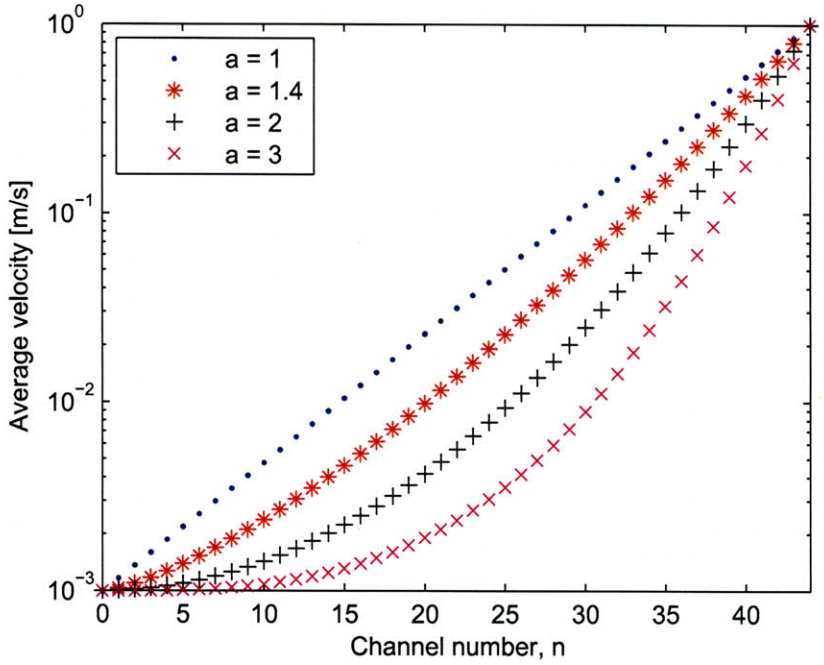

(a)

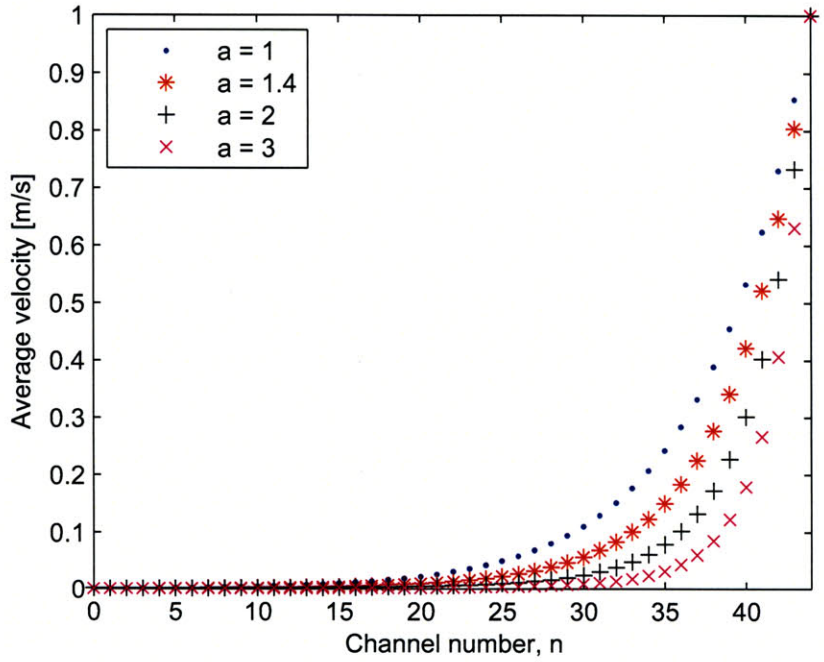

(b)

Figure 5-15. Example of "one-sided" parabolic velocity scaling in a microchannel array, in logarithmic coordinate space: (a) logarithmic scale plot; (b) linear scale plot.

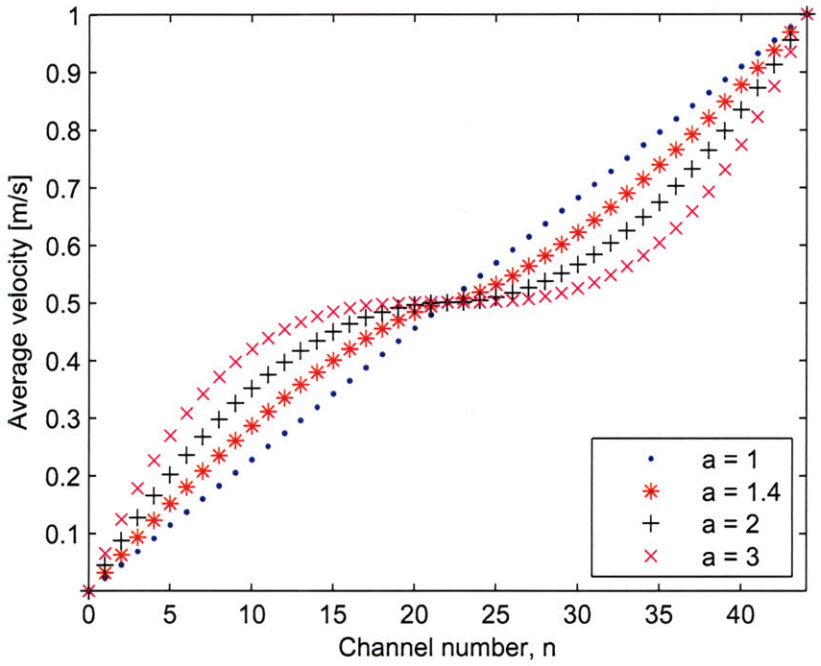

Figure 5-16. Example of "two-sided" parabolic velocity scaling in a microchannel array, in linear coordinate space.

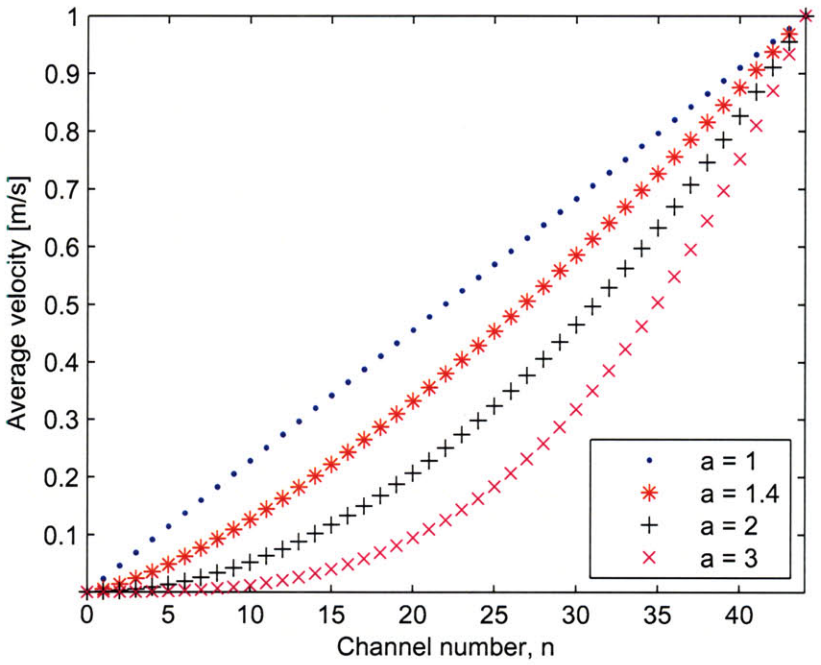

Figure 5-17. Example of "one-sided" parabolic velocity scaling in a microchannel array, in linear coordinate space.

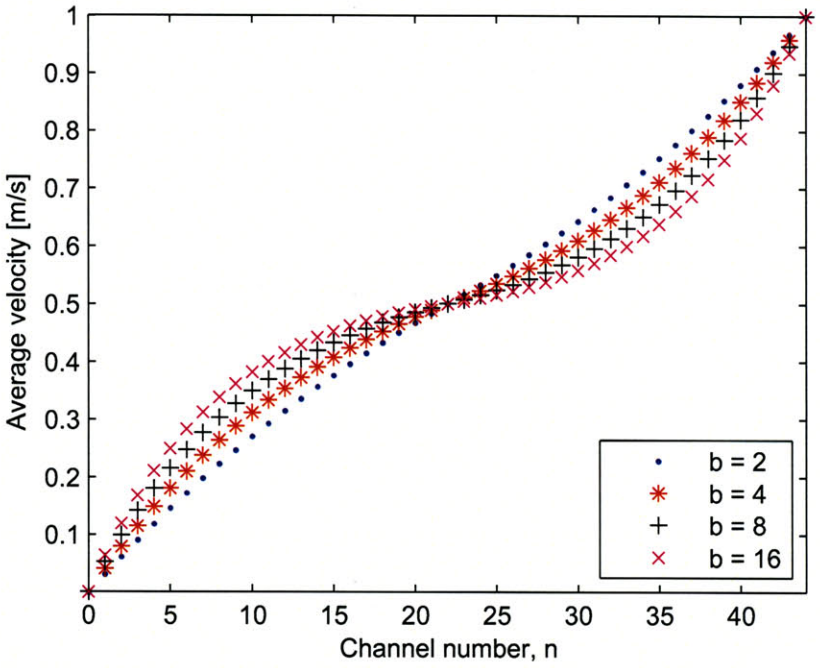

Figure 5-18. Example of "two-sided" power-law velocity scaling in a microchannel array, in linear coordinate space.

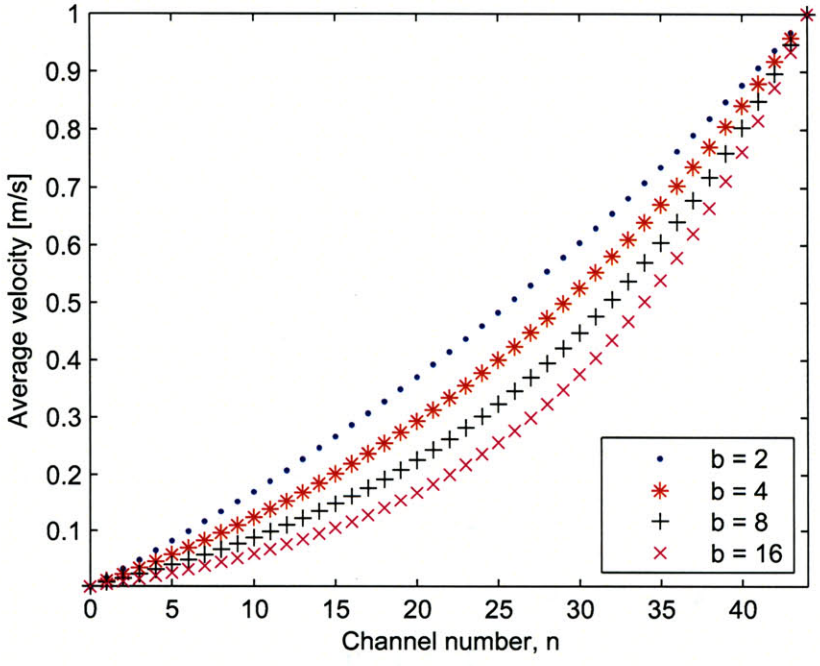

Figure 5-19. Example of "one-sided" power-law velocity scaling in a microchannel array, in linear coordinate space.

5.3.2 Channel geometry calculations

To determine the channel dimensions needed to give the desired progression of velocities in the growth regions, a relationship is first derived for the total pressure drop across one of the microchannels, using models of compressible slip flow in the entry region and incompressible slip flow in the growth region. This is justified by the classification of flow regimes in Fig. 5-3, and verified by Knudsen number calculations presented later. Also, because the pressure drop in the growth region is very small, compressibility in this region is negligible.

The total pressure drop across the array is equal for all channels because they are connected to reservoirs at the entry and exit of the array. For a particular channel n, this is the sum of the pressure drops across its entry ($\Delta p_{e,n}$) and growth ($\Delta p_{g,n}$) regions,

$$\Delta p_{total} = \Delta p_{e,n} + \Delta p_{g,n}. \tag{5.52}$$

A nominal value of Δp_{total} is specified for the calculations; however, Δp_{total} can be adjusted during operation of the device (e.g., 1–25 psi) to quasi-uniformly "tune" the velocities and flow rates in the channels.

Because flow in the growth region is incompressible, the pressure drop across the growth region ($\Delta p_{g,n}$) is independent of the outlet pressure. However, recalling Eq. (5.34), the entry region pressure drop ($\Delta p_{e,n}$) depends on the outlet pressure of the entry region. Furthermore, $\Delta p_{e,n}$ depends on the mass flow rate ($\dot{m}_n$) in the channel. While $\Delta p_{g,n}$ is most always negligible compared to $\Delta p_{e,n}$, $\dot{m}_n$ is formally calculated at the midpoint of the growth region. Using the ideal gas law,

$$\dot{m}_n = A_{g,n} V_{g,n} \left(\frac{\Delta p_{g,n}/2 + p_a}{R_g T} \right), \tag{5.53}$$

where $A_{g,n}$ is the cross-sectional area of the growth region (Eq. 5.24) and p_a is the outlet pressure of the array (assumed to be atmospheric pressure).

This formulation for $\dot{m}_n$ is substituted into the expression for the pressure drop across a circular pipe having compressible slip flow (Eq. 5.34), which is scaled for the triangular cross-section (Eq. 5.27), giving

$$\Delta p_{e,n} = B_{tri} \left(\frac{-C_{2,n} - \sqrt{C_{2,n}^2 - 2C_{1,n}\left(\dot{m}_n L_{e,n} - \frac{C_{1,n}(\Delta p_{g,n} + p_a)^2}{2} - C_{2,n}(\Delta p_{g,n} + p_a) \right)}}{C_{1,n}} \right). \tag{5.54}$$

The constant B_{tri} is independent of w and includes the correction factor for the triangular cross-section, such that

$$B_{tri} = 0.83 \left(\frac{\pi \tan\theta}{\left(1 + \frac{1}{\cos\theta}\right)^2} \right) = 0.49. \tag{5.55}$$

The constants $C_{1,n}$ and $C_{2,n}$ are calculated using the hydraulic diameter of the channel, Eq. (5.23), such that

$$C_{1,n} = -\frac{\pi w_{e,n}^4}{128 \mu R_g T} \left(\frac{\tan\theta}{1 + \frac{1}{\cos\theta}} \right)^4 = -0.0018 \left(\frac{w_{e,n}^4}{128 \mu R_g T} \right), \tag{5.56}$$

and

$$C_{2,n} = \frac{\pi \rho w_{e,n}^3}{2\epsilon} \left(\frac{\tan\theta}{1 + \frac{1}{\cos\theta}} \right)^3 = 0.2173 \left(\frac{\rho w_{e,n}^3}{\epsilon} \right). \tag{5.57}$$

Note that in Eq. (5.54), the pressure at the inlet of the growth region ($\Delta p_{g,n} + p_a$) is substituted for the outlet pressure (p_o). The pressure drop across the growth region is formulated using Eq. (5.33), scaled for a trapezoidal cross-section, giving

$$\Delta p_{g,n} = B_{trap} \left(\frac{128 \mu V_{g,n} L_{g,n}}{\pi} \right) \left(\frac{w_g \tan\theta - d_g}{w_g \tan\theta} \right) \left(\frac{2w_g - \frac{2d_g}{\tan\theta} + \frac{2d_g}{\sin\theta}}{4 w_g d_g - \frac{4d_g^2}{\tan\theta}} \right)^4, \tag{5.58}$$

where

$$B_{trap} = 0.85\pi \left(\frac{4 w_g d_g - \frac{4d_g^2}{\tan\theta}}{2w_g - \frac{2d_g}{\tan\theta} + \frac{2d_g}{\sin\theta}} \right)^2 \left(\frac{w_g \tan\theta}{w_g \tan\theta - d_g} \right). \tag{5.59}$$

Combining Eqs. (5.58) and (5.59) and substituting $L_g = L_{total} - L_e$,

$$\Delta p_{g,n} = 108.8 (L_{total} - L_{e,n}) \mu V_{g,n} \left(\frac{2w_g - \frac{2d_g}{\tan\theta} + \frac{2d_g}{\sin\theta}}{4 w_g d_g - \frac{4d_g^2}{\tan\theta}} \right)^2. \tag{5.60}$$

Having assembled all the terms of Eq. 5.52, this is solved for $L_{e,n}$ numerically using MATLAB™, for each corresponding pair of $w_{e,n}$ and $V_{g,n}$ values and the desired Δp_{total}. To minimize leaks between adjacent channels (section 5.5.1), it is desirable for the entry channels to be as long and as wide as possible, and for the difference in length between adjacent entry channels ($L_{e,n}$ - $L_{e,n-1}$) to be as small as possible. The maximum length of the array and the maximum depth of the entry channels (which must guarantee that the etches self-terminate) limit on these values. In the designs which have been fabricated, the total length of the array is 12.5 mm, and the length of the first entry region is specified to be as close as possible to 5 mm. The width of the entry region must be rounded to the nearest 0.25 μm, as constrained by the mask-writing process. After this starting point, and indexing through the array, the width of each entry region is calculated to the nearest 0.25 μm increment that minimizes the differential length ($L_{e,n}$ - $L_{e,n-1}$).

5.4 Parameters of test devices

Six device designs are detailed and have been fabricated: three "wide range" devices with a linear progression of velocities in logarithmic space, and three "high resolution" devices with a two-sided parabolic progression of velocities in logarithmic space. Table 5.2 lists the common characteristics of the devices, and Table 5.3 compares the values of important design parameters. The devices are designed for a 1:1:1 mixture of CH_4:H_2:Ar, with a total flow rate of 7.50 sccm, at an operating temperature of 900 °C. Note that in all cases the four sacrificial high-flow channels receive most of the flow, to facilitate purging of the device. For example, the array having the highest flow resolution spans the lower 40% of the velocity range using a

logarithmic-parabolic profile, and has a total flow of only 0.0032 sccm (1.04×10^{-5} atm-cc/sec at 20 °C) through the growth channels ($Q_{g,tot}$). This is far less than the flow of 1.87 sccm through each sacrificial channel, and only 0.04% of the total flow through the device.

Because of the strongly nonlinear dependence of the entry channel resistance on w_n, the required L_e varies nonlinearly with w_n and reaches several local maxima as the width increment is changed by the algorithm which calculates the channel geometry. This maximum occurs where the required change in growth velocity specified by $(V_{g,n+1} - V_{g,n})$ balances the decrease in resistance from incrementing w. The velocities in the entry channels are much higher than the velocities in the growth regions; however, because flow is laminar, the sudden expansion at the channel junctions is not a concern.

In practice, scaling the pressure drop across the array scales[4] the $V_{g,n}$ distribution. The first logarithmic-linear design explores a very wide parameter space, and the logarithmic-parabolic design can be tuned to explore a region of this parameter space about a desired nominal velocity, at very high resolution, by adjusting the pressure drop. The total flow rates through the devices can easily be maintained by standard mass flow controllers or high-resolution rotameters; however, the difference in flow rate between adjacent channels is as low as 10^{-5} sccm, which is far below the limits of external gas delivery hardware.

Multi-layer fabrication techniques or methods incorporating channel arrays in series, could be used to create a second controllable pressure reservoir, which would enable bidirectional adjustment of the spread of the velocity distribution in the growth channel regions. Further, a gas mixer could be incorporated in the microchannel network, so each channel receives a different mixture of reactants, or so the concentration of the rate-determining reactant is equal and independent of the flow velocity in each channel.

A less complex array design would have just a parallel array of KOH-etched self-terminating channels, with no time-terminated growth sections. However, this design lacks the two main advantages of the stepped channel design for conducting a parametric reaction study: the uniform cross-section (hence a uniform velocity profile) of each growth region; and the ability to use the length of the entry region to modulate the resistance of the growth section, therefore achieving a velocity resolution far beyond what would be dictated by lithography limits on the width increment between adjacent channels.

[4]The scaling is linear, assuming Δp_e always $\gg \Delta p_g$ and negligible compressibility effects, which would be true to at least first-order. The pressure-flow relation for compressible flow is definitely nonlinear, but the effects of compressibility are more important in determining the pressure drop over long channels, rather than the differentials between channels with slightly different geometries.

Parameter	Value
Total channel length, L_{total}	12.5 mm
Total flow rate (1:1:1 CH_4:Ar:H_2, 900 °C)	7.50 sccm
Resolution of increment in width of entry regions, $\Delta w_{e,min}$	0.25 μm
Pressure drop across array, Δp_{total}	4 psi
Width of growth channels, w_g	100 μm
Depth of growth channels, d_g	55 μm
Center-to-center distance between growth channels	200 μm
Number of sacrificial "dump" channels	4
Length of sacrificial "dump" channels	14 mm

Table 5.2. Common characteristics of first-generation KOH-etched microchannel arrays (total of seventeen devices and six different designs on each 150 mm diameter wafer).

Device	N	N_t	$w_{e,0}$ [μm]	$V_{g,min}$ [m/s]	$V_{g,mid}$	$V_{g,max}$	O_N	a	$Q_{g,tot}$ [sccm]	w_d	Q_d
Wide full (Figs. 5-20 and 5-21)	44	6	6.00	0.0005	0.0224	1.0	3.301	1.00	0.311	181	1.80
Wide low (60% of full, Fig. 5-22)	44	3	5.50	0.0005	0.0049	0.047	1.981	1.00	0.024	184	1.87
Wide high (60%, Fig. 5-23)	44	4	13.25	0.011	0.102	1.00	1.981	1.00	0.496	179	1.75
High-res low (40%, Figs. 5-24 and 5-25)	21	21	6.00	0.0005	0.0023	0.0105	1.320	2.00	0.0032	184	1.87
High-res mid (40%, Fig. 5-26)	21	21	11.25	0.0049	0.0224	0.102	1.320	2.00	0.031	184	1.87
High-res high (40%, Fig. 5-27)	21	21	20.50	0.0478	0.219	1.00	1.320	2.00	0.305	181	1.80

Table 5.3. Calculated flow parameters of fabricated first-generation KOH-etched microchannel arrays.

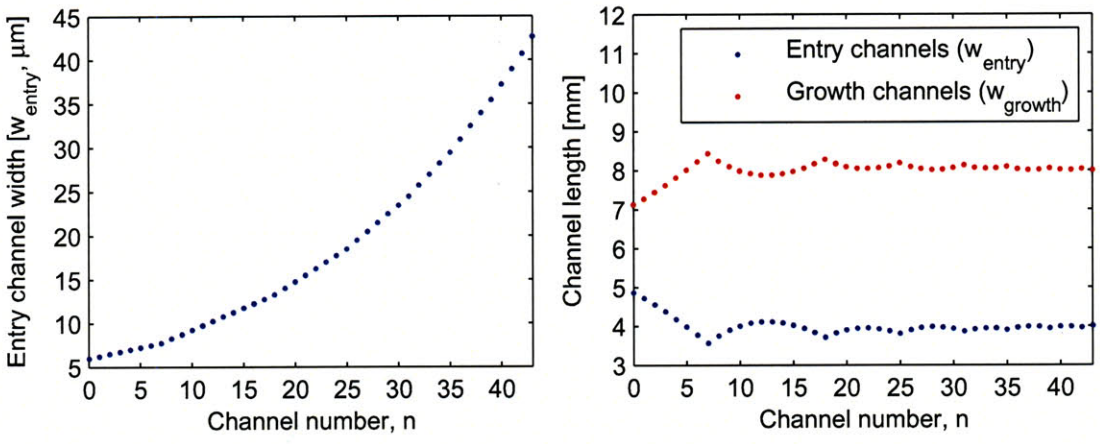

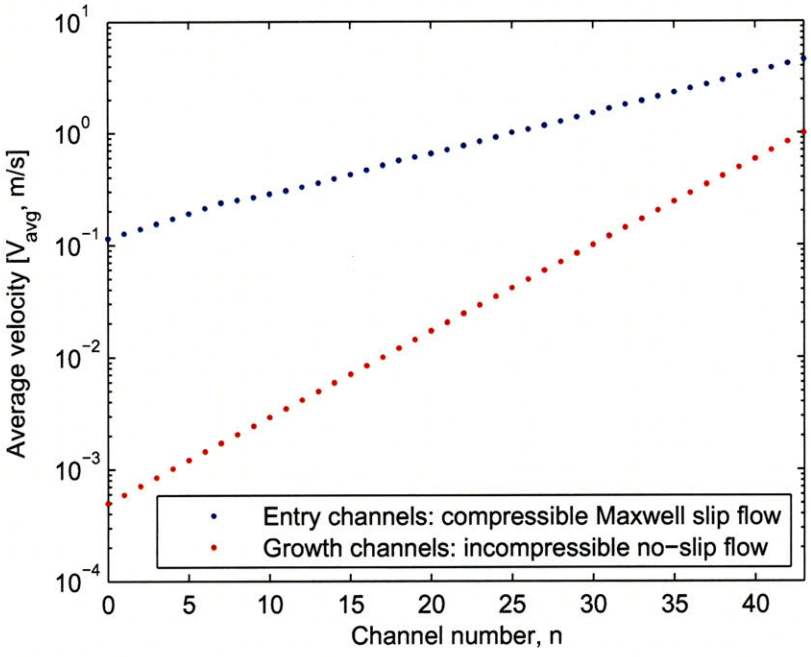

Figure 5-20. Characteristics of logarithmic-linear full velocity range ("wide full") microchannel array: (a) entry region widths; (b) channel lengths; (c) flow velocities.

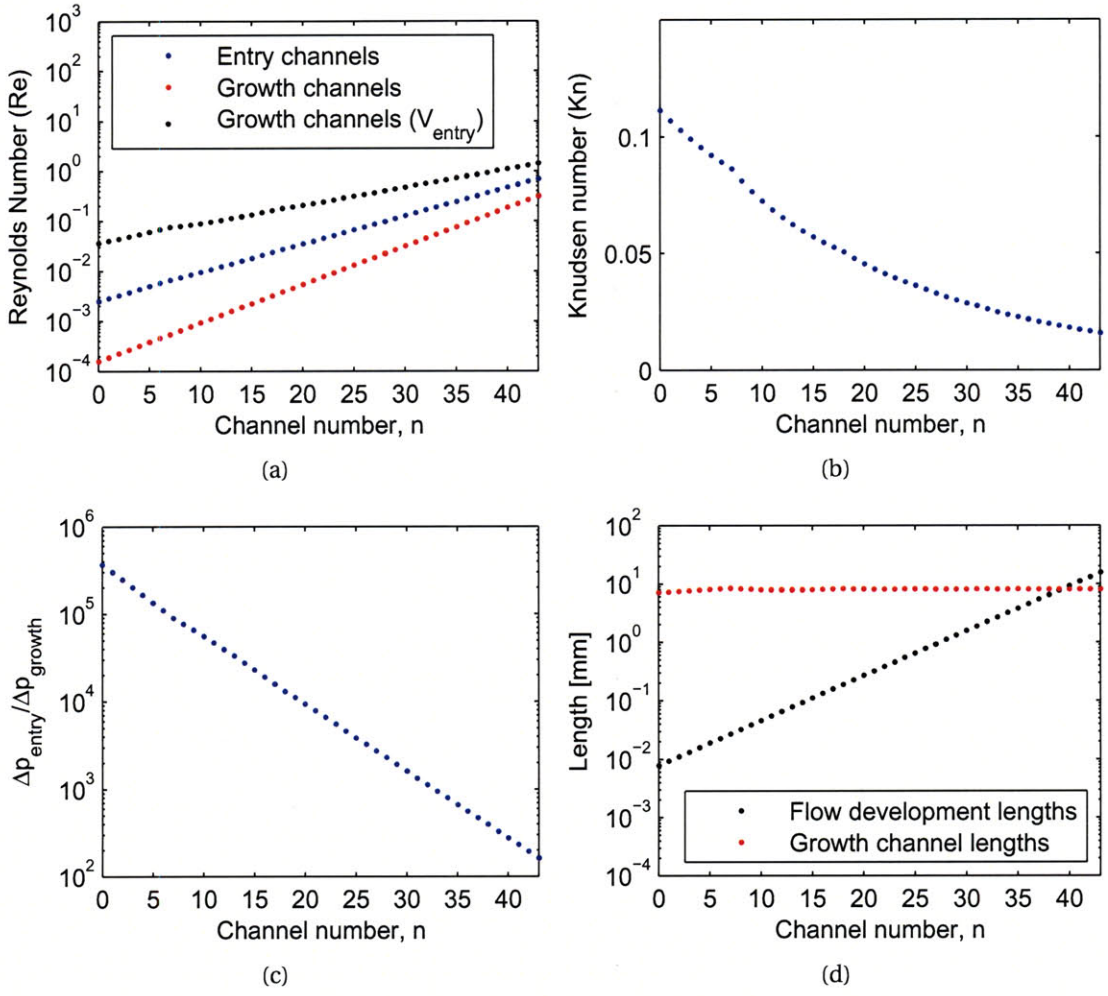

Figure 5-21. Further characteristics of wide full microchannel array: (a) Reynolds numbers of flows in entry and growth regions; (b) Knudsen numbers of flows in entry regions; (c) pressure drop ratios between entry and growth regions; (d) flow development lengths of growth regions.

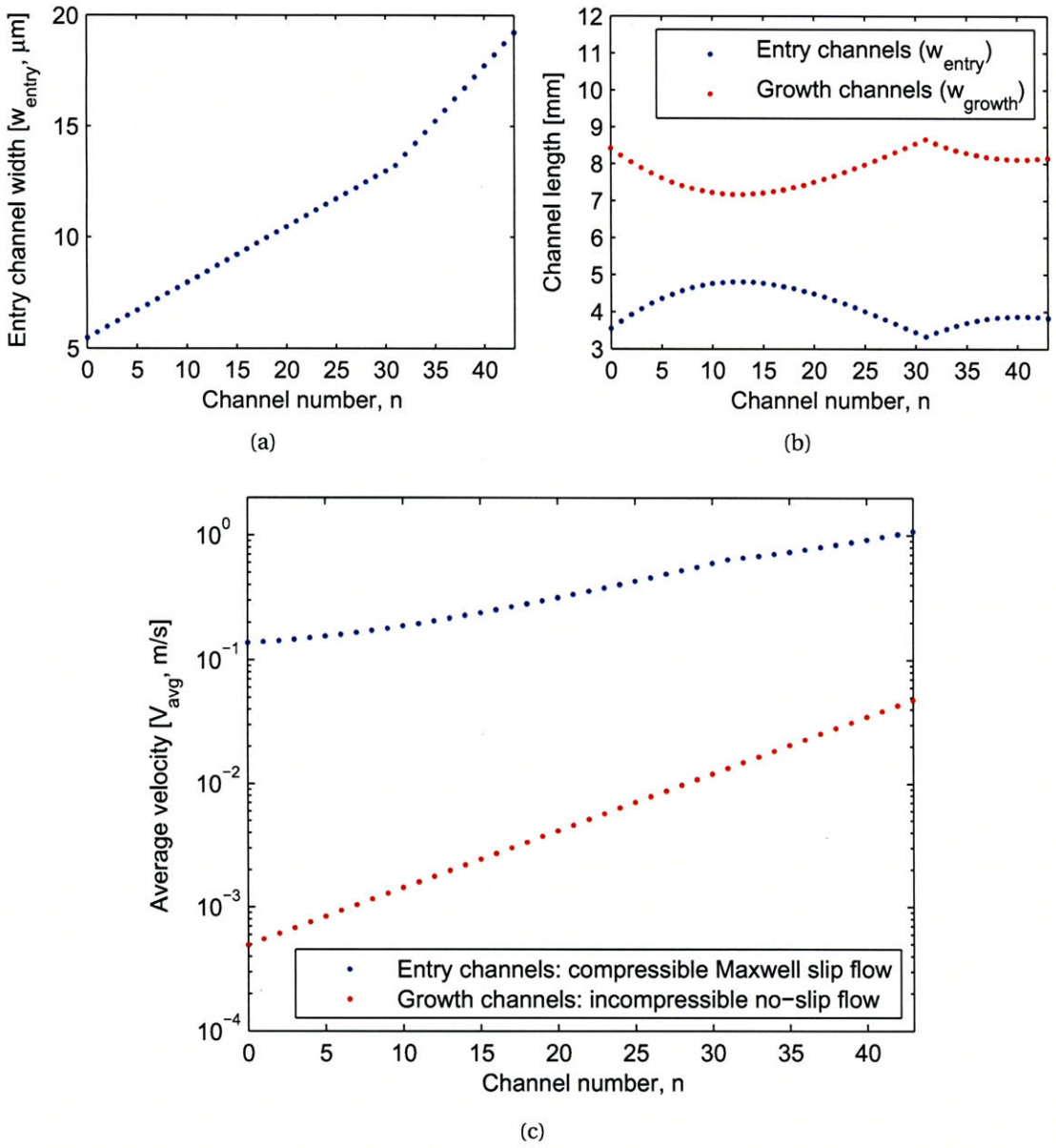

Figure 5-22. Characteristics of logarithmic-linear low-60% (wide low) velocity range microchannel array: (a) entry region widths; (b) channel lengths; (c) flow velocities.

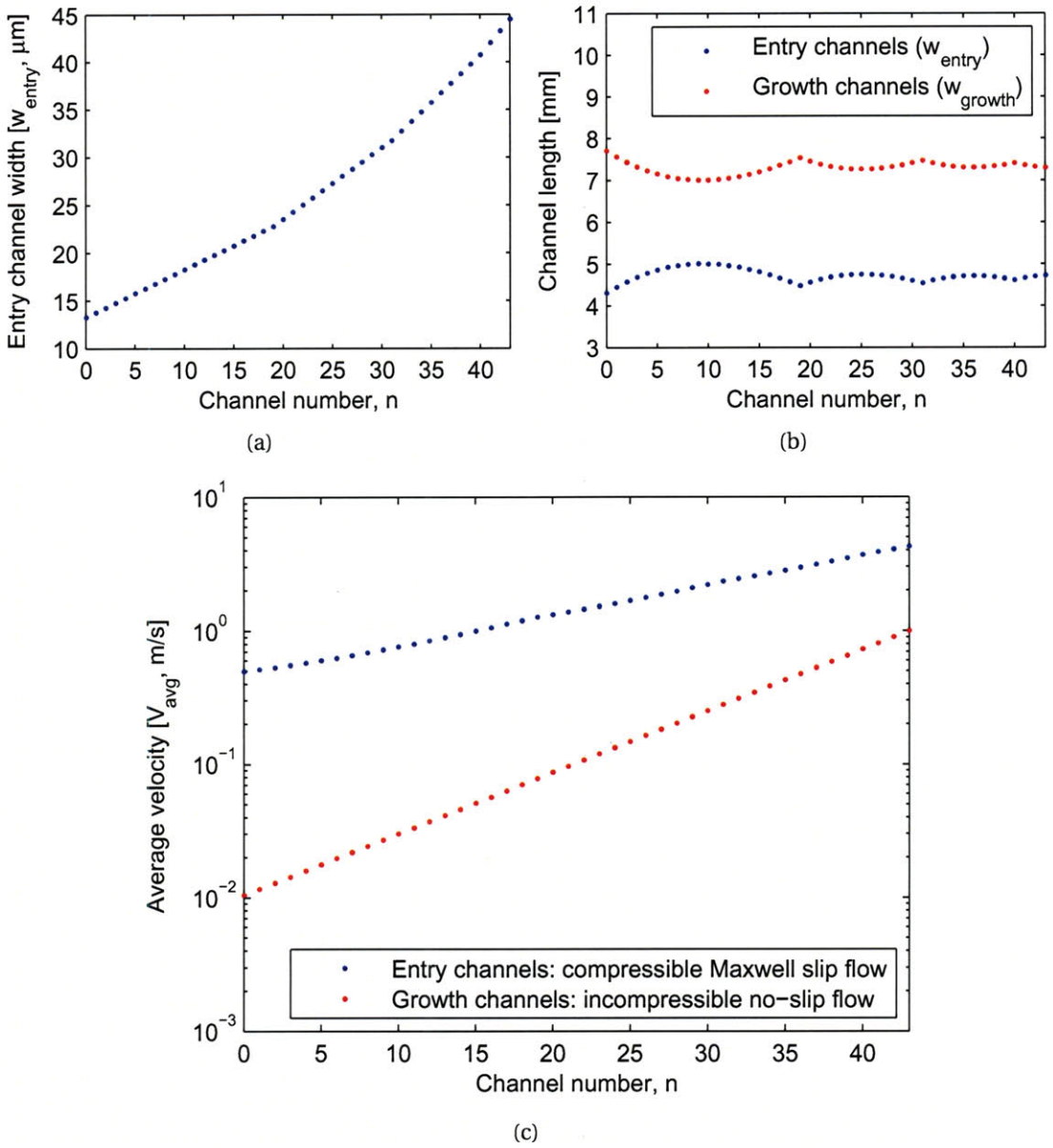

Figure 5-23. Characteristics of logarithmic-linear high-60% (wide high) velocity range microchannel array: (a) entry region widths; (b) channel lengths; (c) flow velocities.

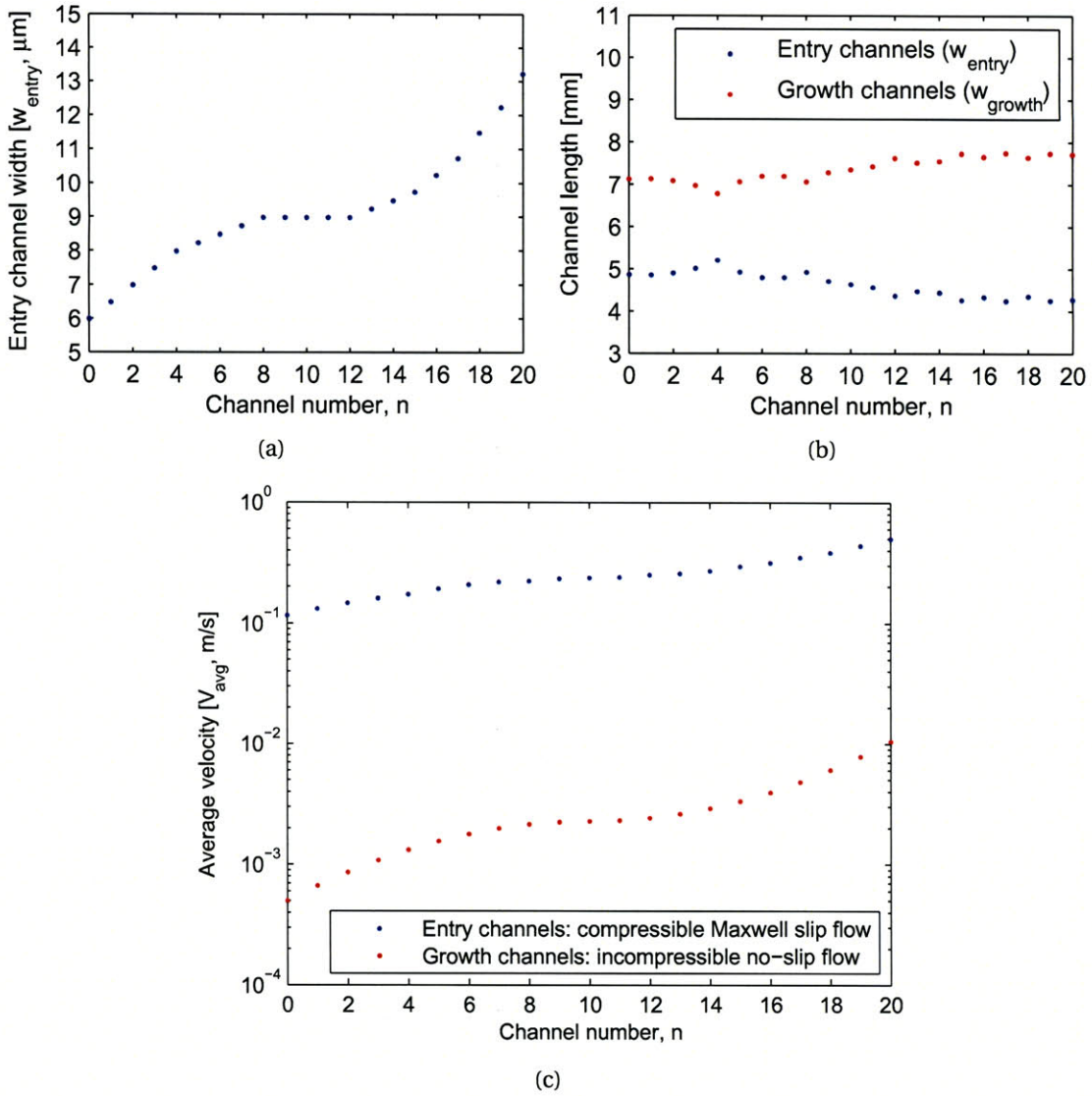

Figure 5-24. Characteristics of logarithmic-parabolic low-40% (high-res low) velocity range microchannel array: (a) entry region widths; (b) channel lengths; (c) flow velocities.

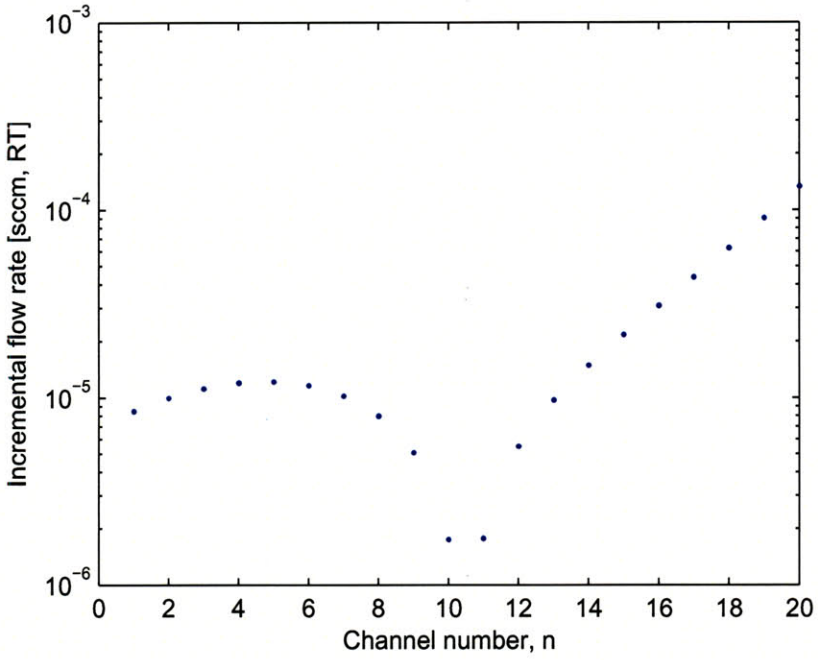

(a)

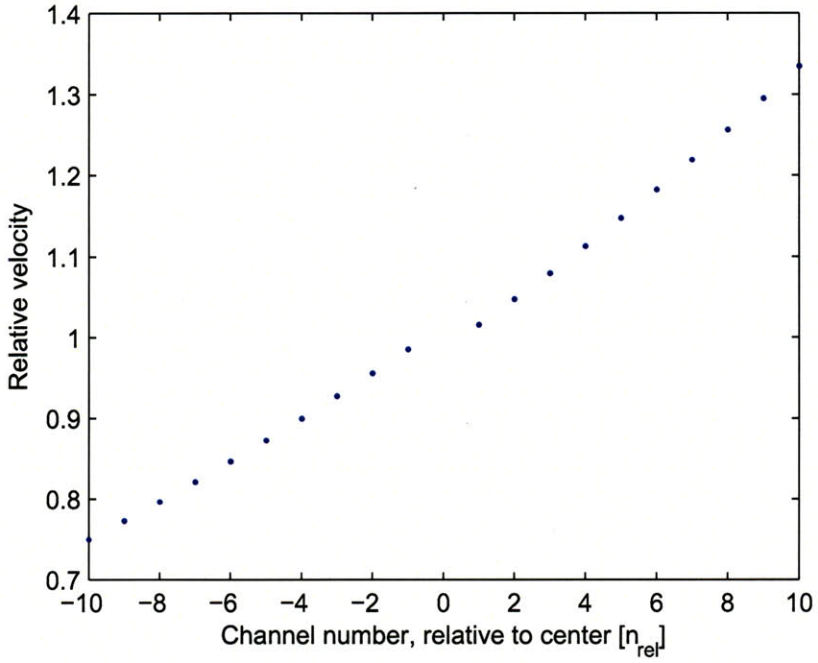

(b)

Figure 5-25. Further characteristics of high-res low velocity range microchannel array: (a) difference of flow rates between adjacent channels; (b) ratio of average velocities (in growth channel regions) between adjacent channels.

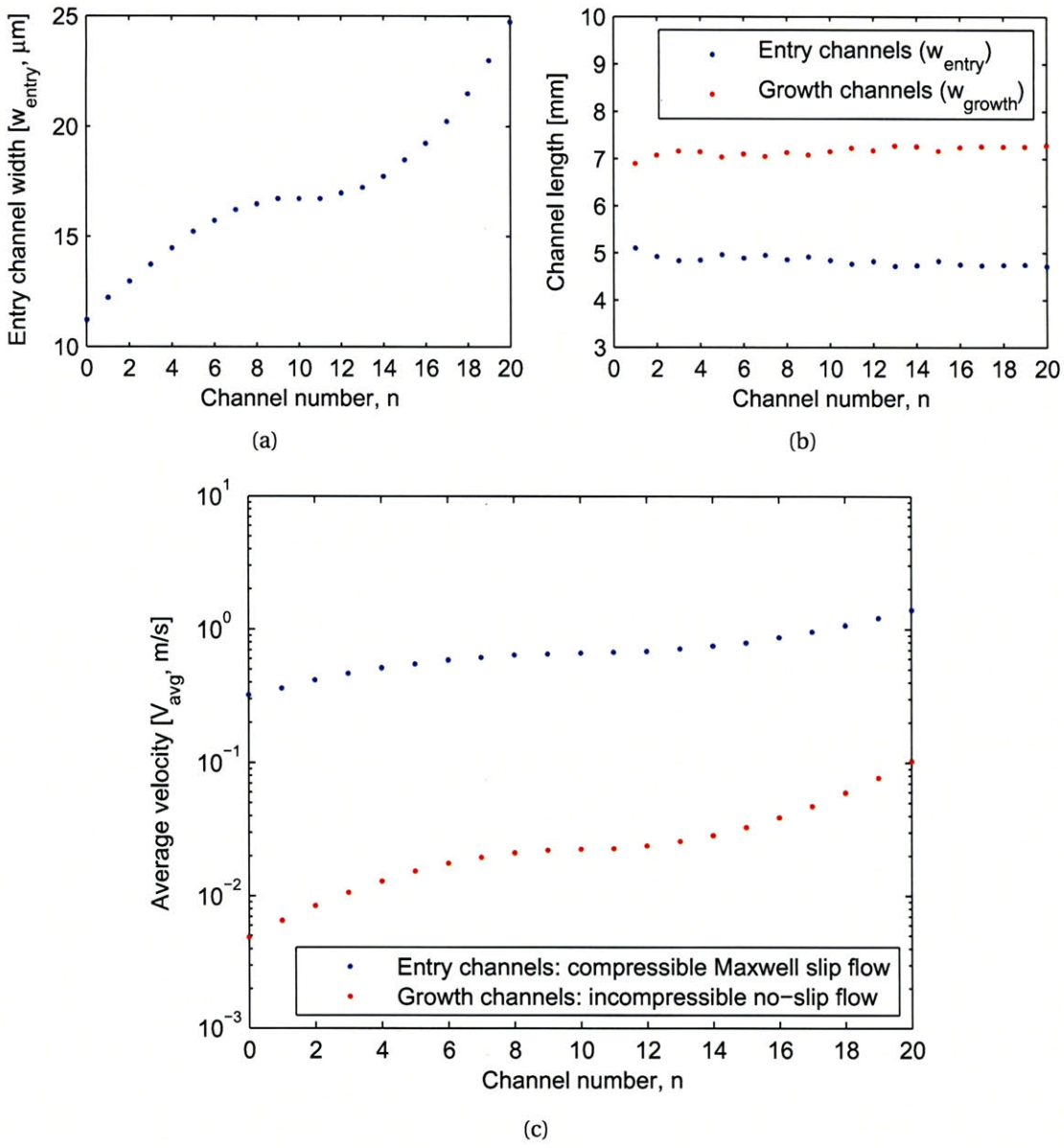

Figure 5-26. Characteristics of logarithmic-parabolic middle-40% (high-res mid) velocity range microchannel array: (a) entry region widths; (b) channel lengths; (c) flow velocities.

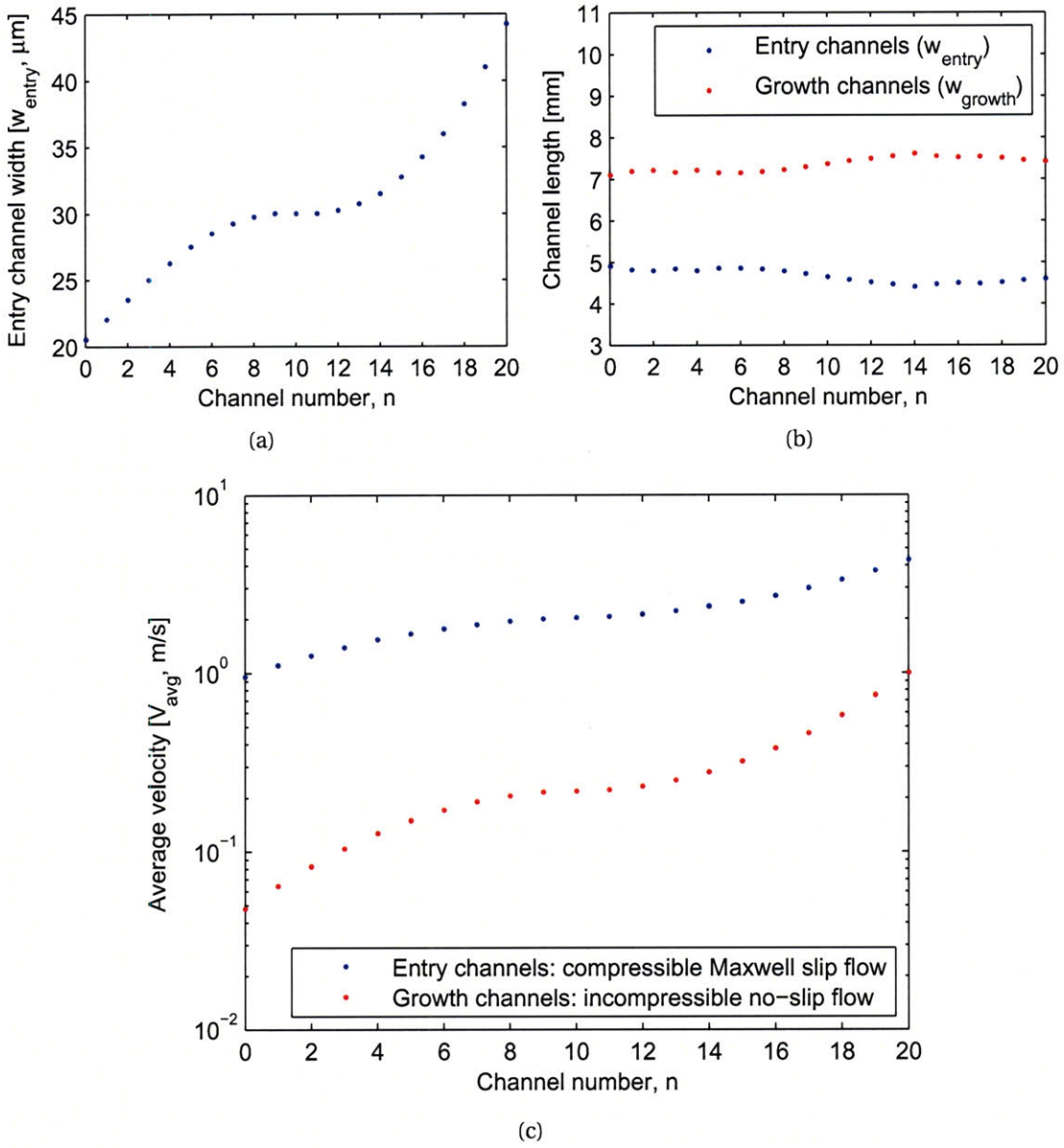

Figure 5-27. Characteristics of logarithmic-parabolic high-40% (high-res high) velocity range microchannel array: (a) entry region widths; (b) channel lengths; (c) flow velocities.

5.5 Error analysis

5.5.1 Models of leaks between channels

For *ex situ* characterization of the nanostructures grown in the microchannels, a reversible non-destructive seal between the enclosing package and the top surface of the device is required. This is accomplished using an interface between a non-polished and a polished silicon surface, where the roughness of the non-polished surface permits leak flows between the pressurized input reservoir and the channels, and between adjacent channels. Modeling of these leaks, and design of compensating features to reduce the leaks, are critical to understand the performance limits of the microchannel array.

The flow through the gap between the sealing surfaces is modeled as a free-molecular flow between two parallel plates. This flow is inversely related to the square of the gap height (h), and is calculated by Karniadakis and Beskok [415] as

$$\dot{M}_{leak} = \frac{wh^2 \Delta p_{leak}}{12L} \left(\sqrt{\frac{\pi}{2R_g T}} \right) \bar{\alpha} \left(1 - \frac{6}{b} \right), \tag{5.61}$$

where w is the width of the gap (assuming $w \gg h$), L is the length of the gap along the flow direction (assuming $l \gg h$), Δp_{leak} is the pressure drop across the gap, and $\bar{\alpha}$ and b are scaling parameters. The gap height is estimated as the RMS roughness of the non-polished surface, which is measured as $\approx 0.15\,\mu$m (Zygo NewView). In practice, the RMS value may be an overestimate of the true gap size because most of the defects in the non-polished surface are pits (Fig. 5-28), which are not continuous flow paths for the leak.

A simple model of the leaks within the microchannel device is based on superposition of four dominant leak types:

- **Mode 1:** Flow leaking between the entry regions of adjacent channels (Fig. 5-29a);
- **Mode 2:** Flow leaking between the output end of the entry region of one channel and the beginning of the growth region of the adjacent channel (Fig. 5-29b);
- **Mode 3:** Flow leaking from the input reservoir, through the gap between the device and the cap, and into the entry regions (Fig. 5-30a);
- **Mode 4:** Flow leaking from the input reservoir, through the gap between the device and the cap, and into the growth regions (Fig. 5-30b).

First, leaks are caused by the length difference between adjacent channels; this length difference is necessitated by the resolution of the lithography process for device fabrication. Points along adjacent entry channels and equidistant from the input reservoir will be at slightly different pressures. Therefore, there will be a leak across the land between the channels, from the longer entry region to the shorter entry region, and to the beginning of the growth region adjacent to the longer entry region. For analysis, this leak is separated into a mode 1 leak between the adjacent entry regions, and a mode 2 leak between the end of the entry region and the beginning of the adjacent growth region. Note that if adjacent entry regions have identical geometry, the mode 1 and mode 2 leaks are absent. Further, when the leaks must be reduced to

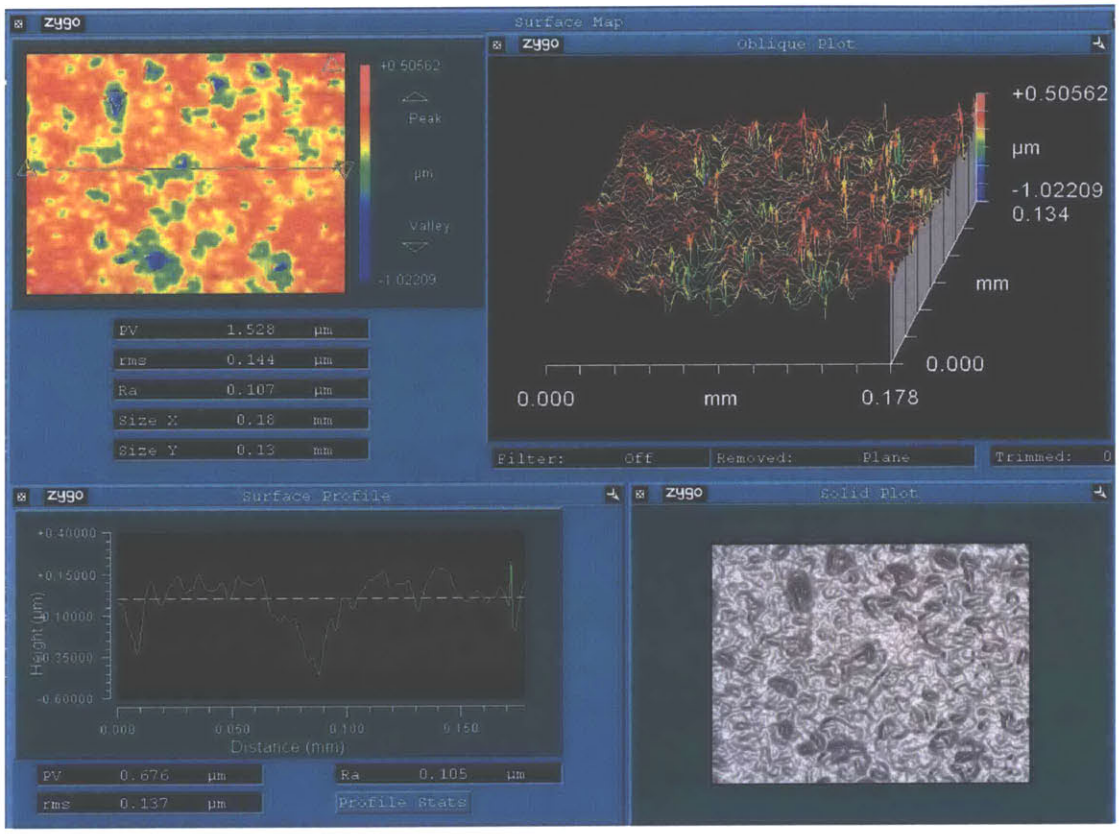

Figure 5-28. Optical surface profilometry measurement (Zygo NewView) of non-polished silicon wafer surface coated with ≈0.5 μm Si_3N_4, giving RMS roughness of 0.15 μm, dominated by pit-type defects. The roughness of the polished surface (≈4 nm) is negligible.

increase the flow resolution of the device, the channels can be patterned in "triplets" (Fig. 5-31), where the middle channel of each triplet is guarded against mode 1 and mode 2 leak flows by the identical adjacent channels.

Second, leaks occur from the input reservoir to the entry and growth regions. These are independent of the relative dimensions of the channels. Mode 3 leaks go from the input reservoir, along the land between adjacent entry regions, and spread into the entry regions. Mode 4 leaks go from the input reservoir, along the land between adjacent entry regions, and dump into the growth regions. Mode 3 and mode 4 leaks are decoupled from each other in the model, such that mode 3 only considers flow leaking into the entry regions, and mode 4 only considers flow which bypasses the entry regions and flows through the gap along the land until it is released into the growth regions.

Figs. 5-29 and 5-30 also show resistance network models for the leak flows, where the resistances are summed by assuming linear pressure-flow relationships. Recalling that the growth regions are always at atmospheric pressure, each leak occurs between an entry "node" at the reservoir pressure and an exit "node" at atmospheric pressure. While gas compressibility dictates a nonlinear pressure-flow relationship in the leak gaps and entry channels, the accuracy of a linear estimate is decidedly within the bounds of error established by other assumptions

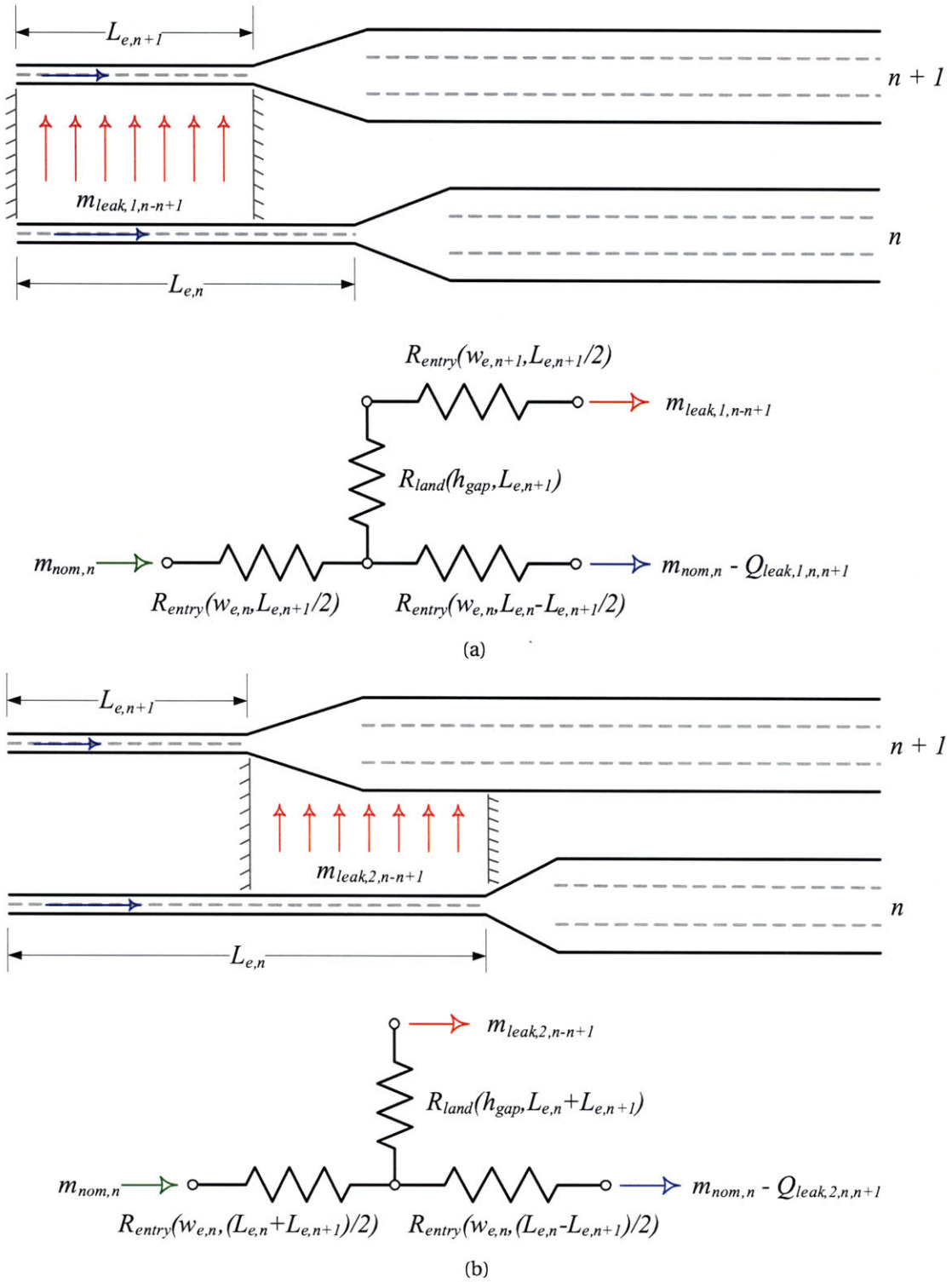

Figure 5-29. Models of (a) mode 1 and (b) mode 2 leaks between adjacent microchannels.

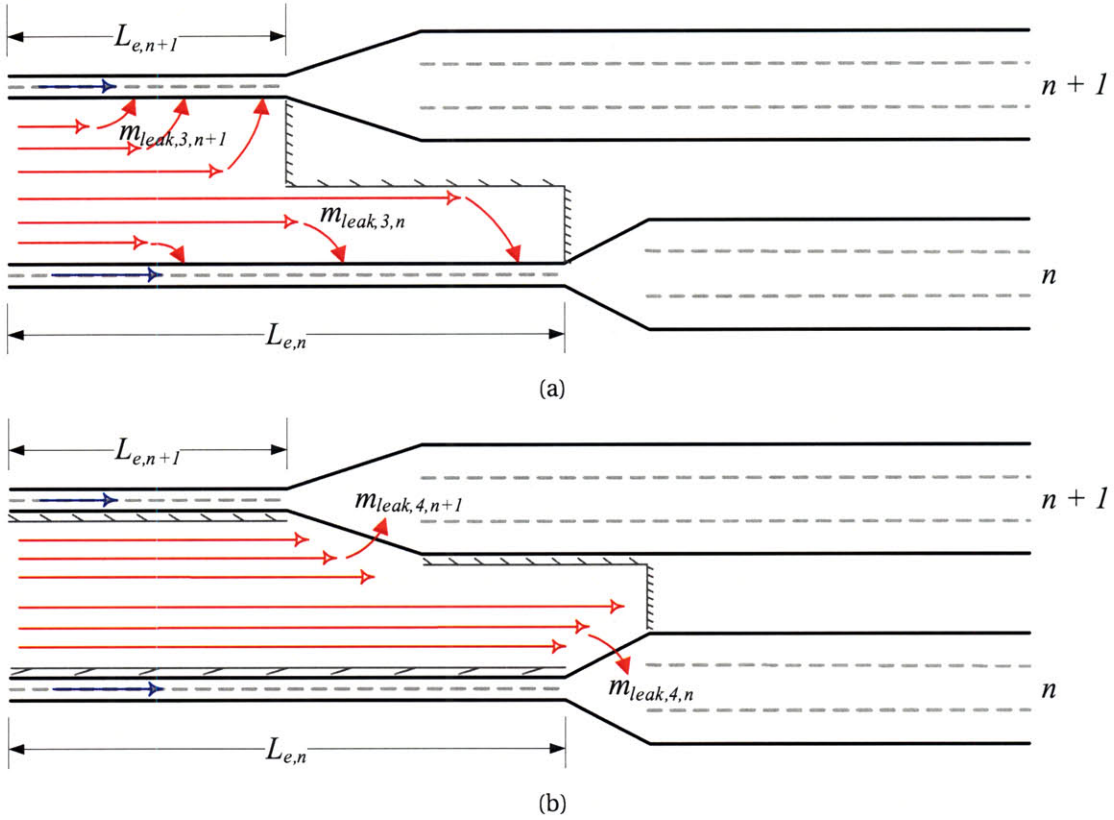

Figure 5-30. Models of (a) mode 3 and (a) mode 4 leaks between adjacent microchannels.

of the model. A particular bounding assumption is our estimate of the effective leak gap height based on a surface measurement of the non-polished side of a silicon wafer.

The leaks between channels are calculated independently, so the total flow in each channel is calculated by summing the nominal flow ($\dot{m}_n$) with the leaks to neighboring channels,

$$\dot{m}_{n,tot} = \dot{m}_n + \dot{m}_{leak,n,n-1} + \dot{m}_{leak,n,n+1}. \tag{5.62}$$

Here, $\dot{m}_{leak,n-1,n-1}$ is the leakage flow from the channel n to channel $n-1$, which is the sum of the individual leak $(n, n-1)$ flows for the four modes.

Leak calculations for the six array designs demonstrate that the mode 1 and mode 2 leaks are dominant; in the low-velocity channels these leaks can introduce up to 100% error in the flow rate through the respective growth channel regions (e.g., Fig. 5-32 for the wide full device). Localized triplet compensation is used to reduce the leaks at points where the differential change in length of the growth regions (e.g., the maxima and minima in 5-20b) causes a single channel to receive positive leak flows from both neighboring channels. Based on this model we expect to achieve a minimum flow of 0.001 m/s compared to the design target of 0.0005 m/s, along with slight reversals in the velocity progression.

All channels of the high-res devices are compensated by the triplet method. For example, calculations for the high-res mid device (Figs. 5-34 and 5-35) show that the compensation method preserves the ordinal velocity progression across the array.

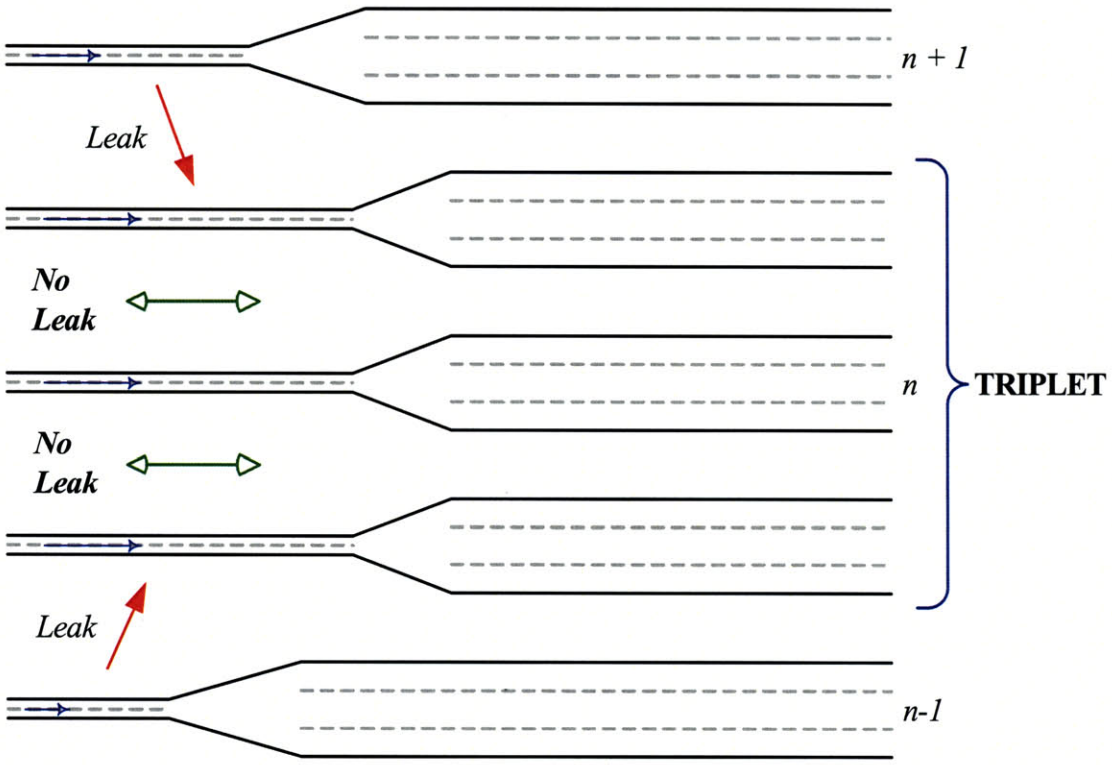

Figure 5-31. "Triplet" channel method of leak compensation, whereby three identical microchannels are fabricated. The middle channel of the "triplet" is guarded against mode 1 and mode 2 leaks by the adjacent channels.

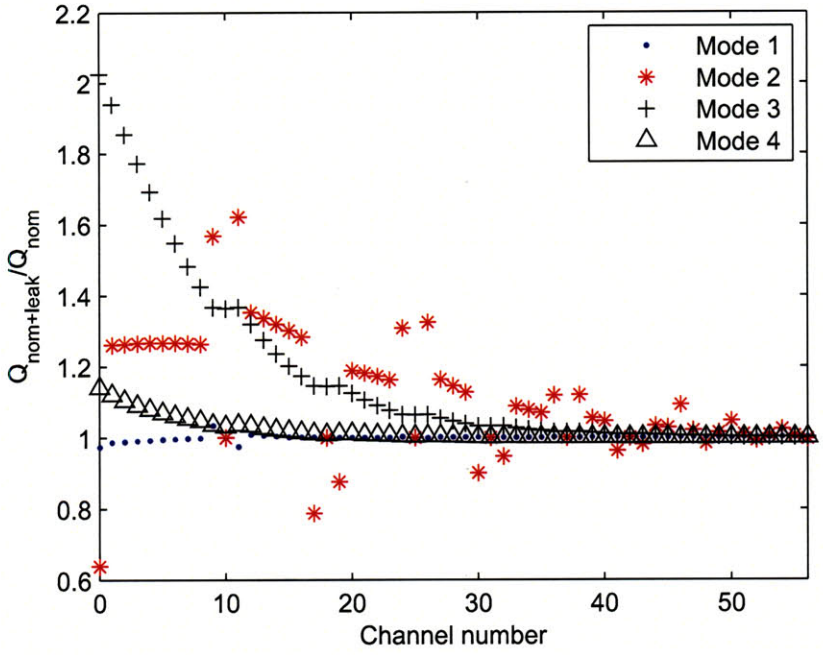

(a)

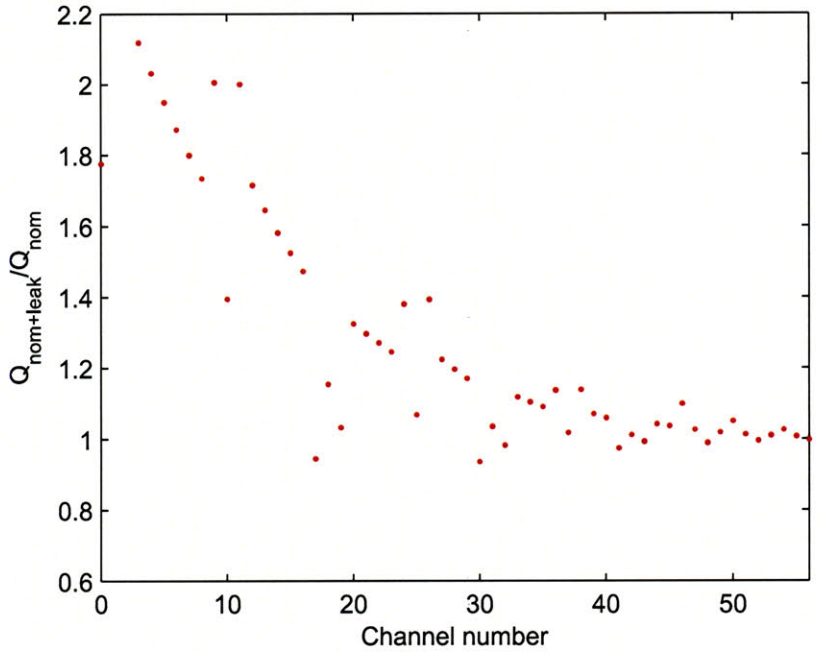

(b)

Figure 5-32. Analysis of leak flows between channels in wide full microchannel device, with localized triplet channel compensation: (a) flow rate errors introduced by each leak mode; (b) sum of flow rate errors caused by all leak modes.

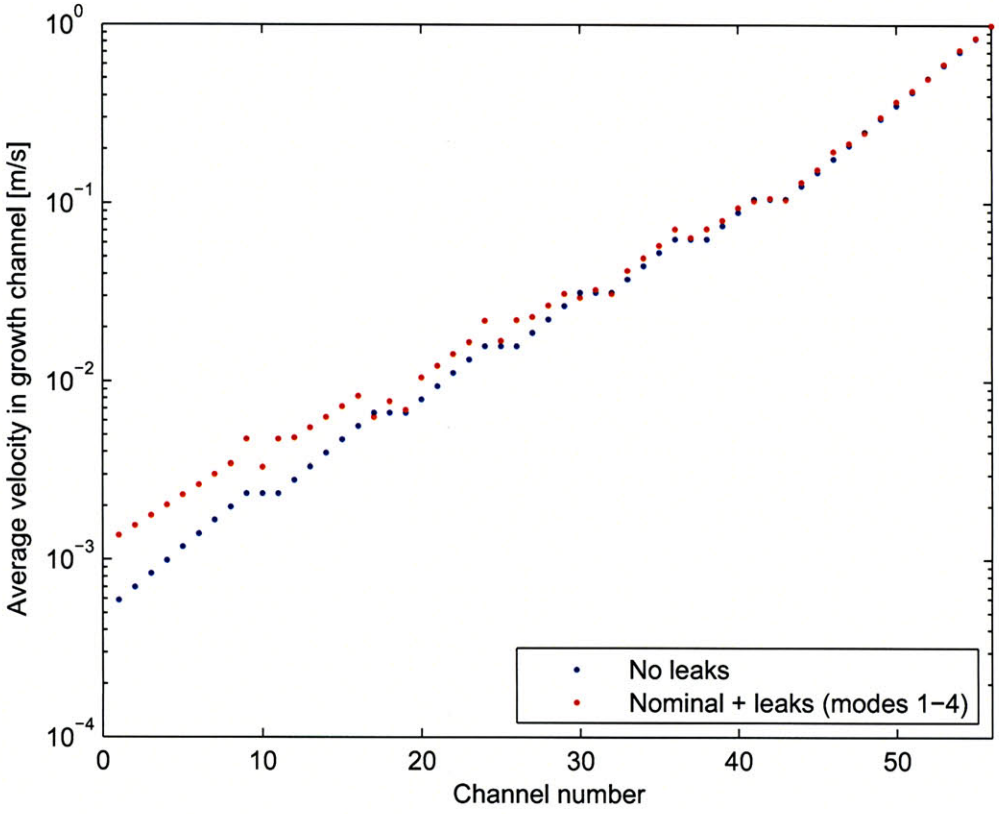

Figure 5-33. Velocities in growth regions of wide full microchannel device with localized triplet channel compensation, plotted with and without leak flows.

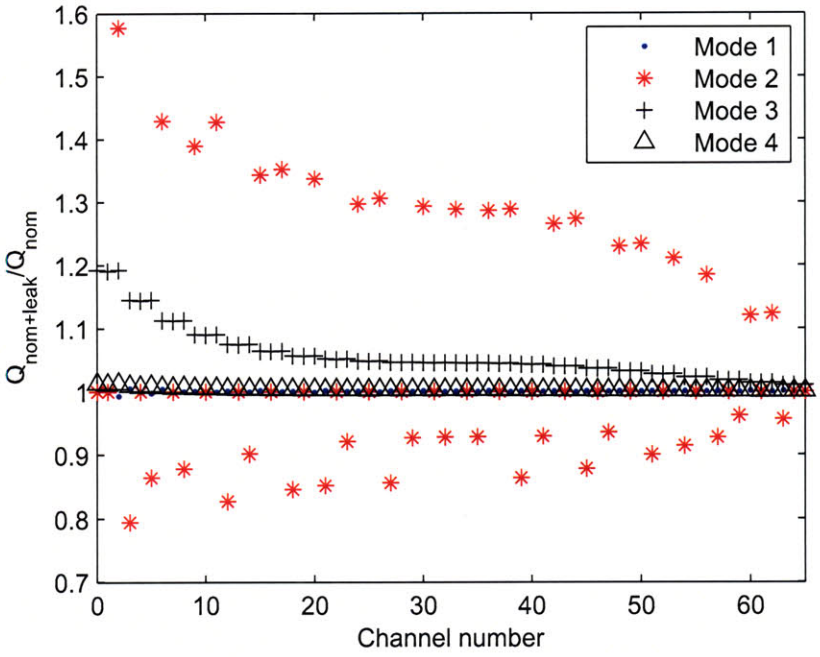

(a)

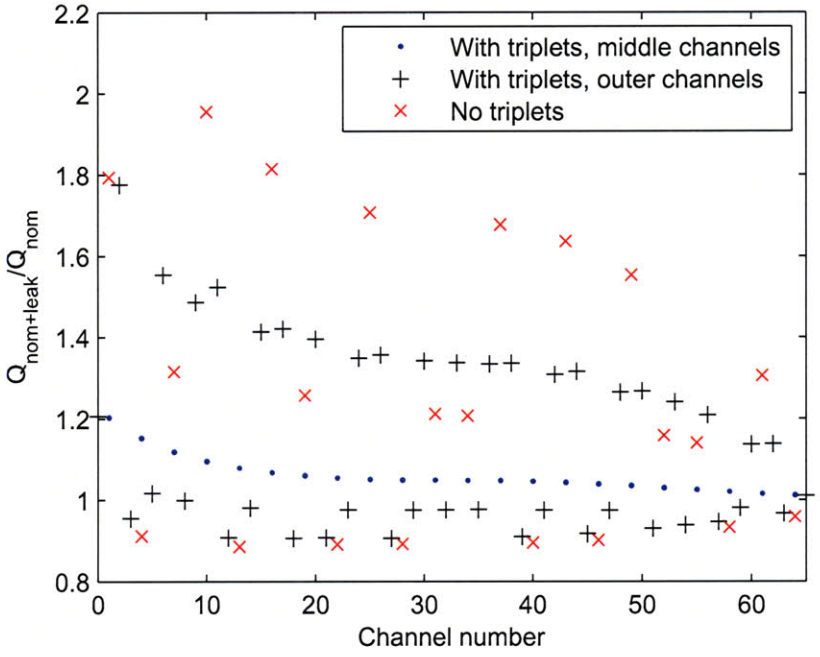

(b)

Figure 5-34. Analysis of leak flows between channels in high-res mid microchannel device, with full triplet channel compensation: (a) flow rate errors introduced by each leak mode; (b) sum of flow rate errors caused by all leak modes.

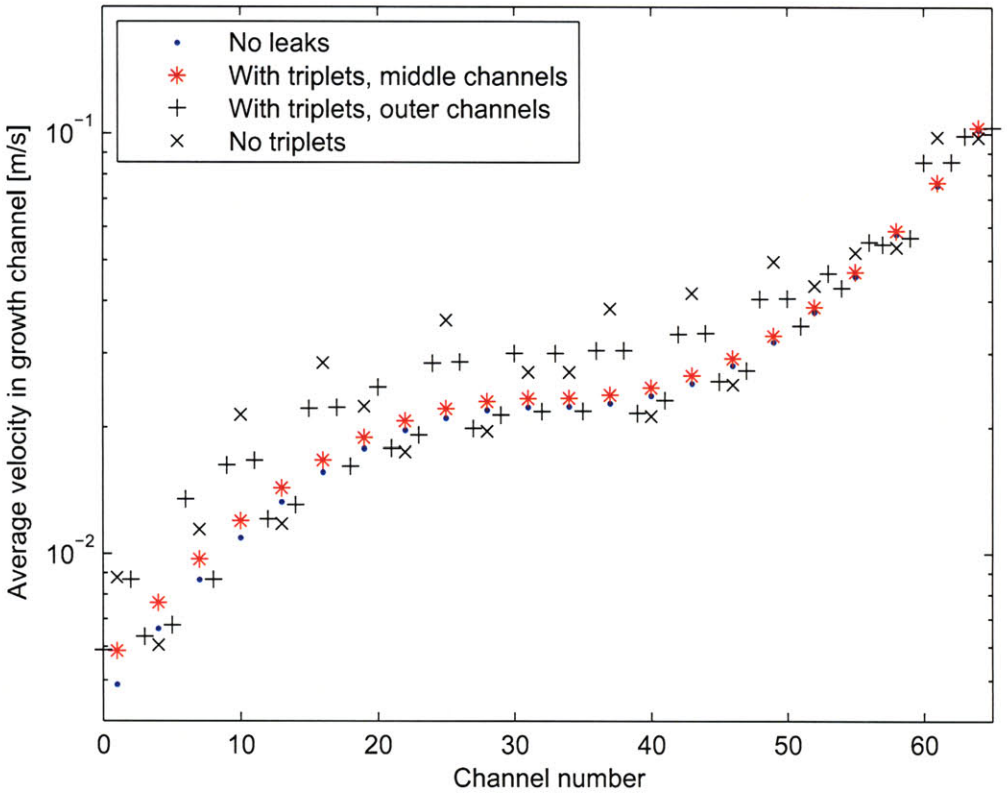

Figure 5-35. Velocities in growth regions of high-res mid microchannel device, with full triplet channel compensation.

5.5.2 Sensitivity to manufacturing variation and changing operating conditions

Errors in the manufacturing process and variations in the operating conditions can alter the progression of velocities in the microchannels. This section briefly presents results of computations for the wide full microchannel device, considering variations of the:

- Lithography alignment (Fig. 5-36), $0 \pm 0.1°$;
- Relative etch rate of (111) planes in KOH (Fig. 5-37), $r_{111}/r_{100} = 0.0005$–0.002;
- Operating temperature (Fig. 5-38, Table 5.4), 800–1000 °C;
- Gas mixture (Figs. 5-39 and 5-40, Table 5.5), 0–100% each of Ar, CH_4, and H_2.

Foremost, the device performance is highly sensitive to variation in the width of the entry channel regions caused by angular misalignment (θ_{mis}) of the lithography pattern (<110>-oriented channels) with respect to the crystallographic orientation of the silicon wafer. This is amplified as a sine error, which is analogous to an Abbe error [422, 423],

$$w_{e,f} = w_{e,i} + L_e(\sin\theta_{mis}). \tag{5.63}$$

Calculations show that alignment within 0.02° is needed to maintain velocity errors within 50% of the nominal values (Fig. 5-36). Standard (100) silicon wafers are cut within a specification of $\pm 0.1°$ between the wafer flat and the (110) plane; therefore, a special pattern must be used for alignment of the lithography pattern to the crystallographic direction. However, unlike some leaks this is a monotonic (and decreasing) error; angular misalignment in either direction will always increase the channel width, giving a lower flow resistance and higher flow rate under a given pressure drop.

Accuracy of the width of the entry regions is also affected by the relative etch rate of (100) and (111) planes in KOH, as etching of the (111) planes undercuts the lithography pattern and therefore increases the width of the channels. Ideally this would be compensated by pre-determining the etch selectivity (r_{111}/r_{100}) and appropriately decreasing the channel widths on the lithography mask, although depending on the magnitude of the error this correction may be less than the precision of the mask-making process. Our fabrication did not calibrate for this error, and at an expected selectivity of $r_{111}/r_{100} = 0.02$ (20% KOH at 80 °C) the velocity error is a maximum of 20% in the initial channels (Fig. 5-37).

We can further consider how variation in one operating condition affects the velocity progression when all other operating conditions are held nominal. For example, increasing or decreasing the operating temperature by 100 °C changes the velocities (Fig. 5-38) and total flow rates (Table 5.4) by only a few percent, owing to opposing trends between the fluid viscosity and fluid density with temperature. Variations in the gas composition more drastically change the fluid properties and therefore significantly shift the velocity progression, as is calculated for the example mixture of $Ar/CH_4/H_2$ (Fig. 5-39). Here, we can adjust the pressure drop (Table 5.5) to compensate (although not without potential consequences in the thermodynamic evolution of the reactant mixture) for the change in fluid properties (Fig. 5-40).

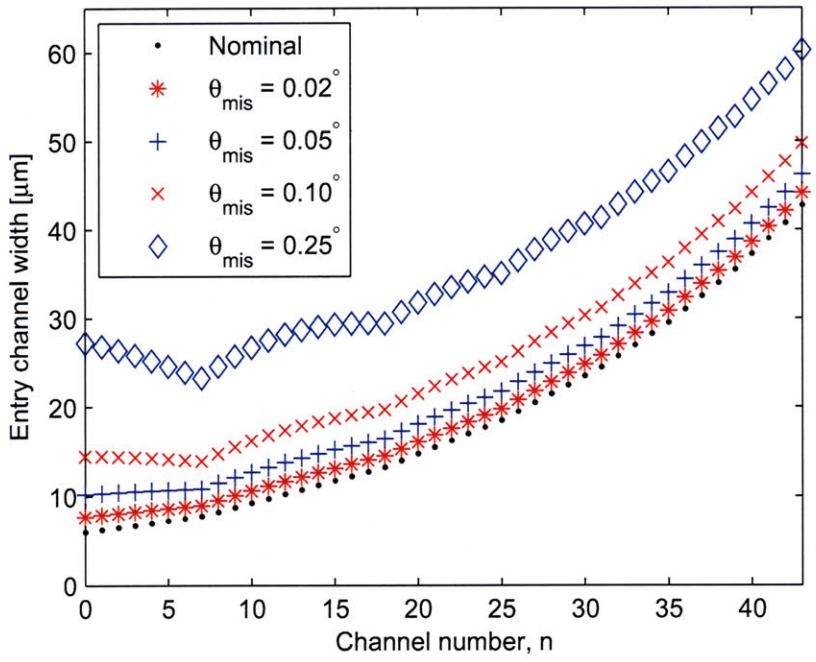

(a)

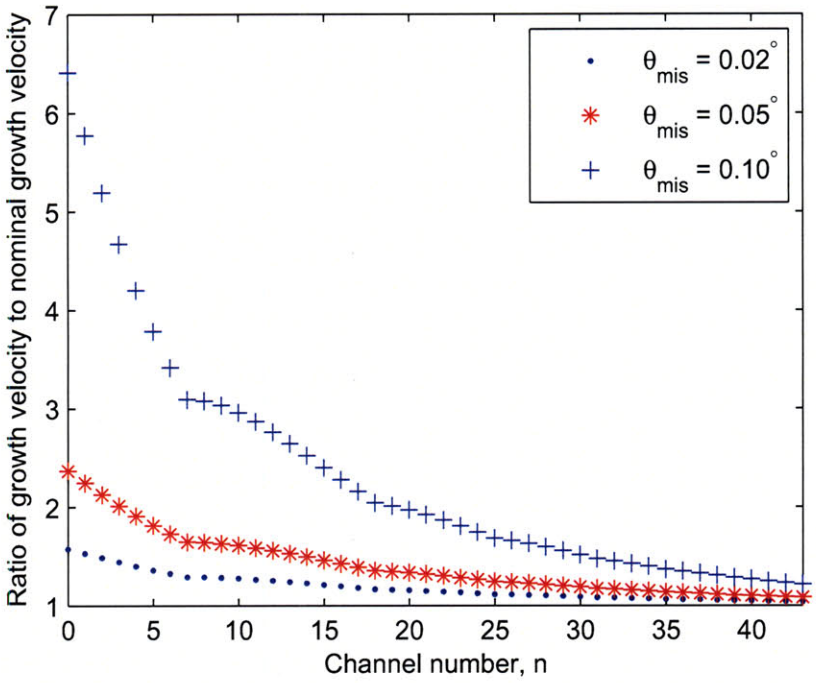

(b)

Figure 5-36. Sensitivity of wide full microchannel array geometry to misalignment of etch pattern, assuming etches are fully self-terminated: (a) final widths of entry regions; (b) velocities in growth regions.

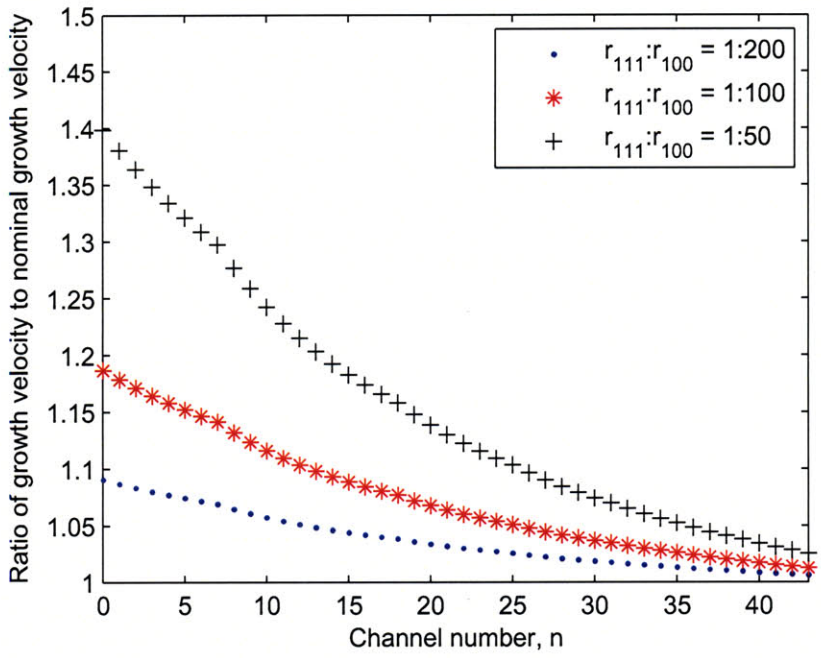

Figure 5-37. Effect of (111) etch rate on growth region velocities in wide full microchannel array, where nominal design assumes no etching of the (111) planes.

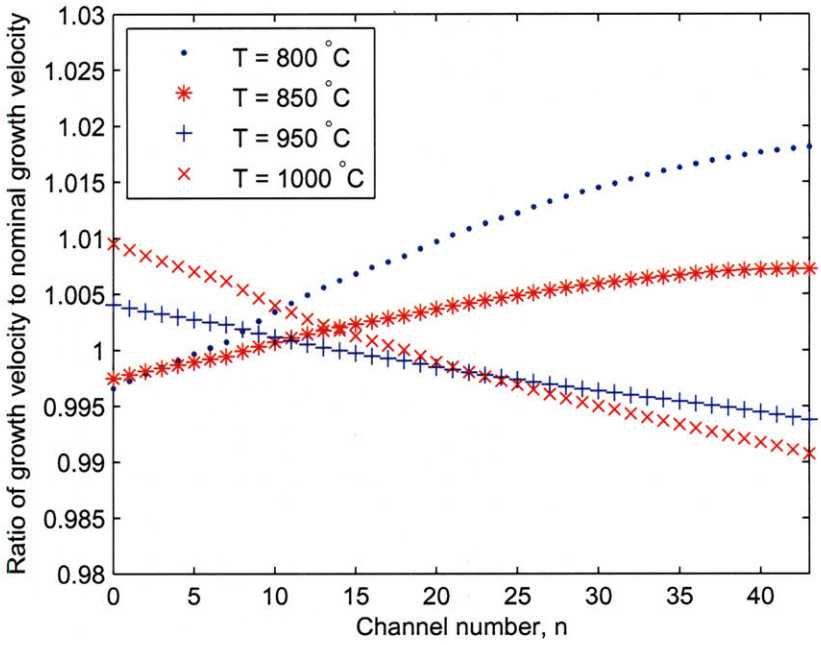

Figure 5-38. Effect of varying temperature on growth region velocities in wide full microchannel array.

Other variable factors not considered here include direct lithography errors affecting the width and length of the entry and growth channel regions, etch timing effects on the depth of the growth regions, and so on.

Temperature [°C]	$Q_{g,tot}$
800	0.345
850	0.327
900	0.311
950	0.297
1000	0.284

Table 5.4. Total room temperature flow rates through microchannel array, at various furnace temperatures (not including flow through dump channels), for total pressure drop of 4.0 psi.

Ar:CH_4:H_2	Δp_{tot} [psi]
0.33:0.33:0.33	4.00
0.50:0.50:0.00	6.00
0.00:0.50:0.50	2.73
0.00:1.00:0.00	3.25
1.00:0.00:0.00	6.19

Table 5.5. Pressure drop correction factors for various compositions of gas mixture flowing through microchannel array.

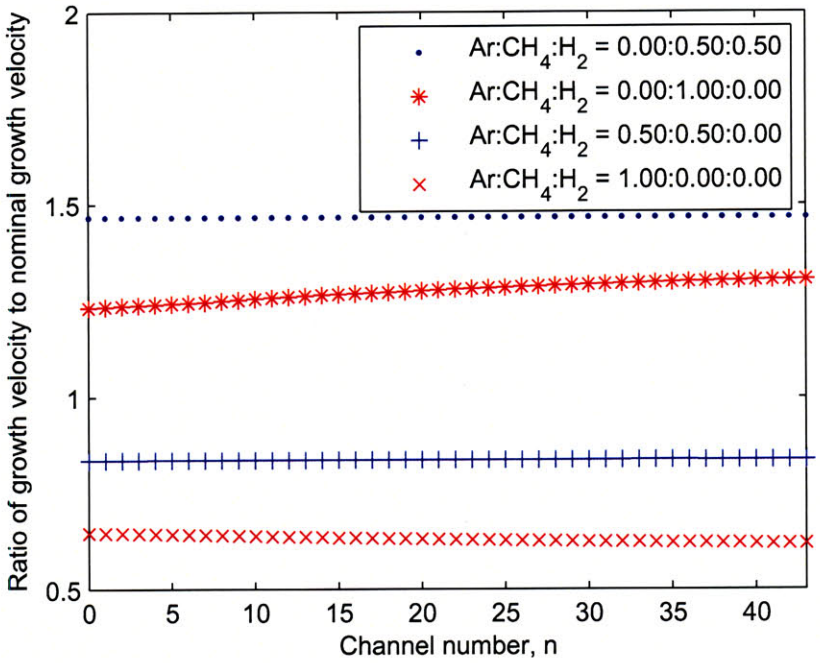

Figure 5-39. Effect of varying relative composition of $Ar/CH_4/H_2$ gas mixture on growth region velocities in wide full microchannel array.

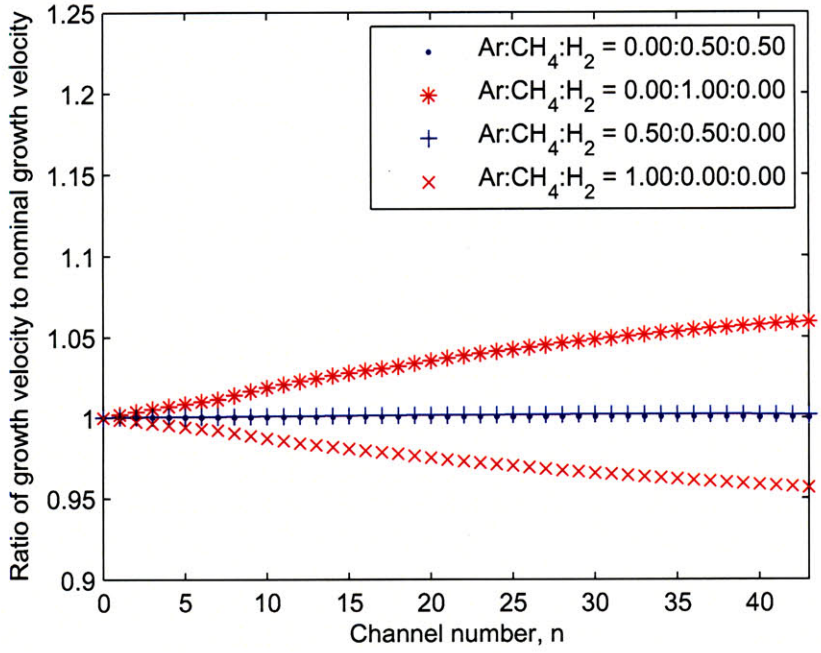

Figure 5-40. Effect of varying relative composition of $Ar/CH_4/H_2$ gas mixture on growth region velocities in wide full microchannel array, when pressure drop is scaled as listed in Table 5.5 to account for mean effects.

5.6 Microfabrication

The microchannel arrays are fabricated by KOH etching of 150 mm diameter, 650 μm thickness, (100)-oriented silicon wafers. Fig. 5-41 summarizes an exemplary fabrication process, where a layer of silicon nitride (Si_3N_4, Si-rich to give low residual stress) masks the KOH etch. A first lithography and etch sequence defines an alignment pattern which reveals the crystallographic orientation of the wafer. The lithography pattern for the devices is aligned to this first pattern, and then the devices are etched by timing the depth of the growth regions of the microchannels (55 μm) to a pre-measured etch rate ($\approx$1.1 μm/min, in 20% KOH in DI-H_2O at 80 °C), and using a depth vernier which is patterned at the periphery of the wafer. Finally, the wafer is divided into devices using a die saw with a 220 μm width water-cooled blade.

As illustrated by the sensitivity calculations, the first etch for crystallographic alignment is necessary to reduce undercutting of the mask openings which amplify the self-terminated widths of the high-aspect-ratio entry channels. For example, 0.1° misalignment of a 5 μm × 1 mm mask opening results in a total undercut of 3.5 μm at each edge, decreasing the fluidic resistance of the channel by approximately a factor of 8.5. The method of Lai et al. [424] is adopted to pattern a set of features on the device wafers to achieve 0.01° alignment of the microchannel pattern to the <110> direction. Practically, we realize that even a thin layer of photoresist significantly reduces visibility of the alignment features, and therefore it is advantageous to inspect the wafer and identify the feature in best alignment with the crystal plane prior to coating the pattern with photoresist. Since all wafers in a box (where all 25 wafers in a typical box are cut from the same silicon boule) are cut with the same flat orientation, the alignment etch was performed on only three wafers per box. Then, the wafer stage was rotated manually to compensate for this pre-measured error on all wafers in the batch.

We must also consider undercutting of convex corners by the KOH etch [425], where the etch rates in these unstable crystallographic directions are much greater than the nominal <100> etch rate. Two critical locations of convex corners in the microchannel device are the expansion between the entry and growth regions of a microchannel and the areas in the growth regions where pyramidal islands are to be created. For these critical <110>-oriented features, the undercutting is conveniently represented by the high etch rate of the {411} planes,

$$r_{411}/r_{100} \cong 4. \tag{5.64}$$

Undercutting at the expansion between the growth and entry regions (Fig. 5-45a-b) is compensated simply by increasing the masked length of the entry channel. For 55 μm etch depth of the growth channels the required compensation length is approximately 220 μm.

Pyramidal islands are fabricated inside the growth channels by defining 'H'-shaped mask structures (Fig. 5-45c-d), where long <110>-oriented beams compensate for undercutting as Sandmaier initially demonstrated [426]. Here, the required length of a <110>-oriented corner-compensating beam is

$$L_{(110)} = d\frac{2r_{411}}{r_{100}} - \frac{w_b}{2\tan(30.96°)}, \tag{5.65}$$

where w_b is the width of the beam.

Misalignment between the edge of a lithographically patterned feature and the <110> direction, as well as edge roughness of the feature cut in the mask, cause scallops to emerge on the

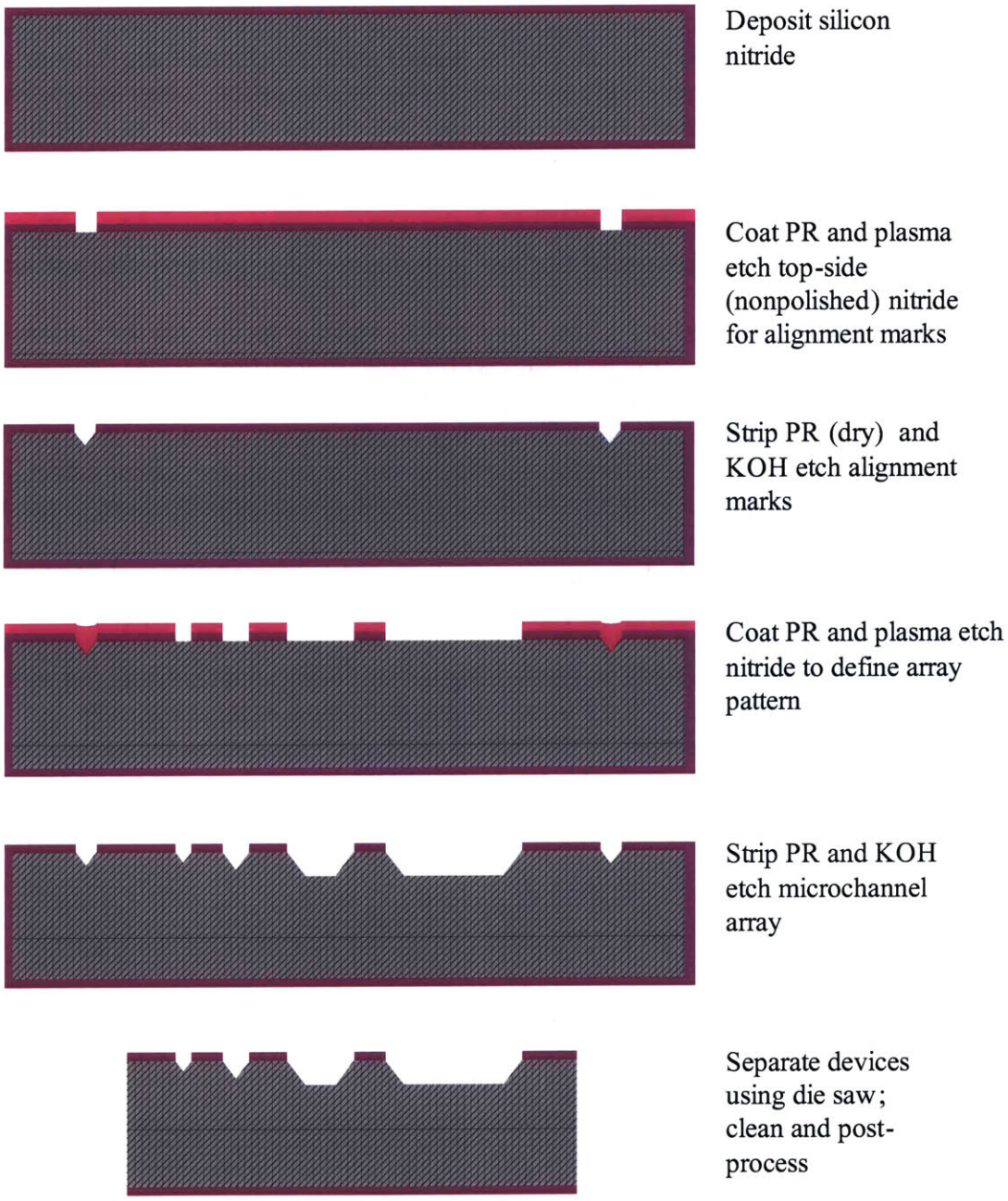

Figure 5-41. Exemplary fabrication process for microchannel array, by KOH-etching of a standard (100)-oriented silicon wafer.

sidewalls of trenches as they are slowly etched to undercut the lithography pattern and form a self-terminating geometry [427, 428]. These scallops do not appear to be detrimental to the microchannel performance; however, observation of these scallops indicates inexact alignment between the feature and the <100> direction.

The literature provides many more approaches to convex corner compensation, including use of (100)-oriented beams [429] which can be packed more efficiently than (110)-oriented features. Enoksson further improves the space efficiency, by slitting the compensating feature to slow undercutting [430]. Further, undercutting can be avoided altogether by a "perfect corner" process where two sequential lithography and etch sequences are used to independently fabricate orthogonal edges of convex-cornered features [431]. Careful timing of unstable undercutting in anitotropic wet etching, in conjunction with compensation methods like those discussed implemented here, is used to fabricate well-defined arrays of very sharp structures such as AFM tips [432].

SIMODE™ software [433] is used to simulate the KOH etching, specifically the undercutting of convex corners, and predicts bulk etch rates within 10% of measured values. This software is extremely useful for visualizing geometries when features are aligned with major crystallographic directions, but detailed agreement is not obtained for structures which are slightly misaligned, or in general where evolution of fast-etching or slow-etching directions is critical [434]. The software greatly overestimates the time taken for slightly misaligned features to achieve a self-terminating geometry; however, the final geometry is correct.

Alternatively, we could fabricate an array using a combination of DRIE and KOH etching [435, 436], and thereby achieve a variety of channel depths along with two-dimensional shape freedom on features such as islands included in the channels. Prior to design of the KOH-etched microchannel array, a DRIE-etched array was designed and fabricated featuring the variety of island shapes indicated in Fig. 5-43, so as to evaluate the effects of local hydrodynamic conditions on the initial growth direction of CNTs from catalyst positioned on the islands. Experimentation using this device was stopped in favor of the KOH-etched array design, and therefore is not discussed further in this thesis.

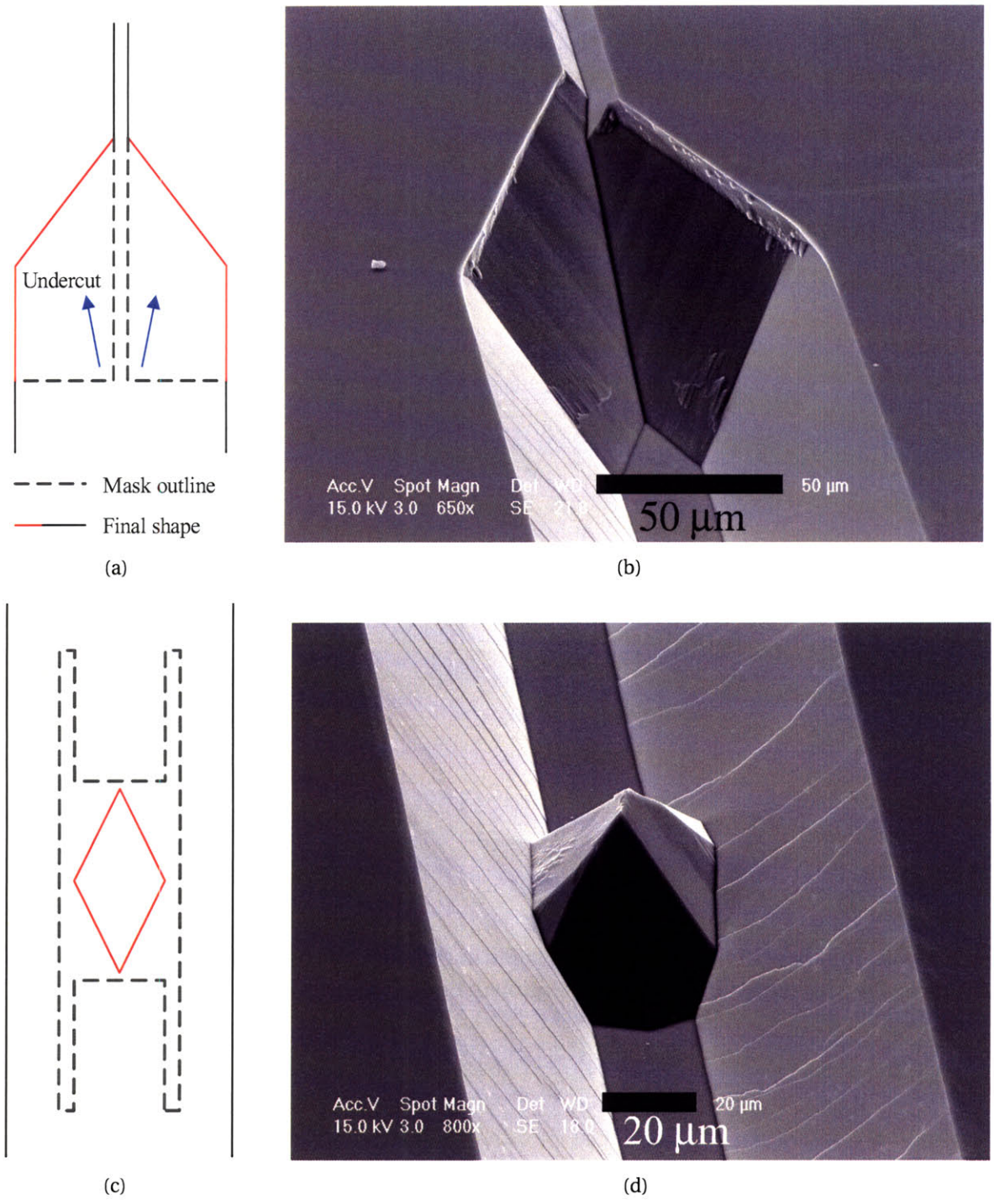

Figure 5-42. Convex corner and undercutting compensation methods, and SEM images of fabricated features for (a)-(b) expansion between entry and growth regions of microchannel, and (c)-(d) pyramidal island inside growth region of microchannel. Note scallops formed on the channel sidewalls because of misalignment between the lithography pattern and the <100> direction.

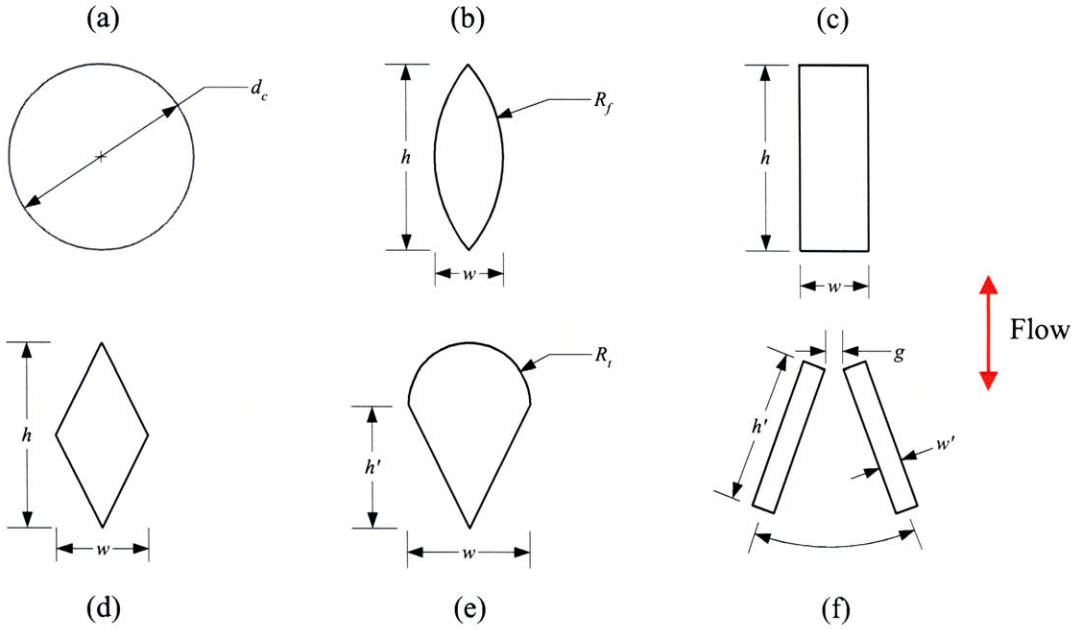

Figure 5-43. Top-view shapes of islands included in DRIE-etched microchannel device, for evaluating local hydrodynamic effects on CNT growth direction.

5.7 Assembly and packaging

For experimentation, the microchannel array is clamped against a second silicon substrate, and the mating interface is between a polished silicon surface and a non-polished surface. This prevents thermally-induced compression bonding of the assembly during high-temperature experimentation. The array can be used to confine growth of nanostructures in two configurations (Fig. 5-44): (1) where the catalyst for growing the nanostructures is placed within the microchannels and the second substrate is a simple cover; (2) where the catalyst is placed on the second substrate. In our experiments, configuration (2) is preferred, as this allows re-use of the microchannel array (after cleaning), and the catalyst can be patterned independently on a polished silicon substrate as discussed in the next section. Patterning the catalyst within the microchannels by lift-off introduces difficulty in uniformly coating the etched topography with photoresist.

The microchannel device and the pattern substrate are held in contact by a compression fixture, which is described in section 6.3. The compression fixture is either a pair of quartz plates preloaded ceramic bolts and high-temperature spring washers in a tube furnace, or a pair of coupons from a quartz wafer preloaded by stainless steel spring clips on a resistively-heated silicon platform.

For fluid entry and exit from the microchannel device, through holes are cut using an excimer laser (248 nm excitation, Resonetics). The device is protected from ablation damage by front-side coating with a 20 μm layer of photoresist, and back-side coating with the die saw tape. The holes are 2 mm diameter, and each hole is cut in approximately 20 minutes by a circular trace of a 170 μm diameter spot. After laser cutting, the devices are delaminated from the tape and the photoresist is dissolved in a "pirahna" solution (3:1 H_2SO_4:H_2O_2). Finally, the devices are rinsed in 2-propanol and blown dry with N_2.

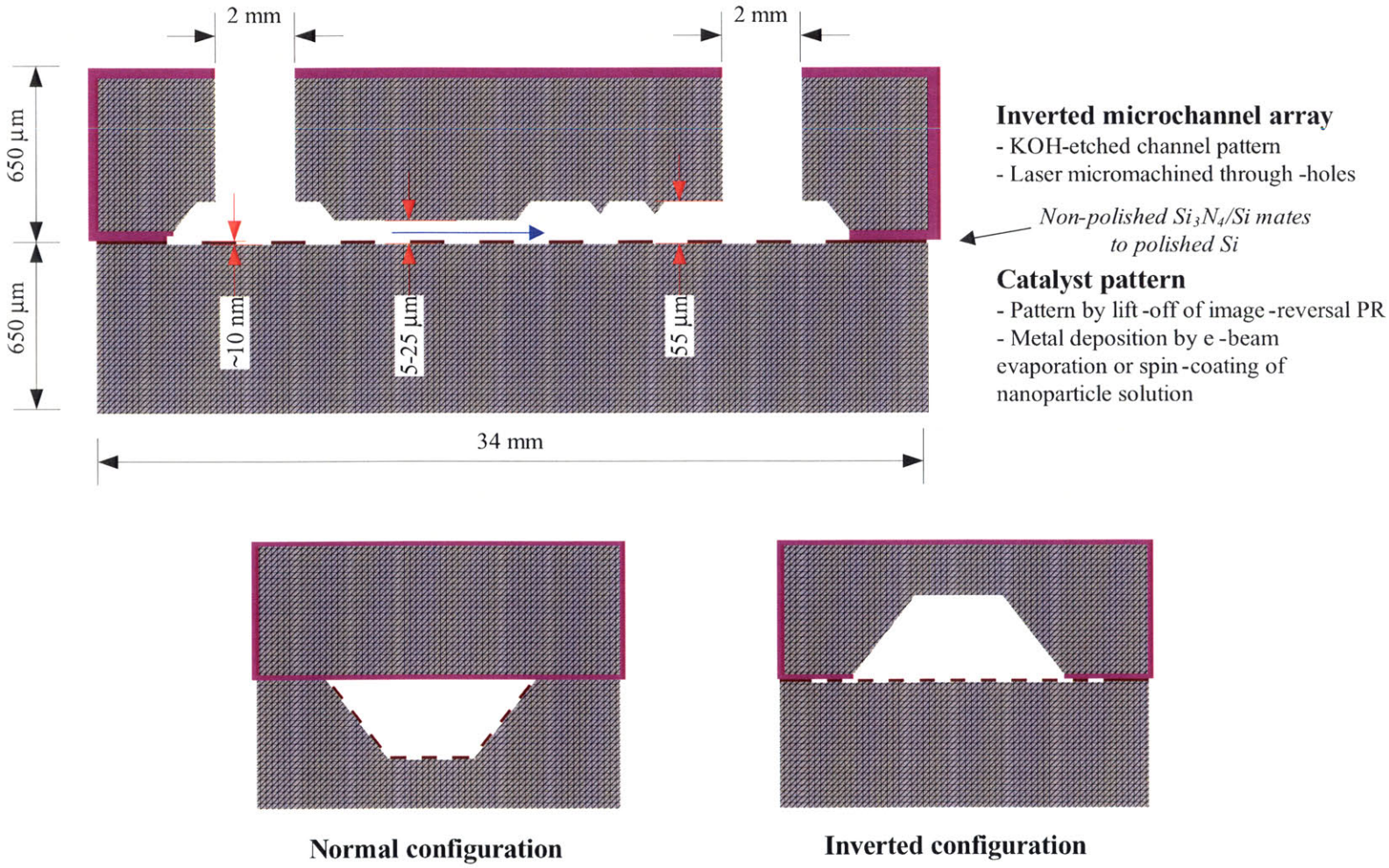

Figure 5-44. Assembly configurations for nanomaterials growth experiments within microchannel array, with top-side access for gas delivery through compression fixture.

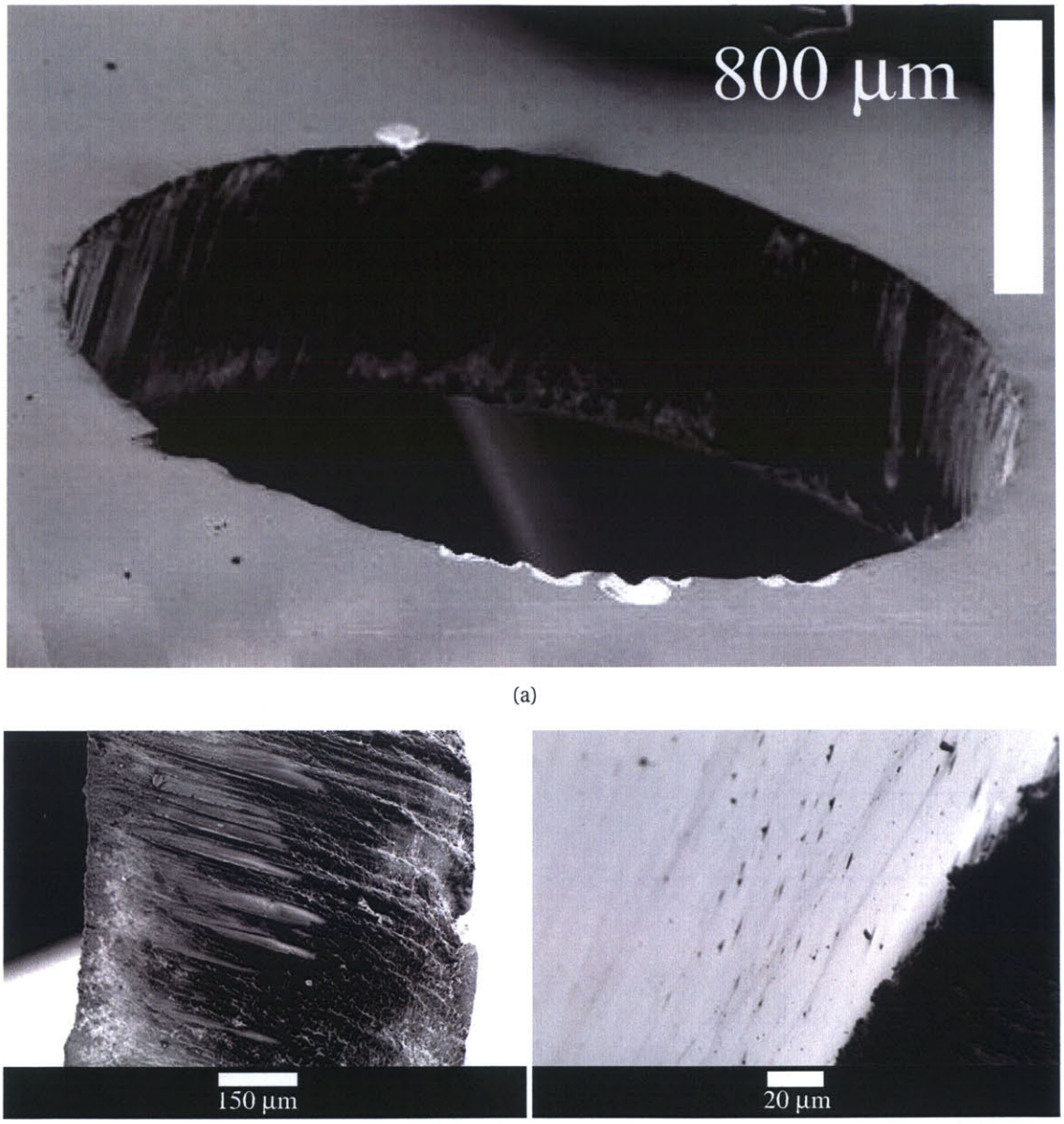

(a)

(b)

(c)

Figure 5-45. SEM images of laser-micromachined through hole in microchannel array: (a) full oblique view of hole; (b) close view of sidewall; (c) close view of surface which was protected by photoresist.

5.8 Design and fabrication of catalyst patterns

For the microchannel tests where the device is mated against a catalyst-coated substrate (Fig. 5-44), thin-film catalysts for CNT growth ($Mo/Fe/Al_2O_3$ [1], Fe/Al_2O_3 [3]) are deposited by e-beam evaporation and patterned by lift-off of image-reversal photoresist (AZ5214E) on bare (with native SiO_2) polished (100) silicon wafers. A variety of pattern sizes, shapes, and arrangements are featured; one particular arrangement has a progression of circular dots (each containing many nanoparticle growth sites) of sequentially increasing and decreasing diameter (Fig. 5-46). With the goal of studying how CNT bundles can be manipulated (i.e., bent, pulled) by gas flows within the microchannel, these dots progress in diameter so as to give a force-deflection relationship which is self-similar with the expected progression of flow velocities in the wide full array.

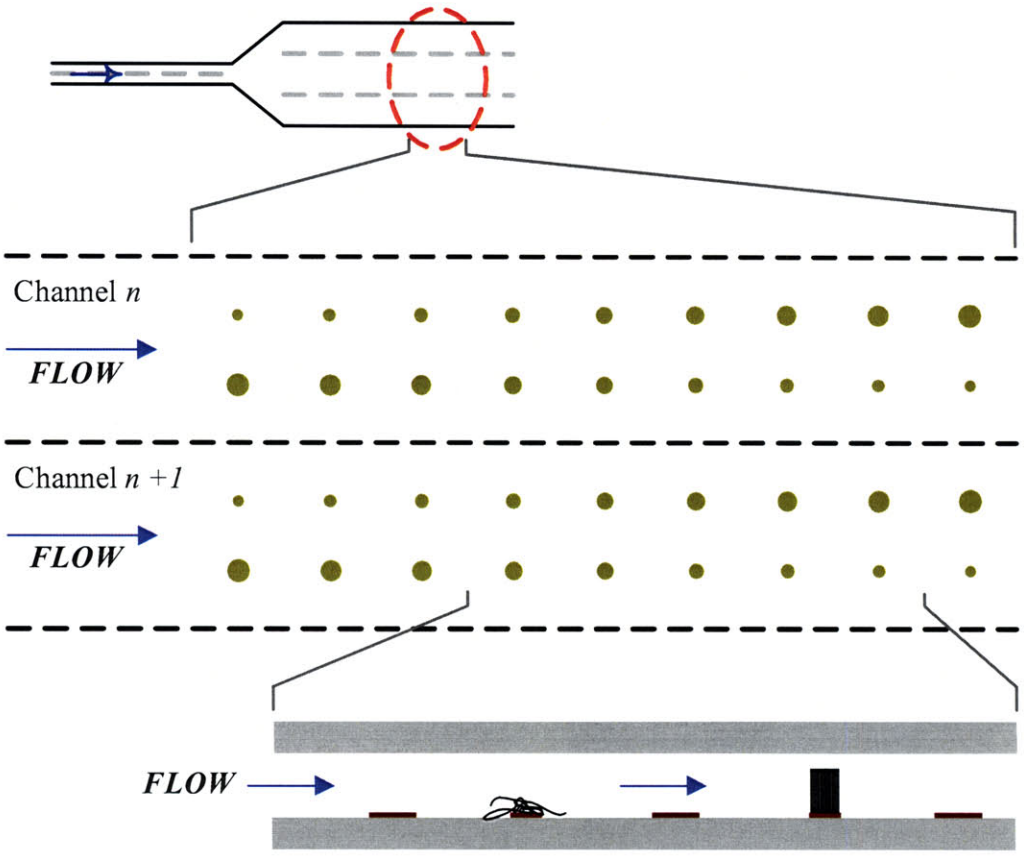

Figure 5-46. Schematic representation of catalyst dot arrangement used for templating CNT growth by mating microchannel device against second substrate which holds catalyst pattern. Catalyst dot diameters range from 3–20 μm.

The diameters of the catalyst dots are calculated by starting from the drag force per unit length on a circular cylinder of diameter d, in cross-flow,

$$f_D = C_D\left(\frac{1}{2}\rho V^2 d\right). \tag{5.66}$$

For low-speed flows (Re < 100) the drag coefficient (C_D) is inversely proportional to Re,

$$C_D \propto \frac{1}{\mathrm{Re}}. \tag{5.67}$$

Similarity is established between the velocity scaling across the channel array and the deflection of the structures caused by flow-induced drag when

$$\frac{V_{g,n+1}}{V_{g,n}} = \frac{\delta_{d,n+1}}{\delta_{d,n}}. \tag{5.68}$$

Modeling a pillar of CNTs as a simply-supported cantilever and substituting Eqs. (5.66, 5.67, and 5.68), the diameter progression of the pillars is governed by

$$d_n = d_1 \left(\frac{V_{g,n}}{V_{g,0}} \right)^{\frac{1}{4}}, \tag{5.69}$$

where $d_1 = 3\ \mu$m is chosen because this value is the smallest possible feature size on a laser-written mask (Advance Reproductions). Recalling the linear-logarithmic scaling progression for the wide-range device (Eq. 5.46),

$$d_n = d_1 \left(\left(10^{O_N}\right)^{\left(\frac{n}{N-1}\right)^a} \right)^{\frac{1}{4}} = 1.045. \tag{5.70}$$

Further experiments were conducted with uniform catalyst coatings on the microchannel devices and on the mating substrates, in both the "normal" and "inverted" configurations. Results of CNT growth experiments in the microchannels are presented in Chapter 7.

Chapter 6

Design and Construction of CNT Growth Systems

This chapter presents the design and construction of furnaces for CVD growth of CNTs on substrates: atmospheric-pressure tube furnaces; and a low-thermal-mass substrate heater using a suspended silicon platform. A new elasto-kinematically constrained tube end cap enables rapid sample exchange and low-stress mechanical and electrical connections to hardware inside furnace tubes. A new "flow reversal" tube furnace configuration enables short- and precise-time growth experiments on small substrate samples. Rapid heating and cooling performance of the suspended platform heater is verified; the platform is implemented in a sealed quartz tube as well as in a custom-built box chamber having versatile mechanical, electrical, and optical access to the reaction surface. The chamber is implemented with non-contact sensing of the platform temperature and *in situ* measurement of the CNT film thickness. Microchannel devices for combinatorial flow studies of CNT growth are packaged in a tube furnace using quartz blocks preloaded by Inconel spring washers, and on the heated platform using thin quartz plates held by stainless steel spring clips.

Lab space for the CNT growth systems was graciously shared by Prof. Yet-Ming Chiang of the MIT Department for Materials Science and Engineering.

6.1 Tube furnaces

Perhaps the simplest apparatus for CVD reactions is a tube furnace, where typically a substrate sample is placed inside a sealed tube, reactive gases are introduced to the tube, and the desired surface reaction takes place on the substrate. The tube is surrounded by an insulated enclosure lined by resistively-heated coils and power to the coils is controlled to maintain a desired temperature in proximity of the tube.

Two horizontal atmospheric-pressure tube furnace systems (e.g., Fig. 6-1) were built[1] and utilized for growing the CNT films discussed in Chapters 2 and 3. The furnaces (Lindberg) are each approximately 0.6×0.5×0.35 m (w×d×h), and are fitted with 0.75 m length quartz tubes (GE fused quartz, cut with fire-polished ends by Finkenbeiner Glass). The furnaces have identical geometry, with ≈50 mm diameter heating coils. One furnace has a 22×26 mm (ID×OD)

[1] Thanks to Pat Kearney for advice regarding the initial tube furnace setup.

quartz tube, and the other has a 42×45 mm tube.

Tanks of high-purity gases (N_2, Ar, He, H_2, CH_4, C_2H_4, CO; BOC, Airgas) are fitted with single-stage pressure regulators (BOC), and are connected to manual needle-valve floating-ball rotameters (Gilmont, Matheson Tri-Gas). All fluid lines are high-purity tygon tubing, and junctions are assembled from threaded brass fittings (McMaster-Carr, Swagelok). Output lines from the flowmeters are connected to a manifold, and the output line of the manifold is connected to the input of the tube furnace. Each furnace output is connected to a glass bubbler which is filled with parrafin oil and provides a slight (≈0.1 psi) back-pressure to stabilize flow inside the tube. The output tube from each bubbler is placed in a fume hood, and this flow is filtered and exhausted from the lab. Quick disconnect tube couplings (Cole-Parmer) enable easy reconfiguration of the gas lines among the flowmeters, manifolds, furnaces, and bubblers.

6.1.1 Quick-change tube end caps using lip seals

A popular furnace tube end cap design which uses face seals is cumbersome to align and seal to the end of a furnace tube; our new design (Fig. 6-2) is "elasto-kinematically" constrained and has two Viton lip seals recessed in grooves in an aluminium cap. This cap easily slides over the end of the tube and self-aligns, sealing against the smooth outer surface of the tube. The seals are spaced to impart sufficient pitch stiffness when the seals soften upon heating, yet the radial compliance of the seals enables low-stress electrical and fluidic connections to components inside the tube [437, 438].

More specifically, the previous design (e.g., Vesuvius McDanel Universal Tube Seal UAC0001 [439], Fig. 6-2d) uses an aluminum plate and a Viton gasket to seal the end of the tube. The plate is held to the end of the tube by three bolts. The plate and gasket must be carefully aligned to the end of the quartz tube to ensure adequate sealing. The quality of the seal depends on the magnitude and uniformity of the bolt tension, and the hose clamp must be tightened sufficiently around the quartz tube to prevent slippage when the bolts holding the plate are tightened. This risks breakage of the quartz tube. This seal design also requires the end of the quartz tube to be smooth (e.g., fire-polished) and orthogonal to the tube axis. It is often difficult to achieve these conditions when a quartz tube is cut in the laboratory.

To realize the new design, an aluminum cap is turned from round stock (2" diameter, alloy 6061), and has two internal grooves to accept lip seals (Chicago Rawhide, #721552 Viton). The cap is easily fitted to the furnace by gently slipping and twisting the assembly onto the quartz tube, forming a self-preloaded seal against the smooth surface of the quartz tube. It seems that the seals soften during the first furnace run, making them easier to seat on the tube. Leak tests, using flowmeters at the input and output of the furnace, confirm that using a single lip seal prevents leakage to a level below 1 sccm. The Viton seals have a maximum working temperature of 232 °C, and sealing is maintained with furnace operation at a hot zone temperature of up to 950 °C for 2 hours. Three screws, using the same hose clamp assembly as the plate-gasket design, are optionally used as retainers. The screws should be fastened with enough free length so the lip seal can slide off the end of the tube (e.g., in case of an explosive reaction inside the tube), without moving the hose clamp assembly.

When a tygon tube is connected directly to a barb fitting threaded into the end cap, the Tygon softens when the furnace is hot. Therefore, a short stainless steel pipe is used to offset the Tygon tubing connection from the cap face (Fig. 6-2c) and keep it at room temperature.

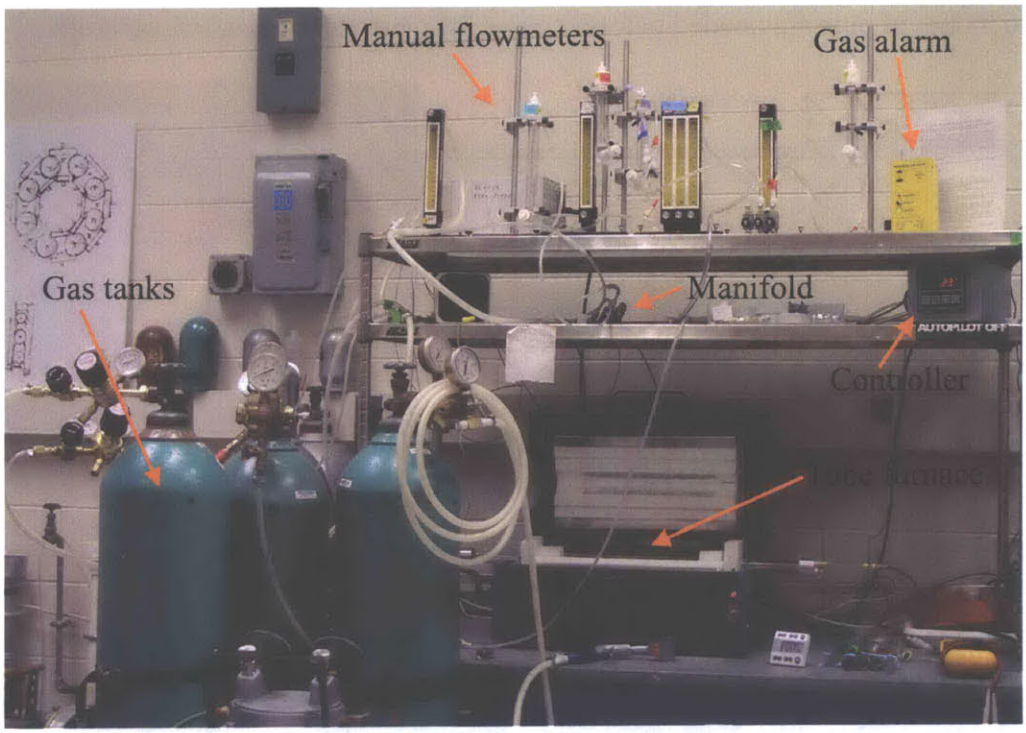

(a)

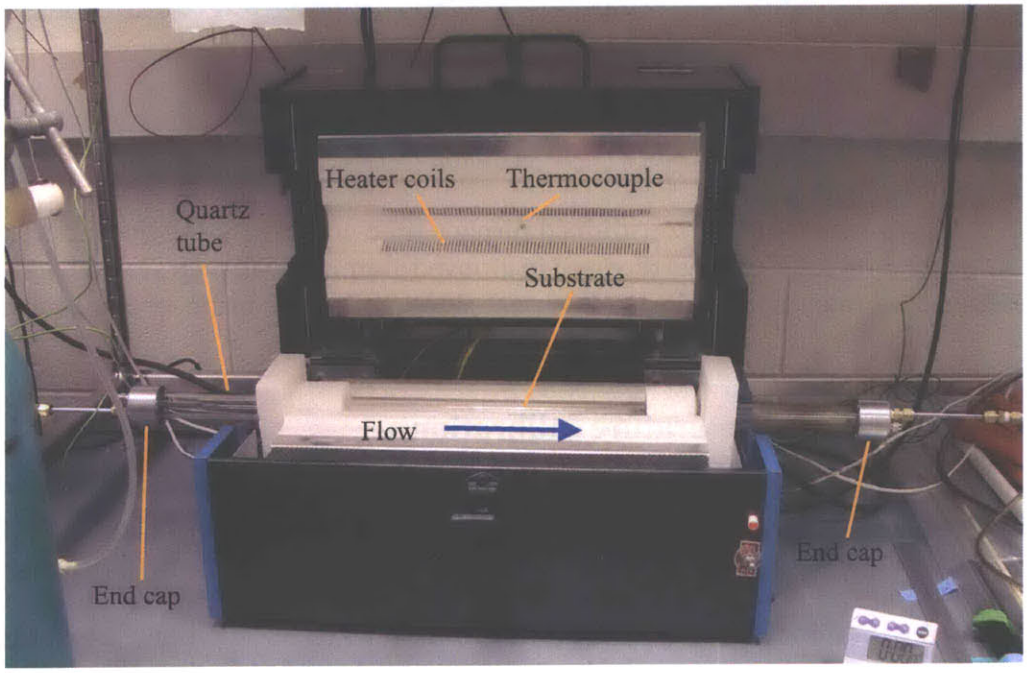

(b)

Figure 6-1. Atmospheric-pressure horizontal-tube furnace system (22 mm ID quartz tube) built for CVD growth of CNTs on substrates, with flow control by manual floating-ball rotameters, and featuring new cap-type tube end seals.

Elementary heat transfer calculations, modeling the stainless steel pipe as a fin [440], show that only two inches of pipe are needed before the end fitting reaches room temperature.

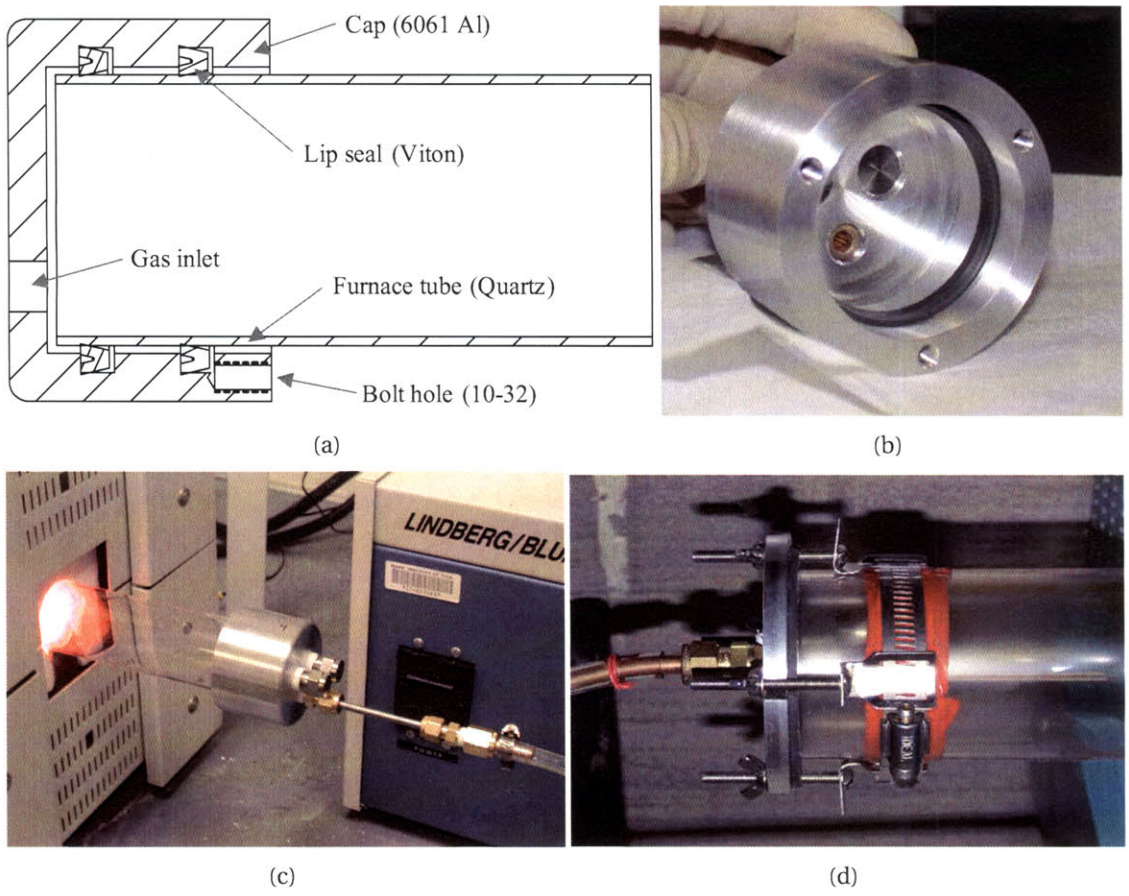

Figure 6-2. Elasto-kinematically constrained furnace tube end caps using lip seals: (a) cross-section drawing showing Viton seal recessed in grooved aluminum; (b) cap seal in hand; (c) cap seal mounted on furnace tube with stainless steel pipe standoff; (d) prior are face seal end cap.

6.1.2 Tube furnace temperature calibration

The temperature inside the tube furnace is measured by sealing a thermocouple inside a two-bore Al_2O_3 pipe (Vesuvius-McDanel) and placing the thermocouple into the center of the furnace at the location of the control thermocouple (Fig. 6-1b). The thermocouple-pipe assembly is fixed in the tube end cap using a Cajon-type fitting (Swagelok Ultra-Torr). The temperature measured by the thermocouple inside the tube is typically higher than the temperature measured by the control thermocouple, as the thermocouple inside the tube sees more uniform radiation from the heat sources surrounding the tube. At steady-state, this "overshoot" is approximately 35 °C for the 22×26 mm tube and 70 °C for the 42×45 mm tube. With the 26 mm OD tube, we can place the control thermocouple closer to the central axis of the furnace tube, and therefore the control temperature is closer to the temperature measured inside the tube.

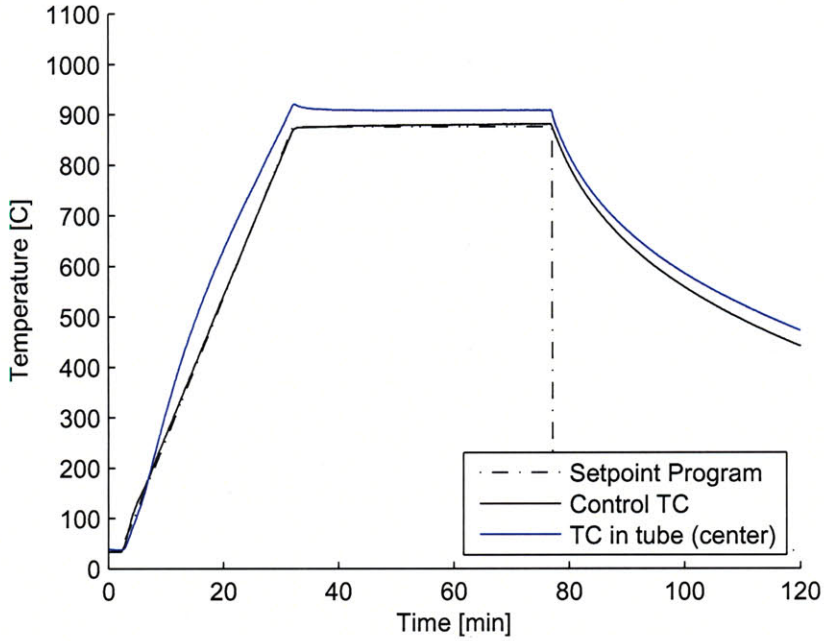

(a)

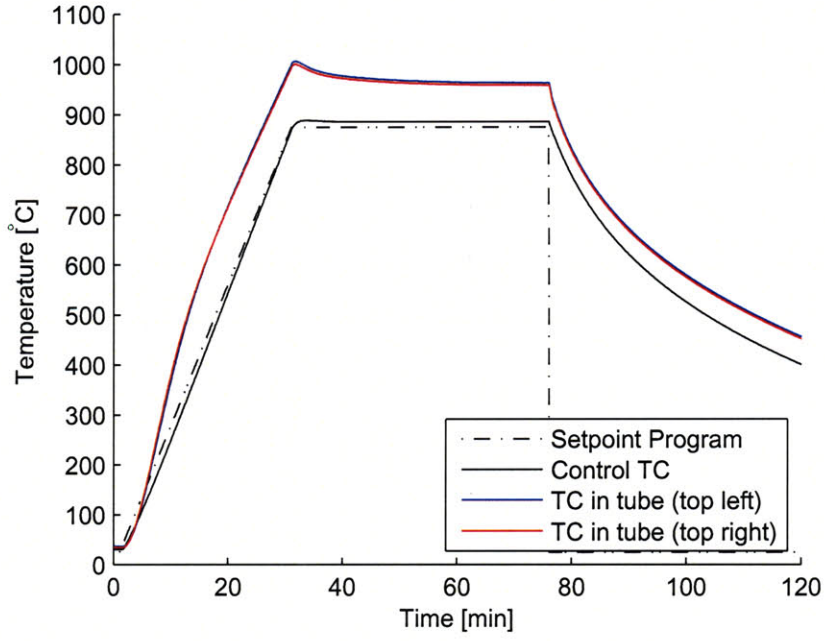

(b)

Figure 6-3. Temperature measurements from a thermocouple mounted inside the furnace tube, compared to values from the furnace control thermocouple during a 30/40/0 minute ramp/hold/step setpoint program: (a) 22×26 mm (ID×OD) furnace tube; (b) 42×45 mm tube.

The temperature measured by the thermocouple inside the tube is a more accurate measure of the temperature of a silicon substrate sample placed inside the tube; therefore, using a 22 mm ID furnace tube, a temperature of 750 °C on the furnace controller is more exactly 785 °C at the sample.

6.1.3 Flow reversal configuration for time-sensitive growth experiments

It takes ≈1 minute to flush the ≈0.5 L gas volume inside our tube furnace; hence, precise studies of the growth time requiring a rapid change of the gas composition over the growth substrate cannot be conducted. To enable such a study, a second quartz tube (6.35 mm OD) is mounted in the end cap of the main tube, and held in place using a Cajon-type fitting. The growth sample is placed in this second tube, and the gas in this tube can be flushed rapidly (approximately 1 s) due to the relatively small internal volume of the tube. This "flow reversal" configuration (Fig. 6-4) features a three-way valve at the output of the small tube, so gas can be directed into the small tube through dedicated supply lines, or drawn into the small tube from the main tube using a vacuum generator or a slight pressure difference between the output bubblers.

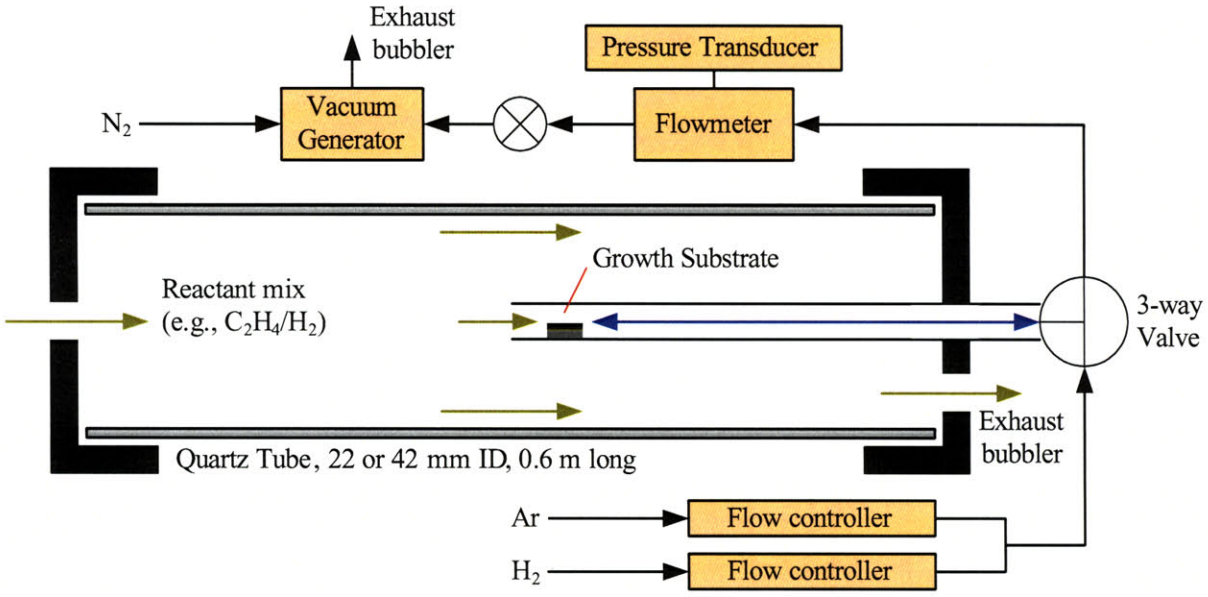

Figure 6-4. Concentric-tube "flow reversal" tube furnace apparatus, where the growth sample is placed in a small tube in the center of the main reaction tube, and gas is purged backward over the sample or drawn rapidly from the main tube.

6.2 Suspended silicon platform heater (developed with Lucas van Laake)

Because of its large thermal mass, a conventional tube furnace as described in the previous sections can be heated no faster than ≈1 °C/s. Studies involving rapid heating and thermal cycling have recently shown that, like temperature itself, temporal temperature variation can be a significant parameter in chemical reactions. For example, a 40% increase in conversion rate of the oxidation of CO was found under fast forced temperature oscillations [441]. In a fluidized bed reactor, rapid heating of the catalyst caused preferential formation of SWNTs [442]. On a substrate, rapid heating caused SWNTs to lift from the substrate, and the SWNTs were subsequently swept upward and aligned by the gas flow, and grew to mm-lengths [214]. In these CNT growth systems, rapid heating has been achieved by quickly moving the catalyst and/or substrate through a temperature gradient. Continuous thermal control has not been achieved for CNT growth, and more broadly has only been achieved in systems based using cartridge heaters [443] or patterned thin-film resistive heaters [444].

We sought direct heating of the growth substrate to enable rapid adjustment of the temperature, as well as to enable flexible access to the growth substrate for performing a variety of experiments which rely on optical, electrical, and/or mechanical access to the reaction surface. This is implemented by resistive heating of a suspended silicon platform [438,445][2], which is simply cut from a highly-doped (p^{++}) silicon wafer and suspended between contact electrodes. Transient thermal performance far surpassing the tube furnace is easily achieved; for example, a 1×5 cm×0.3 mm (W×L×wafer thickness) suspended silicon platform is heated to ≈800 °C in ≈5 seconds using ≈140 W (4.5 A, 30 V) under current control using a conventional variable-output benchtop power supply. Our platform is manufactured without using microfabrication techniques, yet achieves heating and cooling rates equal to or better than existing microsystems [443,447].

Beyond the application to CNT growth discussed here, the platform could be used for many other surface bound high-temperature reactions, while the principle of resistive heating of a silicon element contacted by self-cooled electrodes could be extended for temperature control of microsystems and microreactors as is demonstrated later for our microchannel devices. Direct substrate heating for CNT growth has been utilized previously, such as resistive heating of silicon on a stage [448–450], of a wire [451], of microfabricated traces and bridges [452,453], of carbon cloth coated with catalyst [454–457], and generally of "hot-plate" stages as in plasma-enhanced CVD [458]. However to our knowledge the suspended platform design enables far more rapid thermal control than has previously been achieved over similar-scale areas, and offers flexibility for mounting various substrates on the platform with good thermal contact due to the optical-grade flatness of the polished surface of the silicon platform.

[2] I developed this system in collaboration with Lucas van Laake; Lucas was a visiting graduate student in the MIT Precision Engineering Research Group from April–December 2005. Luuk's Master's thesis [446] at the Technical University of Eindhoven deals in large part with the design and detailed modeling the suspended heater apparatus, and its implementation for CNT film growth.

6.2.1 First-generation prototype: Platform-in-tube

The first-generation prototype (Fig. 6-5) of the suspended platform heater is a segment of silicon wafer clamped between a pair of stainless steel (AISI 304) contact electrodes, which is sealed inside a 48×52×300 mm (ID×OD×L) quartz tube, using the lip seal end cap design. The silicon platform is sandwiched at each end between a pair of stainless steel bars, and the contact is preloaded by gently tightening a bolt which passes through a clearance hole in the top bar and is anchored in a threaded hole in the bottom bar. Electrical and fluid connections are made through Cajon-type fittings in the end caps. Cables from the power supply are routed through the fittings and are terminated in "alligator" clips which are gripped onto the bolts on the contact electrodes.

The heated silicon platform is directly coated with catalyst for CNT growth, or a second substrate coated with catalyst is placed on top of the heated platform. In the latter case, the temperature on the (upward-facing) catalyst surface of the second substrate is ≈20 °C below the temperature of the heated platform. These temperatures are measured (and calibrated to the supply current for a given substrate size) using a fine-wire K-type thermocouple (Omega) which is cemented to the surface. The cement preferably has a high thermal conductivity and is electrically insulating (e.g., Aremco Ceramabond 865), since it must isolate the junction potential of the thermocouple from the current passing through the platform.

6.2.1.1 Heater coil for gas pre-treatment

The gas is routed into the quartz tube through a two- or four-bore Al_2O_3 delivery pipe (6.35 mm OD, 1.8 mm bore ID) which is held in one of the fittings, as shown schematically at the left of Fig. 6-5a. The gas is optionally heated ("pre-treated") while flowing through the delivery pipe; for this, the pipe is heated by passing current through an iron wire wrapped tightly around the pipe ($R \approx 12\,\Omega$ for 24 wraps around the pipe) and packed with insulation inside a firebrick enclosure. Although the gas cools when it exits the pipe and moves toward the substrate, thermal pre-treatment significantly affects the reactivity of the gas and can be utilized to substantially improve the rate and yield of CNT growth. This behavior is discussed more along with the results presented in the Chapter 7. With the suspended platform, localized heating of the growth substrate lets us control the temperature and duration of pre-treatment by independently preheating the gas, whereas in a single-zone tube furnace the thermal pretreatment of the gas is directly coupled to the substrate temperature as the tube, substrate, and gas are heated simultaneously by a single coil.

The effect of pre-treatment has conceptually been studied by others using "hot-filament" CVD [459,460], where the reactant flows across a suspended resistively-heated wire (typically at ≈2000 °C). This thermally activates the reactant and therefore enables growth at relatively low substrate temperatures. Our process is the first approach to decoupling reactant pre-treatment for CNT film growth at atmospheric pressure, and the heated platform reactor offers better flow and temperature control than typical hot-filament apparatuses.

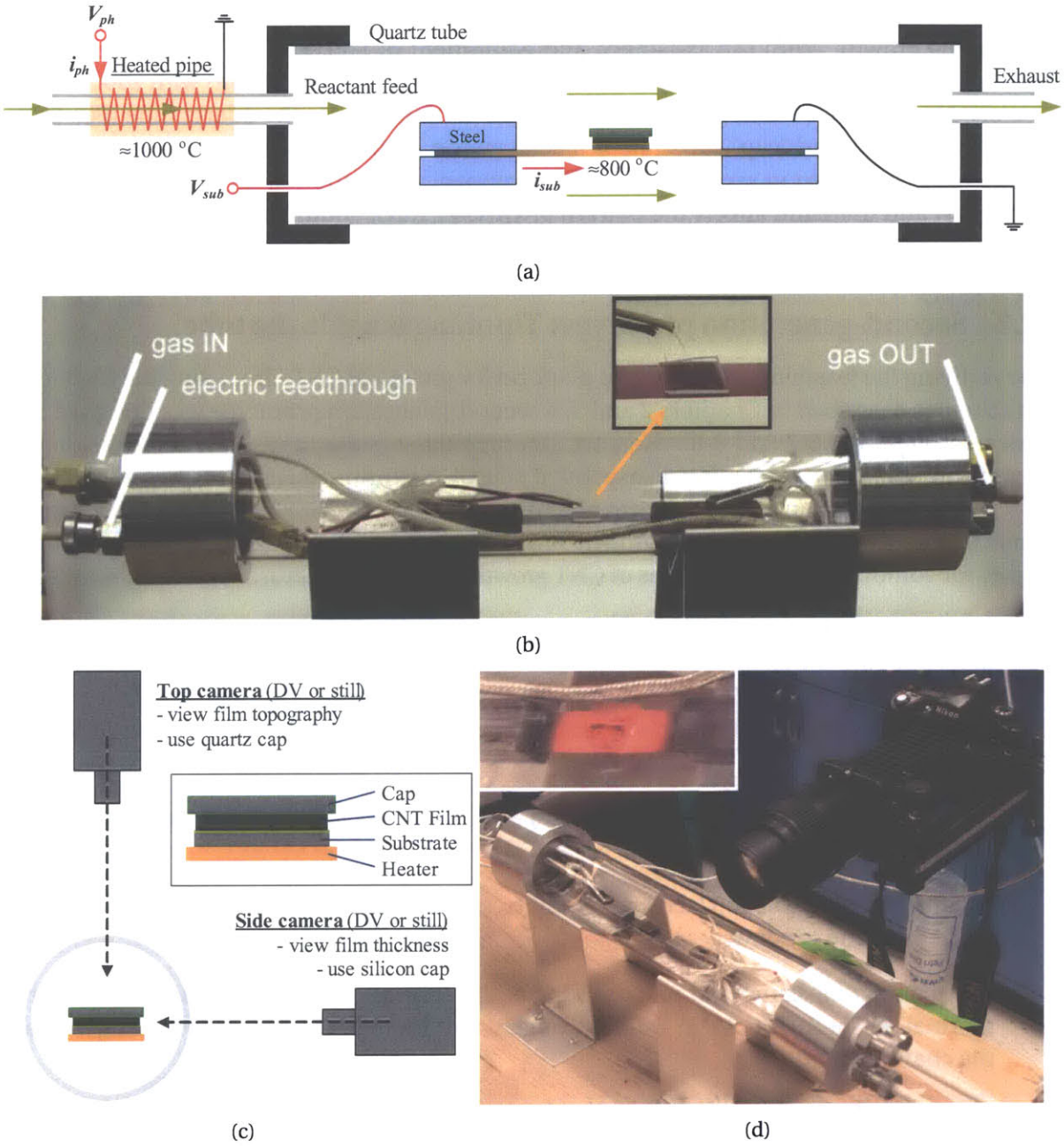

Figure 6-5. First prototype apparatus for CNT film growth on a suspended resistively-heated silicon platform [438], with *in situ* optical imaging: (a) schematic of substrate in sealed quartz tube with heated pipe for optional thermal pre-treatment of reaction gases; (b) laboratory setup with fine-wire thermocouple attached to suspended platform for temperature calibration; (c) configuration for optical imaging of growth from top and side; (d) laboratory setup with digital still camera imaging from side (inset image of CNT growth from catalyst-coated substrate resting on heated platform).

6.2.1.2 Optical imaging setup

Because the heated platform is not enclosed by external heating coils, the substrate is in full view during growth. With the assistance and equipment of Rick Slocum[3], a high-resolution digital still camera (Nikon) and high-definition digital video camera (Canon) with zoom lenses were used to image CNT film growth on the heated platform inside the quartz tube (Fig. 6-5c-d). Optionally a second "cap" substrate is placed on top of the catalyst substrate as an optical reference. As discussed in section 4.1.2.2, this "capped" configuration limit the gas supply to the catalyst and therefore affects the pattern of VA-CNT nucleation; however, after nucleation the VA-CNT growth rate is not limited.

6.2.2 Second-generation prototype: Thinking outside the tube!

After verifying the feasibility of the heated platform for growth of CNT films using the CVD reaction schemes described in Chapters 2 and 3, a second-generation prototype was designed and fabricated (Figs. 6-6, 6-7 and 6-8). Here we "thought outside the tube" (◡̈), and developed a versatile box chamber containing a suspended silicon platform. This system has added flexibility for reconfiguration of the platform and the gas flow paths, for electrical and mechanical connection to the platform and/or growth substrate, and for packaging of the microchannel devices for combinatorial flow studies of CNT growth. The salient features of the apparatus are:

- A "clamshell" chamber design, where easy removal of the top/front half gives open access to reconfigure the chamber from the front and top, while the bottom/back half is stationary with ports (1/4" NPT) for electrical and fluid connections. The chamber seals with an o-ring along the slanted interface, and this is preloaded by two aluminum draw latches (Southco).

- Optical access through large flat windows (1/4" thick borosilicate glass) on the top, front, and bottom of the chamber.

- Separately removable top (screwed), front (screwed), and bottom (latched) access panels, which hold the windows.

- Non-contact measurement and profiling of the substrate temperature using an infrared thermal sensor (IRT/C.3AMF-J-LOE, Exergen) mounted on a linear guide bearing beneath the chamber.

- Mounting of the contact electrodes on a ceramic rail support structure, which allows free expansion and contraction of the platform and electrodes under thermal strains, and thermally and electrically isolates this assembly from the chamber floor.

- An array of threaded holes in the floor of the chamber (M3 on 1" square grid), for fastening components inside the chamber.

[3]Rick's website is `http://100jpegs.com`.

- Gas delivery perpendicular to the platform, through an alumina pipe which can be positioned anywhere from 0–100 mm from the rear edge of the platform. Outside the chamber, the alumina pipe is enclosed by a heating coil for pre-treating the gas, which is identical to the design used with the first generation prototype.

The footprint of the chamber is a 8"×8" (0.5" wall thickness) aluminum extrusion (Alcoa, alloy 6061), which was cut into identical "wedge" sections to form the mating halves of the chamber. Subsequent machining operations[4] defined the access holes on each piece and the o-ring groove on the slanted interface. The top, bottom, and front faceplates were cut from cast aluminum plates using an abrasive waterjet (Omax), and subsequent manual and CNC milling operations defined the o-ring grooves and mounting holes on these pieces as well. Standard-size circular Viton o-rings are chosen because of their temperature stability and low outgassing, and are easily fit to the rectangular-footprint grooves on the chamber.

6.2.2.1 Non-contact temperature sensing and characterization of platform response

The infrared thermal sensor gives an output voltage which is nonlinear with temperature and is readily measurable only above 400 °C. The sensor output is calibrated to the platform temperature by taking simultaneous measurements along with a thermocouple cemented to the opposite (top) surface of the platform. A 9^{th}-order polynomial curve fit (Fig. 6-9) is programmed into software to capture the relationship between sensor output voltage and temperature. Owing to the small yet non-negligible thermal mass of the cement holding the calibration thermocouple to the heated platform, transient measurements reveal a rate-dependent lag of ~10 °C (Fig. 6-10) in the response from the contact thermocouple. Therefore, each calibration point is taken at steady-state, after stabilizing the heater supply current for 1 minute. We still expect a slight error due to a temperature drop from the platform surface to the thermocouple seated in the cement. Not accounting for this error, the curve-fit output from the infrared sensor matches the thermocouple output within 1–2 °C over the 600–900 °C range.

Transient measurements using the calibrated infrared sensor show the step response (Fig. 6-11) and cycling response (Fig. 6-12) at the center of the suspended platform, demonstrating a heating rate of at least 100 °C/s and a cooling rate of at least 50 °C/s. When the current is discontinued, the platform quickly loses heat to the surrounding ambient and to the contact electrodes, which act as heat sinks. Steady-state measurements show the nonlinear relationship between power and temperature (Fig. 6-15a), where the heat loss is dominated by conduction and convection at low temperature, and by radiation at high temperature. The current and voltage applied to heat the platform are converted to and measured as 0–10 V signals using a precision current-sense resistor (Ohmite) and a voltage divider.

Further, the steady-state platform temperature at a particular current varies depending on the convective heat loss, which under similar flow conditions is ordinally governed by the thermal conductivity of the surrounding gas. Lighter gases such as He and H_2 and have higher thermal conductivity than heavier gases such as Air and Ar (Fig. 6-13); therefore, a higher current is required to maintain a particular temperature in the lighter atmospheres (Fig. 6-14). This is especially important when changing the gas atmosphere during an experiment, and in the

[4] Alex St. Claire machined many components for the chamber, as a for-credit undergraduate research (UROP) project during Spring 2006.

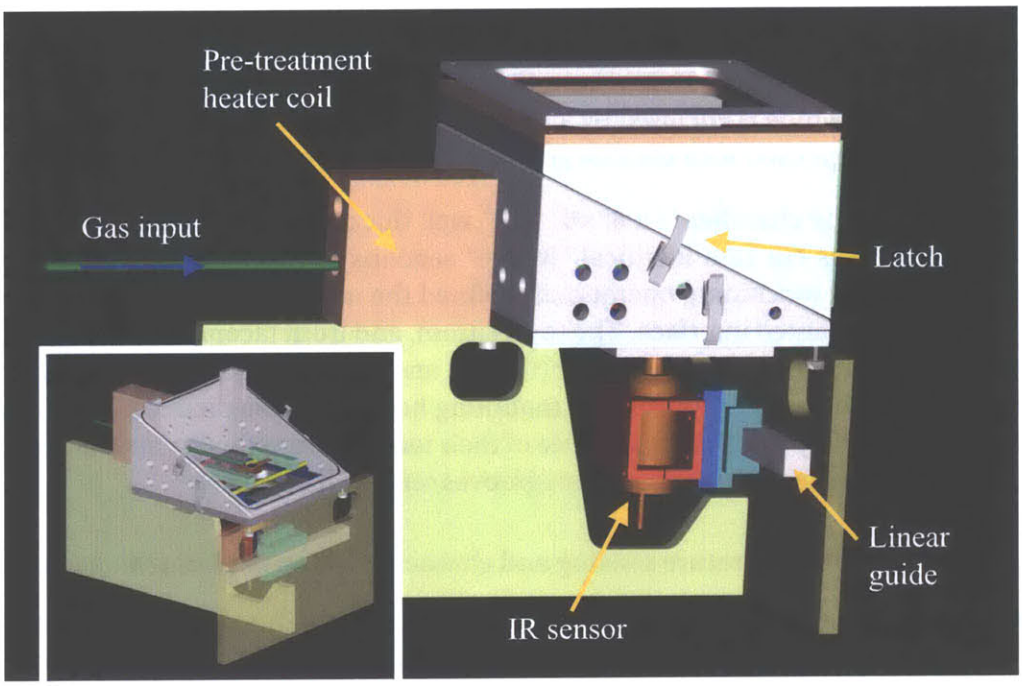

(a)

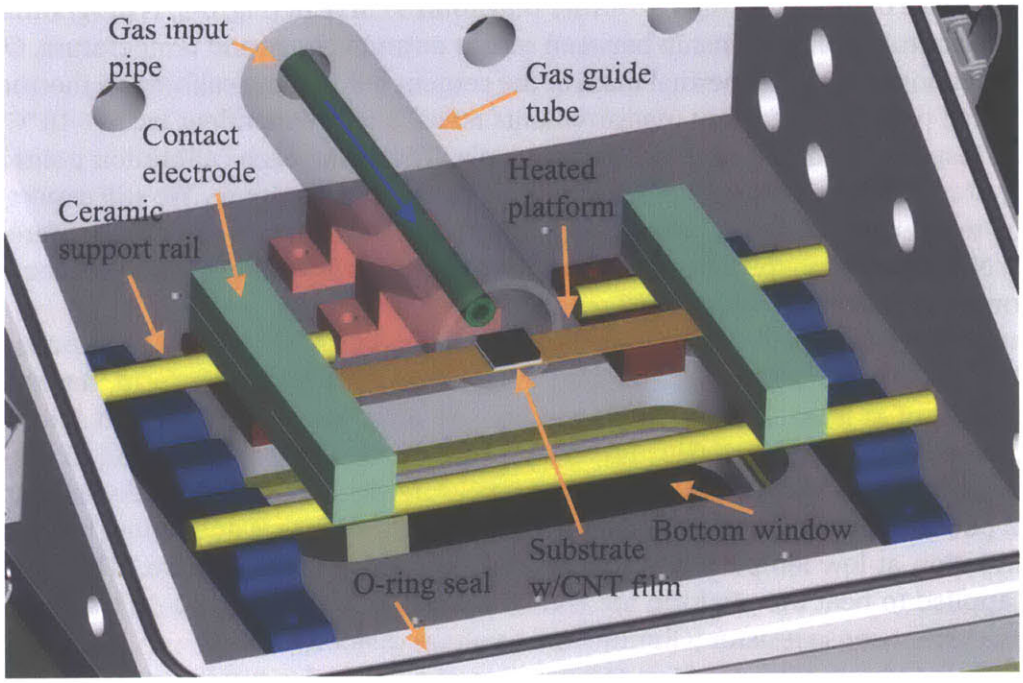

(b)

Figure 6-6. Solid model (Pro ENGINEER Wildfire v2.0) of second-generation prototype ("box") reaction chamber with suspended resistively-heated silicon platform: (f) side rear view, showing infrared thermal sensor mounted on linear guide and gas input through heated pipe enclosed in firebrick (inset is side front view, with cover removed); (b) interior of chamber (cover removed), configured for CNT film growth from catalyst-coated substrate placed on heated platform.

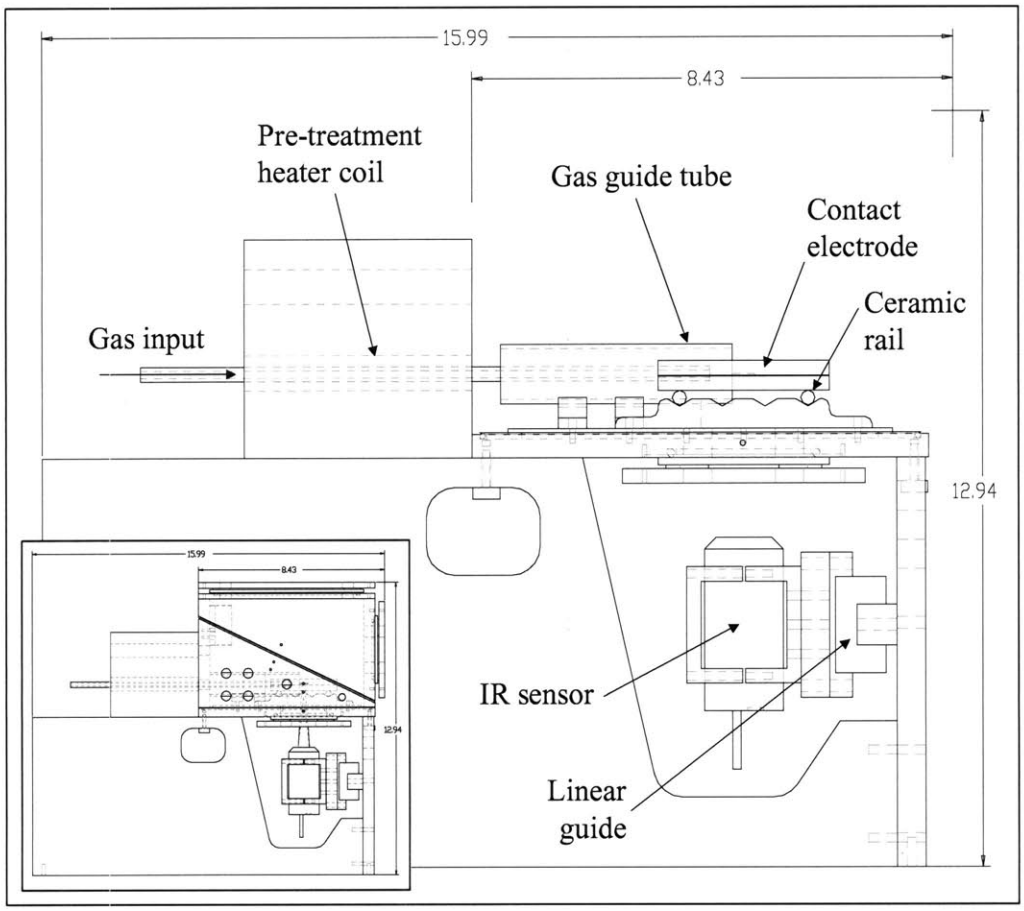

(a)

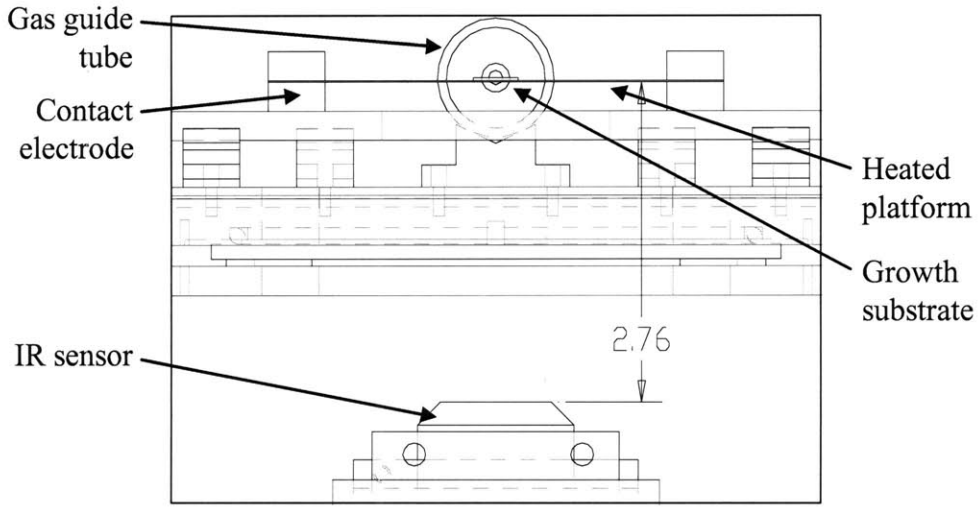

(b)

Figure 6-7. Drawings (Pro ENGINEER Wildfire v2.0) of box reaction chamber with suspended resistively-heated silicon platform: (f) side view, with sidewalls and cover removed (inset shows sidewalls and cover installed); (b) front view, with sidewalls and cover removed.

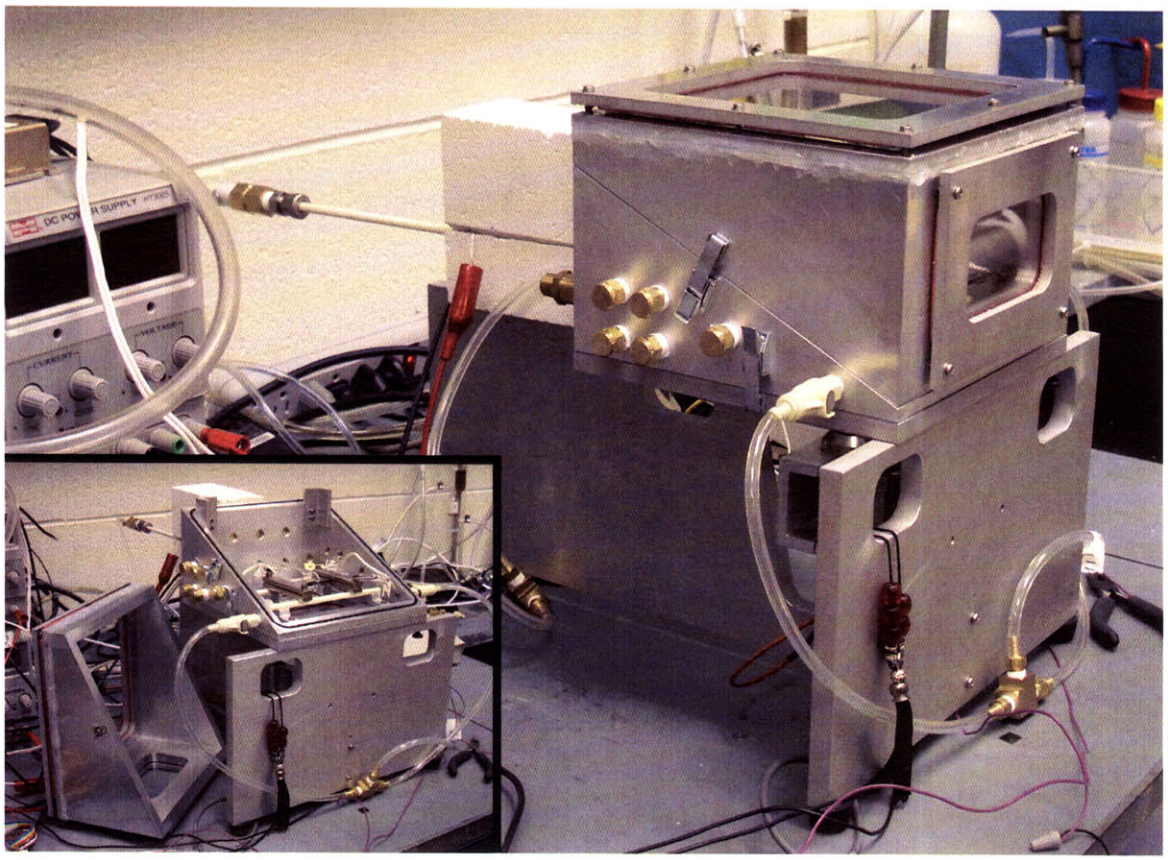

(a)

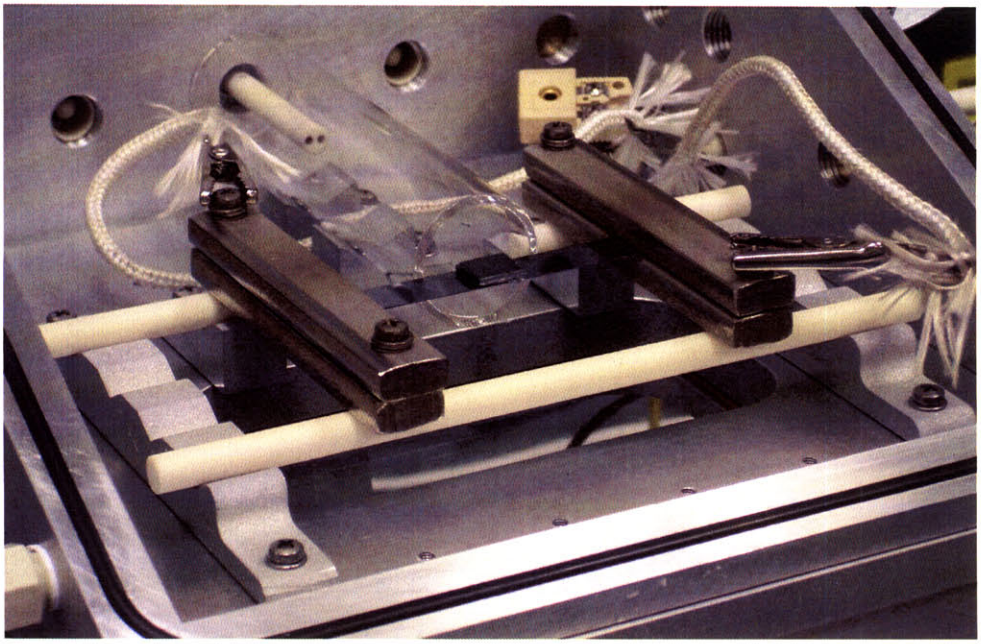

(b)

Figure 6-8. Lab setup of box reaction chamber with heated platform, with components as indicated in Figs. 6-6 and 6-7.

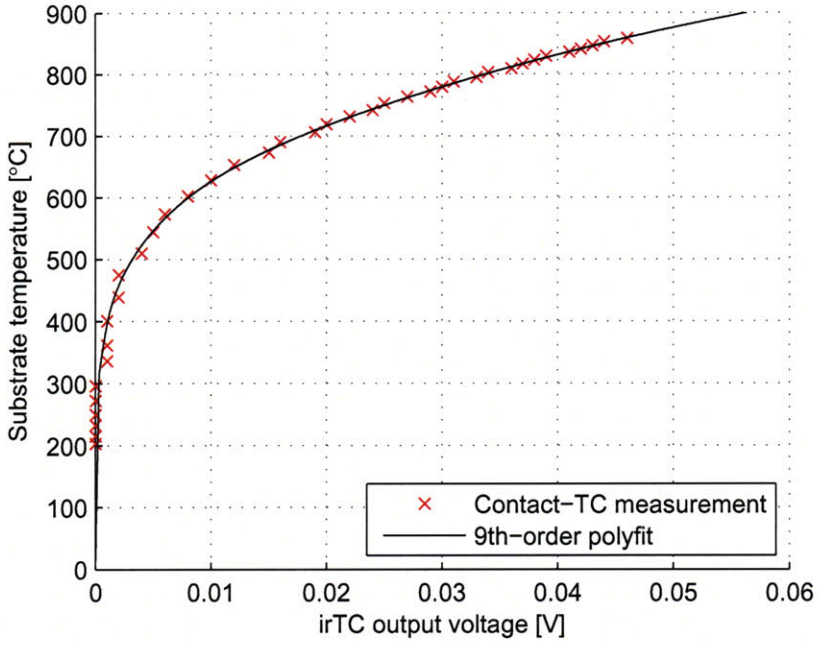

Figure 6-9. Polynomial curve fit response of infrared temperature sensor, calibrated using a thermocouple cemented to the heated platform. The infrared sensor is mounted outside the box chamber and below the heated platform, and is focused on the bottom surface of the heated platform.

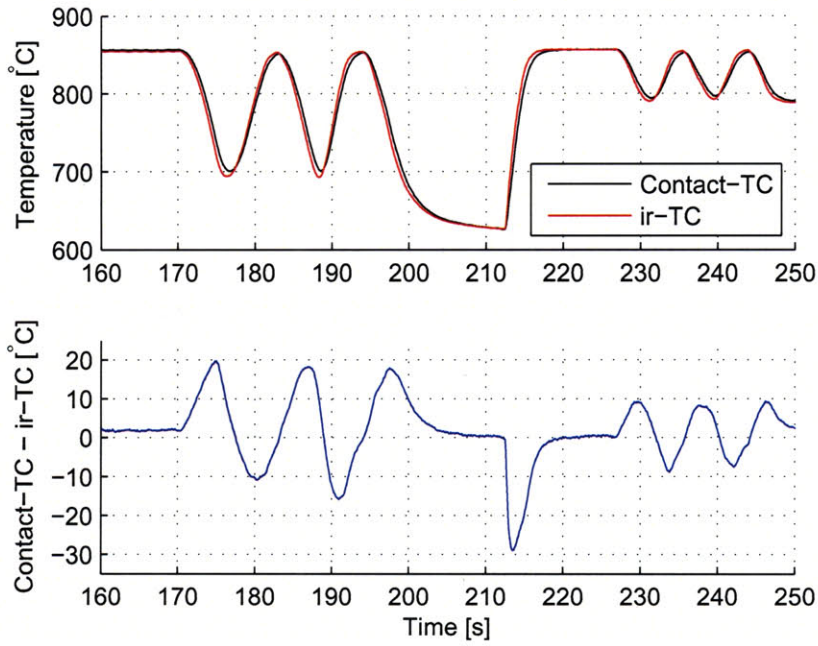

Figure 6-10. Comparison of platform surface temperature readings from contact thermocouple (contact-TC) and from non-contact infrared sensor (ir-TC), demonstrating lag in contact sensor response due to thermal mass of sensor mounting cement.

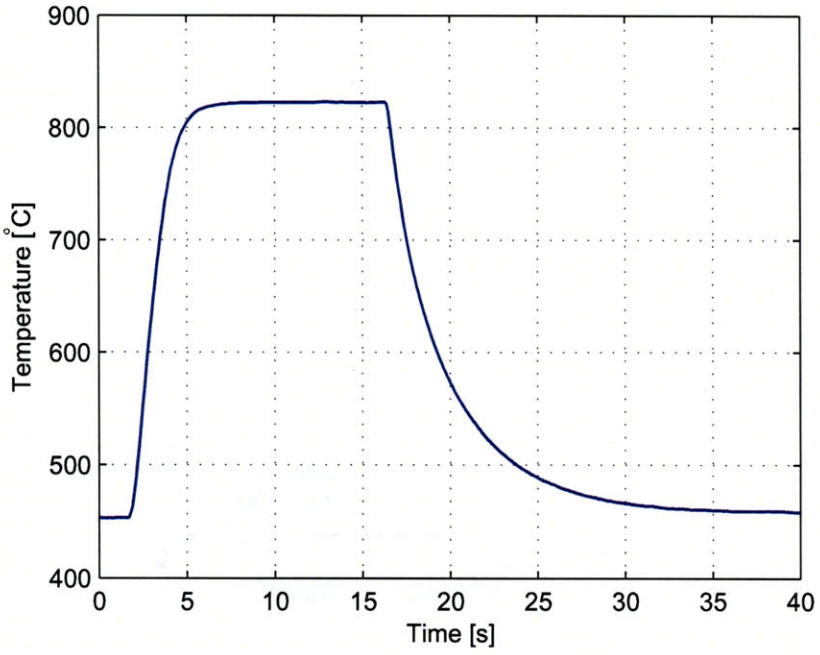

Figure 6-11. Rapid heating response at center of suspended silicon platform (suspended section $\approx 9 \times 48$ mm), when step current (≈ 4.5 A, ≈ 35 V) is applied at $t \approx 2$ s, along with subsequent rapid cooling when current is reduced at $t \approx 17$ s.

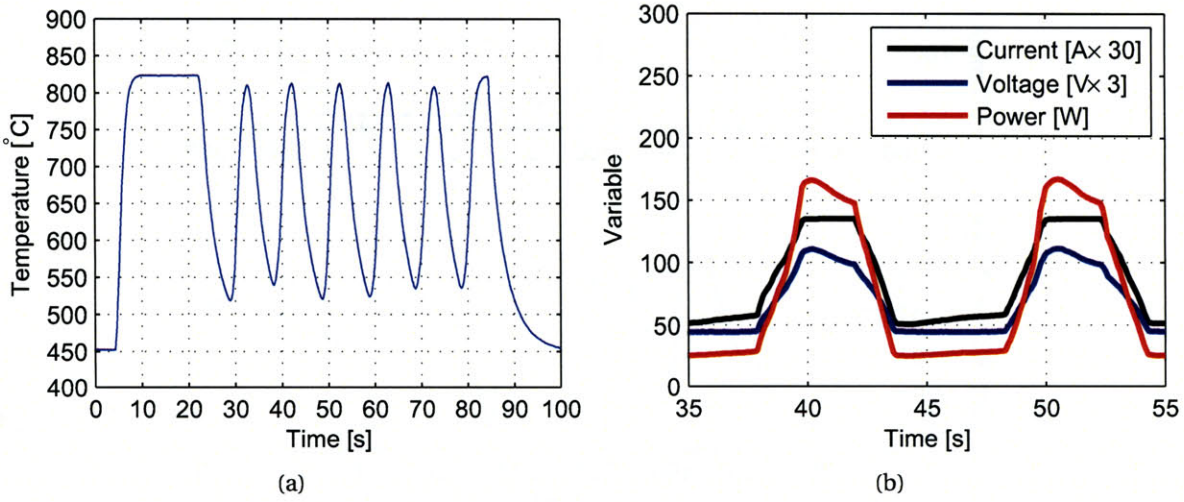

Figure 6-12. Performance of suspended silicon platform heater when current is cycled manually: (b) temperature at center spot; (b) current, voltage, and power trends.

future this will be addressed by feedback control of the platform temperature. We expect that as monatomic and symmetric diatomic molecules, Ar, Air (primarily N_2 and O_2), He, and H_2, are practically transparent to infrared radiation [440] and therefore these temperature differences are not falsely perceived due to absorption in the optical path of the sensor. However, temperature calibration should be performed in each gas atmosphere.

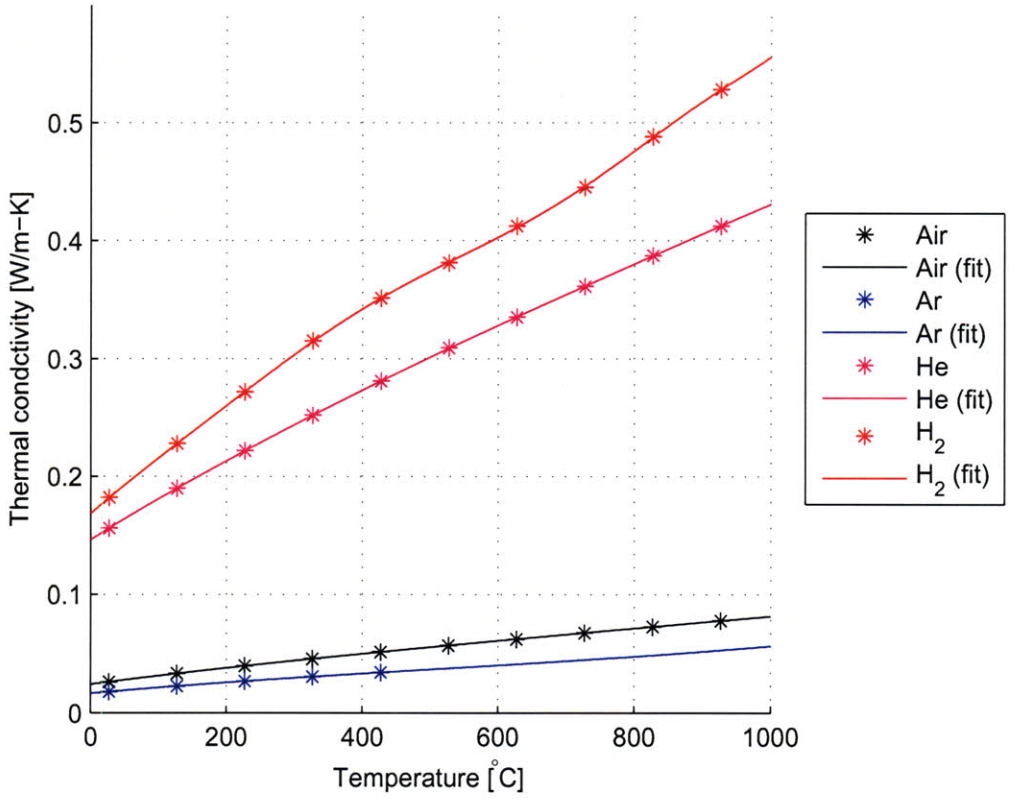

Figure 6-13. Thermal conductivities of carrier gases versus temperature [440]. The convection heat loss is larger and therefore constant-current temperature is lower for a surrounding gas of higher thermal conductivity, as shown in Fig. 6-14.

The resistivity of the suspended silicon platform, measured by dividing the voltage by the current, increases with temperature until ≈700 °C (except for a slight and non-repeatable drop at 300 °C, likely due to a contact effect), and then decreases with temperature (Fig. 6-15b). This trend is typical for highly-doped silicon [461]; in general the resistivity of silicon depends on carrier concentration and carrier mobility. At room temperature, highly-doped silicon is degenerate (this is called the "extrinsic region"), and carrier concentration is approximately equal to the dopant concentration. With increasing temperature, carrier mobility decreases due to scattering, resulting in an increase in resistivity. Above a critical "intrinsic temperature", thermally-activated formation of electron-hole pairs dominates the carrier concentration. In this region, the carrier concentration increases sharply with temperature, causing a sharp decrease in resistivity.

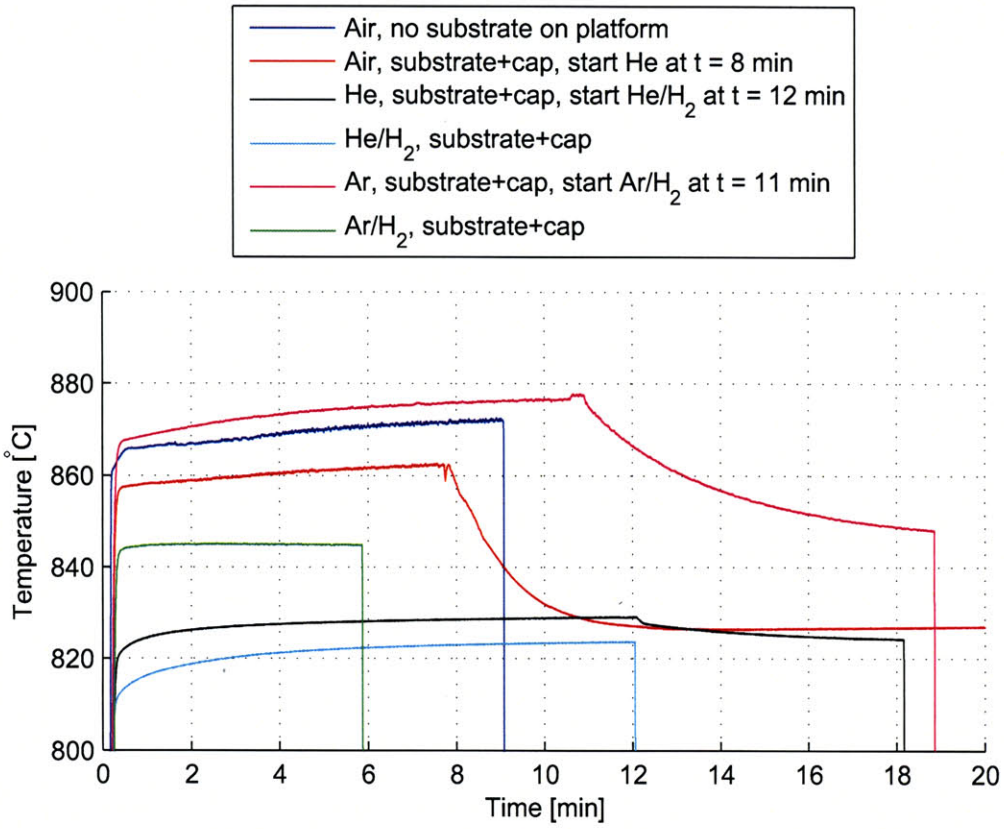

Figure 6-14. Step response (4.87 A) of suspended platform heater in various gas atmospheres, demonstrating sensitivity of platform temperature to variations in convective heat loss.

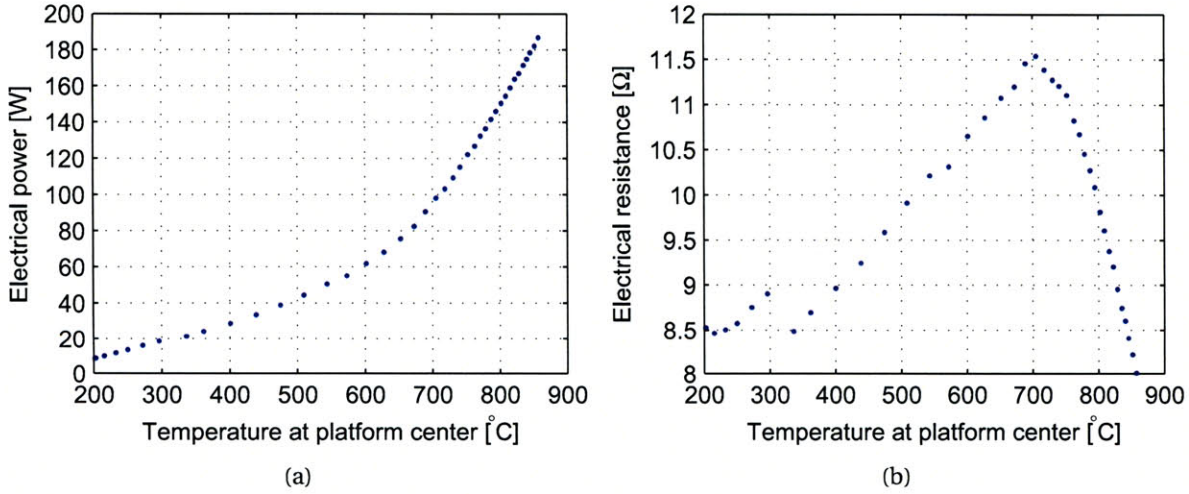

Figure 6-15. Steady-state measurements of (f) electrical power dissipated and (b) resistance versus temperature at center of suspended silicon platform.

Luuk van Laake's work [445, 446] models the thermal behavior of the suspended platform in detail, considering temperature-dependent material properties and convective and radiative heat losses. The model demonstrates excellent (within $\approx$10 °C) agreement with transient temperature profiles across the suspended platform, which are measured with five fine-wire thermocouples cemented along the centerline of the platform (Fig. 6-16). The model can accommodate additional thermal mass on the heated platform; this feature is useful for predicting the thermal performance for example when substrates are placed on the platform or when the microchannel device is clamped to the platform.

Further, we experimentally observe the Thomson effect, where the temperature distribution along the platform is skewed slightly in the direction opposite to current flow through the platform, owing to emission of heat by charge carriers flowing in the direction of a thermal gradient (and vice-versa) [462]. Interestingly, the magnitudes of heat dissipation by the Joule (resistive) and Thomson effects become comparable if the conductor has characteristic dimension of $\approx$1 μm [463], raising issues in observation of heat flow through small suspended structures including thermal micro-actuators [464], suspended heaters for localized growth of nanowires [452], and electrically-heated nanostructures themselves [89].

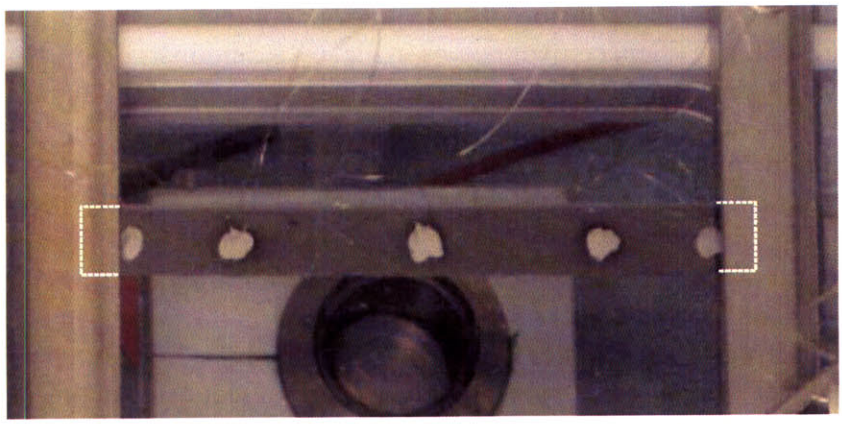

Figure 6-16. Top view of suspended silicon platform with five thermocouples attached for temperature profile measurements. The infrared sensor, positioned to monitor the center spot of the platform, is visible through the bottom window of the chamber. White lines indicate the ends of the silicon platform piece.

6.2.2.2 Laser measurement of film thickness

Optical access through the top window enables direct measurement of the film thickness by reflecting a laser beam from the top surface of the film. A laser-based displacement sensor (Keyence LK-G152) is mounted on an arch which is built around the box (Fig. 6-17). The support posts are aluminum (2"×2" extrusion, alloy 6061), and the cross-beam is cut from 0.5" thick Invar plate (alloy 36, Online Metals). Invar[5] alloy is typically 36% Ni and 64% Fe with

[5]Invar was invented in 1896 by Charles Edouard Guillaume, and he received the Nobel Prize in Physics in 1920 "in recognition of the service he had rendered to precision measurements in Physics by his discovery of anomalies in nickel steel alloys".

slight amounts of C and Cr, and this composition has a very low coefficient of thermal expansion ($\approx 1\times10^{-6}$ /K up to ≈100 °C, compared to $\approx 13\times10^{-6}$ /K for Al). Therefore, Invar is used so the sensor will not drift due to thermal-expansion-induced deflection of the crossbeam caused by heat radiated through the top window. Typically the Keyence sensor is set to 100 μs sampling time with an internal moving average of width 16384 samples, and the analog output of 5 mV/μm is recorded using LabVIEW™.

Gas is delivered to through the ceramic delivery pipe which is placed behind the platform and shielded in a quartz tube. Alternate gas flow configurations using one and two flexible stainless steel hoses (Swagelok) have been tested (Fig. 6-18); however, the configuration with the horizontal delivery pipe gave much more uniform growth in initial experiments and was therefore adopted for all experiments presented in this thesis. The effect of the flow distribution around the platform is clearly vital to the growth process, and this effect must be studied in further detail. Interactions between the (horizontal) forced flow velocity (i.e., dictated by the reactant flow rate and the delivery pipe diameter) with the (vertical) convection velocity (i.e., dictated by natural convection plumes arising due to rapid heating of the reactant in the vicinity of the platform) are likely important.

The measured displacement of the top surface of the cap substrate corresponds to the CNT film thickness, plus thermal expansion of the platform, contact electrodes, and surrounding hardware. Representative displacement curves in Fig. 6-19 demonstrate that these effects can be straightforwardly decoupled to give an accurate measurement of the film thickness versus time.

When the platform is initially heated by supplying a step current (at $t \approx$ -1 min), an upward displacement of 0.1–0.2 mm is suddenly measured, corresponding to thermal expansion. While the design intended that thermal stresses in the platform would be relieved as the contact blocks could slide freely on the ceramic support rails, it is apparent from the magnitude of this initial expansion that the blocks remain fixed and the platform bows upward in response to thermal expansion. After this initial transient decays, the measurement drops by ≈0.03 mm when ethylene is introduced at $t = 0$, presumably because of scattering of the laser beam.

Next, a baseline experiment (black curve in Fig. 6-19) conducted with a bare silicon substrate instead of a catalyst-coated substrate indicates that the displacement measurement drifts upward at < 2 μm/min. This results from ≈ 0.3 °C/min drift of the substrate temperature. The drift is due to the due to heating of the contact electrodes and the ambient gases inside the chamber, which reduces the heat loss from the suspended platform as a constant supply current is maintained. The sensor output has occasional noise fluctuations of ±10 μm, which could be removed by low-pass filtering.

Comparatively, typical growth experiments (red and blue curves in Fig. 6-19) give an upward displacement of ≈100 μm/min, which is easily distinguished from the background drift and therefore represent the growth rate of the CNT film. Under certain conditions which are discussed in section 7.2.3, the reaction terminates naturally and the displacement measurement suddenly levels off (blue curve). Under other conditions (red curve), the reaction proceeds and certain regions of the film stop or slow growing before others, causing the cap to tilt, which can cause the displacement beam to be reflected out of the viewing range of the sensor. In our experiments, this tilt error occurs primarily in the non-sensitive direction of the sensor (Fig. 6-20) and therefore does not affect the measurement accuracy. However, slight tilt in the sensitive direction (side-to-side as viewed from the front of the platform) can introduce significant error

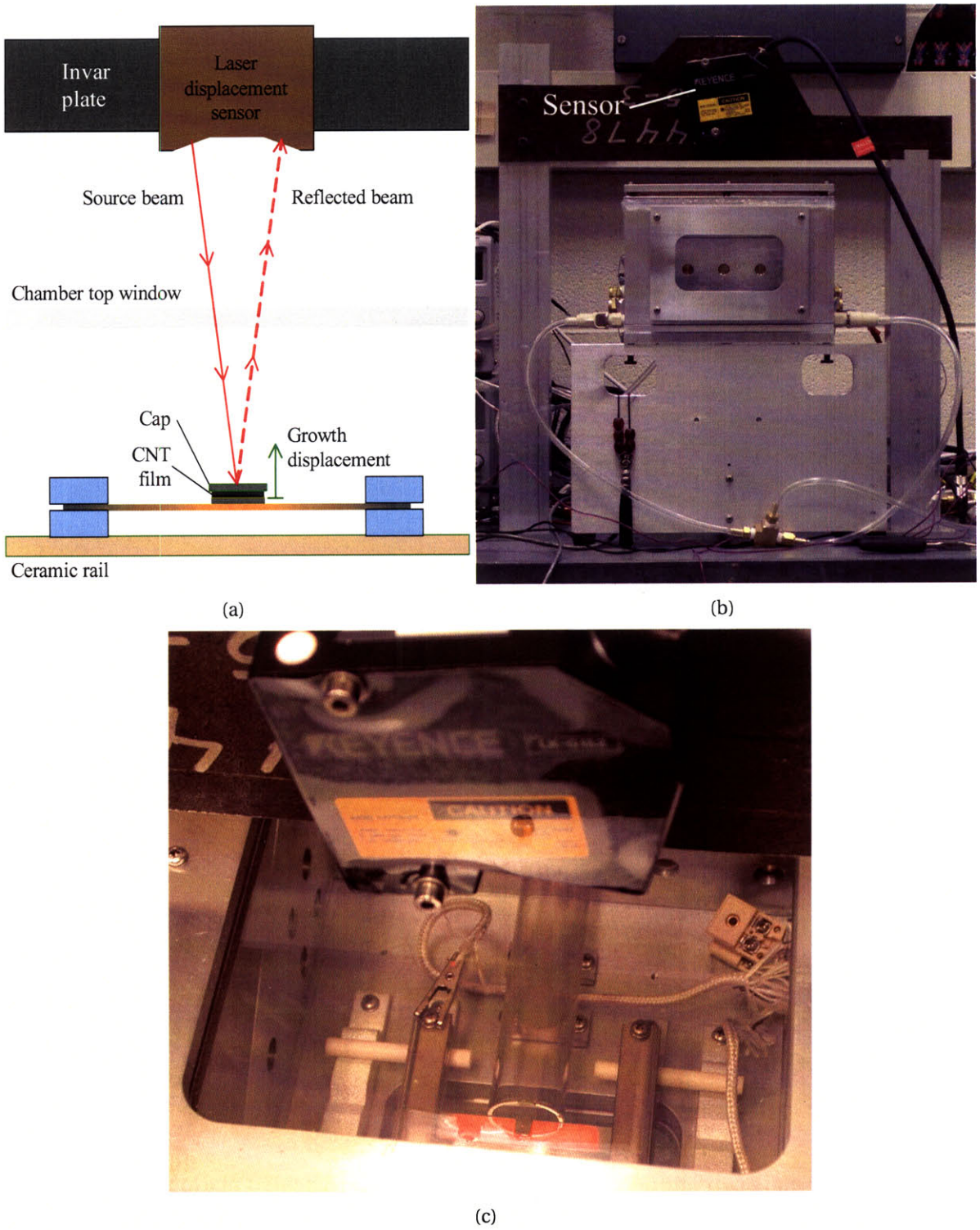

Figure 6-17. Apparatus for real-time measurement of film growth kinetics using laser displacement sensor: (f) schematic of sensor configuration; (b) lab setup with sensor mounted on arch above box chamber; (c) view through top window showing beam spot on Si_3N_4-coated cap on growth substrate.

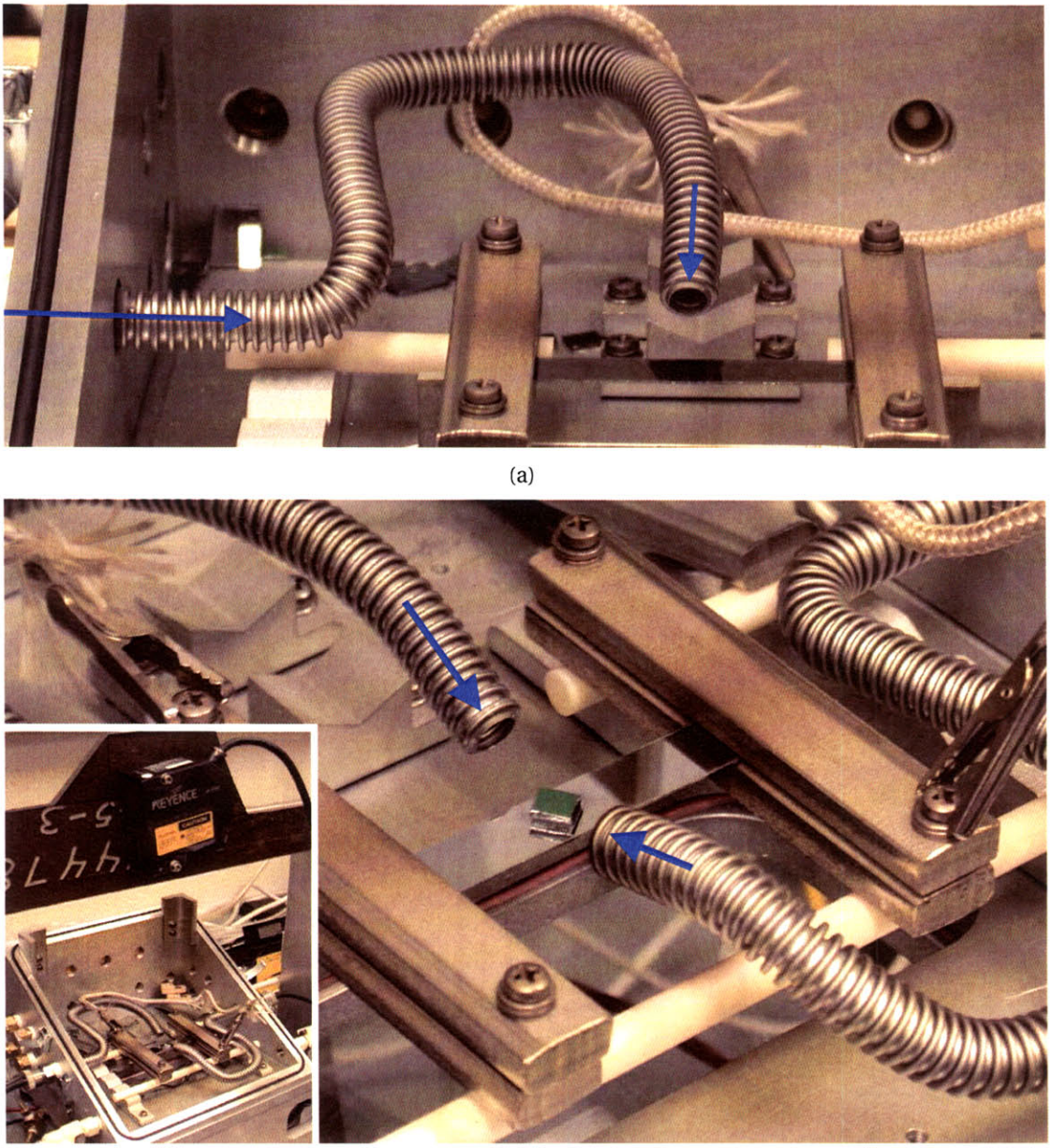

(a)

(b)

Figure 6-18. Alternate configurations for delivery of reactant to heated platform, using flexible stainless steel hoses: (a) single hose, which gave good growth like with delivery through the pipe (Fig. 7-7b); (b) dual hose, which gave poor growth, perhaps due to flow interference.

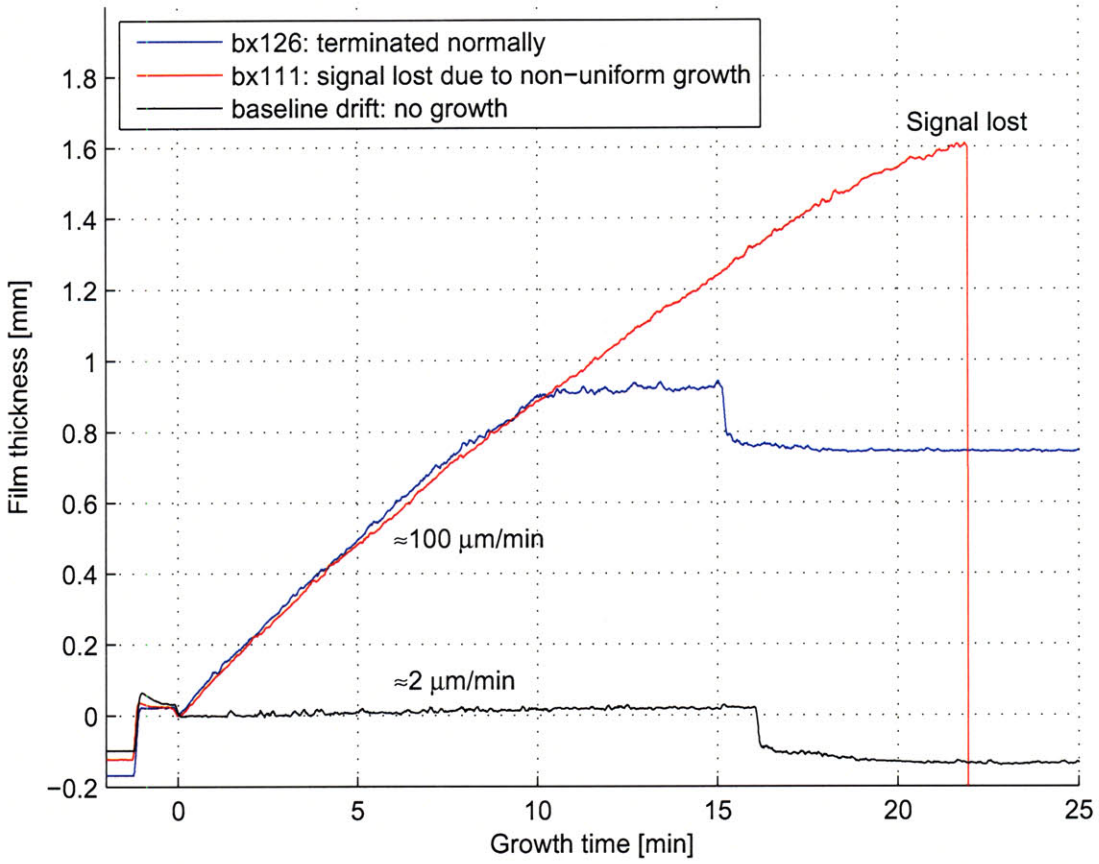

Figure 6-19. Representative values of upward displacement of cap resting on growth substrate, where measured values are shifted to indicate film thickness. This shows the background drift ($\approx 2\ \mu$m/min), compared to typical CNT film growth sequences ($\approx 100\ \mu$m/min) where the reaction terminates uniformly (blue curve) and where the reaction proceeds farther and the beam is eventually lost due to non-uniform growth (red curve).

and must be avoided. Going forward, a mechanism can be implemented to translate the displacement of the highest point of the film to a secondary target which remains flat, and therefore eliminate the effects of tilt errors and enable measurement until final termination of the reaction. Further, displacement measurement from both sides of the substrate would more accurately compensate for thermal drift error in growth kinetics data, especially for experiments with time-varying platform temperature.

Others have measured VA-CNT film growth kinetics by laser reflectivity, where a laser beam is passed into and along the axis of a traditional tube furnace and the growth substrate is mounted perpendicular to the beam [160, 465]. The growth rate is calculated by counting Fabry-Perot fringes as the reflected intensity of the laser decays with increasing CNT film thickness, and by relating the fringe counts to a model of the optical properties of the CNT film and catalyst-coated substrate. Our suspended platform presents an alternative method where it is not necessary to infer the optical properties of the CNT film, where the measurement is insensitive to the temperature of the target, where measurements can be made to mm-thicknesses and be-

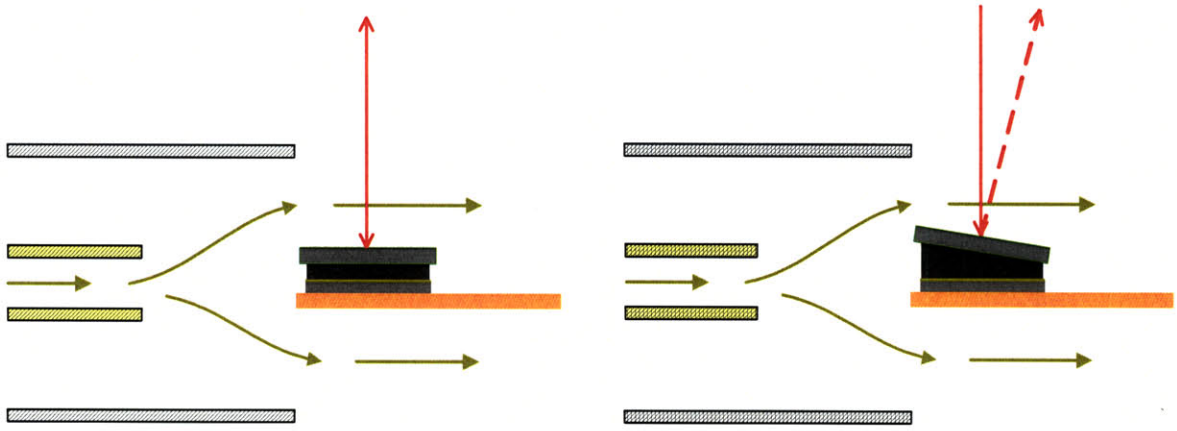

Figure 6-20. Schematic representation of tilt error in non-sensitive direction of laser displacement sensor: (a) uniform film growth, causing translation of beam spot position on detector array; (b) non-uniform film growth, causing reflected beam to divert away from optical sensor.

yond (versus $\approx 10\,\mu$m for the reflection technique of [160]), and where rapid thermal control is simultaneously possible. Growth rate has been determined indirectly by measuring film thickness from many experiments having varying reaction times (e.g., [162]), but this is very time consuming and relies on maintaining exactly the same conditions throughout all experiments. Other methods create witness marks on the sidewall of the film by briefly discontinuing the carbon supply in a tube furnace [161,197], but this may influence growth and further does not give a continuous measurement.

There are many other examples of reaction chambers built for *in situ* monitoring and diagnosis of surface reactions; one recent example is a variable-pressure flow cell used with online IR spectroscopy of CO oxidation [466].

6.3 Packaging of microchannel devices

CNT growth experiments in microchannels are conducted by packaging a microchannel array (Chapter 5) inside a tube furnace or on the resistively-heated silicon platform. The tube furnace package was developed before the heated platform apparatus and was used for initial experiments; later experiments utilized the heated platform.

For experiments in the tube furnace, the array is clamped in a quartz fixture (Fig. 6-21a) which is placed in a 42 mm ID quartz tube. The array is inverted over the growth substrate (coated with a uniform catalyst film or with a catalyst pattern fabricated by lift-off), and is clamped between custom-machined (Ferro-Ceramic Grinding, Wakefield, MA) quartz blocks. Fluid passages in the quartz blocks are aligned with the laser-micromachined through holes in the array. The fixture is clamped using Al_2O_3 bolts (Ceramco), and preloaded using Inconel X750 belleville spring washers (Key Bellevilles). Selection of this spring material is critical, as most metals creep below CNT growth temperatures; in our experiments the Inconel washers retain sufficient elasticity up to 800 °C for 2 hours. A graphite gasket (1/16" thick CraneFoil, John Crane) placed under the growth substrate may also be used to preload the fixture; however this

undesirably outgasses when heated and thereby contaminates the CNT growth catalyst.

Fluid is conveyed to the microchannel array through quartz pipes (3/16" OD, Fig. 6-22) which are affixed to the ends of the quartz blocks, and thereby flow can be pumped into the array by pressurizing the input pipe or drawn into the array by evacuating the output pipe. Knowing the importance of thermal pre-treatment of the reactants for good CNT growth, a preferred configuration draws the gas into the array from the heated atmosphere inside the furnace tube (Figs. 6-23 and 6-24). Here, the reactants flow into the furnace tube and are heated in the same path as for experiments on normal silicon substrates. The front end of the microchannel array is left open by cleaving away a portion of the device die. When the output pipe of the package is evacuated, the thermally pre-treated reactants are drawn into the microchannel array through the open front end. This is similar to the flow reversal configuration presented for short-time experiments with normal substrates, where the evacuation source is a vacuum generator regulated by N_2 line pressure, and the reactants are flushed from the array by reversing the flow using a three-way valve.

On the suspended platform, the the microchannel array and the growth substrate are packaged (Fig. 6-21b) using quartz plates (1 mm thickness, cut from a 150 mm diameter polished quartz wafer) which are held by regular stainless steel binder clips (McMaster-Carr, #12755T81). The suspended platform is sandwiched between the growth substrate and the bottom quartz plate. Holes are drilled through the top quartz plate, and quartz pipes are welded to these holes for flow access to the array (Fig. 6-25a). The device is operated in the same "flow reversal" fashion as with the tube furnace package configuration. Because the growth temperature is maintained locally by the heated platform, the stainless steel clips remain sufficiently below their creep temperature and therefore maintain the clamping force which seals the package. The quartz plates increase the thermal mass of the platform and thereby slow the thermal response; however, the package is readily heated to 800 °C in less than 1 minute (Fig. 6-25b), and with a $\approx 70 \times 20$ mm silicon heater the steady-state power consumption is $\approx$300 W (7 A, 43 V).

An important feature of both packaging arrangements is the design of the mating interface between the microchannel array and the growth substrate; the etched surface of the Si_3N_4-coated microchannel array is non-polished, and the growth substrate is polished (surface roughnesses are as shown in Fig. 3-34). This arrangement prevents bonding between the array and growth substrate at the growth temperatures (and this validated to 1000 °C for 2 hours), enabling the package to be fully disassembled for *ex situ* characterization of the growth substrate and for re-use of the microchannel array after cleaning.

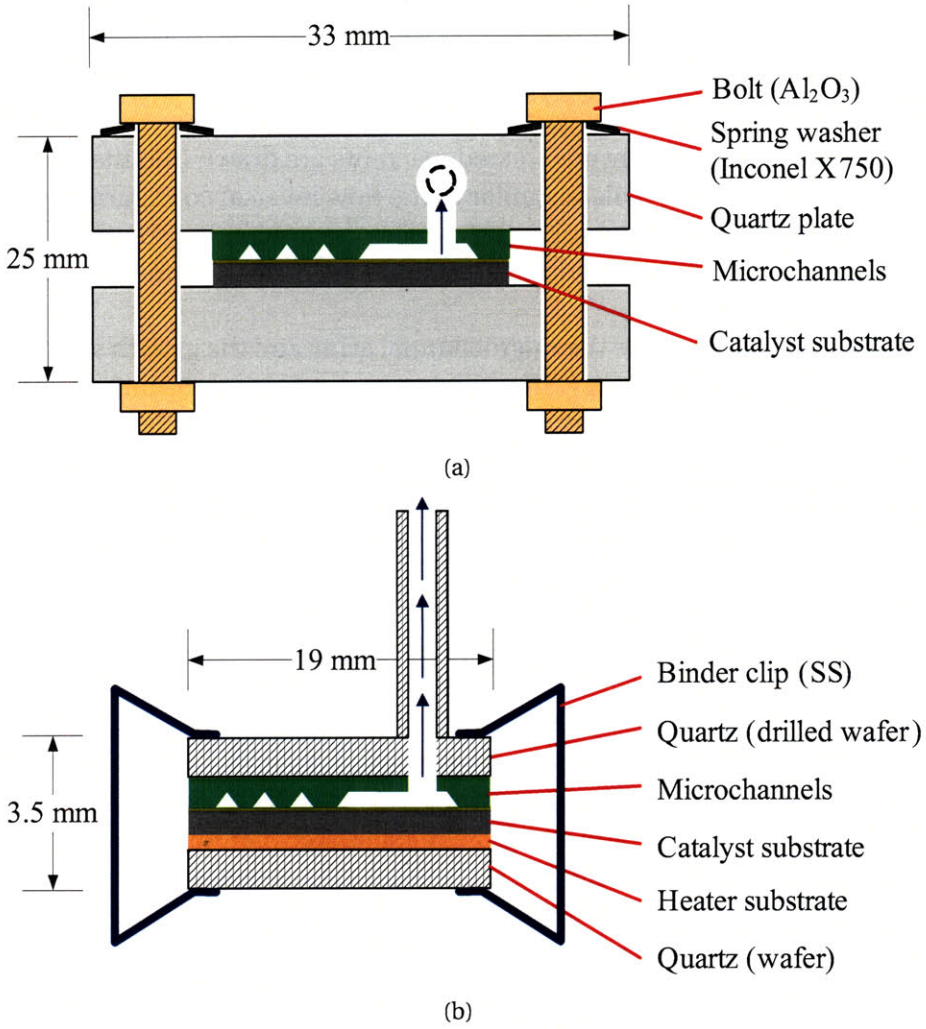

Figure 6-21. Packages for microchannel array device: (f) fixture for tube furnace where the microchannel array is sandwiched between quartz blocks, preloaded using ceramic bolts and Inconel spring washers; (b) fixture for resistively-heated silicon platform, where the microchannel array is sandwiched between thin quartz plates, and the assembly is preloaded using stainless steel binder clips.

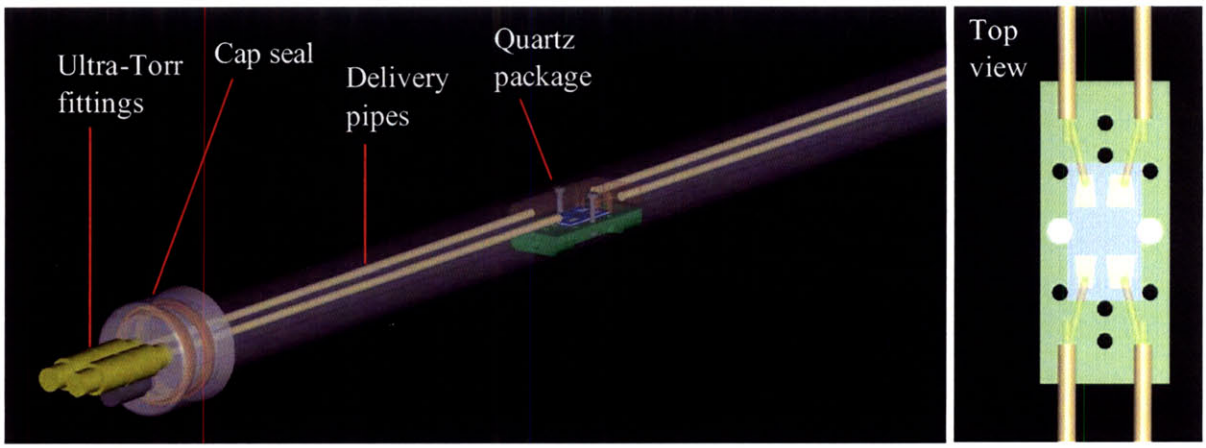

Figure 6-22. Solid model (Pro ENGINEER Wildfire v2.0) of microchannel array package in tube furnace, showing fluid delivery pipes.

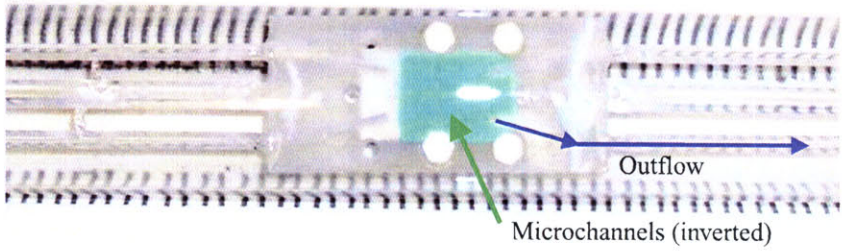

(a)

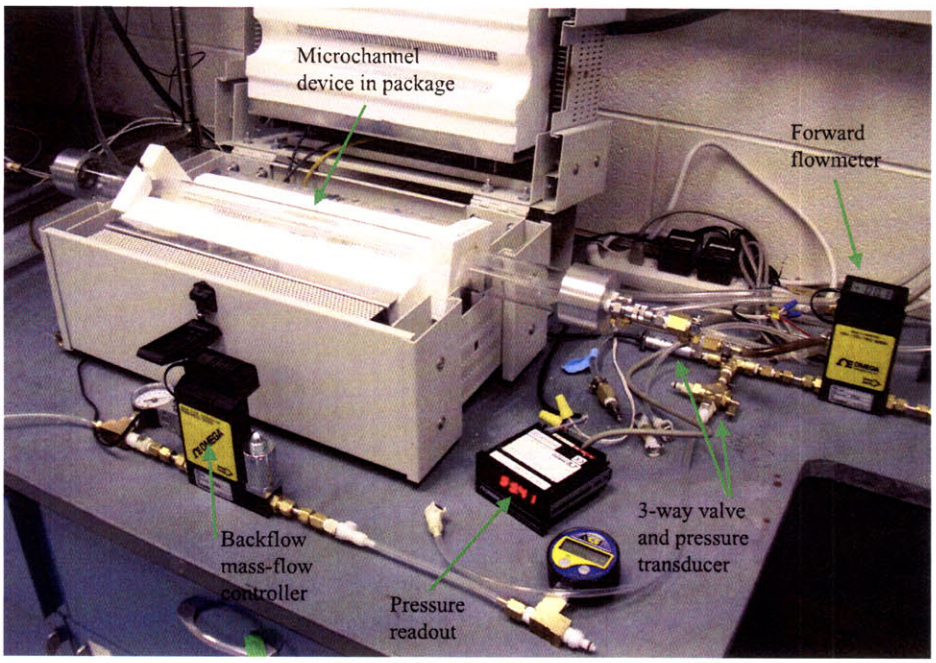

(b)

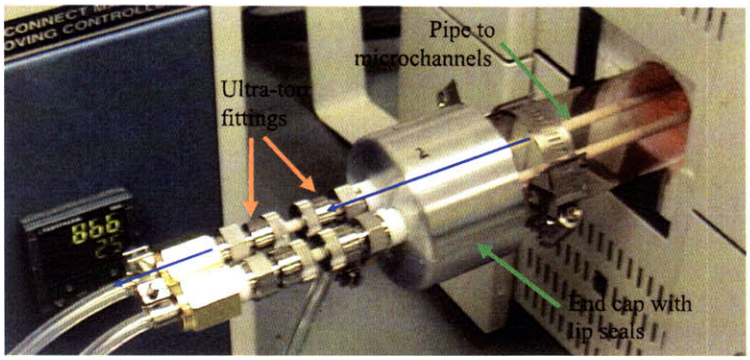

(c)

Figure 6-23. Setup for CNT growth in microchannel array packaged inside tube furnace, in flow reversal configuration: (f) top view of quartz package inside 42 mm OD tube; (b) tube furnace with external instrumentation for pressure and flow control; (c) connections to delivery pipes through tube end caps.

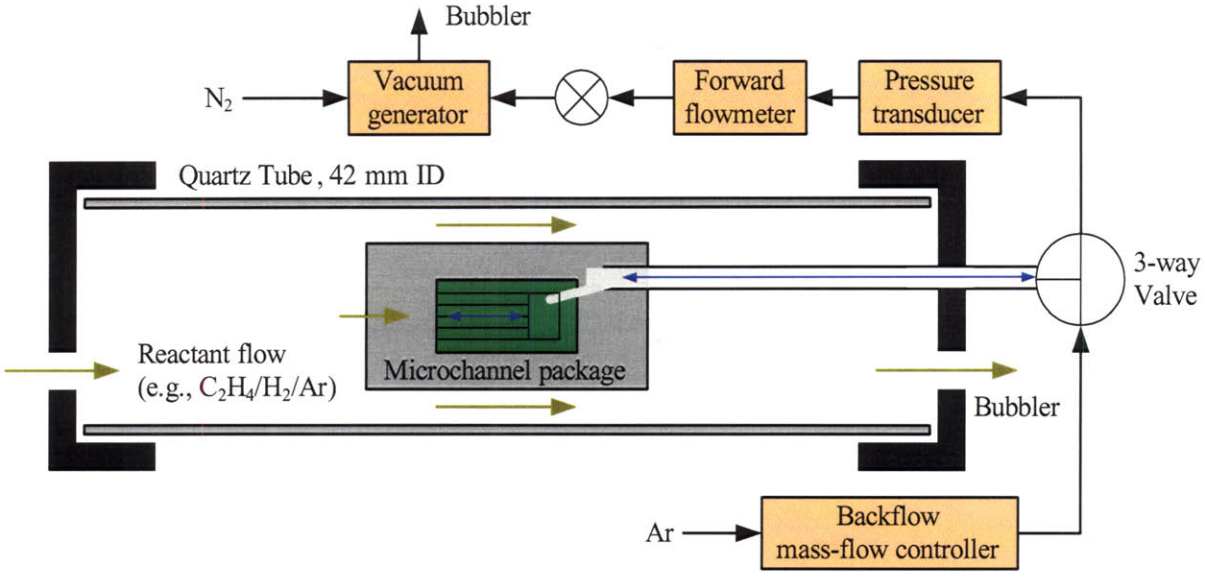

Figure 6-24. Schematic of flow reversal configuration for microchannel array experiments inside tube furnace.

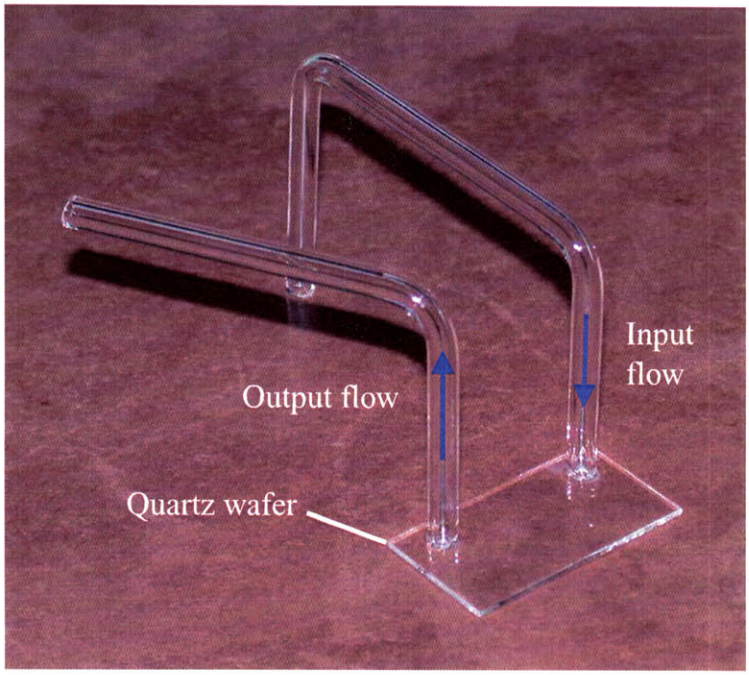

(a)

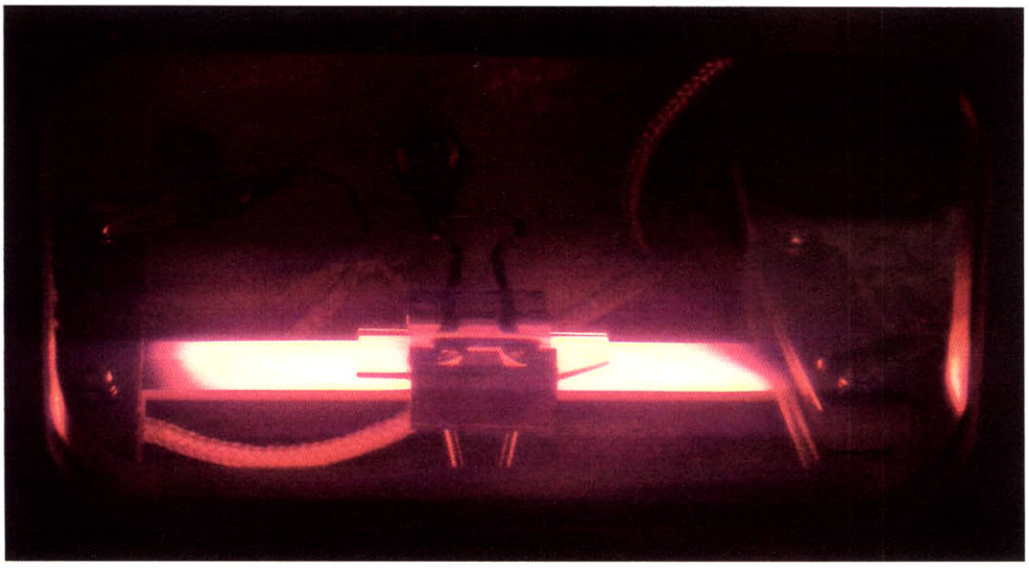

(b)

Figure 6-25. Packaging of microchannel array on heated platform: (f) quartz fixture with wafer interface plate; (b) test heating of 19 mm wide substrate in clamped configuration.

Chapter 7

CNT Growth Studies Using New Furnace Systems

This chapter presents results of CNT growth studies performed using the new furnace systems described in Chapter 6, focusing on experiments conducted under rapid and precision control of flow, temperature, and gas activity. These studies are: an investigation of VA-CNT film nucleation at short growth times by implementing the flow-reversal technique in a horizontal tube furnace; growth of VA-CNT films on the resistively-heated suspended platform by independent thermal control of the gas pre-treatment and growth substrate temperatures, along with laser measurement and optical imaging of the growth kinetics; and preliminary growth studies in microchannel arrays, demonstrating transitions in CNT yield and flow-directed alignment of CNTs.

7.1 Short-time growth experiments using tube furnace in flow-reversal configuration

As described in Chapter 4, films of VA-MWNTs are grown from a Fe/Al_2O_3 catalyst film deposited by electron beam evaporation on silicon wafers. In a normally-configured tube furnace, a film typically grows to 0.9 mm in 15 minutes under a flow of 100/500/200 sccm $C_2H_4/H_2/Ar$ at 750 °C. The CNTs average 9 nm OD with 5 concentric walls [3].

Here, we study the evolution of a CNT film during the initial stage of growth, by rapidly introducing and discontinuing the flow of C_2H_4 to the growth substrate, using the flow reversal apparatus attached to a horizontal tube furnace (Fig. 6-4). The initial stage is when the catalyst is first exposed to the carbon source, causing CNT nucleation. A sufficient density of CNTs begins growth such that the CNTs self-align in the VA-CNT conformation, and then the film thickens while maintaining the alignment.

First, the reactant gas composition is brought to a steady state in the main tube. In the meantime, the growth substrate is pre-conditioned by Ar/H_2 which flows backward through the small tube (Table 7.1). After a pre-conditioning duration of 2 min, the flow through the small tube is reversed and reactants flow from the main tube into the small tube. Growth is terminated by reversing the flow once again: Ar flows backward through the small tube, quickly displacing the reactant gases.

Within 5 s of introducing the reactants to the small tube, a sparse arrangement of tangled CNTs is observed on the substrate (by *ex situ* examination), and a vertically-aligned morphology emerges after 15-30 s of reaction (Fig. 7-2). Due to mechanical and surface hindrance, tangled CNTs do not grow beyond ≈ 1 μm film thickness. We suspect this nucleation period is related to the duration of pre-treatment with H_2, and testing this hypothesis requires further study.

Further, alternating flow reversal steps like the "pulsed" flow experiments presented in section 4.2.3 (e.g., repeatedly introducing Ar/H_2 backward through the small tube), could be used to fabricate precise-thickness CNT multi-layers where H_2 exposure preferentially etches CNTs at the growth site.

	Gas Flow [sccm]	
Time [min]	Main tube	Reversal tube
0–28	400 Ar	← 25 Ar
28–30	100/500/100 $C_2H_4/H_2/Ar$	← 25/75 Ar/H_2
30–(30+t_{rev})	100/500/100 $C_2H_4/H_2/Ar$	→ 25 $C_2H_4/H_2/Ar$ (main tube mix)
(30+t_{rev})–(40+t_{rev})	400 Ar	← 100 Ar
Cool	Trickle Ar	← Trickle Ar

Table 7.1. Gas flow sequence for flow reversal growth experiments in concentric-tube furnace, where t_{rev} is varied as the precise duration of carbon flow over the growth substrate.

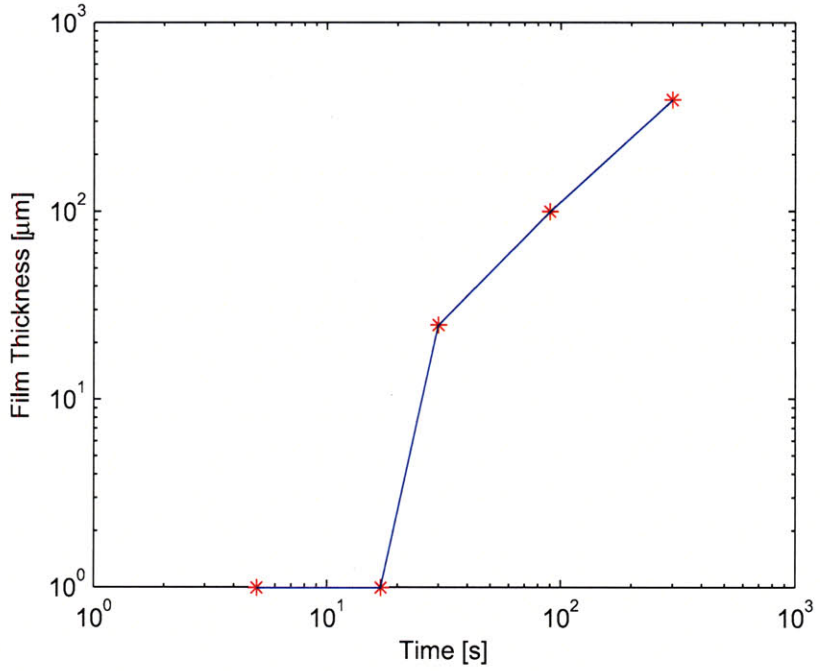

Figure 7-1. Evolution of CNT film thickness at short durations of exposure to C_2H_4 (Table 7.1), revealing dominant VA-CNT nucleation occurs between 15–30 s after C_2H_4 is introduced.

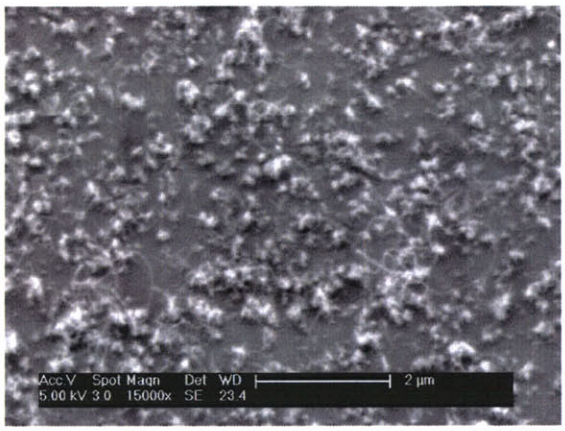

(a) $t = 18\,\mathrm{s}$

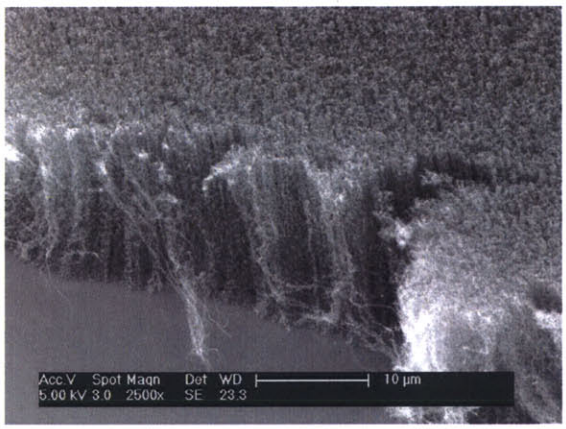

(b) $t = 30\,\mathrm{s}$

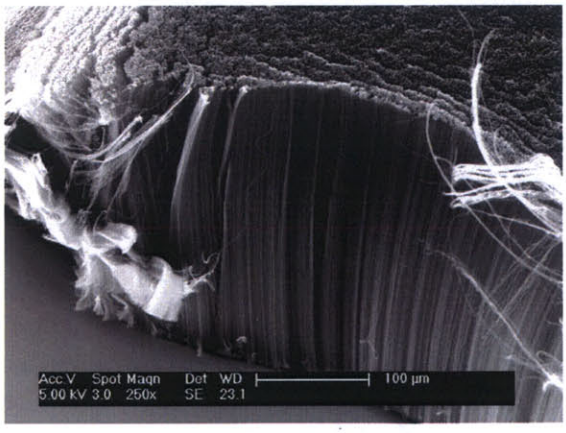

(c) $t = 300\,\mathrm{s}$

Figure 7-2. Evolution of CNT film morphology at short growth times, revealing transition from sparse nucleation of tangled CNTs at $t = 18\,\mathrm{s}$, to VA-CNT film at $t = 30\,\mathrm{s}$, to thick VA-CNT film at $t = 300\,\mathrm{s}$.

7.2 CNT film growth on a resistively-heated silicon platform

An apparatus where the catalyst-coated silicon substrate is placed on a resistively-heated silicon platform (section 6.2, [438,445]) instead of inside an externally-heated quartz tube enables rapid control of the reaction temperature along with optical monitoring of growth. Because the growth temperature is maintained locally at the heated platform, this apparatus reveals the importance of thermal activation of the reactant mixture on the yield and growth rate of CNTs. Pre-treatment (activation) of the gas is an inherent attribute of tube furnace growth systems, as hydrocarbons undergo gas-phase reactions while flowing through the tube. This pre-treatment is strongly coupled to the flow rate of reaction mixture which determines the residence time of the gas in the tube.

Using the heated platform apparatus, the pre-treatment parameters can be chosen independently of the platform temperature. This flexibility enables direct study of the effect of pre-treatment on VA-CNT film growth, along with manipulation of the limiting kinetics, as revealed by *in situ* measurement of the film thickness.

7.2.1 Initial study: importance of thermally pre-treating the reactants

Initial experiments with the heated platform sought to replicate VA-CNT film growth as achieved in a 22 mm ID tube furnace using the Fe/Al_2O_3 catalyst film and 100/500/200 sccm $C_2H_4/H_2/Ar$ (section 4.1, [3]). These experiments used a heated platform sealed inside a quartz tube (section 6.2.1), with a $\approx 1 \times 1$ cm growth substrate placed on the center region of the platform. Directly delivering the gas mixture "fresh" from the supply tanks to the (as in a usual growth experiment, but without heating the gas before it reaches the platform) gives only ≈ 0.1 mm film thickness in 15 min (Fig. 7-3a), compared to ≈ 0.9 mm obtained in the tube furnace under otherwise identical conditions.

However, when the gas is delivered through the tube furnace (750 °C setpoint) prior to entering the heated platform tube, the film thickness reaches ≈ 1 mm in 15 min. The gas returns to room temperature upon exiting the tube furnace, and then is heated a second time when it reaches the platform; therefore it is likely that heating the gas causes thermal decomposition into more reactive species for CNT growth, and these species persist even though the gas is cooled *en route* to the growth site at the platform.

Realizing that dedicated pre-treatment of the gas could significantly increase the film growth rate on the heated platform, while seeking to eliminate the apparent need to first flow the gas through a tube furnace, we turned to experiment with flowing the fresh (not previously heated) reactant through a heated pipe mounted in the inlet fitting of the platform-in-tube apparatus. As discussed in section 6.2.1, this "heated pipe" device (shown schematically in Fig. 6-5a) comprises twenty-four wraps of thin-gauge wire around a four-bore Al_2O_3 pipe which is enclosed in a firebrick housing, and rapidly heats the gas to ≈ 1000 °C[1]. When pre-treating the gas by this method, a VA-CNT film grows to ≈ 2 mm in 15 min (Fig. 7-3b), exceeding all growth rates achieved in the tube furnace. High-magnification SEM imaging indicates that VA-CNT films

[1] This temperature of 1000 °C is far above the self-pyrolysis temperature for C_2H_4 in the reactant mixture. If the reactants flow through the tube furnace at 850 °C or above, soot and oil form in the tube. Conversely, the rapid flow (~0.1 s residence time) through the heat-exchanger tube does not allow enough time for significant pyrolysis yet clearly activates the gas for better CNT growth.

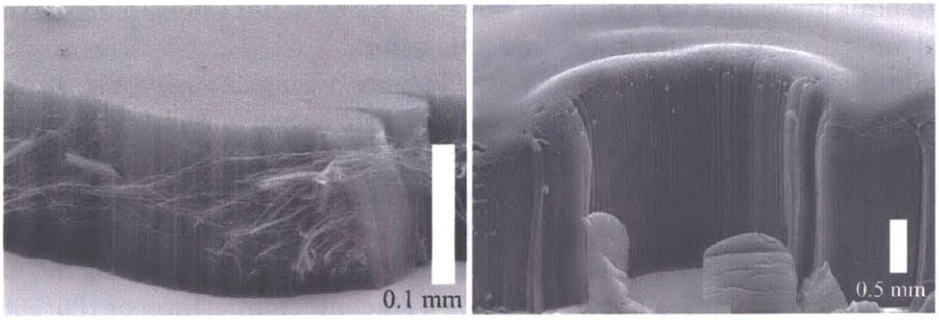

(a) (b)

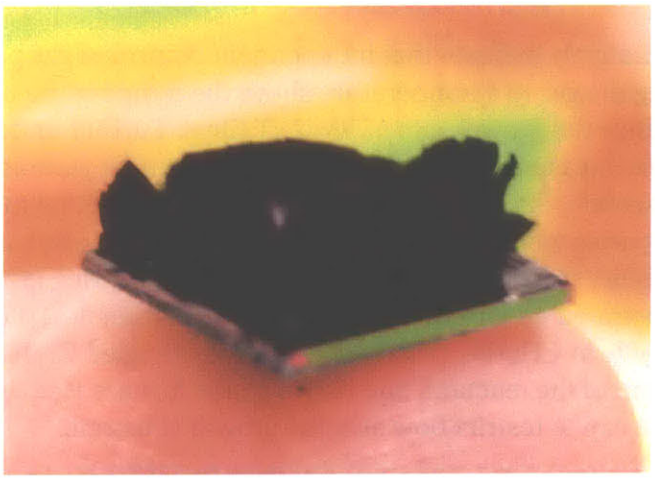

(c)

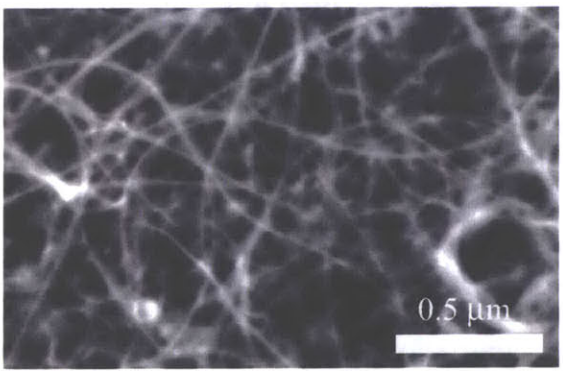

(d)

Figure 7-3. CNT films grown from catalyst-coated silicon substrates rested on the resistively-heated platform: (a) ≈0.1 mm thick VA-CNT film, grown from 1/10 nm Fe/Al_2O_3 in 100/500/200 sccm $C_2H_4/H_2/Ar$ at platform temperature of 800 °C, for 15 min, with no gas pre-treatment, and with H_2 introduced 5 min prior to C_2H_4; (b) ≈2 mm thick VA-CNT film, grown as in (b) with pre-treatment by flowing gas through heated Al_2O_3 delivery pipe; (c) 3+ mm thick VA-CNT film (resting on my fingertip), grown as in (c) but with 100/500/100 sccm $C_2H_4/H_2/CO$; (d) tangled SWNT film, grown in 320/80 sccm CH_4/H_2 at platform temperature of 850 °C.

grown on the heated platform have a comparable areal density of CNTs and comparable CNT diameters to films grown in a tube furnace; however, we have not yet examined these samples by TEM and must do so to further justify this conclusion.

Our studies of VA-CNT film growth in a tube furnace, where changing the configuration of the substrate sample changes the pattern of VA-CNT nucleation on the substrate, suggest that the conversion rate of C_2H_4 or of the appropriate gas-phase precursors may be limiting CNT nucleation and causing sharp transitions in the film structure in regions which receive an insufficient gas flow. Literature indicating that CO can increase the conversion rate of C_2H_4 on Fe catalysts [467] led us to add CO to the reactant mixture for experiments using the heated platform. When replacing Ar with CO, thereby giving a reactant composition of 100/500/100 sccm $C_2H_4/H_2/CO$, a VA-CNT film grows to ≈3 mm in 15 min and some areas reach ≈4 mm in 30 minutes (Fig. 7-3c).

These results qualitatively indicate that independent control of gas pre-treatment, particularly by rapidly heating the gas to a temperature above the temperature of the reaction surface, can significantly enhance the growth rate of VA-CNT films. Further understanding of our process is enabled by *in situ* measurement of the film thickness under various pre-treatment conditions as discussed in section 7.2.3. Moving forward, it will be essential to identify the chemical nature of the active species which enhance growth, perhaps by spectrum analysis (e.g., mass spectrometry, ion mobility spectrometry) of the exhaust gases during growth.

Finally, we demonstrated growth of tangled SWNTs (Chapter 3, [1]) using the heated platform, from $Mo/Fe/Al_2O_3$ in CH_4/H_2 (Fig. 7-3d). Densely tangled CNTs are obtained without dedicated pre-treatment of the reactant, and like in a tube furnace yield is enhanced by placing a second substrate as a cap to restrict flow over the growth substrate.

7.2.2 Optical imaging of VA-CNT film growth

Continuing work with the heated platform apparatus in a quartz tube, VA-CNT film growth from $C_2H_4/H_2/CO$ was imaged digitally using a video camera and a still camera as described in section 6.2.1.2. Imaging from the side reveals the evolution of film thickness, while imaging from the top (typically with a quartz cap used to moderate the gas flow to the catalyst) reveals the evolution of film topography.

Imaging from the side view (Fig. 7-4) shows how VA-CNT film growth lifts the cap which serves as an optical reference, and displacement is visible starting within the first 15 s (still images were taken every 15 s) after introducing the carbon source to the quartz tube. Starting at t≈10 minutes, a significant non-uniformity in film thickness is apparent, as the reference edge of the cap is tilted upward to the right in the images. This tilt increases with continuing growth. Overall we observe that these non-uniformities in growth rate are typical for films which grow rapidly, and emerge as growth slows in some regions of the film (perhaps due to deactivation of the catalyst) while growth remains more rapid in other regions. We can determine the film thickness versus time by measuring relative distances between the substrate and cap on these images; however, this is cumbersome compared to direct laser measurement of the displacement of the cap (section 7.2.3).

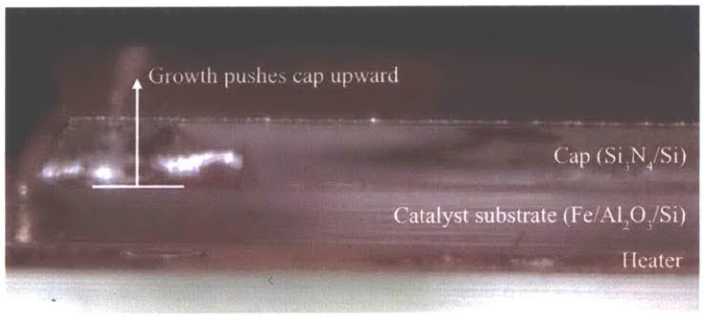

(a) Immediately before introducing C_2H_4, t = 00m:00s

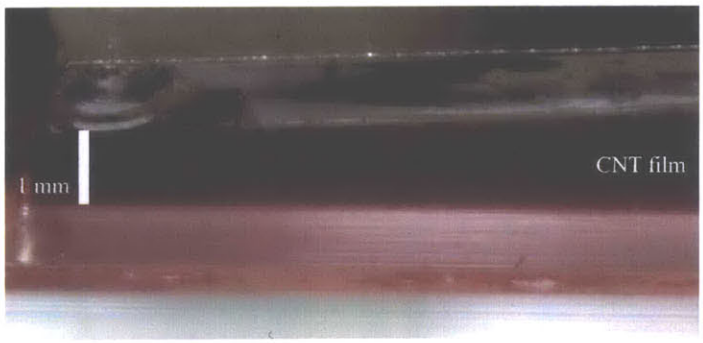

(b) After 10:00 of growth

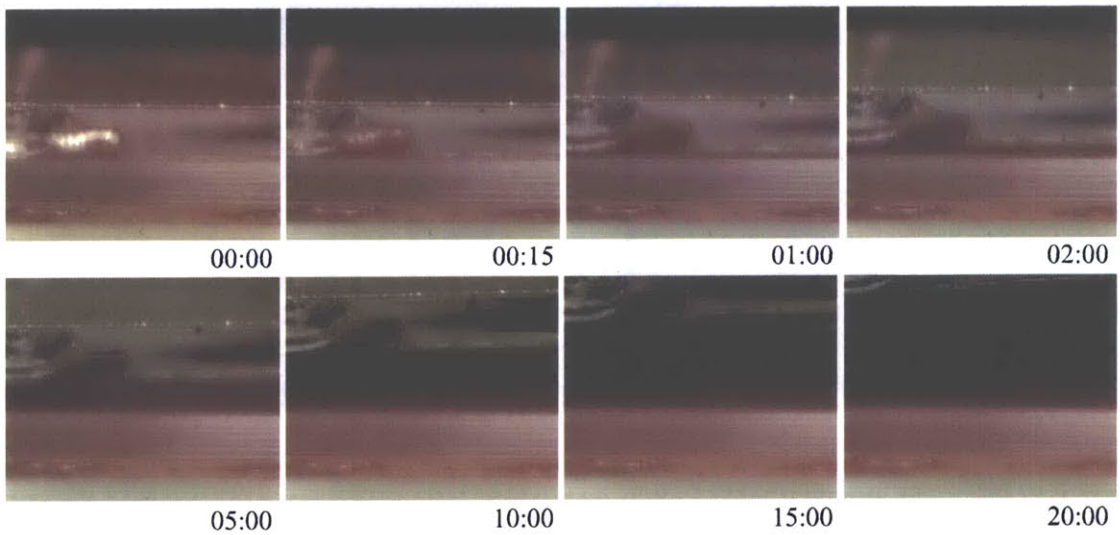

(c)

Figure 7-4. Side-view optical images of a ≈1×1 cm area CNT film during growth on a resistively-heated silicon platform mounted in a quartz tube. The film thickness is ≅2.5 mm after 20 min of growth, in 100/500/100 sccm $C_2H_4/H_2/CO$, with reactant pre-treatment using a heated Al_2O_3 pipe, and with the platform at 800 °C. These images were taken with the assistance of Rick Slocum.

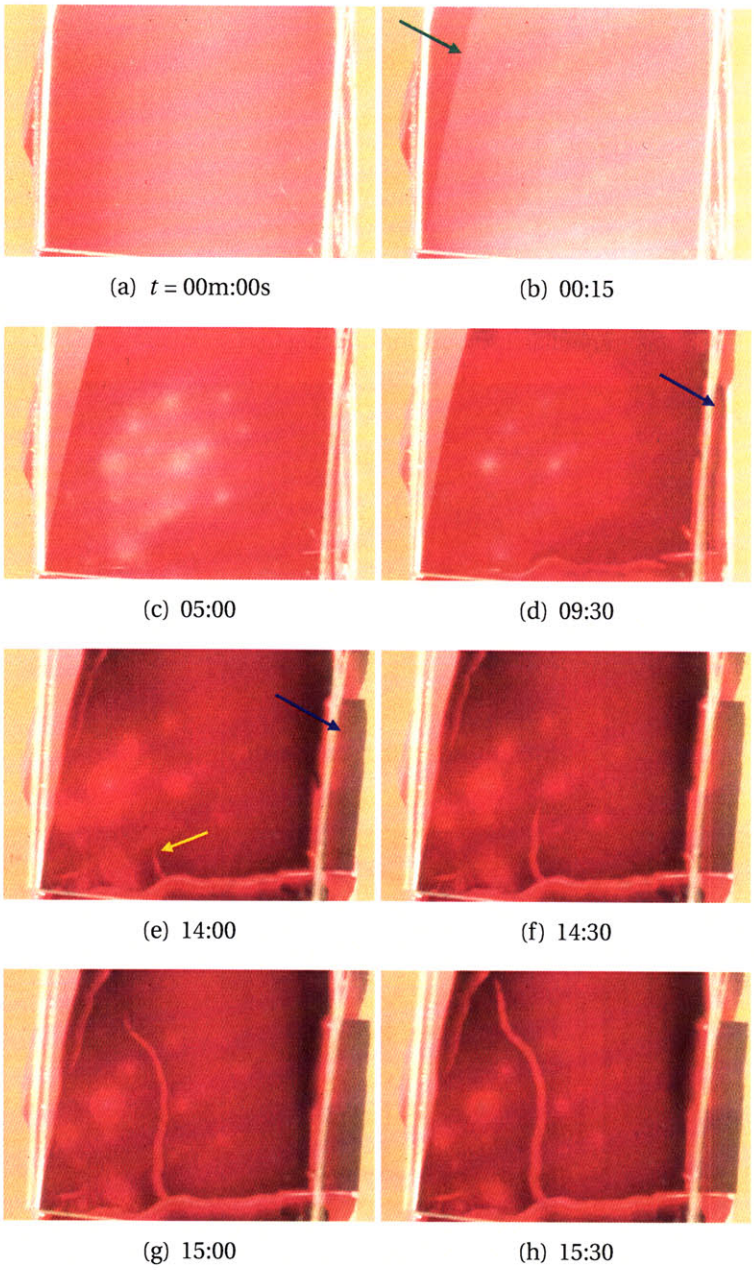

Figure 7-5. Top-view optical images of a $\approx 1 \times 1$ cm area CNT film during growth on a resistively-heated silicon platform: (a)-(b) growth starts within the first 15 s of C_2H_4 supply, where the green arrow indicates the edge of the catalyst film; (c) pits develop in the film where the growth is slower, and these appear as bright spots in the optical image; (d) an edge of the film (blue arrow) breaks away due to stresses and grows to the right; (e)-(h) the edge has grown considerably to the right, and a crack propagates through the middle of the film (yellow arrow). The growth conditions are the same as for Fig. 7-4. These images were taken with the assistance of Rick Slocum.

(a)

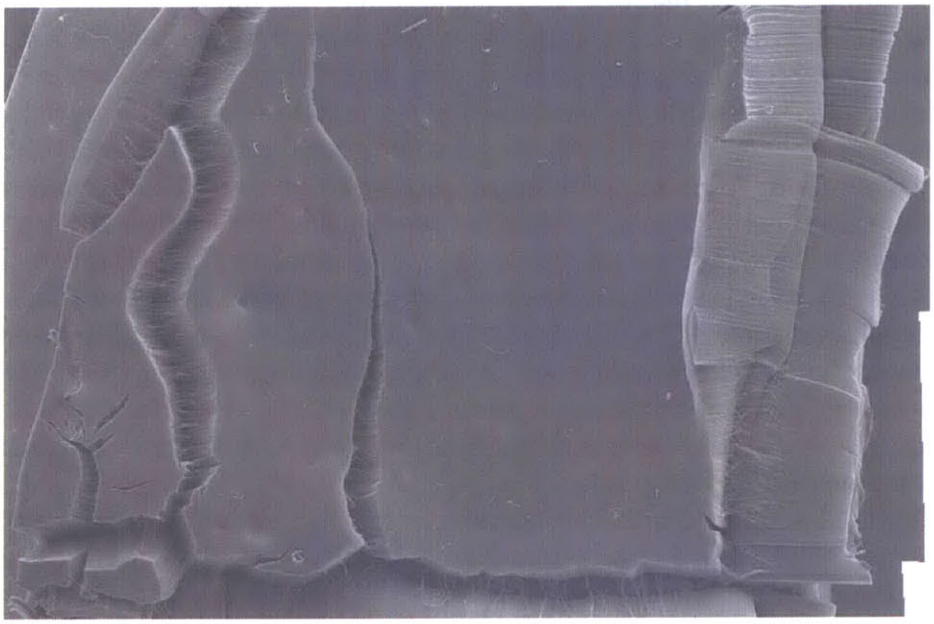

(b)

Figure 7-6. Comparison of (a) final top-view optical image to (b) composite *ex situ* SEM image, of sample with time series shown in Fig. 7-5. The backlight intensity in (a) is greater than in Fig. 7-5. The SEM image was digitally stitched from several frames using Microsoft Expression™ Graphic Designer software. "Pits" in the film which appear as relatively bright spots in the optical images are clearly visible in the SEM image.

Imaging from the top view (Fig. 7-5) concurrently shows that growth begins within the first imaging interval; at t = 15 s, a contrast band appears, corresponding to the edge of the catalyst film (the sample was cut from the perimeter of a silicon wafer, where catalyst was not deposited in a thin band around the perimeter). Within the first 5,min, white spots appear in the images, corresponding to "pits" in the film where the growth rate is suppressed for some reason.

We also see the formation and propagation of "cracks" (splits) in the film is also visible; for example, at t = 9:30 in this experiment, a "wall" of VA-CNTs breaks away from the right side of the sample (Fig. 7-5d) and grows away from the remainder of the film. A broad crack is also visible across the bottom of the image at t = 9:30, and at t = 14:00, another large crack initiates here and cuts across the middle area of the film as shown in the subsequent images. These images confirm that cracks we observed in films grown in the tube furnace likely formed during rather than after growth, and further emphasize the potential importance of mechanical stresses (section 4.2.4) in mediating rapid growth of VA-CNT films.

Comparison with a composite SEM image (Fig. 7-6) taken *ex situ* confirms that we can observe significant micro-scale topographical features of a CNT film by simple optical imaging. It would be interesting to use optical interference profilometry or scanning confocal microscopy to directly assess the film topography during growth.

7.2.3 Measurement and analysis of film growth kinetics

Optical access to the heated platform also enables direct measurement of the thickness of a growing VA-CNT film, using a commercially-available laser displacement sensor, as was described in section 6.2.2.2. Using this setup, we can directly investigate the effects of reactant composition, reactant pre-treatment, and reaction temperature on the film growth kinetics.

For these experiments, a 5×5 mm silicon substrate coated with 1/10 nm Fe/Al_2O_3 is rested on the heated platform. To guarantee uniform reactant access to the catalyst surface, a Si_3N_4-coated cap substrate having microchannels is rested against the catalyst film on the growth substrate, so gas reaches the catalyst predominately by diffusing through the microchannels (Fig. 7-7a). This cap, which is cut from the growth region area of the KOH-etched microchannel array, has its polished surface facing upward. However, the sensor reading is more stable when the beam reflects from a diffuse surface, so a second cap having its non-polished surface facing upward is rested on the microchannel cap. As demonstrated previously (section 4.3) the weight of these caps (giving $p \approx 100\,N/m^2$) is insignificant to the growth process, so the alignment of the CNTs is not measurably degraded.

Gas is delivered to the platform through the ceramic delivery pipe which is placed behind the platform and shielded in a quartz tube (Fig. 7-7b). Typically, the chamber is first purged with He with flows through the delivery pipe and into the main area of the chamber, and then the flow through the delivery pipe is switched to the appropriate mixture for initial processing (e.g., heating in He, He/H_2, or C_2H_4/H_2) of the growth sample. The temperature of the platform is maintained by a constant supply current from a DC power supply; the temperature drift is ≈0.3 °C/min as measured using the calibrated infrared temperature sensor. The displacement of the top surface of the sample stackup is measured throughout the purging, heating, growth, and cooling sequences. The displacement data is shifted and zeroed to subtract thermal expansion movement, giving a continuous measurement of the CNT film thickness versus reaction time.

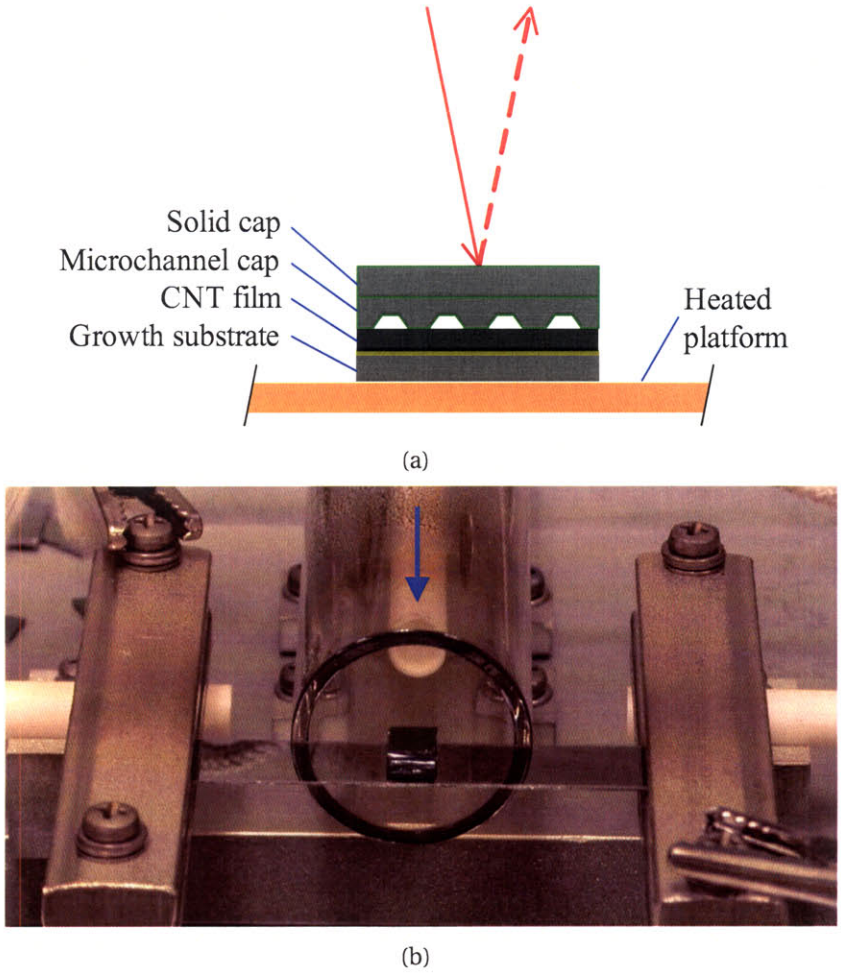

Figure 7-7. Measurement of CNT film thickness on resistively-heated silicon platform: (b) stackup of substrates on heated platform, where microchannels enable uniform gas access to catalyst film upon initial supply of reactant; (b) stackup on suspended platform inside box reaction chamber, with gas delivery through ceramic pipe having open end ≈20 mm from edge of platform, shielded by quartz tube.

To evaluate the effect of thermal pre-treatment of the reactant on the growth kinetics, three furnace configurations are used (Fig. 7-8): direct supply of the reactant mixture to the heated platform; thermal pre-treatment of the reactant in a tube furnace (22 mm ID, Fig. 6-1); and thermal pre-treatment of the reactant mixture in a heated pipe mounted in the inlet to the box chamber. At the inlet to the box chamber (upstream of the heated pipe or downstream of the tube furnace), a three-way valve is used to rapidly switch the flow over the platform. This valve is connected to a stream of He or He/H_2 which is taken directly from the supply tanks, and to a stream of reactant mixture (C_2H_4/H_2 or C_2H_4/He) which is optionally first passed through the tube furnace or the heated pipe. While one stream is directed to the platform via the delivery pipe, the other stream is bypassed to the exhaust, and changing the valve position rapidly changes the gas atmosphere surrounding the growing film.

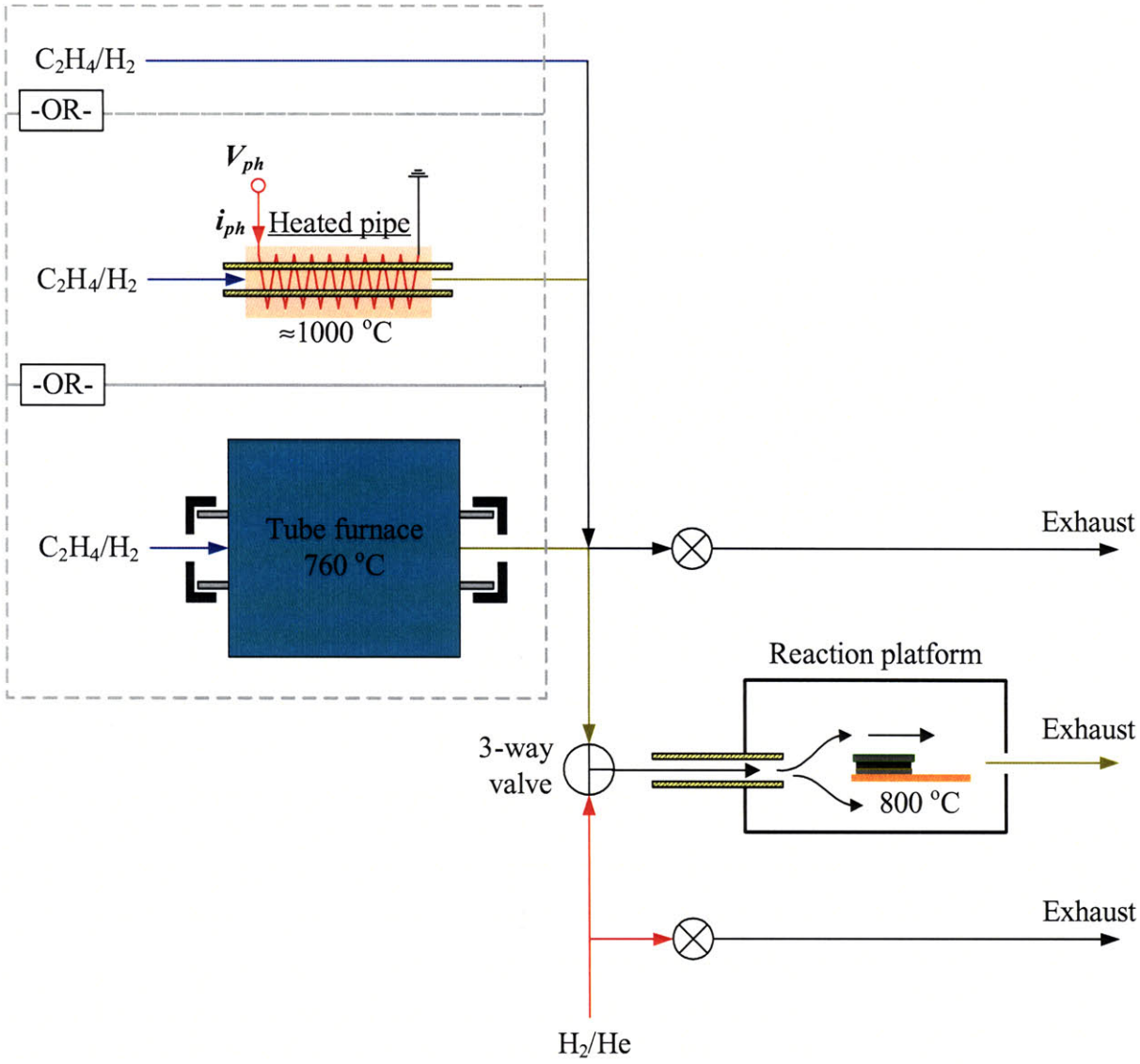

Figure 7-8. Configuration for CNT film growth under controlled gas pre-treatment, where reactant mixture is supplied directly from tanks to heated platform ("fresh"), or first passed through a tube furnace ("activated"), or first passed through a heated pipe which is externally wrapped with a wire coil ("super-activated").

In this configuration, the platform is heated with a flow of He or He/H_2 through the delivery pipe, while a steady composition of reactant mixture is established in the tube furnace (Fig. 7-9). After a desired annealing period has elapsed, the three-way valve is switched. This capability to rapidly introduce or discontinue the reactant flow is especially useful for pinpointing the start of the reaction, and for cycling the gas atmosphere to stop and start growth.

Recalling the significance of pre-conditioning, nucleation, and growth stages for CNT synthesis as described in section 2.5.1, we first present a set of experiments which reveals profound effects of the CVD atmosphere on the CNT film growth kinetics as related to these stages. Referring to the thickness data and process details in Fig. 7-10, we first consider a typical growth experiment (bx111) where the platform is heated in He/H_2 for 1 min before introducing C_2H_4/H_2. The C_2H_4/H_2 mixture is first pre-treated by flowing it through the tube furnace. Upon introduction of the reactant, growth starts almost immediately, and the film thickness increases at a decreasing rate until the sensor signal is lost at $t \approx 22$ min. At this time, the film has thickness $h \approx 1.6$ mm. In an otherwise identical experiment (bx125) where the platform is heated in only He, growth starts ≈3 min after the reactant is introduced, and then continues at a much slower rate than in the previous experiment. From this comparison, we realize that pre-conditioning of the catalyst in a reducing atmosphere (H_2/He) enables immediate and much more rapid CNT growth when the reactant is introduced, and the delay after pre-conditioning in He may represent a time necessary to reduce the Fe catalyst to a metallic state, after which growth begins.

Next, we repeat the sequence of bx111, yet supply C_2H_4/H_2 to the platform without pre-treatment in the tube furnace. Under these conditions (bx101), growth starts immediately, yet the growth rate is ≈30% of that observed using pre-treated reactant. The film reaches only ≈0.5 mm after 22 min of growth, and the experiment is terminated while growth still proceeds (at a gradually decreasing rate) beyond $t = 25$ min. Therefore, we notice that thermal pre-treatment of the reactants, where C_2H_4 decomposes into a variety of higher-order hydrocarbons in addition to H_2 (section 2.5.1.3, [188, 190]), significantly and proportionally increases both the initial and steady growth rates of the VA-CNT film. Further, because the pre-treated mixture cools to room temperature during transfer from the tube furnace to the box chamber, stable products of thermal decomposition of C_2H_4/H_2, rather than unstable radicals, are likely responsible for this difference.

Next (bx124), we supply only fresh C_2H_4 (with a complementary flow of He) to the platform. Growth initially follows the same path as bx101, yet after $t \approx 2.5$ min, the growth rate slows and then growth terminates at $t \approx 5$ min. Comparing bx101 to bx124, it appears that H_2 does not improve the initial growth rate (and therefore may not be critical to nucleation), yet improves the lifetime of the catalyst. In bx124, addition of H_2 to C_2H_4 at $t \approx 6$ min does not appear to reactivate the catalyst, as no additional displacement is observed beyond the initial terminal thickness.

Next (bx122), we return to pre-treating the reactant in the tube furnace, and initially supply pre-treated C_2H_4/He to the platform, and replace He with H_2 at $t = 6$ min. Initial growth proceeds rapidly and slightly faster than bx111, which could be due to a difference the residence time in the tube furnace (due to a difference the total flow rate between C_2H_4/H_2 and C_2H_4/He), or to a greater suitability of pre-treated C_2H_4/He versus pre-treated C_2H_4/H_2. This result confirms that additional H_2 (beyond any H_2 formed when C_2H_4 thermally decomposes in the tube furnace) does not significantly affect the initial growth rate. Finally (bx126) in this series, we initially supply C_2H_4/H_2 to the platform as in bx111, yet switch to pre-treated C_2H_4/He at

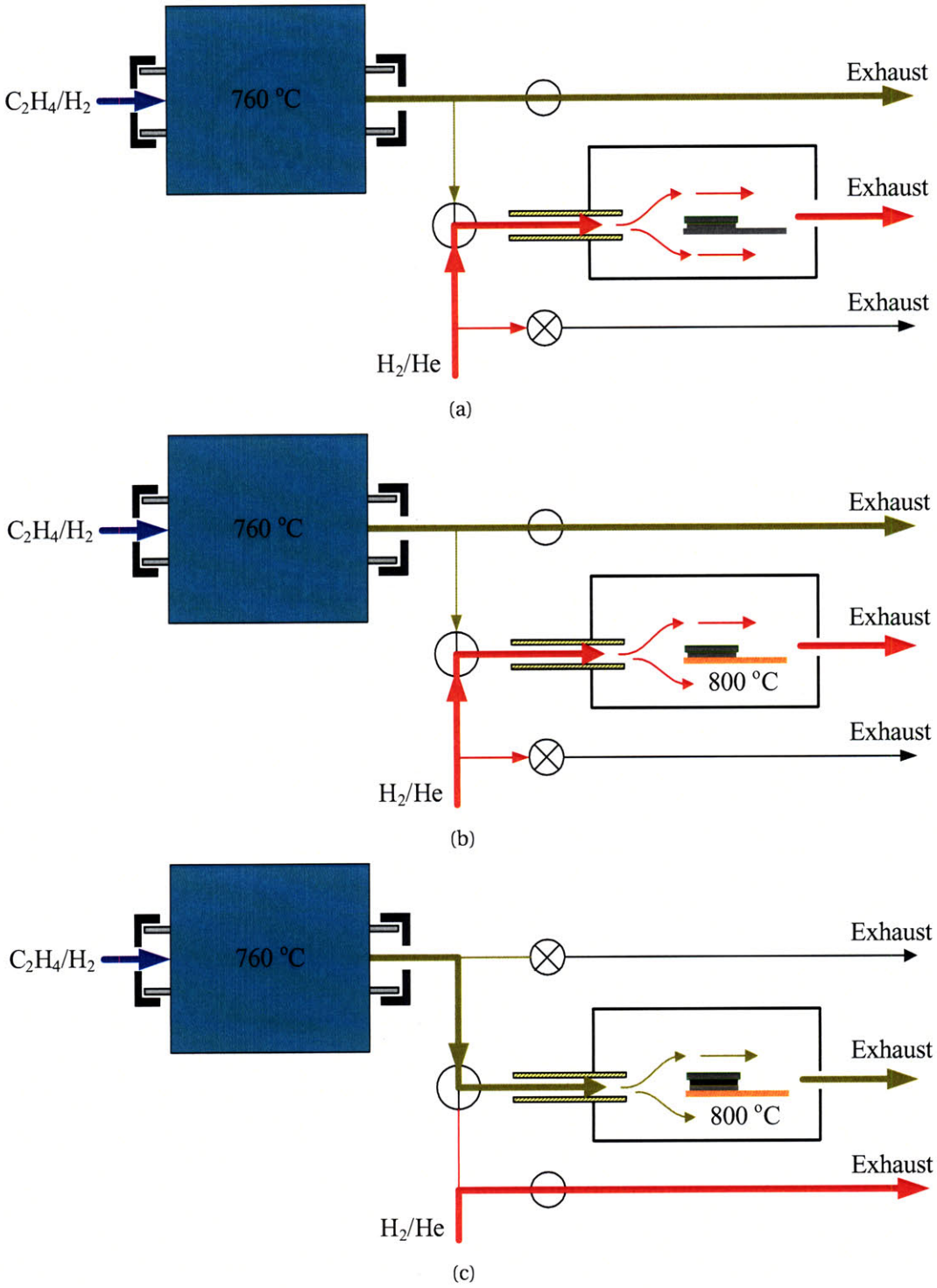

Figure 7-9. Typical sequence for CNT film growth with activation of reactant mixture in tube furnace: (a) purge heated platform chamber with inert or reducing gas mixture (e.g., He/H_2), while establishing steady reactant flow through tube furnace and directing this flow to exhaust; (b) heat platform in inert or reducing atmosphere; (c) rapidly introduce activated reactant mixture to heated platform by switching three-way valve.

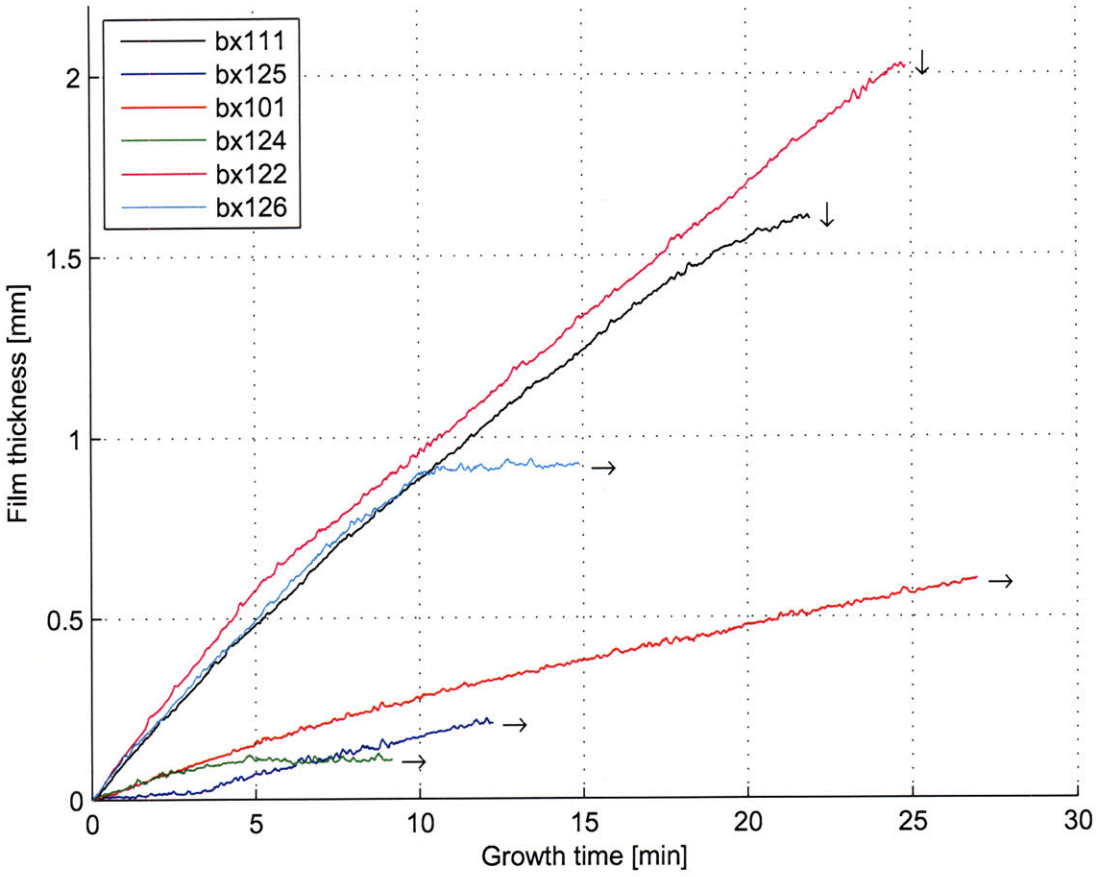

		Reaction sequence	
ID	Heating flow [sccm]	Time [min]	Flow [sccm]
bx111	100/500 He/H_2	0–(end)	100/500 C_2H_4/H_2, pre-treated
bx125	600 He	0–(end)	100/500 C_2H_4/H_2, pre-treated
bx101	100/500 He/H_2	0–(end)	100/500 C_2H_4/H_2, fresh
bx124	100/500 He/H_2	0–6	100/500 C_2H_4/He, fresh
		6–(end)	100/500 C_2H_4/H_2, fresh
bx122	100/500 He/H_2	0–6	100/500 C_2H_4/He, pre-treated
		6–(end)	100/500 C_2H_4/H_2, pre-treated
bx126	100/500 He/H_2	0–3	100/500 C_2H_4/H_2, pre-treated
		3–12	100/500 C_2H_4/He, pre-treated
		12–(end)	100/500 C_2H_4/H_2, pre-treated

Figure 7-10. Measurements of VA-CNT film growth kinetics, comparing effects of heating atmosphere (H_2 vs. He), nucleation atmosphere (C_2H_4 vs. C_2H_4/H_2, with and without pre-treatment in tube furnace), and growth atmosphere (C_2H_4 vs. C_2H_4/H_2, with and without pre-treatment in tube furnace). All experiments were at a platform temperature (T_p) of 810 °C. For all experiments where the gas was pre-treated by first flowing through the tube furnace, the furnace was held at T_f = 760 °C. A downward arrow (↓) at the end of the curve indicates that the sensor signal was lost due to tilting of the cap, while a rightward arrow (→) indicates that the experiment was terminated by turning off the heated platform at this time.

t = 6 min. As expected, initial growth is identical to bx111; however, growth abruptly stops at $t \approx 10$ min. This confirms that H_2 can improve the lifetime of the catalyst, as the absence of additional H_2 in the later stage of this experiment causes premature termination of growth.

In the next series of experiments (Fig. 7-11) we pre-treat the reactant mixture by flowing it through the heated pipe mounted in the inlet to the box chamber. This rapidly heats the flow to ≈1000 °C in ≈0.1 s, and like with the tube furnace the flow rapidly cools before reaching the heated platform. Our initial experiment (bx106) with C_2H_4/H_2 through the heated pipe (at the same composition yet a lower total flow than in the previous series) gives very rapid (≈ 200 μm/min) initial growth, yet growth terminates within ≈3 min at $h \approx 0.45$ mm.

Increasing the total flow (bx107; therefore decreasing the residence time) to match that from the previous series slows the initial growth rate yet increases the catalyst lifetime compared to bx106. Significantly decreasing the temperature (voltage) applied to the heated pipe gives very little initial growth (bx108). Increasing the power to the nominal value at t = 5 min increases the growth rate rapidly, and the then the sensor signal is lost at $t \approx 11$ min. Starting with a moderate voltage to the heated pipe gives ≈40 μm/min initial growth, and growth continues for a much longer duration, beyond $t \approx 19$ min when the experiment is stopped.

Adding a slight flow of CO to the C_2H_4/H_2 mixture (bx114) moderately decreases the initial growth rate compared to the first experiment (bx106), yet the catalyst lifetime is prolonged significantly, and the signal is not lost until the film is beyond $h \approx 1.3$ mm at $t \approx 17$ min. This change in growth kinetics may be because of a direct chemical effect of CO on the growth reaction or on the thermal evolution of the mixture during pre-treatment, or simply due to the change in residence time of the gas mixture in the pipe. Coincidentally, a nearly identical kinetic progression occurs (bx116) when we decrease the platform temperature from T_p = 810 °C to T_p = 775 °C, yet maintain the same flow and composition as in bx106.

The results of this series further demonstrate the coupling between thermal pre-treatment of the reactant mixture and the growth kinetics, and indicate an inverse relationship between the initial growth rate and the apparent lifetime of the catalyst. Combined with the results of the first series, we see that no or "gentle" pre-treatment (e.g., bx122, bx109) gives slow (≈25 μm/min) and uniform growth; relatively "moderate" pre-treatment (e.g., bx111, bx107) gives more rapid growth (≈100 μm/min) yet the signal is lost indicating significant non-uniformities (early termination in certain areas) in the later stage of the experiment; and "heavy" pre-treatment gives very rapid (≈200 μm/min) initial growth accompanied by rapid deactivation of the catalyst.

In the third series (Fig. 7-12), we study the effect of platform temperature on the film growth kinetics, using a reactant mixture of C_2H_4/H_2 pre-treated in the tube furnace. For the three temperatures tested (695–810 °C), the growth rate and final thickness increase with platform temperature. Additional experiments should be conducted to determine the kinetics at higher temperatures; however, the growth rate increases beyond 750 °C, whereas the maximum growth rate in the tube furnace alone is observed at 750 °C (section 4.2.1.1). This suggests that the decrease in growth rate above 750 °C in the tube furnace is due to excessive thermal decomposition of the reactants, rather than excessive heating of the catalyst.

The fourth series (Fig. 7-13) studies the effect of tube furnace pre-treatment temperature on the film growth kinetics, revealing that the growth rate increases with increasing pre-treatment temperature from 720 °C, to 740 °C, to 760 °C. At 780 °C and 800 °C, the growth rate remains nearly identical to that at 760 °C, yet the catalyst lifetime (presumably related to when the signal is lost) decreases significantly. Above 800 °C, significant pyrolysis occurs in the tube furnace, as

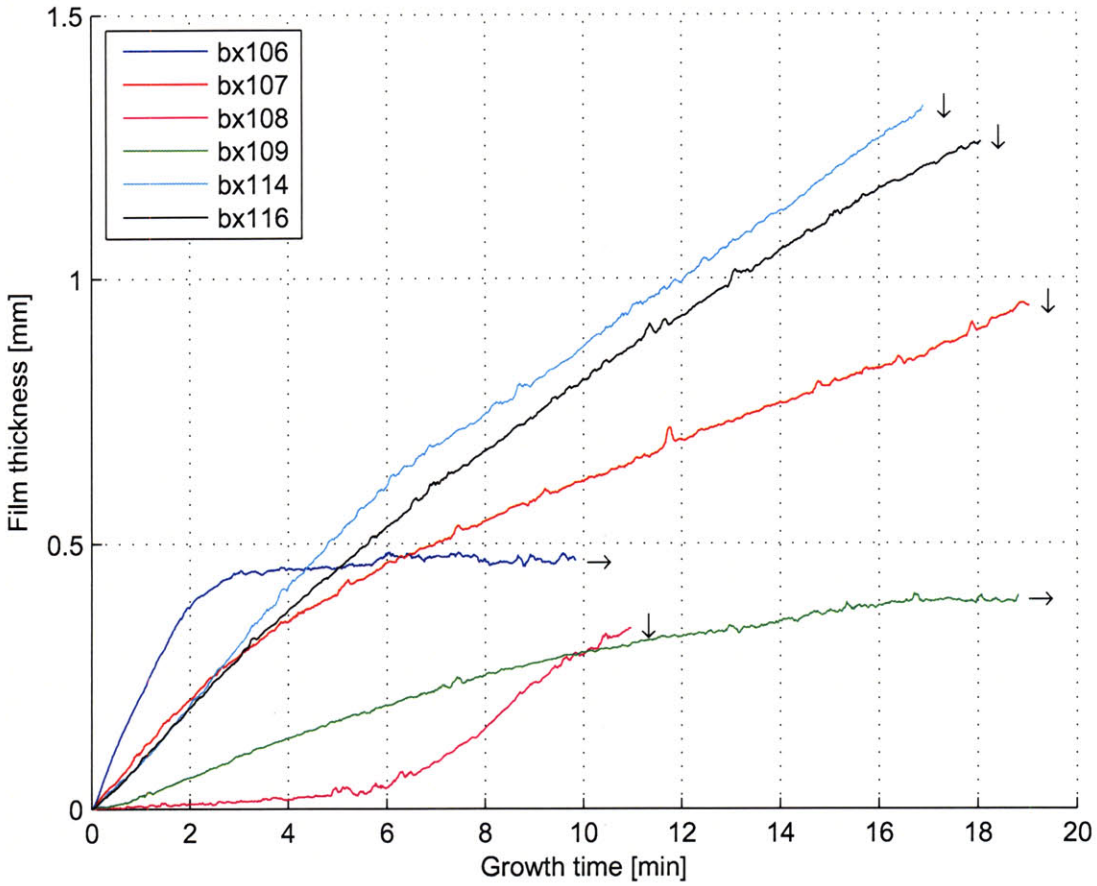

ID	T_p [°C]	HP [V]	Reaction flow [sccm]	Note
bx106	810	27.4	50/200 C_2H_4/H_2	Nominal case.
bx107	810	27.4	100/500 C_2H_4/H_2	Increase total flow.
bx108	810	16.0	50/200 C_2H_4/H_2	Low HP power; increase later.
bx109	810	23.0	50/200 C_2H_4/H_2	Medium HP power.
bx114	810	27.4	50/200/50 $C_2H_4/H_2/CO$	Add CO to flow.
bx116	775	27.4	50/200 C_2H_4/H_2	Decrease T_p

Figure 7-11. Study of reactant pre-treatment by delivering gas through heated pipe (HP), demonstrating sensitivity of initial growth rate and catalyst lifetime to pre-treatment temperature (HP voltage), gas composition, and residence time (flow rate). In all experiments the platform was rapidly heated and the sample was pre-treated for 1 minute, in a flow of 50/200 sccm He/H_2 through the heated pipe.

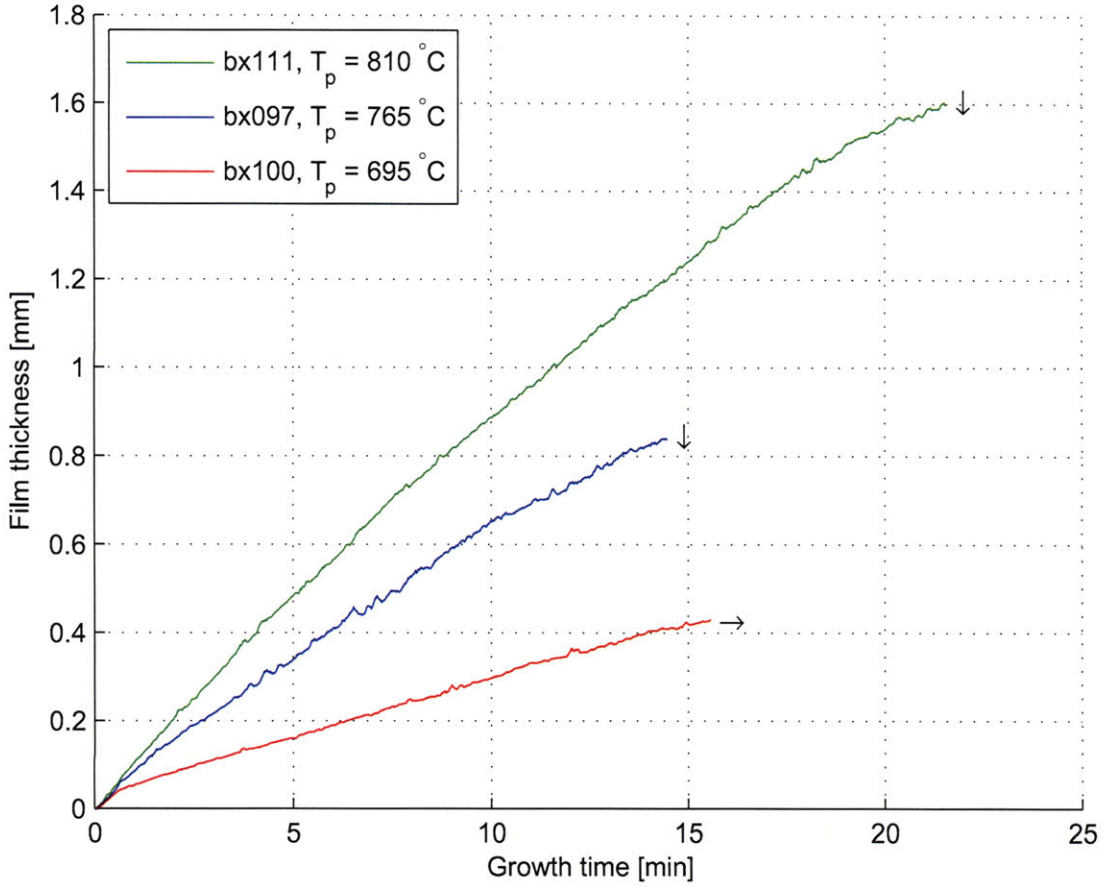

Figure 7-12. Effect of platform temperature on film growth kinetics, with reactant flow of 100/500 sccm C_2H_4/H_2, through tube furnace at T_f = 760 °C.

oil condenses in the output region and clogs the output fitting. This trend indicates a particular active precursor may be formed at or just below 760 °C (in conjunction with the residence time for 600 sccm total flow), and heating the reactant beyond this temperature does not increase the activity of the mixture but instead increases the formation of precursors (e.g., long chain hydrocarbons) which may deactivate the catalyst (e.g., by encapsulating the active surfaces). However, we noted previously that rapidly heating the reactant to ≈1000 °C in the heated pipe gives a significant increase in the growth rate. This reinforces that the relationship between pre-treatment temperature, residence time, and growth kinetics is highly coupled, and that the chemical effects of thermal pre-treatment must be studied in further detail, such as by chemical analysis of the pre-treated gas streams (e.g., mass spectrometry, gas chromatography, or ion mobility spectroscopy). Further, the CNTs must be studied by SEM, TEM, and Raman spectroscopy, to determine how their structure, quality, and areal density may vary for growth using various thermally-activated reactant chemistries.

We can quantitatively compare the growth kinetics under various reaction conditions by fitting curves to the measured progressions of film thickness versus reaction time. In general, VA-CNT film growth kinetics may be limited by diffusion of the reactant to the catalyst, which

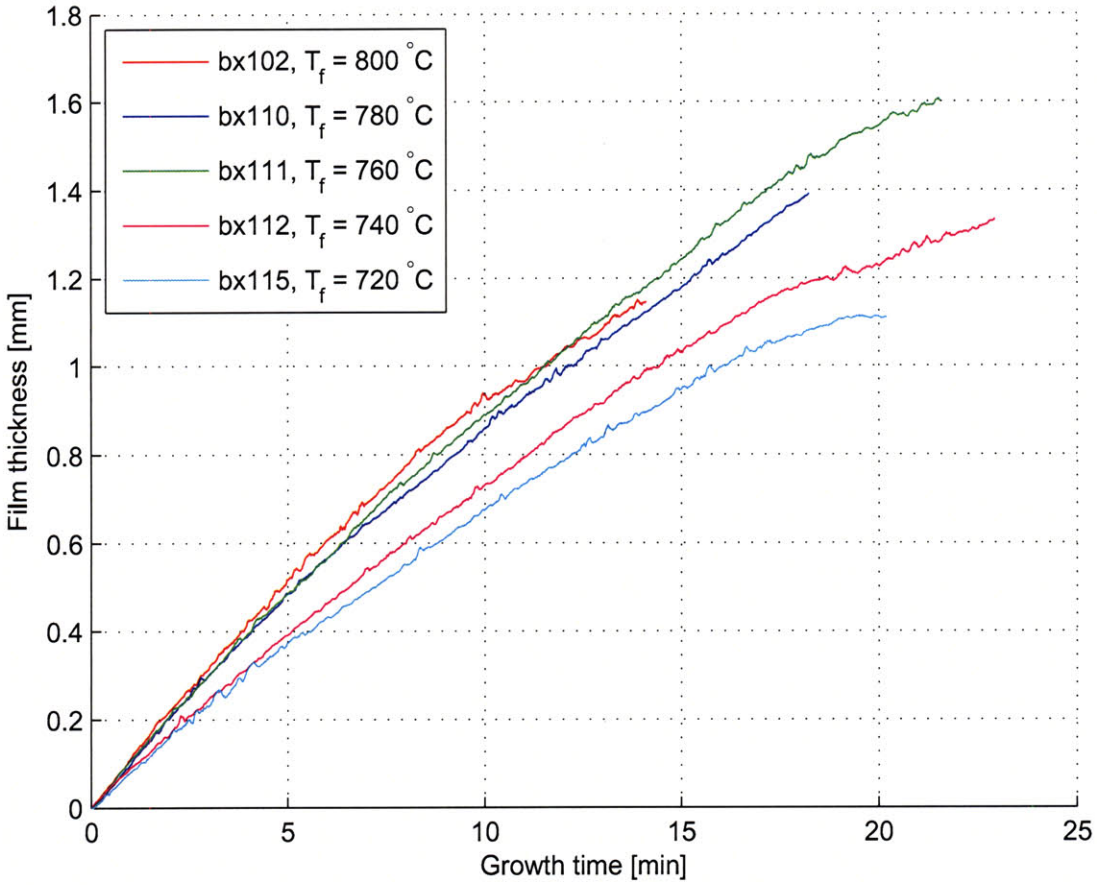

Figure 7-13. Effect of tube furnace pre-treatment temperature on film growth kinetics, with reactant flow of 100/500 sccm, and platform temperature of T_p = 810 °C. In all experiments the sensor signal is lost before the reaction fully terminates. A decrease in the time it takes for the signal to be lost ordinally indicates a decrease in the catalyst lifetime, because some areas of the film .

remains at the substrate surface and is therefore increasingly starved of reactant as the film thickens. Alternatively, the film thickness may be limited by the catalyst lifetime; regardless of the reactant supply, the film will no longer thicken if the catalyst is encapsulated by amorphous carbon or otherwise becomes unable to convert the reactant into CNTs. As demonstrated by our experiments, the balance between these limiting factors depends on the reaction conditions.

Accordingly, we study functional forms which have previously been attributed to diffusion-limited and catalyst-limited kinetics. After the well-known Deal-Grove model for thermal oxidation of silicon [468], as adopted for VA-CNT growth by Zhu et al. [197], a diffusion-limited growth reaction progresses as:

$$h = 0.5\sqrt{\left(A^2 + 4Bt\right)} - 0.5A. \tag{7.1}$$

In the constants

$$A = \frac{2D}{k_s} \tag{7.2}$$

and

$$B = \frac{4DC_0}{M}, \tag{7.3}$$

D is the coefficient of gas diffusion through the film, k_s is the rate constant assuming a first-order reaction at the catalyst surface, C_0 is the concentration of active precursors at the catalyst surface, and M is the number of precursor molecules incorporated into a unit volume of the growing film.

Alternatively, we can test the decay-limited model proposed by Futaba et al. [162], where

$$h = \beta\tau_0\left(1 - e^{-t/t_0}\right). \tag{7.4}$$

Here, β is the initial film growth rate, and τ_0 represents the catalyst lifetime. This is a classic model of radioactive decay; in this situation, it suggests that a catalyst has a fixed number of growth "steps" before it stops producing a CNT.

Clearly, neither model appropriately considers all aspects of the growth kinetics. One one hand, the diffusion-limited model predicts that growth will slow gradually as it becomes more difficult for precursors to diffuse to the catalyst, yet growth will never stop. Further, this model assumes perfect and constant efficiency of the catalyst, and neglects other critical aspects such as the polydispersity of the reactant mixture and diffusion of reaction products away from the catalyst. On the other hand, the decay-limited model neglects possible diffusion limitation, assuming there is always a sufficient supply of reactant to maintain the growth rate limited by the catalyst.

Fitting selected data (Fig. 7-14) to these models illustrates that both the diffusion-limited and decay-limited functional forms adequately represent the observed kinetics of our process before growth terminates. However, when abrupt termination is observed (e.g., bx126, bx106), the decay-limited model does not adequately capture the termination trend. Therefore, it appears that our VA-CNT growth process is diffusion-limited, yet this is interrupted by sudden (or very rapid) deactivation of the catalyst before the growth rate becomes negligibly small due to diffusion limitation.

Additional complexity arises when the growth rate first increases when C_2H_4/H_2 is introduced and then decreases, as observed in experiment bx109 (Fig. 7-15). Here, a power law fit,

$$h = mt^n \tag{7.5}$$

is appropriate for the initial stage until the growth rate reaches a maximum, and then a quadratic fit is appropriate as the growth rate decreases. Basic curve fitting does not aid our scientific understanding here; however, this example further illustrates that more complex kinetic relations are needed to consider both activation, steady growth, and deactivation of the growth process. Further, the kinetics of the initial growth stage change (Fig. 7-16) when the platform is heated in the reactant atmosphere of C_2H_4/H_2 rather than pre-conditioned in He/H_2, or when the reactant is gradually introduced to the box chamber rather than rapidly introduced using the three-way valve configuration.

Next, we fit the models to the kinetic data measured at different platform temperatures (Fig. 7-17; constant tube furnace pre-treatment temperature), and at different tube furnace pre-treatment temperatures (Fig. 7-18; constant platform temperature). Once again, we see that the

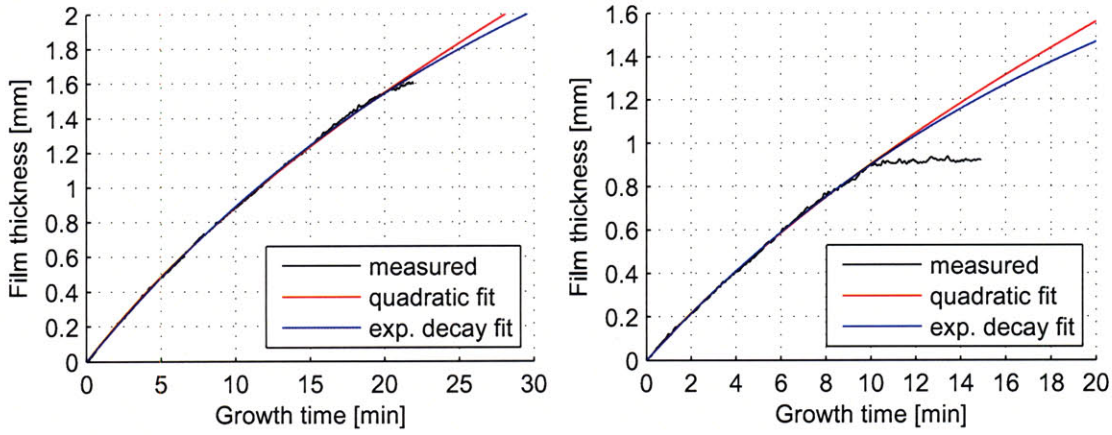

(a) bx111

(b) bx126

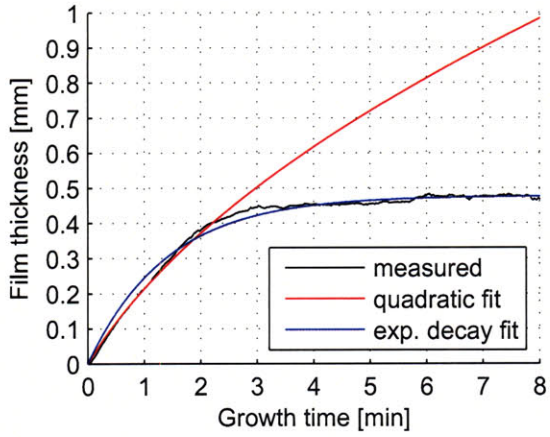

(c) bx106

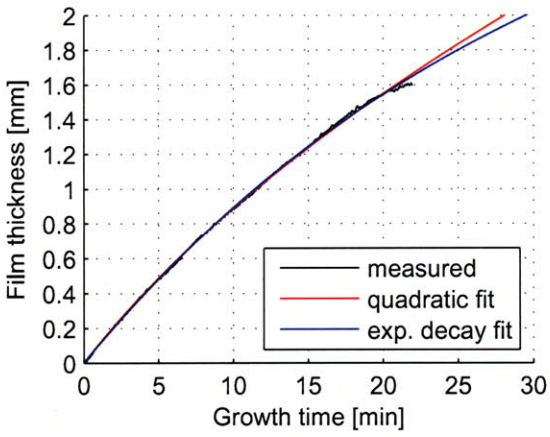

(d) bx107

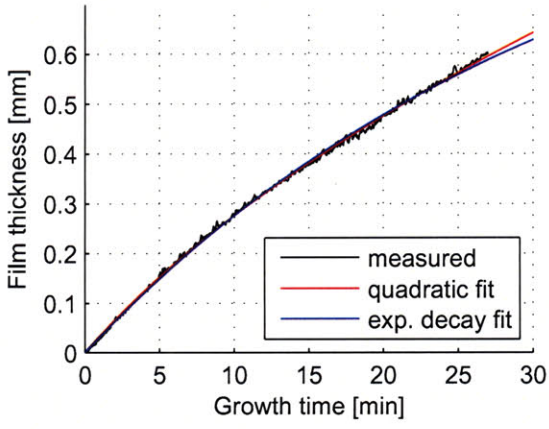

(e) bx101

Figure 7-14. Fitting of measured CNT film growth kinetics to diffusion-limited (quadratic) and decay-limited (exponential decay) models.

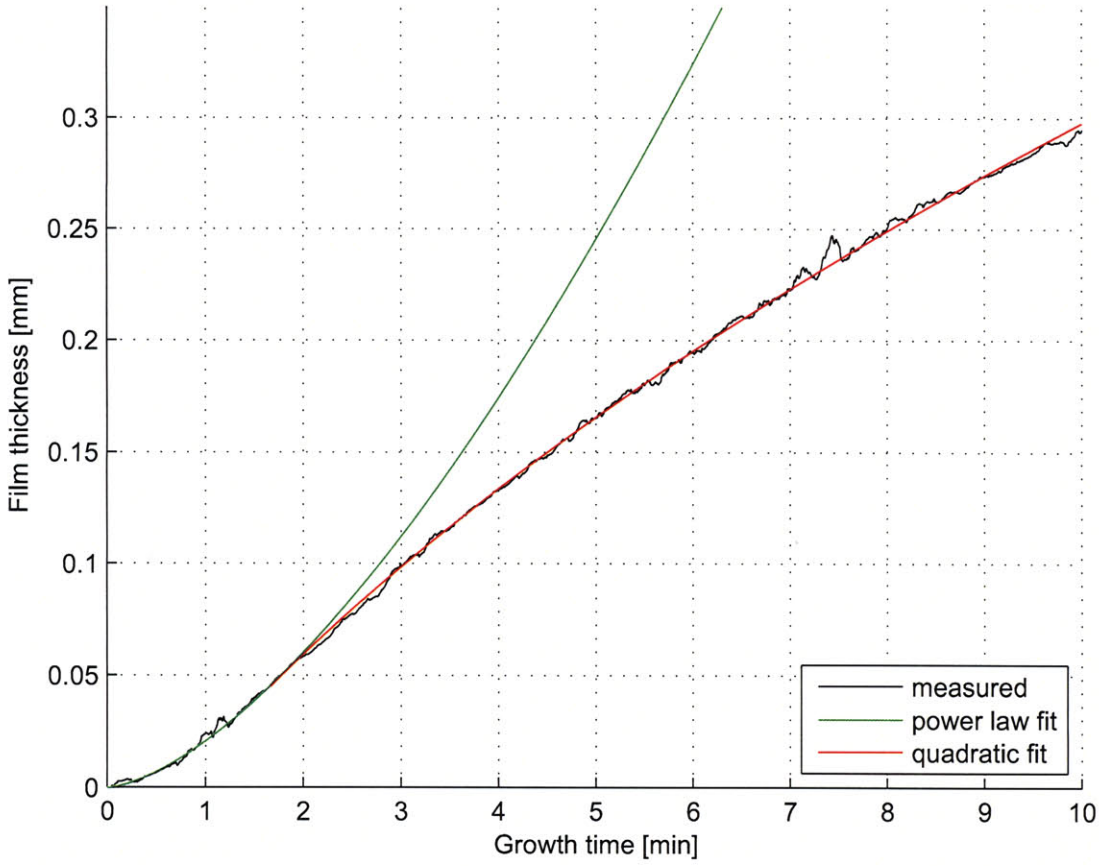

Figure 7-15. Piecewise curve fit to kinetic data (bx109) exhibiting initially increasing growth rate, and subsequently decreasing rate.

diffusion-limited and decay-limited models both fit the initial kinetics very well, and both predict (inaccurately) that growth can proceed to extreme thicknesses.

Assuming C_0 and M are constant throughout this series, the diffusion coefficient (D) is directly related to the fit constant B. Further, dividing

$$\frac{B}{A} = \frac{2C_0 k_s}{M} \propto k_s \tag{7.6}$$

we estimate the reaction rate constant (k_s). Plotting these parameters versus the relevant temperature (Fig. 7-19) demonstrates that the diffusion coefficient increases linearly with platform temperature (as would be expected for a diffusion-limited reaction, and as shown by Zhu et al. [197]), and the reaction rate constant also increases linearly with platform temperature. However, the diffusion coefficient does not monotonically vary with the tube furnace temperature, indicating that the changing chemical nature of the precursor due to thermal pre-treatment affects the perceived diffusivity of active reactant through the film. Further, the rate constant increases monotonically yet nonlinearly with tube furnace temperature, verifying that pre-treatment alters the chemical activity of the reactants. The rapid increase in rate constant between T_f = 740 °C and T_f = 760 °C may suggest that a particularly active precursor is being

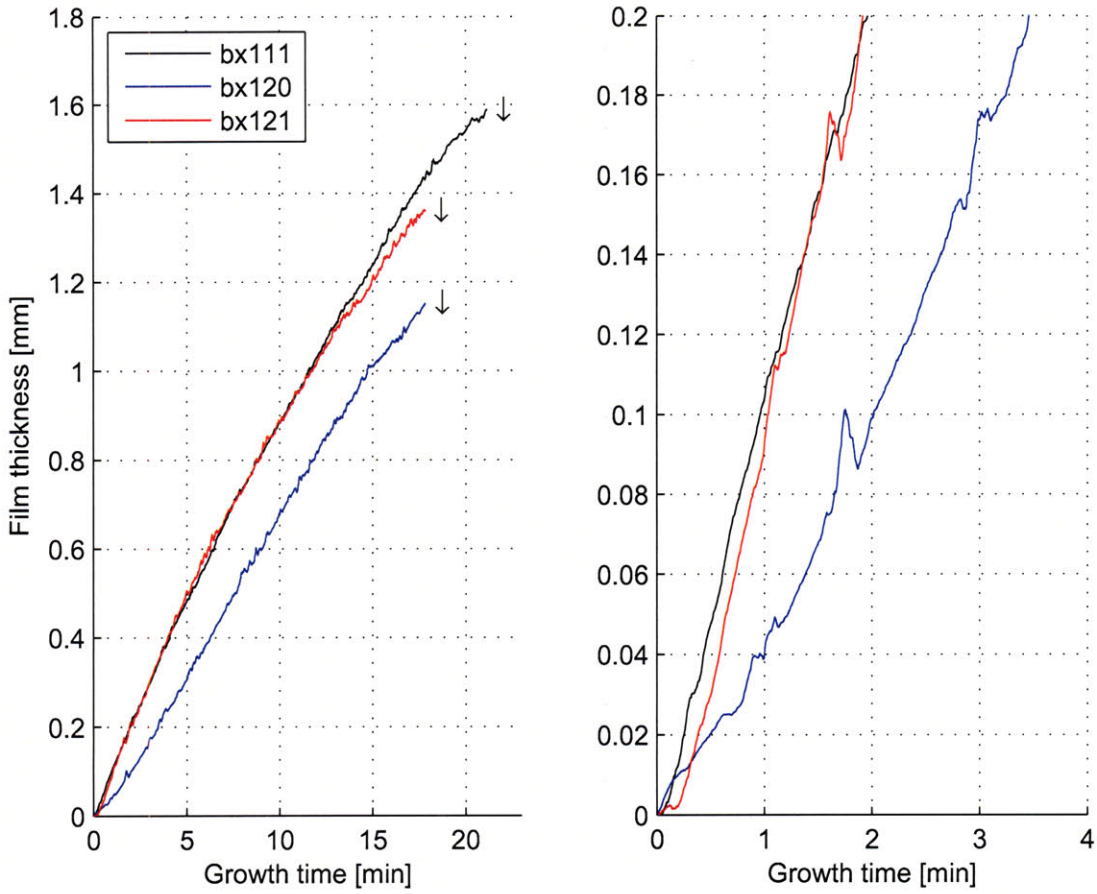

ID	Details
bx111	Heat in 100/500 sccm He/H_2, hold 1 minute Rapidly switch to 100/500 sccm C_2H_4/H_2
bx120	Heat in 100/500 sccm C_2H_4/H_2 (grow immediately)
bx121	Heat in 100/500 sccm He/H_2, hold 1 minute Gradually replace He with 100 sccm C_2H_4

Figure 7-16. Effect of gas introduction and platform heating sequence on initial growth kinetics.

formed by thermal decomposition of the reactant at this temperature.

Measuring the film thickness during experiments where the reactant supply is periodically discontinued and then reintroduced (Fig. 7-20) demonstrates that growth can be stopped, started, deactivated, and reactivated in a continuous fashion (as also shown in section 4.2.3 for growth experiments in the tube furnace). The incremental growth achieved in consecutive periods of reactant supply decreases with increasing total reaction time; however, comparison of the total film thickness between 1 min and 5 min pause intervals (bx129 vs. bx132) indicates that additional exposure to H_2 alone can increase the catalyst lifetime. SEM imaging of the film grown with 5 min pause intervals reveals distinct interfaces between the CNT layers (Fig. 7-21).

As a final example of the versatility of this reaction system, we demonstrate that real-time changes in the growth rate can be observed when the platform temperature is adjusted during

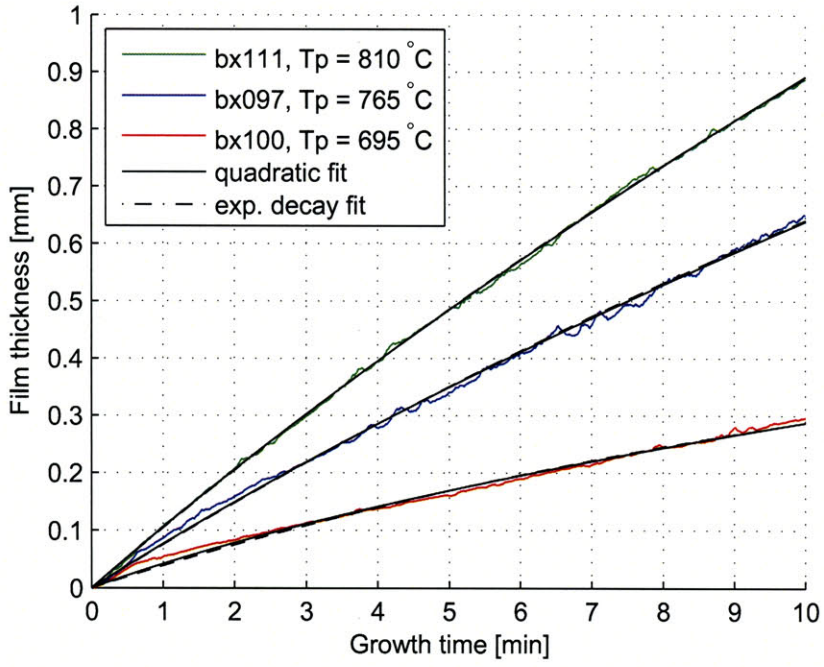

(a)

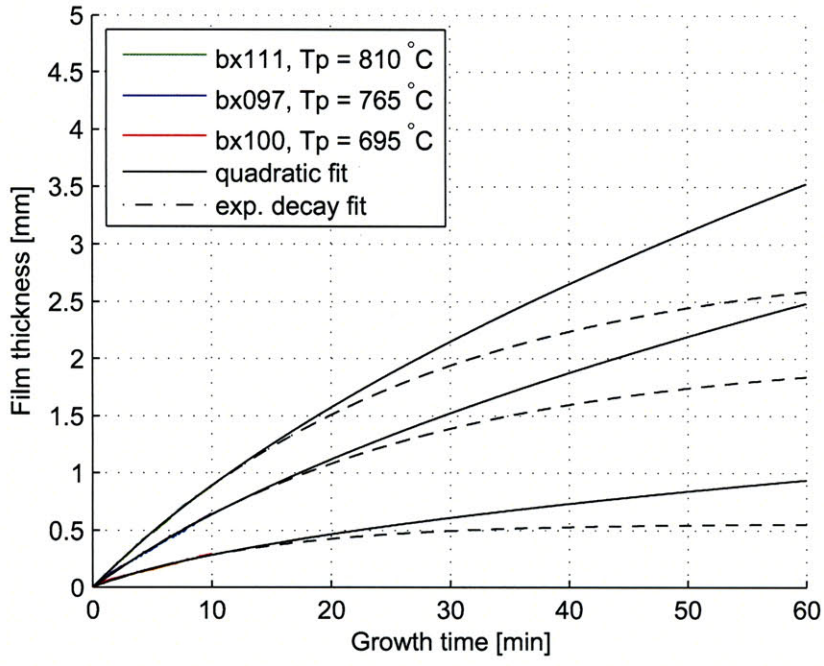

(b)

Figure 7-17. Curve fits to initial 10 min of kinetic data for growth experiments at different platform temperatures (other parameters described in Fig. 7-12).

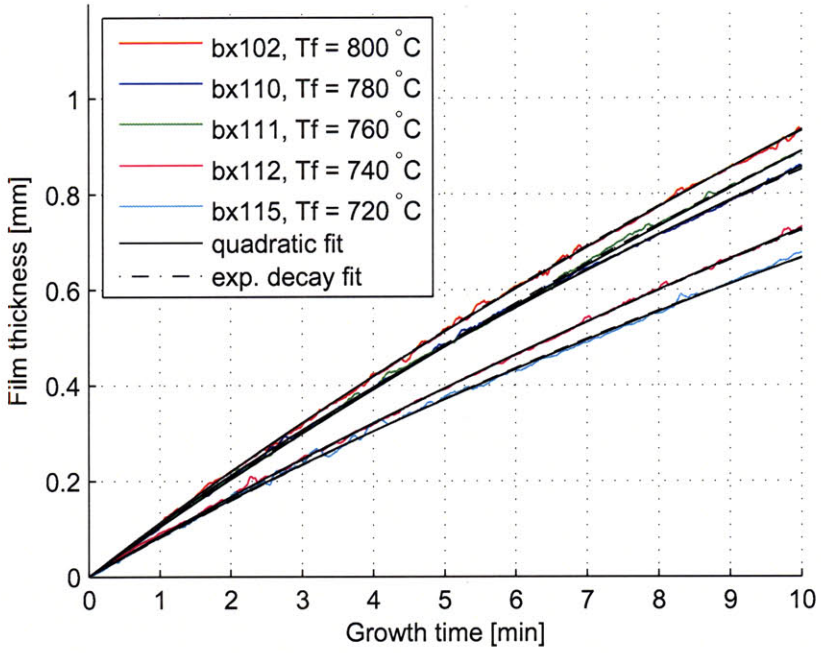

(a)

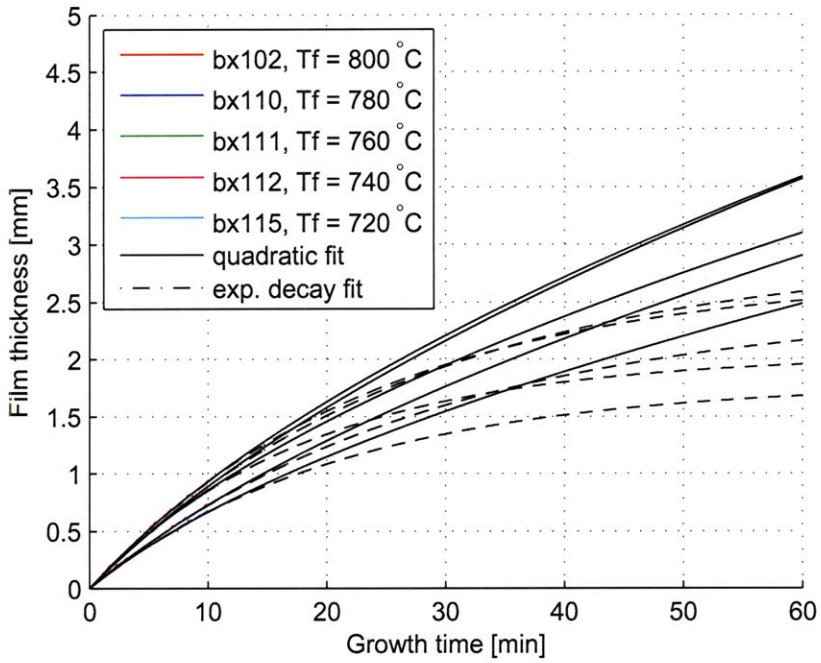

(b)

Figure 7-18. Curve fits to initial 10 min of kinetic data for growth experiments at different tube furnace temperatures (other parameters described in Fig. 7-13).

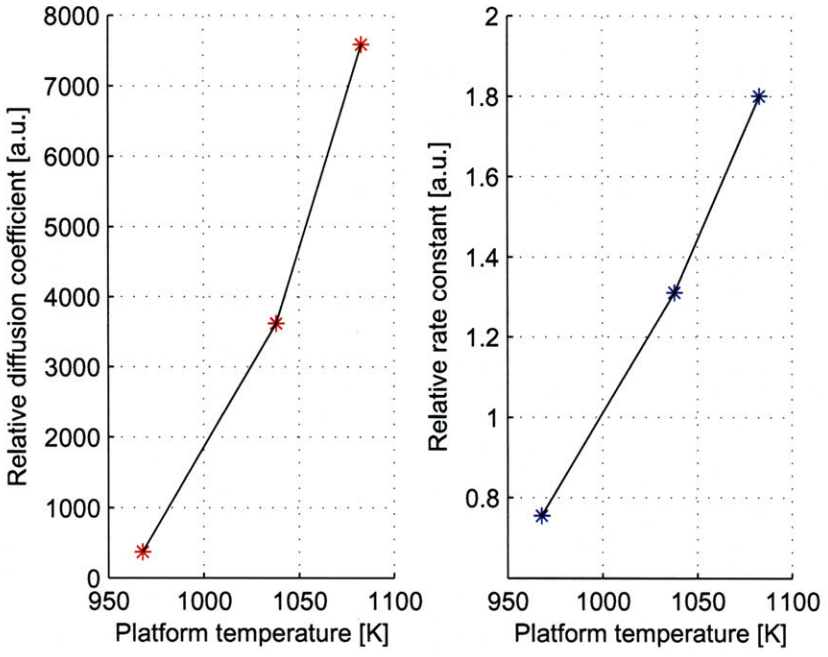

(a)

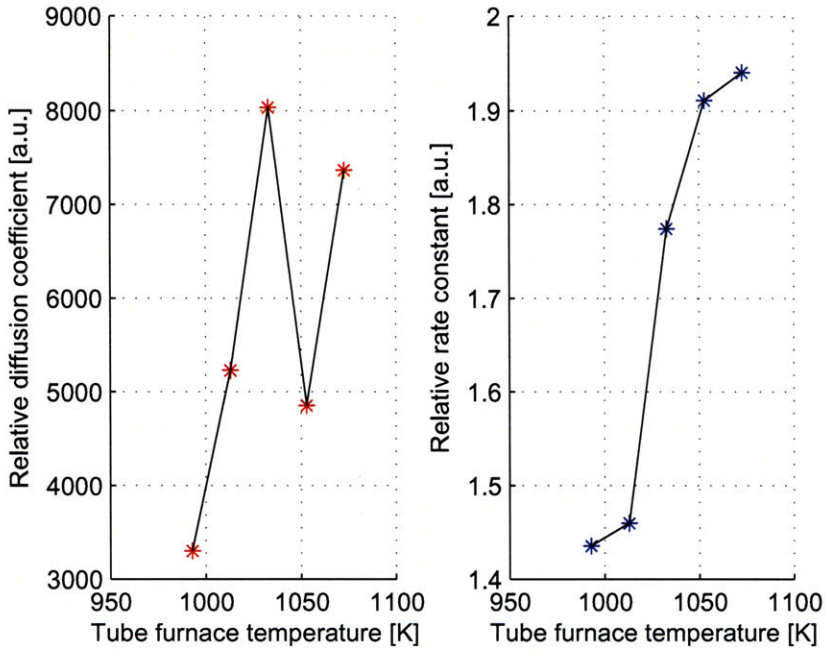

(b)

Figure 7-19. Kinetic parameters extracted from fits using diffusion-limited reaction model (a) for series with different platform temperatures, and (b) for series with different tube furnace temperatures.

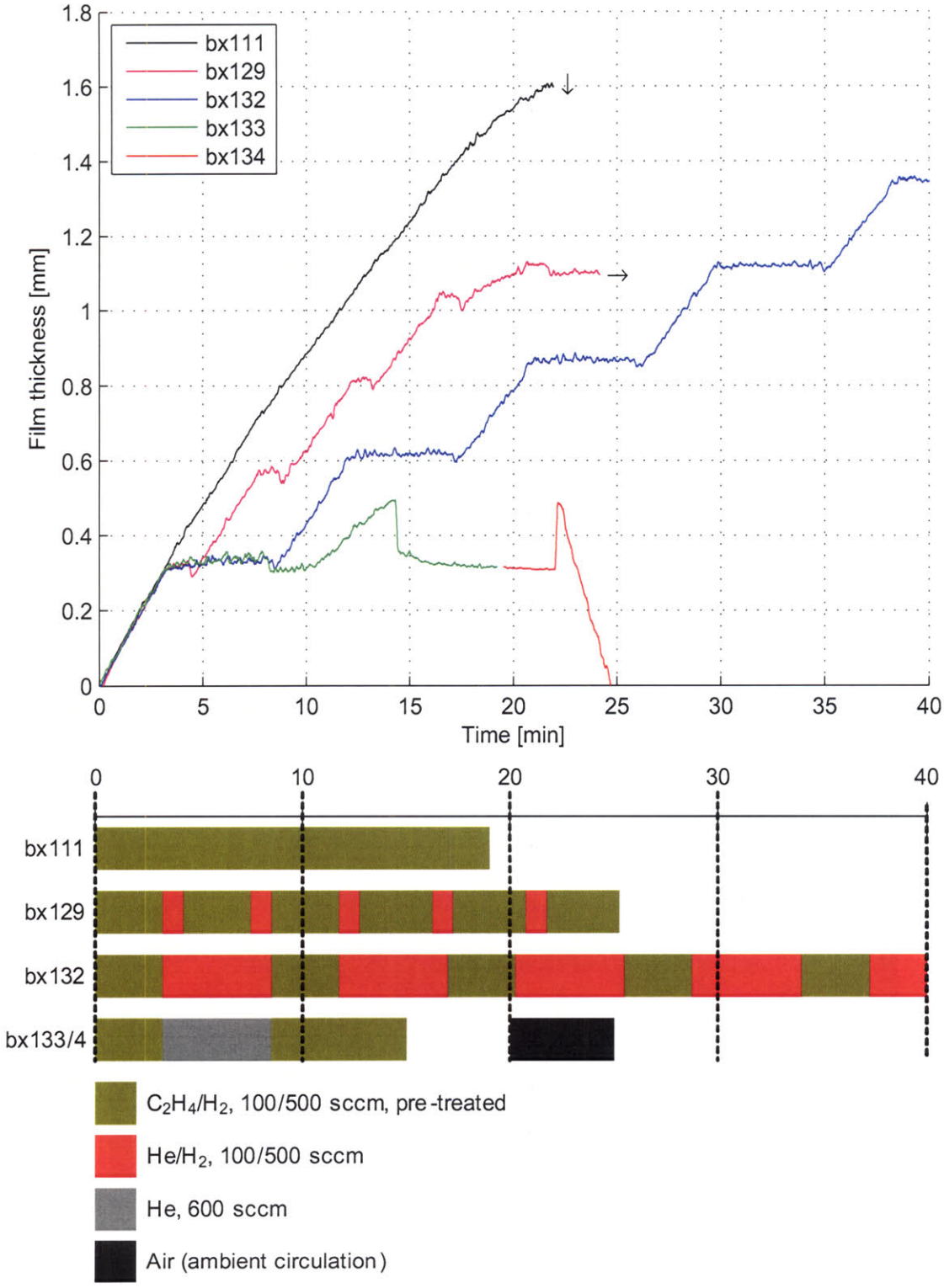

Figure 7-20. Kinetics of VA-CNT film growth under periodically-varying reactant flows, demonstrating pausing and re-starting of growth by alternating C_2H_4/H_2 with He/H_2, and deactivation and re-activation (with delay) by alternating C_2H_4/H_2 with He. The film is etched rapidly by exposure to air. All experiments were at $T_p = 810\,°C$ and $T_f = 760\,°C$.

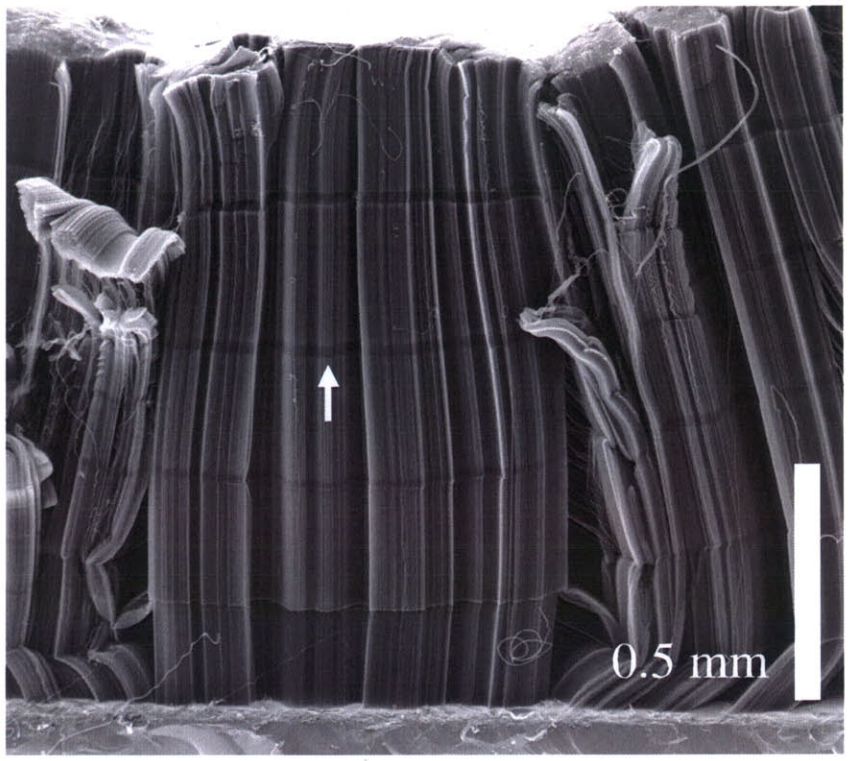

(a)

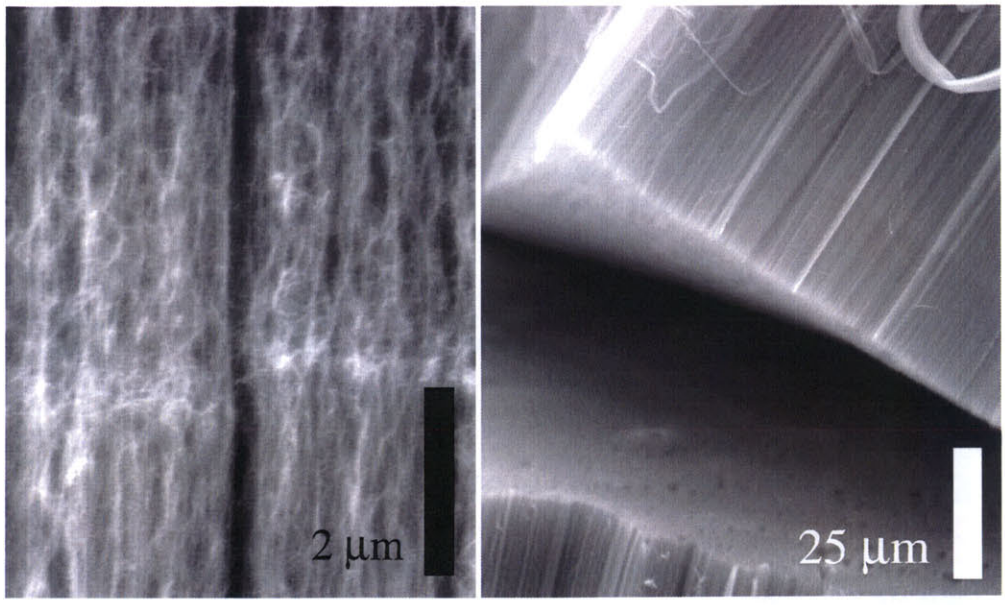

(b) (c)

Figure 7-21. SEM images of VA-CNT film grown on heated platform, with periodic reaction cycle of 3 min C_2H_4/H_2 and 5 min He/H_2: (a) wide view of film, showing distinct CNT layers grown in each cycle; (b) close view of interface between adjacent layers, at white arrow in (a); (c) split between adjacent layers.

growth (Fig. 7-22). Combining this with the capability to independently pre-treat and rapidly introduce and discontinue the reactant flow, we may be able to identify particular reaction conditions suitable for both high-density nucleation and extended catalyst lifetime, thereby giving taller and more dense VA-CNT films.

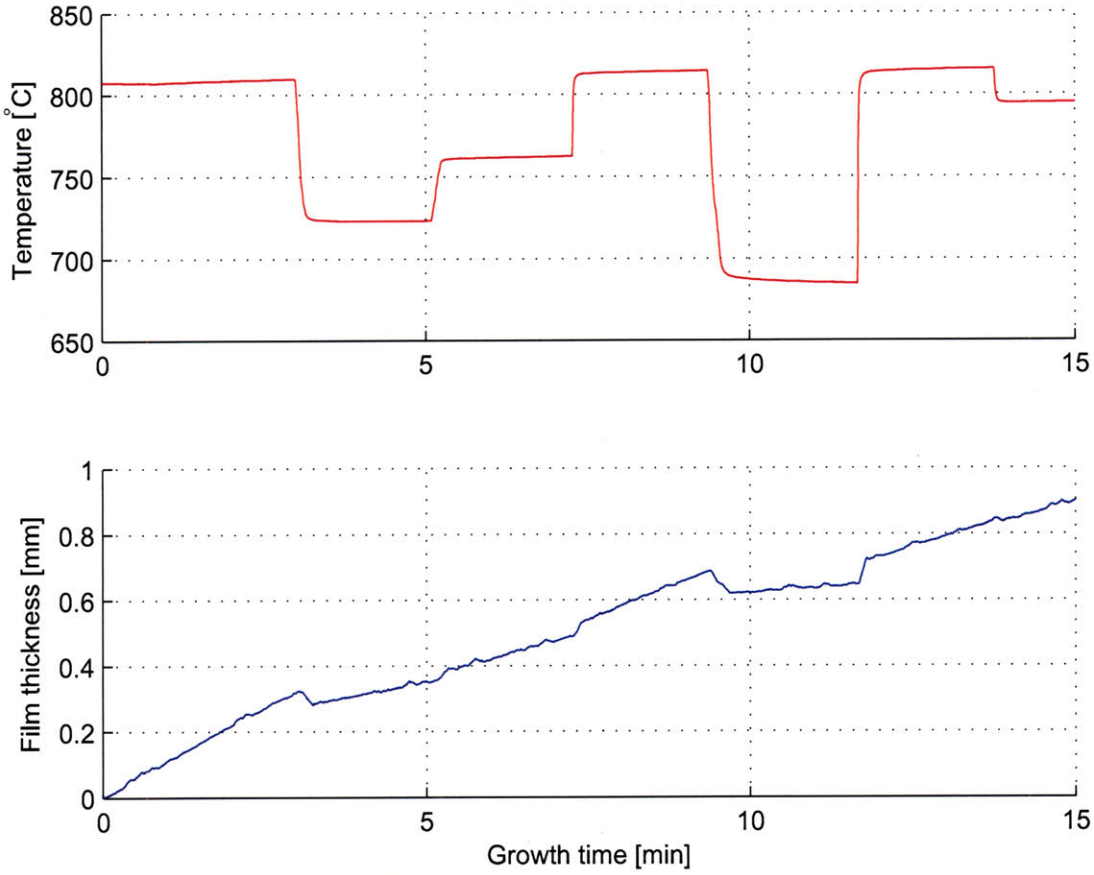

Figure 7-22. Kinetics of VA-CNT film growth when platform temperature is varied during the reaction cycle, while a flow of 100/500 sccm C_2H_4/H_2 is maintained. The reactant flow was pre-treated at T_f = 760 °C.

7.3 CNT growth in microchannel arrays

Growing CNTs in microchannels offers the potential to study the limiting aspects of the CVD reaction, as well as to perform a large number of experiments in parallel, where the difference in reaction conditions between neighboring channels is very small yet a microchannel array spans a wide range of conditions. This section presents results of initial CNT growth experiments using the "wide full" KOH-etched microchannel array detailed in Chapter 5. These experiments were designed with the goal of simultaneously growing and aligning CNTs in the direction of reactant flow through the microchannels. The experiments were conducted with the microchannel array packaged inside the 42 mm tube furnace (section 6.3) in the flow-reversal configuration.

7.3.1 Flow-directed alignment of isolated CNTs

We first sought to grow flow-aligned CNTs with the microchannel array in the "normal" configuration (Fig. 5-44) where catalyst is deposited on the microchannel surfaces, and the device is mated against a second (nonpolished) substrate having through-holes for gas delivery via the quartz fixture. A uniform catalyst film (not patterned) of $Mo/Fe/Al_2O_3$ was deposited on the array, and growth was conducted by drawing CH_4/H_2 through the array inside the tube furnace at 825 °C. Initial experiments quickly demonstrated that it would be difficult to achieve flow-aligned growth of CNTs with these process parameters; the $Mo/Fe/Al_2O_3$ catalyst gives a densely tangled mat of CNTs, and this entanglement "traps" the CNTs against each other or against the surface before they can be aligned by the gas flow.

To further test this observation, we first grew CNTs on a microchannel array placed by itself (open, as for Fig. 3-15) in the tube furnace, so a uniform tangled CNT film grew over the surfaces of the microchannels, and occasional CNTs grew to span across the narrow microchannels. We then packaged this device inside the quartz fixture, and heated it to 550 °C under Ar flow ($\ll$1–1 m/s across the array) through the microchannels. SEM examination of the CNTs before and after this high-temperature gas flow demonstrates that the CNTs did not move in response to the strong flow through the channels; therefore, anchoring of CNTs on the microchannel surfaces is quite strong. Based on this limiting test case, we would not expect flow-aligned CNTs by direct growth in the microchannel arrays as we attempted during our initial experiment.

To improve the likelihood of flow-aligned CNT growth, we sought to decrease the density of CNT nucleation sites on the microchannel surfaces, so CNTs could grow longer before becoming entangled. This could have been achieved using an alternate catalyst preparation technique, such as by coating the substrate with a low-concentration metal salt solution [261] or by using a solution of catalyst nanoparticles (e.g., from apoferritin [469]). However, recalling how the $Mo/Fe/Al_2O_3$ catalyst film breaks up when processed above ≈900 °C (Fig. 7-2(c)), we simply repeated the initial growth experiment at T = 915 °C. At this condition, CNTs only grow from apparent cracks in the film, and flow alignment of short CNTs was achieved (Fig. 7-24).

However, because the CNTs grown at the conditions of film breakup are short and appear to be of poor quality, we did not do further work here. Instead, we sought to develop a CVD reaction which grew CNTs at much higher yield and growth rate, so the CNTs would initially crowd and self-align at the surface, and then become aligned by the gas flow after reaching a sufficient length. This was the initial motivation to work with the Fe/Al_2O_3 catalyst film in

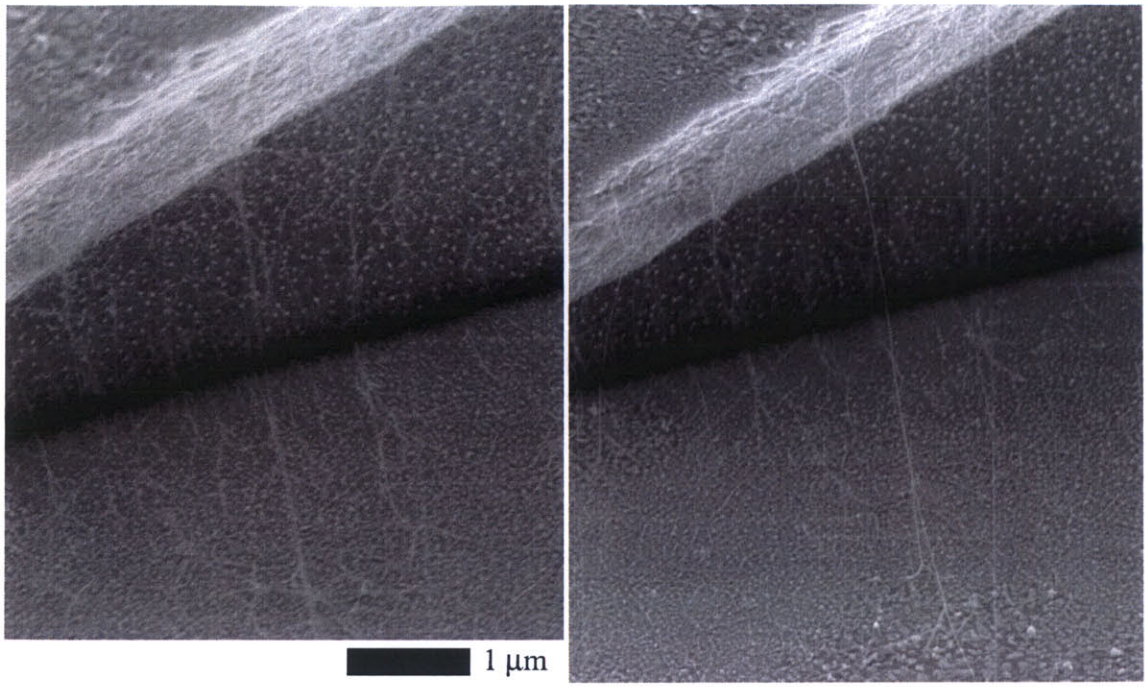

Figure 7-23. Stability of anchored suspended CNTs: (a) CNTs grown across a KOH-etched groove in tube furnace ("open" configuration) from $Mo/Fe/Al_2O_3$ catalyst in CH_4/H_2; (b) same CNTs after ≈1 m/s Ar flow through microchannel in tube furnace at 550 °C. The image in (b) is sharper perhaps due to oxidative cleaning of the CNTs by the flow exposure, yet the CNTs are identically placed, qualitatively demonstrating the strength of anchoring.

the more active CVD environment of C_2H_4, which concurrently led to the work presented in Chapter 4.

7.3.2 Chemically-induced evolution of CNT yield

While the reaction of Fe/Al_2O_3 in $C_2H_4/H_2/Ar$ routinely gave VA-CNT growth in the 22 mm ID tube furnace, attempts to replicate these experiments in the 42 mm ID tube furnace were initially unsuccessful. When the same reactant mixture and flow were introduced to the larger tube, the reactants significantly decomposed before reaching the sample, because the slower flow velocity allowed a greater residence time for the gas to thermally evolve. This unfavorable condition gave very low CNT yield and was not sufficient for experiments with the microchannel fixture, which due to its dimensions necessitated use of the larger tube furnace. Soot formed in the gas phase and was drawn into the microchannels, causing the channels to clog (Fig. 7-25).

To remedy this, a modified end cap was constructed (Fig. 7-26a-b) for the furnace tube, so the gas could be introduced to the open end of the quartz fixture through a 22 mm ID quartz tube nested concentrically within the 42 mm ID tube (Fig. 7-26c). This cap has four internal grooves and four lip seals: two seals for the smaller tube, and two seals for the larger tube. Using this setup, we could maintain the same reactant flow as we had previously found to give best

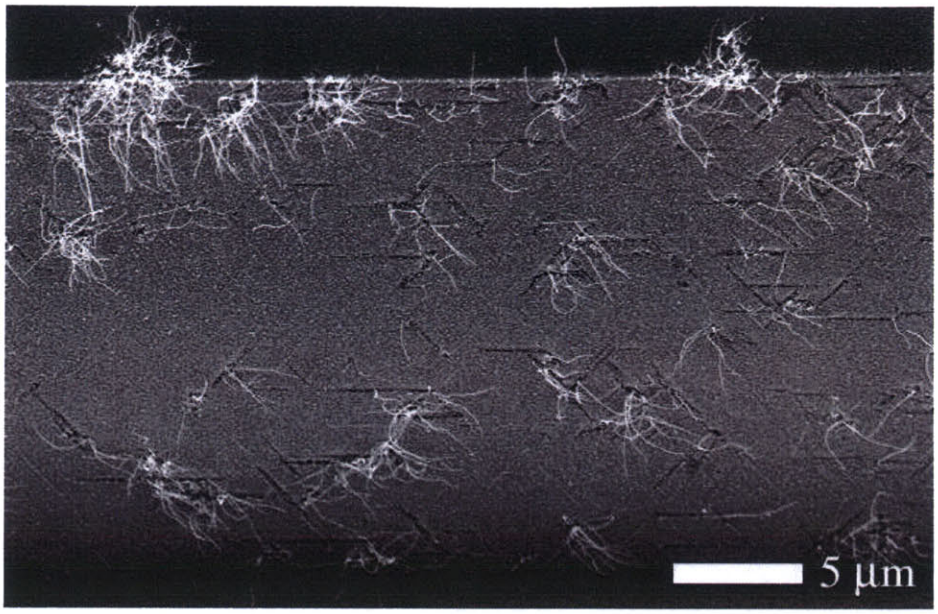

(a)

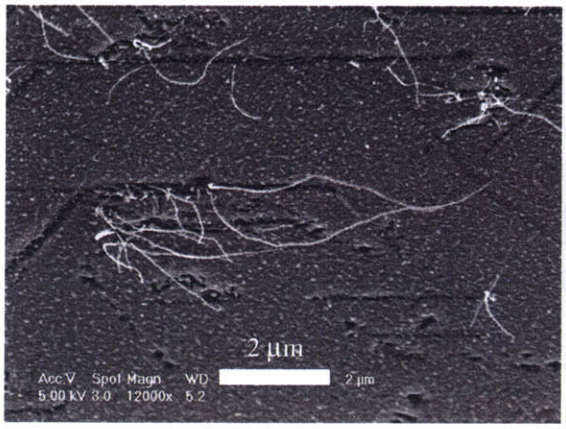

(b)

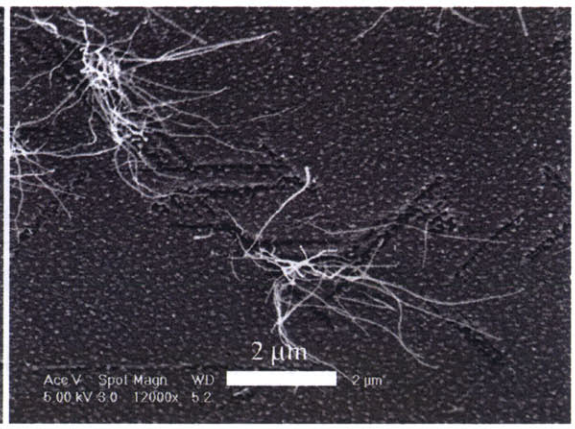

(c)

Figure 7-24. Flow-directed alignment of individual CNTs grown from $Mo/Fe/Al_2O_3$ in ≈ 1 m/s CH_4/H_2 flow through a KOH-etched microchannel groove, at 915 °C.

growth in the 22 mm ID tube furnace, while packaging the microchannel array in the 42 mm ID tube. We suspect that a suitable growth condition could have been found for direct flow into the larger tube, likely by increasing the total flow of reactant while maintaining the same composition. However, our flowmeters did not accommodate a sufficient increase in the flow rates. Therefore, the new end cap was sought as a more direct method of finding a good growth condition, and enabled quick acquisition of the two limiting results discussed next.

First, at a low flow velocity of $C_2H_4/H_2/Ar$ (corresponding to $\Delta p \approx 0.1$ psi) through the microchannel array, we observe a gradual transition from tangled to self-aligned CNT growth from lithographically-patterned (section 5.8) dots of Fe/Al_2O_3 catalyst along each microchannel. As the microchannel device is isothermal, this transition reflects an increase in the activity of the

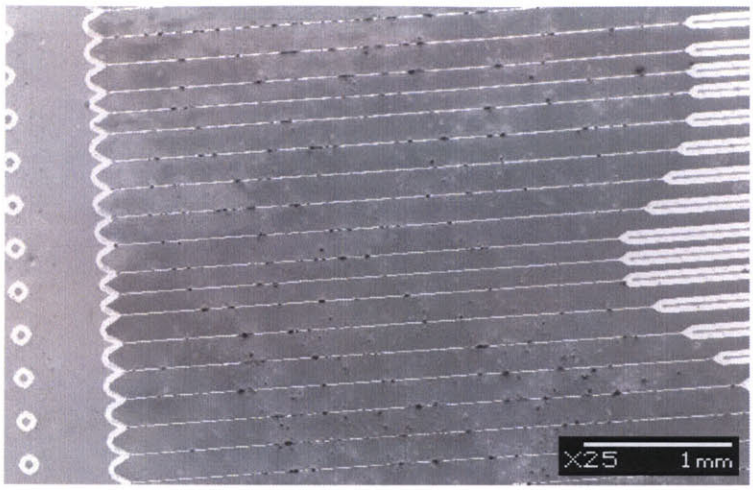

(a)

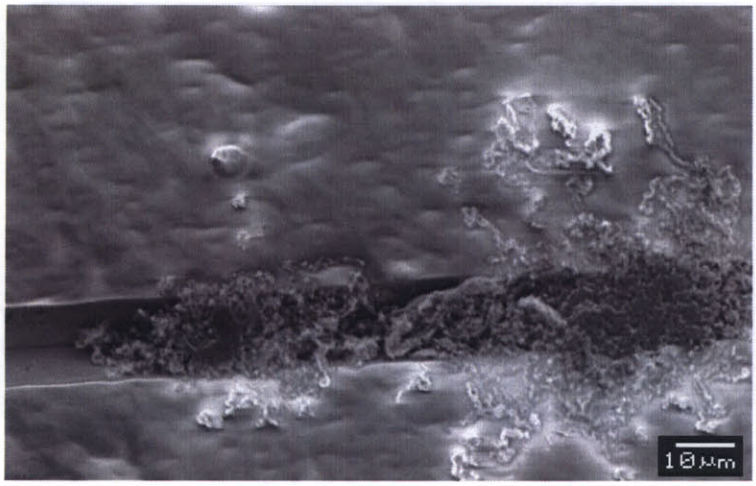

(b)

Figure 7-25. SEM images of soot-clogged triangular-groove entry regions of microchannel device: (a) wide view of array; (b) close view of individual groove.

reactant mixture, which significantly increases the yield and quality of CNTs growing from the catalyst. At the upstream extent of flow through the channel (Fig. 7-27b), the CNTs are sparse; then the density and length (judged by examining the CNTs extending from the perimeter of the catalyst area) increases (Fig. 7-27c-e); and then the density is sufficient to cause the structure to grow away upward and away from the substrate (Fig. 7-27f-g). This justifies our earlier conclusion (section 4.1.2.2) that a gradient in reactant supply caused by the gas flow over flat silicon substrates mediates a tangled-to-aligned morphology transition.

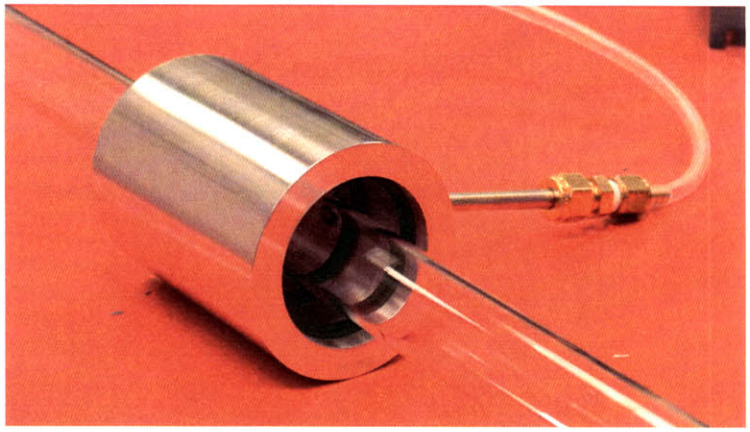

(a)

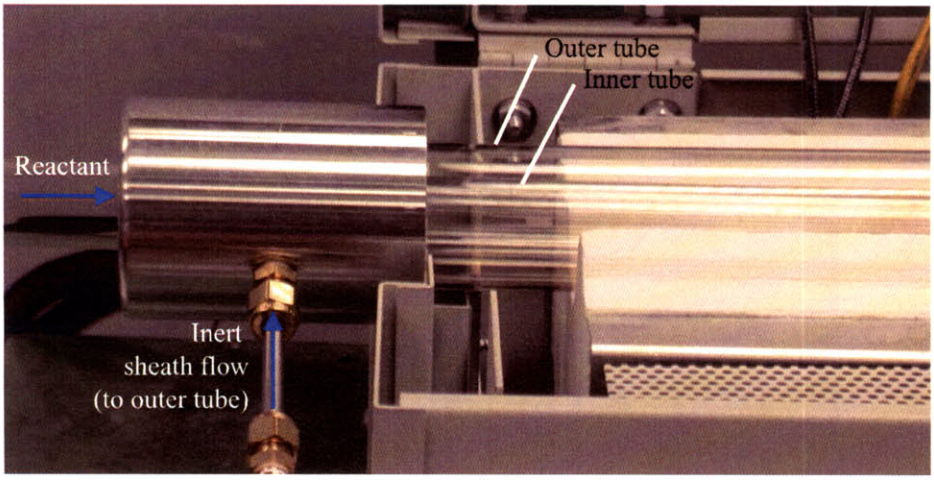

(b)

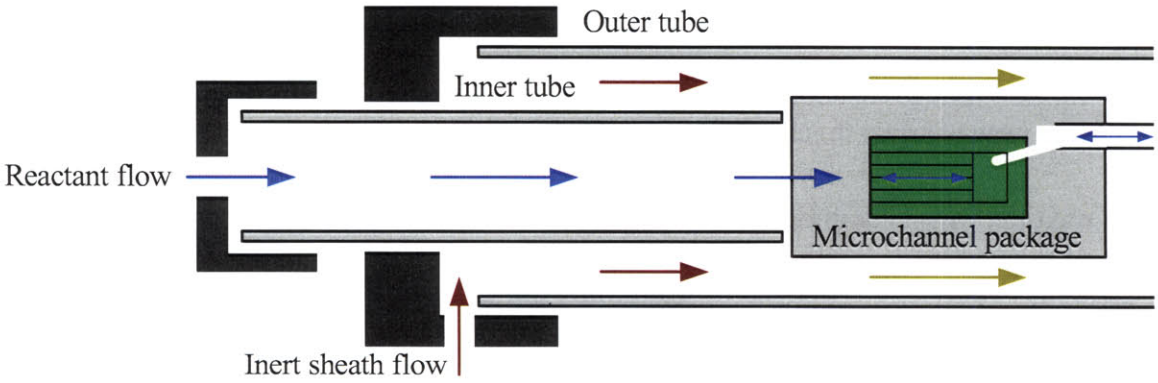

(c)

Figure 7-26. Tube end cap accommodating 26×22 mm (OD×ID) quartz tube inside of 45×42 mm tube: (f) cap with small tube installed, showing lip seals for large tube; (b) cap mounted in tube furnace; (c) schematic of tube furnace configuration with flow through 22 mm ID tube directed to open end of quartz fixture (in flow-reversal configuration).

(a)

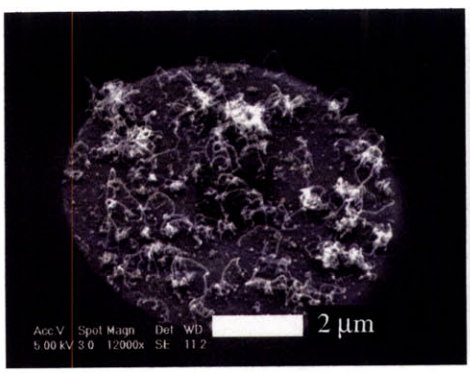

(b) $x \approx 1\,\text{mm}$

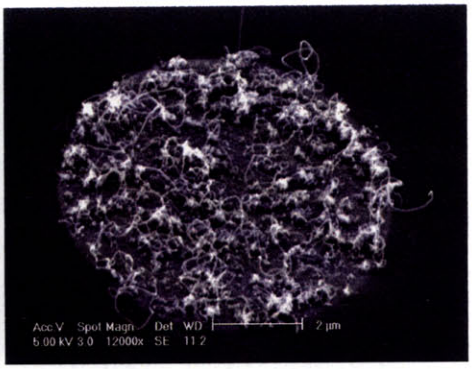

(c) $x \approx 2\,\text{mm}$

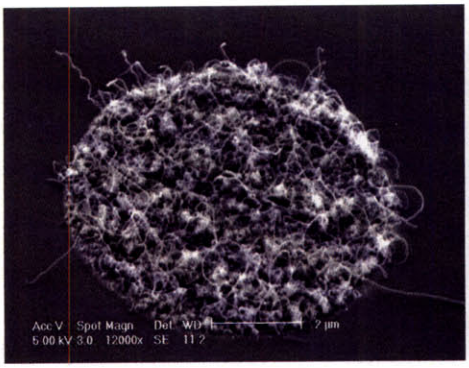

(d) $x \approx 3\,\text{mm}$

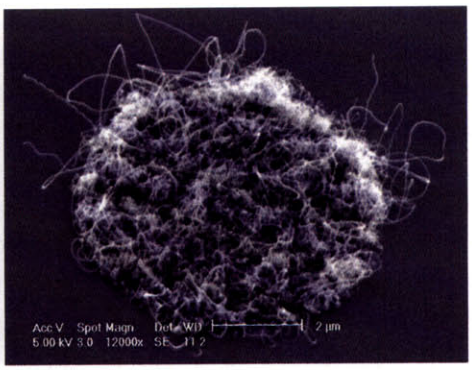

(e) $x \approx 4\,\text{mm}$

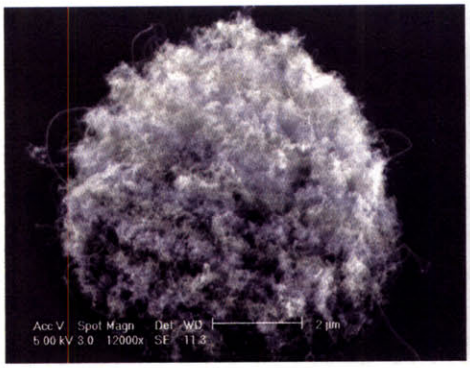

(f) $x \approx 5\,\text{mm}$

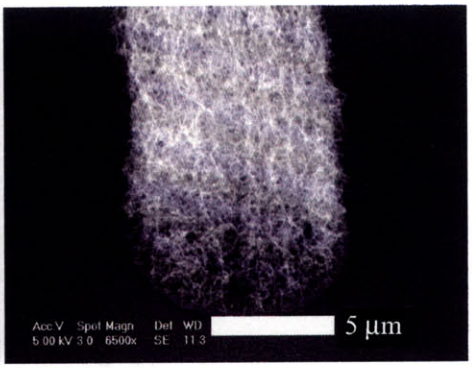

(g) $x \approx 6\,\text{mm}$

Figure 7-27. Transition from tangled to aligned CNT growth from ≈7 μm diameter dots of Fe/Al_2O_3 catalyst, confined in a gentle flow of $C_2H_4/H_2/Ar$ through a microchannel. A flow of 100/500/200 sccm $C_2H_4/H_2/Ar$ was supplied to the inner quartz furnace tube, at 750 °C. Images (b)–(f) are at the same scale.

7.3.3 Flow-directed alignment of CNT microstructures

Using a mixture of $C_2H_4/H_2/CO$ to give a more reactive flow, and at a much higher flow velocity (corresponding to $\Delta p = 4$ psi) through the microchannels, all patterned areas of catalyst in the channels exhibit self-aligned growth. In the channels having the highest flow velocity ($\approx$1 m/s) the CNT microstructures grow in the direction of the gas flow through the channels (Fig. 7-28). Smaller diameter strands exhibit stronger flow-directed alignment owing to their lower stiffness; for example, a 3 μm diameter structure becomes horizontally-oriented by the flow, whereas strands larger than 8 μm do not deflect in response to the flow. We hypothesize that each strand initially grows vertically from the catalyst substrate, and is gradually deflected by the gas flow when it grows to a sufficient length to induce the required drag force.

Flow-induced deformations of CNT structures can later be correlated to models of the flow-induced forces on nanoscale structures. Preliminary models of fluid shear forces on CNTs and CNT bundles were developed in collaboration with Michael Franzkowiak, during his work at MIT as a visiting graduate student in 2003 [470].

7.3.4 Combinatorial grow-molding

Finally, with the microchannel array mated against a substrate coated with a uniform film of Fe/Al_2O_3 catalyst, and using the mixture of $C_2H_4/H_2/CO$ at $\Delta p = 4$ psi, we demonstrate grow-molding of 3D-shaped CNT microstructures using directed gas flows. This contrasts with the grow-molding process of section 4.3.2.2 where the gas diffuses into the cavities between the template and catalyst-coated substrate. Likewise, the CNTs grow to fill the flow paths in the microchannel array, so the geometry of the array is replicated on the catalyst substrate (Fig. 7-29). However, here we observe that the penetration depth to which CNT growth fills a microchannel depends ordinally on the velocity through the microchannel. Channels with a higher velocity are filled farther along their length.

This result suggests that the initial supply of reactant determines whether the CNTs start to grow in the aligned or tangled configuration. The supply of active species in the reactant is depleted with flow along the channel. At a downstream location in each channel, a transition from aligned-to-tangled growth is observed. This is where the gas chemistry is insufficient to nucleate (section 2.5.1.2) a high density of CNTs—a reverse analogue of the tangled-to-aligned transition induced in a slow flow over patterned catalyst (Fig. 7-27).

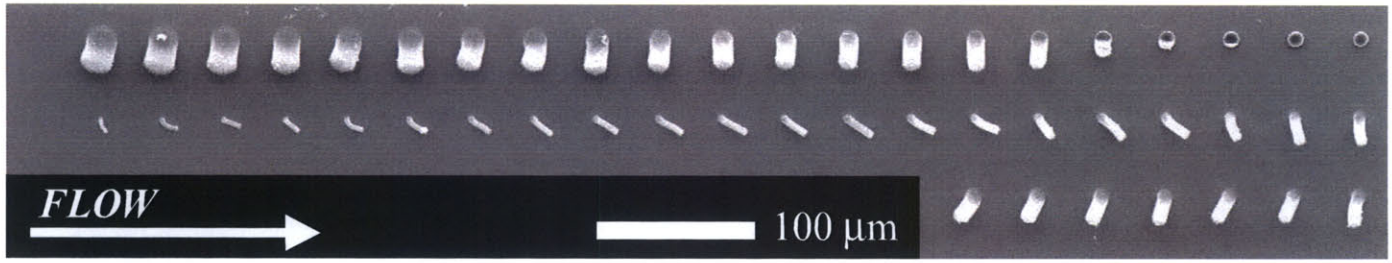

(a)

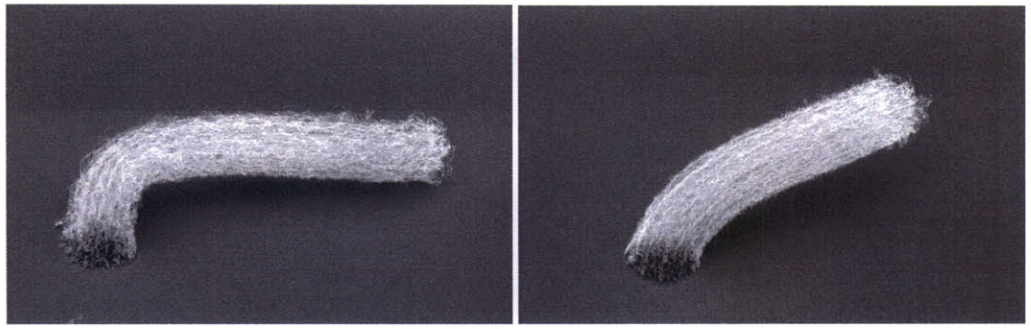

(b) 3 μm diameter

(c) 5 μm diameter

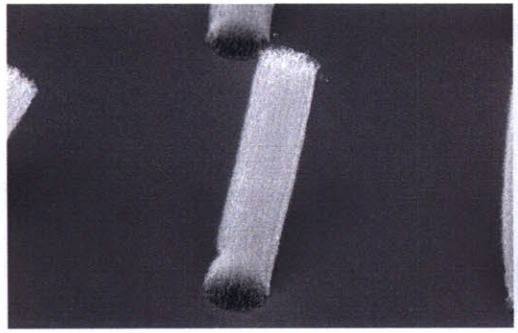

(d) 8 μm diameter

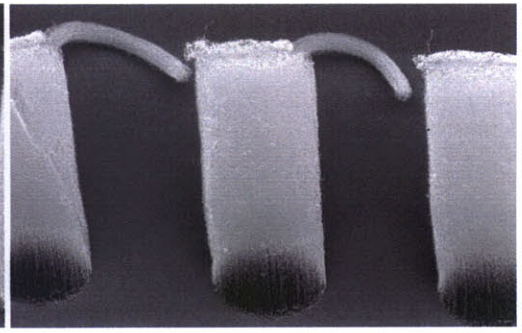

(e) 18 μm diameter

Figure 7-28. Flow-aligned growth of CNT microstructures from patterned Fe/Al_2O_3 catalyst, at ≈1 m/s flow of $C_2H_4/H_2/CO$ through the microchannel array, at 750 °C: (f) progression in alignment along area of catalyst pattern enclosed by a single microchannel; (b)–(e) individual strands, where degree of alignment is inversely proportional to strand diameter (stiffness).

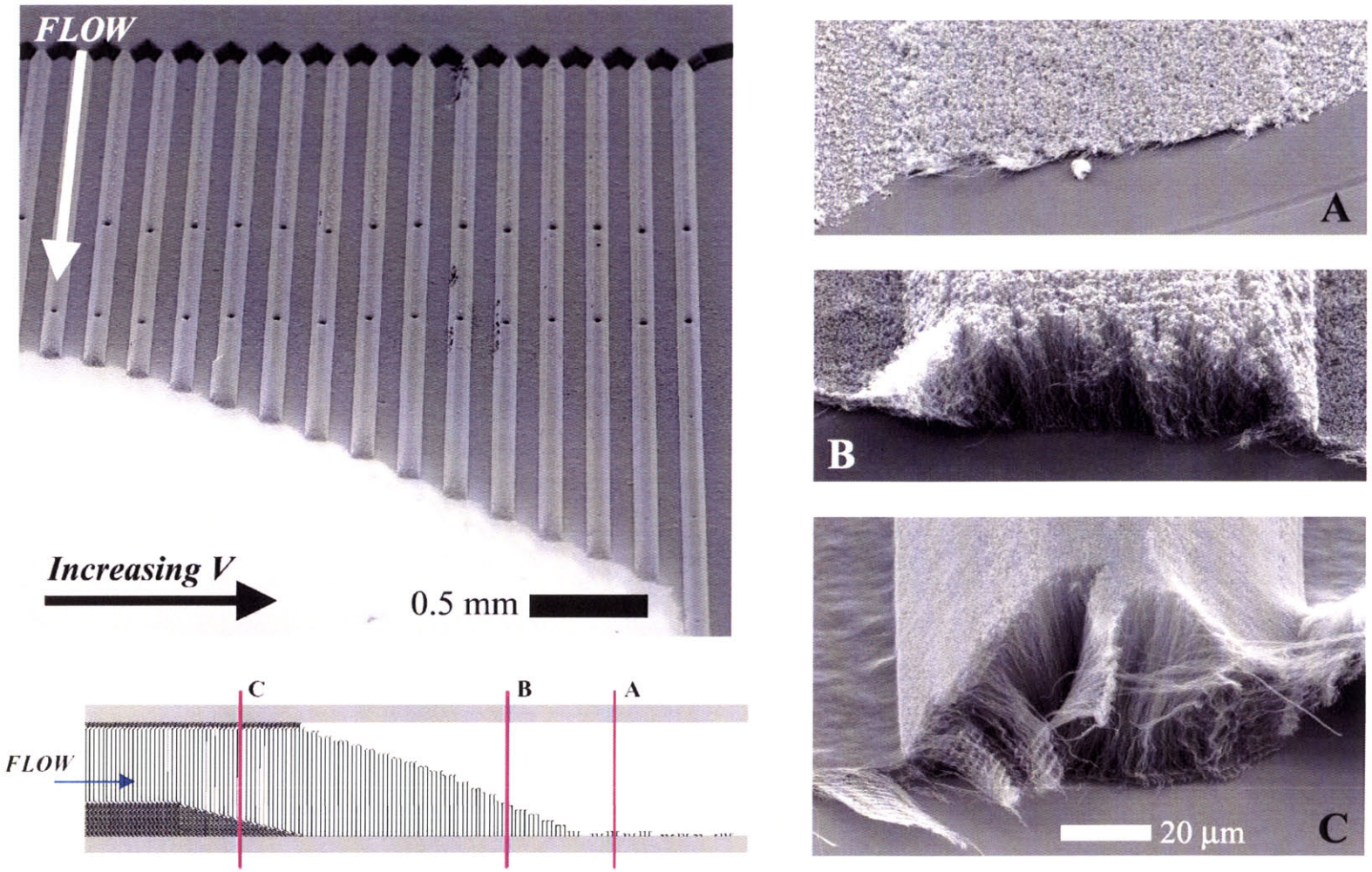

Figure 7-29. Initial experiment with CNT grow-molding using directed gas flow through microchannel array, where flow velocity determines extent of VA-CNT growth by limiting initial gas supply. Supply depletion with flow through microchannel causes transition from aligned (microformed) growth to sparsely tangled growth.

7.3.5 Summary

These experiments constitute our initial observations of CNT growth behavior in microchannel flows. The summary in Table 7.2 comprises limiting results obtained in conventional furnace systems, as well as new results which would not be observed in these systems. There should be significant interest in future work with this system, starting with combinatorial studies of CNT growth. These studies could assess the evolution of CNT quality, yield, and alignment *along* the flow direction of each microchannel, along with the distribution of growth results *across* the array. Tests with the array packaged on the heated platform are also warranted, and these would facilitate management of the chemical activity by pre-treatment of the input flow, along with rapid adjustment of the array temperature.

	Catalyst Arrangement	
CVD conditions	*Uniform film*	*Sparse/Patterned dots*
$Mo/Fe/Al_2O_3$ in CH_4/H_2	No alignment Rigid anchoring G/D and G/Si transitions?	Alignment with flow
Fe/Al_2O_3 in $C_2H_4/H_2/Ar$	Grow-molding VA→Tangled transition	Tangled→VA transition Alignment with flow

Table 7.2. Summary of initial CNT growth experiments in microchannel arrays.

Chapter 8

Artistic Visualizations of CNT Structures

Studying the growth of VA-CNT structures—from chemically and mechanically-mediated nucleation to ordered and lithographically-patterned growth—leads to a plethora of beautiful images taken using scanning electron microscopes, arising from both expected and unexpected experimental results.

Ryan Wartena's[1] creative and enthusiastic efforts have catalyzed many of these artistic interpretations of VA-CNT structures, starting with our entry in the 2005 Materials Research Society Science-as-Art Competition (Fig. 8-2).

Conversations with Felice Frankel inspired me to visualize these structures in new ways and to pursue them as a medium of broader scientific communication. Felice also featured the "Seed of Life" image and described how we used of the digital image stitching technique developed by Michael Cohen at Microsoft, in her monthly column in American Scientist [471].

Some of our most enjoyable and notable efforts are shown on the following pages. An online gallery of images is maintained `http://www.nanobliss.com`.

[1] Ryan's website is `http://awonderfulofnew.org`.

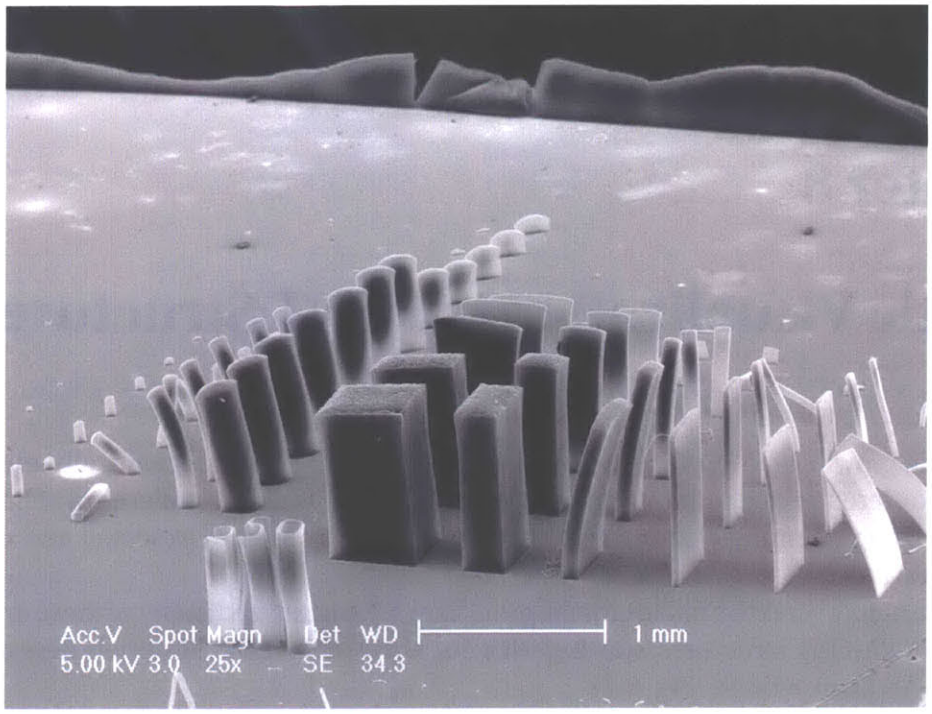

(a) Unaltered SEM image.

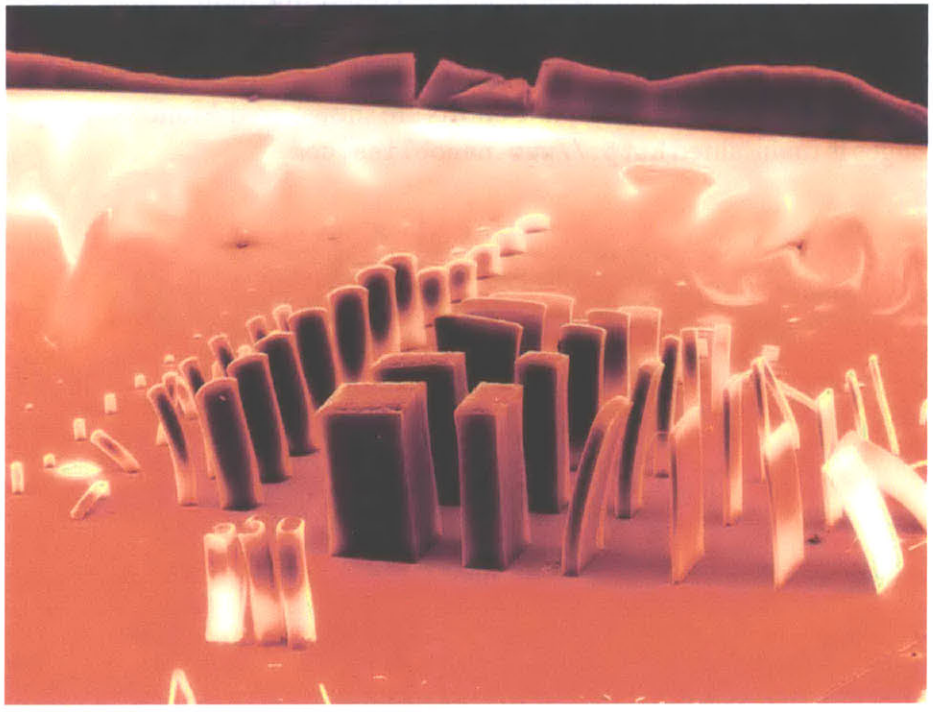

(b) Image digitally-enhanced by Ryan Wartena, using Adobe Photoshop.

Figure 8-1. *Making the Desertlands.*

Figure 8-2. *Making the Desertlands*, framed as displayed in the 2005 MRS Science-as Art Competition, approx. 23×17.5".

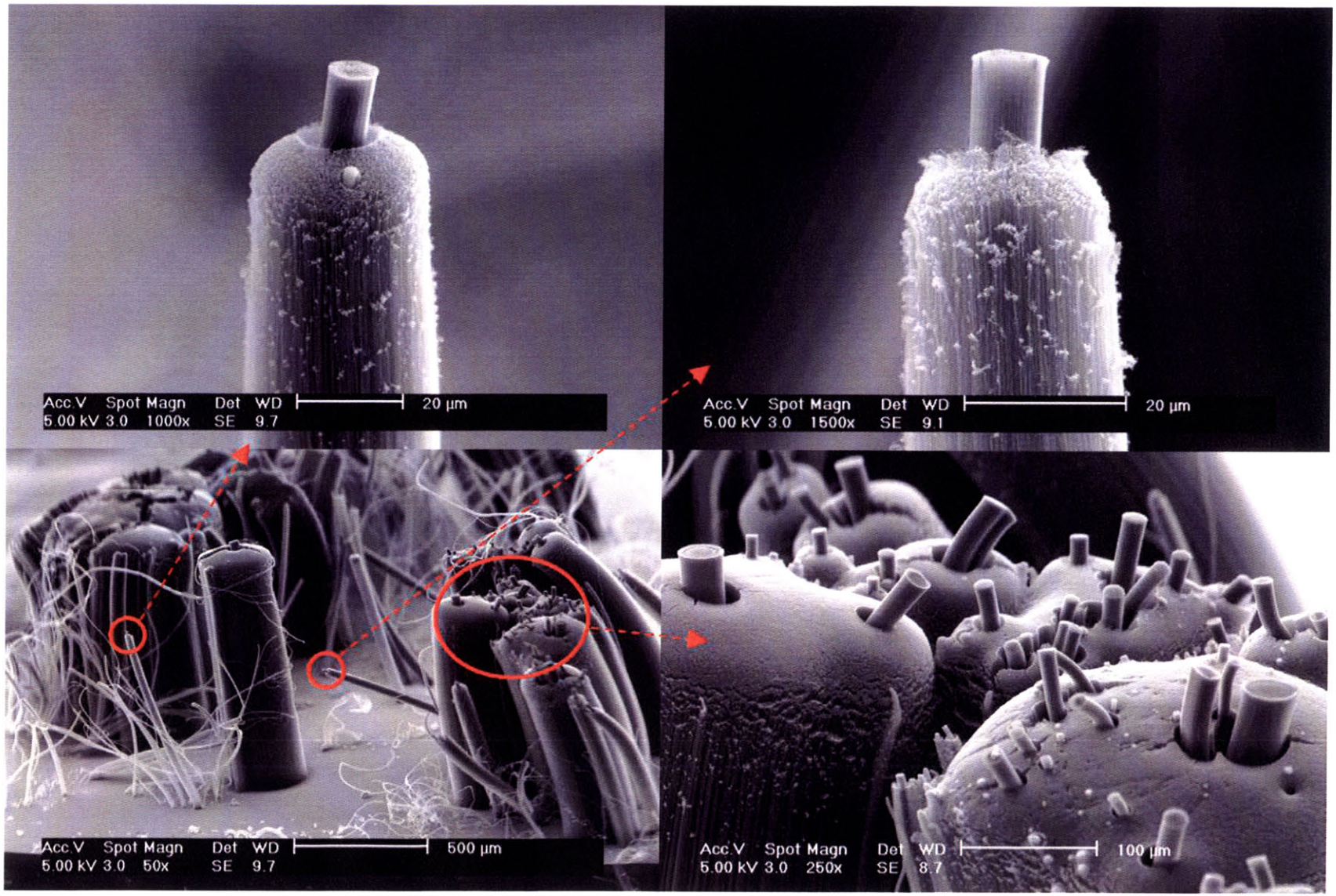

Figure 8-3. CNT structures imaged for the "Absolut Nano" rendering, grown in $C_2H_4/H_2/Ar$ after rapid heating of Fe/Al_2O_3 catalyst film in Ar (section 4.2.6).

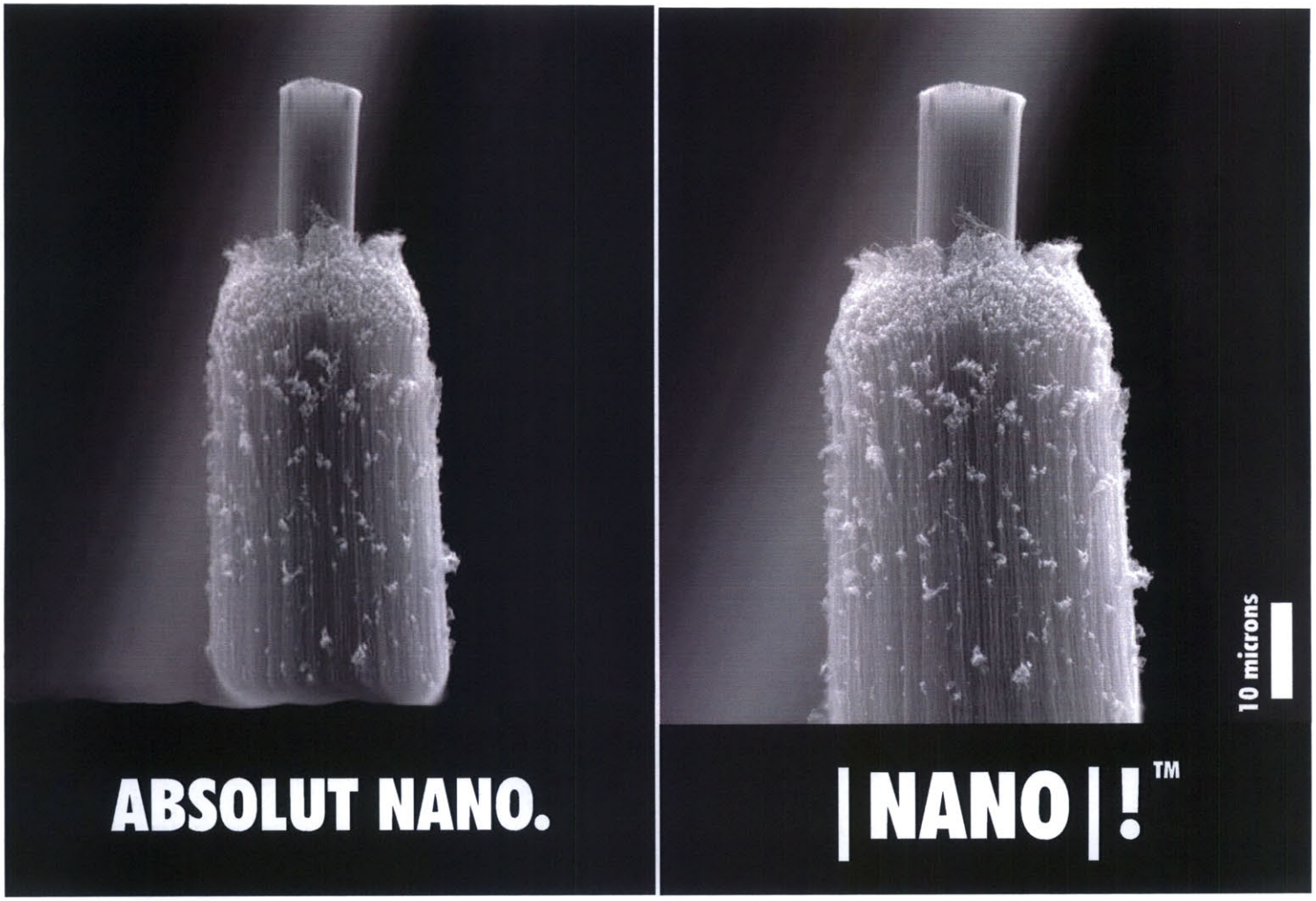

(a) (b)

Figure 8-4. *Absolutely.* Rendering (a) was proposed to the Absolut Spirits Corporation as it is emblematic of their well-known advertising campaign, but unfortunately they rejected all unsolicited submissions.

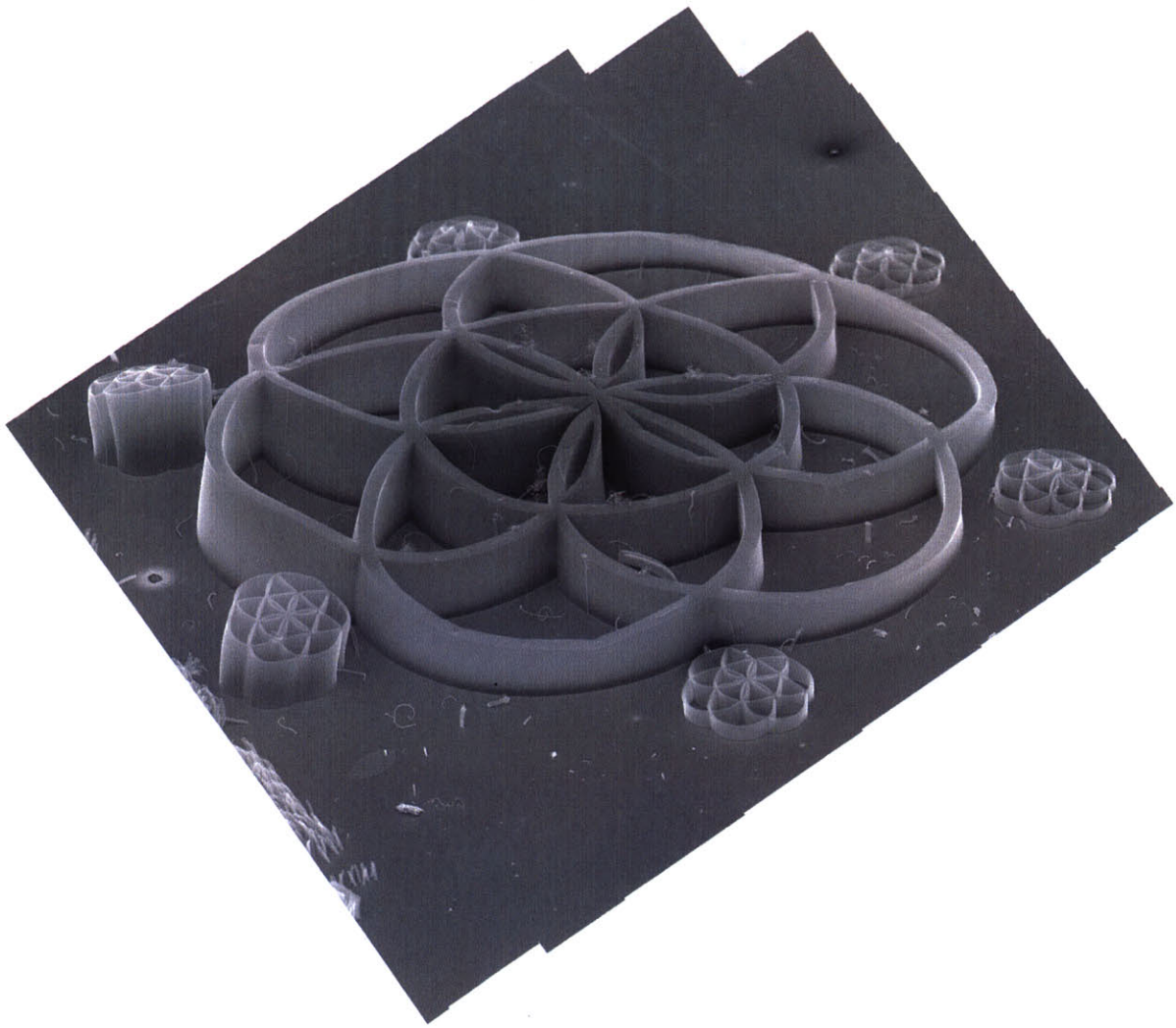

Figure 8-5. *Seed of Life* (angled view). This arrangement of circles having 6-fold symmetry was first found at the Temple of Osiris at Abydos, Egypt. The composite image shown was stitched from several individual frames taken under planar translation of the sample stage in the SEM. The images were processed using Microsoft Expression™ Graphic Designer software, in collaboration with Felice Frankel at MIT and Michael Cohen of Microsoft Research. Felice describes the image and technique in "Needlework" [471].

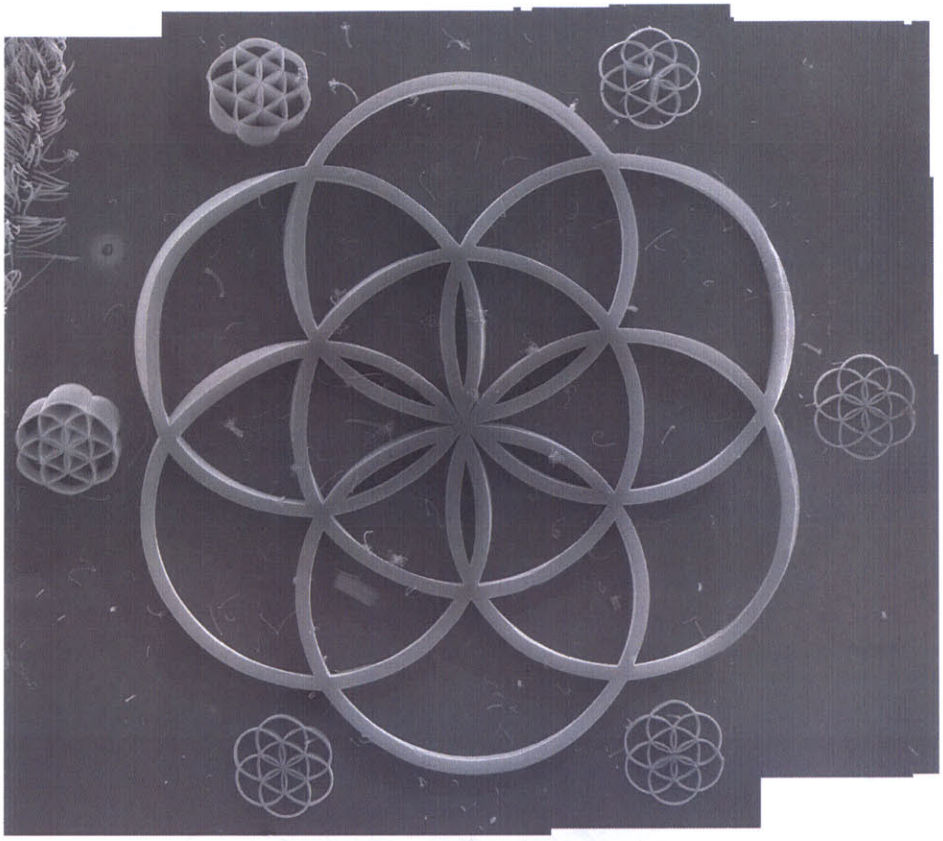

(a) Composite SEM image, stitched from several frames (otherwise unaltered).

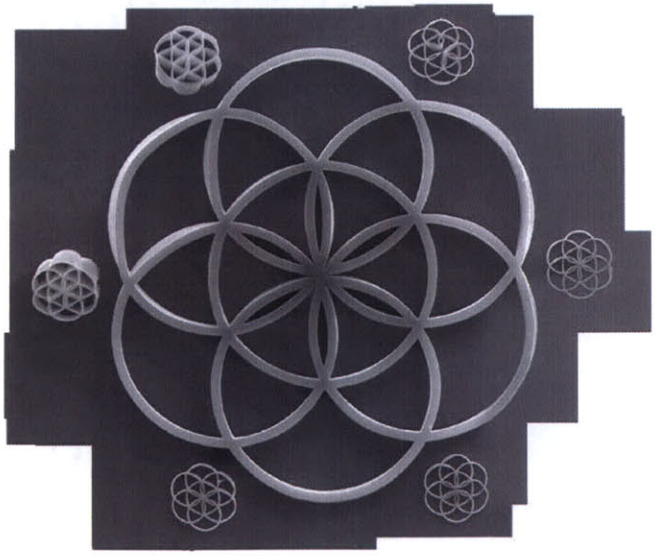

(b) Image digitally cleaned by Felice Frankel.

Figure 8-6. *Seed of Life* (top view).

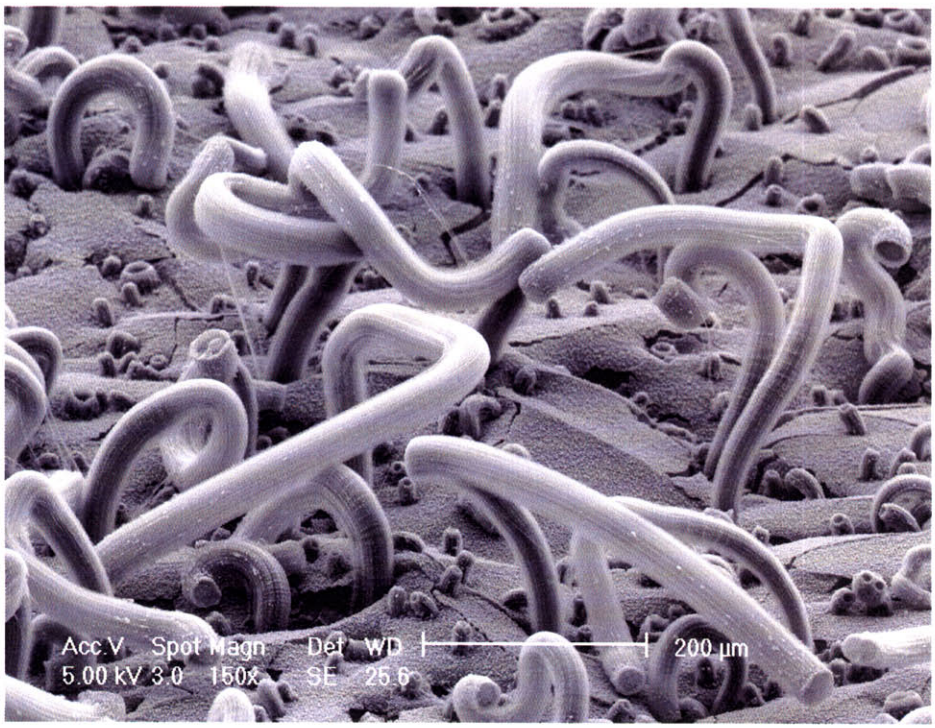

(a) Unaltered SEM image.

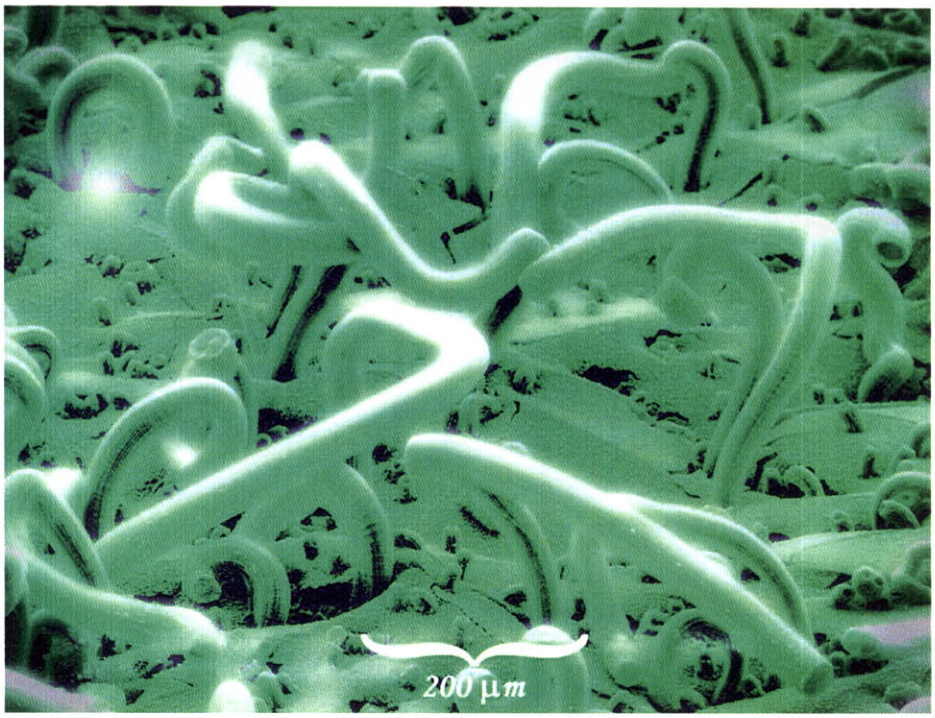

(b) Image digitally-enhanced by Ryan Wartena, using Adobe Photoshop.

Figure 8-7. *Growing the Green Fields.*

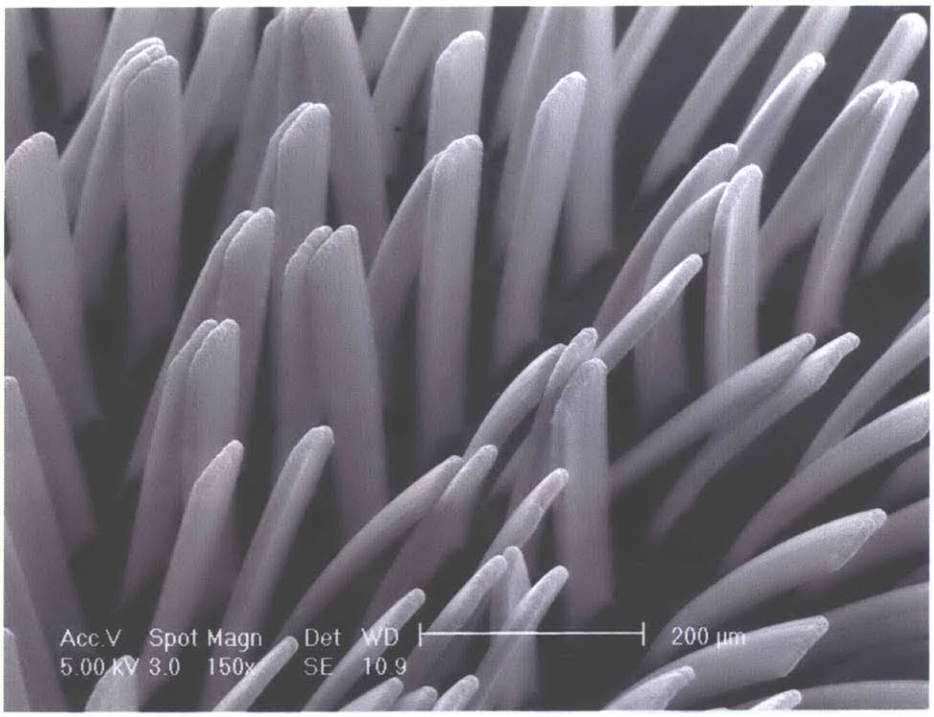

(a) Unaltered SEM image.

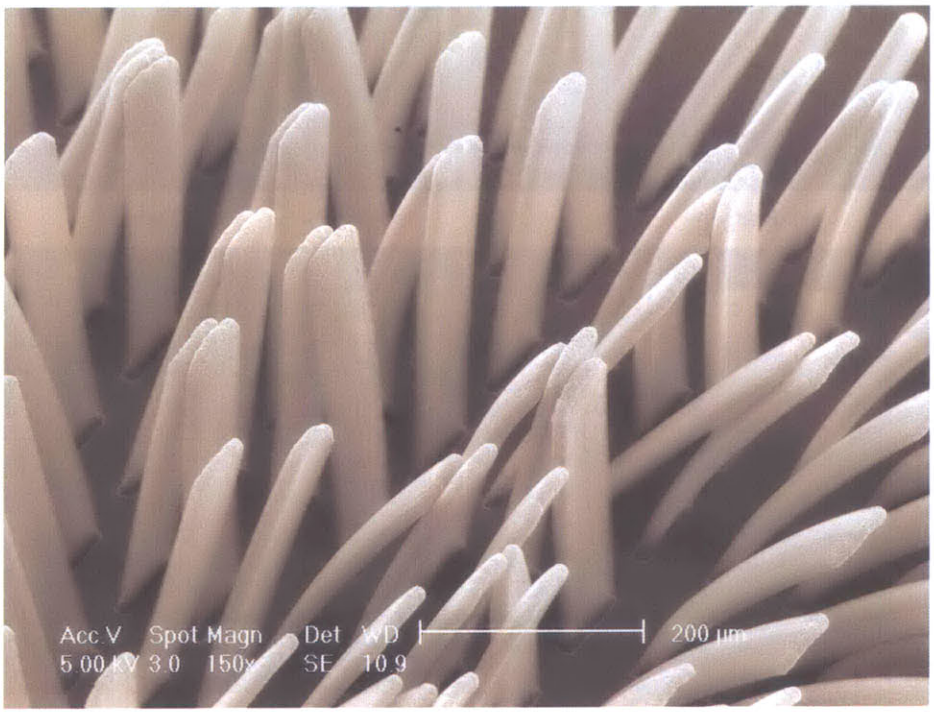

(b) Image with sepia tone.

Figure 8-8. *Whispers.*

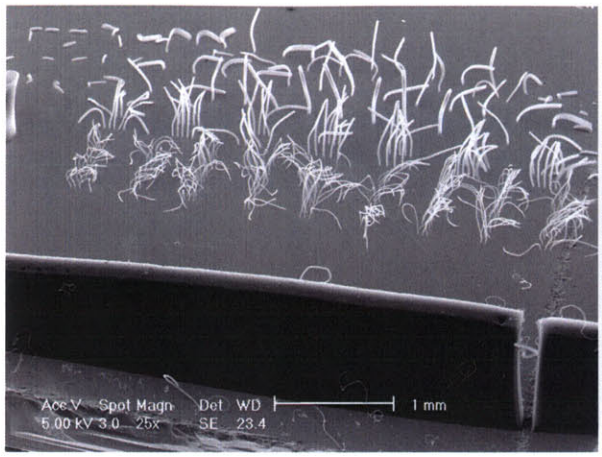

(a) *Across the Fence.*

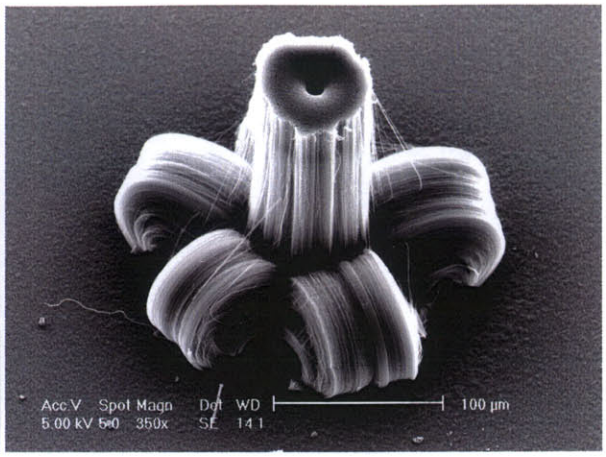

(b) *Banana.*

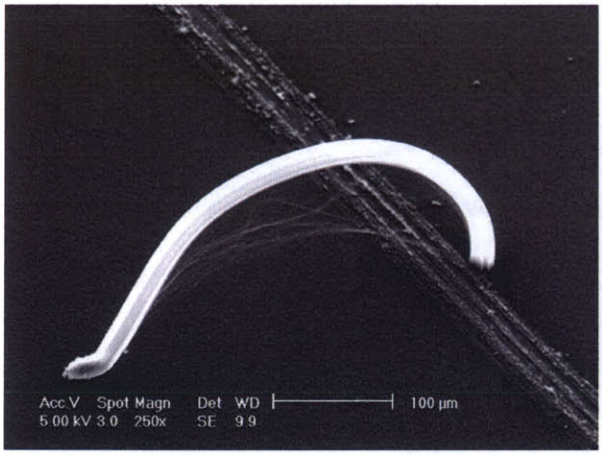

(c) *Bridge.*

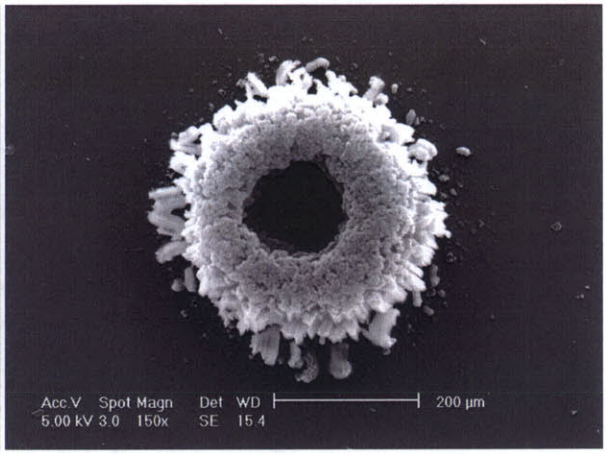

(d) *Daisy.*

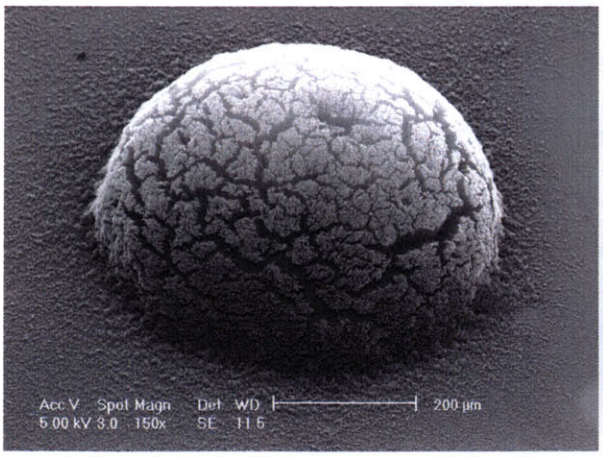

(e) *Dome.*

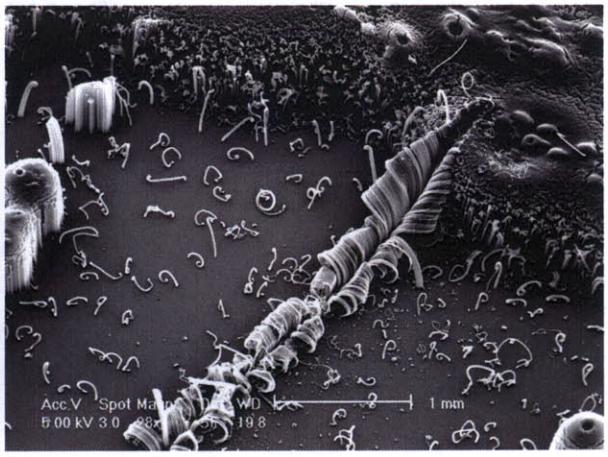

(f) *Garden.*

Figure 8-9.

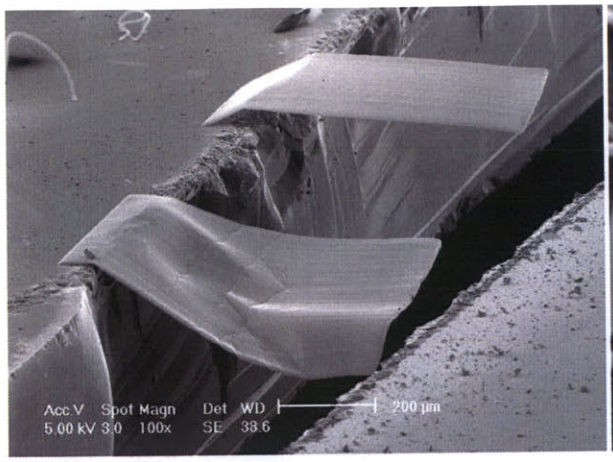

(a) *Walk the Plank.*

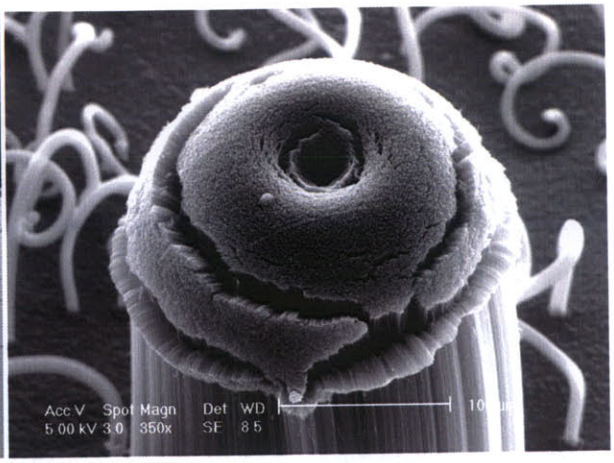

(b) *Rose.*

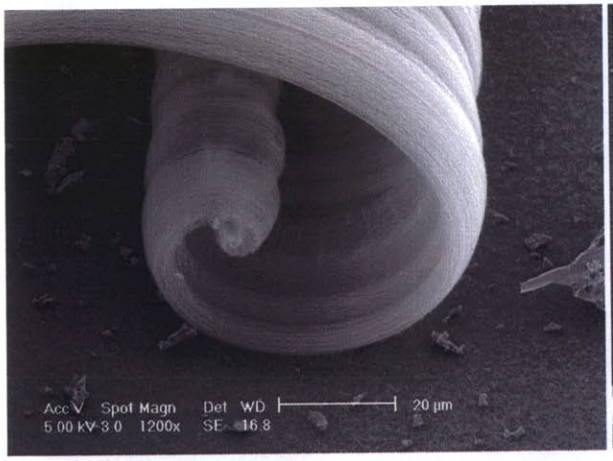

(c) *Scroll.*

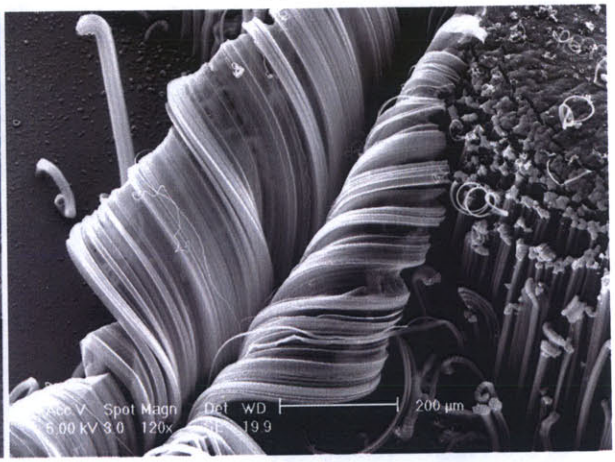

(d) *Split.*

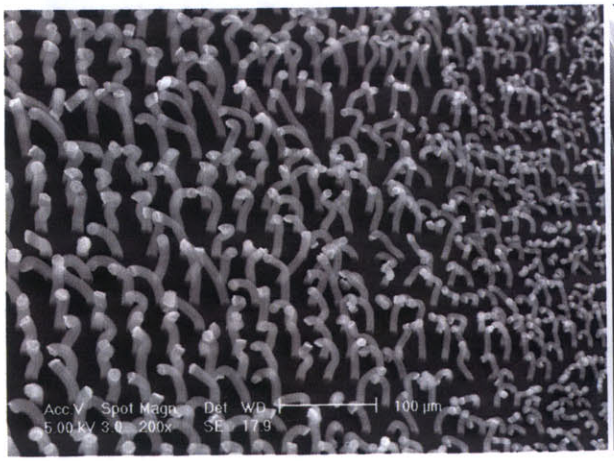

(e) *Sprouts.*

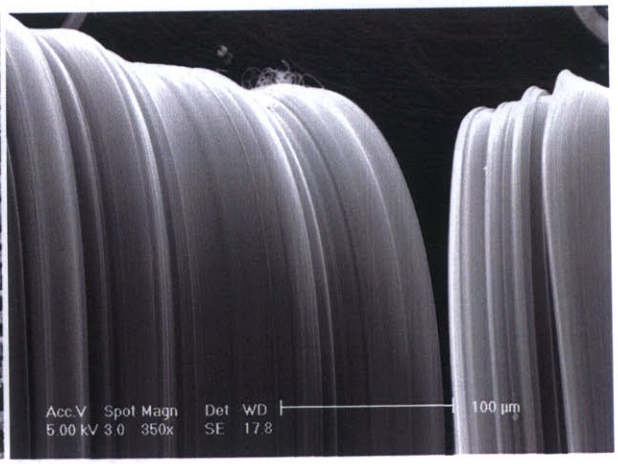

(f) *Waterfall.*

Figure 8-10.

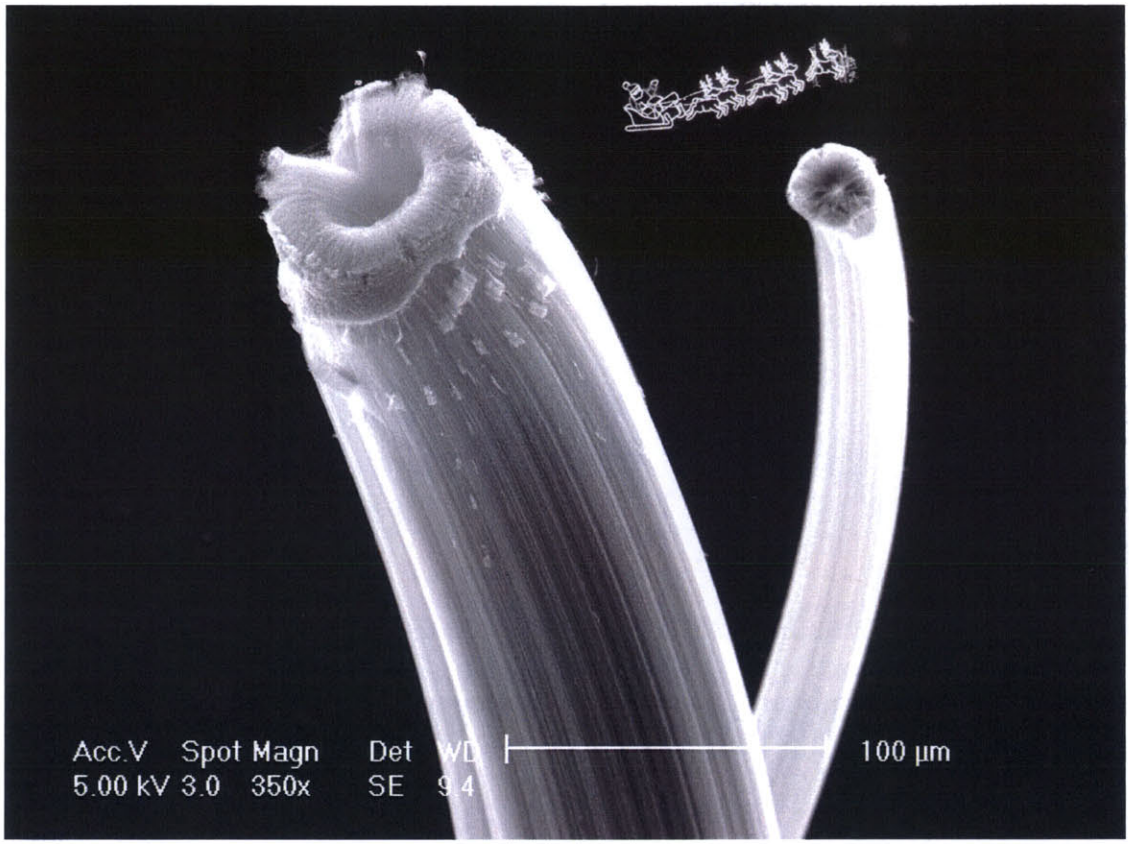

Figure 8-11. *Merry Christmas from the small world!*

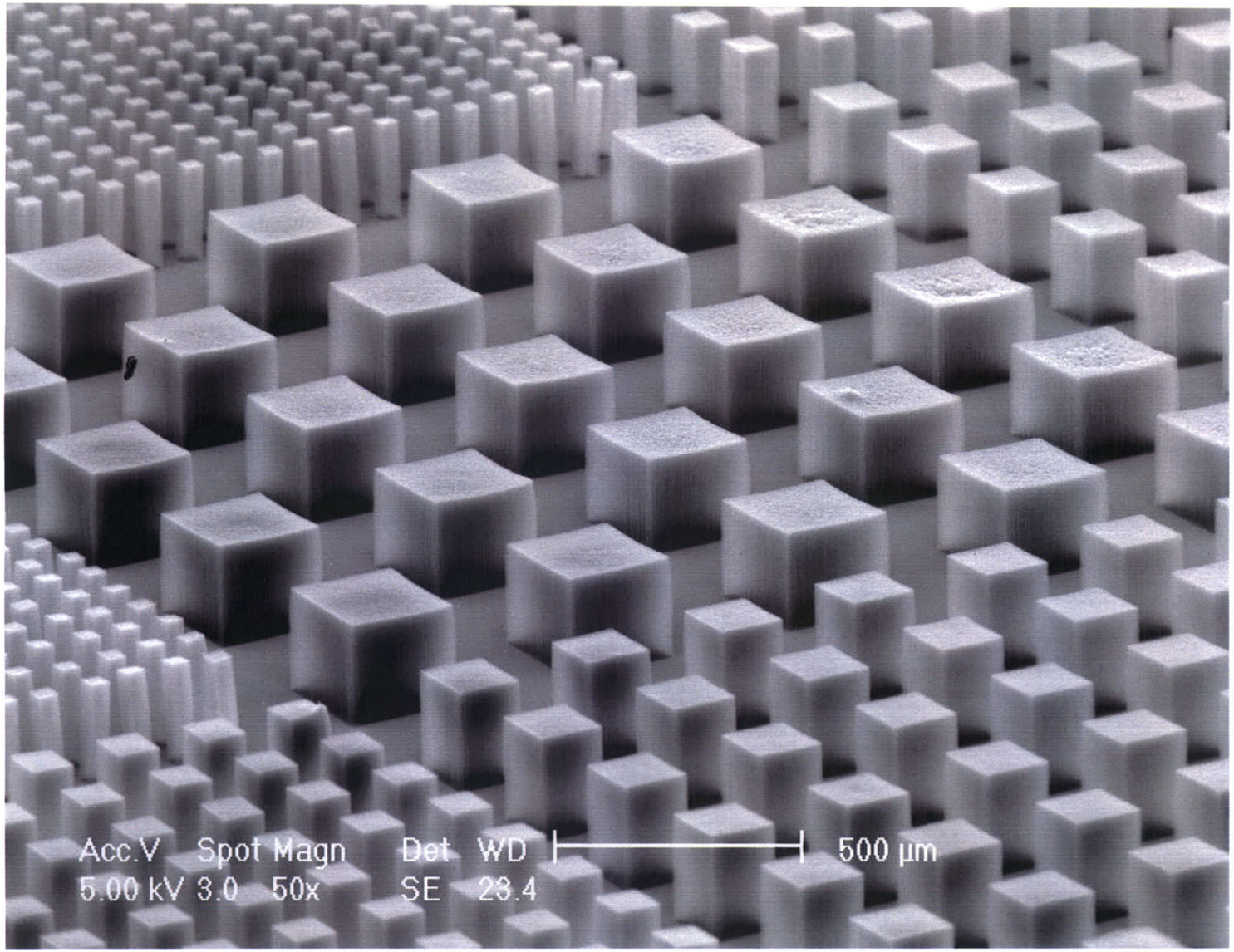

Figure 8-12. *City Blocks.*

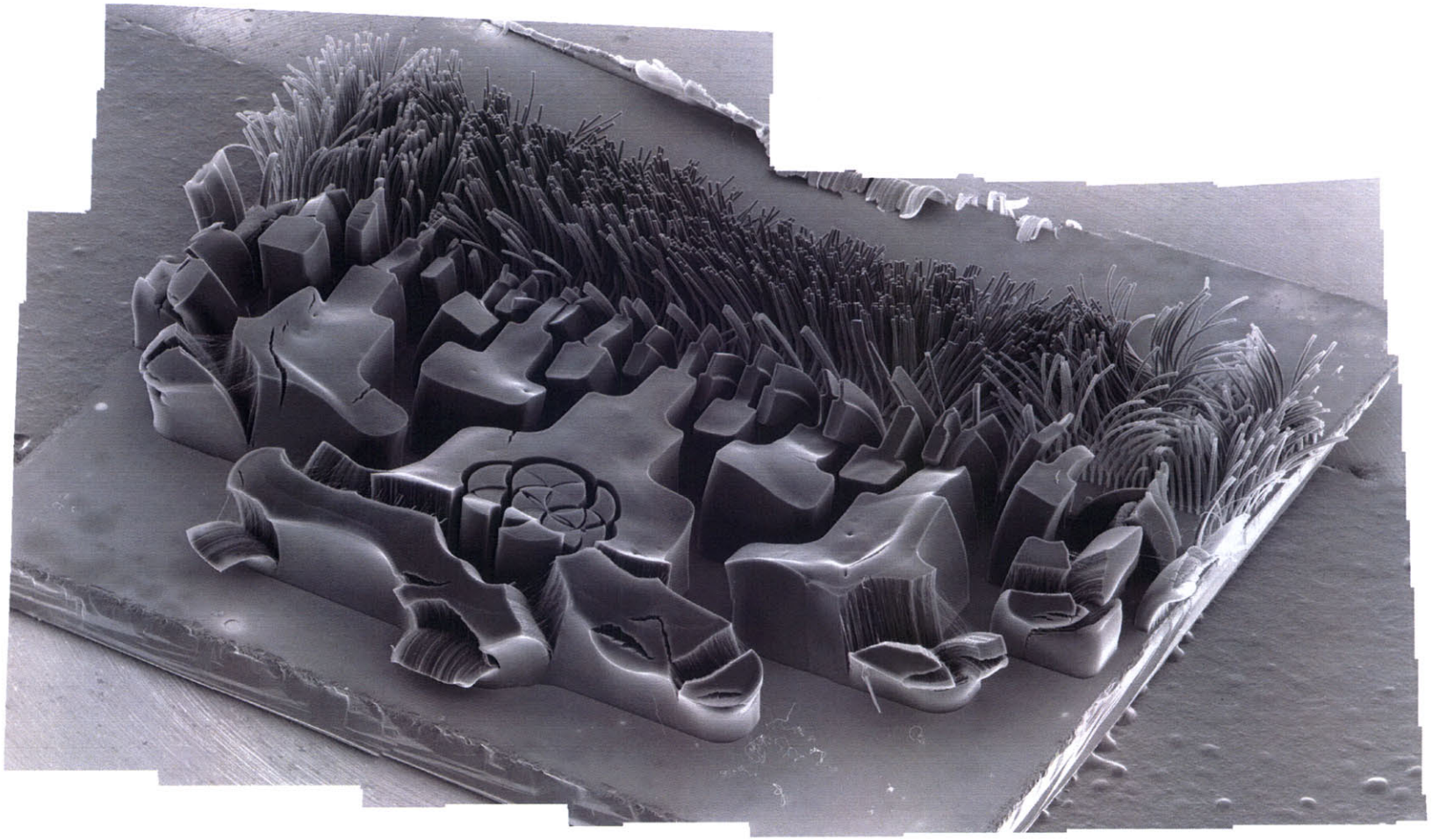

Figure 8-13. *Windblown* or *Carbon Nano-Piccasos (CNPs).*

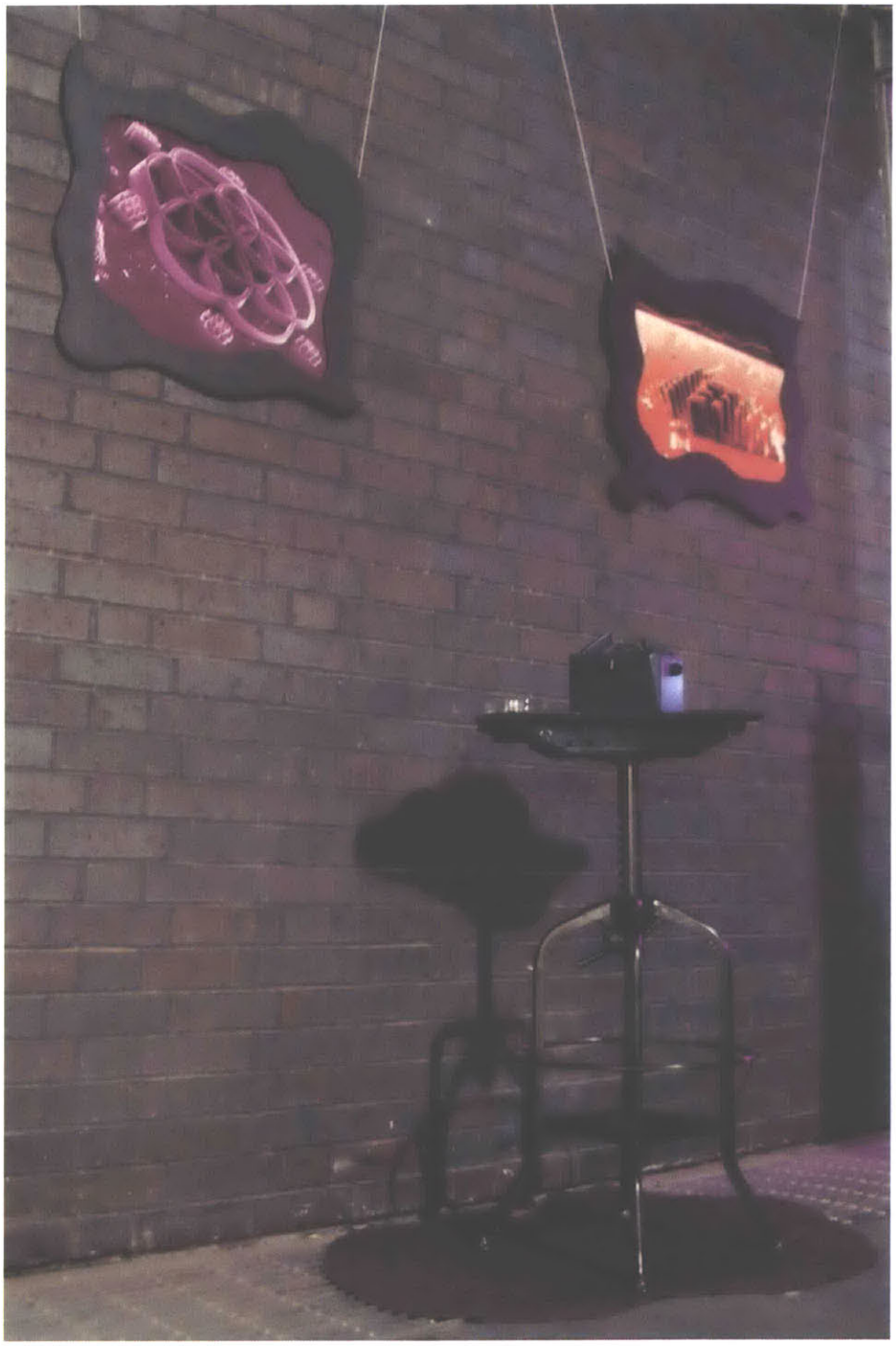

Figure 8-14. "Growing Architecture Initial Experiments" exhibit of CNT visualizations and samples at CollisionCollective C9 show in Cambridge, MA, February 2006. The exhibit was designed, built, and installed by Ryan Wartena and Ammon Embry-Pelrine.

Chapter 9

Findings and Next Steps

9.1 Contributions of this work

This thesis has explored synthesis of carbon nanotubes by catalytic chemical vapor deposition on catalyst-coated substrates: from development and understanding of basic catalysts, reaction schemes, and characterization techniques; to creation and utilization of new machines and methods for applying directed forces, flows, and thermal and chemical gradients to control and understand growth. The major contributions of this work include:

- A rigorous study of growth of tangled films of SWNTs from a $Mo/Fe/Al_2O_3$ catalyst film [1]:
  - A process for single-stage deposition of the catalyst by e-beam evaporation;
  - A parametric study of growth results in a CH_4/H_2 atmosphere, relating to CNT yield and quality as measured by Raman spectroscopy;
  - A study of the effects of thermal activation of the gas atmosphere, where the gas activity is manipulated by changing the size and configuration of the sample in the furnace tube.
- The first demonstration of conformal CNT film growth on bulk micromachined surfaces, on sloped and vertical sidewalls of RIE-etched and KOH-etched silicon structures [1,2].
- Very high-yield growth films and microstructures of vertically-aligned MWNTs using a Fe/Al_2O_3 catalyst in C_2H_4/H_2, with nearly the fastest growth rates and tallest structures yet reported [3], along with:
  - Observations of size-dependencies and loading-dependencies growth of CNT microstructures from lithographically-patterned catalyst films;
  - Manipulation of spatial transitions between tangled and aligned morphologies by changing the flow configuration of the substrate sample inside the furnace tube and the annealing sequence in H_2;
  - Novel observations of mechanical stress effects on growth, possibly causing structural "collapse" of the emerging layer of the growing CNT film;

- Demonstration of the ability to pause, restart, stop, and regenerate growth by temporally adjusting the reactant composition in a tube furnace.

- Rapid growth of aligned MWNTs on the surfaces of commercially-available Al_2O_3 fiber cloth and hoses [358], using catalyst deposited from a metal salt solution.

- Processes for structuring CNTs by applying mechanical pressure during growth [4]:
  - Control of the film microstructure by placing a weight on the catalyst prior to growth, where the pressure causes the CNTs to transition from aligned to "collapsed" and causes significant defects in the CNT walls;
  - Characterization of the force output capability of CNT growth, and comparison to the energetics of the growth reaction and post-growth deformation, revealing that relatively slight forces are needed to deform CNTs during growth;
  - "Grow-molding" of CNTs into three-dimensional microforms, and fabrication of multi-layer film architectures (e.g., having consecutive aligned and collapsed layers).

- New apparatuses for studying and controlling growth of nanomaterials on substrates:
  - A "flow-reversal" configuration for rapid adjustment of the reactant composition inside a tube furnace, along with a new tube end-cap design [437];
  - A microchannel array for combinatorial and high-throughput nanomaterials growth experiments, which is capable of dozens of parallel experiments over a velocity range exceeding 10^3 [404];
  - A suspended resistively-heated silicon reaction platform (developed with Lucas van Laake) enabling rapid thermal and chemical control of the reaction conditions [438, 445];
  - Implementation of the suspended reaction platform in a quartz tube, and in a custom reaction chamber featuring flexible mechanical, optical, and electrical access to the platform along with non-contact measurement of the platform temperature;
  - Assembly and packaging schemes for reversibly-sealed operation of the microchannel array at up to 1000 °C, in a tube furnace or on the resistively-heated platform.

- Novel CNT growth experiments using the new apparatuses developed in this work:
  - A study of the initial stages of VA-CNT film growth using the flow-reversal tube furnace setup, demonstrating that a VA-CNT morphology emerges after a brief incubation period, which likely depends on the nature and duration of catalyst pretreatment in H_2 [437];
  - Optical imaging of VA-CNT film growth on the heated platform, revealing how nonuniformities and cracks develop during later stages of film growth;
  - *In situ* measurement of VA-CNT film growth kinetics on the heated platform, along with control of the initial growth rate and catalyst lifetime by dedicated thermal pretreatment of the reactant mixture;

- Demonstration of enhanced VA-CNT film growth by rapid thermal pre-treatment of $C_2H_4/H_2/CO$ and independent control of the platform temperature, where the film reaches 3 mm thickness in only 15 minutes;
- Initial CNT growth experiments in the microchannel array, demonstrating alignment of isolated CNTs and CNT strands directed by the gas flow through the microchannels, evolution of CNT yield causing a transition from a tangled to a self-aligned morphology, and combinatorial "grow-molding" of CNT microforms [472].

In addition, several enjoyable research collaborations have broadened the focus of this work, and are leading to initial applications of CNTs grown by the methods presented here. These projects are listed below; some have been mentioned in this thesis, while for brevity, others have not been addressed in further detail. These are generating exciting results and will dictate important directions as the research continues.

- (with E. J. Garcia and B. Wardle at MIT) Creating "nanostitched" composite architectures having enhanced interlaminar strength and multifunctional performance, using VA-CNTs grown directly on fiber surfaces and VA-CNTs assembled at fiber interfaces [388, 389].
- (with O. Yaglioglu at MIT) Creating electrical contact surfaces and electromechanical probes utilizing VA-CNT structures grown from lithographically-patterned catalysts.
- (with R. Bennett and R. Cohen at MIT) CNT growth from catalyst nanoparticle films organized by block copolymers, where control of the film morphology and CNT areal density is achieved by varying the spatial density of catalyst on the substrate [346, 473, 474].
- (with B.O. Boskovic at the University of Cambridge) Plasma-enhanced growth of CVD of CNTs and CNFs on silicon "micrograss" surfaces [2, 295].
- (with H. Taylor at MIT) Studying micro-scale chemical loading effects on CNT growth from patterned catalysts, and physical embossing of CNT films into three-dimensional topographies.
- (with D. Lucca at Oklahoma State University) Surface analysis of catalyst films before and after CNT growth to determine mechanisms of film evolution and catalyst deactivation.
- (with G. Nessim and C. V. Thompson at MIT) Studying the roles of H_2 and O_2 in the preparation, evolution, activity, and lifetime of catalyst nanoparticles for CNT growth.

9.2 Key questions and next steps

The study of CNTs is a fast-moving field, where results and publications are rapidly growing in frequency and impact. However, as identified in Chapter 1 and explored throughout this thesis, many key questions in understanding the growth behavior of CNTs must be answered before we realize the extraordinary properties of individual CNTs at macroscopic scales. Some of the more important questions are introduced below.

- What is the atomic mechanism of carbon addition at the catalyst, and how might this change depending on the reaction conditions? This can range from surface diffusion over solid catalysts at lower temperatures to bulk diffusion through liquid catalysts at higher temperatures. The former condition could be rigorously exploited to grow individual CNTs for electronic devices, whereas the latter condition could enable more rapid and extended growth of aligned CNTs for large-scale materials applications.

- What are the precise roles of hydrogen and oxygen in mediating growth of CNTs, and how can we best balance the accumulation of graphitic and amorphous carbon to maintain the activity of the growth catalyst? Can CNTs be grown to indefinite lengths by proper maintenance of the catalyst efficiency?

- What determines the chirality of a CNT and can chirality-selective processes be implemented? Alternatively, must we resort to sorting and separating multi-chiral ensembles of CNTs rather than growing CNTs of a desired chirality? In addition to chirality, what precisely determines the number of walls of a CNT, for example mediating selectivity among SWNTs, DWNTs, and MWNTs?

- Is there an ideal or primary precursor for CNT growth; in other words, which molecule is best suited for direct conversion into CNTs under a particular reaction condition?

- How do the mechanical, electrical, and thermal properties of CNTs relate to the type and density of defects in the walls? What are practical and scalable techniques for making low-resistance electrical and thermal contact to CNTs, so these properties can be measured and utilized?

- How can controlled doping of CNTs be practically realized to tune their electrical and surface properties? How can CNTs be mechanically, thermally, and electrically interconnected to one another to improve their properties as a bulk ensemble?

These challenges provide innumerable exciting opportunities for future research and development of commercial applications of CNTs and many other nanostructured materials. This research will continue at MIT through 2006 and at the University of Michigan starting in 2007, and will have the following initial thrusts.

- Further development of the heated platform apparatus for *in situ* monitoring and control of substrate-bound CNT growth, seeking to discover methods and reaction conditions for synthesis of macroscopic-length strands of high-quality CNTs.

- Creation of a machine for continuous industrial-scale production and application of large-area VA-CNT films, capable of re-dressing and/or regeneration of the growth catalyst and continuous transfer of the VA-CNT film to a secondary substrate.

- Further development of the microfluidic platform for combinatorial and high-throughput studies of CNT growth, along with modeling of the laminar flows and chemical gradients the microchannels, to verify observed reaction kinetics and fluid interactions with nanostructures.

- Characterization of the bulk mechanical, thermal, electrical, and interfacial transport properties of long CNTs in mm-thick CNT films, to reveal how these properties scale to macroscopic lengths and number densities. These measurements will be correlated to the structural quality and defect density of the CNTs, and associated analytical models.

- Creation of multifunctional composite materials using interlayers of aligned CNTs and CNTs grown directly on the surfaces of ceramic and carbon fibers, particularly for lightweight aerospace and wind turbine structures.

- Development of CNT-supported catalysts for energy conversion systems such as fuel cells, along with CNT-based devices to study the effects of electronic control on catalytic reactions.

A broad ultimate goal is to fabricate macroscopic CNT strands of arbitrary length, which would be the most fantastic mechanical material known; however, many of the challenges just mentioned must be overcome before this is, if ever, achieved. In the meantime, preliminary calculations show that feasible improvements to the efficiency of CNT growth from substrate-bound catalysts could make ordered CNT-based materials, such as strands of closely-wound mm-length aligned CNTs, available at a competitive price of $100/kg.

With this three-and-a-half years of hard and exciting work as a starting example, it is likely that many scientific advances and commercial applications can spring from further enthusiastic effort in this exciting area of research. As mechanical engineers, our ability to grasp multidisciplinary problems can push the forefront of nanoscience discoveries, while we simultaneously develop robust approaches for utilizing and integrating these discoveries in large-scale applications. This will also accelerate understanding of the physical properties of newly discovered materials and interactions, and catalyze our visions of yet further new materials and their applications, new characterization tools, and ground-breaking experimental techniques.

Bibliography

[1] A. J. Hart, A. H. Slocum, and L. Royer. Growth of conformal single-walled carbon nanotube films from Mo/Fe/Al_2O_3 deposited by electron beam evaporation. *Carbon*, 44(2):348–359, 2006.

[2] A. J. Hart, B. O. Boskovic, A. T. H. Chuang, V. B. Golovko, J. Robertson, B. F. G. Johnson, and A. H. Slocum. Uniform and selective CVD growth of carbon nanotubes and nanofibres on arbitrarily microstructured silicon surfaces. *Nanotechnology*, 17(5):1397–1403, 2006.

[3] A. J. Hart and A. H. Slocum. Flow-mediated nucleation and rapid growth of millimeter-scale aligned carbon nanotube structures from a thin-film catalyst. *Journal of Physical Chemistry B*, 110:8250–8257, 2006.

[4] A. J. Hart and A. H. Slocum. Force output, control of film structure, and microscale shape transfer by carbon nanotube growth under mechanical pressure. *Nano Letters*, 6(6):1254–1260, 2006.

[5] M. S. Dresselhaus and P. Avouris. Introduction to carbon materials research. In M. S. Dresselhaus, G. Dresselhaus, and P. Avouris, editors, *Carbon Nanotubes: Synthesis, Structure, Properties, and Applications*. Springer, Berlin, 2001.

[6] M. S. Dresselhaus, G. Dresselhaus, and P. Avouris, editors. *Carbon Nanotubes: Synthesis, Structure, Properties, and Applications*. Springer, Berlin.

[7] S.V. Rotkin and S. Subramoney, editors. *Applied Physics of Carbon Nanotubes*. Springer, New York, 2005.

[8] R. H. Baughman, A. A. Zakhidov, and W. A. de Heer. Carbon nanotubes - the route toward applications. *Science*, 297(5582):787–792, 2002.

[9] M. Endo, T. Hayashi, Y.A. Kim, M. Terrones, and M.S. Dresselhaus. Applications of carbon nanotubes in the twenty-first century. *Philosophical Transactions of the Royal Society*, 362(1823):2223–2238, 2004.

[10] M. Endo, T. Hayashi, Y. A. Kim, and H. Muramatsu. Development and application of carbon nanotubes. *Japanese Journal of Applied Physics*, 45(6A):4883–4892, 2006.

[11] B. W. Smith, M. Monthioux, and D. E. Luzzi. Encapsulated C_{60} in carbon nanotubes. *Nature*, 396(6709):323–324, 1998.

[12] M. S. Dresselhaus, Y. M. Lin, O. Rabin, A. Jorio, A. G. Souza, M. A. Pimenta, R. Saito, G. G. Samsonidze, and G. Dresselhaus. Nanowires and nanotubes. *Materials Science and Engineering C*, 23(1-2):129–140, 2003.

[13] S. Iijima. Helical microtubules of graphitic carbon. *Nature*, 354(6348):56–58, 1991.

[14] S. Iijima and T. Ichihashi. Single-shell carbon nanotubes of 1-nm diameter. *Nature*, 363(6430):603–605, 1993.

[15] T. V. Hughes and C. R. Chambers. Manufacture of carbon filaments, *U.S. Patent 405,480*, 1889.

[16] T. A. Edison. Electric lamp, *U.S. Patent 223,898*, 1880.

[17] T. A. Edison. Manufacture of filaments for incandescent electric lamps, *U.S. Patent 470,925*, 1892.

[18] W. R. Davis, R. J. Slawson, and G. R. Bigby. An unusual form of carbon. *Nature*, 171:756, 1953.

[19] H. F. Kaufmann, D. J. Griffiths, and J. S. Mackay. Process for making fibrous carbon, *U.S. Patent 2,796,331*, 1957.

[20] R. Bacon. Growth, structure, and properties of graphite whiskers. *Journal of Applied Physics*, 31:283–289, 1960.

[21] R. T. K. Baker, M. A. Barber, P. S. Harris, F. S. Feates, and R. J. Waite. Nucleation and growth of carbon deposits from the nickel catalyzed decomposition of acetylene. *Journal of Catalysis*, 26(1):51–62, 1972.

[22] R. T. K. Baker, P. S. Harris, R. B. Thomas, and R. J. Waite. Formation of filamentous carbon from iron, cobalt and chromium catalyzed decomposition of acetylene. *Journal of Catalysis*, 30(1):86–95, 1973.

[23] A. Oberlin, M. Endo, and T. Koyama. Filamentous growth of carbon through benzene decomposition. *Journal of Crystal Growth*, 32(3):335–349, 1976.

[24] J. Abrahamson, P.G. Wiles, and B.L. Rhoades. Structure of carbon fibers found on carbon arc anodes. In *14th Biennial Conference on Carbon*, pages 254–255, University Park, PA, 1979.

[25] H. W. Kroto, J. R. Heath, S. P. O'Brien, R. F. Curl, and R. E. Smalley. C_{60}: Buckminsterfullerene. *Nature*, 318:162–163, 1985.

[26] M. Endo. Grow carbon fibers in the vapor phase. *Chemtech*, 18:568–576, 1988.

[27] M. Endo. Large scale production of carbon nanotubes and their current application. In *Fifth International Conference on the Science and Application of Nanotubes*, San Luis Potosi, Mexico, 2004.

[28] E. T. Thostenson, C. Y. Li, and T. W. Chou. Nanocomposites in context. *Composites Science and Technology*, 65(3-4):491–516, 2005.

[29] J. N. Coleman, U. Khan, W. J. Blau, and Y. K. Gun'ko. Small but strong: A review of the mechanical properties of carbon nanotube-polymer composites. *Carbon*, 44(9):1624–1652, 2006.

[30] E. H. Hong, K. H. Lee, S. H. Oh, and C. G. Park. In-situ synthesis of carbon nanotubes on organic polymer substrates at atmospheric pressure. *Advanced Materials*, 14(9):676–679, 2002.

[31] B. J. Yoon, E. H. Hong, S. E. Jee, D. M. Yoon, D. S. Shim, G. Y. Son, Y. J. Lee, K. H. Lee, H. S. Kim, and C. G. Park. Fabrication of flexible carbon nanotube field emitter arrays by direct microwave irradiation on organic polymer substrate. *Journal of the American Chemical Society*, 127(23):8234–8235, 2005.

[32] K. S. Suslick. Sonochemistry. *Science*, 247(4949):1439–1445, 1990.

[33] S. H. Jeong, J. H. Ko, J. B. Park, and W. J. Park. A sonochemical route to single-walled carbon nanotubes under ambient conditions. *Journal of the American Chemical Society*, 126(49):15982–15983, 2004.

[34] A.K. Pal, R.K. Roy, S.K. Mandal, S. Gupta, and B. Deb. Electrodeposited carbon nanotube thin films. *Thin Solid Films*, 476(2):288–294, 2005.

[35] M.K. Beyer and H. Clausen-Schaumann. Mechanochemistry: The mechanical activation of covalent bonds. *Chemical Reviews*, 105(8):2921–2948, 2005.

[36] J. J. Gilman. Mechanochemistry. *Science*, 274(5284):65–65, 1996.

[37] M. K. Beyer. Coupling of mechanical and chemical energy: Proton affinity as a function of external force. *Angewandte Chemie-International Edition*, 42(40):4913–4915, 2003.

[38] D. Bensimon. Force: A new structural control parameter? *Structure*, 4(8):885–889, 1996.

[39] J. H. Shin, L. Mahadevan, and P. Matsudaira. Force generated by an actin spring. *Biophysical Journal*, 84(2):571A, 2003.

[40] E. L. Grishchuk, M. I. Molodtsov, F. I. Ataullakhanov, and J. R. McIntosh. Force production by disassembling microtubules. 438(7066):384–388, 2005.

[41] M. S. Dresselhaus and M. Endo. Relation of carbon nanotubes to other carbon materials. In M. S. Dresselhaus, G. Dresselhaus, and P. Avouris, editors, *Carbon Nanotubes: Synthesis, Structure, Properties, and Applications*. Springer, Berlin, 2001.

[42] High-performance structural fibers for advanced polymer matrix composites. Technical report, National Materials Advisory Board, National Academy of Sciences, 2005.

[43] G. G. Tibbetts. Why are carbon filaments tubular? *Journal of Crystal Growth*, 66(3):632–638, 1984.

[44] J. R. Bradley and G. G. Tibbetts. Improved yield of carbon fibers by pyrolysis of natural gas in stainless steel tubes. *Carbon*, 23(4):423–430, 1985.

[45] G. G. Tibbetts. Lengths of carbon fibers grown from iron catalyst particles in natural gas. *Journal of Crystal Growth*, 73(3):431–438, 1985.

[46] G. G. Tibbetts, M. G. Devour, and E. J. Rodda. An adsorption-diffusion isotherm and its application to the growth of carbon filaments on iron catalyst particles. *Carbon*, 25(3):367–375, 1987.

[47] G. G. Tibbetts and E. J. Rodda. A lengthening rate model for carbon filaments. In *Biennial Conference on Carbon*, pages 372–3. American Carbon Society, 1989.

[48] G. G. Tibbetts. Growing carbon fibers with a linearly increasing temperature sweep: Experiments and modeling. *Carbon*, 30(3):399–406, 1992.

[49] G. G. Tibbetts, C. A. Bernardo, D. W. Gorkiewicz, and R. L. Alig. Role of sulfur in the production of carbon-fibers in the vapor-phase. *Carbon*, 32(4):569–576, 1994.

[50] G. G. Tibbetts and M. P. Balogh. Increase in yield of carbon fibres grown above the iron/carbon eutectic. *Carbon*, 37(2):241–247, 1999.

[51] M. Endo, Y. A. Kim, T. Hayashi, Y. Fukai, K. Oshida, M. Terrones, T. Yanagisawa, S. Higaki, and M. S. Dresselhaus. Structural characterization of cup-stacked-type nanofibers with an entirely hollow core. *Applied Physics Letters*, 80(7):1267–1269, 2002.

[52] K. B. K. Teo, C. Singh, M. Chhowalla, and W. I. Milne. Catalytic synthesis of carbon nanotubes and nanofibers. In H. S. Nalwa, editor, *Encyclopedia of Nanoscience and Nanotechnology*. 2004.

[53] N. M. Rodriguez, A. Chambers, and R. T. K. Baker. Catalytic engineering of carbon nanostructures. *Langmuir*, 11(10):3862–3866, 1995.

[54] M. S. Dresselhaus, G. Dresselhaus, and R. Saito. Physics of carbon nanotubes. *Carbon*, 33(7):883–891, 1995.

[55] S. Reich, L. Li, and J. Robertson. Structure and formation energy of carbon nanotube caps. *Physical Review B*, 72(16), 2005.

[56] S. J. Tans, A. R. M. Verschueren, and C. Dekker. Room-temperature transistor based on a single carbon nanotube. *Nature*, 393(6680):49–52, 1998.

[57] A. Javey, J. Guo, Q. Wang, M. Lundstrom, and H. Dai. Ballistic carbon nanotube field-effect transistors. *Nature*, 424(6949):654–657, 2003.

[58] Z. Chen, J. Appenzeller, Y. M. Lin, J. Sippel-Oakley, A. G. Rinzler, J. Tang, S. J. Wind, P. M. Solomon, and P. Avouris. An integrated logic circuit assembled on a single carbon nanotube. *Science*, 311(5768):1735, 2006.

[59] B. Q. Wei, R. Vajtai, and P. M. Ajayan. Reliability and current carrying capacity of carbon nanotubes. *Applied Physics Letters*, 79(8):1172–1174, 2001.

[60] M. Nihei, A. Kawabata, D. Kondo, M. Horibe, S. Sato, and Y. Awano. Electrical properties of carbon nanotube bundles for future via interconnects. *Japanese Journal of Applied Physics*, 44(4A):1626–1628, 2005.

[61] M. Horibe, M. Nihei, D. Kondo, A. Kawabata, and Y. Awano. Carbon nanotube growth technologies using tantalum barrier layer for future ULSIs with Cu/low-k interconnect processes. *Japanese Journal of Applied Physics*, 44(7A):5309–5312, 2005.

[62] S. J. Wind, J. Appenzeller, and P. Avouris. Lateral scaling in carbon-nanotube field-effect transistors. *Physical Review Letters*, 91(5):058301, 2003.

[63] H. J. Li, W. G. Lu, J. J. Li, X. D. Bai, and C. Z. Gu. Multichannel ballistic transport in multiwall carbon nanotubes. *Physical Review Letters*, 95(8), 2005.

[64] H. T. Soh, C. F. Quate, A. F. Morpurgo, C. M. Marcus, J. Kong, and H. J. Dai. Integrated nanotube circuits: Controlled growth and ohmic contacting of single-walled carbon nanotubes. *Applied Physics Letters*, 75(5):627–629, 1999.

[65] N. Nemec, D. Tomanek, and G. Cuniberti. Contact dependence of carrier injection in carbon nanotubes: An ab initio study. *Physical Review Letters*, 96(7):076802, 2006.

[66] L. B. Zhu, Y. Y. Sun, D. W. Hess, and C. P. Wong. Well-aligned open-ended carbon nanotube architectures: An approach for device assembly. *Nano Letters*, 6(2):243–247, 2006.

[67] I. Takesue, J. Haruyama, N. Kobayashi, S. Chiashi, S. Maruyama, T. Sugai, and H. Shinohara. Superconductivity in entirely end-bonded multiwalled carbon nanotubes. *Physical Review Letters*, 96(5):057001, 2006.

[68] Y. W. Fan, B. R. Goldsmith, and P. G. Collins. Identifying and counting point defects in carbon nanotubes. *Nature Materials*, 4(12):906–911, 2005.

[69] J. Kong, N. R. Franklin, C. Zhou, M. G. Chapline, S. Peng, K. Cho, and H. Dai. Nanotube molecular wires as chemical sensors. *Science*, 287(5453):622–625, 2000.

[70] H. E. Romero, K. Bolton, A. Rosen, and P. C. Eklund. Atom collision-induced resistivity of carbon nanotubes. *Science*, 307(5706):89–93, 2005.

[71] P. G. Collins, K. Bradley, M. Ishigami, and A. Zettl. Extreme oxygen sensitivity of electronic properties of carbon nanotubes. *Science*, 287(5459):1801–1804, 2000.

[72] P. Poncharal, Z. L. Wang, D. Ugarte, and W. A. de Heer. Electrostatic deflections and electromechanical resonances of carbon nanotubes. *Science*, 283(5407):1513–1516, 1999.

[73] M. S. Dresselhaus, G. Dresselhaus, J. C. Charlier, and E. Hernandez. Electronic, thermal and mechanical properties of carbon nanotubes. *Philosophical Transactions of the Royal Society*, 362(1823):2065–2098, 2004.

[74] J. Gaillard, M. Skove, and A. M. Rao. Mechanical properties of chemical vapor deposition-grown multiwalled carbon nanotubes. *Applied Physics Letters*, 86(23):233109, 2005.

[75] A. Krishnan, E. Dujardin, T. W. Ebbesen, P. N. Yianilos, and M. M. J. Treacy. Young's modulus of single-walled nanotubes. *Physical Review B*, 58(20):14013–14019, 1998.

[76] A. H. Barber, R. Andrews, L. S. Schadler, and H. D. Wagner. On the tensile strength distribution of multiwalled carbon nanotubes. *Applied Physics Letters*, 87:203106–1–3, 2005.

[77] P. Kim, L. Shi, A. Majumdar, and P. L. McEuen. Thermal transport measurements of individual multiwalled nanotubes. *Physical Review Letters*, 8721(21), 2001.

[78] Y. L. Li, I. A. Kinloch, and A. H. Windle. Direct spinning of carbon nanotube fibers from chemical vapor deposition synthesis. *Science*, 304(5668):276–278, 2004.

[79] M. Motta, Y. L. Li, I. Kinloch, and A. Windle. Mechanical properties of continuously spun fibers of carbon nanotubes. *Nano Letters*, 5(8):1529–1533, 2005.

[80] M. Zhang, K. R. Atkinson, and R. H. Baughman. Multifunctional carbon nanotube yarns by downsizing an ancient technology. *Science*, 306(5700):1358–1361, 2004.

[81] A. B. Dalton, S. Collins, J. Razal, E. Munoz, V. H. Ebron, B. G. Kim, J. N. Coleman, J. P. Ferraris, and R. H. Baughman. Continuous carbon nanotube composite fibers: properties, potential applications, and problems. *Journal of Materials Chemistry*, 14(1):1–3, 2004.

[82] L. M. Ericson, H. Fan, H. Q. Peng, V. A. Davis, W. Zhou, J. Sulpizio, Y. Wang, R. Booker, J. Vavro, C. Guthy, A. N. G. Parra-Vasquez, M. J. Kim, S. Ramesh, R. K. Saini, C. Kittrell, G. Lavin, H. Schmidt, W. W. Adams, W. E. Billups, M. Pasquali, W. F. Hwang, R. H. Hauge, J. E. Fischer, and R. E. Smalley. Macroscopic, neat, single-walled carbon nanotube fibers. *Science*, 305(5689):1447–1450, 2004.

[83] MatWeb Material Property Data, `http://www.matweb.com`.

[84] M. F. Yu, O. Lourie, M. J. Dyer, K. Moloni, T. F. Kelly, and R. S. Ruoff. Strength and breaking mechanism of multiwalled carbon nanotubes under tensile load. *Science*, 287(5453):637–640, 2000.

[85] D. A. Walters, L. M. Ericson, M. J. Casavant, J. Liu, D. T. Colbert, K. A. Smith, and R. E. Smalley. Elastic strain of freely suspended single-wall carbon nanotube ropes. *Applied Physics Letters*, 74(25):3803–3805, 1999.

[86] J. Y. Huang, S. Chen, Z. Q. Wang, K. Kempa, Y. M. Wang, S. H. Jo, G. Chen, M. S. Dresselhaus, and Z. F. Ren. Superplastic carbon nanotubes. 439(7074):281, 2006.

[87] T. Dumitrica, M. Hua, and B. I. Yakobson. Symmetry-, time-, and temperature-dependent strength of carbon nanotubes. *Proceedings of the National Academy of Sciences*, 103(16):6105–6109, 2006.

[88] J. Hone. Phonons and thermal properties of carbon nanotubes. In M. S. Dresselhaus, G. Dresselhaus, and P. Avouris, editors, *Carbon Nanotubes: Synthesis, Structure, Properties, and Applications*. Springer, Berlin, 2001.

[89] E. Pop, D. Mann, Q. Wang, K. Goodson, and H. J. Dai. Thermal conductance of an individual single-wall carbon nanotube above room temperature. *Nano Letters*, 6(1):96–100, 2006.

[90] H. Y. Chiu, V. V. Deshpande, H. W. C. Postma, C. N. Lau, C. Miko, L. Forro, and M. Bockrath. Ballistic phonon thermal transport in multiwalled carbon nanotubes. *Physical Review Letters*, 95(22):226101, 2005.

[91] T. W. Tombler, C. W. Zhou, L. Alexseyev, J. Kong, H. J. Dai, L. Lei, C. S. Jayanthi, M. J. Tang, and S. Y. Wu. Reversible electromechanical characteristics of carbon nanotubes under local-probe manipulation. *Nature*, 405(6788):769–772, 2000.

[92] J. Cao, Q. Wang, and H. J. Dai. Electromechanical properties of metallic, quasimetallic, and semiconducting carbon nanotubes under stretching. *Physical Review Letters*, 90(15):157601, 2003.

[93] U. D. Venkateswaran, A. M. Rao, E. Richter, M. Menon, A. Rinzler, R. E. Smalley, and P. C. Eklund. Probing the single-wall carbon nanotube bundle: Raman scattering under high pressure. *Physical Review B*, 59(16):10928–10934, 1999.

[94] S. B. Cronin, A. K. Swan, M. S. Unlu, B. B. Goldberg, M. S. Dresselhaus, and M. Tinkham. Resonant Raman spectroscopy of individual metallic and semiconducting single-wall carbon nanotubes under uniaxial strain. *Physical Review B*, 72(3):035425, 2005.

[95] J. Cumings and A. Zettl. Low-friction nanoscale linear bearing realized from multiwall carbon nanotubes. *Science*, 289(5479):602–604, 2000.

[96] A. M. Fennimore, T. D. Yuzvinsky, W. Q. Han, M. S. Fuhrer, J. Cumings, and A. Zettl. Rotational actuators based on carbon nanotubes. *Nature*, 424(6947):408–410, 2003.

[97] J. C. Meyer, M. Paillet, and S. Roth. Single-molecule torsional pendulum. *Science*, 309(5740):1539–1541, 2005.

[98] K. Jensen, C. Girit, W. Mickelson, and A. Zettl. Tunable nanoresonators constructed from telescoping nanotubes. *Physical Review Letters*, 96(21):215503, 2006.

[99] C. Stampfer, T. Helbling, D. Obergfell, B. Schoberle, M. K. Tripp, A. Jungen, S. Roth, V. M. Bright, and C. Hierold. Fabrication of single-walled carbon-nanotube-based pressure sensors. *Nano Letters*, 6(2):233–237, 2006.

[100] T. Rueckes, K. Kim, E. Joselevich, G. Y. Tseng, C. L. Cheung, and C. M. Lieber. Carbon nanotube-based nonvolatile random access memory for molecular computing. *Science*, 289(5476):94–97, 2000.

[101] Nantero NRAM^{TM}, `http://www.nantero.com/nram.html`.

[102] Brittanica guide to the Nobel Prizes: Hermann Staudinger, http://www.britannica.com/nobel/micro/564_55.html.

[103] B. Crist. The ultimate strength and stiffness of polymers. *Annual Review of Materials Science*, pages 295–323, 1995.

[104] Y. Wang, L.M. Ericson, C. Kittrell, M.J. Kim, H. Shan, H. Fan, S. Ripley, S. Ramesh, R.H. Hauge, W.W. Adams, M. Pasquali, and R.E. Smalley. Revealing the substructure of single-walled carbon nanotube fibers. *Chemistry of Materials*, 2005.

[105] Yijun Li, Kunlin Wang, Jinquan Wei, Zhiyi Gu, Zhicheng Wang, Jianbin Luo, and Dehai Wu. Tensile properties of long aligned double-walled carbon nanotube strands. *Carbon*, 43(1):31–35, 2005.

[106] J. K. W. Sandler, J. E. Kirk, I. A. Kinloch, M. S. P. Shaffer, and A. H. Windle. Ultra-low electrical percolation threshold in carbon-nanotube-epoxy composites. *Polymer*, 44(19):5893–5899, 2003.

[107] Y. B. Yi, L. Berhan, and A. M. Sastry. Statistical geometry of random fibrous networks, revisited: Waviness, dimensionality, and percolation. *Journal of Applied Physics*, 96(3):1318–1327, 2004.

[108] F. M. Du, J. E. Fischer, and K. I. Winey. Effect of nanotube alignment on percolation conductivity in carbon nanotube/polymer composites. *Physical Review B*, 72(12), 2005.

[109] S. I. Cha, K. T. Kim, S. N. Arshad, C. B. Mo, and S. H. Hong. Extraordinary strengthening effect of carbon nanotubes in metal-matrix nanocomposites processed by molecular-level mixing. *Advanced Materials*, 17(11):1377–1381, 2005.

[110] D. Blond, V. Barron, M. Ruether, K. P. Ryan, V. Nicolosi, W. J. Blau, and J. N. Coleman. Enhancement of modulus, strength, and toughness in poly(methyl methacrylate)-based composites by the incorporation of poly(methyl methacrylate)-functionalized nanotubes. *Advanced Functional Materials*, 16(12):1608–1614, 2006.

[111] H. D. Wagner. Nanotube-polymer adhesion: a mechanics approach. *Chemical Physics Letters*, 361(1-2):57–61, 2002.

[112] C. A. Cooper, S. R. Cohen, A. H. Barber, and H. D. Wagner. Detachment of nanotubes from a polymer matrix. *Applied Physics Letters*, 81(20):3873–3875, 2002.

[113] A. H. Barber, S. R. Cohen, and H. D. Wagner. Measurement of carbon nanotube-polymer interfacial strength. *Applied Physics Letters*, 82(23):4140–4142, 2003.

[114] J. N. Coleman, W. J. Blau, A. B. Dalton, E. Munoz, S. Collins, B. G. Kim, J. Razal, M. Selvidge, G. Vieiro, and R. H. Baughman. Improving the mechanical properties of single-walled carbon nanotube sheets by intercalation of polymeric adhesives. *Applied Physics Letters*, 82(11):1682–1684, 2003.

[115] J. N. Coleman, M. Cadek, R. Blake, V. Nicolosi, K. P. Ryan, C. Belton, A. Fonseca, J. B. Nagy, Y. K. Gun'ko, and W. J. Blau. High-performance nanotube-reinforced plastics: Understanding the mechanism of strength increase. *Advanced Functional Materials*, 14(8):791–798, 2004.

[116] M. J. Yang, V. Koutsos, and M. Zaiser. Interactions between polymers and carbon nanotubes: A molecular dynamics study. *Journal of Physical Chemistry B*, 109(20):10009–10014, 2005.

[117] H. Dai. Nanotube growth and characterization. In M. S. Dresselhaus, G. Dresselhaus, and P. Avouris, editors, *Carbon Nanotubes: Synthesis, Structure, Properties, and Applications*. Springer, Berlin, 2001.

[118] M. L. Terranova, V. Sessa, and M. Rossi. The world of carbon nanotubes: An overview of CVD growth methodologies. *Chemical Vapor Deposition*, 12(6):315–325, 2006.

[119] W. Kratschmer, Lowell D. Lamb, K. Fostiropoulos, and Donald R. Huffman. Solid C_{60}: a new form of carbon. 347(6291):354–358, 1990.

[120] J. B. Howard, J. T. Mckinnon, Y. Makarovsky, A. L. Lafleur, and M. E. Johnson. Fullerenes C_{60} and C_{70} in flames. *Nature*, 352(6331):139–141, 1991.

[121] A. Goel, P. Hebgen, J. B. Vander Sande, and J. B. Howard. Combustion synthesis of fullerenes and fullerenic nanostructures. *Carbon*, 40(2):177–182, 2002.

[122] M. J. Height, J. B. Howard, J. W. Tester, and J. B. V. Sande. Flame synthesis of single-walled carbon nanotubes. *Carbon*, 42(11):2295–2307, 2004.

[123] M. J. Height, J. B. Howard, J. W. Tester, and J. B. V. Sande. Carbon nanotube formation and growth via particle-particle interaction. *Journal of Physical Chemistry B*, 109(25):12337–12346, 2005.

[124] A. Evelyn, S. Mannick, and P. A. Sermon. Unusual carbon-based nanofibers and chains among diesel-emitted particles. *Nano Letters*, 3(1):63–64, 2003.

[125] A. Thess, R. Lee, P. Nikolaev, H. J. Dai, P. Petit, J. Robert, C. H. Xu, Y. H. Lee, S. G. Kim, A. G. Rinzler, D. T. Colbert, G. E. Scuseria, D. Tomanek, J. E. Fischer, and R. E. Smalley. Crystalline ropes of metallic carbon nanotubes. *Science*, 273(5274):483–487, 1996.

[126] D. M. Yoon, B. J. Yoon, K. H. Lee, H. S. Kim, and C. G. Park. Synthesis of carbon nanotubes from solid carbon sources by direct microwave irradiation. *Carbon*, 44(7):1339–1343, 2006.

[127] E. G. Gamaly and T. W. Ebbesen. Mechanism of carbon nanotube formation in the arc-discharge. *Physical Review B*, 52(3):2083–2089, 1995.

[128] H. W. Zhu, X. S. Li, B. Jiang, C. L. Xu, Y. F. Zhu, D. H. Wu, and X. H. Chen. Formation of carbon nanotubes in water by the electric-arc technique. *Chemical Physics Letters*, 366(5-6):664–669, 2002.

[129] A. A. Puretzky, H. Schittenhelm, X. D. Fan, M. J. Lance, L. F. Allard, and D. B. Geohegan. Investigations of single-wall carbon nanotube growth by time-restricted laser vaporization. *Physical Review B*, 65(24):245425, 2002.

[130] M. H. Rummeli, E. Borowiak-Palen, T. Gemming, T. Pichler, M. Knupfer, M. Kalbac, L. Dunsch, O. Jost, S. R. P. Silva, W. Pompe, and B. Buchner. Novel catalysts, room temperature, and the importance of oxygen for the synthesis of single-walled carbon nanotubes. *Nano Letters*, 5(7):1209–1215, 2005.

[131] J. Hahn, J. H. Han, J. E. Yoo, H. Y. Jung, and J. S. Suh. New continuous gas-phase synthesis of high purity carbon nanotubes by a thermal plasma jet. *Carbon*, 42(4):877–883, 2004.

[132] J. Hahn, S. B. Heo, and J. S. Suh. Catalyst free synthesis of high-purity carbon nanotubes by thermal plasma jet. *Carbon*, 43(12):2638–2641, 2005.

[133] R.S. Wagner and W.C. Ellis. The vapor-liquid-solid mechanism of crystal growth and its application to silicon. *Transactions of the Metallurgical Society of AIME*, 223:1053–1064, 1965.

[134] J. W. Snoeck, G. F. Froment, and M. Fowles. Filamentous carbon formation and gasification: Thermodynamics, driving force, nucleation, and steady-state growth. *Journal of Catalysis*, 169(1):240–249, 1997.

[135] F. Ding, A. Rosen, and K. Bolton. Dependence of SWNT growth mechanism on temperature and catalyst particle size: Bulk versus surface diffusion. *Carbon*, 43(10):2215–2217, 2005.

[136] S. Hofmann, G. Csanyi, A. C. Ferrari, M. C. Payne, and J. Robertson. Surface diffusion: The low activation energy path for nanotube growth. *Physical Review Letters*, 95(3), 2005.

[137] Y. Y. Wu and P. D. Yang. Direct observation of vapor-liquid-solid nanowire growth. *Journal of the American Chemical Society*, 123(13):3165–3166, 2001.

[138] Y. Cui, L. J. Lauhon, M. S. Gudiksen, J. F. Wang, and C. M. Lieber. Diameter-controlled synthesis of single-crystal silicon nanowires. *Applied Physics Letters*, 78(15):2214–2216, 2001.

[139] S. Kodambaka, J. Tersoff, M. C. Reuter, and F. M. Ross. Diameter-independent kinetics in the vapor-liquid-solid growth of si nanowires. *Physical Review Letters*, 96(9):096105, 2006.

[140] T. Hayashi, Y. A. Kim, T. Matoba, M. Esaka, K. Nishimura, T. Tsukada, M. Endo, and M. S. Dresselhaus. Smallest freestanding single-walled carbon nanotube. *Nano Letters*, 3(7):887–889, 2003.

[141] S. M. Huang, X. Y. Cai, and J. Liu. Growth of millimeter-long and horizontally aligned single-walled carbon nanotubes on flat substrates. *Journal of the American Chemical Society*, 125(19):5636–5637, 2003.

[142] L. X. Zheng, M. J. O'Connell, S. K. Doorn, X. Z. Liao, Y. H. Zhao, E. A. Akhadov, M. A. Hoffbauer, B. J. Roop, Q. X. Jia, R. C. Dye, D. E. Peterson, S. M. Huang, J. Liu, and Y. T. Zhu. Ultralong single-wall carbon nanotubes. *Nature Materials*, 3:673–676, 2004.

[143] M. Terrones, N. Grobert, J. Olivares, J. P. Zhang, H. Terrones, K. Kordatos, W. K. Hsu, J. P. Hare, P. D. Townsend, K. Prassides, A. K. Cheetham, H. W. Kroto, and D. R. M. Walton. Controlled production of aligned-nanotube bundles. *Nature*, 388(6637):52–55, 1997.

[144] S. S. Fan, M. G. Chapline, N. R. Franklin, T. W. Tombler, A. M. Cassell, and H. J. Dai. Self-oriented regular arrays of carbon nanotubes and their field emission properties. *Science*, 283(5401):512–514, 1999.

[145] V. I. Merkulov, A. V. Melechko, M. A. Guillorn, D. H. Lowndes, and M. L. Simpson. Alignment mechanism of carbon nanofibers produced by plasma-enhanced chemical-vapor deposition. *Applied Physics Letters*, 79(18):2970–2972, 2001.

[146] A. V. Melechko, V. I. Merkulov, D. H. Lowndes, M. A. Guillorn, and M. L. Simpson. Transition between 'base' and 'tip' carbon nanofiber growth modes. *Chemical Physics Letters*, 356(5-6):527–533, 2002.

[147] R. T. K. Baker, G. R. Gadsby, R. B. Thomas, and R. J. Waite. The production and properties of filamentous carbon. *Carbon*, 13(3):211–214, 1975.

[148] G. A. Jablonski, F. W. Geurts, A. Sacco, and R. R. Biederman. Carbon deposition over Fe, Ni, and Co foils from CO-H_2-CH_4-CO_2-H_2O, C-CO_2, CH_4-H_2, and CO-H_2-H_2O gas mixtures: Morphology. *Carbon*, 30(1):87–98, 1992.

[149] C. P. Deck and K. S. Vecchio. Prediction of carbon nanotube growth success by the analysis of carbon-catalyst binary phase diagrams. *Carbon*, 44(2):267–275, 2006.

[150] W. Q. Deng, X. Xu, and W. A. Goddard. A two-stage mechanism of bimetallic catalyzed growth of single-walled carbon nanotubes. *Nano Letters*, 4(12):2331–2335, 2004.

[151] B. Q. Wei, R. Vajtai, Y. Jung, J. Ward, R. Zhang, G. Ramanath, and P. M. Ajayan. Assembly of highly organized carbon nanotube architectures by chemical vapor deposition. *Chemistry of Materials*, 15(8):1598–1606, 2003.

[152] M. Glerup, H. Kanzow, R. Almairac, M. Castignolles, and P. Bernier. Synthesis of multi-walled carbon nanotubes and nano-fibres using the aerosol method with metal-ions as the catalyst precursors. *Chemical Physics Letters*, 377(3-4):293–298, 2003.

[153] A. G. Nasibulin, A. Moisala, D. P. Brown, H. Jiang, and E. I. Kauppinen. A novel aerosol method for single walled carbon nanotube synthesis. *Chemical Physics Letters*, 402(1-3):227–232, 2005.

[154] C. L. Cheung, A. Kurtz, H. Park, and C. M. Lieber. Diameter-controlled synthesis of carbon nanotubes. *Journal of Physical Chemistry B*, 106(10):2429–2433, 2002.

[155] F. Larouche, O. Smiljanic, X. L. Sun, and B. L. Stansfield. Solutal bernard-marangoni instability as a growth mechanism for single-walled carbon nanotubes. *Carbon*, 43(5):986–993, 2005.

[156] R. L. Vander Wal and L. J. Hall. Carbon nanotube synthesis upon stainless steel meshes. *Carbon*, 41(4):659–672, 2003.

[157] A. Kukovecz, D. Mehn, E. Nemes-Nagy, R. Szabo, and I. Kiricsi. Optimization of CCVD synthesis conditions for single-wall carbon nanotubes by statistical design of experiments (DoE). *Carbon*, 43(14):2842–2849, 2005.

[158] G. A. Jablonski, F. W. A. H. Geurts, and A. Sacco. Carbon deposition over Fe, Ni, and Co foils from CO-H_2-CH_4-CO_2-H_2O, C-CO_2, CH_4-H_2, and CO-H_2-H_2O gas mixtures: Kinetics. *Carbon*, 30(1):99–106, 1992.

[159] O. A. Louchev, T. Laude, Y. Sato, and H. Kanda. Diffusion-controlled kinetics of carbon nanotube forest growth by chemical vapor deposition. *Journal of Chemical Physics*, 118(16):7622–7634, 2003.

[160] A. A. Puretzky, D. B. Geohegan, S. Jesse, I. N. Ivanov, and G. Eres. In situ measurements and modeling of carbon nanotube array growth kinetics during chemical vapor deposition. *Applied Physics A*, 81(2):223–240, 2005.

[161] K. Liu, K. Jiang, C. Feng, Z. Chen, and S. Fan. A growth mark method for studying growth mechanism of carbon nanotube arrays. *Carbon*, 43(14):2850–2856, 2005.

[162] D. N. Futaba, K. Hata, T. Yamada, K. Mizuno, M. Yumura, and S. Iijima. Kinetics of water-assisted single-walled carbon nanotube growth revealed by a time-evolution analysis. *Physical Review Letters*, 95:056104, 2005.

[163] R. T. K. Baker, J. R. Alonzo, J. A. Dumesic, and D. J. C. Yates. Effect of the surface state of iron on filamentous carbon formation. *Journal of Catalysis*, 77(1):74–84, 1982.

[164] K. Nishimura, N. Okazaki, L. J. Pan, and Y. Nakayama. In situ study of iron catalysts for carbon nanotube growth using X-ray diffraction analysis. *Japanese Journal of Applied Physics*, 43(4A):L471–L474, 2004.

[165] H. J. Dai, A. G. Rinzler, P. Nikolaev, A. Thess, D. T. Colbert, and R. E. Smalley. Single-wall nanotubes produced by metal-catalyzed disproportionation of carbon monoxide. *Chemical Physics Letters*, 260(3-4):471–475, 1996.

[166] D. E. Resasco, W. E. Alvarez, F. Pompeo, L. Balzano, J. E. Herrera, B. Kitiyanan, and A. Borgna. A scalable process for production of single-walled carbon nanotubes (SWNTs) by catalytic disproportionation of CO on a solid catalyst. *Journal of Nanoparticle Research*, 4(1-2):131–136, 2002.

[167] A. Moisala, A. G. Nasibulin, and E. I. Kauppinen. The role of metal nanoparticles in the catalytic production of single-walled carbon nanotubes - a review. *Journal of Physics: Condensed Matter*, 15(42):S3011–S3035, 2003.

[168] A. R. Harutyunyan, T. Tokune, and E. Mora. Liquefaction of catalyst during carbon single-walled nanotube growth. *Applied Physics Letters*, 86(15):153113, 2005.

[169] A. R. Harutyunyan, T. Tokune, and E. Mora. Liquid as a required catalyst phase for carbon single-walled nanotube growth. *Applied Physics Letters*, 87(5):–, 2005. 051919.

[170] S. Iijima and T. Ichihashi. Structural instability of ultrafine particles of metals. *Physical Review Letters*, 56(6):616–619, 1986.

[171] R. Sharma, P. Rez, Michael M. J. Treacy, and S. J. Stuart. In situ observation of the growth mechanisms of carbon nanotubes under diverse reaction conditions. *Journal of Electron Microscopy*, 54(3):231–237, 2005.

[172] M. Lin, J. P. YingTan, C. Boothroyd, K. P. Loh, E. S. Tok, and Y. L. Foo. Direct observation of single-walled carbon nanotube growth at the atomistic scale. *Nano Letters*, 6(3):449–452, 2006.

[173] S. Helveg, C. Lopez-Cartes, J. Sehested, P. L. Hansen, B. S. Clausen, J. R. Rostrup-Nielsen, F. Abild-Pedersen, and J. K. Norskov. Atomic-scale imaging of carbon nanofibre growth. *Nature*, 427(6973):426–429, 2004.

[174] H. Zhu, K. Suenaga, A. Hashimoto, K. Urita, K. Hata, and S. Iijima. Atomic-resolution imaging of the nucleation points of single-walled carbon nanotubes. *Small*, 1(12):1180–1183, 2005.

[175] F. Ding, K. Bolton, and A. Rosen. Nucleation and growth of single-walled carbon nanotubes: A molecular dynamics study. *Journal of Physical Chemistry B*, 108(45):17369–17377, 2004.

[176] J. Y. Raty, F. Gygi, and G. Galli. Growth of carbon nanotubes on metal nanoparticles: a microscopic mechanism from *ab initio* molecular dynamics simulations. *Physical Review Letters*, 95:096103, 2005.

[177] R. Seidel, G. S. Duesberg, E. Unger, A. P. Graham, M. Liebau, and F. Kreupl. Chemical vapor deposition growth of single-walled carbon nanotubes at 600 °C and a simple growth model. *Journal of Physical Chemistry B*, 108(6):1888–1893, 2004.

[178] S. M. Bachilo, L. Balzano, J. E. Herrera, F. Pompeo, D. E. Resasco, and R. B. Weisman. Narrow (n,m)-distribution of single-walled carbon nanotubes grown using a solid supported catalyst. *Journal of the American Chemical Society*, 125(37):11186–11187, 2003.

[179] G. Lolli, L. A. Zhang, L. Balzano, N. Sakulchaicharoen, Y. Q. Tan, and D. E. Resasco. Tailoring (n,m) structure of single-walled carbon nanotubes by modifying reaction conditions and the nature of the support of CoMo catalysts. *Journal of Physical Chemistry B*, 110(5):2108–2115, 2006.

[180] Y. H. Miyauchi, S. H. Chiashi, Y. Murakami, Y. Hayashida, and S. Maruyama. Fluorescence spectroscopy of single-walled carbon nanotubes synthesized from alcohol. *Chemical Physics Letters*, 387(1-3):198–203, 2004.

[181] K. Koziol, M. Shaffer, and A. Windle. Three-dimensional internal order in multiwalled carbon nanotubes grown by chemical vapor deposition. *Advanced Materials*, 17:760–763, 2005.

[182] C. Ducati, K. Koziol, S. Friedrichs, T. J. V. Yates, M. S. Shaffer, P. A. Midgley, and A. H. Windle. Crystallographic order in multi-walled carbon nanotubes synthesized in the presence of nitrogen. *Small*, 2(6):774–784, 2006.

[183] J. F. Colomer, L. Henrard, P. Launois, G. Van Tendeloo, A. A. Lucas, and P. Lambin. Bundles of identical double-walled carbon nanotubes. *Chemical Communications*, (22):2592–2593, 2004.

[184] N. R. Franklin and H. J. Dai. An enhanced CVD approach to extensive nanotube networks with directionality. *Advanced Materials*, 12(12):890–894, 2000.

[185] H. J. Jeong, S. Y. Jeong, Y. M. Shin, J. H. Han, S. C. Lim, S. J. Eum, C. W. Yang, N. G. Kim, C. Y. Park, and Y. H. Lee. Dual-catalyst growth of vertically aligned carbon nanotubes at low temperature in thermal chemical vapor deposition. *Chemical Physics Letters*, 361(3-4):189–195, 2002.

[186] M. Endo, H. Muramatsu, T. Hayashi, Y. A. Kim, M. Terrones, and M.S. Dresselhaus. 'Buckypaper' from coaxial nanotubes. *Nature*, 433:476, 2005.

[187] H. Muramatsu, T. Hayashi, Y. A. Kim, M. Endo, M. Terrones, and M. S. Dresselhaus. Growth of double-walled carbon nanotubes using a conditioning catalyst. *Journal of Nanoscience and Nanotechnology*, 5(3):404–408, 2005.

[188] R. Brukh and S. Mitra. Mechanism of carbon nanotube growth by CVD. *Chemical Physics Letters*, 424(1-3):126–132, 2006.

[189] Y. A. Kim, H. Muramatsu, T. Hayashi, M. Endo, M. Terrones, and M. S. Dresselhaus. Fabrication of high-purity, double-walled carbon nanotube buckypaper. *Chemical Vapor Deposition*, 12(6):327–330, 2006.

[190] G. D. Towell and J. J. Martin. Kinetic data from nonisothermal experiments: Thermal decomposition of ethane, ethylene, and acetylene. *AIChE Journal*, 7(4):693–698, 1961.

[191] G. Eres, A. A. Kinkhabwala, H. Cui, D. B. Geohegan, A. A. Puretkzy, and D. H. Lowndes. Molecular beam-controlled nucleation and growth of vertically-aligned single-wall carbon nanotube arrays. *Journal of Physical Chemistry B*, 109:16684–16694, 2005.

[192] A. I. La Cava, C. A. Bernardo, and D. L. Trimm. Studies of deactivation of metals by carbon deposition. *Carbon*, 20(3):219–223, 1982.

[193] J. W. Ward, B. Q. Wei, and P. M. Ajayan. Substrate effects on the growth of carbon nanotubes by thermal decomposition of methane. *Chemical Physics Letters*, 376(5-6):717–725, 2003.

[194] Y. J. Tian, Z. Hu, Y. Yang, X. Chen, W. J. Ji, and Y. Chen. Thermal analysis-mass spectroscopy coupling as a powerful technique to study the growth of carbon nanotubes from benzene. *Chemical Physics Letters*, 388(4-6):259–262, 2004.

[195] Y. J. Tian, Z. Hu, Y. Yang, X. Z. Wang, X. Chen, H. Xu, Q. Wu, W. J. Ji, and Y. Chen. *In situ* TA-MS study of the six-membered-ring-based growth of carbon nanotubes with benzene precursor. *Journal of the American Chemical Society*, 126(4):1180–1183, 2004.

[196] W. E. Alvarez, B. Kitiyanan, A. Borgna, and D. E. Resasco. Synergism of Co and Mo in the catalytic production of single-wall carbon nanotubes by decomposition of CO. *Carbon*, 39(4):547–558, 2001.

[197] L. Zhu, D.W. Hess, and C.-P. Wong. Monitoring carbon nanotube growth by formation of nanotube stacks and investigation of the diffusion-controlled kinetics. *Journal of Physical Chemistry B*, 110(11):5445–5449, 2006.

[198] R. D. Bennett, A. J. Hart, and R. E. Cohen. Controlling the morphology of carbon nanotube films by varying the areal density of catalyst nanoparticles using block copolymer micellar thin films. *Advanced Materials*, 18:2274–2279, 2006.

[199] D. N. Futaba, K. Hata, T. Namai, T. Yamada, K. Mizuno, Y. Hayamizu, M. Yumura, and S. Iijima. 84% catalyst activity of water-assisted growth of single walled carbon nanotube forest characterization by a statistical and macroscopic approach. *Journal of Physical Chemistry B*, 110(15):8035–8038, 2006.

[200] I. Chorkendorff and J. W. Niemantsverdriet. *Concepts of Modern Catalysis and Kinetics*. Wiley-VCH, Weinheim, Germany, 2003.

[201] Y. Nishiyama and Y. Tamai. Effect of hydrogen on carbon deposition catalyzed by copper-nickel alloys. *Journal of Catalysis*, 45(1):1–5, 1976.

[202] N. Yoshida, N. Matsumoto, and S. Kishimoto. Role of hydrogen in catalytic decomposition of ethylene on nickel. *Journal of Catalysis*, 92(1):177–179, 1985.

[203] G. Zhang, D. Mann, L. Zhang, A. Javey, Y. Li, E. Yenilmez, Q. Wang, J. P. McVittie, Y. Nishi, J. Gibbons, and H. Dai. Ultra-high-yield growth of vertical single-walled carbon nanotubes: Hidden roles of hydrogen and oxygen. *Proceedings of the National Academy of Sciences*, 102(45):16141–16145, 2005.

[204] Y. Murakami, S. Chiashi, Y. Miyauchi, M. H. Hu, M. Ogura, T. Okubo, and S. Maruyama. Growth of vertically aligned single-walled carbon nanotube films on quartz substrates and their optical anisotropy. *Chemical Physics Letters*, 385(3-4):298–303, 2004.

[205] K. Hata, D. N. Futaba, K. Mizuno, T. Namai, M. Yumura, and S. Iijima. Water-assisted highly efficient synthesis of impurity-free single-walled carbon nanotubes. *Science*, 306(5700):1362–1364, 2004.

[206] M. Cantoro, S. Hofmann, S. Pisana, V. Scardaci, A. Parvez, C. Ducati, A.C. Ferrari, A.M. Blackburn, K.-Y. Wang, and J. Robertson. Catalytic chemical vapor deposition of single-wall carbon nanotubes at low temperatures. *Nano Letters*, 6(6):1107–1112, 2006.

[207] H. M. Cheng, F. Li, G. Su, H. Y. Pan, L. L. He, X. Sun, and M. S. Dresselhaus. Large-scale and low-cost synthesis of single-walled carbon nanotubes by the catalytic pyrolysis of hydrocarbons. *Applied Physics Letters*, 72(25):3282–3284, 1998.

[208] H. W. Zhu, C. L. Xu, D. H. Wu, B. Q. Wei, R. Vajtai, and P. M. Ajayan. Direct synthesis of long single-walled carbon nanotube strands. *Science*, 296(5569):884–886, 2002.

[209] M. S. Motta, A. M. Moisala, I. A. Kinloch, and A. H. Windle. Role of sulphur on the production of carbon nanotubes by chemical vapour deposition. In *Seventh International Conference on the Science and Application of Nanotubes*, page 95, Nagano, Japan, 2006.

[210] A. G. Nasibulin, D. P. Brown, P. Queipo, D. Gonzalez, H. Jiang, and E. I. Kauppinen. An essential role of CO_2 and H_2O during single-walled CNT synthesis from carbon monoxide. *Chemical Physics Letters*, 417(1-3):179–184, 2006.

[211] N. R. Franklin, Y. M. Li, R. J. Chen, A. Javey, and H. J. Dai. Patterned growth of single-walled carbon nanotubes on full 4-inch wafers. *Applied Physics Letters*, 79(27):4571–4573, 2001.

[212] D. Takagi, Y. Homma, and Y. Kobayashi. Selective growth of individual single-walled carbon nanotubes suspended between pillar structures. *Physica E-Low-Dimensional Systems & Nanostructures*, 24(1-2):1–5, 2004.

[213] Y. Homma, D. Takagi, and Y. Kobayashi. Suspended architecture formation process of single-walled carbon nanotubes. *Applied Physics Letters*, 88(2):023115, 2006.

[214] S. M. Huang, M. Woodson, R. Smalley, and J. Liu. Growth mechanism of oriented long single walled carbon nanotubes using "fast-heating" chemical vapor deposition process. *Nano Letters*, 4(6):1025–1028, 2004.

[215] L. Huang, B. White, M.Y. Sfeir, M. Huang, H.X. Huang, S. Wind, J. Hone, and S. O'Brien. Cobalt ultrathin film catalyzed ethanol chemical vapor deposition of single-walled carbon nanotubes. *Journal of Physical Chemistry B*, 110(23):11103–11109, 2006.

[216] Iuliana Radu, Yael Hanein, and David H. Cobden. Oriented growth of single-wall carbon nanotubes using alumina patterns. *Nanotechnology*, (5):473–476, 2004.

[217] C. Kocabas, S. H. Hur, A. Gaur, M. A. Meitl, M. Shim, and J. A. Rogers. Guided growth of large-scale, horizontally aligned arrays of single-walled carbon nanotubes and their use in thin-film transistors. *Small*, 1(11):1110–1116, 2005.

[218] Ariel Ismach, Lior Segev, Ellen Wachtel, and Ernesto Joselevich. Atomic-step-templated formation of single wall carbon nanotube patterns. *Angewandte Chemie - International Edition*, 43(45):6140–6143, 2004.

[219] Y. G. Zhang, A. L. Chang, J. Cao, Q. Wang, W. Kim, Y. M. Li, N. Morris, E. Yenilmez, J. Kong, and H. J. Dai. Electric-field-directed growth of aligned single-walled carbon nanotubes. *Applied Physics Letters*, 79(19):3155–3157, 2001.

[220] X. Q. Chen, T. Saito, H. Yamada, and K. Matsushige. Aligning single-wall carbon nanotubes with an alternating-current electric field. *Applied Physics Letters*, 78(23):3714–3716, 2001.

[221] M. Chhowalla, K. B. K. Teo, C. Ducati, N. L. Rupesinghe, G. A. J. Amaratunga, A. C. Ferrari, D. Roy, J. Robertson, and W. I. Milne. Growth process conditions of vertically aligned carbon nanotubes using plasma enhanced chemical vapor deposition. *Journal of Applied Physics*, 90(10):5308–5317, 2001.

[222] T. Kato, G. H. Jeong, T. Hirata, R. Hatakeyama, and K. Tohji. Freestanding individual single-walled carbon nanotube synthesis based on plasma sheath effects. *Japanese Journal of Applied Physics*, 43(10A):L1278–L1280, 2004.

[223] C. M. Yeh, M. Y. Chen, J. S. Syu, J.-Y. Gan, and J. Hwang. Effect of gravity on the growth of vertical single-walled carbon nanotubes in a chemical vapor deposition process. *Applied Physics Letters*, 89:033117, 2006.

[224] G. W. Wang, Y. P. Zhao, and G. T. Yang. The stability of a vertical single-walled carbon nanotube under its own weight. *Materials & Design*, 25(6):453–457, 2004.

[225] W. C. Hu, D. W. Gong, Z. Chen, L. M. Yuan, K. Saito, C. A. Grimes, and P. Kichambare. Growth of well-aligned carbon nanotube arrays on silicon substrates using porous alumina film as a nanotemplate. *Applied Physics Letters*, 79(19):3083–3085, 2001.

[226] R. Krishnan, H. Q. Nguyen, C. V. Thompson, W. K. Choi, and Y. L. Foo. Wafer-level ordered arrays of aligned carbon nanotubes with controlled size and spacing on silicon. *Nanotechnology*, 16(6):841–845, 2005.

[227] G. W. Meng, Y. J. Jung, A. Y. Cao, R. Vajtai, and P. M. Ajayan. Controlled fabrication of hierarchically branched nanopores, nanotubes, and nanowires. *Proceedings of the National Academy of Sciences*, 102(20):7074–7078, 2005.

[228] M. S. Strano, M. L. Usery, P. W. Barone, D. A. Heller, and S. K. Baik. The selective chemistry of single walled carbon nanotubes. In S.V. Rotkin and S. Subramoney, editors, *Applied Physics of Carbon Nanotubes*. Springer-Verlag, Berlin, 2005.

[229] C. A. Dyke and J. M. Tour. Covalent functionalization of single-walled carbon nanotubes for materials applications. *Journal of Physical Chemistry A*, 108(51):11151–11159, 2004.

[230] W. Wenseleers, I. I. Vlasov, E. Goovaerts, E. D. Obraztsova, A. S. Lobach, and A. Bouwen. Efficient isolation and solubilization of pristine single-walled nanotubes in bile salt micelles. *Advanced Functional Materials*, 14(11):1105–1112, 2004.

[231] B. Messer, J. H. Song, and P. D. Yang. Microchannel networks for nanowire patterning. *Journal of the American Chemical Society*, 122(41):10232–10233, 2000.

[232] Y. Huang, X. F. Duan, Q. Q. Wei, and C. M. Lieber. Directed assembly of one-dimensional nanostructures into functional networks. *Science*, 291(5504):630–633, 2001.

[233] C. A. P. Petit and J. D. Carbeck. Combing of molecules in microchannels (COMMIC): A method for micropatterning and orienting stretched molecules of DNA on a surface. *Nano Letters*, 3(8):1141–1146, 2003.

[234] H. J. Xin and A. T. Woolley. Directional orientation of carbon nanotubes on surfaces using a gas flow cell. *Nano Letters*, 4(8):1481–1484, 2004.

[235] N. Chakrapani, B. Q. Wei, A. Carrillo, P. M. Ajayan, and R. S. Kane. Capillarity-driven assembly of two-dimensional cellular carbon nanotube foams. *Proceedings of the National Academy of Sciences*, 101(12):4009–4012, 2004.

[236] V. V. Tsukruk, H. Ko, and S. Peleshanko. Nanotube surface arrays: Weaving, bending, and assembling on patterned silicon. *Physical Review Letters*, 92(6):065502, 2004.

[237] J. Hedberg. Air flow technique for large scale dispersion and alignment of carbon nanotubes on various substrates. *Applied Physics Letters*, 86, 2005.

[238] M. D. Lynch and D. L. Patrick. Organizing carbon nanotubes with liquid crystals. *Nano Letters*, 2(11):1197–1201, 2002.

[239] I. Dierking, G. Scalia, P. Morales, and D. LeClere. Aligning and reorienting carbon nanotubes with nematic liquid crystals. *Advanced Materials*, 16(11):865–869, 2004.

[240] M. A. Meitl, Y. X. Zhou, A. Gaur, S. Jeon, M. L. Usrey, M. S. Strano, and J. A. Rogers. Solution casting and transfer printing single-walled carbon nanotube films. *Nano Letters*, 4(9):1643–1647, 2004.

[241] R. Krupke, F. Hennrich, H. von Lohneysen, and M. M. Kappes. Separation of metallic from semiconducting single-walled carbon nanotubes. *Science*, 301(5631):344–347, 2003.

[242] M. Zheng, A. Jagota, M. S. Strano, A. P. Santos, P. Barone, S. G. Chou, B. A. Diner, M. S. Dresselhaus, R. S. Mclean, G. B. Onoa, G. G. Samsonidze, E. D. Semke, M. Usrey, and D. J. Walls. Structure-based carbon nanotube sorting by sequence-dependent DNA assembly. *Science*, 302(5650):1545–1548, 2003.

[243] M. Zheng, A. Jagota, E. D. Semke, B. A. Diner, R. S. Mclean, S. R. Lustig, R. E. Richardson, and N. G. Tassi. DNA-assisted dispersion and separation of carbon nanotubes. *Nature Materials*, 2(5):338–342, 2003.

[244] M. Endo, H. Muramatsu, T. Hayashi, Y. A. Kim, G. Van Lier, J. C. Charlier, H. Terrones, M. Terrones, and M. S. Dresselhaus. Atomic nanotube welders: Boron interstitials triggering connections in double-walled carbon nanotubes. *Nano Letters*, 5(6):1099–1105, 2005.

[245] A. Kis, G. Csanyi, J. P. Salvetat, T. N. Lee, E. Couteau, A. J. Kulik, W. Benoit, J. Brugger, and L. Forro. Reinforcement of single-walled carbon nanotube bundles by intertube bridging. *Nature Materials*, 3(3):153–157, 2004.

[246] H.Z. Geng, X.B. Zhang, S.H. Mao, A. Kleinhammes, H. Shimoda, Y. Wu, and O. Zhou. Opening and closing of single-wall carbon nanotubes. *Chemical Physics Letters*, 399(1-3):109–113, 2004.

[247] J. Q. Wei, L. J. Ci, B. Jiang, Y. H. Li, X. F. Zhang, H. W. Zhu, C. L. Xu, and D. H. Wu. Preparation of highly pure double-walled carbon nanotubes. *Journal of Materials Chemistry*, 13(6):1340–1344, 2003.

[248] H. Igarashi, H. Murakami, Y. Murakami, S. Maruyama, and N. Nakashima. Purification and characterization of zeolite-supported single-walled carbon nanotubes catalytically synthesized from ethanol. *Chemical Physics Letters*, 392(4-6):529–532, 2004.

[249] D. Chattopadhyay, I. Galeska, and F. Papadimitrakopoulos. Complete elimination of metal catalysts from single wall carbon nanotubes. *Carbon*, 40(7):985–988, 2002.

[250] B. W. Clare and D. L. Kepert. Opening of carbon nanotubes by addition of oxygen. *Inorganica Chimica Acta*, 343:1–17, 2003.

[251] L. Thien-Nga, K. Hernadi, E. Ljubovic, S. Garaj, and L. Forro. Mechanical purification of single-walled carbon nanotube bundles from catalytic particles. *Nano Letters*, 2(12):1349–1352, 2002.

[252] A. R. Harutyunyan, B. K. Pradhan, J. P. Chang, G. G. Chen, and P. C. Eklund. Purification of single-wall carbon nanotubes by selective microwave heating of catalyst particles. *Journal of Physical Chemistry B*, 106(34):8671–8675, 2002.

[253] M. Terrones. Science and technology of the twenty-first century: Synthesis, properties and applications of carbon nanotubes. *Annual Review of Materials Research*, 33:419–501, 2003.

[254] E. S. Snow, J. P. Novak, P. M. Campbell, and D. Park. Random networks of carbon nanotubes as an electronic material. *Applied Physics Letters*, 82(13):2145–2147, 2003.

[255] A. Star, T. R. Han, V. Joshi, J. C. P. Gabriel, and G. Gruner. Nanoelectronic carbon dioxide sensors. *Advanced Materials*, 16(22):2049–2052, 2004.

[256] S. Ghosh, A. K. Sood, and N. Kumar. Carbon nanotube flow sensors. *Science*, 299(5609):1042–1044, 2003.

[257] Y. Tzeng, Y. Chen, and C. Liu. Electrical contacts between carbon-nanotube coated electrodes. *Diamond and Related Materials*, 12(3-7):774–779, 2003.

[258] S. C. Qu, C. K. M. Fung, R. H. M. Chan, and W. J. Li. Development of an automated microinjection system for fabrication of carbon nanotube sensors. In *Fifth World Congress on Intelligent Control and Automation*, pages 5613–5618, Hangzhou, China, 2004.

[259] R. L. Vander Wal, T. M. Ticich, and V. E. Curtis. Substrate-support interactions in metal-catalyzed carbon nanofiber growth. *Carbon*, 39(15):2277–2289, 2001.

[260] C. N. Satterfield. *Heterogeneous Catalysis in Industrial Practice.* McGraw-Hill, New York, 2nd edition, 1991.

[261] J. Kong, H. T. Soh, A. M. Cassell, C. F. Quate, and H. J. Dai. Synthesis of individual single-walled carbon nanotubes on patterned silicon wafers. *Nature*, 395(6705):878–881, 1998.

[262] C. J. Lee, D. W. Kim, T. J. Lee, Y. C. Choi, Y. S. Park, W. S. Kim, Y. H. Lee, W. B. Choi, N. S. Lee, J. M. Kim, Y. G. Choi, and S. C. Yu. Synthesis of uniformly distributed carbon nanotubes on a large area of Si substrates by thermal chemical vapor deposition. *Applied Physics Letters*, 75(12):1721–1723, 1999.

[263] S. Maruyama, Y. Miyauchi, T. Edamura, Y. Igarashi, S. Chiashi, and Y. Murakami. Synthesis of single-walled carbon nanotubes with narrow diameter-distribution from fullerene. *Chemical Physics Letters*, 375(5-6):553–559, 2003.

[264] Y. M. Shin, S. Y. Jeong, H. J. Jeong, S. J. Eum, C. W. Yang, C. Y. Park, and Y. H. Lee. Influence of morphology of catalyst thin film on vertically aligned carbon nanotube growth. *Journal of Crystal Growth*, 271(1-2):81–89, 2004.

[265] A. Muller, S. K. Das, P. Kogerler, H. Bogge, M. Schmidtmann, A. X. Trautwein, V. Schunemann, E. Krickemeyer, and W. Preetz. A new type of supramolecular compound: Molybdenum-oxide-based composites consisting of magnetic nanocapsules with encapsulated keggin-ion electron reservoirs cross-linked to a two-dimensional network. *Angewandte Chemie - International Edition*, 39(19):3414–3417, 2000.

[266] L. An, J. M. Owens, L. E. McNeil, and J. Liu. Synthesis of nearly uniform single-walled carbon nanotubes using identical metal-containing molecular nanoclusters as catalysts. *Journal of the American Chemical Society*, 124(46):13688–13689, 2002.

[267] G. S. Choi, Y. S. Cho, K. H. Son, and D. J. Kim. Mass production of carbon nanotubes using spin-coating of nanoparticles. *Microelectronic Engineering*, 66(1-4):77–82, 2003.

[268] Y. Murakami, Y. Miyauchi, S. Chiashi, and S. Maruyama. Direct synthesis of high-quality single-walled carbon nanotubes on silicon and quartz substrates. *Chemical Physics Letters*, 377(1-2):49–54, 2003.

[269] H. Kind, J. M. Bonard, C. Emmenegger, L. O. Nilsson, K. Hernadi, E. Maillard-Schaller, L. Schlapbach, L. Forro, and K. Kern. Patterned films of nanotubes using microcontact printing of catalysts. *Advanced Materials*, 11(15):1285–1289, 1999.

[270] A. M. Cassell, N. R. Franklin, T. W. Tombler, E. M. Chan, J. Han, and H. J. Dai. Directed growth of free-standing single-walled carbon nanotubes. *Journal of the American Chemical Society*, 121(34):7975–7976, 1999.

[271] L. P. H. Jeurgens, W. G. Sloof, F. D. Tichelaar, and E. J. Mittemeijer. Growth kinetics and mechanisms of aluminum-oxide films formed by thermal oxidation of aluminum. *Journal of Applied Physics*, 92(3):1649–1656, 2002.

[272] T. de los Arcos, M. G. Garnier, P. Oelhafen, D. Mathys, J. W. Seo, C. Domingo, J. V. Garci-Ramos, and S. Sanchez-Cortes. Strong influence of buffer layer type on carbon nanotube characteristics. *Carbon*, 42(1):187–190, 2004.

[273] L. Delzeit, B. Chen, A. Cassell, R. Stevens, C. Nguyen, and M. Meyyappan. Multilayered metal catalysts for controlling the density of single-walled carbon nanotube growth. *Chemical Physics Letters*, 348(5-6):368–374, 2001.

[274] R. G. Lacerda, K. B. K. Teo, A. S. Teh, M. H. Yang, S. H. Dalal, D. A. Jefferson, J. H. Durrell, N. L. Rupesinghe, D. Roy, G. A. J. Amaratunga, W. I. Milne, F. Wyczisk, P. Legagneux, and M. Chhowalla. Thin-film metal catalyst for the production of multi-wall and single-wall carbon nanotubes. *Journal of Applied Physics*, 96(8):4456–4462, 2004.

[275] T. de los Arcos, Z. M. Wu, and P. Oelhafen. Is aluminum a suitable buffer layer for carbon nanotube growth? *Chemical Physics Letters*, 380(3-4):419–423, 2003.

[276] S. Qi and B. Yang. Methane aromatization using Mo-based catalysts prepared by microwave heating. *Catalysis Today*, 98(4):639–645, 2004.

[277] T. de los Arcos, M. G. Garnier, J. W. Seo, P. Oelhafen, V. Thommen, and D. Mathys. The influence of catalyst chemical state and morphology on carbon nanotube growth. *Journal of Physical Chemistry B*, 108(23):7728–7734, 2004.

[278] J. Kong, A. M. Cassell, and H. J. Dai. Chemical vapor deposition of methane for single-walled carbon nanotubes. *Chemical Physics Letters*, 292(4-6):567–574, 1998.

[279] H. J. Dai, J. Kong, C. W. Zhou, N. Franklin, T. Tombler, A. Cassell, S. S. Fan, and M. Chapline. Controlled chemical routes to nanotube architectures, physics, and devices. *Journal of Physical Chemistry B*, 103(51):11246–11255, 1999.

[280] N. A. Vasileva, R. A. Buyanov, and I. N. Klimik. The catalytic pyrolysis of hydrocarbons. *Kinetics and Catalysis*, 21(1):175–179, 1980.

[281] I. T. Han, B. K. Kim, H. J. Kim, M. H. Yang, Y. W. Jin, S. Jung, N. Lee, S. K. Kim, and J. M. Kim. Effect of Al and catalyst thicknesses on the growth of carbon nanotubes and application to gated field emitter arrays. *Chemical Physics Letters*, 400(1-3):139–144, 2004.

[282] A. Y. Cao, P. M. Ajayan, G. Ramanath, R. Baskaran, and K. Turner. Silicon oxide thickness-dependent growth of carbon nanotubes. *Applied Physics Letters*, 84(1):109–111, 2004.

[283] A. Jorio, M. A. Pimenta, A. G. Souza, R. Saito, G. Dresselhaus, and M. S. Dresselhaus. Characterizing carbon nanotube samples with resonance Raman scattering. *New Journal of Physics*, 5:139.1–139.17, 2003.

[284] V. Kayastha, Y. K. Yap, S. Dimovski, and Y. Gogotsi. Controlling dissociative adsorption for effective growth of carbon nanotubes. *Applied Physics Letters*, 85(15):3265–3267, 2004.

[285] I. T. Han, H. J. Kim, Y. J. Park, Y. W. Jin, J. E. Jung, J. M. Kim, B. K. Kim, N. Lee, and S. K. Kim. Synthesis of highly crystalline multiwalled carbon nanotubes by thermal chemical vapor deposition using buffer gases. *Japanese Journal of Applied Physics*, 43(6A):3631–3635, 2004.

[286] J. sF. Moulder and J. Chastain. *Handbook of X-ray Photoelectron Spectroscopy: a reference book of standard spectra for identification and interpretation of XPS data.* Perkin-Elmer Corporation, Eden Prairie, MN, 1992.

[287] T. C. Lin, G. Seshadri, and J. A. Kelber. A consistent method for quantitative XPS peak analysis of thin oxide films on clean polycrystalline iron surfaces. *Applied Surface Science*, 119(1-2):83–92, 1997.

[288] H. Knösinger and P. Ratnasamy. Catalytic aluminas. *Catalysis Reviews*, 17:31–69, 1978.

[289] H. Ago, K. Nakamura, N. Uehara, and M. Tsuji. Roles of metal-support interaction in growth of single- and double-walled carbon nanotubes studied with diameter-controlled iron particles supported on MgO. *Journal of Physical Chemistry B*, 108(49):18908–18915, 2004.

[290] E.W. Wong, M.J. Bronikowski, M.E. Hoenk, R.S. Kowalczyk, and B.D. Hunt. Submicron patterning of iron nanoparticle monolayers for carbon nanotube growth. *Chemistry of Materials*, 17(2):237–241, 2005.

[291] H. M. Christen, A. A. Puretzky, H. Cui, K. Belay, P. H. Fleming, D. B. Geohegan, and D. H. Lowndes. Rapid growth of long, vertically aligned carbon nanotubes through efficient catalyst optimization using metal film gradients. *Nano Letters*, 4(10):1939–1942, 2004.

[292] H. Jansen, M. Deboer, R. Legtenberg, and M. Elwenspoek. The black silicon method: a universal method for determining the parameter setting of a fluorine-based reactive ion etcher in deep silicon trench etching with profile control. *Journal of Micromechanics and Microengineering*, 5(2):115–120, 1995.

[293] H. Jansen, H. Gardeniers, M. deBoer, M. Elwenspoek, and J. Fluitman. A survey on the reactive ion etching of silicon in microtechnology. *Journal of Micromechanics and Microengineering*, 6(1):14–28, 1996.

[294] Y. J. Jung, B. Q. Wei, R. Vaitai, and P. M. Ajayan. Mechanism of selective growth of carbon nanotubes on SiO_2/Si patterns. *Nano Letters*, 3(4):561–564, 2003.

[295] B. O. Boskovic, A. J. Hart, A. T. H. Chuang, V. B. Golovko, and B. F. G. Johnson. Carbon nanotube synthesis on arbitrary three-dimensional surfaces. In *International Carbon Conference*, Aberdeen, Scotland, 2006.

[296] M. J. Madou. *Fundamentals of Microfabrication.* CRC Press, London, UK, 2002.

[297] S. Hofmann, M. Cantoro, B. Kleinsorge, C. Casiraghi, A. Parvez, J. Robertson, and C. Ducati. Effects of catalyst film thickness on plasma-enhanced carbon nanotube growth. *Journal of Applied Physics*, 98(3):34308–1, 2005.

[298] B. O. Boskovic, V. B. Golovko, M. Cantoro, B. Kleinsorge, A. T. H. Chuang, C. Ducati, S. Hofmann, J. Robertson, and B. F. G. Johnson. Low temperature synthesis of carbon nanofibres on carbon fibre matrices. *Carbon*, 43:2643–2648, 2005.

[299] V. B. Golovko, H. W. Li, B. Kleinsorge, S. Hofmann, J. Geng, M. Cantoro, Z. Yang, D. A. Jefferson, B. F. G. Johnson, W. T. S. Huck, and J. Robertson. Submicron patterning of co colloid catalyst for growth of vertically aligned carbon nanotubes. *Nanotechnology*, 16(9):1636–1640, 2005.

[300] S. Herminghaus. Roughness-induced non-wetting. *Europhysics Letters*, 52(2):165–170, 2000.

[301] L. Feng, S. H. Li, Y. S. Li, H. J. Li, L. J. Zhang, J. Zhai, Y. L. Song, B. Q. Liu, L. Jiang, and D. B. Zhu. Super-hydrophobic surfaces: From natural to artificial. *Advanced Materials*, 14(24):1857–1860, 2002.

[302] A. Otten and S. Herminghaus. How plants keep dry: A physicist's point of view. *Langmuir*, 20(6):2405–2408, 2004.

[303] K. K. S. Lau, J. Bico, K. B. K. Teo, M. Chhowalla, G. A. J. Amaratunga, W. I. Milne, G. H. McKinley, and K. K. Gleason. Superhydrophobic carbon nanotube forests. *Nano Letters*, 3(12):1701–1705, 2003.

[304] H. B. Peng, T. G. Ristroph, G. M. Schurmann, G. M. King, J. Yoon, V. Narayanamurti, and J. A. Golovchenko. Patterned growth of single-walled carbon nanotube arrays from a vapor-deposited Fe catalyst. *Applied Physics Letters*, 83(20):4238–4240, 2003.

[305] C.V. Raman. The molecular scattering of light, Nobel Lecture, December 11, 1930.

[306] A. M. Rao, E. Richter, S. Bandow, B. Chase, P. C. Eklund, K. A. Williams, S. Fang, K. R. Subbaswamy, M. Menon, A. Thess, R. E. Smalley, G. Dresselhaus, and M. S. Dresselhaus. Diameter-selective Raman scattering from vibrational modes in carbon nanotubes. *Science*, 275(5297):187–191, 1997.

[307] S. K. Doorn. Raman spectroscopy and imaging of ultralong carbon nanotubes. *Journal of Physical Chemistry B*, 109:3751–3758, 2005.

[308] A. C. Dillon, P. A. Parilla, J. L. Alleman, T. Gennett, K. M. Jones, and M. J. Heben. Systematic inclusion of defects in pure carbon single-wall nanotubes and their effect on the Raman D-band. *Chemical Physics Letters*, 401(4-6):522–528, 2005.

[309] S. Osswald, E. Flahaut, H. Ye, and Y. Gogotsi. Elimination of D-band in Raman spectra of double-wall carbon nanotubes by oxidation. *Chemical Physics Letters*, 402(4-6):422–427, 2005.

[310] Y. A. Kim, T. Hayashi, K. Osawa, M. S. Dresselhaus, and M. Endo. Annealing effect on disordered multi-wall carbon nanotubes. *Chemical Physics Letters*, 380(3-4):319–324, 2003.

[311] P. Buffat and J. P. Borel. Size effect on the melting temperature of gold particles. *Physical Review A*, 13(6):2287 LP – 2298, 1976.

[312] Y. Q. Hou, D. M. Zhuang, G. Zhang, M. S. Wu, and J. J. Liu. Preparation of diamond films by hot filament chemical vapor deposition and nucleation by carbon nanotubes. *Applied Surface Science*, 185(3-4):303–308, 2002.

[313] L. T. Sun, J. L. Gong, Z. Y. Zhu, D. Z. Zhu, S. X. He, Z. X. Wang, Y. Chen, and G. Hu. Nanocrystalline diamond from carbon nanotubes. *Applied Physics Letters*, 84(15):2901–2903, 2004.

[314] B. Wei, J. Zhang, J. Liang, and D. Wu. The mechanism of phase transformation from carbon nanotube to diamond. *Carbon*, 36(7-8):997–1001, 1998.

[315] L. T. Sun, J. L. Gong, D. Z. Zhu, Z. Y. Zhu, and S. X. He. Diamond nanorods from carbon nanotubes. *Advanced Materials*, 16(20):1849–1853, 2004.

[316] Z. W. Pan, S. S. Xie, B. H. Chang, C. Y. Wang, L. Lu, W. Liu, M. Y. Zhou, and W. Z. Li. Very long carbon nanotubes. *Nature*, 394(6694):631–632, 1998.

[317] H. Cui, G. Eres, J. Y. Howe, A. Puretkzy, M. Varela, D. B. Geohegan, and D. H. Lowndes. Growth behavior of carbon nanotubes on multilayered metal catalyst film in chemical vapor deposition. *Chemical Physics Letters*, 374(3-4):222–228, 2003.

[318] L. Delzeit, C. V. Nguyen, B. Chen, R. Stevens, A. Cassell, J. Han, and M. Meyyappan. Multiwalled carbon nanotubes by chemical vapor deposition using multilayered metal catalysts. *Journal of Physical Chemistry B*, 106(22):5629–5635, 2002.

[319] C. N. R. Rao, R. Sen, B. C. Satishkumar, and A. Govindaraj. Large aligned-nanotube bundles from ferrocene pyrolysis. *Chemical Communications*, (15):1525–1526, 1998.

[320] Z. J. Zhang, B. Q. Wei, G. Ramanath, and P. M. Ajayan. Substrate-site selective growth of aligned carbon nanotubes. *Applied Physics Letters*, 77(23):3764–3766, 2000.

[321] C. Singh, M. S. P. Shaffer, K. K. K. Koziol, I. A. Kinloch, and A. H. Windle. Towards the production of large-scale aligned carbon nanotubes. *Chemical Physics Letters*, 372(5-6):860–865, 2003.

[322] C. J. Lee, S. C. Lyu, H. W. Kim, C. Y. Park, and C. W. Yang. Large-scale production of aligned carbon nanotubes by the vapor phase growth method. *Chemical Physics Letters*, 359(1-2):109–114, 2002.

[323] C.P. Deck and K.S. Vecchio. Growth of well-aligned carbon nanotube structures in successive layers. *Journal of Physical Chemistry B*, 109:12353–12357, 2005.

[324] G. Eres, A. A. Puretzky, D. B. Geohegan, and H. Cui. In situ control of the catalyst efficiency in chemical vapor deposition of vertically aligned carbon nanotubes on predeposited metal catalyst films. *Applied Physics Letters*, 84(10):1759–1761, 2004.

[325] G. Zhong, T. Iwasaki, K. Honda, I. Ohdomari, and H. Kawarada. Very high yield growth of vertically aligned single-walled carbon nanotubes by point-arc microwave plasma CVD. *Chemical Vapor Deposition*, 11(3):127–130, 2005.

[326] M. Hiramatsu, H. Nagao, M. Taniguchi, H. Amano, Y. Ando, and M. Hori. High-rate growth of films of dense, aligned double-walled carbon nanotubes using microwave plasma-enhanced chemical vapor deposition. *Japanese Journal of Applied Physics*, 44(20-23):L693–L695, 2005.

[327] W. K. Chu, J. W. Mayer, and M. A. Nicolet. *Backscattering Spectrometry*. Academic Press, New York, 1978.

[328] V. K. Kayastha, Y. K. Yap, Z. Pan, I. N. Ivanov, A. A. Puretzky, and D. B. Geohegan. High-density vertically aligned multiwalled carbon nanotubes with tubular structures. *Applied Physics Letters*, 86(25):253105, 2005.

[329] C. J. Lee and J. Park. Growth model for bamboolike structured carbon nanotubes synthesized using thermal chemical vapor deposition. *Journal of Physical Chemistry B*, 105(12):2365–2368, 2001.

[330] Y. T. Lee, J. Park, Y. S. Choi, H. Ryu, and H. J. Lee. Temperature-dependent growth of vertically aligned carbon nanotubes in the range 800-1100 °C. *Journal of Physical Chemistry B*, 106(31):7614–7618, 2002.

[331] T. Shimada, T. Sugai, C. Fantini, M. Souza, L. G. Cancado, A. Jorio, M. A. Pimenta, R. Salto, A. Gruneis, G. Dresselhaus, M. S. Dresselhaus, Y. Ohno, T. Mizutani, and H. Shinohara. Origin of the 2450 cm^{-1} Raman bands in HOPG, single-wall and double-wall carbon nanotubes. *Carbon*, 43(5):1049–1054, 2005.

[332] S. Bandow, S. Asaka, Y. Saito, A. M. Rao, L. Grigorian, E. Richter, and P. C. Eklund. Effect of the growth temperature on the diameter distribution and chirality of single-wall carbon nanotubes. *Physical Review Letters*, 80(17):3779–3782, 1998.

[333] K. E. Kim, K. J. Kim, W. S. Jung, S. Y. Bae, J. Park, J. Choi, and J. Choo. Investigation on the temperature-dependent growth rate of carbon nanotubes using chemical vapor deposition of ferrocene and acetylene. *Chemical Physics Letters*, 401(4-6):459–464, 2005.

[334] C. Hedlund, H. O. Blom, and S. Berg. Microloading effect in reactive ion etching. *Journal of Vacuum Science & Technology A*, 12(4):1962–1965, 1994.

[335] J. Karttunen, J. Kiihamaki, and S. Franssila. Loading effects in deep silicon etching. In *Micromachining and Microfabrication Process Technology VI*, volume 4174 of *Proceedings of SPIE*, pages 90–97, 2000.

[336] S. Agrawal, A. Kumar, M. J. Frederick, and G. Ramanath. Hybrid microstructures from aligned carbon nanotubes and silica particles. *Small*, 1(8-9):823–826, 2005.

[337] T. A. El-Aguizy, J. H. Jeong, Y. B. Jeon, W. Z. Li, Z. F. Ren, and S. G. Kim. Transplanting carbon nanotubes. *Applied Physics Letters*, 85(24):5995–5997, 2004.

[338] T. Jeong, J. Heo, J. Lee, S. Lee, W. Kim, H. Lee, S. Park, J. M. Kim, T. Oh, C. Park, J. B. Yoo, B. Gong, N. Lee, and S. Yu. Improvement of field emission characteristics of carbon nanotubes through metal layer intermediation. *Applied Physics Letters*, 87(6):063112, 2005.

[339] T. J. Imholt, C. A. Dyke, B. Hasslacher, J. M. Perez, D. W. Price, J. A. Roberts, J. B. Scott, A. Wadhawan, Z. Ye, and J. M. Tour. Nanotubes in microwave fields: Light emission, intense heat, outgassing, and reconstruction. *Chemistry of Materials*, 15(21):3969–3970, 2003.

[340] A. V. Krasheninnikov and K. Nordlund. Irradiation effects in carbon nanotubes. *Nuclear Instruments and Methods in Physics Research B*, 216:355–366, 2004.

[341] A. Cao, V. P. Veedu, X. Li, Z. Yao, M. N. Ghasemi-Nejhad, and P. M. Ajayan. Multifunctional brushes made from carbon nanotubes. *Nature Materials*, 4:540–545, 2005.

[342] J. Rostrup-Nielsen and D. L. Trimm. Mechanisms of carbon formation on nickel-containing catalysts. *Journal of Catalysis*, 48(1-3):155–165, 1977.

[343] L. Zhu, Y. Xiu, D.W. Hess, and C. P. Wong. Aligned carbon nanotube stacks by water-assisted selective etching. *Nano Letters*, 5(12):2641–2645, 2005.

[344] B. Yurdumakan, N. R. Raravikar, P. M. Ajayan, and A. Dhinojwala. Synthetic gecko foothairs from multiwalled carbon nanotubes. *Chemical Communications*, (30):3799–3801, 2005.

[345] M. He, X. Wang, J. Zhang, Z. Liu, and C. Robinson. Iron catalysts reactivation for efficient CVD growth of SWNT with base-growth mode on surface. *Journal of Physical Chemistry B*, 108(34):12665–12668, 2004.

[346] R. D. Bennett, A. J. Hart, and R. E. Cohen. Strategies for controlling the planar arrangement of micellar templated inorganic nanoclusters and their applications in carbon nanotube synthesis. In *Materials Research Society Fall Meeting*, Boston, MA, 2005.

[347] S. Arepalli, P. Nikolaev, O. Gorelik, V. G. Hadjiev, W. Holmes, B. Files, and L. Yowell. Protocol for the characterization of single-wall carbon nanotube material quality. *Carbon*, 42(8-9):1783–1791, 2004.

[348] G. S. B. McKee and K.S. Vecchio. Thermogravimetric analysis of synthesis variation effects on CVD generated multiwalled carbon nanotubes. *Journal of Physical Chemistry B*, 110:1179–1186, 2006.

[349] A. C. Dillon, T. Gennett, K. M. Jones, J. L. Alleman, P. A. Parilla, and M. J. Heben. A simple and complete purification of single-walled carbon nanotube materials. *Advanced Materials*, 11(16):1354–1358, 1999.

[350] J. F. AuBuchon, L. H. Chen, and S. H. Jin. Control of carbon capping for regrowth of aligned carbon nanotubes. *Journal of Physical Chemistry B*, 109:6044–6048, 2005.

[351] O. Yaglioglu, A. J. Hart, and A. H. Slocum. Electromechanical characterization of carbon nanotube contact surfaces. In *6th International Conference of the European Society of Precision Engineering and Nanotechnology*, pages 406–409, Baden, Austria, 2006.

[352] J. F. Despres, E. Daguerre, and K. Lafdi. Flexibility of graphene layers in carbon nanotubes. *Carbon*, 33(1):87–89, 1995.

[353] S. Iijima, C. Brabec, A. Maiti, and J. Bernholc. Structural flexibility of carbon nanotubes. *Journal of Chemical Physics*, 104(5):2089–2092, 1996.

[354] L. B. Freund and S. Suresh. *Thin Film Materials: stress, defect formation, and surface evolution.* Cambridge University Press, Cambridge, UK, 2003.

[355] S. S. Fan, L. Liu, and M. Liu. Monitoring the growth of carbon nanotubes by carbon isotope labelling. *Nanotechnology*, 14(10):1118–1123, 2003.

[356] A. G. Nasibulin, P. V. Pikhitsa, H. Jiang, and E. I. Kauppinen. Correlation between catalyst particle and single-walled carbon nanotube diameters. *Carbon*, 43(11):2251–2257, 2005.

[357] *Handbook of Chemistry and Physics.* CRC Press, London, UK, 87th. edition, 2003-2004.

[358] A. J. Hart and A. H. Slocum. Versatility of the Fe/Al_2O_3 system for high-yield carbon nanotube growth by thermal CVD of C_2H_4. In *Sixth International Conference on the Science and Application of Nanotubes*, page 28, Gotëborg, Sweden, 2005.

[359] C. Bower, W. Zhu, S. H. Jin, and O. Zhou. Plasma-induced alignment of carbon nanotubes. *Applied Physics Letters*, 77(6):830–832, 2000.

[360] J. F. AuBuchon, L. H. Chen, A. I. Gapin, D. W. Kim, C. Daraio, and S. H. Jin. Multiple sharp bendings of carbon nanotubes during growth to produce zigzag morphology. *Nano Letters*, 4(9):1781–1784, 2004.

[361] H. Ko, S. Peleshanko, and V. V. Tsukruk. Combing and bending of carbon nanotube arrays with confined microfluidic flow on patterned surfaces. *Journal of Physical Chemistry B*, 108(14):4385–4393, 2004.

[362] E. Kim, Y. Xia, and G. M. Whitesides. Polymer microstructures formed by moulding in capillaries. 376(6541):581–584, 1995.

[363] X. M. Zhao, Y. N. Xia, and G. M. Whitesides. Fabrication of three-dimensional microstructures: Microtransfer molding. *Advanced Materials*, 8(10):837–840, 1996.

[364] V. Piotter, W. Bauer, T. Benzler, and A. Emde. Injection molding of components for microsystems. *Microsystem Technologies*, 7(3):99–102, 2001.

[365] B. Q. Wei, Z. J. Zhang, G. Ramanath, and P. M. Ajayan. Lift-up growth of aligned carbon nanotube patterns. *Applied Physics Letters*, 77(19):2985–2987, 2000.

[366] Z. X. Chen, J. Merikhi, I. Koehler, and P. K. Bachmann. Sandwich growth of carbon nanotubes. *Diamond and Related Materials*, 15(1):104–108, 2006.

[367] X. S. Li, A. Y. Cao, Y. J. Jung, R. Vajtai, and P. M. Ajayan. Bottom-up growth of carbon nanotube multilayers: Unprecedented growth. *Nano Letters*, 5(10):1997–2000, 2005.

[368] M. Pinault, V. Pichot, H. Khodja, P. Launois, C. Reynaud, and M. Mayne-L'Hermite. Evidence of sequential lift in growth of aligned multiwalled carbon nanotube multilayers. *Nano Letters*, 5(12):2394–2398, 2005.

[369] G. L. Che, B. B. Lakshmi, E. R. Fisher, and C. R. Martin. Carbon nanotubule membranes for electrochemical energy storage and production. *Nature*, 393(6683):346–349, 1998.

[370] A. Srivastava, O. N. Srivastava, S. Talapatra, R. Vajtai, and P. M. Ajayan. Carbon nanotube filters. *Nature Materials*, 3(9):610–614, 2004.

[371] S. Amelinckx, X. B. Zhang, D. Bernaerts, X. F. Zhang, V. Ivanov, and J. B. Nagy. A formation mechanism for catalytically grown helix-shaped graphite nanotubes. *Science*, 265(5172):635–639, 1994.

[372] J. Abrahamson. The surface energies of graphite. *Carbon*, 11(4):337–362, 1973.

[373] S. M. Carr, W. E. Lawrence, and M. N. Wybourne. Buckling cascade of free-standing mesoscopic beams. *Europhysics Letters*, 69(6):952–958, 2005.

[374] B. Roman and A. Pocheau. Buckling cascade of thin plates: Forms, constraints, and stability. *Europhysics Letters*, 45(5):602–608, 1999.

[375] A. Cao, P. L. Dickrell, W. G. Sawyer, M. N. Ghasemi-Nejhad, and P. M. Ajayan. Supercompressible foamlike carbon nanotube films. *Science*, 310(5752):1307–1310, 2005.

[376] S. Akita, H. Nishijima, T. Kishida, and Y. Nakayama. Influence of force acting on side face of carbon nanotube in atomic force microscopy. *Japanese Journal of Applied Physics*, 39(6B):3724–3727, 2000.

[377] R. C. Hibbeler. *Statics and Mechanics of Materials.* Prentice-Hall, 1993.

[378] J. E. Huber, N. A. Fleck, and M. F. Ashby. The selection of mechanical actuators based on performance indices. *Proceedings of the Royal Society of London*, 453(1965):2185–2205, 1997.

[379] M. Zupan, M. F. Ashby, and N. A. Fleck. Actuator classification and selection - the development of a database. *Advanced Engineering Materials*, 4(12):933–940, 2002.

[380] W.J. Arora, A.J. Nichol, H.I. Smith, and G. Barbastathis. Membrane folding to achieve three-dimensional nanostructures: Nanopatterned silicon nitride folded with stressed chromium hinges. *Applied Physics Letters*, 88:053108, 2006.

[381] H. Rajoria and N. Jalili. Passive vibration damping enhancement using carbon nanotube-epoxy reinforced composites. *Composites Science and Technology*, 65(14):2079–2093, 2005.

[382] H. J. Li, X. B. Wang, Y. L. Song, Y. Q. Liu, Q. S. Li, L. Jiang, and D. B. Zhu. Super-"amphiphobic" aligned carbon nanotube films. *Angewandte Chemie-International Edition*, 40(9):1743–1746, 2001.

[383] Y Murakami and S. Maruyama. Detachment of vertically aligned single-walled carbon nanotube films from substrates and their re-attachment to arbitrary surfaces. *Chemical Physics Letters*, 422(4-6):575–580, 2006.

[384] O. Breuer and U. Sundararaj. Big returns from small fibers: A review of polymer/carbon nanotube composites. *Polymer Composites*, 25(6):630–645, 2004.

[385] E. T. Thostenson, Z. F. Ren, and T. W. Chou. Advances in the science and technology of carbon nanotubes and their composites: A review. *Composites Science and Technology*, 61(13):1899–1912, 2001.

[386] N. A. Koratkar, B. Q. Wei, and P. M. Ajayan. Multifunctional structural reinforcement featuring carbon nanotube films. *Composites Science and Technology*, 63(11):1525–1531, 2003.

[387] M. Cadek, J. N. Coleman, K. P. Ryan, V. Nicolosi, G. Bister, A. Fonseca, J. B. Nagy, K. Szostak, F. Beguin, and W. J. Blau. Reinforcement of polymers with carbon nanotubes: The role of nanotube surface area. *Nano Letters*, 4(2):353–356, 2004.

[388] E. J. Garcia, A. J. Hart, B. L. Wardle, and A. H. Slocum. Fabrication and testing of long carbon nanotubes grown on the surface of fibers for hybrid composites. In *47th AIAA/ASME/ASCE/AHS/ASC Structures, Structural Dynamics, and Materials Conference*, Newport, RI, 2006.

[389] E. J. Garcia, A. J. Hart, B. L. Wardle, and A. H. Slocum. Fabrication of CNT/polymer nanocomposites and characterization of their mechanical properties using nanoindentation/compression tests, . In *ASME IMECE Conference (accepted)*, Chicago, IL, 2006.

[390] E.J. Garcia. *Characterization of Composites with Aligned Carbon Nanotubes (CNTs) as Reinforcement.* M.S. Thesis, Massachusetts Institute of Technology, 2006.

[391] L. J. Ci, Z. G. Zhao, and J. B. Bai. Direct growth of carbon nanotubes on the surface of ceramic fibers. *Carbon*, 43(4):883–886, 2005.

[392] E. T. Thostenson, W. Z. Li, D. Z. Wang, Z. F. Ren, and T. W. Chou. Carbon nanotube/carbon fiber hybrid multiscale composites. *Journal of Applied Physics*, 91(9):6034–6037, 2002.

[393] R. A. Shatwell. Method and apparatus for the production of carbon nanostructures, *U.S. Patent Application 2005/0152826*, 2005.

[394] K. Kwok and W. K. S. Chiu. Continuous deposition of carbon nanotubes on a moving substrate by open-air laser-induced chemical vapor deposition. *Carbon*, 43(12):2571–2578, 2005.

[395] J. Sun, L. Gao, and X. Jin. Reinforcement of alumina matrix with multi-walled carbon nanotubes. *Ceramics International*, 31(6):893–896, 2005.

[396] G. D. Zhan and A. K. Mukherjee. Carbon nanotube reinforced alumina-based ceramics with novel mechanical, electrical, and thermal properties. *International Journal of Applied Ceramic Technology*, 1(2):161–171, 2004.

[397] G. D. Zhan, J. D. Kuntz, J. L. Wan, and A. K. Mukherjee. Single-wall carbon nanotubes as attractive toughening agents in alumina-based nanocomposites. *Nature Materials*, 2(1):38–42, 2003.

[398] V. P. Veedu, A. Y. Cao, X. S. Li, K. G. Ma, C. Soldano, S. Kar, P. M. Ajayan, and M. N. Ghasemi-Nejhad. Multifunctional composites using reinforced laminae with carbon-nanotube forests. *Nature Materials*, 5(6):457–462, 2006.

[399] B. L. Wardle, A. J. Hart, E. J. Garcia, and A. H. Slocum. Production of reinforced composite materials and aligned carbon nanotubes, *U.S. Provisional Patent Application*, filed May 19, 2006.

[400] M. Audier, A. Oberlin, and M. Coulon. Study of biconic microcrystals in the middle of carbon tubes obtained by catalytic disproportionation of CO. *Journal of Crystal Growth*, 57(3):524–534, 1982.

[401] R. L. Vander Wal and L. J. Hall. Nanotube coated metals: New reinforcement materials for polymer matrix composites. *Advanced Materials*, 14(18):1304–1308, 2002.

[402] D. Park, Y. H. Kim, and J. K. Lee. Pretreatment of stainless steel substrate surface for the growth of carbon nanotubes by PECVD. *Journal of Materials Science*, 38(24):4933–4939, 2003.

[403] M. Karwa, Z. Iqbal, and S. Mitra. Scaled-up self-assembly of carbon nanotubes inside long stainless steel tubing. *Carbon*, 44(7):1235–1242, 2006.

[404] A. J. Hart and A. H. Slocum. Design and fabrication of microchannel arrays for combinatorial studies of nanomaterials growth. In *5th International Conference of the European Society of Precision Engineering and Nanotechnology*, pages 81–84. Montpellier, France, 2005.

[405] A. J. Hart and A. H. Slocum. Methods and devices for growth and/or assembly of nanostructures using small channel environments, *U.S. Provisional Patent Application*, filed May 6, 2005.

[406] G. Kolb and V. Hessel. Micro-structured reactors for gas phase reactions. *Chemical Engineering Journal*, 98(1-2):1–38, 2004.

[407] E. M. Chan, R. A. Mathies, and A. P. Alivisatos. Size-controlled growth of CdSe nanocrystals in microfluidic reactors. *Nano Letters*, 3(2):199–201, 2003.

[408] B. K. H. Yen, A. Gunther, M. A. Schmidt, K. F. Jensen, and M. G. Bawendi. A microfabricated gas-liquid segmented flow reactor for high-temperature synthesis: The case of CdSe quantum dots. *Angewandte Chemie-International Edition*, 44(34):5447–5451, 2005.

[409] S. D. Senturia. *Microsystem Design.* Kluwer Academic Publishers, Boston, MA, 2002.

[410] Y. C. Ho, C. G. Cassandras, C. H. Chen, and L. Dai. Ordinal optimisation and simulation. *Journal of the Operational Research Society*, 51(4):490–500, 2000.

[411] H. M. Christen, I. Ohkubo, C. M. Rouleau, G. E. Jellison, A. A. Puretzky, D. B. Geohegan, and D. H. Lowndes. A laser-deposition approach to compositional-spread discovery of materials on conventional sample sizes. *Measurement Science and Technology*, (1):21–31, 2005.

[412] A. Ludwig, J. Cao, J. Brugger, and I. Takeuchi. MEMS tools for combinatorial materials processing and high-throughput characterization. *Measurement Science and Technology*, 16(1):111–118, 2005.

[413] E. B. Arkilic, M. A. Schmidt, and K. S. Breuer. Gaseous slip flow in long microchannels. *Journal of Microelectromechanical Systems*, 6(2):167–178, 1997.

[414] S. A. Schaff and P. L. Chambre. *Flow of Rarefied Gases.* Princeton University Press, Princeton, NJ, 1961.

[415] G. E. Karniadakis and A. Beskok. *Micro Flows.* Springer-Verlag, New York, NY, 2002.

[416] F. M. White. *Fluid Mechanics.* McGraw-Hill, New York, 1994.

[417] L. B. Loeb. *The Kinetic Theory of Gases.* Dover Publications, 1961.

[418] E. B. Arkilic, K. S. Breuer, and M. A. Schmidt. Mass flow and tangential momentum accommodation in silicon micromachined channels. *Journal of Fluid Mechanics*, 437:29–43, 2001.

[419] H. B. Ma and G. P. Peterson. Laminar friction factor in microscale ducts of irregular cross section. *Microscale Thermophysical Engineering*, 1(3):253–265, 1997.

[420] G.L. Morini, M. Lorenzini, and M. Spiga. A criterion for experimental validation of slip-flow models for incompressible rarefied gases through microchannels. *Microfluidics and Nanofluidics*, 1(2):190–196, 2005.

[421] K. Pong. Non-linear pressure distribution in uniform microchannels. In *Applications of Microfabrication to Fluid Mechanics, ASME Winter Annual Meeting*, pages 51–56, Chicago, IL, 1994.

[422] E. Abbe. Gesammelte Abhandlungen. pages 319–338. G. Fischer Verlag, Jena, Germany, 1905.

[423] A. H. Slocum. *Precision Machine Design.* Prentice Hall, Englewood Cliffs, N.J., 1992.

[424] J. M. Lai, W. H. Chieng, and Y. C. Huang. Precision alignment of mask etching with respect to crystal orientation. *Journal of Micromechanics and Microengineering*, 8(4):327–329, 1998.

[425] A. C. Weber. *Precision Passive Alignement of Wafers.* M.S. Thesis, Massachusetts Institute of Technology, 2002.

[426] H. Sandmaier, H.L. Offereins, K. Kuhl, and W. Lang. Corner compensation techniques in anisotropic etching of (100)-silicon using aqueous KOH. In *International Conference on Solid-State Sensors and Actuators*, pages 456–459, 1991.

[427] D. L. Kendall. A new theory for the anisotropic etching of silicon and some underdeveloped chemical micromachining concepts. *Journal of Vacuum Science & Technology A*, 8(4):3598–3605, 1990.

[428] J. Frühauf, S. Krönert, and R. Krüger-Sehm. Precision of etched bulk silicon structures with dimensions up to the mm-range. In *International Topical Meeting of the European Society of Precision Engineering and Nanotechnology*, Aachen, Germany, 2003.

[429] Q. X. Zhang, L. T. Liu, and Z. J. Li. A new approach to convex corner compensation for anisotropic etching of (100) Si in KOH. *Sensors and Actuators A*, 56(3):251–254, 1996.

[430] P. Enoksson. New structure for corner compensation in anisotropic KOH etching. *Journal of Micromechanics and Microengineering*, 7(3):141–144, 1997.

[431] J. H. Jerman. Micromachining process for making perfect exterior corner in an etchable substrate, *U.S. Patent 5,338,400*, 1994.

[432] Y. Mita. A convex-corner preservation principle in bulk micromachining and its application to nano-point needles. In *12th International Conference on Solid State Sensors, Actuators, and Microsystems*, pages 1683–1686, Boston, MA, 2003.

[433] J. Frühauf, K. Trautmann, J. Wittig, and D. Zielke. A simulation tool for orientation-dependent etching. *Journal of Micromechanics and Microengineering*, 3(3):113–115, 1993.

[434] B. Hannemann and J. Fruhauf. New and extended possibilities of orientation dependent etching in microtechnics. In *11th Annual International Workshop on Microelectromechanical Systems*, pages 234–239, 1998.

[435] Huai-Yuan Chu and Weileun Fang. A novel convex corner compensation for wet anisotropic etching on (100) silicon wafer. In *17th IEEE International Conference on Micro Electro Mechanical Systems*, pages 253–256, Maastricht, The Netherlands, 2004.

[436] Huai-Yuan Chu and Weileun Fang. Bulk micromachining fabrication platform using the integration of DRIE and wet anisotropic etching. *Microsystem Technologies*, 11:141–150, 2005.

[437] A. J. Hart, L. C. van Laake, and A. H. Slocum. Precision design of tube furnace systems for growth of carbon nanotube films. In *6th International Conference of the European Society of Precision Engineering and Nanotechnology*, pages 413–416, Baden, Austria, 2006.

[438] L. C. van Laake, A. J. Hart, and A. H. Slocum. Design and modeling of a suspended silicon substrate heater and its application to novel studies of carbon nanotube growth. In *6th International Conference of the European Society of Precision Engineering and Nanotechnology*, pages 381–384, Baden, Austria, 2006.

[439] Vesvius McDanel Company. Tube end seals, `http://www.techceramics.com/products.html`, 2003.

[440] J.H. Leinhard-IV and J.H. Leinhard-V. *A Heat Transfer Textbook.* Phlogiston Press, Cambridge, MA, 2001.

[441] H. A. Hansen, J. L. Olsen, S. Jensen, O. Hansen, and U. J. Quaade. Rate enhancement in microfabricated chemical reactors under fast forced temperature oscillations. *Catalysis Communications*, 7(5):272–275, 2006.

[442] Y. L. Li, I. A. Kinloch, M. S. P. Shaffer, C. Singh, J. F. Geng, B. F. G. Johnson, and A. H. Windle. Growth of single-walled carbon nanotubes by the rapid heating of a supported catalyst. *Chemistry of Materials*, 16(26):5637–5643, 2004.

[443] J. J. Brandner, G. Emig, M. A. Liauw, and K. Schubert. Fast temperature cycling in microstructure devices. *Chemical Engineering Journal*, 101(1-3):217–224, 2004.

[444] S. L. Firebaugh, K. F. Jensen, and M. A. Schmidt. Investigation of high-temperature degradation of platinum thin films with an in situ resistance measurement apparatus. *Journal of Microelectromechanical Systems*, 7(1):128–135, 1998.

[445] L. C. van Laake, A. J. Hart, and A. H. Slocum. A suspended silicon platform heater apparatus for rapid thermal control of surface reactions, with application to carbon nanotube film growth. *Review of Scientific Instruments (submitted)*, 2006.

[446] L. C. van Laake. *A New Setup for Fast Carbon Nanotube Growth: Rapid Thermal Control and In-Situ Monitoring.* M.S. Thesis, Technical University of Eindhoven, 2006.

[447] K. F. Jensen. Microreaction engineering - is small better? *Chemical Engineering Science*, 56(2):293–303, 2001.

[448] S. Chiashi, Y. Murakami, Y. Miyauchi, and S. Maruyama. Cold wall CVD generation of single-walled carbon nanotubes and in situ Raman scattering measurements of the growth stage. *Chemical Physics Letters*, 386(1-3):89–94, 2004.

[449] P. Finnie, J. Bardwell, I. Tsandev, M. Tomlinson, M. Beaulieu, J. Fraser, and J. Lefebvre. Cold wall chemical vapor deposition of single walled carbon nanotubes. *Journal of Vacuum Science & Technology A*, 22(3):747–751, 2004.

[450] P. Finnie, A. Li-Pook-Than, J. Lefebvre, and D.G. Austing. Optimization of methane cold wall chemical vapor deposition for the production of single walled carbon nanotubes and devices. *Carbon (in press)*, 2006.

[451] M. Croci, J. M. Bonard, O. Noury, T. Stockli, and A. Chatelain. Cold atmosphere CVD: A simple method for the growth of carbon nanotubes. *Chemical Vapor Deposition*, 8(3):89–92, 2002.

[452] O. Englander, D. Christensen, and L. W. Lin. Local synthesis of silicon nanowires and carbon nanotubes on microbridges. *Applied Physics Letters*, 82(26):4797–4799, 2003.

[453] S. Dittmer, O. A. Nerushev, and E. E. B. Campbell. Low ambient temperature CVD growth of carbon nanotubes. *Applied Physics A*, 84(3):243–246, 2006.

[454] O. Smiljanic, T. Dellero, A. Serventi, G. Lebrun, B. L. Stansfield, J. P. Dodelet, M. Trudeau, and S. Desilets. Growth of carbon nanotubes on ohmically heated carbon paper. *Chemical Physics Letters*, 342(5-6):503–509, 2001.

[455] X. Sun, B. Stansfield, J. P. Dodelet, and S. Desilets. Growth of carbon nanotubes on carbon paper by ohmically heating silane-dispersed catalytic sites. *Chemical Physics Letters*, 363(5-6):415–421, 2002.

[456] X. Sun, R. Li, B. Stansfield, J.P. Dodelet, and S. Desilets. 3D carbon nanotube network based on a hierarchical structure grown on carbon paper backing. *Chemical Physics Letters*, 394(4-6):266–270, 2004.

[457] J. P. Dodelet, X. Sun, and S. Desilets. Process for preparing carbon nanotubes, U.S. Patent 6,887,451, 2005.

[458] K. B. K. Teo, D. B. Hash, R. G. Lacerdo, N. L. Rupesinghe, M. S. Bell, S. H. Dalal, D. Bose, T. R. Govindan, B. A. Cruden, M. Chhowalla, G. A. J. Amaratunga, J. M. Meyyappan, and W. I. Milne. The significance of plasma heating in carbon nanotube and nanofiber growth. *Nano Letters*, 4(5):921–926, 2004.

[459] S. Chaisitsak, A. Yamada, and M. Konagai. Hot filament enhanced cvd synthesis of carbon nanotubes by using a carbon filament. *Diamond and Related Materials*, 13(3):438–444, 2004.

[460] Y. Ishikawa and H. Jinbo. Synthesis of multiwalled carbon nanotubes at temperatures below 300°C by hot-filament assisted chemical vapor deposition. *Japanese Journal of Applied Physics*, 44(12-15):L394–L397, 2005.

[461] G. L. Pearson and J. Bardeen. Electrical properties of pure silicon and silicon alloys containing boron and phosphorus. *Physical Review*, 75:865–883, 1949.

[462] J. Tauc. *Photo and thermoelectric effects in semiconductors.* International series of monographs on semiconductors. Pergamon Press, New York, 1962.

[463] A. Jungen, M. Pfenninger, M. Tonteling, C. Stampfer, and C. Hierold. Electrothermal effects at the microscale and their consequences on system design. *Journal of Micromechanics and Microengineering*, 16(8):1633–1638, 2006.

[464] J. Qiu, J. H. Lang, A. H. Slocum, and A. C. Weber. A bulk-micromachined bistable relay with U-shaped thermal actuators. *Journal of Microelectromechanical Systems*, 14(5):1099–1109, 2005.

[465] D. B. Geohegan, A. A. Puretzky, I. N. Ivanov, S. Jesse, G. Eres, and J. Y. Howe. In situ growth rate measurements and length control during chemical vapor deposition of vertically aligned multiwall carbon nanotubes. *Applied Physics Letters*, 83(9):1851–1853, 2003.

[466] Z. Zhao, T. Diemant, T. Haring, H. Rauscher, and R. J. Behm. Small-volume, ultrahigh-vacuum-compatible high-pressure reaction cell for combined kinetic and in situ IR spectroscopic measurements on planar model catalysts. *Review of Scientific Instruments*, 76(12):123903, 2005.

[467] N. M. Rodriguez, M. S. Kim, and R. T. K. Baker. Promotional effect of carbon monoxide on the decomposition of ethylene over an iron catalyst. *Journal of Catalysis*, 144(1):93–108, 1993.

[468] B. E. Deal and A. S. Grove. General relationship for the thermal oxidation of silicon. *Journal of Applied Physics*, 36(12):3770–3778, 1965.

[469] Y. M. Li, W. Kim, Y. G. Zhang, M. Rolandi, D. W. Wang, and H. J. Dai. Growth of single-walled carbon nanotubes from discrete catalytic nanoparticles of various sizes. *Journal of Physical Chemistry B*, 105(46):11424–11431, 2001.

[470] M. Franzkowiak. *Analytical and Numerical Fluid Modeling of a Microchannel Device for Growing Aligned Carbon Nanotubes.* M.S. Thesis, Aachen University of Technology, 2003.

[471] F. Frankel. Needlework. *American Scientist*, pages 66–67, Jan–Feb 2006.

[472] A. J. Hart and A. H. Slocum. Combinatorial flow studies of carbon nanotube growth using microchannel arrays. In *Materials Research Society Fall Meeting*, Boston, MA, 2005.

[473] R. D. Bennett, A. J. Hart, and R. E. Cohen. Controlling the morphology of carbon nanotube films by varying the areal density of catalyst nanoparticles using block copolymer micellar thin films. *Advanced Materials*, 18:2274–2279, 2006.

[474] R. D. Bennett, A. J. Hart, A. C. Miller, R. E. Cohen, P. T. Hammond, and D. J. Irvine. Patterning of block copolymer micellar thin films using microcontact printing and applications in carbon nanotube synthesis. *Langmuir (in press)*, 2006.